U.S.NRC
United States Nuclear Regulatory Commission
Protecting People and the Environment

NUREG/CR-7286
ORNL/TM-2020/1584

Reactor Pressure Vessel Fluence Evaluation Methodology for Extended Beltline Locations

Office of Nuclear Regulatory Research

AVAILABILITY OF REFERENCE MATERIALS IN NRC PUBLICATIONS

NRC Reference Material

As of November 1999, you may electronically access NUREG-series publications and other NRC records at the NRC's Library at www.nrc.gov/reading-rm.html. Publicly released records include, to name a few, NUREG-series publications; *Federal Register* notices; applicant, licensee, and vendor documents and correspondence; NRC correspondence and internal memoranda; bulletins and information notices; inspection and investigative reports; licensee event reports; and Commission papers and their attachments.

NRC publications in the NUREG series, NRC regulations, and Title 10, "Energy," in the *Code of Federal Regulations* may also be purchased from one of these two sources:

1. **The Superintendent of Documents**
   U.S. Government Publishing Office
   Washington, DC 20402-0001
   Internet: www.bookstore.gpo.gov
   Telephone: (202) 512-1800
   Fax: (202) 512-2104

2. **The National Technical Information Service**
   5301 Shawnee Road
   Alexandria, VA 22312-0002
   Internet: www.ntis.gov
   1-800-553-6847 or, locally, (703) 605-6000

A single copy of each NRC draft report for comment is available free, to the extent of supply, upon written request as follows:

Address: **U.S. Nuclear Regulatory Commission**
Office of Administration
Digital Communications and Administrative Services Branch
Washington, DC 20555-0001
E-mail: distribution.resource@nrc.gov
Facsimile: (301) 415-2289

Some publications in the NUREG series that are posted at the NRC's Web site address www.nrc.gov/reading-rm/doc-collections/nuregs are updated periodically and may differ from the last printed version. Although references to material found on a Web site bear the date the material was accessed, the material available on the date cited may subsequently be removed from the site.

Non-NRC Reference Material

Documents available from public and special technical libraries include all open literature items, such as books, journal articles, transactions, *Federal Register* notices, Federal and State legislation, and congressional reports. Such documents as theses, dissertations, foreign reports and translations, and non-NRC conference proceedings may be purchased from their sponsoring organization.

Copies of industry codes and standards used in a substantive manner in the NRC regulatory process are maintained at—

The NRC Technical Library
Two White Flint North
11545 Rockville Pike
Rockville, MD 20852-2738

These standards are available in the library for reference use by the public. Codes and standards are usually copyrighted and may be purchased from the originating organization or, if they are American National Standards, from—

American National Standards Institute
11 West 42nd Street
New York, NY 10036-8002
Internet: www.ansi.org
(212) 642-4900

Legally binding regulatory requirements are stated only in laws; NRC regulations; licenses, including technical specifications; or orders, not in NUREG-series publications. The views expressed in contractor prepared publications in this series are not necessarily those of the NRC.

The NUREG series comprises (1) technical and administrative reports and books prepared by the staff (NUREG–XXXX) or agency contractors (NUREG/CR–XXXX), (2) proceedings of conferences (NUREG/CP–XXXX), (3) reports resulting from international agreements (NUREG/IA–XXXX),(4) brochures (NUREG/BR–XXXX), and (5) compilations of legal decisions and orders of the Commission and the Atomic and Safety Licensing Boards and of Directors' decisions under Section 2.206 of the NRC's regulations (NUREG–0750).

U.S.NRC
United States Nuclear Regulatory Commission
Protecting People and the Environment

NUREG/CR-7286
ORNL/TM-2020/1584

Reactor Pressure Vessel Fluence Evaluation Methodology for Extended Beltline Locations

Manuscript Completed: June 2021
Date Published: May 2022

Prepared by:
J. Risner
A. Alpan
J. Yang (formerly with ORNL)

Oak Ridge National Laboratory
Oak Ridge, TN 37831-6283

J. Wallace, NRC Project Manager

Office of Nuclear Regulatory Research

DISCLAIMER

This report was prepared as an account of work sponsored by an agency of the U.S. Government. Neither the U.S. Government nor any agency thereof, nor any employee, makes any warranty, expressed or implied, or assumes any legal liability or responsibility for any third party's use, or the results of such use, of any information, apparatus, product, or process disclosed in this publication, or represents that its use by such third party complies with applicable law.

This report does not contain or imply legally binding requirements. Nor does this report establish or modify any regulatory guidance or positions of the U.S. Nuclear Regulatory Commission and is not binding on the Commission.

ABSTRACT

It has become increasingly challenging to accurately predict neutron fluence and displacements per atom (dpa) in reactor pressure vessels (RPVs) as plant life extensions and power uprates expand the area of concern, causing neutron damage to locations in the so-called extended beltline region. At this writing, the only available guidance on RPV fluence calculations is from analyses that only address the traditional beltline region. This study evaluated the impact of multiple physical parameters on fast fluence (E > 1 MeV) estimates to ascertain the degree to which extended beltline fluence evaluations are more sensitive to those parameters compared with traditional beltline evaluations. In addition, key calculational parameters in the widely used discrete ordinates method were evaluated to determine their impact on extended beltline fluence estimates. Hybrid radiation transport calculations, which employ the current state of the art in radiation transport simulations, were used as benchmark solutions in the absence of measured data in extended beltline locations. These hybrid calculations utilize continuous-energy Monte Carlo calculations and eliminate the discretizations in space, energy, and angle that impose accuracy limitations on discrete ordinates calculations. This report details the results of the physical and calculational parameter studies and provides insights into where modifications in analysis methodology may be necessary to obtain calculational uncertainty in the extended beltline region comparable to that specified for traditional beltline fluence analyses.

.

TABLE OF CONTENTS

LIST OF FIGURES

LIST OF TABLES

EXECUTIVE SUMMARY

Regulatory Guide (RG) 1.190, "Calculational and Dosimetry Methods for Determining Pressure Vessel Neutron Fluence," describes the application and qualification of a methodology acceptable to the U.S. Nuclear Regulatory Commission (NRC) for determining the best-estimate neutron fluence experienced by materials in the beltline region of light water reactor (LWR) reactor pressure vessels (RPVs). Although the beltline region is not explicitly defined in RG 1.190, NUREG/CR-1511, "Reactor Pressure Vessel Status Report," states that materials with a projected neutron fluence greater than 1.0×10^{17} neutrons per square centimeter (n/cm^2) at end of license experience sufficient neutron damage to be included in the beltline.

Subsequent to the issuance of RG 1.190, the continuing trend of plant life extension and power uprates for both pressurized water reactors (PWRs) and boiling water reactors (BWRs) has led to growing concern about lifetime fluence levels in materials outside the traditional beltline region and in the RPV internals. The regions of the RPV that lie outside the traditional beltline are referred to as the extended beltline region.

Although the fundamental radiation transport phenomena for fluence levels in the extended beltline region are the same as those for the traditional beltline region, the characteristics and limitations of the numerical methods used to solve the transport equation, as well as the different transport paths from the core to the reactor vessel, result in additional considerations when determining fluence outside the beltline region relative to calculations within the beltline region. In addition, calculation of other neutron responses of interest—including damage as measured by displacements per atom (dpa) and a variety of dosimetry reactions that serve as measured data for use in benchmarking transport methods—may be more sensitive to the selection of transport methods and parameters in the extended beltline.

The primary objectives of this report are to identify transport phenomena that are important in calculation of RPV fluence levels in the extended beltline region and to evaluate radiation transport methodologies to determine which ones are best suited to such analyses. PWR and BWR reference models were used with discrete ordinates calculations, which represent the most widely used technique for RPV fluence evaluations. PWR and BWR reference models were also used with hybrid radiation transport calculations, which represent the current state of the art.

Sensitivity of extended beltline neutron transport calculations to physical parameters

A variety of physical parameters, including coolant density, neutron fission spectra, changes in the geometry of the cavity gap region, changes in the composition of the bioshield concrete, and the presence of a bioshield liner and reflective metallic thermal insulation were evaluated using high-fidelity hybrid radiation transport calculations. These studies provide key insights into how these parameters often affect fast neutron flux levels in the extended beltline region more significantly than in the traditional beltline region. Some factors, such as changes in concrete composition, changes in cavity gap width, and the presence or absence of a steel bioshield liner, have little to no effect on flux levels within the traditional beltline region, but they do have significant effects in extended beltline locations. Of particular concern are the effects that physical parameter variations have on neutron flux and dpa rates in the PWR model's vessel supports.

Sensitivity of extended beltline discrete ordinates calculations to angular quadrature and multigroup cross-section libraries

Regulatory Guide 1.190 provides guidance on the selection of discrete ordinates angular quadrature sets and multigroup (MG) cross-section libraries for RPV fluence calculations in the traditional beltline region but does not provide guidance for locations in the extended beltline region. In this work, an extensive set of calculational parameter studies was performed to assess typical discrete ordinates parameter selections for cases in which calculations extend beyond the traditional beltline region, particularly for locations in the vicinity of nozzles and vessel supports.

Quadrature sensitivity studies confirmed that the commonly used S8 quadrature set is not suitable for extended beltline fluence calculations. Furthermore, localized deficiencies in S8 solutions in the traditional beltline region may be significant, particularly for vessel dosimetry calculations. Even though the higher-order S16 quadrature provides improvements in the accuracy of discrete ordinates solutions, it is still likely inadequate for extended beltline applications in the nozzle and vessel support locations.

More recently developed quadruple range (QR) quadratures were also evaluated. These quadrature sets were developed specifically to improve solution accuracy with models that have material discontinuities parallel to the coordinate axes in areas such as the edges of fuel assemblies and/or the streaming paths along a coordinate axis. Of particular importance is the ability of a quadrature set to accurately model neutron streaming paths in the cavity gap between an RPV and the concrete bioshield.

Quadrature sets that are best suited for use in extended beltline applications were selected by comparing Denovo discrete ordinates calculations having various quadrature selections to Shift Monte Carlo solutions that used the same MG library that was used by the Denovo calculations. These studies demonstrated that the QR quadratures provide superior solution accuracy. However, even the use of high-order QR quadratures can still produce solutions with localized differences of 10% or more in the extended beltline region.

Multigroup cross-section library sensitivity

One of the most significant areas of potential solution inaccuracy in discrete ordinates calculations is the use of MG cross-section libraries. With respect to RPV fluence calculations, this area is of particular concern for extended beltline regions where the neutron flux spectra may be significantly different from those used to generate an MG library. For instance, the flux weighting spectra that were used to develop the widely used BUGLE-B7 MG library are based on one-dimensional transport calculations at the core midplane of simplified PWR and BWR models.

The method chosen to evaluate MG libraries in this study uses hybrid Shift calculations. Because Shift can be run with either MG or continuous-energy (CE) cross-section data, these calculations provide a means of comparing various MG libraries with a more accurate CE solution. Various MG libraries were evaluated, including VITAMIN-B7 (199 neutron energy groups) and BUGLE-B7 (47 neutron groups), both of which were developed specifically for LWR shielding analyses. MG libraries from the SCALE code system containing 200 to 1,597 neutron groups were evaluated. In addition, two libraries developed specifically to address neutron transport through energy ranges important for RPV flux and response calculations were also evaluated. All of these calculations were performed using the PWR model.

In addition to assessing the impact of MG libraries on fast fluence calculations in the extended beltline region, analyses were also performed to evaluate the ability of MG libraries to provide accurate calculation of neutron dpa rates and for nine dosimetry reaction rates that are often used in RPV fluence benchmark analyses. This set of 11 neutron responses (fast flux, dpa rate, and dosimetry reaction rates) was used to assess the adequacy of MG libraries over a wide range of neutron energies. The results of these studies suggest that whereas the BUGLE-B7 library is generally adequate for the calculation of all these quantities at locations radially out through the inner portion of the RPV in the traditional beltline region, it is not well suited to the calculation of most of these 11 responses at locations in the extended beltline region.

The accuracy of MG solutions can be improved by using a very fine group structure. However, libraries with up to several hundred energy groups could increase the amount of computer memory required for cross-section storage by more than two orders of magnitude and would also lead to much longer run times. Therefore, MG solutions may not be practical for routine RPV analyses.

Recommendations for analysis methodology

Results from the analyses performed in this study suggest that the discretization of the angular and energy variables in MG discrete ordinates transport calculations poses significant challenges for RPV fluence evaluations in the extended beltline region. Even though it may be possible to adequately address quadrature effects without a significant cost increase in computing requirements, the use of MG cross-section libraries—even with hundreds of energy groups—produced solutions that often underpredicted more accurate CE calculations in extended beltline locations, including the vessel supports in the PWR model. This underprediction is particularly noteworthy for calculation of dpa rates and of some dosimetry reaction rates.

Hybrid radiation transport methods provide a significant advantage in these analyses because the Monte Carlo calculations that are performed in the final stage of the hybrid calculational sequence are not subject to angular discretization or to the approximations made in MG cross-section libraries.

ACKNOWLEDGMENTS

The work described in this report was sponsored by the U.S. Nuclear Regulatory Commission (NRC), Office of Nuclear Regulatory Research (RES). The authors thank Jay Wallace for his support and guidance as the NRC project manager. His insights, questions, and encouragement have been invaluable to the success of this project and report. A number of NRC staff contributed constructive comments on draft versions of this report, on earlier documents, and in public meetings held during the course of this project. Among those contributors, special thanks are due to Ben Parks, Nate Hudson, Dan Widrevitz, and Amrit Patel. The authors also thank Oak Ridge National Laboratory (ORNL) staff members Katherine Royston and Tara Pandya for their reviews of this work, and Rose Raney and Kathy Jones for final document preparation.

ABBREVIATIONS AND ACRONYMS

1D	one-dimensional
2D	two-dimensional
3D	three-dimensional
ADAMS	Agencywide Documents Access and Management System
ANS	American Nuclear Society
ANSI	American National Standards Institute
ASTM	American Society for Testing and Materials
B&W	Babcock and Wilcox
BAF	bottom of active fuel
BOL	beginning of life
BWR	boiling water reactor
CE	continuous energy
C/M	calculated-to-measured ratio
CPU	central processing unit
DOM	the dominant axial zone in a GE14 BWR fuel assembly
dpa	displacements per atom
DSA	diffusion synthetic acceleration
DTW	directional theta weighted
EFPY	effective full-power year
ENDF	Evaluated Nuclear Data File
EOL	end of life
EVND	ex-vessel neutron dosimetry
IAEA	International Atomic Energy Agency
IRDF	International Reactor Dosimetry File
LD	linear discontinuous
LWR	light water reactor
MCNP	Monte Carlo N-Particle
MG	multigroup
NAT	the natural U axial zone at the bottom of each rod in a GE14 BWR fuel assembly
NPP	nuclear power plant
NRC	United States Nuclear Regulatory Commission
N-T	the natural U axial zone at the top of each rod in a GE14 BWR fuel assembly
N-V	the natural uranium vanished rod axial zone in a GE14 BWR fuel assembly
ORNL	Oak Ridge National Laboratory
PNNL	Pacific Northwest National Laboratory
PCA	Pool Critical Assembly [Pressure Vessel Facility Benchmark]
PCR	partial-current rebalance
PDF	probability distribution function
PLE	the plenum axial zone in a GE14 BWR fuel assembly
PSZ	the power shaping axial zone in a GE14 BWR fuel assembly
PWR	pressurized water reactor
PWROG	PWR Owners Group
QR	quadruple range
RPV	reactor pressure vessel
RVI	reactor vessel internals
SC	step characteristic
SI	source iteration

SLR	subsequent license renewal
SPEO	subsequent period of extended operation
TAF	top of active fuel
TLD	trilinear discontinuous
TSA	transport synthetic acceleration
TW	theta weighted
VAN	the vanished rod axial zone in a GE14 BWR fuel assembly
VF	void fraction
Voxel	volume element
VR	variance reduction
WBN1	Watts Bar Nuclear Plant Unit 1
WDD	weighted diamond difference

1 INTRODUCTION

For the past several decades, the main region of concern for reactor pressure vessel (RPV) fluence calculations has been the portion of the RPV referred to as the beltline region, which can be defined [1] as "the region adjacent to the reactor core that must be evaluated to account for the effects of radiation on fracture toughness." With the continuing trend of plant life extension and power uprates for both pressurized water reactors (PWRs) and boiling water reactors (BWRs) throughout the United States, there is growing concern about lifetime fluence levels in regions above and below what has historically been considered the beltline region and in reactor vessel internals (RVI).

Regulatory Guide 1.190 [2] describes the application and qualification of a methodology acceptable to the U.S. Nuclear Regulatory Commission (NRC) for determining the best-estimate neutron fluence experienced by materials in the beltline region of light water reactor (LWR) RPVs. This methodology is also acceptable for determining the overall uncertainty associated with those best-estimate values. However, Regulatory Guide 1.190 does not specifically define the beltline region.

In Title 10 of the Code of Federal Regulations (CFR) Part 50 [3], Section II of Appendix G defines the beltline region as "The region of the reactor vessel (shell material including welds, heat affected zones, and plates or forgings) that directly surrounds the effective height of the active core and adjacent regions of the reactor vessel that are predicted to experience sufficient radiation damage to be considered in the selection of the most limiting material with regard to radiation damage." 10 CFR Part 50, Section III of Appendix H [3] requires that reactor vessels for which the peak neutron fluence at the end of the design life of the vessel exceeds 10^{17} cm^{-2} (E > 1 MeV) must have their beltline materials monitored by a surveillance program complying with American Society for Testing and Materials (ASTM) E185-2 [4], as modified by Appendix H.

Section 2.3 of NUREG/CR-1511 [5] states that "The NRC staff considered materials with a projected neutron fluence of greater than 1.0E17 neutrons per square centimeter (n/cm^2) at end of license to experience sufficient neutron damage to be included in the beltline."

An International Atomic Energy Agency (IAEA) Nuclear Energy Series report on the integrity of RPVs in nuclear power plants (NPPs) [6] refers to the beltline as "the region of shell material directly surrounding the effective height of the fuel element assemblies, plus an additional volume of shell material both below and above the active core, with an [end-of-life] fluence of more than 10^{21} m^{-2} (E > 1 MeV) (10^{17} cm^{-2})." This definition is consistent with that given in NUREG/CR-1511.

Chapter 12 of the IAEA report [6] states that typical end-of-life design neutron fluences are on the order of 10^{18} n/cm^2 for BWRs and on the order of 10^{19} n/cm^2 for PWRs. Values of 4×10^{18} n/cm^2 for BWRs, 4×10^{19} n/cm^2 for Westinghouse PWRs, and 1.2×10^{19} n/cm^2 for Babcock and Wilcox (B&W) PWRs are provided in the IAEA assessment [6]. The PWR fluence values are noted as corresponding to a lifetime of 32 effective full-power years (EFPYs). Lifetime is not noted for BWRs.

In the context of the current report, the portion of the RPV where the end-of license fluence would be expected to exceed 10^{17} n/cm^2 for plant operations consistent with those in the original operating license is referred to as the traditional beltline region, or simply the beltline region. Locations above and below the traditional beltline region are referred to as the extended beltline region.

While the fundamental radiation transport phenomena for fluence levels in the extended beltline region are the same as those for the traditional beltline region, the characteristics and limitations of the numerical methods used to solve the transport equation, as well as the different transport paths from the core to the reactor vessel, result in additional considerations for the determination of fluence outside the beltline region relative to calculations within the beltline region.

This report discusses the use of PWR and BWR reference models for the evaluation of RPV fast (E > 1 MeV) neutron fluence and displacements per atom (dpa) and describes studies that were performed to evaluate transport phenomena that must be specifically addressed for such calculations in the extended beltline region. Parameter sensitivity studies are performed to assess the accuracy that can be expected for extended beltline fluence calculations using discrete ordinates transport codes, which are the most common method currently used for RPV fluence analyses. Modern hybrid radiation transport methods that combine both deterministic and Monte Carlo calculations are discussed and contrasted with the discrete ordinates method.

2 AN OVERVIEW OF RADIATION TRANSPORT CALCULATIONAL METHODS

The neutral particle radiation transport calculations performed for reactor physics and radiation shielding analyses are typically based on obtaining solutions to the steady-state Boltzmann transport equation. Detailed discussions of the derivation and application of the Boltzmann equation for nuclear reactor analyses can be found in the literature [8], [9], and [10].

The steady-state Boltzmann transport equation for fixed-source shielding calculations can be written as[1]

$$\Omega \cdot \nabla\phi(\mathrm{r},\mathrm{E},\Omega) + \sigma(\mathrm{r},\mathrm{E})\phi(\mathrm{r},\mathrm{E},\Omega) = \int_0^\infty \int_{4\pi} \sigma_s(\mathrm{r},\mathrm{E}' \longrightarrow \mathrm{E},\Omega' \longrightarrow \Omega)\phi(\mathrm{r},\mathrm{E}',\Omega')\mathrm{d}\Omega'\mathrm{d}\mathrm{E}' + q_e(\mathrm{r},\mathrm{E},\Omega), \quad (1)$$

where

Ω = a unit vector in the direction of particle travel,
ϕ = the particle flux,
r = the particle's position,
E = the particle's energy,
σ = the macroscopic total cross section,
σ_s = the macroscopic scattering cross section, and
q_e = external (flux-independent) sources

For the problems encountered in reactor physics and shielding analyses, the angular distribution of scattered particles depends only on the cosine of the scattering angle between the incoming and exiting particles, and Eq. (1) can be written as

$$\Omega \cdot \nabla\phi(\mathrm{r},\mathrm{E},\Omega) + \sigma(\mathrm{r},\mathrm{E})\phi(\mathrm{r},\mathrm{E},\Omega) = \int_0^\infty \int_{4\pi} \sigma_s(\mathrm{r},\mathrm{E}' \longrightarrow \mathrm{E},\omega)\phi(\mathrm{r},\mathrm{E}',\Omega')\mathrm{d}\Omega'\mathrm{d}\mathrm{E}' + q_e(\mathrm{r},\mathrm{E},\Omega), \quad (2)$$

where

$$\omega = \Omega' \cdot \Omega.$$

Exact analytical solutions for the transport equation exist only for very simple cases (e.g., monoenergetic particles in a one-dimensional system). For realistic shielding problems, a variety of methods have been developed to solve the transport equation using numerical techniques. The primary computational methods used to solve neutral particle transport theory problems have traditionally been either deterministic or stochastic. Deterministic methods were pioneered by Carlson and Lathrop in the 1950s and 1960s and are described in numerous Los Alamos Scientific Laboratory Reports, conference proceedings, and journal articles. A thorough description of the early development of the method, including an extensive list of references, can be found in Chapter 3 of the book by Greenspan et al. [11]. Stochastic methods are based

[1] Throughout this section, **boldface** symbols are used to represent vector quantities.

on the Monte Carlo technique pioneered by Ulam, Von Neumann, et al. [12]. Current state-of-the-art radiation transport calculations utilize both deterministic and stochastic codes in the hybrid radiation transport methodology. A paper by Mosher et al. [13] provides a more current discussion of the development and implementation of hybrid methods for radiation shielding calculations. The computer codes used in this report are briefly described in Section 2.4.

2.1 Deterministic Calculations

Modern computer codes based on deterministic methods are generally referred to as discrete ordinates or S_N codes. Although there are differences among the major discrete ordinates transport codes currently in use, all of them are based on discretizing the spatial, energy, and angular variables and solving the resulting set of equations using numerical methods. The techniques used to discretize energy, space, and angle are discussed in this section.

2.1.1 Energy Discretization

Energy discretization in the discrete ordinates method is accomplished through the multigroup (MG) approximation. In this method, the energy range of interest [E_{min}, E_{max}] is divided into G intervals or groups. The standard convention is to establish group one as the highest energy group, with an upper group boundary E_0 equal to E_{max}, and a lower group boundary of E_1. The group numbers increase as energy decreases. The energy E lies within group g if $E_g < E \leq E_{g-1}$.[2]

For a given energy group g, the group flux and external source at position r with direction Ω are defined as

$$\phi_g(r,\Omega) = \int_{E_g}^{E_{g-1}} \phi_g(r,E,\Omega)\ dE \tag{3}$$

and

$$q_g(r,\Omega) = \int_{E_g}^{E_{g-1}} q_g(r,E,\Omega)\ dE. \tag{4}$$

A set of MG cross sections is generated by averaging the continuous-energy (CE) cross-section data over the energy groups using an appropriate weighting function. A brief overview of MG cross-section libraries is provided in APPENDIX A.

[2] While most deterministic codes (e.g. DORT, TORT, PARTISN) follow this convention, Denovo uses group zero for the highest energy group. In this case the energy E lies within the group g if $E_{g+1} < E \leq E_g$. The notation used throughout this section follows the standard convention, with group numbers beginning with one.

Applying the MG approximation to Eq. (2) yields the MG transport equation for the flux in group g:

$$\Omega \cdot \nabla \phi_g(r,\Omega) + \sigma_g(r)\phi(r,\Omega) = \sum_{g'=1}^{G} \int_{4\pi} \sigma_{s,gg'}(r,\omega)\phi_g(r,\Omega')d\Omega' + q_g(r,\Omega). \quad (5)$$

The standard approach in discrete ordinates calculations is to represent the angular dependence of the scattering cross section using a Legendre polynomial expansion:

$$\sigma_{s,gg'}(r,\omega) = \sum_{n=0}^{N} \frac{2n+1}{4\pi} P_n(\omega)\sigma_{sn,gg'}(r), \quad (6)$$

where P_n is the Legendre polynomial of order n, and the $\sigma_{sn,gg'}$ values are referred to as the moments of the scattering cross section. The zeroth moment, $\sigma_{sn,gg'}$, is the total cross section for scattering from group g′ to group g. MG cross-section libraries used for LWR shielding analyses typically represent the angular distribution of scattering cross sections using a maximum order N in Eq. (6) ranging from three to seven.

For the hypothetical scenario of particle transport in a medium in which all scattering is isotropic, a P_0 expansion would be adequate. In actual practice, scattering is rarely isotropic. The degree of anisotropy in a scattering cross section is dependent on the isotope and the neutron energy. In general, neutron scattering becomes increasingly anisotropic as the neutron energy increases and/or the mass of the scattering nucleus decreases [14].

2.1.2 Spatial Discretization

In discrete ordinates transport calculations, the problem geometry is discretized into cells or voxels. Depending on the size and complexity of the system being modeled, the number of cells can range from thousands to tens or even hundreds of millions. For the majority of discrete ordinates codes, a regular structured mesh is employed. Typical mesh geometries for structured mesh codes are two-dimensional (2D) and three-dimensional (3D) Cartesian geometry and one-dimensional (1D), 2D, or 3D cylindrical geometry. In most shielding analyses, including the calculation of fluxes in a reactor system, either a 3D cylindrical or 3D Cartesian geometry is applied. While some unstructured mesh discrete ordinates codes are available, the discussion in this report is limited to the more widely used structured mesh codes.

Most shielding calculations are performed using models that include a wide variety of components, not all of which are best represented by a single coordinate system. For example, cylindrical geometry is well suited to modeling the cylindrical portions of an RPV, but not the lower hemispherical RPV head, fuel assemblies, or many of the core internals. In addition, a cylindrical coordinate system with its Z-axis oriented with the vertical axis of an RPV is not well suited to modeling the cylindrical nozzles whose axes are orthogonal to the Z-axis of the coordinate system.

Each spatial cell in a deterministic transport model is filled with a single material. A material may be an isotope, an element, a compound such as water, an engineering material such as stainless steel or concrete, or a mixture of any of these, such as a region represented by a homogenization of steel and water. In typical discrete ordinates calculations, the boundaries

where material changes occur will not necessarily coincide perfectly with voxel boundaries, so some voxels will overlap two or more distinct materials. Early discrete ordinates codes such as DORT [15],[16] and TORT [15],[17],[18] assign the material with the maximum volume fraction in such a voxel. Some modern discrete ordinates codes like Denovo [19] and PARTISN [20] perform volume weighting of the materials in such cells and create a mixed material to better model radiation transport through that cell. An example of the effect of material mixing is seen in Figure 2-1 and Figure 2-2. In Figure 2-1 the voxels that include the RPV clad (a stainless steel layer with a thickness of 0.56 cm) are modeled as either coolant, stainless steel (RPV clad), or carbon steel (RPV base metal). With material mixing (Figure 2-2), the same voxels are modeled as mixtures of two or three of those materials. While the use of material mixing provides a more accurate transport solution, it also increases the memory requirements for a given calculation. Codes like Denovo allow the user to specify a tolerance level for the creation of unique mixed materials.

In addition to the approximation introduced by discretizing a transport model into cells, discrete ordinates solutions are also affected by the differencing scheme that is used to relate the directional flux at the center of a spatial cell center to the flux at the cell boundaries. Differencing schemes that are used in current discrete ordinates codes include the following:

- weighted diamond difference (WDD)
- theta weighted (TW)
- directional theta weighted (DTW)
- linear discontinuous (LD)
- trilinear discontinuous (TLD)
- step characteristic (SC)

Various publications [18] [19], [21], [22] provide useful information regarding the characteristics and application of these schemes. The most commonly used differencing schemes in RPV fluence calculations are TW and DTW. The LD scheme is used for the majority of the Denovo calculations performed in this analysis. The SC scheme is often used in the discrete ordinates step(s) of a hybrid radiation transport sequence (Section 2.3).

The accuracy that can be obtained in a discrete ordinates solution is dependent on the differencing scheme and the spatial mesh intervals. Furthermore, the mesh and differencing scheme can be interdependent. For example, the LD scheme tends to give very accurate results on well-refined meshes, but it also tends to be sensitive to the aspect ratio of the mesh cells. There are no universal rules that can be applied to ensure that a spatial mesh and differencing scheme are appropriate for a discrete ordinates calculation.

Determination that a solution has converged with respect to the spatial discretization is typically obtained by parameter studies for a given model. Petrovic and Haghighat [23] present meshing parameter studies for 2D cylindrical Rθ vessel fluence calculations using DORT. Davidson and Burre [24] present meshing studies for 2D cylindrical RZ and 3D XYZ discrete ordinates calculations of gamma transport using DORT, TORT, and PARTISN models of spent fuel sources in a fuel cask. Regulatory Guide 1.190 provides general guidelines for spatial mesh in 2D cylindrical (Rθ and RZ) geometries, but it has no recommendations for Cartesian geometries.

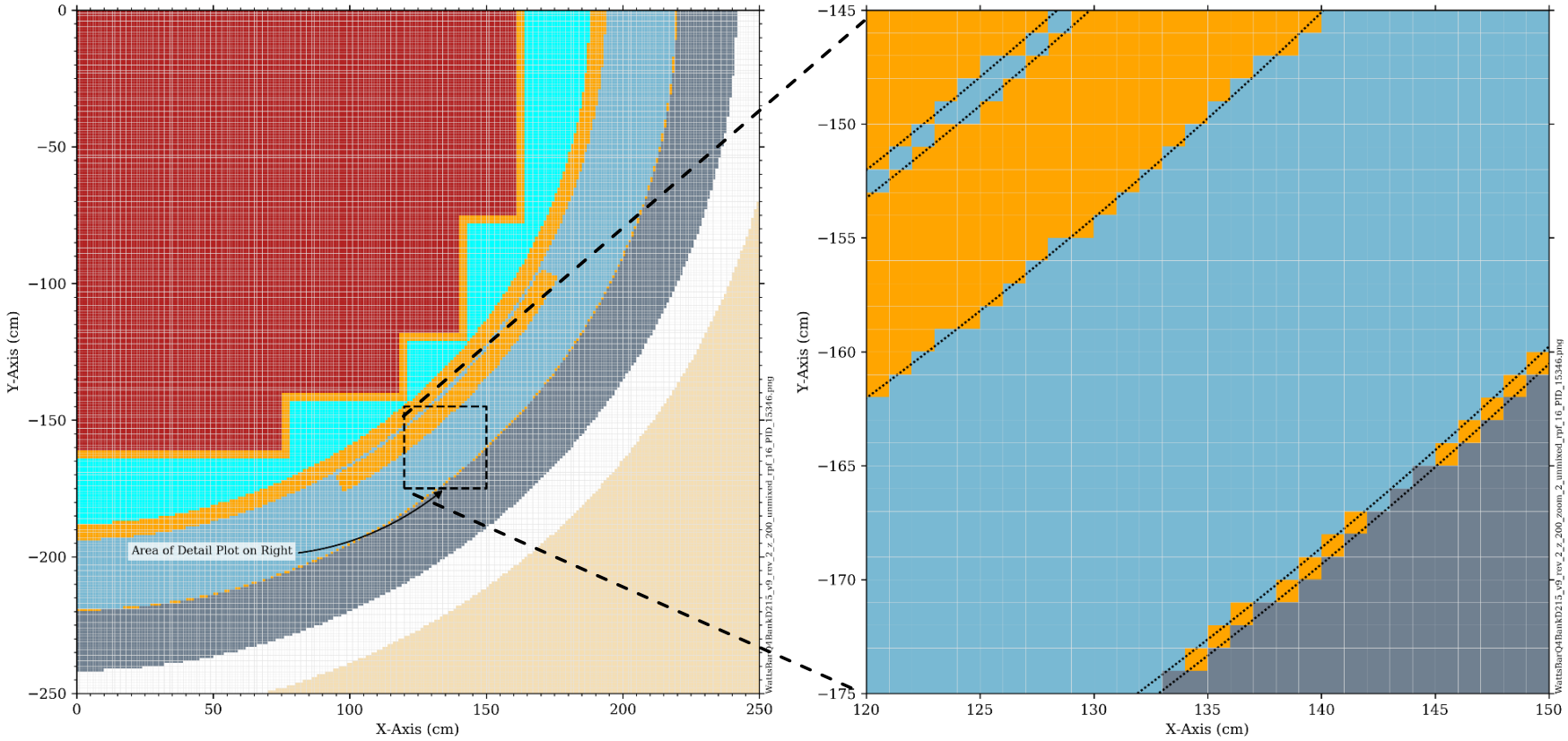

Figure 2-1 Two-dimensional slice of the PWR reference model at Z = 200 cm for a Denovo calculation with uniform 1 cm mesh intervals in X, Y, and Z. Material mixing is suppressed in the Denovo spatial discretization The detail plot on the right shows a close-up of a region that includes the core barrel, neutron pad, coolant, RPV clad, and RPV base metal. The light gray lines are the Denovo spatial mesh, and the dotted black lines in the right-hand view represent the radial boundaries of the core barrel, neutron pad, RPV clad, and RPV base metal.

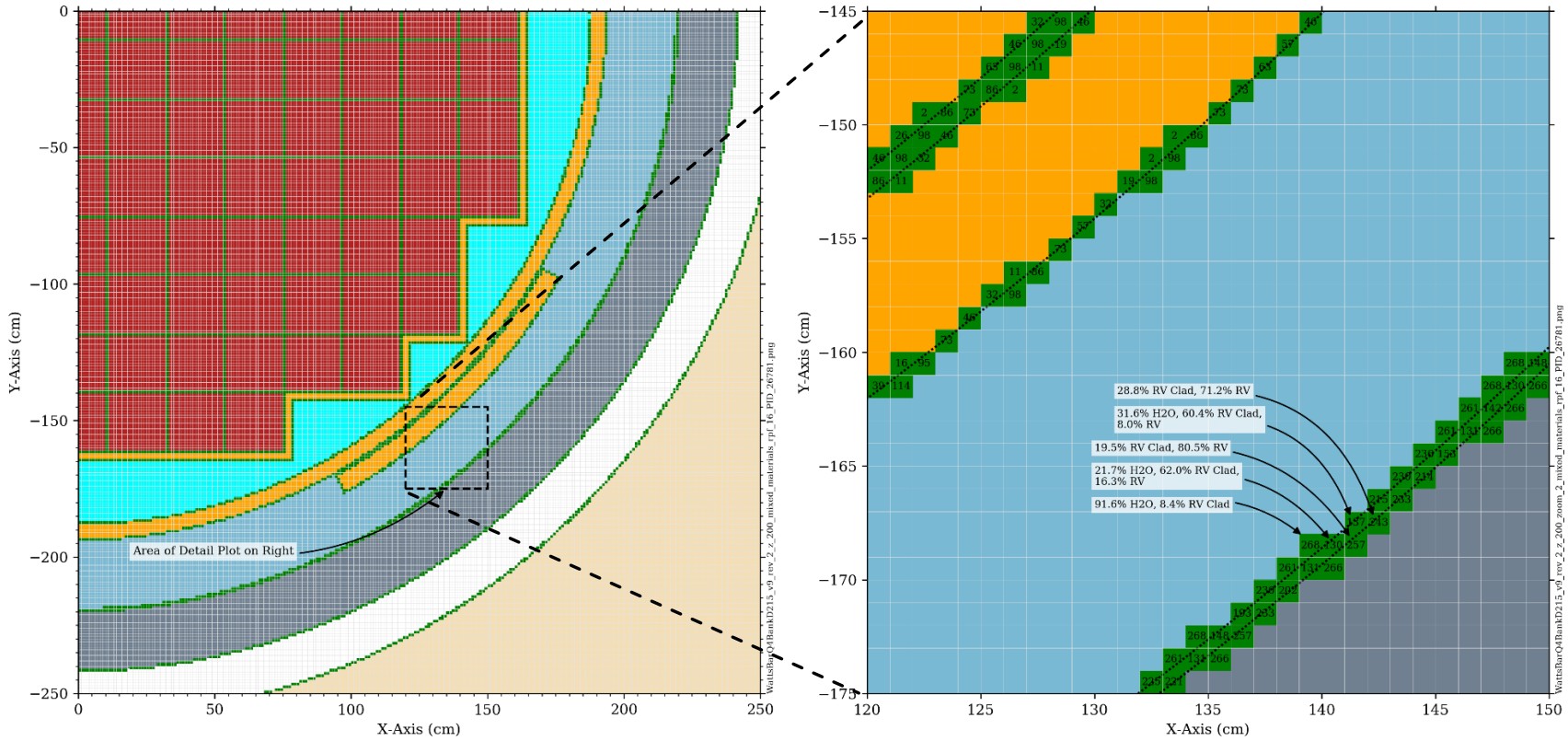

Figure 2-2 Two-dimensional slice of the PWR reference model at Z = 200 cm for a Denovo calculation with uniform 1 cm mesh intervals in X, Y, and Z. Material mixing is applied in the Denovo spatial discretization *Voxels with mixed materials are shaded green. The detail plot on the right shows a close-up of a region that includes the core barrel, neutron pad, coolant, RPV clad, and RPV base metal. The light gray lines are the Denovo spatial mesh and the dotted black lines represent the radial boundaries of the core barrel, neutron pad, RPV clad, and RPV base metal. The integers in each of the mixed material voxels are mixed material numbers. The volume fractions for several voxels along the RPV clad and RPV base metal are shown.*

2.1.3 Angular Discretization

In discrete ordinates calculations, particle travel is allowed only in a finite set of discrete directions. The angular flux in each of these directions is calculated using transport sweeps to solve the discrete ordinates equations. The scalar flux is then formed by integrating the angular fluxes using numerical quadrature, with each quadrature direction having a specified quadrature weight. The accuracy that can be obtained in solving the transport equation using the discrete ordinates method is dependent on several factors, including the set of quadrature weights and ordinates that is used. While there is no standard procedure for choosing an adequate set, Duderstadt and Martin [8] suggest that the following criteria should be considered:

1. Projection invariance. In cases where there is no a priori knowledge concerning the angular flux in the solution space, it is reasonable to select a quadrature set that is invariant with respect to allowable orientations of the physical domain. For 3D Cartesian geometry, this means quadrature ordinates should be invariant under arbitrary 90° rotations about the coordinate axes, and 180° reflections about the XY, XZ, or YZ planes. These conditions are met by the widely used level-symmetric S_N quadrature sets[3]. Regulatory Guide 1.190 states that an S8 fully symmetric angular quadrature must be used as a minimum for determining the fluence in the vessel, with the potential need for higher-order quadratures (i.e., quadratures with a greater number of ordinates) in reactor cavity fluence calculations.

2. Positivity of the scalar flux. The scalar flux should always be positive. Choosing a quadrature set in which all the weights are positive will ensure integration of a positive scalar flux provided the angular fluxes are positive. Level-symmetric S_N quadratures have negative weights for orders exceeding S20, which limits their ability to use increasing quadrature orders as a means of confirming that a solution has converged with respect to quadrature.

3. Accurate evaluation of angular integrals. The flux moments and the source should be integrated accurately with a minimum number of directions and weights.

While projection invariance is desirable in general, in some cases noninvariant quadratures are better suited to a particular application. Abu-Shumays [25],[26] developed quadruple range (QR) quadratures to accurately integrate functions that are discontinuous across octant boundaries of the unit sphere. Because the QR sets have directions closer to the coordinate axes than level-symmetric S_N sets with the same number of angles, the QR sets often provide superior solutions for models which have material interfaces along any of the coordinate axes and/or particle streaming through gaps that are parallel to a coordinate axis [27], such as the cavity gap between an LWR's RPV and bioshield.

[3] The notation S_N refers to a quadrature set with N/2 direction cosines with respect to each of the coordinate axes. Thus, for example, the S8 quadrature shown in Figure 2-3 in has four direction cosines with respect to the X, Y, and Z axes. While the value of *N* is often written as a subscript, the convention in this report is to avoid subscripts, which could become difficult to read for some of the QR quadrature sets considered in Section 7.

Figure 2-3 shows the quadrature ordinates and weights for the level symmetric S8 and S16 quadratures, which are widely used in RPV fluence calculations. Figure 2-4 shows the ordinates and weights for S16 and QR8T[4] quadratures, each with 36 angles per octant in a triangular arrangement. Note that the QR8T quadrature has ordinates closer to each of the coordinate system axes. Consequently, QR8T quadrature is likely to be more appropriate than S16 quadrature for problems in which particle streaming near the coordinate axes is a significant transport path. This behavior is illustrated in Section 7.

Numerous other types of quadrature sets have been developed in attempts to improve the accuracy and/or efficiency of discrete ordinates solutions. Carew et al. [28],[29] developed uniformly distributed equal weight quadratures and uniform Gauss weight quadratures to provide the ability to systematically increase quadrature order while maintaining positive weights. This work was motivated by the inability of the standard level symmetric SN sets to be refined beyond order 20. Longoni and Haghighat [30] developed an ordinate splitting technique for problems in which the particle flux is peaked along certain directions of the unit sphere. Ahrens [31] developed new quadratures that are invariant under the icosahedral rotation group, but not under 90°and 180°rotations. Fromowitz and Zeigler [32] developed large quadrature sets with more than approximately 1,000 angles per octant. These were developed to reduce ray effects[5] in problems that have significant regions with low-scattering or nonscattering media.

A recent paper by Manalo, Ahrens, and Sjoden [33] provides an overview of their work in quadrature development. While many of the quadrature sets discussed in the references can be used directly in standard discrete ordinates radiation transport codes such as TORT, PARTISN, and Denovo, methods such as the ordinate splitting technique [30] require modifications to the transport sweep routines.

[4] For QR quadratures the notation QR*N*T refers to a QR set with N direction cosines with respect to the Z-axis and a triangular arrangement of azimuthal angles on the polar levels. The notation QR*M*x*N* refers to a QR set with M polar levels and N azimuthal angles on each polar level.

[5] Ray effects can occur in multidimensional discrete ordinates calculations, particularly those with highly localized sources and regions with minimal or no scattering. Ray effects are characterized by nonphysical oscillations in the angular flux solution and even in the scalar flux. Examples of ray effects are presented in Section 7.

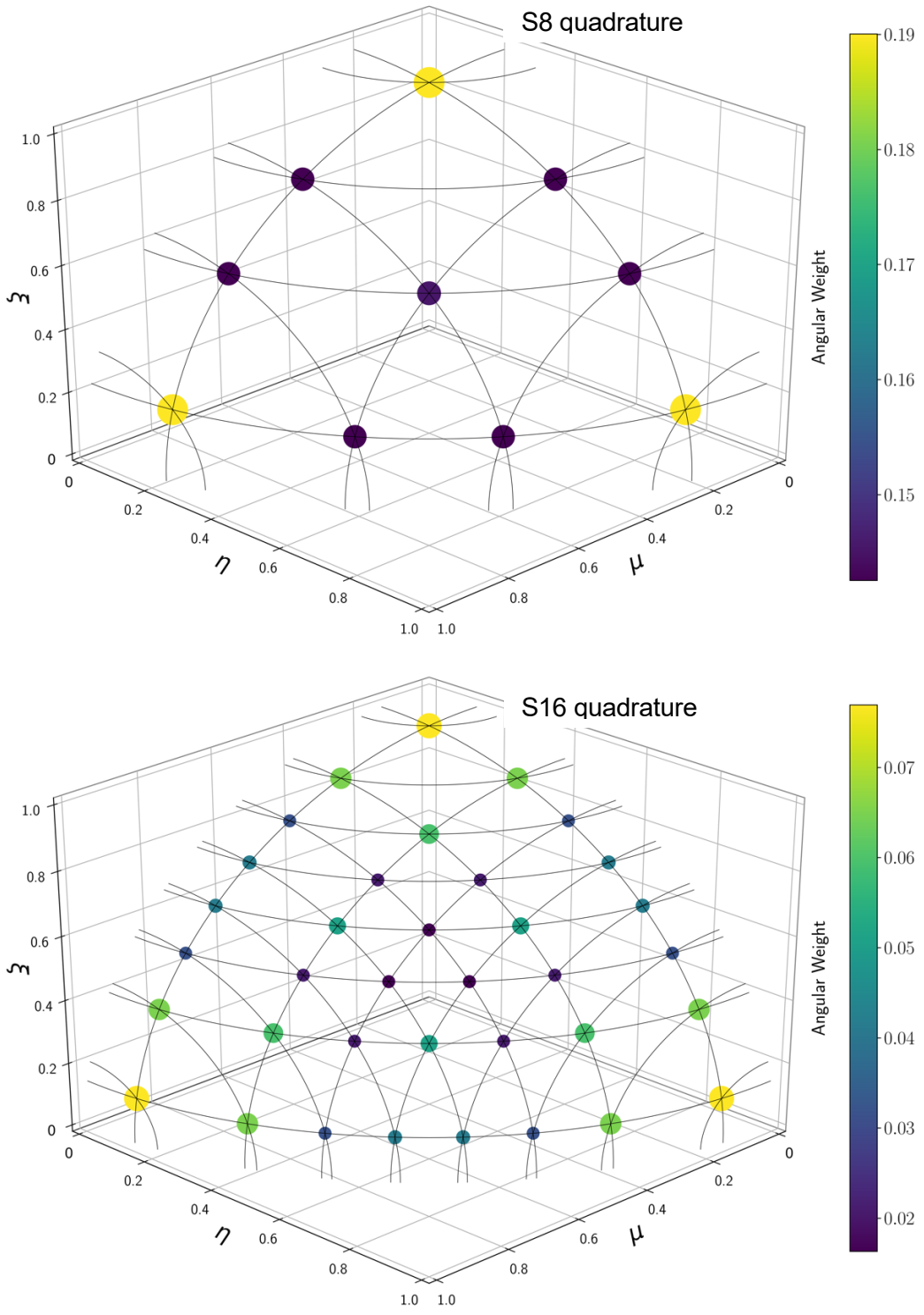

Figure 2-3 Level symmetric S8 and S16 quadrature ordinates and weights in one octant of the unit sphere *The circles represent the direction cosines in X, Y, and Z on the unit sphere. Associated weights are indicated by circle color and size. These sets are rotationally invariant.*

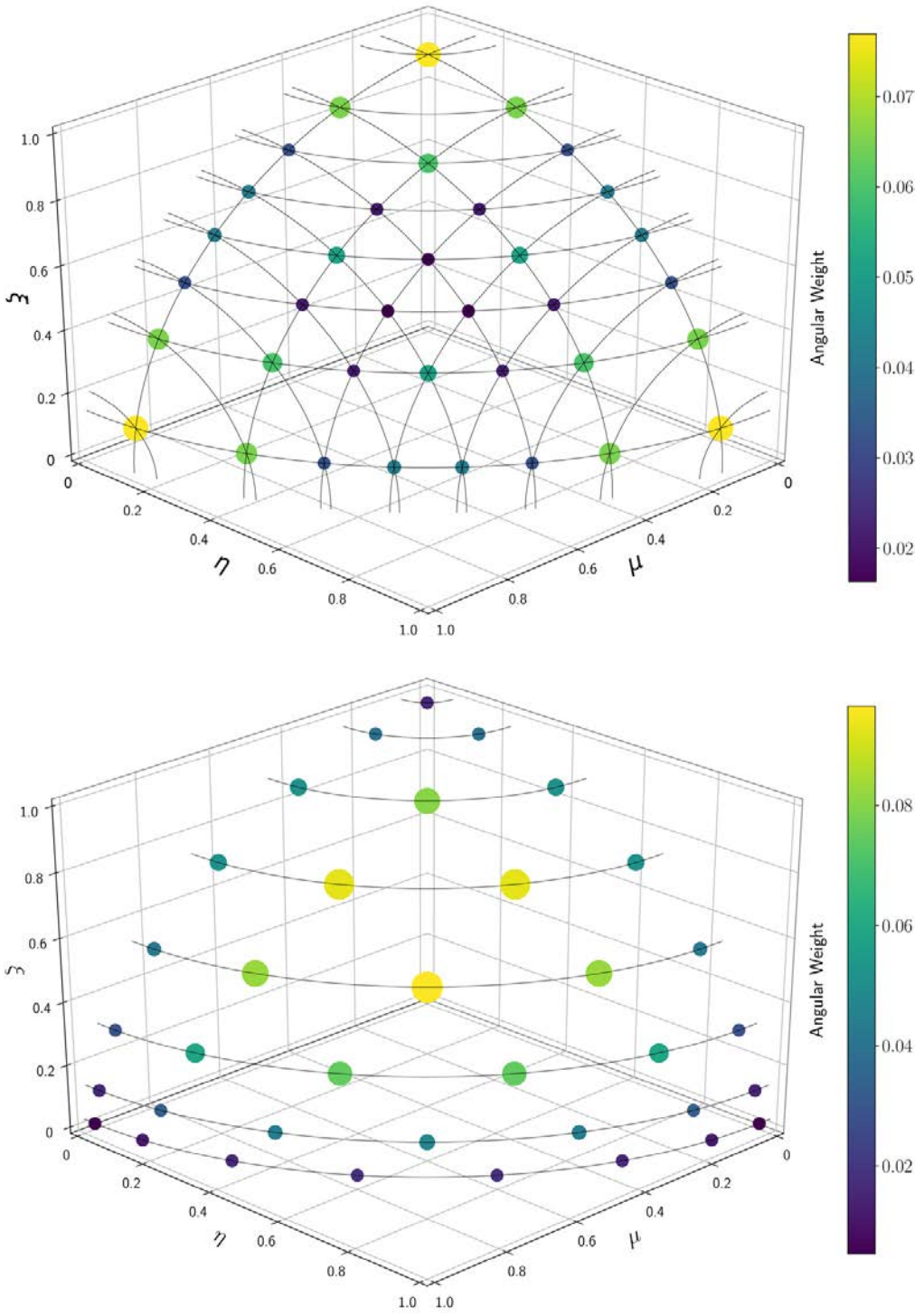

Figure 2-4 S16 and QR8T quadrature ordinates and weights in one octant of the unit sphere *The circles represent the direction cosines in X, Y, and Z on the unit sphere* *The associated weights are indicated by circle color and size. The S16 set is rotationally invariant, while the QR8T set is not. Both sets have eight polar levels and 36 angles per octant.*

2.1.4 Solution of the Discrete Ordinates Transport Equations

Discretization of a transport model in energy, space, and angle in a discrete ordinates calculation produces a set of linear equations which are solved iteratively until a specified convergence criterion is met. Because the number of unknowns for discrete ordinates calculations is generally very large, substantial computing resources are required for many applications of this method. For example, the Denovo calculations for this study typically included more than 10^{10} unknowns based on mesh spacing, MG library, and quadrature selection.

Because these calculations are computationally expensive, a variety of acceleration techniques have been developed to reduce the time required to obtain a converged solution. The most commonly used acceleration techniques in discrete ordinates codes include diffusion synthetic acceleration (DSA), coarse mesh finite difference rebalance (CMFD), partial-current rebalance (PCR), and transport synthetic acceleration (TSA). The primary acceleration technique in Denovo is based on Krylov methods, which can be substantially more efficient than other acceleration schemes.

The usual output of a discrete ordinates calculation is the scalar flux in every mesh cell in each energy. The scalar fluxes can be combined with MG response functions to obtain other quantities of interest, such as reaction rates, displacements per atom (dpa) rates, or dose rates.

2.2 Stochastic Calculations

Radiation transport computer programs based on stochastic methods are generally referred to as Monte Carlo codes. Monte Carlo radiation transport calculations are based on the simulation of particle histories. Each history is based on sampling probability distribution functions (PDFs) that govern each event as a particle is born (e.g., a neutron is created by fission), undergoes various interactions as it traverses through the model phase space, and is finally absorbed or escapes the boundary of the model.

As particle histories are accumulated, the model phase space is populated with a distribution of particle positions, energies, and directions. The population in one or more region(s) of interest can be obtained through the use of particle tallies. These tallies can be very localized, or they can encompass large portions of the model (Section 2.2.3).

Monte Carlo calculations inherently provide higher-fidelity solutions than discrete ordinates calculations, as they do not require the discretization in energy, space, and angle imposed by all discrete ordinates codes. Because of this, Monte Carlo simulations are generally considered to be the most accurate method for high-fidelity radiation transport calculations. Until the advent of hybrid radiation transport (Section 2.3), Monte Carlo calculations were generally used on a very limited basis due to the amount of central processing unit (CPU) time required to achieve a well-converged solution.

The Monte Carlo calculations in this study used the MCNP [34] and Shift [35] computer codes.

2.2.1 Continuous-Energy Cross Sections

Monte Carlo calculations can use either CE or MG cross-section data. CE cross-section libraries should be used whenever possible, as they provide a higher fidelity modeling of the physics involved in particle transport.

CE libraries used in Monte Carlo calculations include data for all reaction types that are present in the Evaluated Nuclear Data Files (ENDF) data [36],[37]. The cross-section values are given on an energy grid that is sufficiently dense that linear-linear interpolation between the energy grid points reproduces the evaluated cross sections within a specified tolerance. The data libraries used by MCNP have cross sections that are reproduced to a tolerance of 1% or less, with many of the more recent evaluations having tolerances of 0.1%. The data libraries used by Shift have tolerances of 0.1%. In addition to the cross-section values, CE libraries include kinematic data that provide PDFs for the energy and angular distributions of secondary particles.

2.2.2 Spatial Modeling Capabilities

Unlike discrete ordinates calculations, in which the problem geometry is defined based on a mesh grid, Monte Carlo calculations provide the ability to exactly model the majority of the geometric features in most radiation transport problems. Both MCNP and Shift allow modeling of linear and quadratic surfaces (planes, spheres, cylinders, cones, ellipsoids, hyperboloids, paraboloids), as well as elliptical or circular torii with axes parallel to the X-, Y-, or Z-axis.

This aspect of Monte Carlo modeling is particularly beneficial in vessel fluence analyses, as the vessel, closure head, nozzles, and reactor vessel internals (RVIs) can all be represented without the meshing artifacts that occur with discrete ordinates codes. Because there are no approximations made when modeling the surfaces listed in the previous paragraph, Monte Carlo models are sometimes referred to as exact geometric models. It must be kept in mind, though, that the exactness refers to the representation of the model as defined by the analyst. It is incumbent on the analyst to construct a model that is a faithful representation of the geometry of the system being modeled and to consider modeling issues (e.g., tolerances, as-built dimensions) that may cause the geometry model to deviate from the actual system being modeled.

2.2.3 Monte Carlo Tallies

Radiation transport calculations that are performed using the discrete ordinates method provide a solution that contains the particle flux as a function of position and energy throughout the model phase space. In contrast, the output of a Monte Carlo calculation provides the flux—or response(s) based on the flux—only for locations and energy intervals that are specified in the problem input. These user defined regions of interest in the model are referred to as tallies. The most commonly used types of Monte Carlo tallies are briefly defined below, and further details can be found in the literature [34], [38], [10].

Cell tallies are used to obtain the particle flux in one or more cells that are part of the model geometry definition. For example, if the core barrel is modeled as a single cell, then a cell tally for the core barrel will provide the average flux in the core barrel over specified energy intervals.

Surface tallies are used to obtain the particle flux crossing a given surface that is a boundary between two adjacent cells.

Point detector tallies are deterministic estimates of the flux at a point in space rather than the flux averaged over a cell or surface. Point detectors are also referred to as next event estimators, as they involve the computation of the contribution to a point detector tally at source and collision events throughout a particle history, as if the next event were a particle trajectory directly to the detector point without further collision.

Mesh tallies provide estimates of the flux in every voxel of a Cartesian or cylindrical mesh that is superimposed over the problem geometry. In the limiting case, a mesh tally can provide a global solution with spatial resolution that can be comparable to, or even finer than, the spatial mesh of a discrete ordinates calculation of the same model. Until fairly recently, the use of mesh tallies in many Monte Carlo simulations was impractical because the problem run times that would be necessary to achieve acceptable convergence were unacceptably long. With the advent of hybrid radiation transport methods (Section 2.3), highly detailed mesh tallies are now feasible for many shielding analyses, including vessel fluence calculations.

Monte Carlo tallies provide estimates of the mean and variance for the tally quantities of interest. The standard approach for reporting tally results is to provide the mean and the relative error. Given a mean value μ and a variance σ^2, the tally relative error RE is given by

$$\mathrm{RE} = \frac{\sigma}{\mu}. \tag{7}$$

Monte Carlo tallies are generally considered reliable if the relative error is less than 10%, except in the case of point detectors. Because point detectors are more prone to false convergence than other tally types, it is recommended that they be converged to less than 5% relative error for reliability.

2.2.4 Analog Monte Carlo and Variance Reduction Methods

The simplest type of Monte Carlo radiation transport calculation is an analog calculation. In analog calculations, the natural probabilities for all the events that occur during a particle history are used. This approach is referred to as analog because it is directly analogous to the events that occur naturally during each particle's history.

Analog Monte Carlo simulations can work well when a significant fraction of the source particles contribute to the tally (or tallies) of interest. For deep penetration shielding calculations, though, the fraction of source particles that reach a tally region can be very small. For these problems, an analog simulation is not feasible because few of the source particles reach the tally region, and the statistical error associated with the tally mean is unacceptably high.

An example is a simplified one-dimensional radial geometry that is representative of the PWR reference model at the core midplane. For an analog calculation with 10^7 source neutrons, only 188 neutrons "survive" to reach the RPV. Obtaining a well-converged solution to this type of problem requires either extremely long computational times or the use of variance reduction methods, which are used to reduce the statistical uncertainties associated with each tally value.

Before discussing variance reduction methods, it is necessary to introduce the concept of a particle's weight. Weight can be defined as "an adjustment for deviating from a direct physical simulation of the transport process" [34]. In an analog Monte Carlo simulation, every particle has a unit weight, as no adjustments are made to the natural probability distributions that govern each event in the particle histories.

Most variance reduction techniques alter or bias the natural probability distributions in an effort to improve the statistical convergence of the problem tallies. The purpose of these biasing techniques is to increase the number of particles that contribute to the tallies of interest without erroneously affecting the mean tally results. At every instance in which a biased distribution is sampled, the particle weight must be adjusted so that the biased weight is given by

$$w_{biased} = w_{unbiased} \times \frac{pdf_{unbiased}}{pdf_{biased}}. \quad (8)$$

Some of the more commonly used variance reduction methods are briefly discussed in this section. Further details on these and other variance reduction methods can be found in the references.

1. Source biasing

   Source biasing can be illustrated using the example of Monte Carlo calculations of RPV fluence. It is well known that within the beltline region of a typical LWR, the outermost fuel assemblies dominate the neutron flux levels in the RPV. Furthermore, for the calculation of the flux of neutrons with energies above 1 MeV, it is clear that only neutrons born with an energy above 1 MeV have any chance of reaching the RPV with an energy of at least 1 MeV. It is also known that the probability of a source neutron reaching the RPV increases as the source energy increases.

   a. The fraction of source neutrons that reach the RPV can thus be increased by biasing the probabilities that govern the spatial and energy sampling of the source. The simplest example would be a case in which the spatial distribution of source neutrons in the core is uniform. In this case, any location within the core has an equal probability of being sampled as source particles are generated. Because neutrons born near the outer edge of the core have a significantly higher probability of reaching the vessel compared to neutrons born in the interior modules, the distribution used to sample the starting location can be biased so that more neutrons are born near the outer edge of the core. In doing so, the weight assigned to each source particle must be modified by the ratio of the unbiased and biased probability distributions, as shown in Eq. (8).
   b. In a similar manner, the energy distribution of the source neutrons can be biased by sampling from a probability distribution that is more heavily weighted toward higher neutron energies. An example of the effects of spatial and energy biasing for an RPV fluence calculation is provided in Section 2.3.4.

2. Implicit capture

   Implicit capture is a variance reduction method that is particularly useful for deep penetration shielding problems in which a particle's history may be terminated very close to a tally region. When implicit capture is used, a particle is not terminated if it undergoes an absorption reaction. Instead, the particle undergoes a scattering interaction and has its weight reduced. Given an absorption cross section Σ_a and a total cross section Σ_t, a particle whose weight is w_i is scattered and assigned a weight w_o of

$$w_o = w_i \times \left(1 - \frac{\Sigma_a}{\Sigma_t}\right). \quad (9)$$

3. Particle splitting and Russian roulette

Particle splitting and Russian roulette are variance reduction methods used to control the population of particles in various regions of the problem space. Using these methods, many particles of low weight are tracked in important regions, whereas in unimportant regions, only a few particles of high weight are tracked. The weight of each particle is adjusted at each splitting or rouletting event to ensure that the simulation remains unbiased.

An example of splitting would be a problem in which an optically thick shield—that is, a shield with a thickness of many mean free paths—is placed between a source and a detector where the flux is to be tallied in the simulation. The shield can be split into multiple layers in the Monte Carlo model, with the particles being split each time they exit one layer and enter a layer nearer the detector. With each split of a single particle into N particles, the weight of the N particles is reduced by a factor of 1/N.

The Russian roulette technique is essentially the opposite of splitting. Particles that are moving into unimportant regions of the model or whose weight has fallen below a specified value can be rouletted. In this process, a random number is generated and compared to a parameter such as 1/d, where d is a parameter in the range [2,10] [46]. If the random number is greater than 1/d, then the history is terminated. If it is not, then the history is continued, and the particle weight is increased by a factor of d.

Splitting and rouletting can also be performed based on energy for cases in which certain energy ranges are more important than others.

4. Weight windows

The weight-window variance reduction technique provides splitting and rouletting of particles as a function of space or of both space and energy. The technique is illustrated in Figure 2-5.

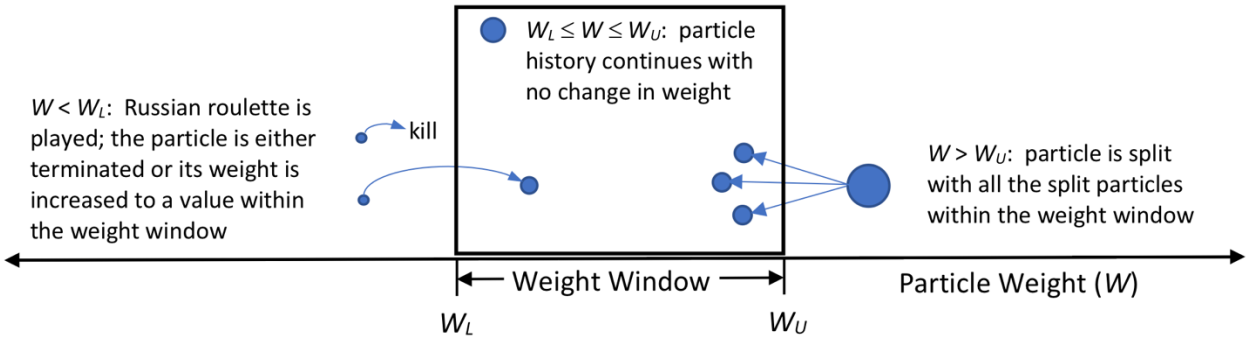

Figure 2-5 Illustration of weight windows as a variance reduction method for Monte Carlo calculations *Particles of weight W enter the weight window, which has lower and upper bounds of W_L and W_U. The size of each particle in the figure is proportional to its weight.*

For each phase space (space or space-energy) cell in the weight-window map, the user supplies a lower weight bound W_L. The upper weight bound W_U is calculated as a user specified multiple of the lower weight bound. These bounds define a window of acceptable particle weights. If a particle's weight is above the upper bound, then it is split so that all of the split particles are within the weight window. In the illustration, the particle that enters with a weight W above the weight window's upper boundary W_U is split into three particles, each of which has weight W/3. If a particle's weight is below the lower bound, then Russian roulette is played. The particle history is either terminated, or the particle continues with its weight increased to a value within the window. In the illustration, the particle is killed with a 50% probability or continued with a weight of 2W. Particles with weights within the lower and upper bounds are continued with no change in weight.

Judicious use of variance reduction techniques can make it possible to obtain well-converged Monte Carlo simulations in substantially less time than in analog simulations. The hybrid radiation transport method provides an efficient, effective means of generating space-energy weight windows and source biasing parameters that can reduce Monte Carlo run times by orders of magnitude.

2.3 Hybrid Methods

Hybrid methods are a class of techniques used to obtain a solution to the Boltzmann transport equation using a combination of deterministic and stochastic calculations. The deterministic calculations in hybrid calculation sequences are used to generate variance reduction (VR) parameters (space- and energy-dependent weight windows and source biasing parameters) that are then used in Monte Carlo transport calculations to obtain the desired quantities of interest. Hybrid calculations can be run using ADVANTG [39] and MCNP, and they can also be run with the Denovo and Shift codes in Exnihilo, the massively parallel radiation transport code suite developed at Oak Ridge National Laboratory (ORNL).

2.3.1 Particle Importance and Adjoint Flux Calculations

Hybrid radiation transport methods are based on the concept of particle importance. A particle's importance is a measure of how likely it is to contribute to a response of interest, such as the flux or a reaction rate at a particular location within a particular energy range. For example, a neutron with an energy of 2 MeV in the downcomer region of a PWR has a much greater probability of contributing to the fast fluence in the RPV than a neutron of the same energy in an inner assembly of the core. Therefore, the neutron in the downcomer has a greater importance than the equivalent-energy neutron within the core.

The particle importance as a function of space and energy can be obtained by solving the adjoint form of the Boltzmann transport equation [9]. In an adjoint calculation, the adjoint source is the response of interest at a specified location or locations. For example, if the response of interest is the fast fluence in the beltline region of the RPV, then the adjoint source is taken to be the flux of neutrons with energy greater than 1 MeV within the RPV over the axial extent of the beltline region. Figure 2-6 shows the resulting adjoint flux, and hence the importance, for neutrons that will reach the RPV with energies greater than 1 MeV. As expected, the outermost fuel pins are the most important core regions with respect to RPV fluence.

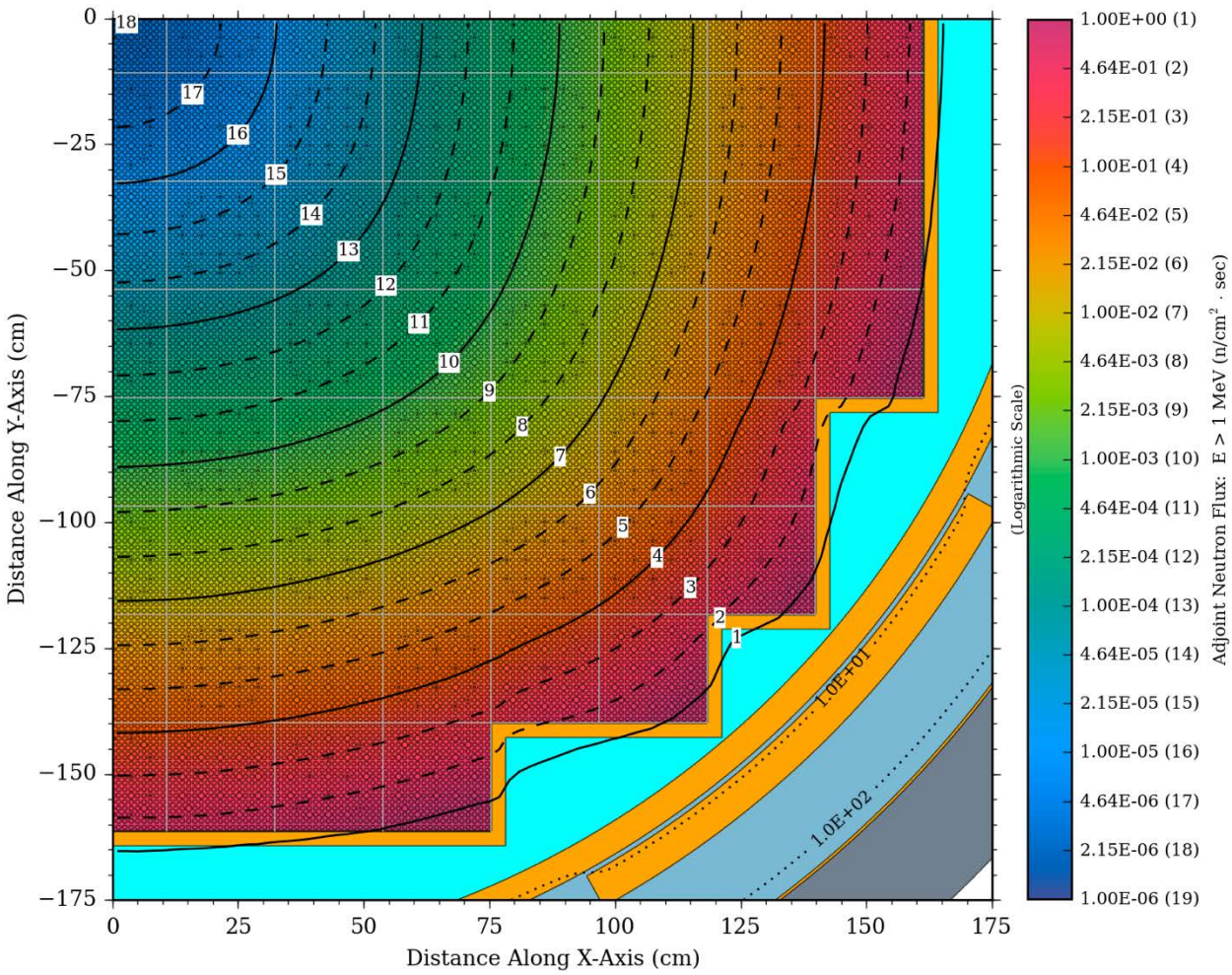

Figure 2-6 **Adjoint fast (E > 1 MeV) neutron flux for the PWR reference model with homogenized fuel assemblies. Plan view at Z= 200 cm** *The adjoint source region is in the reactor from an elevation of 0–400 cm.*

2.3.2 Hybrid Calculations Using the Cadis Methodology

The Consistent Adjoint Driven Importance Sampling (CADIS) methodology [40],[41] was developed to generate space-energy weight windows and consistently biased sources to accelerate the convergence of source-detector type problems in which a single localized response (tally) is the quantity of interest in a Monte Carlo simulation. The basic steps of a hybrid calculation sequence using the CADIS methodology are listed here. A detailed derivation can be found in the references.

1. The adjoint flux for the problem of interest is solved using a discrete ordinates calculation. The adjoint source is modeled as the response of interest (e.g., the flux or dpa rate) at the location where the Monte Carlo tally will be computed. As noted in Section 2.3.1, the adjoint scalar flux $\varphi^{+}_{g}(r)$ represents the importance of a particle such as a neutron at a given location and energy in contributing to the response of interest at the adjoint source location (i.e., the Monte Carlo tally location).

2. Weight-window target values $w_g(r)$ for the Monte Carlo calculations are constructed as

$$w_g(r) = \frac{R}{\phi_g^+(r)}, \tag{10}$$

where R is an estimate of the response of interest based on the adjoint calculation.

3. A source distribution q that is biased in space and energy in a manner that is consistent with the weight windows is constructed as

$$\hat{q}_g(r) = \frac{q_g(r)\phi_g^+(r)}{R}, \tag{11}$$

where $q_g(r)$ is the source for the forward transport problem.

4. The Monte Carlo calculation is run using the space-energy weight windows from Eq. (10) and the biased source definition from Eq. (11).

The CADIS methodology has been applied to a wide range of shielding calculations. It can provide speedups of orders of magnitude in obtaining a well-converged Monte Carlo solution.

2.3.3 Hybrid Calculations Using the FW-Cadis Methodology

While the CADIS method is very effective for providing substantial speedups in the convergence of Monte Carlo simulations for a single tally, it is not well suited to Monte Carlo simulations in which tallies at multiple locations or mesh tallies are the quantities of interest. To converge multiple tallies to the same relative uncertainty in a single Monte Carlo simulation using CADIS, the adjoint source corresponding to each tally must be weighted inversely with the expected tally value [43].

In the FW-CADIS (Forward-Weighted CADIS) method, a forward discrete ordinates calculation, is performed to estimate the response of interest at each location to be tallied in the Monte Carlo simulation. The inverse of those response values is then used to weight the adjoint source strength at each location. Using this adjoint source, the CADIS methodology outlined in Steps 1–4 of Section 2.3.2 is used to construct weight windows and a biased source for use in the Monte Carlo simulation.

2.3.4 A FW-CADIS Example

The FW-CADIS methodology can be illustrated with the following example. Consider a Monte Carlo simulation that is performed to obtain the fast (E > 1 MeV) neutron flux in the RPV of the PWR reference model over an axial range that extends from the top of the lower head to the bottom of the closure head. The flux will be obtained using a cylindrical mesh tally in a Monte Carlo simulation. The first step of the FW-CADIS sequence is a discrete ordinates calculation that provides an estimate of the fast flux for the entire solution space. The inverse of the discrete ordinates forward flux is then used to weight an adjoint source that corresponds to the cylindrical mesh tally for the Monte Carlo simulation.

Using the adjoint source derived from the forward discrete ordinates solution, an adjoint discrete ordinates calculation is then run to construct the space-energy weight windows and the biased source for the Monte Carlo simulation.

Figure 2-7 illustrates the weight window lower bounds for two energy groups from the SCALE [42] 27N19G cross-section library that is often used for generating variance reduction parameters. (Recall from Eq. 10 that the weight window bounds are inversely proportional to the adjoint flux, so regions of high importance have correspondingly low weight window bounds.) The left side of the figure shows the weight window's lower bounds for neutrons with energies between 6.3763 and 20.0 MeV (group 1 of the 27-group structure). The right side shows the lower bounds for neutrons with energies between 0.90718 and 1.4227 MeV (group 5). It is clear from this figure that the higher energy neutrons are much more important in all regions of the model space and that they are attenuated much less rapidly. (Note that since weight window bounds are inversely proportional to the importance estimate provided by the adjoint flux, locations with higher weight window bounds are less likely to contribute to the tallies of interest.)

Because the outer regions of the core have higher importance with regard to contributions to the flux in the RPV, the spatial source distribution is biased so that more particles are sampled from the outer assemblies, with their source weights reduced to maintain an unbiased[6] simulation. Figure 2-8 shows the spatial distribution and particle weights for 10^6 source neutrons in an MCNP simulation. The left side of the figure shows the distribution for a case with no VR applied. As expected, all the source neutrons have a weight of 1.0, and they are distributed uniformly throughout the core for this example calculation, which has a spatially uniform source. The right side illustrates the spatial distribution for an MCNP simulation using variance reduction parameters from ADVANTG. The spatial distribution that will be sampled in the Monte Carlo simulation is strongly biased toward the outer assemblies, with the source weights being reduced by several orders of magnitude because of the higher sampling probability from the biased distribution. Only a few source points are sampled from the interior portion of the core, and their weights are increased by several orders of magnitude to offset their low sampling probability.

In addition to the spatial biasing of the source in the reactor core, the energy distribution is biased in a manner that is consistent with the weight windows. Figure 2-9 shows the adjoint flux spectra at five locations within the core. In addition to the decrease in the magnitude of the adjoint flux at locations further from the edge of the core, it is also clear that the spectrum of the adjoint flux changes significantly as a function of location. In particular, for the two locations furthest from the edge of the core (Locations 1 and 2), the variation in the spectrum is 10 orders of magnitude or more. This is consistent with the fact that neutrons born with energies in the lower part of the energy range of interest are much less likely to be transported from the inner assemblies to the RPV than neutrons born near the periphery of the core.

The effect of biasing the source in energy is illustrated in Figure 2-10. The left side of this figure shows the energy distribution for neutrons born with energies greater than 1 MeV when sampled from a Watt fission spectrum. The right side shows the energy distribution for the biased source. It can be seen that the source is biased toward higher energies, which is consistent with the greater importance of high-energy neutrons contributing to the fast neutron flux in the RPV.

[6] In Monte Carlo terminology, an unbiased simulation is sometimes referred to as a *fair game*.

The result of applying the weight windows and source biasing to a Monte Carlo simulation is illustrated in Figure 2-11. The left side of this figure shows the collision locations and particle weights for the small number of the 10^6 source neutrons that are transported to the RPV in a simulation with no variance reduction applied. Note that some of the particle weights are below 1.0, even though weight windows have not been applied. These variations are due to the use of the default implicit capture method in the MCNP simulation. The right side of the figure shows the collision locations and particle weights for the simulation using ADVANTG-generated weight windows and source biasing. Here it can be seen that there is an increase of several orders of magnitude in the number of particles experiencing collisions in the RPV, with all of those collisions occurring with particles whose weight has been reduced to provide an unbiased simulation.

2.3.5 Accuracy Considerations for the Discrete Ordinates Forward and Adjoint Calculations in Hybrid Calculations

One of the key factors of the hybrid radiation transport method is that the deterministic calculations performed to generate space-energy weight windows and source biasing parameters do not need to be highly accurate. Moderate-fidelity discrete ordinates calculations are capable of producing variance reduction parameters that are highly effective in reducing the computational time required to achieve well-converged Monte Carlo tallies. Consequently, the Denovo calculations that are run to generate variance reduction parameters with ADVANTG and Shift are typically performed using broad-group cross-section libraries and relatively coarse angular and spatial discretizations. This approach reduces the discrete ordinates run time and computational resource requirements (e.g., number of processors and amount of memory) while still providing highly effective variance reduction.

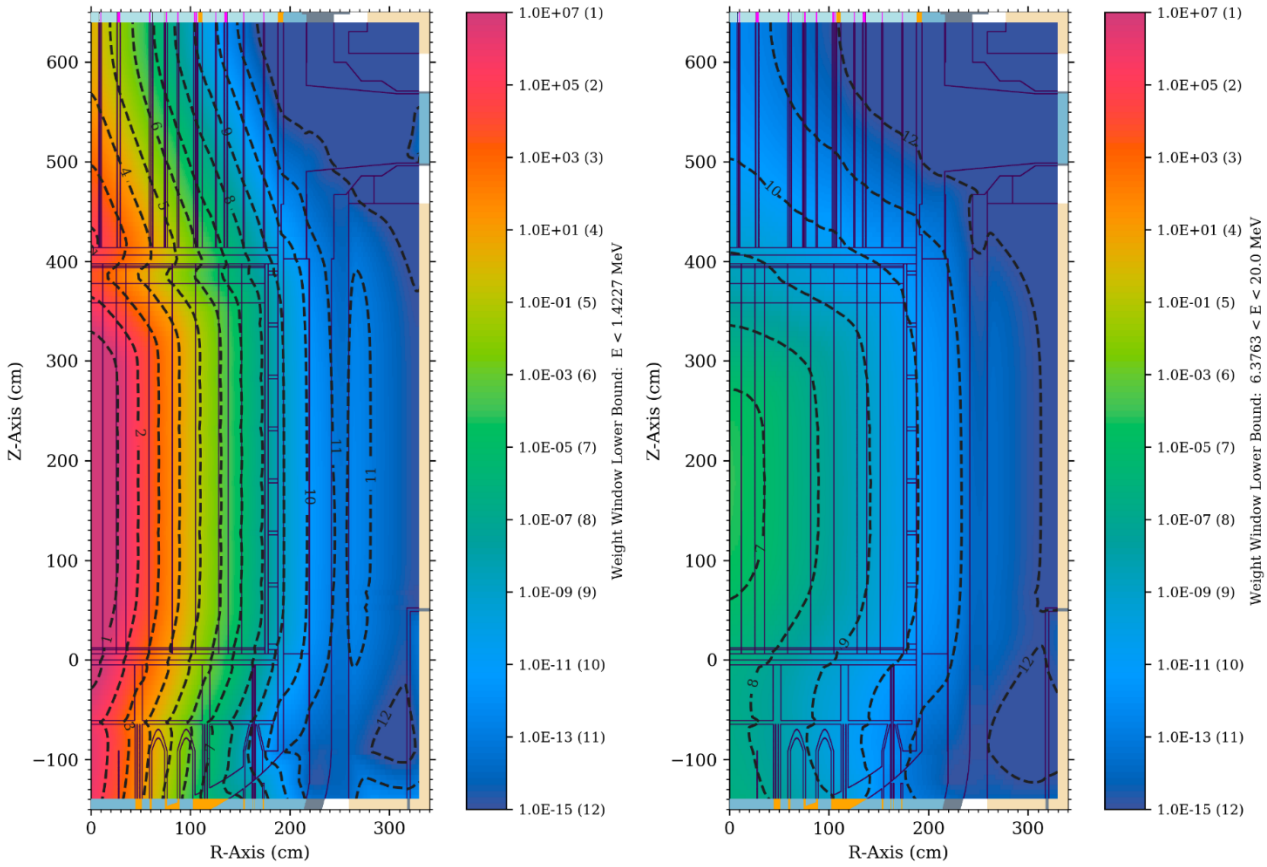

Figure 2-7 ADVANTG-generated weight-window lower bounds for neutrons with energies from 6.3763–20.0 MeV and for those with energies from 0.90718–1.4227 MeV *The adjoint source region for the ADVANTG calculation is the RPV, including the inlet and outlet nozzles, from Z=-100 cm to 648 cm.*

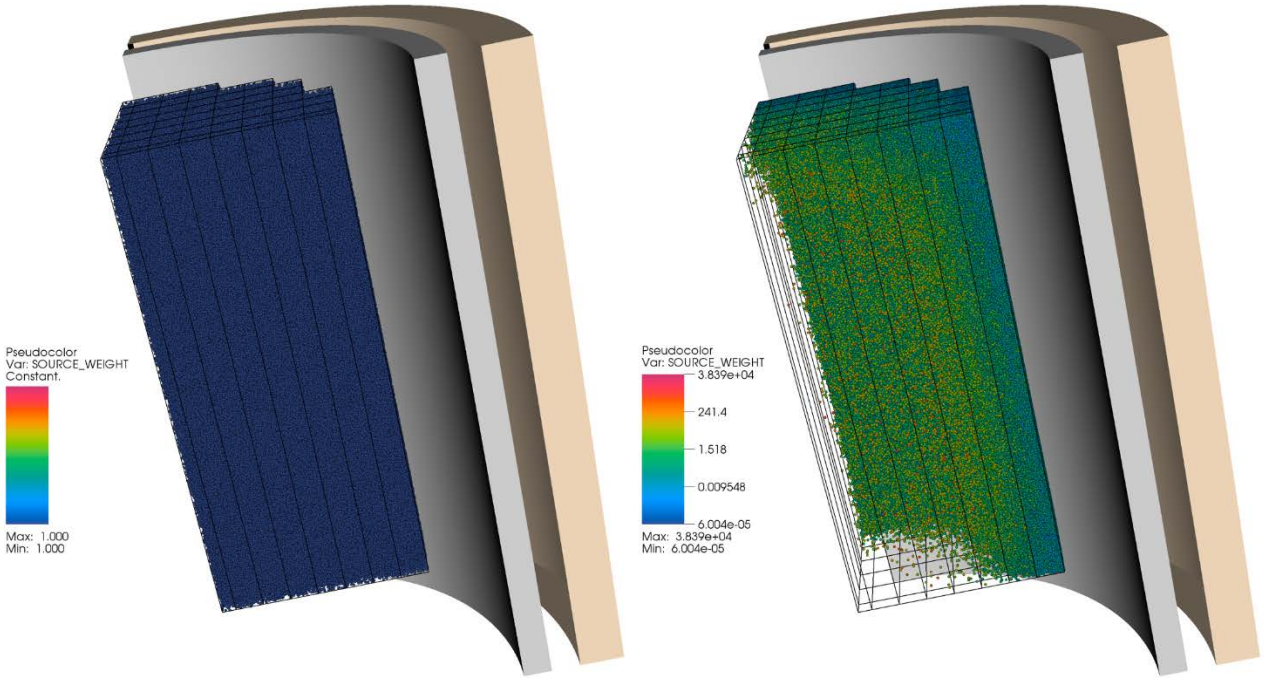

Figure 2-8 Spatial distribution and weights of 10^6 source neutrons for an analog MCNP simulation and an MCNP simulation using weight windows and source biasing generated by ADVANTG *The adjoint source region for the ADVANTG calculation is the RPV, including the inlet and outlet nozzles, from Z = -100 cm to 648 cm Note that the biased source samples are primarily from the outermost assemblies, which is consistent with the adjoint fluxes and weight windows shown in Figure 2-6 and Figure 2-7.*

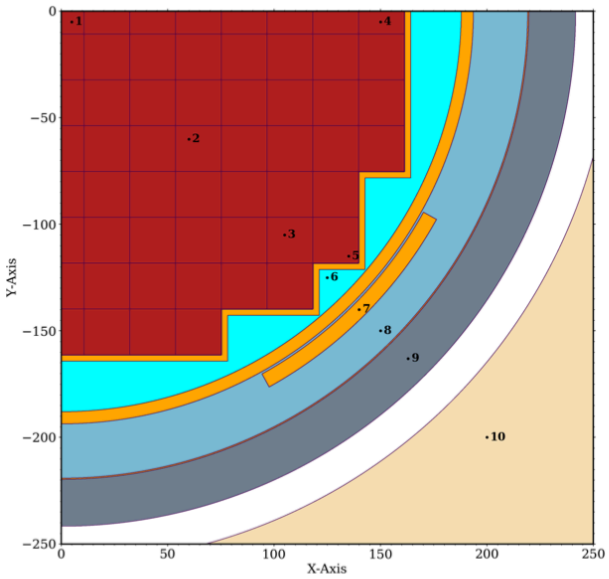

(a) Geometry plan view at z = 200 cm for the PWR reference model with homogenized assemblies. The location numbers correspond to the flux spectra shown in **(b)**.

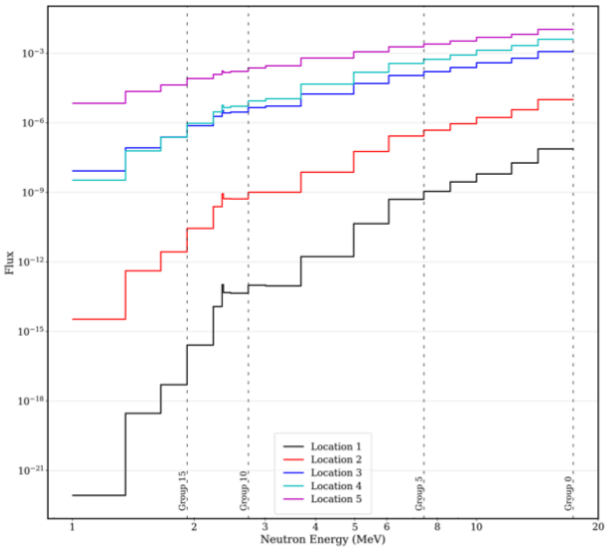

(b) Groupwise adjoint flux spectra at locations 1-5 from **(a)**. The adjoint source is uniform in energy throughout the RV. The group numbers correspond to the BUGLE-B7 group structure. The local peaks in each spectrum for the energy group from 2.3457 to 2.3653 MeV are caused by a resonance minimum in the O-16 cross section in that energy range.

Figure 2-9 Plan view of the PWR reference model with homogenized assemblies at Z = 200 cm, and the adjoint flux spectra at five locations in the core *The slight uptick in the adjoint flux spectrum in group 13 is due to an antiresonance in the ^{16}O scattering cross section.*

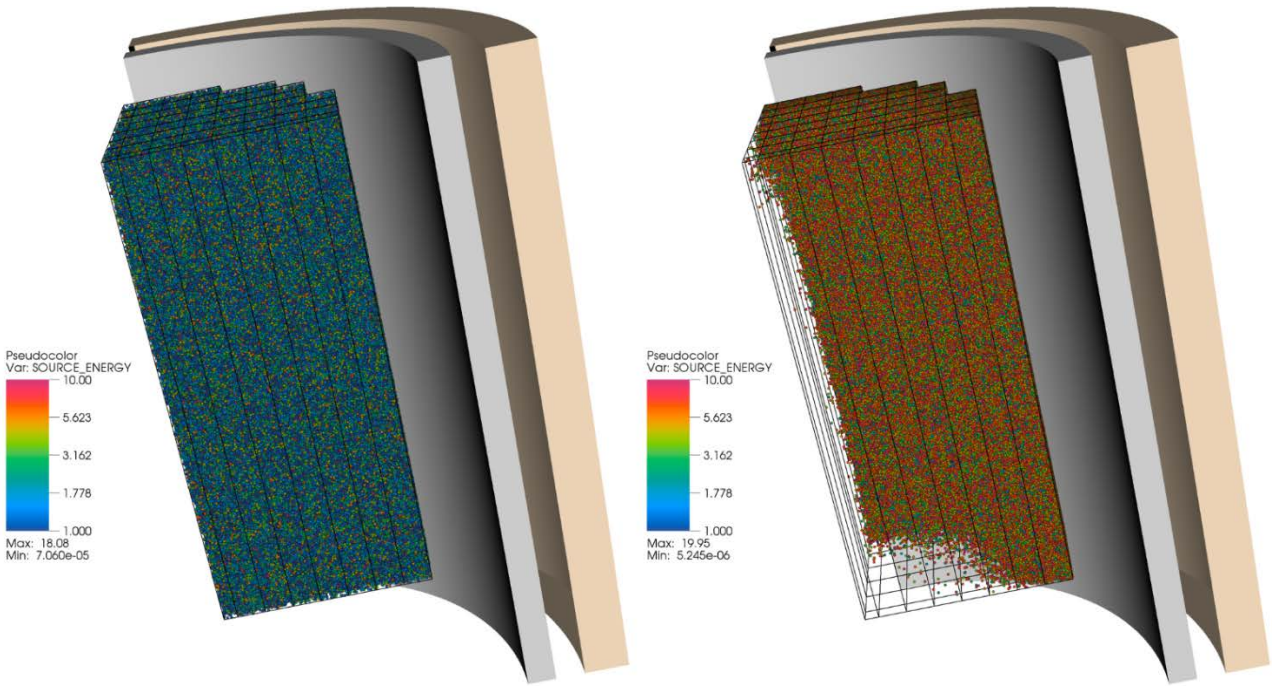

Figure 2-10 Spatial distribution and energies of 10^6 source neutrons for an analog MCNP simulation and an MCNP simulation using weight windows and source biasing generated by ADVANTG *The adjoint source region for the ADVANTG calculation is the RPV, including the inlet and outlet nozzles, from Z = -100 cm to 648 cm. Note that the biased source samples are primarily from the outermost assemblies, consistent with the adjoint fluxes and weight windows shown in Figure 2-6 and Figure 2-7.*

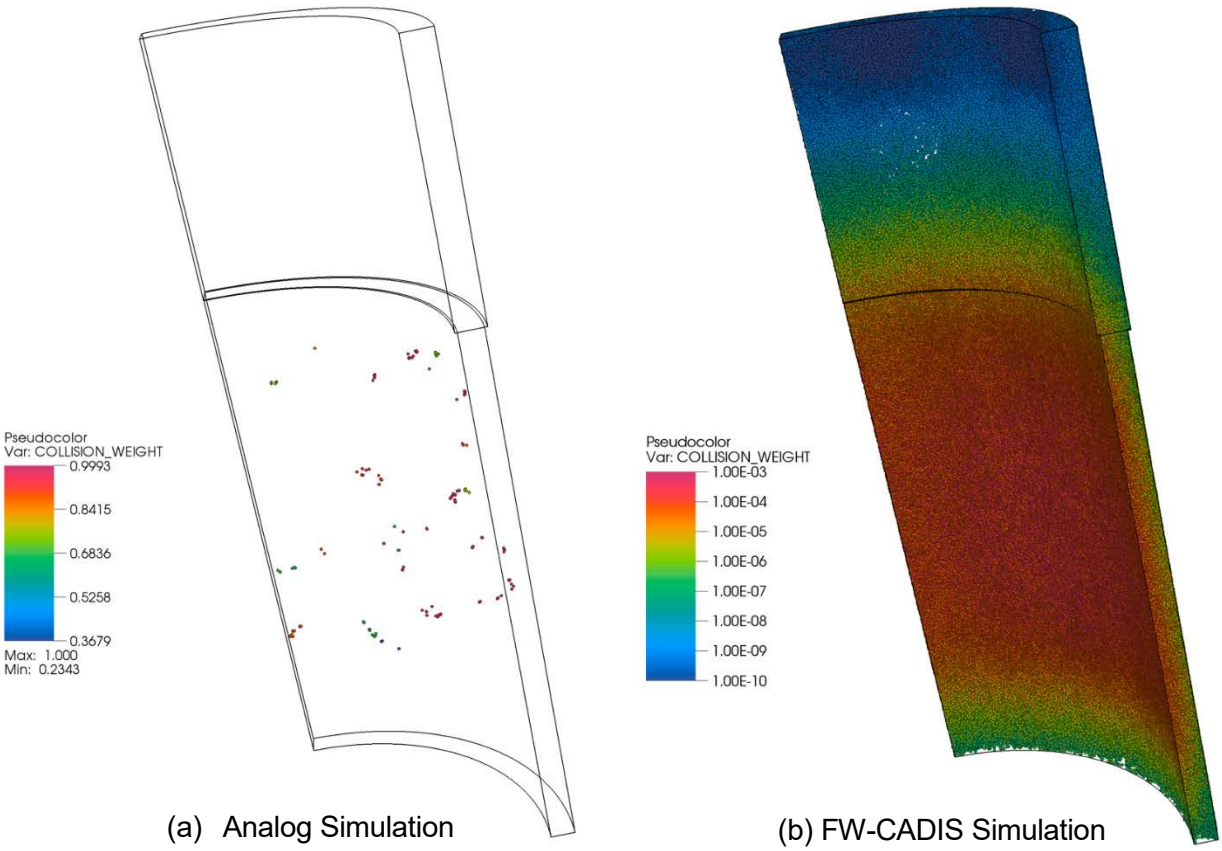

(a) Analog Simulation

(b) FW-CADIS Simulation

Figure 2-11 Spatial distribution and weights of fast (E > 1 MeV) neutrons that enter the RPV from the sampling of 10^6 source neutrons View (a) is for an analog simulation, and view (b) is for a simulation using weight windows and source biasing parameters from ADVANTG

2.4 Computer Codes Used in this Study

The radiation transport calculations used for the analyses in this report were performed using the deterministic and hybrid methods. The codes used for these calculations are briefly described in this section.

2.4.1 Deterministic Calculations

The deterministic calculations used for the work presented in this report, including the deterministic portion of all hybrid calculations, were performed using the Denovo code, which has superseded the 2D DORT and 3D TORT codes in the DOORS package [15]. Codes in the DOORS package were developed at ORNL but are no longer maintained. The final version of DOORS (DOORS3.2a) was released in May 2007. Denovo has been used for all subsequent discrete ordinates code development at ORNL.

While DORT and TORT support cylindrical and Cartesian geometries, Denovo is limited to Cartesian geometry. However, the use of mixed materials (Section 2.1.2) in Denovo reduces the solution artifacts that can occur with Cartesian representation of cylindrical surfaces, such as the inner and outer radius of the RPV, when no material mixing is performed. Comparison of Denovo and hybrid calculations (which provide exact modeling of both cylindrical and Cartesian geometry in the Monte Carlo calculation) in later sections of this report demonstrates that with adequate space, energy, and angular discretization, Denovo is capable of producing solutions that capture the peak fast fluence values at the inner surfaces of RPVs.

2.4.2 Hybrid Calculations

The hybrid calculations presented in this report were run using two hybrid sequences: MCNP/ADVANTG and Shift. In the first approach, the ADVANTG code is used to generate space-energy weight windows and a consistently biased source for use in MCNP Monte Carlo calculations. The deterministic portion of the hybrid sequence, which is driven by ADVANTG, uses the Denovo discrete ordinates code. After the variance reduction parameters are generated by ADVANTG, they are used in an MCNP calculation to obtain the final Monte Carlo solution.

When hybrid calculations are run using Shift, Denovo is first executed to generate the variance reduction parameters (weight windows and source biasing), as with the ADVANTG/MCNP sequence. Shift then runs a Monte Carlo simulation using those variance reduction parameters in the same manner as the ADVANTG/ MCNP sequence.

Because the deterministic calculations in a hybrid sequence only require moderate fidelity to generate effective variance reduction parameters, the Denovo calculations in the ADVANTG/MCNP hybrid sequence are typically performed with space, energy, and angular discretizations that are relatively coarse compared to what would be appropriate for a deterministic-only calculation.

3 LITERATURE REVIEW OF CALCULATIONAL METHODS USED FOR REACTOR PRESSURE VESSEL FLUENCE CALCULATIONS

The RPV fluence calculational methodologies developed by nuclear power industry companies that follow Regulatory Guide 1.190 and are approved by the NRC are predominantly based on the 2D/1D FLUX synthesis technique, which synthesizes 3D solutions from 2D and 1D calculations [44],[45],[46]. The 2D/1D flux synthesis technique has been shown to provide acceptable results when applied to RPV dosimetry at axial regions that directly surround the active core height. However, this methodology has limitations when used in the extended beltline region of the RPV. Recently, the 3D RAPTOR-M3G code [47] has been approved by the NRC as a fluence methodology for the RPV traditional beltline region.

There is no currently approved methodology for fluence analysis in the RPV extended beltline region. However, numerous 60-calendar-year NPP heat-up and cooldown limit curve reports have been submitted to the NRC that have used the 2D/1D fluence rate methodology in the RPV extended beltline region [48], [49], [50], [51], [52].

Recent NPP subsequent license renewal (SLR) applications for 80-calendar-year operation ([53], [54], [55]) have also used the 2D/1D fluence rate synthesis methodology in the RPV extended beltline region. Volume 2 of NUREG-2191 [56] states the following in Section X.M2:

> … The methods developed and approved using the guidance contained in RG 1.190 are specifically intended for determining neutron fluence in the region of the RPV close to the active fuel region of the core and are not intended to apply to vessel regions significantly above and below the active fuel region of the core, nor to RVI components. Therefore, the use of RG 1.190-adherent methods to estimate neutron fluence for the RPV regions significantly above and below the active fuel region of the core and RVI components may require additional justification, even if those methods were approved by the NRC for RPV neutron fluence calculations …

The following excerpts from the SLR applications provide a representative sample of the statements that were made to justify the use of the 2D/1D fluence rate synthesis methodology in the RPV extended beltline region:

> … End-of-license (life) 80-year fluence in PTN [Turkey Point] RPV regions above the active fuel region (e.g., in nozzle locations) are currently projected to exceed the 1×10^{17} n/cm^2 threshold prior to the end of the [subsequent period of extended operation] SPEO, whereas RPV locations below the active fuel region do not, as described in Section 4.2.1. FPL follows related industry efforts, such as those from the Pressurized Water Reactor Owners Group (PWROG), and will use the information from those efforts to provide additional justification for fluence determinations in those areas prior to entering the SPEO [53].

> … The methods and assumptions used for the original beltline region are considered appropriate for the beltline region that has been extended to encompass materials projected to experience fluence in excess of 1×10^{17} n/cm^2 (E > 1 MeV) at 70 EFPY, since the extended region does not extend significantly above or below the active fuel region and no additional reactor vessel plate materials (heat numbers) or welds are projected to experience fluence in excess of 1×10^{17} n/cm^2 (E > 1 MeV) … [55].

> … Some of the inlet and outlet nozzles are projected to experience neutron fluence in excess of 1×10^{17} n/cm^2. These inlet and outlet nozzles are treated as extended beltline material for subsequent license renewal … Studies to date have shown that the DORT model calculates fluence in the Z direction above the core more conservatively than three-dimensional models such as RAPTOR-M3G … The fluence projections used in the SLR application conservatively utilized a constant material mixture of 90% water and 10% steel above and below the core. A sensitivity study was performed to show that this assumption was conservative compared to an analysis based upon more representative plant specific material mixture data above and below the core" [54].

Publications focused on fluence calculations in the RPV extended beltline region or on RVI components above and below the core height are limited [57], [58], [59], [60], [61]. Hopkins et al. [57] present results from analysis of ex-vessel capsules in a PWR at nozzle support elevations using the 2D/1D fluence rate synthesis technique. Comparison of calculations to measurements demonstrates the limitations of this analysis methodology in the region of the nozzles and supports. In a paper by Chen et al. [58], 3D transport calculations and 2D/1D fluence rate synthesis calculations are compared at the core barrel inner and outer radii in a PWR. Their work concludes that the 2D/1D fluence rate synthesis technique cannot accurately capture some important details of 3D geometry. Even within the active core height, the 2D/1D fluence rate synthesis technique can provide inadequate results with complex geometries, such as RPV internal structures with irregular shapes. Lippincott and Manahan [59] demonstrate that in regions above and below the core of a BWR, the separability of the azimuthal and axial fluence rate shape in the 2D/1D fluence rate synthesis technique does not hold. Amiri et al. [60] present the results of a dosimetry evaluation that was performed for above-core zirconium alloy samples in a PWR. The results indicate that the use of core-averaged, cycle-specific axial power distributions can cause significant underestimation of fluence with the 2D/1D fluence rate synthesis technique. Fischer and Kim [61] performed retrospective dosimetry analysis for PWR top support plug samples from scrap surveillance capsule material. Their comparisons of measurements with calculations using the 3D RAPTOR-M3G code generally demonstrate good agreement.

An objective of the ongoing PWROG program is to qualify the fluence determination in the RPV extended beltline locations. This program involves collecting measurements in the RPV extended beltline regions of operating PWRs [62]. The measurement data collected from this PWROG program will provide valuable information for validating fluence methodologies in the RPV extended beltline region.

4 ANALYSIS MODELS

4.1 PWR Model

The PWR reference model is based on Watts Bar Nuclear Plant Unit 1 (WBN1). WBN1 is a Westinghouse four-loop design with a licensed power of 3,456 MWt. The fuel assemblies are a Westinghouse 17 × 17 design with three ^{235}U enrichments: 2.11, 2.619, and 3.1 wt%. Geometry and material specifications for the core were obtained from Godfrey [63]. Materials and dimensions for internal structures, the RPV, and the inlet and outlet nozzles were adopted from several sources [64],[65],[66],[67],[68],[69]. This four-loop model has quarter-core symmetry, and calculations were performed using a quarter-core model.

The model was developed using MCNP geometry. The MCNP model can be used to run MCNP with ADVANTG for hybrid radiation transport, Shift through Omnibus for hybrid radiation transport, and Denovo through Omnibus for deterministic calculations. Selected parameters in the PWR model are provided in Table 4-1. The material definitions are provided in Table 4-2.

Elevation and plan views of the PWR model are shown in Figure 4-1 through Figure 4-5.

Table 4-1 Selected model parameters for the PWR reference model

Parameter	Measurement
Thermal power	3,456 MW(t)
Core operating pressure	2,250 PSIA
Coolant temp:	
Inlet	559 °F
Outlet	622.5 °F
Core	592.5 °F
Baffle plate thickness	2.85 cm
Core barrel:	
Inner radius	187.96 cm
Outer radius	193.68 cm
Neutron pad:	
Inner radius	194.64 cm
Outer radius	201.63 cm
RPV liner inner radius:	
Below Z = 402.59 cm	219.15 cm
Above Z = 402.59 cm	216.45 cm
RPV inner radius:	
Below Z = 402.59 cm	219.71 cm
Above Z = 402.59 cm	217.01 cm
RPV outer radius:	
Below Z = 402.59 cm	241.7 cm
Above Z = 402.59 cm	244.32 cm
Bioshield inner radius:	
Below Z = 630.48 cm	259.08 cm
Above Z = 630.48 cm	277.73 cm

Table 4-2 Material definitions in the PWR reference model The isotope identifiers are of the form ZZAAA, where ZZ is the atomic number (e.g., 8 for oxygen) and AAA is the atomic mass (e.g., 16). The units are atoms/b·cm, where 1 b = 10^{-24} cm^2

Material	Density (g/cm^3)	Isotope	Atom density (atoms/b·cm)
UO_2 fuel; 2.11% enrichment	10.257	8016	4.5758E-02
		92234	4.0480E-06
		92235	4.8879E-04
		92236	2.2375E-06
		92238	2.2384E-02
UO_2 fuel; 2.619% enrichment	10.257	8016	4.5760E-02
		92234	5.0949E-06
		92235	6.0671E-04
		92236	2.7680E-06
		92238	2.2266E-02
UO_2 fuel; 3.1% enrichment	10.257	8016	4.5763E-02
		92234	6.1184E-06
		92235	7.1811E-04
		92236	3.2985E-06
		92238	2.2154E-02
Zircaloy 4	6.56	24050	3.3011E-06
		24052	6.3658E-05
		24053	7.2184E-06
		24054	1.7968E-06
		26054	8.6828E-06
		26056	1.3630E-04
		26057	3.1478E-06
		26058	4.1891E-07
		40090	2.1886E-02
		40091	4.7728E-03
		40092	7.2953E-03
		40094	7.3931E-03
		40096	1.1911E-03
		50112	4.6805E-06
		50114	3.1847E-06
		50115	1.6406E-06
		50116	7.0159E-05
		50117	3.7058E-05
		50118	1.1687E-04
		50119	4.1449E-05
		50120	1.5721E-04
		50122	2.2341E-05
		50124	2.7938E-05
		72174	3.5413E-09
		72176	1.1642E-07
		72177	4.1167E-07
		72178	6.0379E-07
		72179	3.0145E-07
		72180	7.7642E-07

Table 4-2. Material definitions in the PWR reference model (continued)

Material	Density (g/cm^3)	Isotope	Atom density (atoms/b·cm)
Inconel	8.19	14028	4.0487E-03
		14029	2.0568E-04
		14030	1.3574E-04
		22046	2.1251E-04
		22047	1.9165E-04
		22048	1.8989E-03
		22049	1.3936E-04
		22050	1.3343E-04
		24050	6.1820E-04
		24052	1.1921E-02
		24053	1.3518E-03
		24054	3.3649E-04
		26054	3.6134E-04
		26056	5.6723E-03
		26057	1.3100E-04
		26058	1.7433E-05
		28058	4.1759E-02
		28060	1.6086E-02
		28061	6.9923E-04
		28062	2.2295E-03
		28064	5.6778E-04
Stainless steel 304	8.0	6012	3.1745E-04
		6013	3.4334E-06
		14028	1.5819E-03
		14029	8.0363E-05
		14030	5.3038E-05
		15031	6.9991E-05
		24050	7.6489E-04
		24052	1.4750E-02
		24053	1.6725E-03
		24054	4.1633E-04
		25055	1.7538E-03
		26054	3.4476E-03
		26056	5.4121E-02
		26057	1.2499E-03
		26058	1.6634E-04
		28058	5.3084E-03
		28060	2.0448E-03
		28061	8.8885E-05
		28062	2.8340E-04
		28064	7.2175E-05

Table 4-2. Material definitions in the PWR reference model (continued)

Material	Density (g/cm^3)	Isotope	Atom density (atoms/b·cm)
Low-Alloy carbon steel (RPV)	7.7879	6012	9.7048E-04
		6013	1.0496E-05
		14028	3.4216E-04
		14029	1.7326E-05
		14030	1.1501E-05
		24050	5.5180E-06
		24052	1.0641E-04
		24053	1.2065E-05
		24054	3.0035E-06
		25055	1.1200E-03
		26054	4.8320E-03
		26056	7.5117E-02
		26057	1.7199E-03
		26058	2.2931E-04
		28058	3.0311E-04
		28060	1.1588E-04
		28061	5.0171E-06
		28062	1.5940E-05
		28064	4.0403E-06
Pyrex	2.2458	5010	9.6145E-04
		5011	3.8944E-03
		8016	4.6688E-02
		14028	1.8164E-02
		14029	9.2273E-04
		14030	6.0898E-04
B_4C	1.76	5010	1.5269E-02
		5011	6.1458E-02
		6012	1.8976E-02
		6013	2.0524E-04
AgInCd	10.2	47107	2.3616E-02
		47109	2.1940E-02
		48106	3.4152E-05
		48108	2.4316E-05
		48110	3.4124E-04
		48111	3.4971E-04
		48112	6.5927E-04
		48113	3.3387E-04
		48114	7.8494E-04
		48116	2.0464E-04
		49113	3.4426E-04
		49115	7.6804E-03

Table 4-2. Material definitions in the PWR reference model (continued)

Material	Density (g/cm^3)	Isotope	Atom density (atoms/b·cm)
Upper core plate support column and control rod guide tube	5.581	1001	1.6540E-02
		5010	3.5277E-06
		5011	1.4199E-05
		6012	2.1163E-04
		6013	2.2890E-06
		8016	8.2701E-03
		14028	1.0546E-03
		14029	5.3575E-05
		14030	3.5358E-05
		15031	4.6661E-05
		24050	5.0993E-04
		24052	9.8334E-03
		24053	1.1150E-03
		24054	2.7756E-04
		25055	1.1692E-03
		26054	2.2984E-03
		26056	3.6080E-02
		26057	8.3326E-04
		26058	1.1089E-04
		28058	3.5389E-03
		28060	1.3632E-03
		28061	5.9257E-05
		28062	1.8894E-04
		28064	4.8116E-05
Type 04 concrete	2.35	1001	7.7679E-03
		8016	4.4081E-02
		11023	1.0479E-03
		12024	1.1744E-04
		12025	1.4868E-05
		12026	1.6370E-05
		13027	2.3884E-03
		14028	1.4675E-02
		14029	7.4547E-04
		14030	4.9199E-04
		16032	5.3526E-05
		16033	4.2261E-07
		16034	2.3948E-06
		16036	5.6349E-09
		19039	6.4646E-04
		19040	8.1103E-08
		19041	4.6653E-05
		20040	2.8262E-03
		20042	1.8862E-05
		20043	3.9357E-06
		20044	6.0814E-05
		20046	1.1661E-07

Table 4-2. Material definitions in the PWR reference model (continued)

Material	Density (g/cm^3)	Isotope	Atom density (atoms/b·cm)
Type 04 concrete (continued)		20048	5.4518E-06
		26054	1.8281E-05
		26056	2.8697E-04
		26057	6.6274E-06
		26058	8.8198E-07
Homogenized top nozzle	3.9041	1001	2.6768E-02
		2004	3.6442E-09
		5010	2.1140E-05
		5011	7.5484E-06
		6012	1.1046E-04
		6013	1.1947E-06
		8016	1.3384E-02
		14028	5.5045E-04
		14029	2.7963E-05
		14030	1.8455E-05
		15031	2.4355E-05
		24050	2.6615E-04
		24052	5.1325E-03
		24053	5.8199E-04
		24054	1.4487E-04
		25055	6.1027E-04
		26054	1.1997E-03
		26056	1.8832E-02
		26057	4.3492E-04
		26058	5.7879E-05
		28058	1.8471E-03
		28060	7.1151E-04
		28061	3.0929E-05
		28062	9.8615E-05
		28064	2.5114E-05
		47107	1.6658E-03
		47109	1.5476E-03
		48106	2.4090E-06
		48108	1.7152E-06
		48110	2.4071E-05
		48111	2.4668E-05
		48112	4.6503E-05
		48113	2.3550E-05
		48114	5.5369E-05
		48116	1.4435E-05
		49113	2.4283E-05
		49115	5.4176E-04

Table 4-2. Material definitions in the PWR reference model (continued)

Material	Density (g/cm^3)	Isotope	Atom density (atoms/b·cm)
Homogenized bottom nozzle	3.6885	1001	2.7718E-02
		5010	5.9117E-06
		5011	2.3795E-05
		6012	1.2989E-04
		6013	1.4049E-06
		8016	1.3859E-02
		14028	6.4729E-04
		14029	3.2883E-05
		14030	2.1702E-05
		15031	2.8639E-05
		24050	3.1298E-04
		24052	6.0355E-03
		24053	6.8438E-04
		24054	1.7036E-04
		25055	7.1763E-04
		26054	1.4107E-03
		26056	2.2145E-02
		26057	5.1143E-04
		26058	6.8062E-05
		28058	2.1721E-03
		28060	8.3669E-04
		28061	3.6370E-05
		28062	1.1596E-04
		28064	2.9533E-05
Inlet coolant	0.7419	1001	4.9548E-02
		5010	1.0568E-05
		5011	4.2535E-05
		8016	2.4774E-02
Core average coolant	0.7025	1001	4.6917E-02
		5010	1.0006E-05
		5011	4.0276E-05
		8016	2.3458E-02
Outlet coolant	0.6584	1001	4.3971E-02
		5010	9.3782E-06
		5011	3.7748E-05
		8016	2.1986E-02

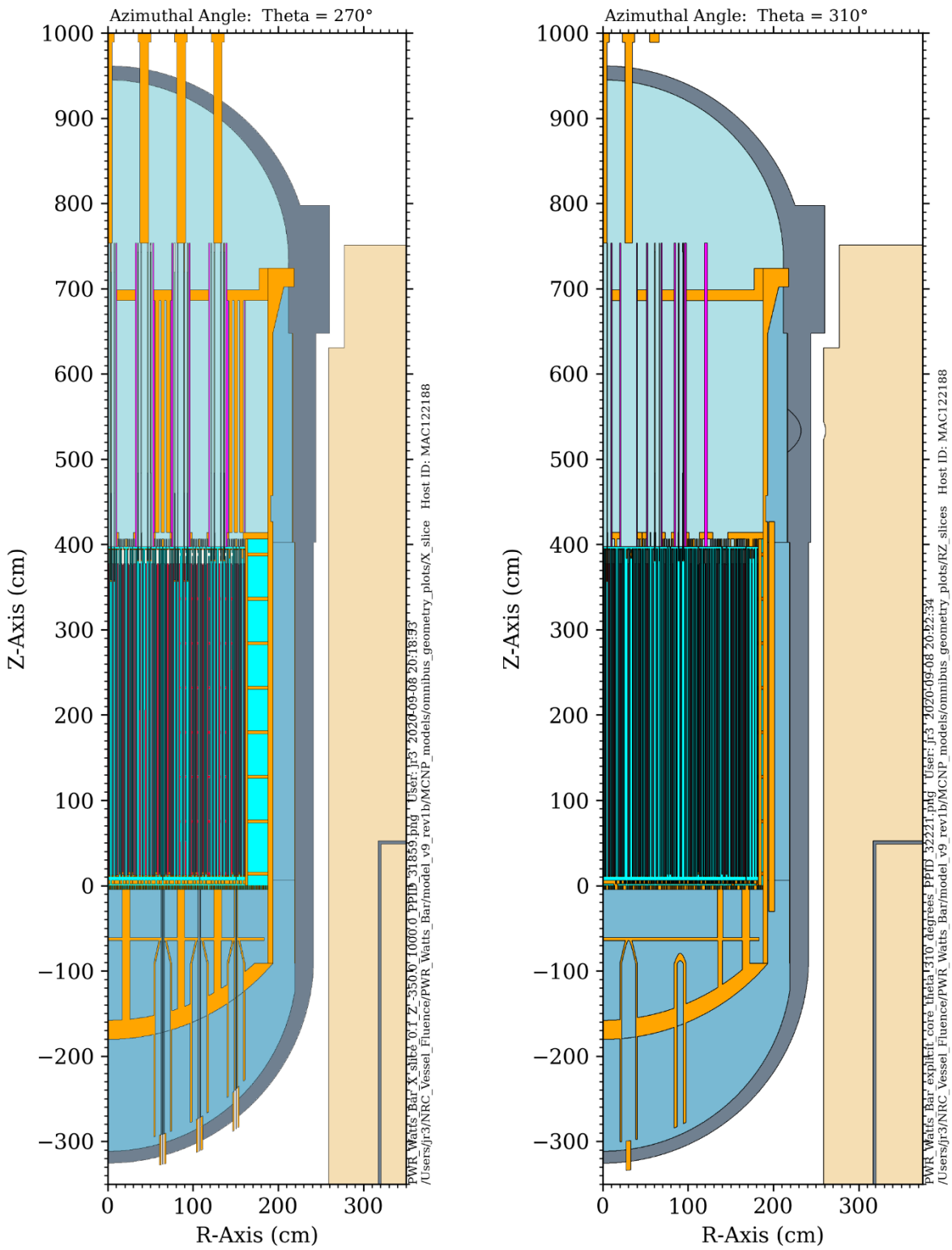

Figure 4-1 Elevation views of the PWR model at azimuthal angles of 270° and 310° *These are the azimuthal locations with the maximum and minimum amounts of water, respectively, between the core and the RPV.*

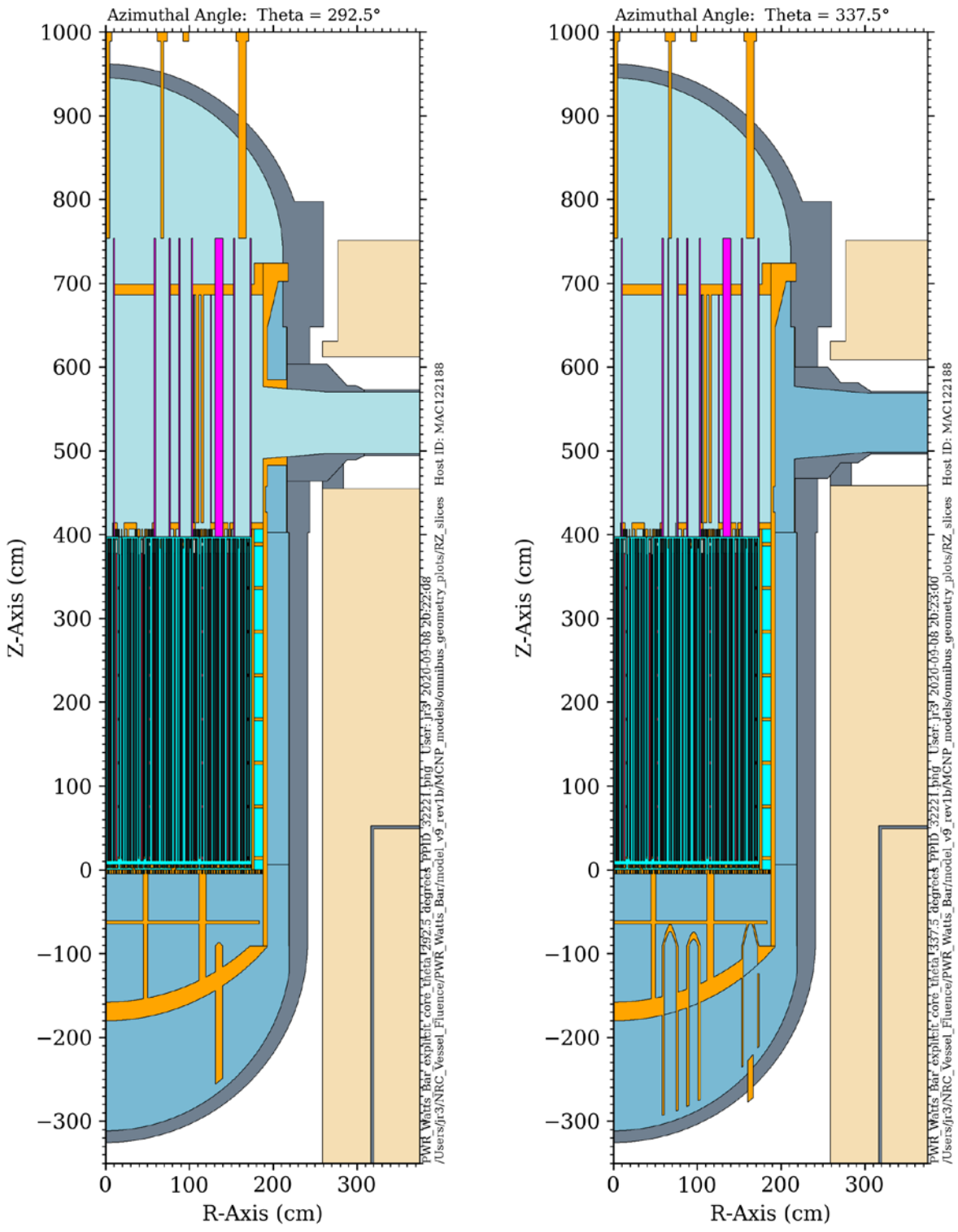

Figure 4-2 Elevation views of the PWR model at azimuthal angles of 292.5° and 337.5°
These are the azimuthal locations of the outlet and inlet nozzles, respectively.

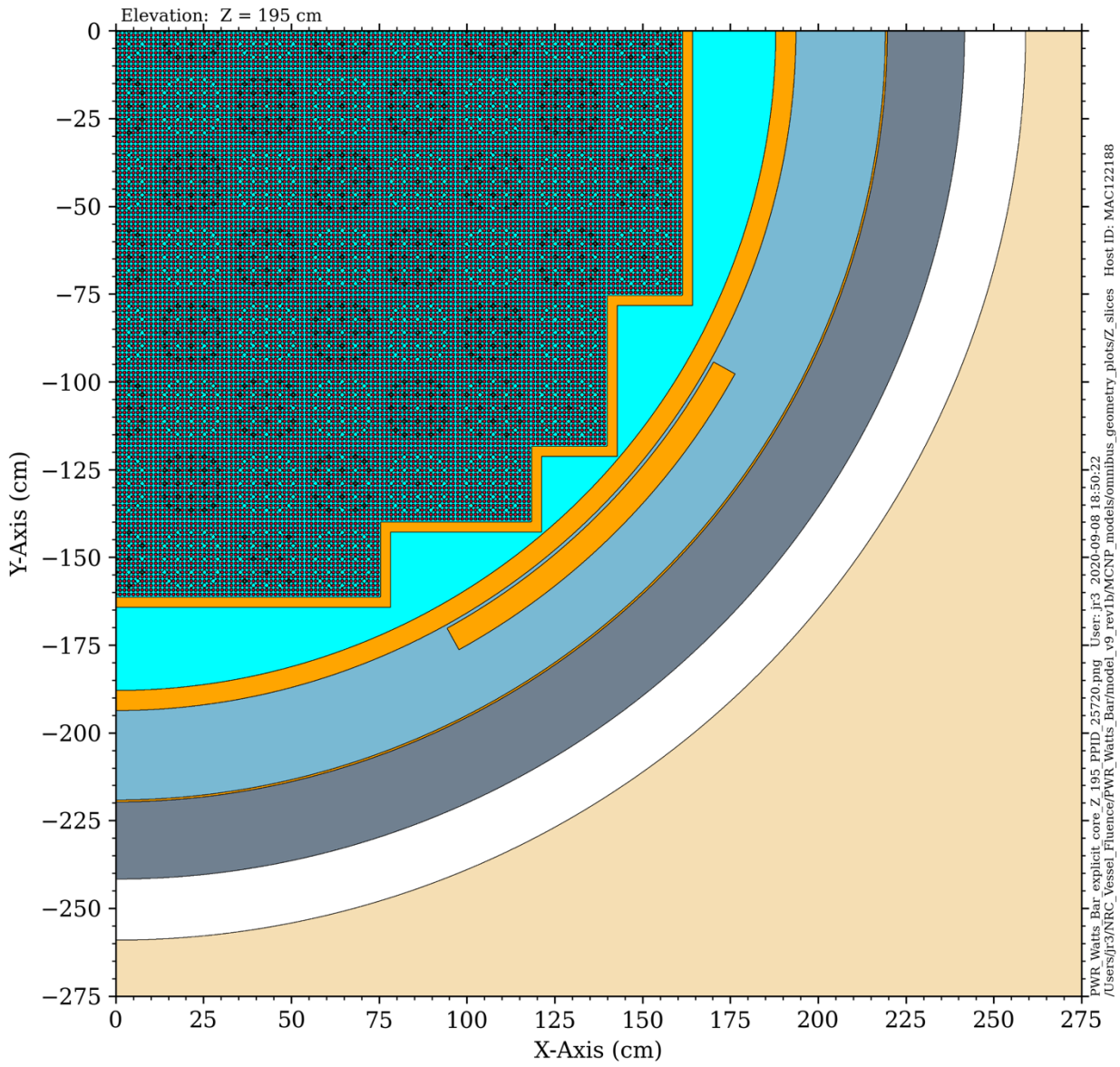

Figure 4-3 Plan view of the PWR model at the core midplane (Z = 195 cm)

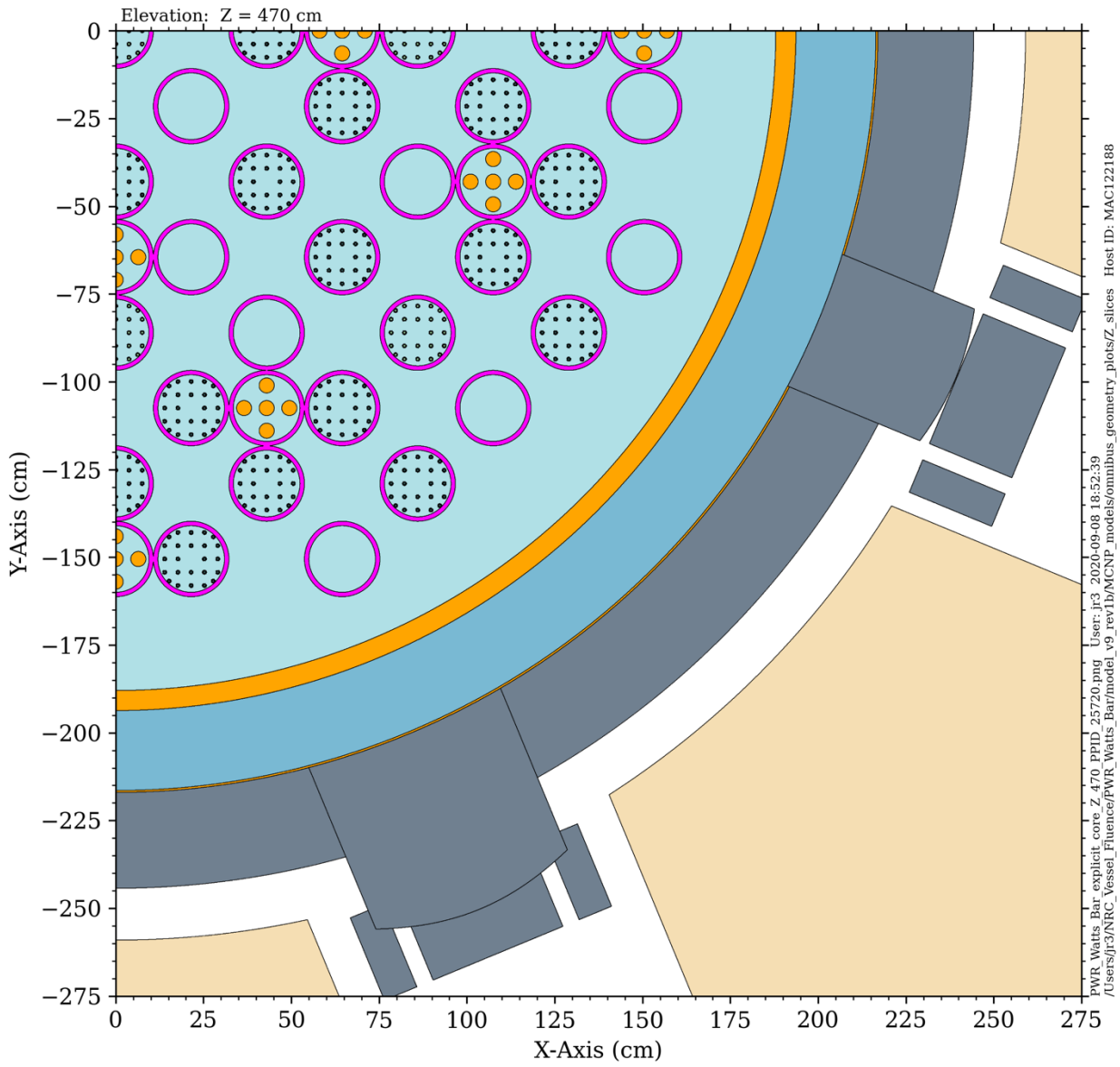

Figure 4-4 Plan view of the PWR model at an elevation of Z = 470 cm *This elevation intersects the vessel supports and the bottom portion of the inlet and outlet nozzles.*

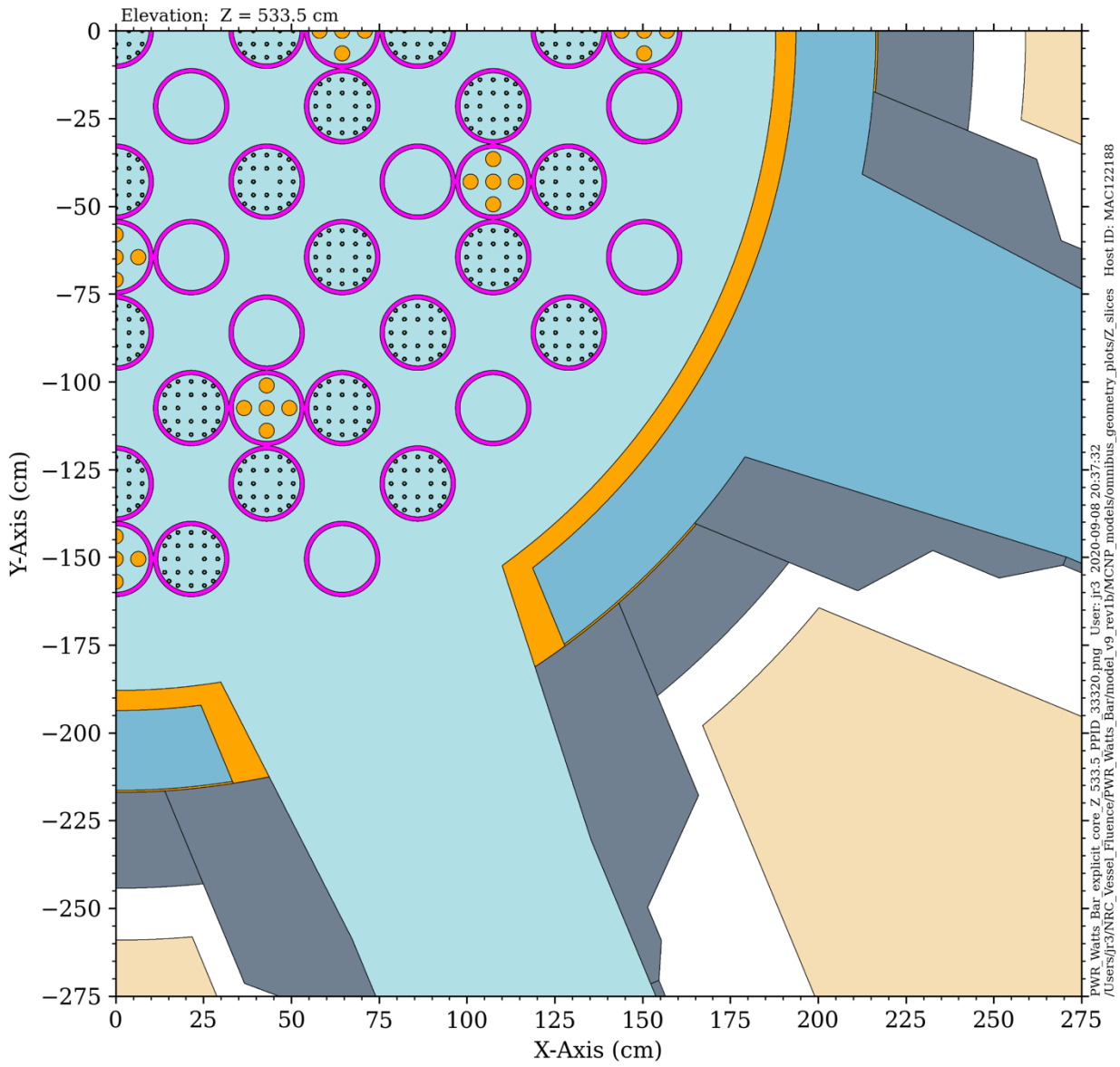

Figure 4-5 Plan view of the PWR model at an elevation of Z = 533.5 cm *This elevation is through the centerline of the inlet and outlet nozzles.*

4.2 BWR Model

The BWR reference model is based on Hatch Unit 2, which is a GE-4 design with a licensed power of 2,804 MWt. Modeling dimensions and materials were taken from NUREG/CR-6115 [70] and the Hatch Nuclear Plant Unit No. 2 Updated Final Safety Analysis Report [71]. The initial model used a core design with fuel assemblies based on a GE 7 × 7 design with four different ^{235}U enrichments. An update to the model during the course of the project replaced the 7 × 7 assembly design with the GE14 design, which has a 10 × 10 lattice. Figure 4-6 shows a typical fuel lattice arrangement in the GE14 assembly design [72]. This design has seven ^{235}U enrichment levels, as well as natural uranium. There are seven axial zones: natural uranium at the bottom of each rod (NAT), the power shaping zone (PSZ), the dominant zone (DOM), the plenum zone (PLE), the vanished rod zone (VAN), the natural uranium vanished rod zone (N-V), and the natural uranium top zone (N-T). Some fuel pins in the PSZ, DOM, PLE, and VAN zones contain Gd as a burnable poison. Void fractions (VFs) in the fuel assembly axial zones are discussed in the parameter study of Section 5.4. The baseline model uses average VFs based on data from NUREG/CR-7224 [73].

The model was developed using MCNP geometry. The MCNP model can be used to run MCNP with ADVANTG for hybrid radiation transport, Shift through Omnibus for hybrid radiation transport, and Denovo through Omnibus for deterministic calculations. Key dimensions in the BWR model are provided in Table 4-3. The material definitions are provided in Table 4-4.

Elevation and plan views of the BWR model are shown in Figure 4-7 through Figure 4-13. Full- and quarter-core models were constructed. Because the model has quarter-core symmetry at elevations below the feedwater inlet nozzle, quarter-core calculations were performed to reduce memory and CPU requirements for the MCNP, Shift, and Denovo calculations.

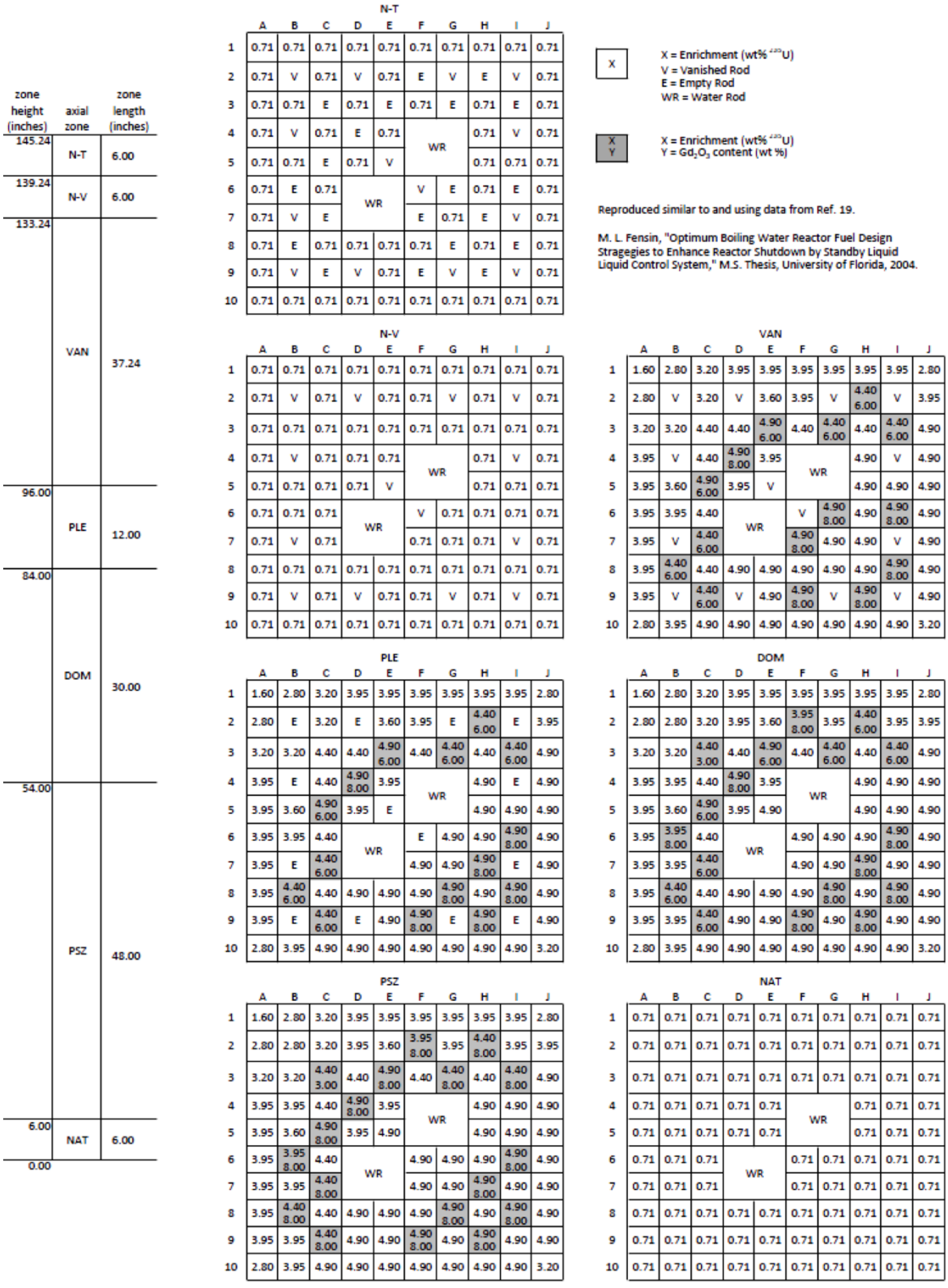

Figure 4-6 Typical GE14 10 × 10 fuel lattice

Table 4-3 Selected model parameters for the BWR reference model

Parameter	Measurement
Thermal power	2,804 MW(t)
Core operating pressure	1,246 PSIA
Coolant temp	
Feedwater inlet	425.8 °F
Recirc pump suction	534 °F
Recirc pump discharge	535 °F
Core inlet	534.6 °F
Core outlet	553.3 °F
Steam dome	551.8 °F
Shroud	
Inner radius	222.32 cm
Outer radius	225.50 cm
RPV	
Liner inner radius	277.34 cm
Inner radius	278.13 cm
Outer radius	293.05 cm
Concrete bioshield	
Inner radius	309.05 cm
Thickness*	30.48 cm

* The thickness used in the calculations.

Table 4-4 Material definitions in the BWR reference model

Material	Density (g/cm^3)	Isotope	Atom density (atoms/b·cm)
UO_2 fuel; 0.71% enrichment	10.5	8016	4.6848E-02
		92234	1.5054E-06
		92235	1.6842E-04
		92236	7.7146E-07
		92238	2.3253E-02
UO_2 fuel; 1.6% enrichment	10.4	8016	4.6394E-02
		92234	3.3591E-06
		92235	3.7582E-04
		92236	1.7214E-06
		92238	2.2816E-02
UO_2 fuel; 2.8% enrichment	10.4	8016	4.6400E-02
		92234	5.8783E-06
		92235	6.5767E-04
		92236	3.0124E-06
		92238	2.2533E-02
UO_2 fuel; 3.2% enrichment	10.4	8016	4.6402E-02
		92234	6.7181E-06
		92235	7.5162E-04
		92236	3.4428E-06
		92238	2.2439E-02
UO_2 fuel; 3.6% enrichment	10.4	8016	4.6404E-02
		92234	7.5578E-06
		92235	8.4556E-04
		92236	3.8731E-06
		92238	2.2345E-02
UO_2 fuel; 3.95% enrichment	10.4	8016	4.6406E-02
		92234	8.2925E-06
		92235	9.2777E-04
		92236	4.2496E-06
		92238	2.2263E-02
UO_2 fuel; 4.4% enrichment	10.4	8016	4.6408E-02
		92234	9.2372E-06
		92235	1.0335E-03
		92236	4.7337E-06
		92238	2.2157E-02
UO_2 fuel; 4.9% enrichment	10.4	8016	4.6411E-02
		92234	1.0287E-05
		92235	1.1509E-03
		92236	5.2716E-06
		92238	2.2039E-02

Table 4-4 Material definitions in the BWR reference model (continued)

Material	Density (g/cm^3)	Isotope	Atom density (atoms/b·cm)
UO_2 fuel; 3.95% enrichment	10.26	8016	4.6210E-02
8.0 wt% Gd_2O_3		64152	5.4544E-06
		64154	5.9453E-05
		64155	4.0363E-04
		64156	5.5826E-04
		64157	4.2681E-04
		64158	6.7744E-04
		64160	5.9616E-04
		92234	7.5264E-06
		92235	8.4206E-04
		92236	3.8570E-06
		92238	2.0206E-02
UO_2 fuel; 4.4% enrichment	10.26	8016	4.5944E-02
3.0 wt% Gd_2O_3		64152	2.0454E-06
		64154	2.2295E-05
		64155	1.5136E-04
		64156	2.0935E-04
		64157	1.6005E-04
		64158	2.5404E-04
		64160	2.2356E-04
		92234	8.8394E-06
		92235	9.8896E-04
		92236	4.5299E-06
		92238	2.1203E-02
UO_2 fuel; 4.4% enrichment	10.26	8016	4.6105E-02
6.0 wt% Gd_2O_3		64152	4.0908E-06
		64154	4.4590E-05
		64155	3.0272E-04
		64156	4.1869E-04
		64157	3.2010E-04
		64158	5.0808E-04
		64160	4.4712E-04
		92234	8.5661E-06
		92235	9.5837E-04
		92236	4.3898E-06
		92238	2.0547E-02

Table 4-4 Material definitions in the BWR reference model (continued)

Material	Density (g/cm^3)	Isotope	Atom density (atoms/b·cm)
UO_2 fuel; 4.4% enrichment	10.26	8016	4.6212E-02
8.0 wt% Gd_2O_3		64152	5.4544E-06
		64154	5.9453E-05
		64155	4.0362E-04
		64156	5.5826E-04
		64157	4.2681E-04
		64158	6.7744E-04
		64160	5.9616E-04
		92234	8.2291E-06
		92235	9.3798E-04
		92236	4.2964E-06
		92238	2.0110E-02
UO_2 fuel; 4.9% enrichment	10.26	8016	4.6107E-02
6.0 wt% Gd_2O_3		64152	4.0908E-06
		64154	4.4590E-05
		64155	3.0272E-04
		64156	4.1869E-04
		64157	3.2010E-04
		64158	5.0808E-04
		64160	4.4712E-04
		92234	9.4481E-06
		92235	1.0673E-03
		92236	4.8886E-06
		92238	2.0438E-02
UO_2 fuel; 4.9% enrichment	10.26	8016	4.6214E-02
8.0 wt% Gd_2O_3		64152	5.4544E-06
		64154	5.9453E-05
		64155	4.0363E-04
		64156	5.5826E-04
		64157	4.2681E-04
		64158	6.7744E-04
		64160	5.9616E-04
		92234	9.3364E-06
		92235	1.0446E-03
		92236	4.7846E-06
		92238	2.0003E-02
B_4C	1.7643	5010	1.5306E-02
		5011	6.1610E-02
		6012	1.9023E-02
		6013	2.0575E-04
Al_2O_3	3.97	8016	7.0363E-02
		13027	4.6895E-02

Table 4-4 Material definitions in the BWR reference model (continued)

Material	Density (g/cm^3)	Isotope	Atom density (atoms/b·cm)
Zircaloy-2	6.56	24050	3.3012E-06
		24052	6.3660E-05
		24053	7.2185E-06
		24054	1.7968E-06
		26054	5.5819E-06
		26056	8.7624E-05
		26057	2.0236E-06
		26058	2.6931E-07
		28058	2.5201E-05
		28060	9.7075E-06
		28061	4.2198E-07
		28062	1.3454E-06
		28064	3.4265E-07
		40090	2.1891E-02
		40091	4.7738E-03
		40092	7.2969E-03
		40094	7.3947E-03
		40096	1.1913E-03
		50112	4.6806E-06
		50114	3.1847E-06
		50115	1.6406E-06
		50116	7.0161E-05
		50117	3.7059E-05
		50118	1.1687E-04
		50119	4.1450E-05
		50120	1.5721E-04
		50122	2.2341E-05
		50124	2.7939E-05
		72174	3.5412E-09
		72176	1.1642E-07
		72177	4.1167E-07
		72178	6.0378E-07
		72179	3.0145E-07
		72180	7.7642E-07
Zircaloy-4	6.56	24050	3.3012E-06
		24052	6.3660E-05
		24053	7.2185E-06
		24054	1.7968E-06
		26054	8.6829E-06
		26056	1.3630E-04
		26057	3.1478E-06
		26058	4.1892E-07
		40090	2.1888E-02
		40091	4.7733E-03
		40092	7.2961E-03

Table 4-4 Material definitions in the BWR reference model (continued)

Material	Density (g/cm^3)	Isotope	Atom density (atoms/b·cm)
Zircaloy-4 (continued)		40094	7.3940E-03
		40096	1.1912E-03
		50112	4.6806E-06
		50114	3.1847E-06
		50115	1.6406E-06
		50116	7.0160E-05
		50117	3.7059E-05
		50118	1.1687E-04
		50119	4.1450E-05
		50120	1.5721E-04
		50122	2.2341E-05
		50124	2.7939E-05
Stainless steel 304	8.0	6012	3.1774E-04
		6013	3.4366E-06
		14028	3.1641E-03
		14029	1.6067E-04
		14030	1.0591E-04
		15031	6.2216E-05
		16032	5.7049E-05
		16033	4.5673E-07
		16034	2.5781E-06
		16036	1.2019E-08
		24050	7.8503E-04
		24052	1.5139E-02
		24053	1.7166E-03
		24054	4.2730E-04
		25055	1.3154E-03
		26054	3.3955E-03
		26056	5.3302E-02
		26057	1.2310E-03
		26058	1.6382E-04
		28058	5.3085E-03
		28060	2.0448E-03
		28061	8.8886E-05
		28062	2.8341E-04
		28064	7.2176E-05

Table 4-4 Material definitions in the BWR reference model (continued)

Material	Density (g/cm^3)	Isotope	Atom density (atoms/b·cm)
Low-alloy carbon steel (RPV)	7.7879	6012	9.7048E-04
		6013	1.0496E-05
		14028	3.4216E-04
		14029	1.7326E-05
		14030	1.1501E-05
		24050	5.5181E-06
		24052	1.0641E-04
		24053	1.2065E-05
		24054	3.0035E-06
		25055	1.1200E-03
		26054	4.8320E-03
		26056	7.5117E-02
		26057	1.7199E-03
		26058	2.2932E-04
		28058	3.0311E-04
		28060	1.1588E-04
		28061	5.0171E-06
		28062	1.5940E-05
		28064	4.0403E-06
Jet pumps, risers	7.9273	24050	6.7422E-04
		24052	1.3002E-02
		24053	1.4742E-03
		24054	3.6698E-04
		26054	3.7636E-03
		26056	5.8508E-02
		26057	1.3396E-03
		26058	1.7862E-04
		28058	4.7081E-03
		28060	1.8000E-03
		28061	7.7929E-05
		28062	2.4758E-04
		28064	6.2756E-05
Upper axial reflector	2.5675	1001	9.8222E-03
		6012	3.7936E-05
		6013	4.1031E-07
		8016	4.9112E-03
		14028	1.3326E-04
		14029	6.7477E-06
		14030	4.4792E-06
		24050	1.2247E-04
		24052	2.3590E-03
		24053	2.6746E-04
		24054	6.6582E-05
		25055	2.4594E-04
		26054	5.5654E-04
		26056	8.6518E-03

Table 4-4 Material definitions in the BWR reference model (continued)

Material	Density (g/cm^3)	Isotope	Atom density (atoms/b·cm)
Upper axial reflector (cont.)		26057	1.9809E-04
		26058	2.6412E-05
		28058	9.4444E-04
		28060	3.6106E-04
		28061	1.5632E-05
		28062	4.9644E-05
		28064	1.2589E-05
		40090	3.8652E-03
		40091	8.4289E-04
		40092	1.2884E-03
		40094	1.3057E-03
		40096	2.1035E-04
Top guide	1.3466	1001	1.2153E-02
		8016	6.0767E-03
		40090	3.9563E-03
		40091	8.6278E-04
		40092	1.3188E-03
		40094	1.3365E-03
		40096	2.1531E-04
Type 04 concrete	2.35	1001	7.7679E-03
		8016	4.4081E-02
		11023	1.0479E-03
		12024	1.1744E-04
		12025	1.4868E-05
		12026	1.6370E-05
		13027	2.3884E-03
		14028	1.4675E-02
		14029	7.4547E-04
		14030	4.9199E-04
		16032	5.3526E-05
		16033	4.2261E-07
		16034	2.3948E-06
		16036	5.6349E-09
		19039	6.4646E-04
		19040	8.1103E-08
		19041	4.6653E-05
		20040	2.8262E-03
		20042	1.8862E-05
		20043	3.9357E-06
		20044	6.0814E-05
		20046	1.1661E-07
		20048	5.4518E-06
		26054	1.8281E-05
		26056	2.8697E-04
		26057	6.6274E-06
		26058	8.8198E-07

Table 4-4 Material definitions in the BWR reference model (continued)

Material	Density (g/cm^3)	Isotope	Atom density (atoms/b·cm)
Core inlet coolant	0.7537	1001	5.0399E-02
		8016	2.5200E-02
Core outlet coolant	0.0389	1001	2.5991E-03
(within the shroud dome)		8016	1.2995E-03
Recirc pump suction	0.7540	1001	5.0421E-02
		8016	2.5210E-02
Recirc pump discharge	0.7549	1001	5.0480E-02
		8016	2.5240E-02
Feedwater inlet	0.8463	1001	5.6591E-02
		8016	2.8296E-02
Coolant – Zone Nat*	0.7386	1001	4.9392E-02
		8016	2.4696E-02
Coolant – Zone PSZ*	0.7160	1001	4.7880E-02
		8016	2.3940E-02
Coolant – Zone DOM*	0.6142	1001	4.1076E-02
		8016	2.0538E-02
Coolant – Zone PLE*	0.4710	1001	3.1500E-02
		8016	1.5750E-02
Coolant – Zone VAN*	0.3957	1001	2.6460E-02
		8016	1.3230E-02
Coolant – Zone N-V*	0.3241	1001	2.1672E-02
		8016	1.0836E-02
Coolant – Zone N-T*	0.3241	1001	2.1672E-02
		8016	1.0836E-02

* Densities within the fuel assemblies correspond to the average VF (VF) condition. See Section 5.4 for a discussion of the variation in VFs.

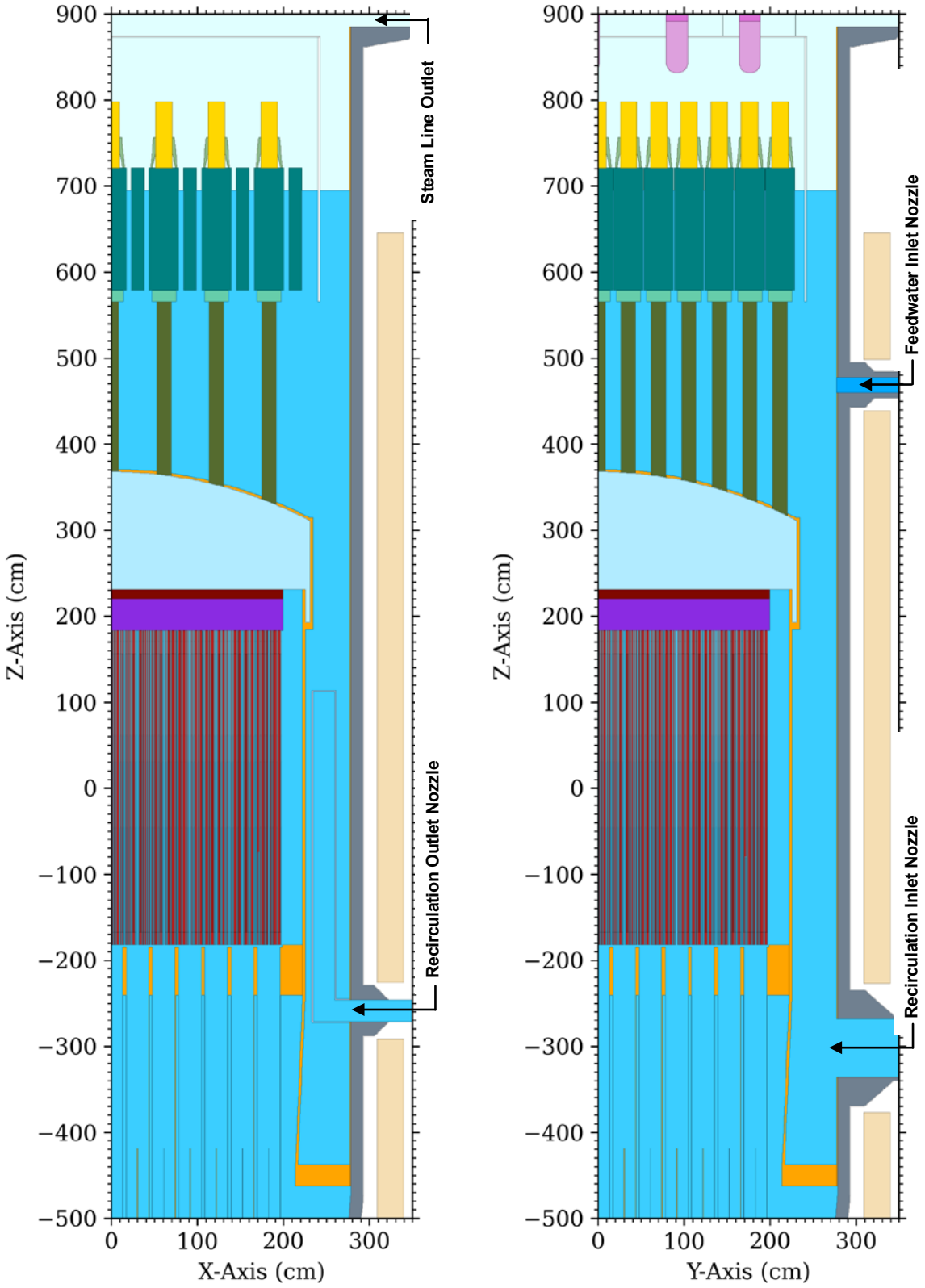

Figure 4-7 Elevation views of the BWR model at locations through the first row of fuel pins nearest the X- and Y-reflecting boundaries

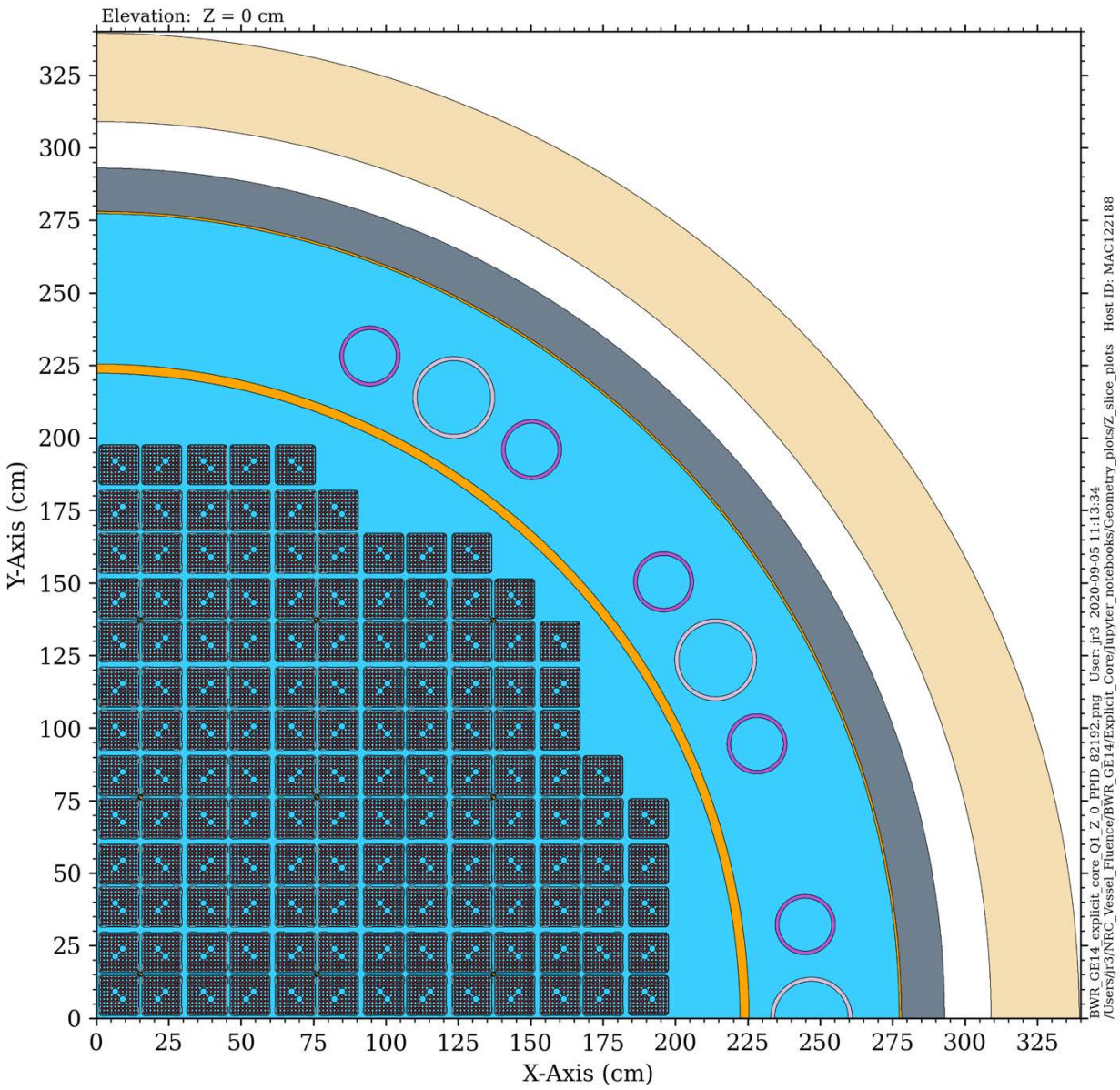

Figure 4-8 Plan view of the BWR model at the core midplane (Z = 0)

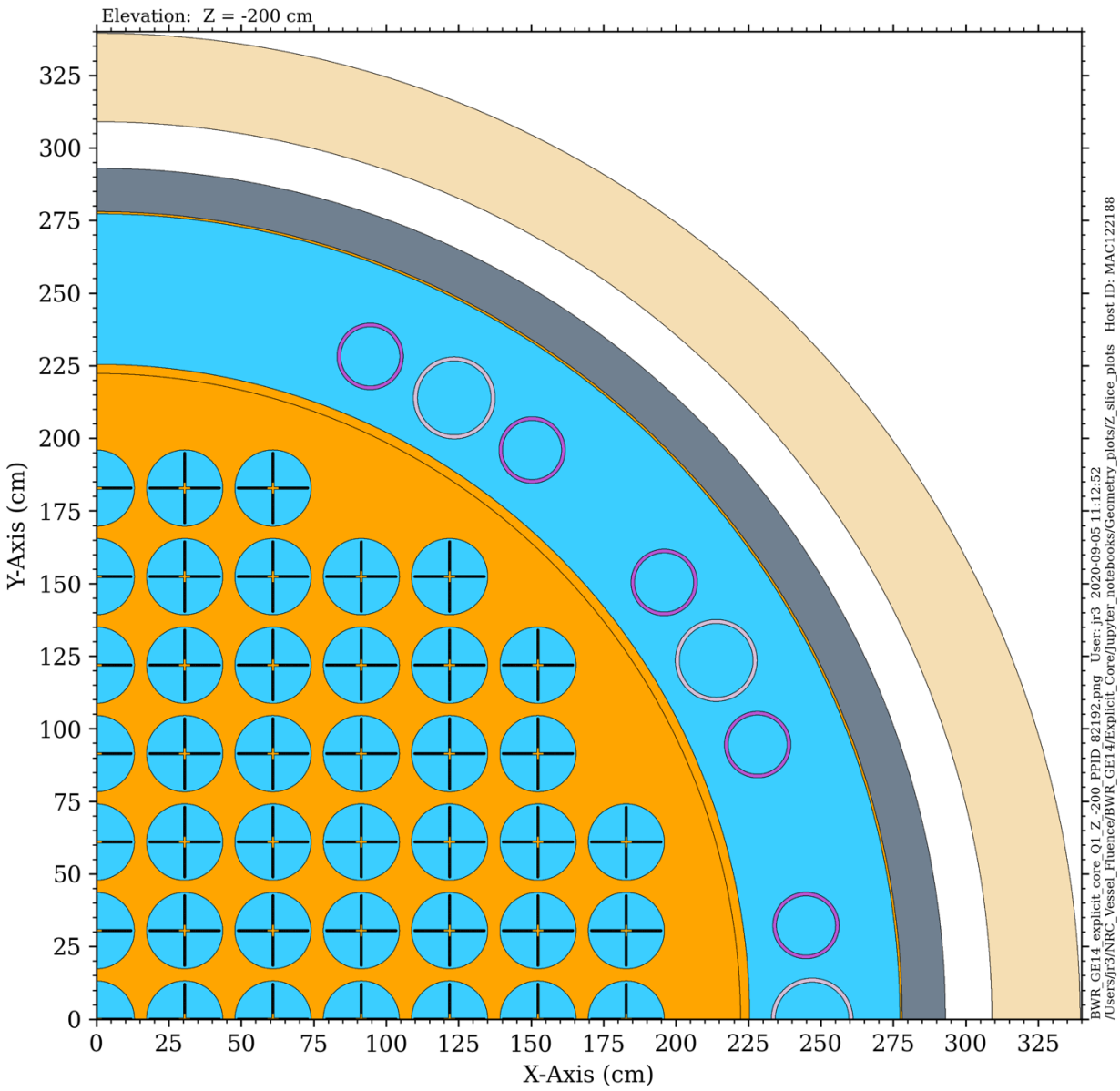

Figure 4-9 Plan view of the BWR model through the bottom core pate (Z = -200 cm)

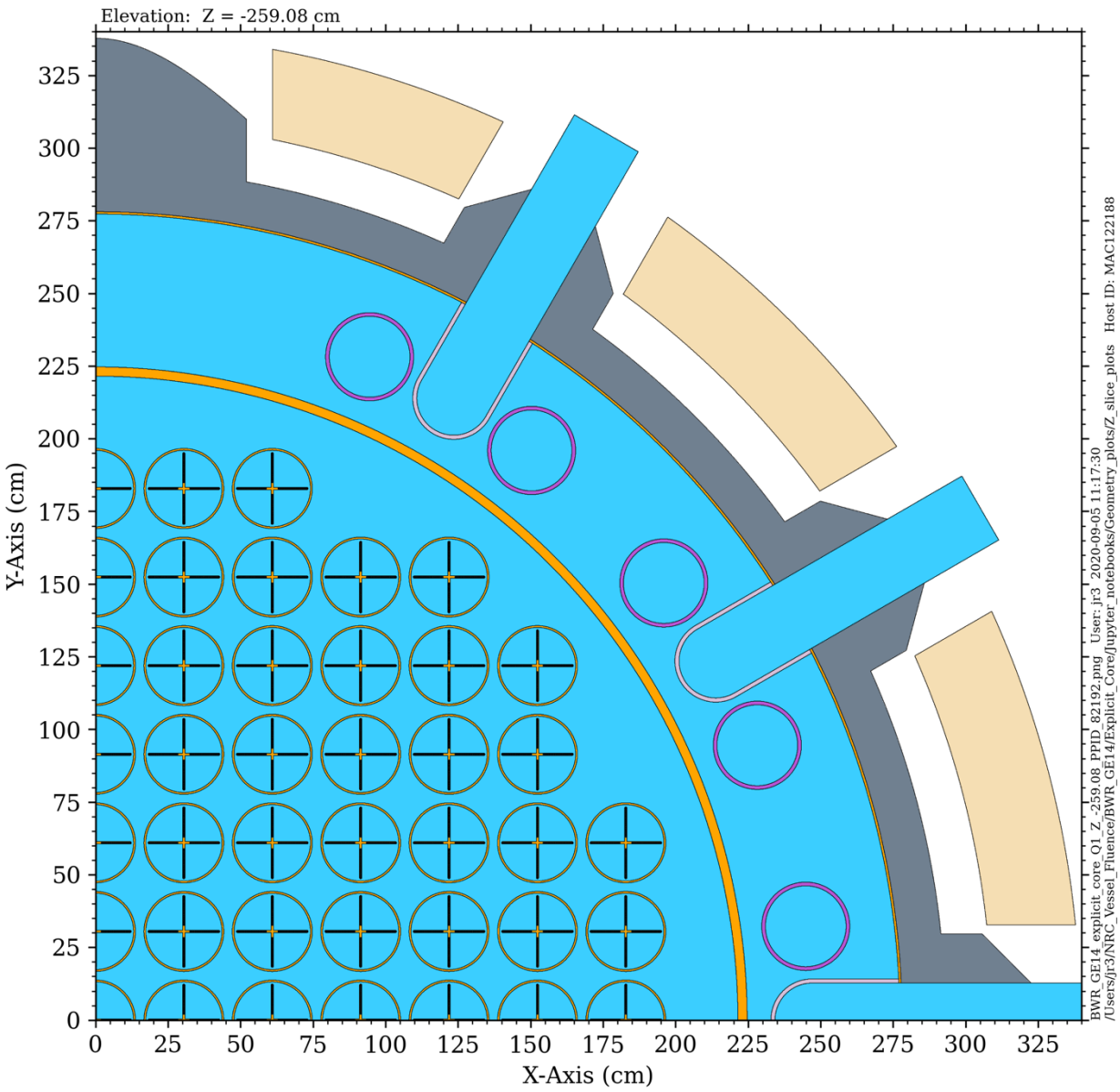

Figure 4-10 Plan view of the BWR model at the midplane of the recirculation outlet nozzles (Z = -259.08 cm)

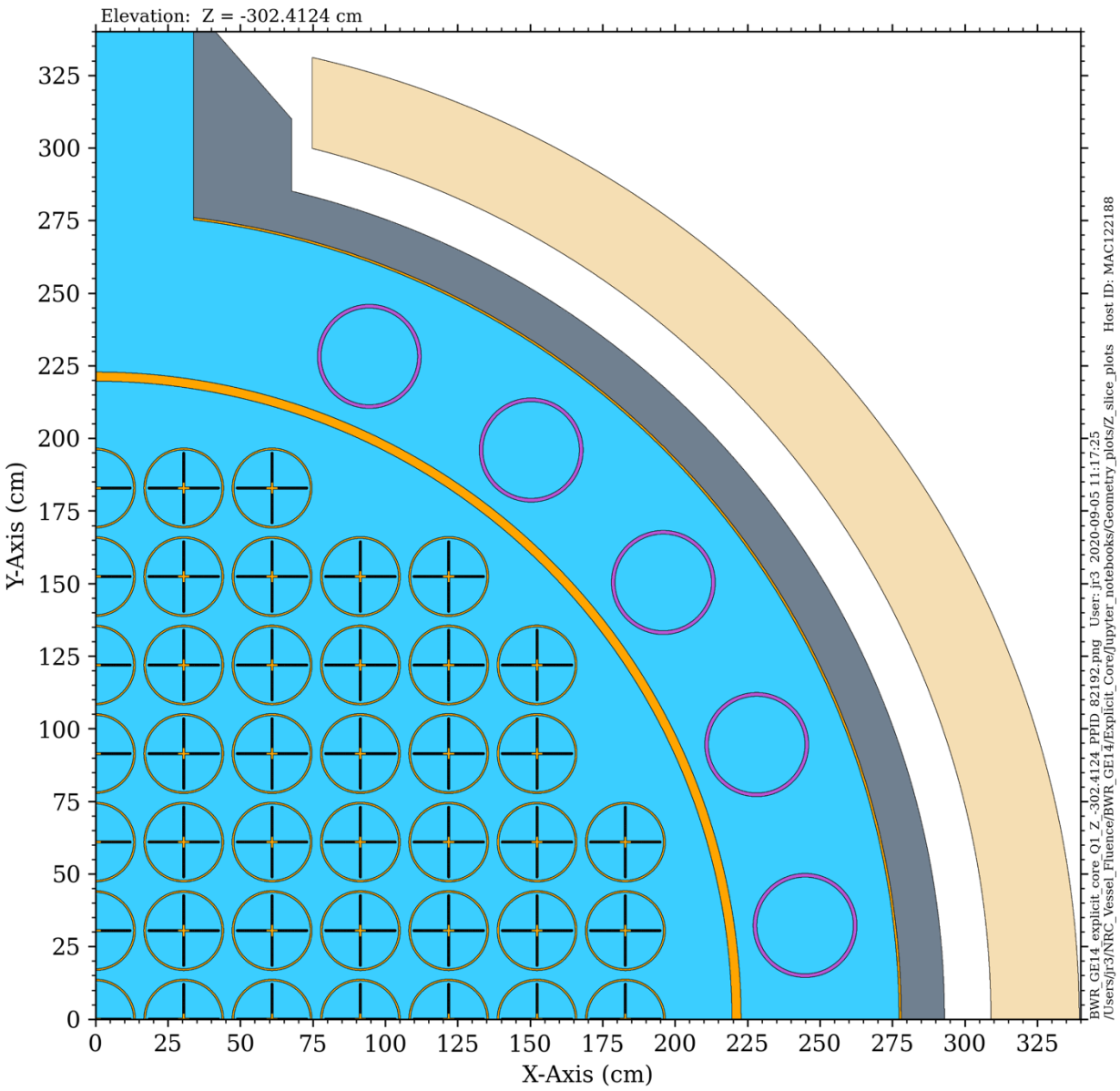

Figure 4-11 Plan view of the BWR model at the midplane of the recirculation inlet nozzles (Z = -302.41 cm)

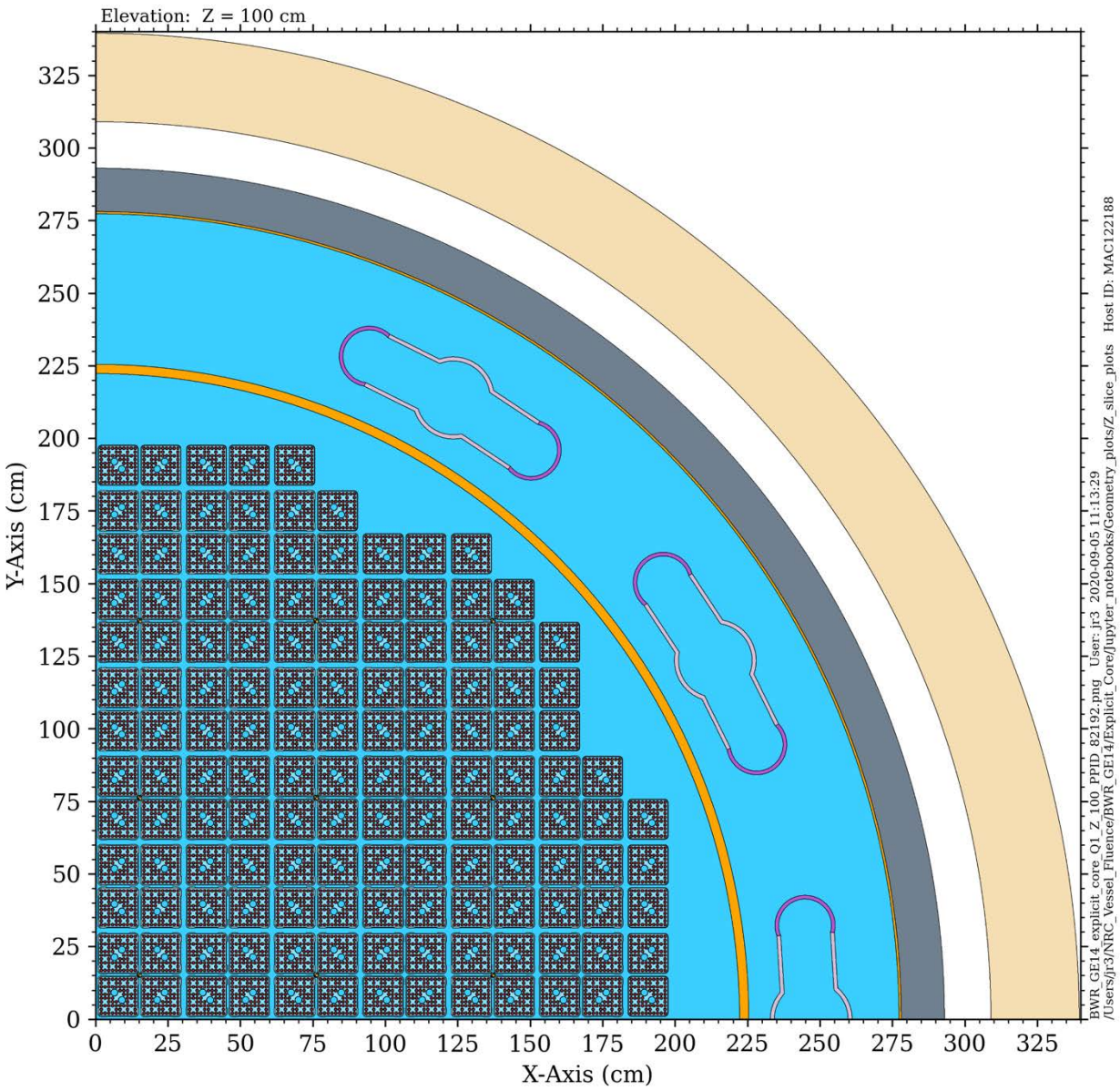

Figure 4-12 Plan view of the BWR model through the jet pump to riser connection (Z = 100 cm)

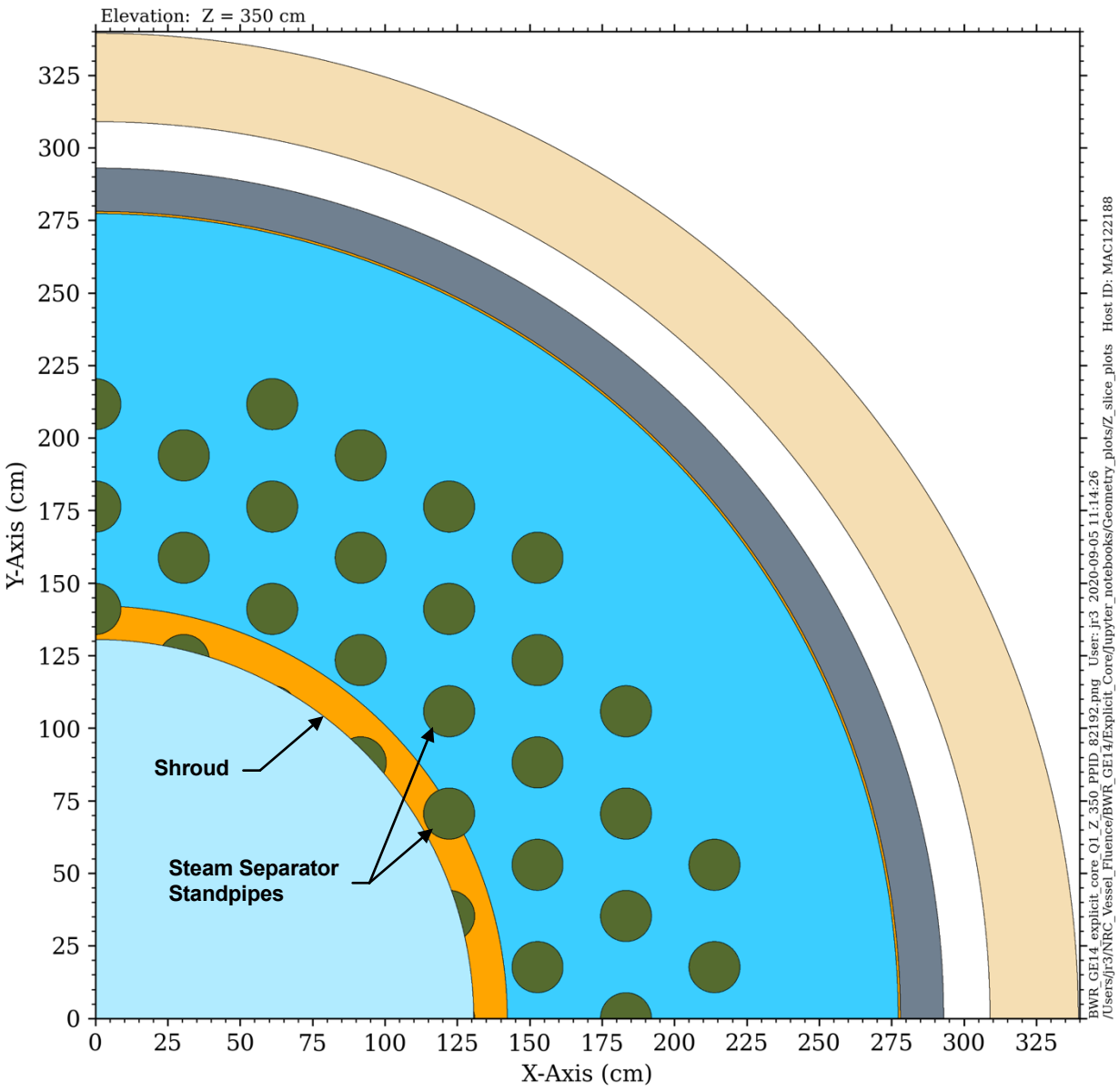

Figure 4-13 Plan view of the BWR model through the shroud dome (Z = 350 cm)

5 SENSITIVITY ANALYSES OF SELECTED PHYSICAL PARAMETERS FOR EXTENDED BELTLINE FLUENCE CALCULATIONS

5.1 Baseline Calculations

Baseline calculations with the PWR and BWR models were performed using hybrid FW-CADIS radiation transport with the Shift Monte Carlo code. CE cross sections based on ENDF/B-VII.1 were used. These calculations provide high-fidelity solutions that are typically converged to within 1% in mesh tally voxels in the regions of interest. Parameter studies with the PWR and BWR models employ pinwise spatially uniform core sources. While not representative of any actual operating condition, this distribution provides a convenient means of isolating the effects of individual parameters—whether modifications in the physical construction of the models or variations in analysis parameters. The fission nuclides included in the source definitions are discussed in Section 5.1 and Section 5.2. All radiation transport calculations in this report are normalized to the full-power values noted in Sections 4.1 and 4.2.

The baseline calculations in Sections 5.1.1 and 5.1.2 form the foundation for many of the parameter studies addressed in Section 5. In some cases, particularly for those presented in Sections 7 and 8, calculations are run using a neutron source representing a single fissile isotope—typically ^{235}U—for parameter studies. These cases are noted in the relevant sections.

The purpose of the parameter studies described in this section was to identify sensitivities to physical parameters and modeling techniques that may be more pronounced in the extended beltline region than in the traditional beltline region. This information provides insights into optimal calculation strategies.

Much of the data analysis in this report is based on interpretation of mesh tally plots that provide information on the model geometry and the solution (or ratio of solutions in parameter studies) being plotted. Examples of mesh tally plots are provided in APPENDIX B. Examination of those plots will aid in understanding the features of the 2D data plots throughout Sections 5, 6, 7, 8, and 9.

5.1.1 PWR Model

The baseline calculation for the PWR model employs a source with fission fractions based on a pseudo beginning-of-life (BOL) source. Fission fractions for six fissile isotopes (^{235}U, ^{238}U, ^{239}Pu, ^{240}Pu, ^{241}Pu, and ^{242}Pu) as a function of PWR burnup were obtained from NUREG/CR-6115, Table 2.1.1.1 [70]. The fractions for ^{240}Pu and ^{242}Pu were excluded since they are below 0.05%, even at the highest reported burnup values. The remaining data are provided below in Table 5-1.

Table 5-1. Fraction of fissions by isotope as a function of burnup for a PWR

Exposure (MWD)	^{235}U	^{238}U	^{239}Pu	^{241}Pu
150	0.9281	0.06172	0.01018	4.258E-7
500	0.9051	0.06214	0.03270	1.499E-5
10,000	0.5570	0.07074	0.3395	0.03342
20,000	0.3564	0.07819	0.4647	0.09988
40,000	0.1231	0.09120	0.5828	0.2035

For fresh fuel, there is no fission from the Pu isotopes, so only the ^{235}U and ^{238}U spectra are required. The pseudo-BOL source was obtained by using the ^{238}U fission fraction at the lowest recorded burnup (6.172% at 150 MWD) and assigning the remainder (93.828%) to ^{235}U. Note that of all the fissile isotopes considered, the ^{238}U fission fraction has the smallest variation with burnup. With increasing burnup, the relative contributions of ^{235}U, ^{239}Pu, and ^{241}Pu change significantly, but their sum varies by only a few percent throughout the lifetime of the fuel.

Plan views of the fast (E > 1 MeV) neutron flux for the baseline PWR calculation are shown in Figure 5-1, Figure 5-2, and Figure 5-3. Figure 5-1 shows the fast flux at the core midplane (Z = 195 cm), where the highest flux levels occur. Figure 5-2 and Figure 5-3 show the fast neutron flux at Z = -70 cm and at Z = 470 cm, respectively. These elevations are approximately 80 cm below and 90 cm above the axial extents of the fuel (Figure 4-2).

The peak fast neutron flux at the core midplane for the baseline solution is 4.31×10^{10} n/cm^2•sec. (Table 1 of IAEA's report [6] lists a fast flux of 4×10^{10} n/cm^2•sec for a Westinghouse PWR.) The peak fast flux levels in the RPV at the elevations of Z = -70 cm and Z = 470 cm are approximately three orders of magnitude lower than the peak flux in the RPV at the core midplane. The elevation at Z = 470 cm is noteworthy, as it includes critical weld locations for the nozzles, as well as the vessel supports.

If the spatially uniform source of this baseline calculation were realistic, then the peak EOL fast fluence levels at Z = -70 cm and Z = 470 cm would be less than 1×10^{17} n/cm^2, which is the value above which 10 CFR Part 50 [3], Section III, Appendix H, requires monitoring of beltline materials using a surveillance program complying with ASTM E185-82 [4]. With typical axial power distributions, the neutron flux levels in the upper and lower regions of the fuel are lower than the core average, so the fast flux values at these elevations with the baseline model are likely to be conservative with respect to lifetime exposure. However, as discussed in Section 6.1, the peak dpa values at these locations exceed the values estimated based on the fast flux due to the increasing contribution to damage from neutrons with energies less than 1 MeV.

Elevation views of the fast neutron flux for the baseline PWR calculation are shown in Figure 5-4, Figure 5-5, and Figure 5-6. Figure 5-4 is an elevation view at 270.5°, which is the azimuthal location with the maximum amount of water between the core and the RPV. Figure 5-5 is an elevation view at 315.5°, which is at or near the location of the peak fast flux in the RPV (Figure 5-1). Figure 5-6 shows the fast flux at an azimuthal angle of 292.5°, which is through the centerline of the outlet nozzle.

The elevation views show clear evidence of a condition known as cavity streaming, in which fast neutrons that enter the cavity gap between the RPV and the concrete bioshield scatter into directions that transport them vertically upward and downward in the gap. At elevations of ~50 to ~60 cm above and below the active fuel region, the fast flux radial profile through the RPV is no longer monotonically decreasing from the RPV inner surface to the RPV outer surface.

The effect of cavity streaming neutrons is illustrated further in Figure 5-7 and Figure 5-8. These plots provide 1D normalized radial fast flux profiles through the RPV at 270.5° and 315.5°, respectively. At each of these azimuthal locations, 1D radial profiles are shown at elevations ranging from ~100 cm below the core to ~110 cm above the core. Each plot also includes a solid dashed line that represents the attenuation formula in Eq. (3) of RG 1.99 [78]. A number of observations can be made from these two figures.

1. At elevations within or nearly within the height of the fuel (Z = 0 cm, Z = 195 cm, and Z = 400 cm), the fast neutron flux is attenuated with a nearly exponential behavior that decreases more rapidly than the RG 1.99 formula would suggest. As discussed in Section 6, the RG 1.99 equation was developed based on the attenuation behavior of dpa rates rather than fast flux, and at elevations within the core height, the equation is conservative for predictions of fast flux attenuation.
2. At elevations outside of an axial range extending from ~50 cm below the fuel (Z = -40 cm) to ~50 cm above the fuel (Z = 430 cm), the slope of the fast flux profile changes, and there is no longer a monotonic fast flux decrease through the entire RPV thickness.
3. For elevations lower than ~-75 cm and higher than ~480 cm, the peak fast flux is no longer at the inner surface of the RPV, but rather at the outer surface. In these regions, the radial flux profile is dominated by cavity streaming neutrons. Note that based on the discussion above regarding peak EOL fluences at Z = -70 cm and Z = 470 cm, these locations would be expected to have EOL fluence levels below the monitoring threshold of 1×10^{17} n/cm^2.

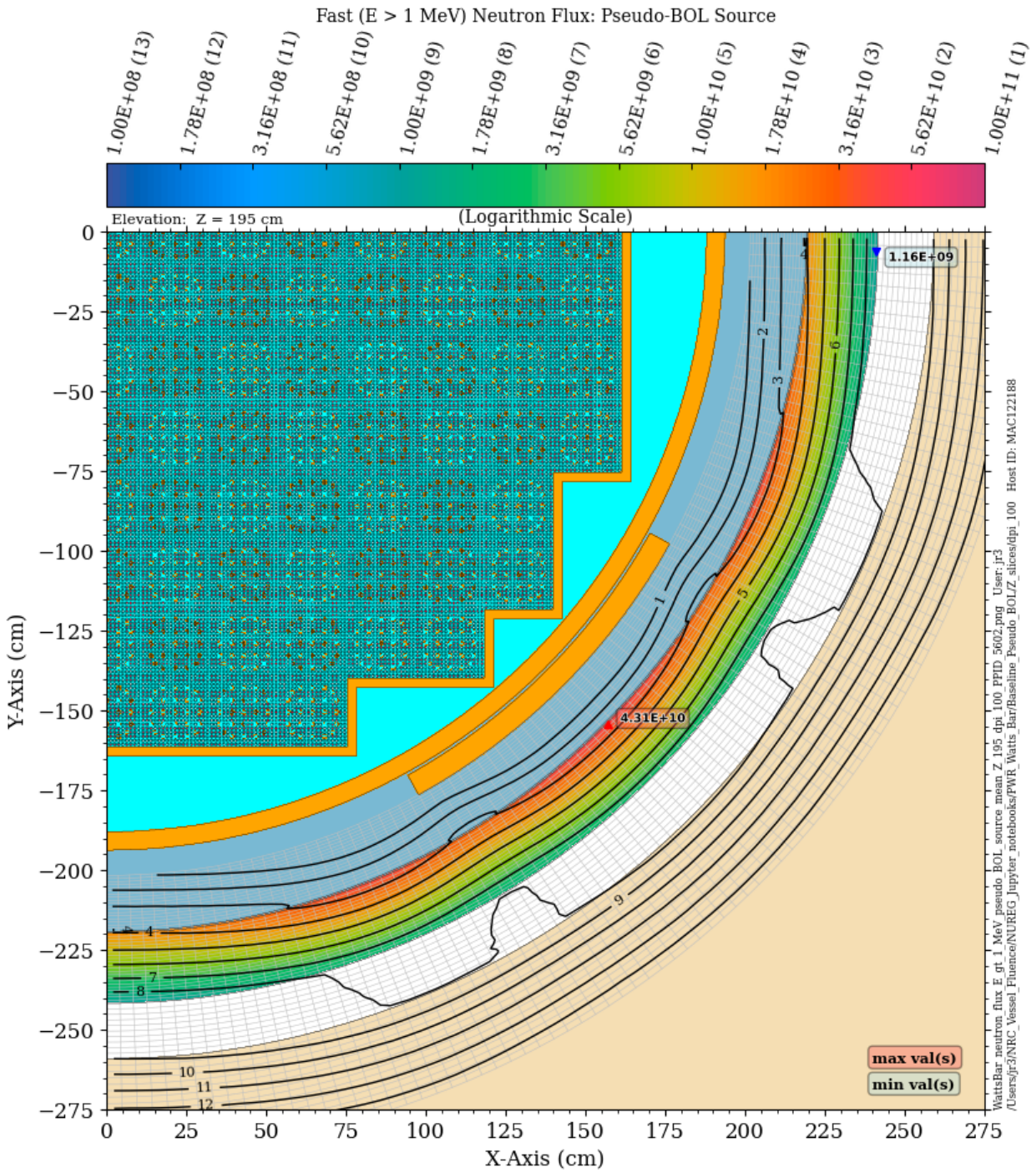

Figure 5-1 Fast neutron flux in the baseline PWR model with a pseudo-BOL fission source. Plan view at the core midplane elevation

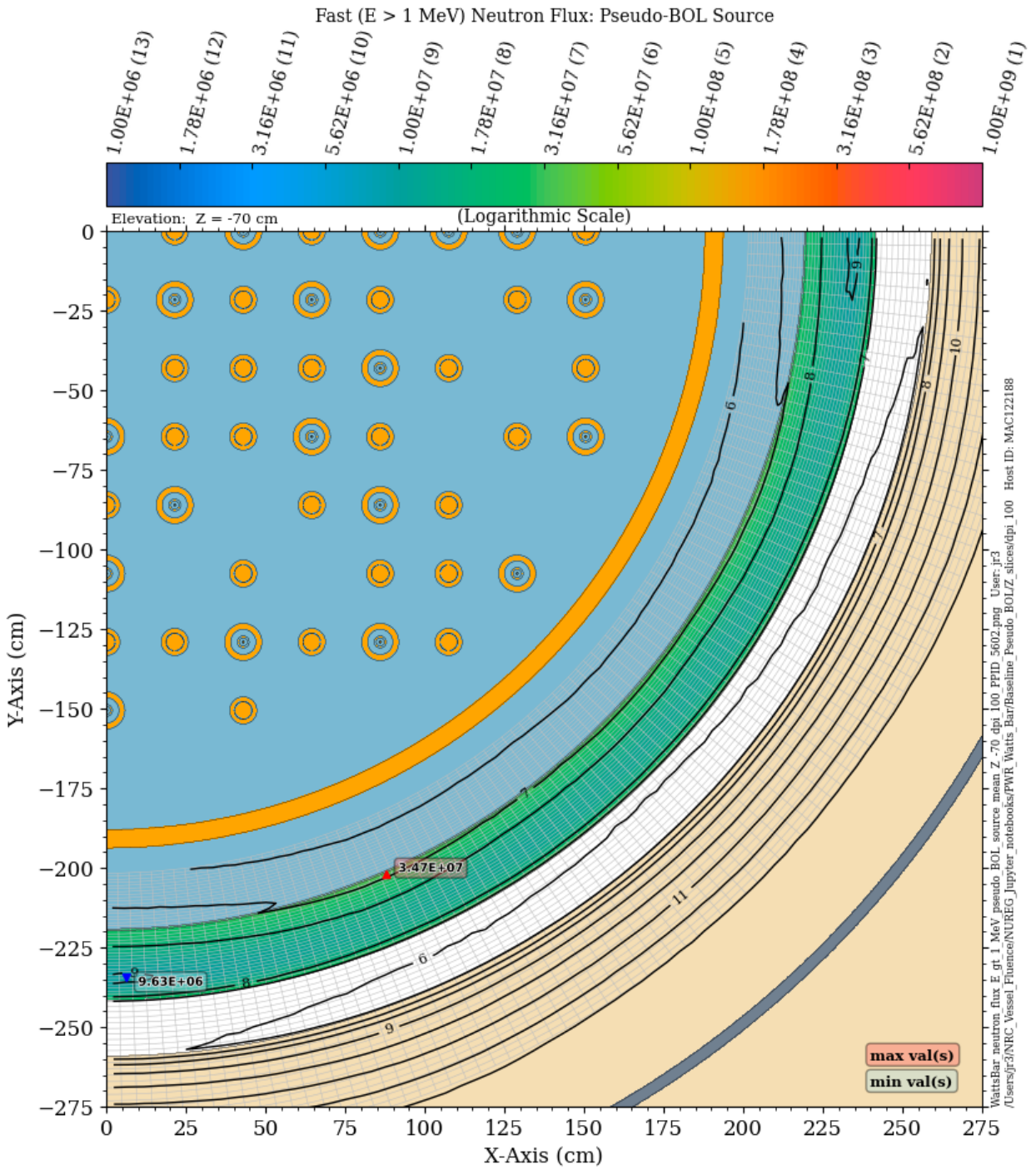

Figure 5-2 Fast neutron flux in the baseline PWR model with a pseudo-BOL fission source. Plan view at an elevation at Z = -70 cm

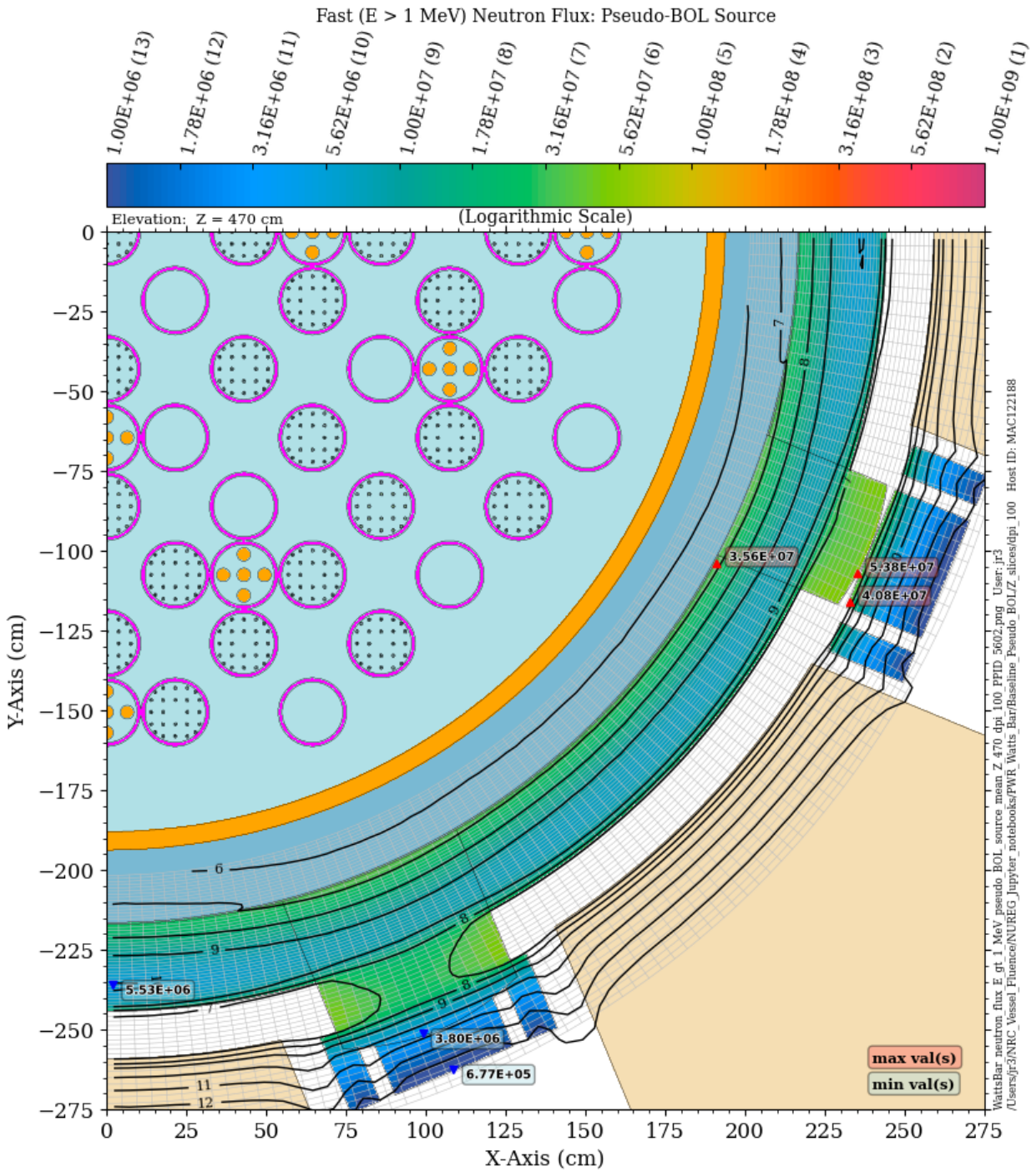

Figure 5-3 Fast neutron flux in the baseline PWR model with a pseudo-BOL fission source. Plan view through the vessel supports at an elevation of Z = 470 cm

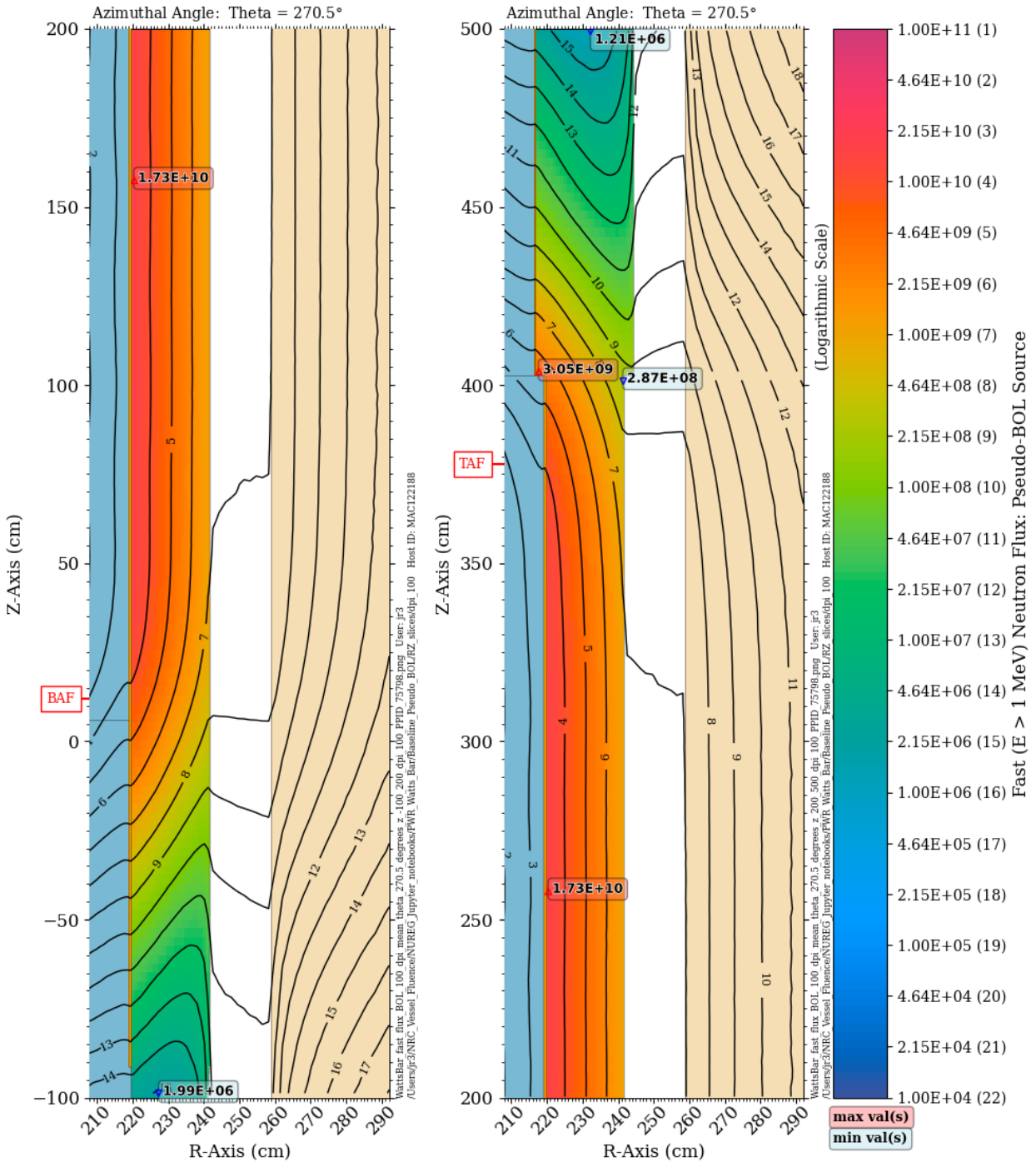

Figure 5-4 Fast neutron flux in the baseline PWR model with a pseudo-BOL fission source. Elevation view at an azimuthal angle of 270.5° *This is the azimuthal location with the maximum amount of water between the core and the RPV.*

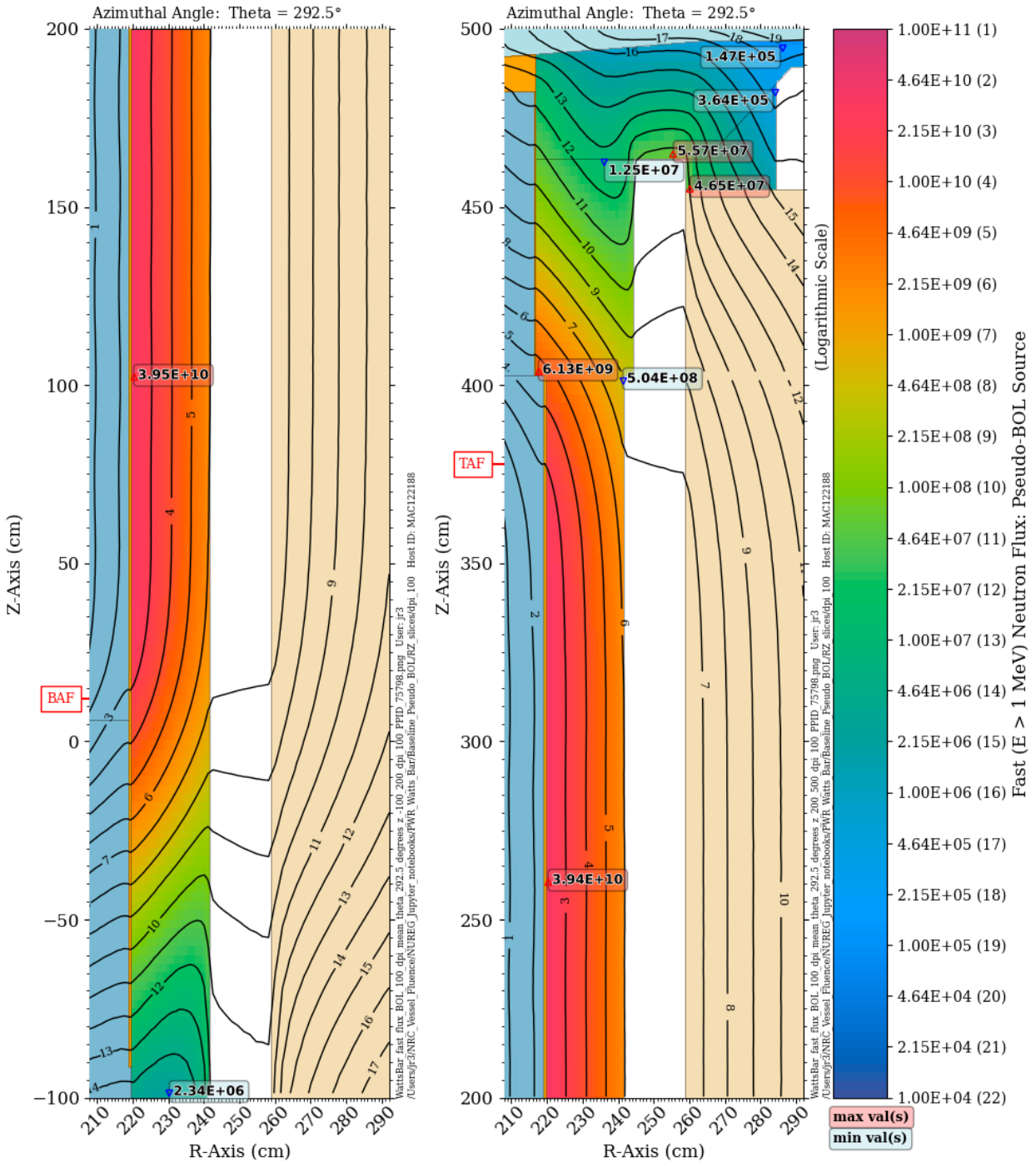

Figure 5-5 Fast neutron flux in the baseline PWR model with a pseudo-BOL fission source. Elevation view at an azimuthal angle of 292.5°

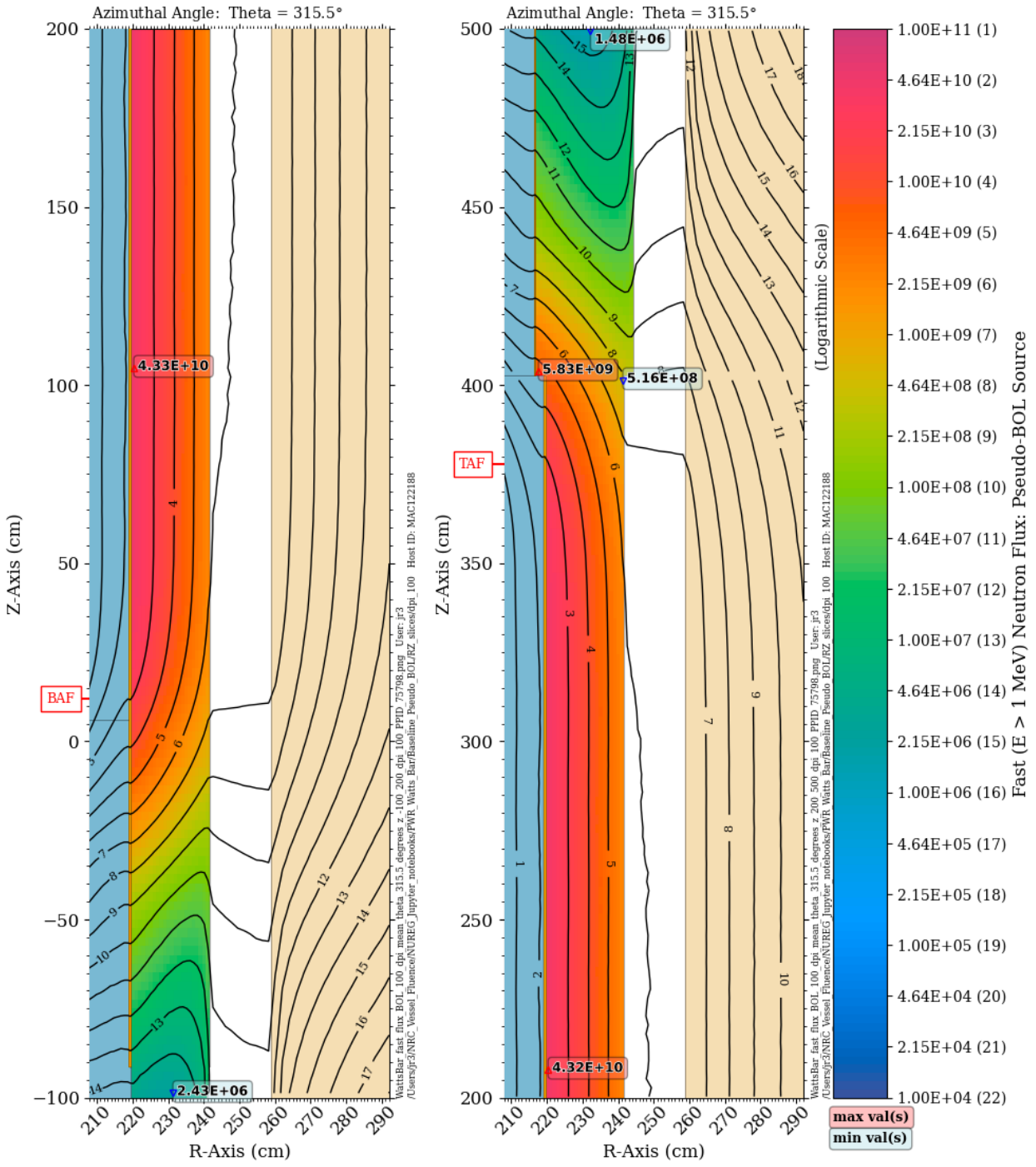

Figure 5-6 Fast neutron flux in the baseline PWR model with a pseudo-BOL fission source. Elevation view at an azimuthal angle of 315.5°

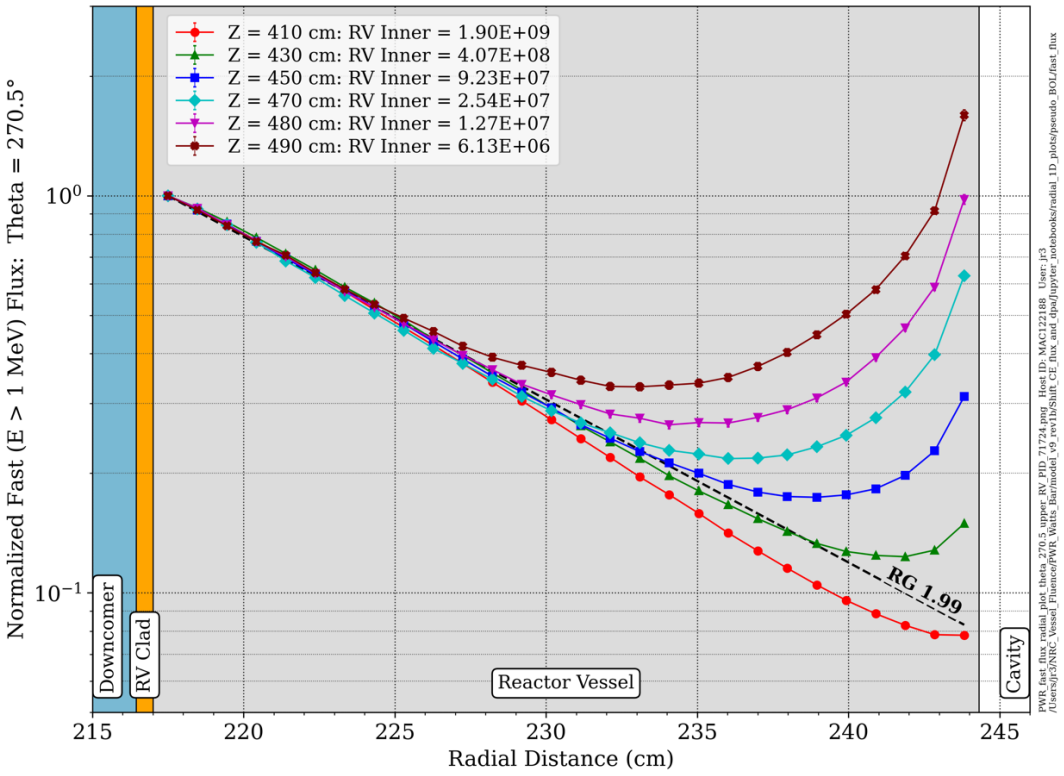

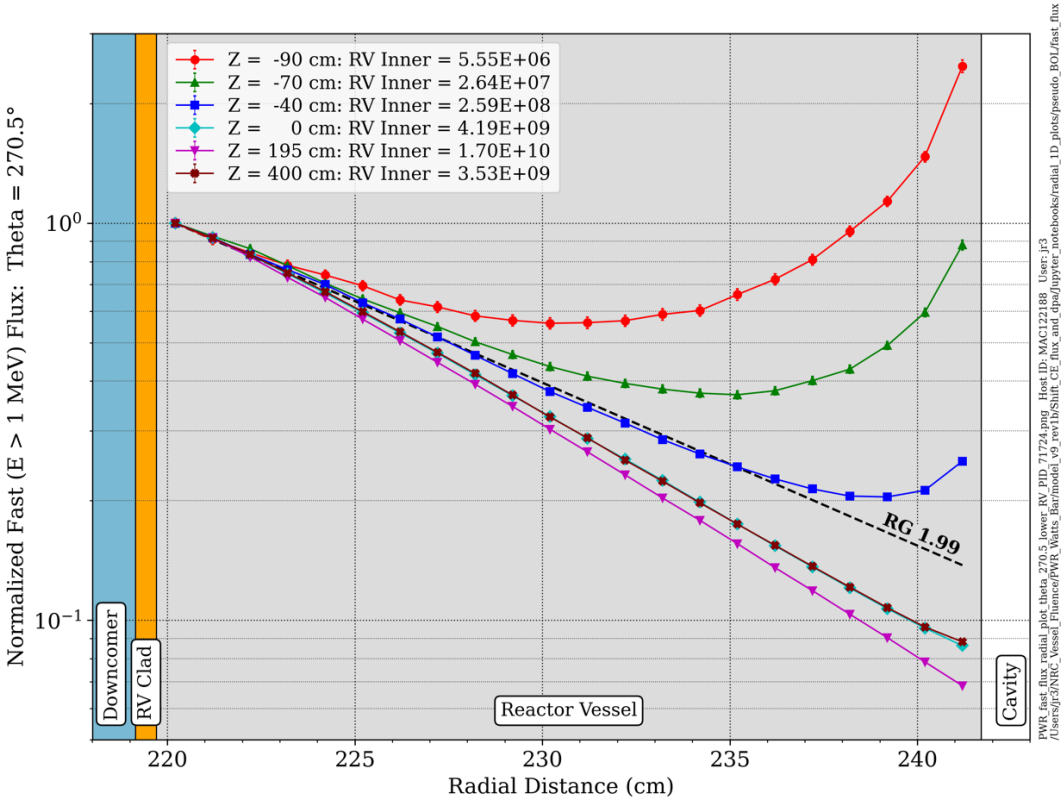

Figure 5-7 Normalized radial fast neutron flux profiles in the PWR model with a pseudo-BOL fission source. Azimuthal angle of 270.5° *The profiles are normalized to the flux at the RPV inner diameter at each elevation.*

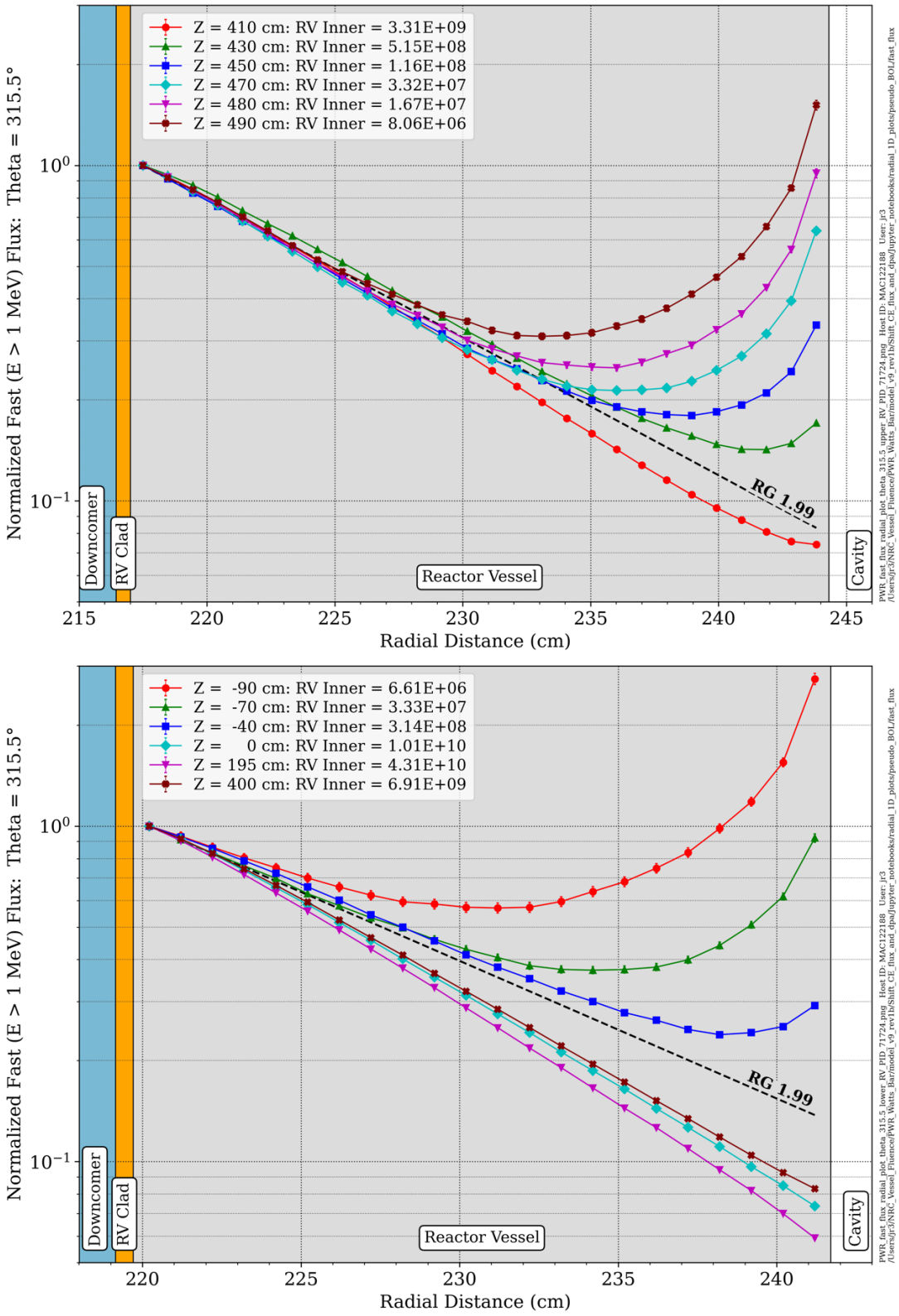

Figure 5-8 Normalized radial fast neutron flux profiles in the PWR model with a pseudo-BOL fission source. Azimuthal angle of 315.5° *The profiles are normalized to the flux at the RPV inner diameter at each elevation.*

5.1.2 BWR Model

The baseline calculation for the BWR model employs a source with fission fractions based on a pseudo-BOL source. Fission fractions for four fissile isotopes (^{235}U, ^{238}U, ^{239}Pu, and ^{241}Pu) as a function of BWR burnup were obtained from NUREG/CR-6115, Table 2.2.1.1 [70]. The data are provided below in Table 5-2.

Table 5-2. Fraction of fissions by isotope as a function of burnup for a BWR

Exposure (MWD/T)	^{235}U	^{238}U	^{239}Pu	^{241}Pu
4.33	0.7651	0.0733	0.1566	0.0
5.92	0.7190	0.0733	0.1936	0.0059
6.62	0.7085	0.0733	0.2096	0.0074
11.13	0.6153	0.0766	0.2814	0.0220
14.12	0.5630	0.0766	0.3220	0.0373
15.66	0.5370	0.0766	0.3400	0.0440
17.88	0.5070	0.0766	0.3580	0.0533

For fresh fuel, there is no fission from the Pu isotopes, so only the ^{235}U and ^{238}U spectra are required. The pseudo-BOL source was obtained by using the ^{238}U fission fraction at the lowest tabulated burnup (7.33% at 4.33 MWD/T) and assigning the remainder (92.67%) to ^{235}U. Note that, as with the PWR model, there is very little change in the ^{238}U fission fraction with burnup. With increasing burnup, the relative contributions of the ^{235}U, ^{239}Pu, and ^{241}Pu change significantly, but their sum remains nearly constant throughout the lifetime of the fuel.

Plan views of the fast neutron flux in the BWR model are shown in Figure 5-9, Figure 5-10, and Figure 5-11. Figure 5-9 shows the fast flux at the core midplane, where the highest flux levels occur. Note that the maximum fast flux level at the core midplane in the BWR RPV is nearly an order of magnitude lower than that at the core midplane in the PWR RPV (Figure 5-1). This difference is consistent with PWR and BWR fluence estimates in IAEA's publication [6] and Nuclear Power – Control, Reliability, and Human Factors [7]. Figure 5-10 shows the fast flux at an elevation through the recirculation outlet nozzles at Z = -250 cm. The peak RPV fast flux at this elevation is approximately two orders of magnitude lower than at the core midplane. Figure 5-11 shows the fast flux above the shroud dome at an elevation of Z = 375 cm. At this elevation, the peak RPV fast flux level is also approximately two orders of magnitude lower than at the core midplane. If the spatially uniform source of this baseline calculation were realistic, then the peak EOL fast fluence at Z = -250 cm and Z = 375 cm would be less than 1×10^{17} n/cm^2, which is the threshold for requirement of a surveillance program, as noted in Section 5.1.1.

Elevation views of the fast neutron flux for the baseline BWR calculation are shown in Figure 5-12 and Figure 5-13. Figure 5-12 is an elevation view at 0.5°, which is the location with the minimum fast flux incident to the RPV. Figure 5-13 is an elevation view at 44.5°, which has the maximum fast flux incident to the RPV. By comparison with the PWR figures in Section 5.1.1, it is clear that the effects of cavity streaming neutrons are less pronounced in the BWR model than the PWR model, particularly at elevations above the top of the core. This is also illustrated in Figure 5-14 and Figure 5-15. At all elevations above the core midplane up to a distance of almost 200 cm above the top of the fuel, the normalized fast flux decreases monotonically (or nearly so) in the RPV, and it is bounded by (i.e., below) RG 1.99 Eq. (3). The fast neutron flux profile through the BWR RPV only ceases to display monotonic attenuation at the 44.5° azimuthal angle for elevations more than approximately 50 cm below the active core. At increasing distances below the active core, the fast neutron flux profile in the RPV is dominated by cavity streaming neutrons.

The reason for this behavior in the BWR model is the significant difference in the neutron flux attenuation at elevations below and above the fuel. For the lower elevations, the neutron flux is significantly attenuated by the water, and to a lesser extent, by the structures between the core and the RPV. This is clearly demonstrated in the lower axial portions of Figure 5-12 and Figure 5-13. At locations above the core midplane, there is less neutron attenuation from the core to the RPV due to (1) the coolant density within the fuel assemblies decreasing with increasing height as the VFs increase, and (2) neutrons that have transport paths through the shroud dome (with coolant in the steam phase) have significantly less attenuation than those transported through coolant in the liquid phase. Thus, for the BWR model, cavity, streaming is significant only for elevations in the lower extended beltline region, where EOL fast fluence values are likely to be less than 1×10^{17} n/cm^2.

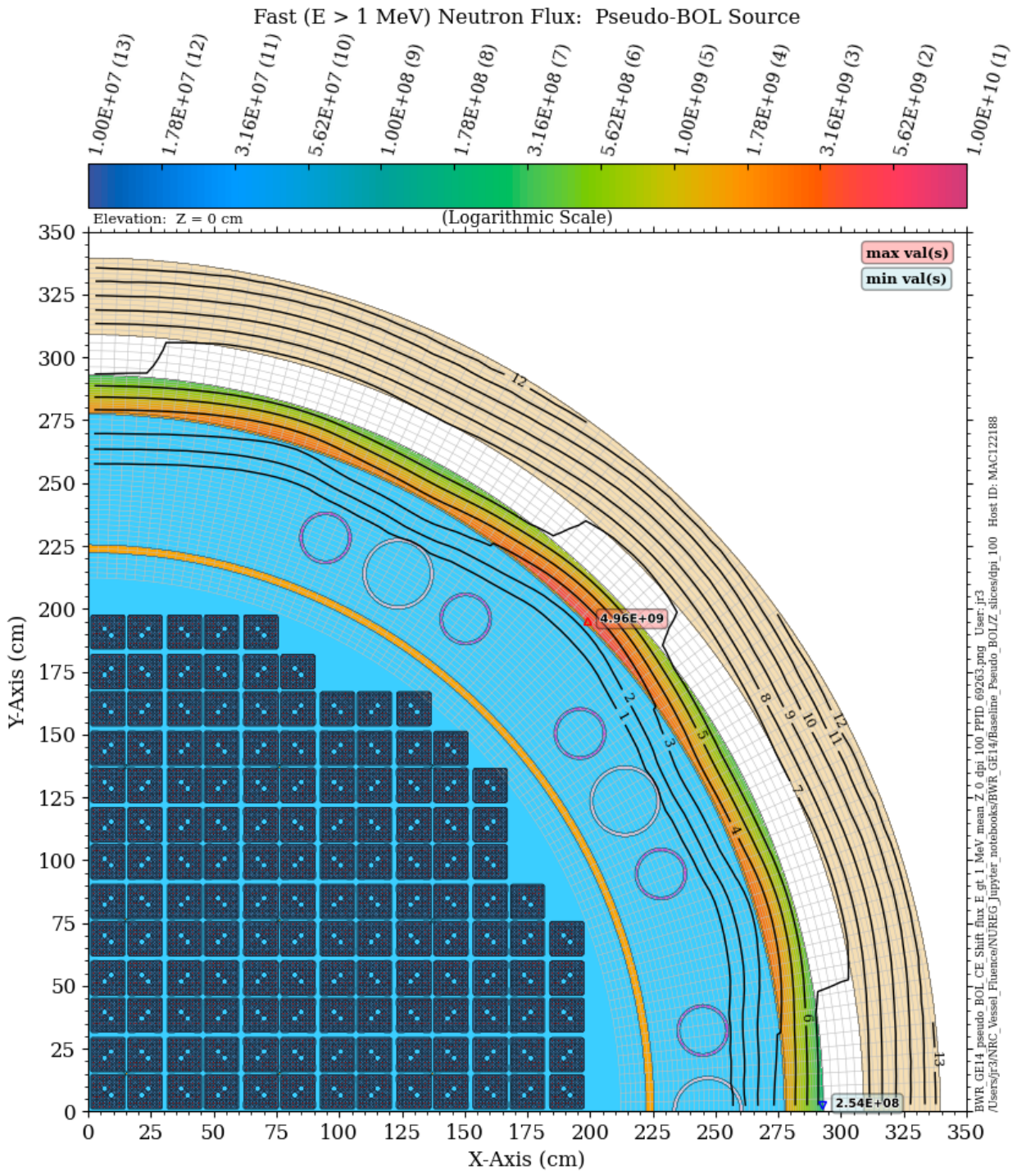

Figure 5-9 Fast neutron flux in the baseline BWR model with a pseudo-BOL fission source. Plan view at the core midplane

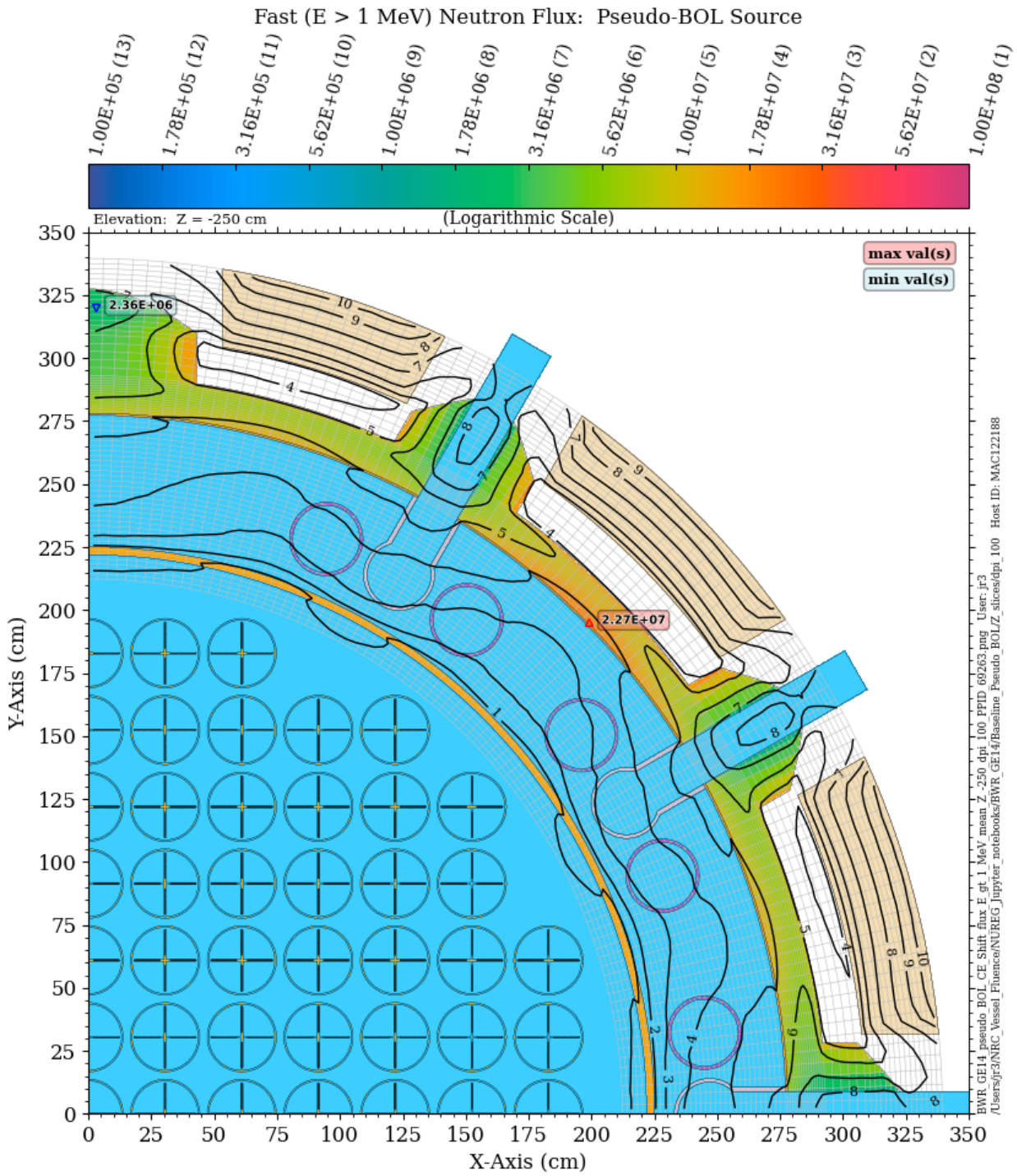

Figure 5-10 Fast neutron flux in the baseline BWR model with a pseudo-BOL fission source. Plan view through the recirculation outlet nozzles at Z = -250 cm

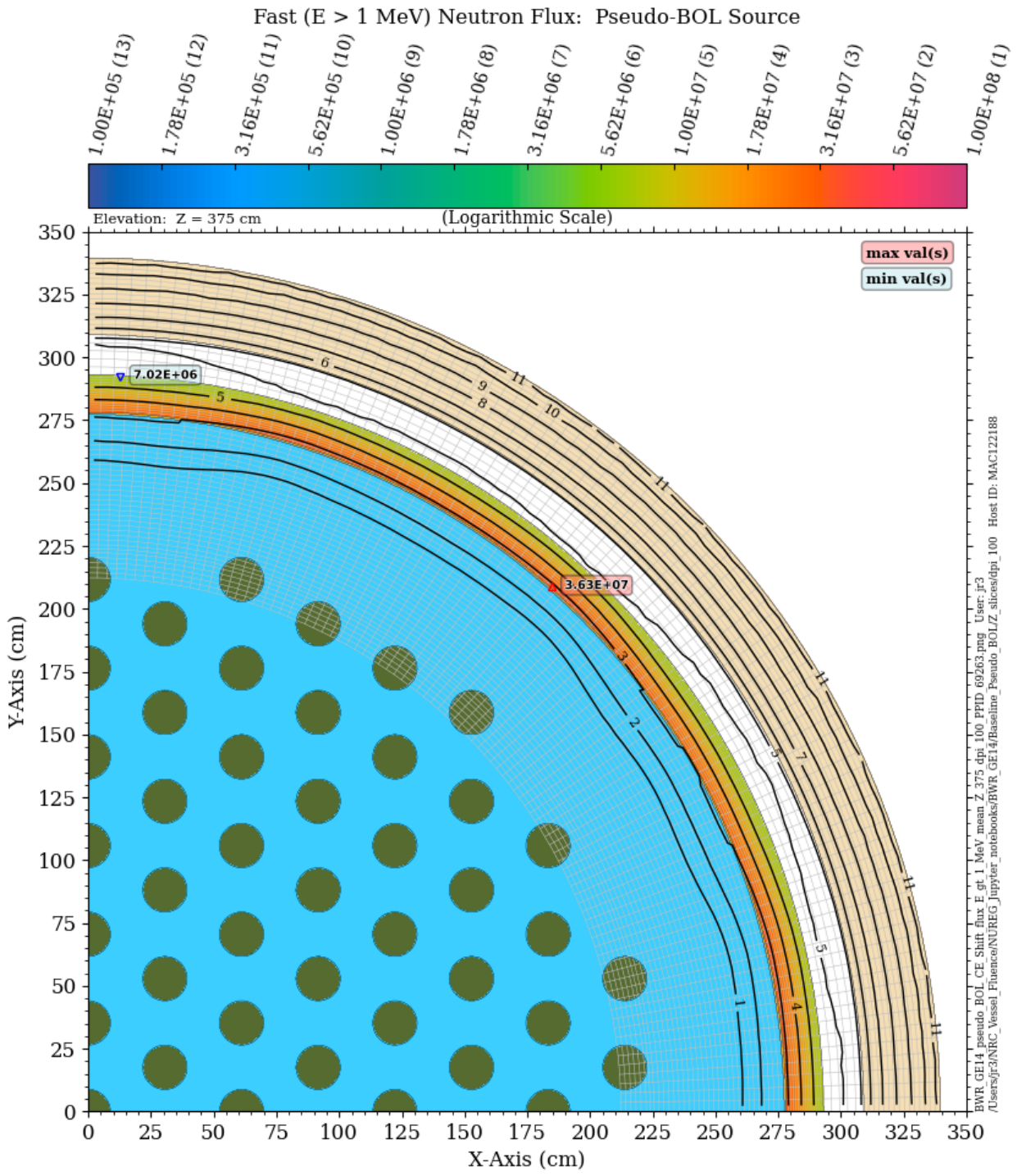

Figure 5-11 Fast neutron flux in the baseline BWR model with a pseudo-BOL fission source. Plan view above the core shroud dome at an elevation of Z = 375 cm

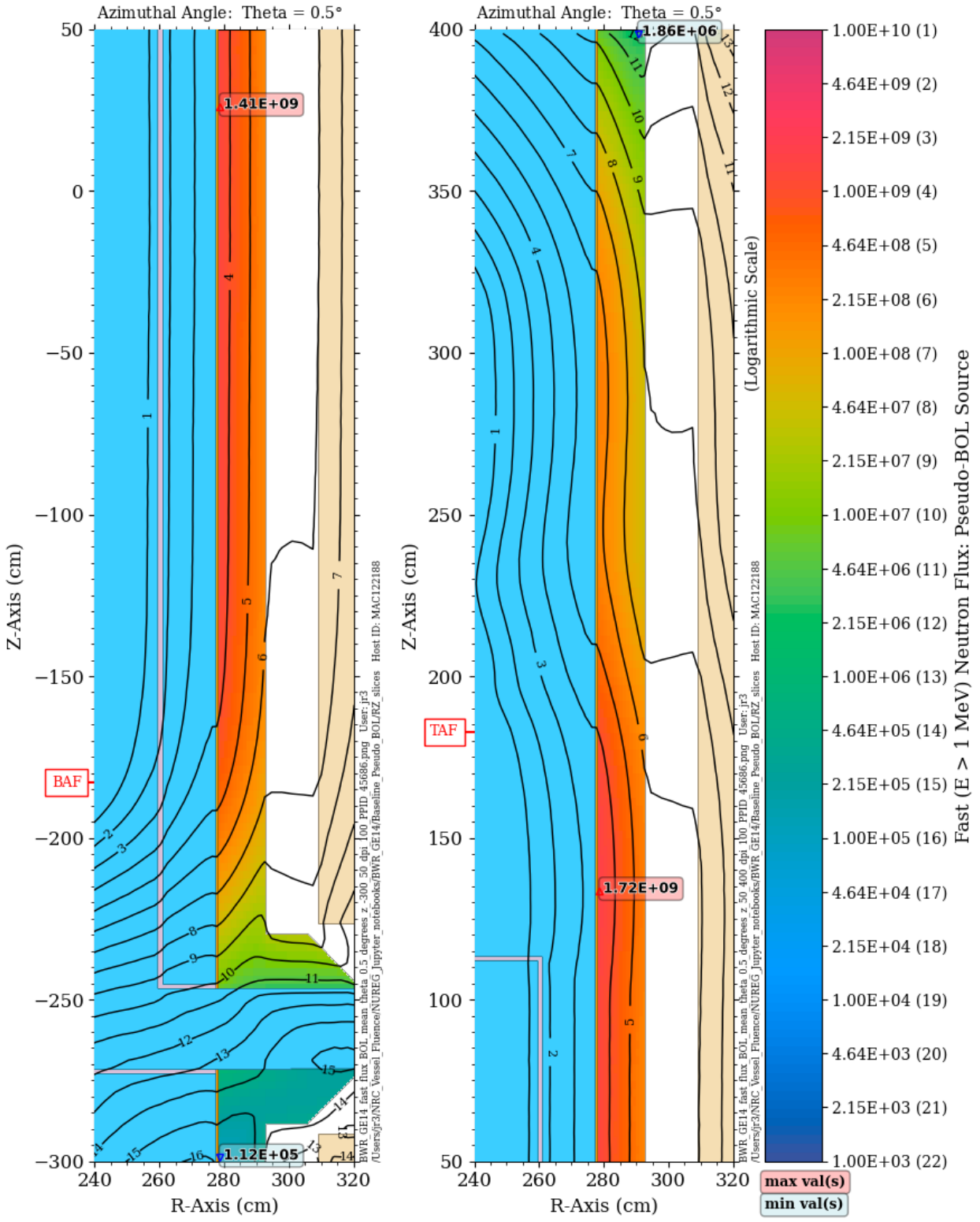

Figure 5-12 Fast neutron flux in the baseline BWR model with a pseudo-BOL fission source. Elevation view through the recirculation outlet nozzle at an azimuthal angle of 0.5°

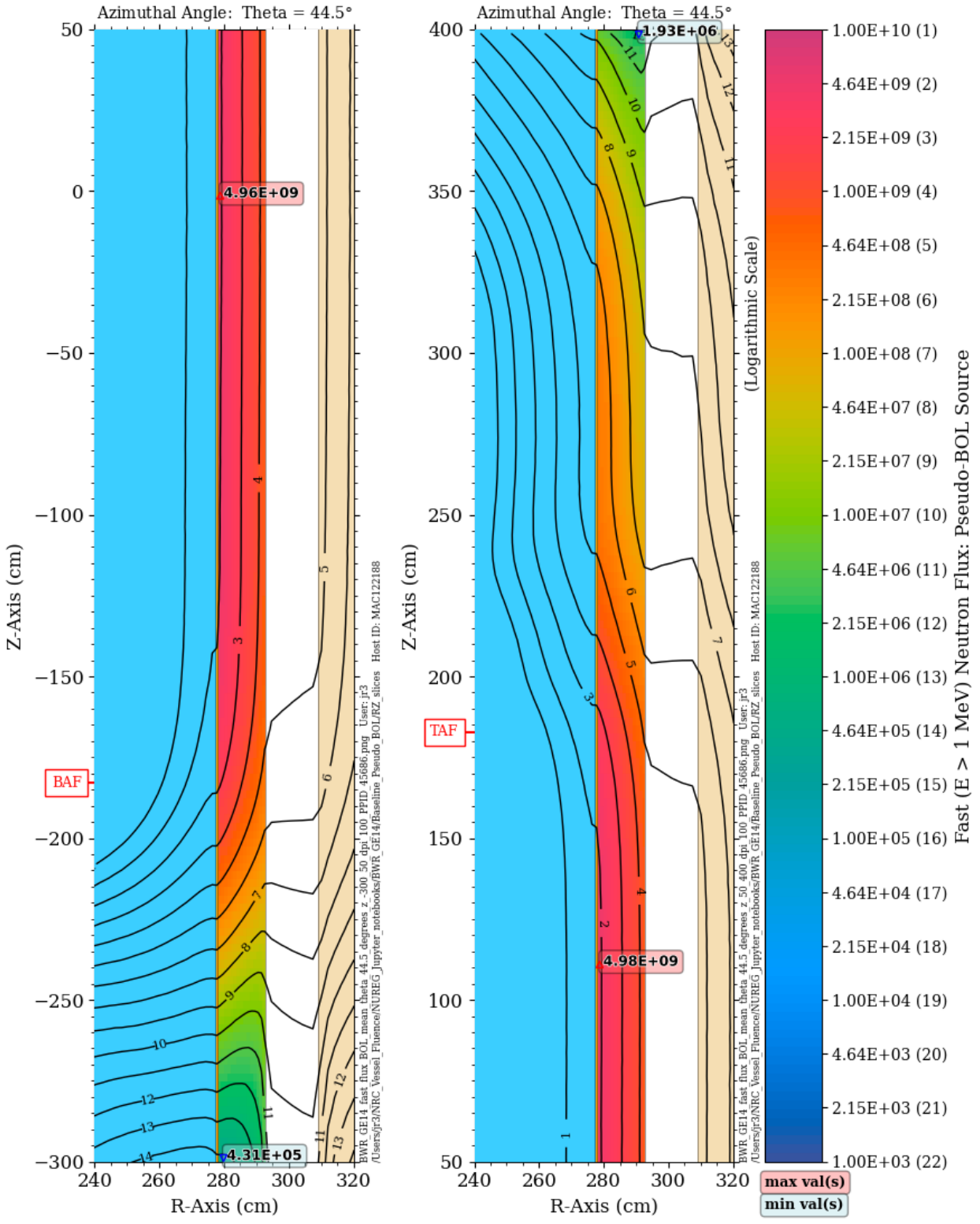

Figure 5-13 Fast neutron flux in the baseline BWR model with a pseudo-BOL fission source. Elevation view at an azimuthal angle of 44.5°

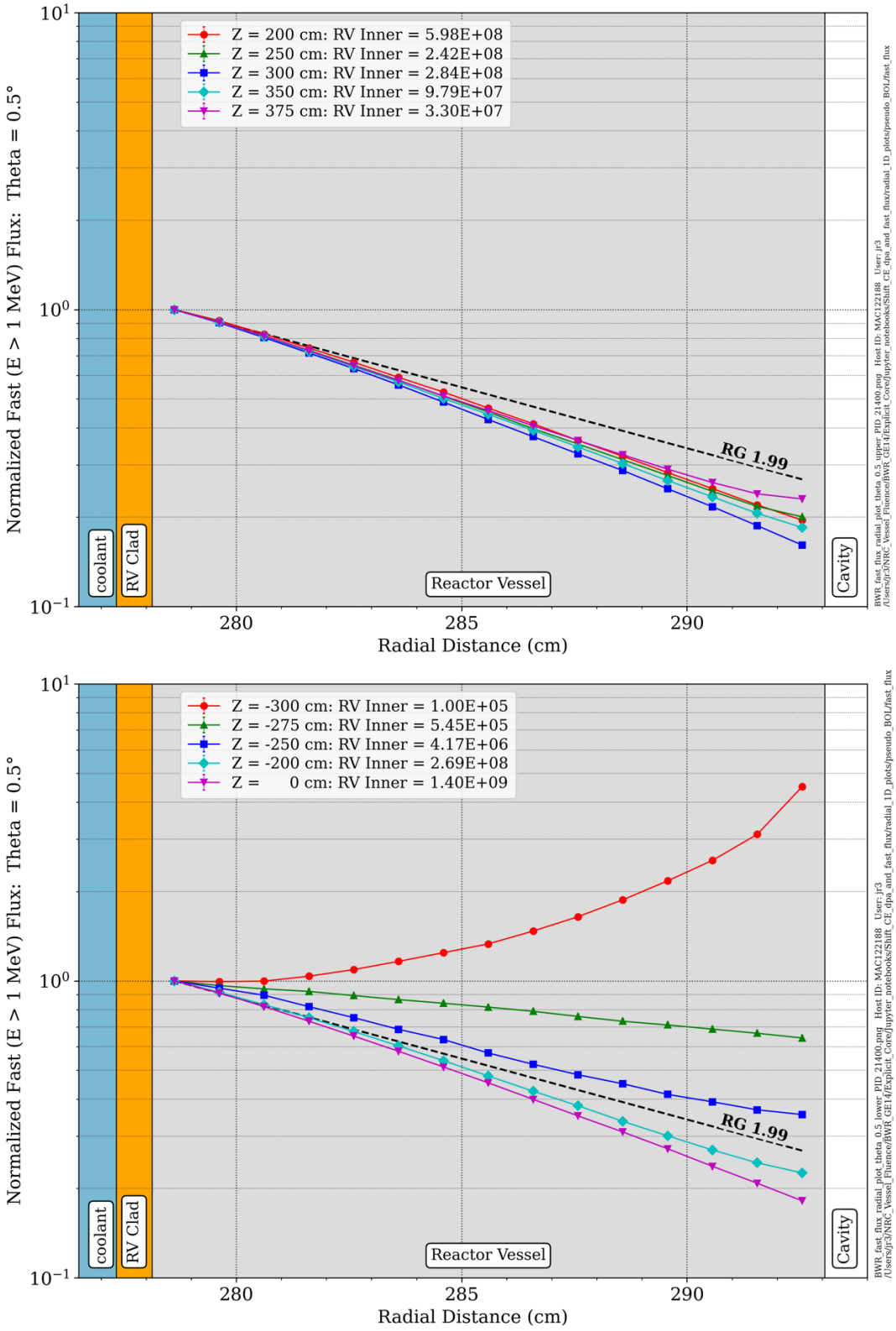

Figure 5-14 Normalized radial fast neutron flux profiles in the BWR model with a pseudo-BOL fission source. Azimuthal angle of 0.5° *The profiles are normalized to the flux at the RPV inner diameter at each elevation.*

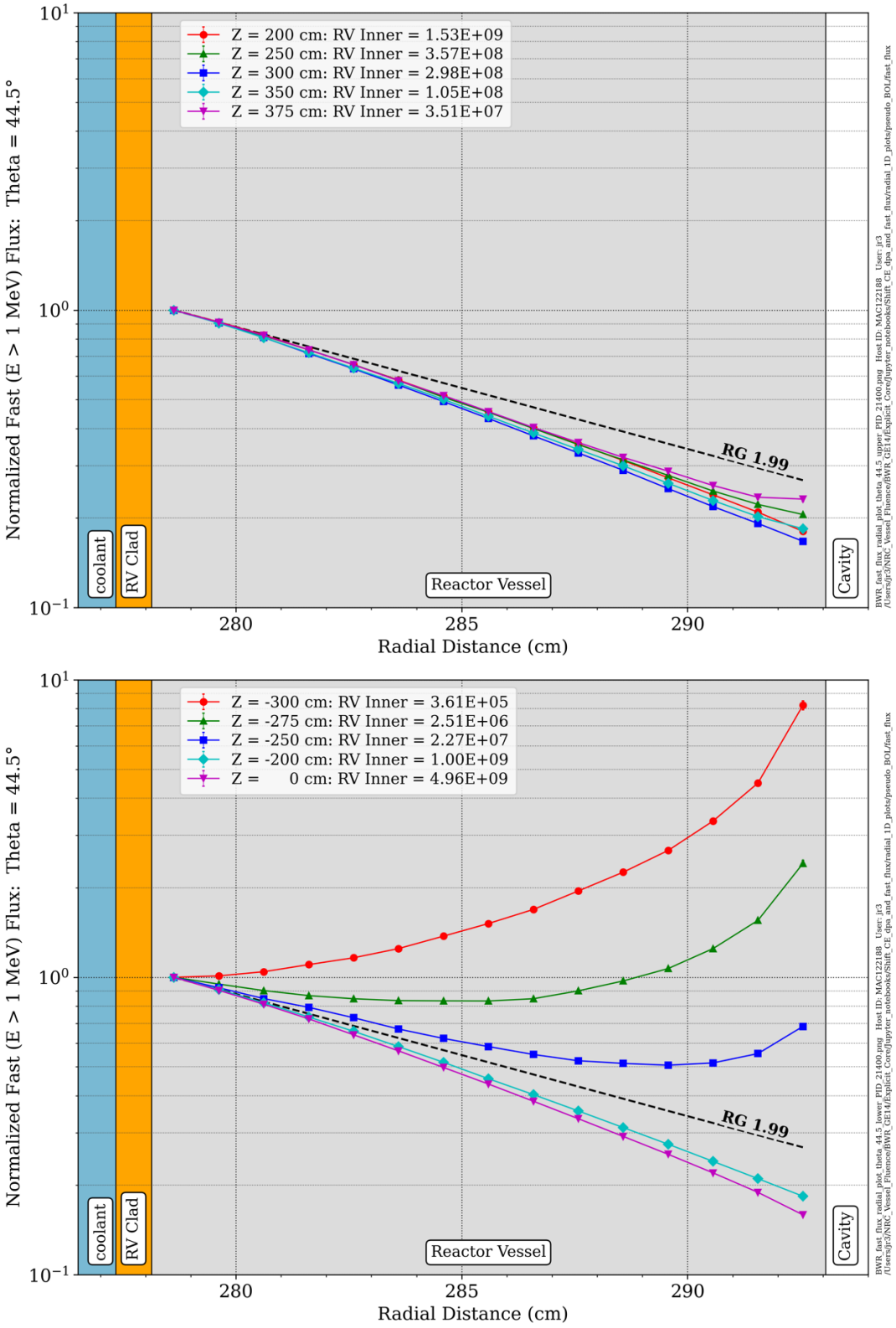

Figure 5-15 Normalized radial fast neutron flux profiles in the BWR model with a pseudo-BOL fission source. Azimuthal angle of 44.5° *The profiles are normalized to the flux at the RPV inner diameter at each elevation.*

5.2 Fission Spectrum Changes with Burnup

As LWR fuel is burned up, the fraction of fissions by isotope changes. In general, the fraction of fissions from ^{235}U decreases monotonically, while the fission fractions from ^{239}Pu, ^{241}Pu, and, to a lesser degree ^{238}U, increase monotonically. While some fission can occur in ^{240}Pu and ^{242}Pu, the fraction of fissions in those isotopes is very low, even in high-burnup assemblies.

Changes in the fission fraction contributions with burnup affect RPV fluence in three ways:

1. They result in changes in the energy spectrum of the fission neutrons. Relative to ^{235}U, the spectrum of prompt fission neutrons from ^{238}U is "softer," i.e., shifted toward lower energies, while the spectra for ^{239}Pu and ^{241}Pu are "harder," i.e., shifted toward higher energies. This is shown in Figure 5-16.
2. They cause changes in the value of $\bar{\nu}$, the average number of neutrons emitted per fission. The values of $\bar{\nu}$ for ^{235}U, ^{238}U, ^{239}Pu, and ^{241}Pu are provided in Table 5-3 based on cross-section data in work by Rearden and Jessee [42]. With increasing fuel burnup, the average number of neutrons released per fission increases due to the increasing contributions of ^{239}Pu and ^{241}Pu.
3. They lead to changes in K, the energy released in fission. Values of K for ^{235}U, ^{238}U, ^{239}Pu, and ^{241}Pu were obtained from work by James [74] and are provided in Table 5-3. The number of fissions required per second for a given power level is inversely proportional to K. Consequently, the fission rate per unit power is slightly lower with the Pu isotopes compared to with the U isotopes. However, this effect is small (less than 4%) compared to the increasing values of $\bar{\nu}$.

Table 5-3 Values of nu-bar ($\bar{\nu}$) and kappa (K) used in the fissile isotope parameter study

Isotope	$\bar{\nu}$ (neutrons/fission)	K (MeV/fission)
^{235}U	2.44	202.7
^{238}U	2.56	205.9
^{239}Pu	2.88	207.2
^{241}Pu	2.95	210.6

The baseline calculations in Sections 5.1.1 and 5.1.2 employed pseudo-BOL sources based on data from Table 5-1 and Table 5-2. In the same manner, pseudo end-of-life (pseudo EOL) sources were used to evaluate fast flux levels based on the maximum-depletion data in Table 5-1 and Table 5-2. A comparison of the pseudo BOL and pseudo EOL sources is shown in Table 5-4. The BWR EOL ^{241}Pu fraction includes 5.33% from Table 5-2 and the residual fraction of 0.51%.

Table 5-4 Isotopic fission fractions for the pseudo BOL and pseudo EOL sources used in the PWR and BWR models

Isotope	PWR		BWR	
	BOL	EOL	BOL	EOL
^{235}U	93.828%	12.31%	92.67%	50.70%
^{238}U	6.172%	9.12%	7.33%	7.66%
^{239}Pu	0.0%	58.28%	0.0%	35.80%
^{241}Pu	0.0%	20.35%	0.0%	5.84%

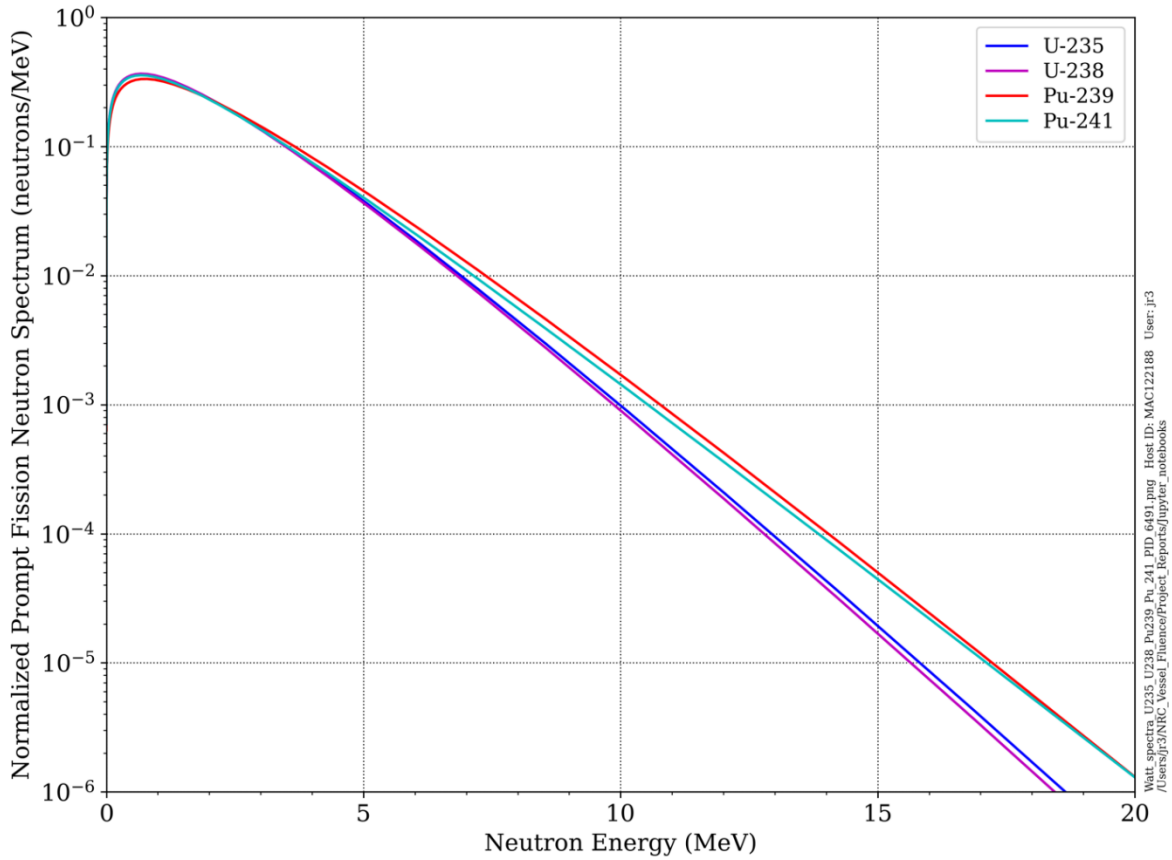

Figure 5-16 **Prompt fission neutron spectra of ^{235}U, ^{238}U, ^{239}Pu, and ^{241}Pu** *All spectra are normalized to an integrated value of 1.0*

If there were no differences in the prompt fission neutron spectra for the four isotopes of interest, then the fast flux in the RPV (and at all locations) would be expected to increase with burnup based on changes in $\bar{\nu}$ and K. Using the data from Table 5-3 and Table 5-4, the expected flux increase from the pseudo BOL to the pseudo EOL sources would be ~12.5% for the PWR model and ~6.5% for the BWR model. However, as discussed in the following paragraph, the shift in the prompt neutron fission spectrum with increasing burnup plays an important role in the overall effect of changes in the fission fractions.

A significant amount of neutron attenuation between the outer fuel assemblies and the RPV occurs in water, especially for the BWR model. Hydrogen is particularly effective in moderating (reducing the energy of) neutrons, as a neutron can lose more than 99.9999% of its energy in a single scatter with ^{1}H. In contrast, a neutron can lose at most ~22.1% of its energy in a single scatter from ^{16}O, and at most, it will only lose ~6.9% in a single scatter from ^{56}Fe. Because the neutron scattering cross section in hydrogen decreases monotonically with neutron energy for energies greater than about 10 keV, a shift in the neutron energy spectrum toward higher energies (as is the case with ^{239}Pu and ^{241}Pu relative to ^{235}U and ^{238}U) will lead to higher fast neutron flux levels in the RPV, even with no consideration of changes in $\bar{\nu}$ and K.

Therefore, it is clear that the fast neutron flux in the RPV of both the PWR and BWR models will increase with increasing fuel burnup. This effect is quantitively addressed in Section 5.2.1 and Section 5.2.2.

5.2.1 Fission Spectrum Effects in the PWR Model

The fast flux levels in the PWR with a pseudo EOL fission source were calculated using the EOL fission fractions from Table 5-4. Ratio plots showing the increase in the fast neutron flux in the RPV from the pseudo EOL relative to the pseudo BOL source are shown in Figure 5-17 through Figure 5-22. At the core midplane, the increase in the fast flux in the RPV ranges from ~23 to 34%. As noted above, ~12.5% of this increase can be attributed to the changes in $\bar{\nu}$ and K. The minimum increases occur in the azimuthal portion of the RPV that is aligned with the neutron pad. This portion of the RPV has the least amount of water between the core and the RPV due to the proximity of the corner fuel assemblies to the core barrel, as well as the displacement of water by steel due to the neutron pad. In contrast, the maximum increase occurs at an azimuthal location with substantially more water between the core and the RPV. This results in a lower fast flux magnitude, but it causes an increase in the EOL/BOL ratio because the spectrum changes are magnified by transmission through a greater amount of water.

At the elevations of Z = -70 cm and Z = 470 cm, the EOL/BOL ratios are greater than at the core midplane, ranging from ~30 to 50%, with the maximum ratios occurring near the inner surface of the RPV. These higher ratios are consistent with the increase in the amount of water through which neutrons are transported to reach the inner portion of the RPV at elevations above and below the active fuel height.

5.2.2 Fission Spectrum Effects in the BWR Model

The fast flux levels in the BWR with a pseudo EOL fission source were calculated using the EOL fission fractions from Table 5-4. Ratio plots of the increase in the fast neutron flux in the RPV from the pseudo EOL to the pseudo BOL sources are shown in Figure 5-23 through Figure 5-27. At the core midplane elevation, the fast flux in the RPV increases by ~20–24%. As noted above, ~6.5% of this increase is due to changes in $\bar{\nu}$ and K, and the remainder is due to the effect of the harder neutron spectrum at EOL. At an elevation of Z = -250 cm, the fast flux increases by ~22–30%. This slightly greater increase is consistent with neutron transport through a greater amount of water than at the core midplane. In a similar manner, the fast flux at Z = 375 cm increases by 24–28%.

BWR cores with higher burnup than that specified in Table 5-3 will experience even greater increases in the RPV fast flux as the contributions from ^{239}Pu and ^{241}Pu increase. A conservative upper limit for this increase can be obtained by comparing the flux with a ^{239}Pu source to that with a ^{235}U source. The ^{239}Pu-to-^{235}U fast flux ratios at the three selected elevations are shown in Figure 5-28, Figure 5-29, and Figure 5-30. While these are a conservative upper limit, as noted, they do indicate that higher burnup BWR fuel would be likely to result in greater EOL/BOL fast flux ratios in the RPV.

5.2.3 Summary

The fast flux levels in the RPV of a PWR and BWR are likely to increase with burnup levels as the contribution of neutrons from the fission of ^{239}Pu and ^{241}Pu increases. These Pu isotopes have a greater average number of neutrons per fission and harder neutron spectra compared to ^{235}U and ^{238}U. The use of core designs with higher fuel burnup could lead to even greater increases in the fast flux as increasing levels of fission occur in the Pu isotopes. The actual variation in the fast neutron flux levels in the RPV as a function of core lifetime will depend on core loading patterns and operating parameters.

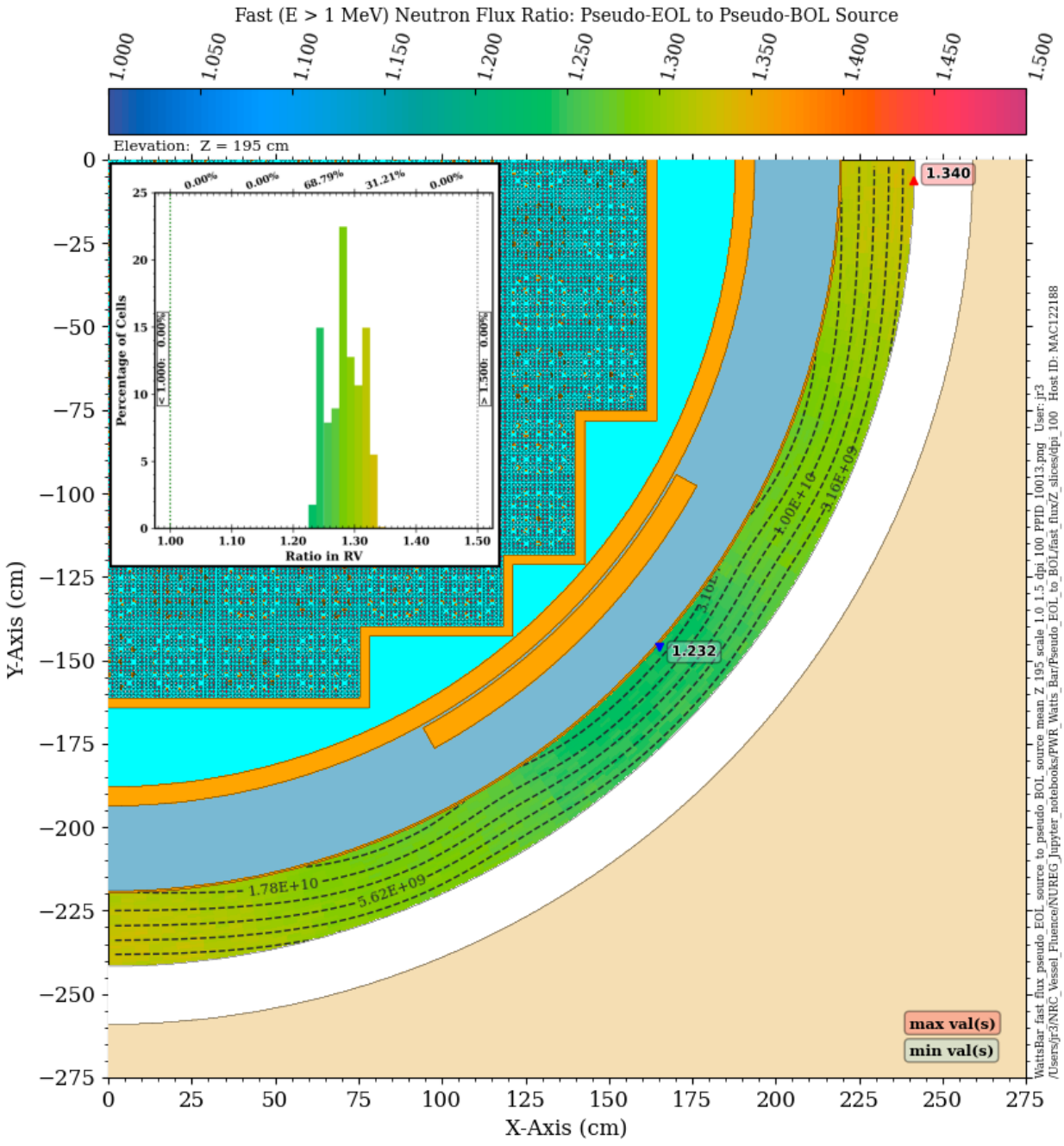

Figure 5-17 Fast neutron flux ratio for a pseudo EOL source relative to a pseudo BOL source in the PWR model. Elevation at Z = 195 cm *The dashed contour lines represent the fast flux with the pseudo-BOL source.*

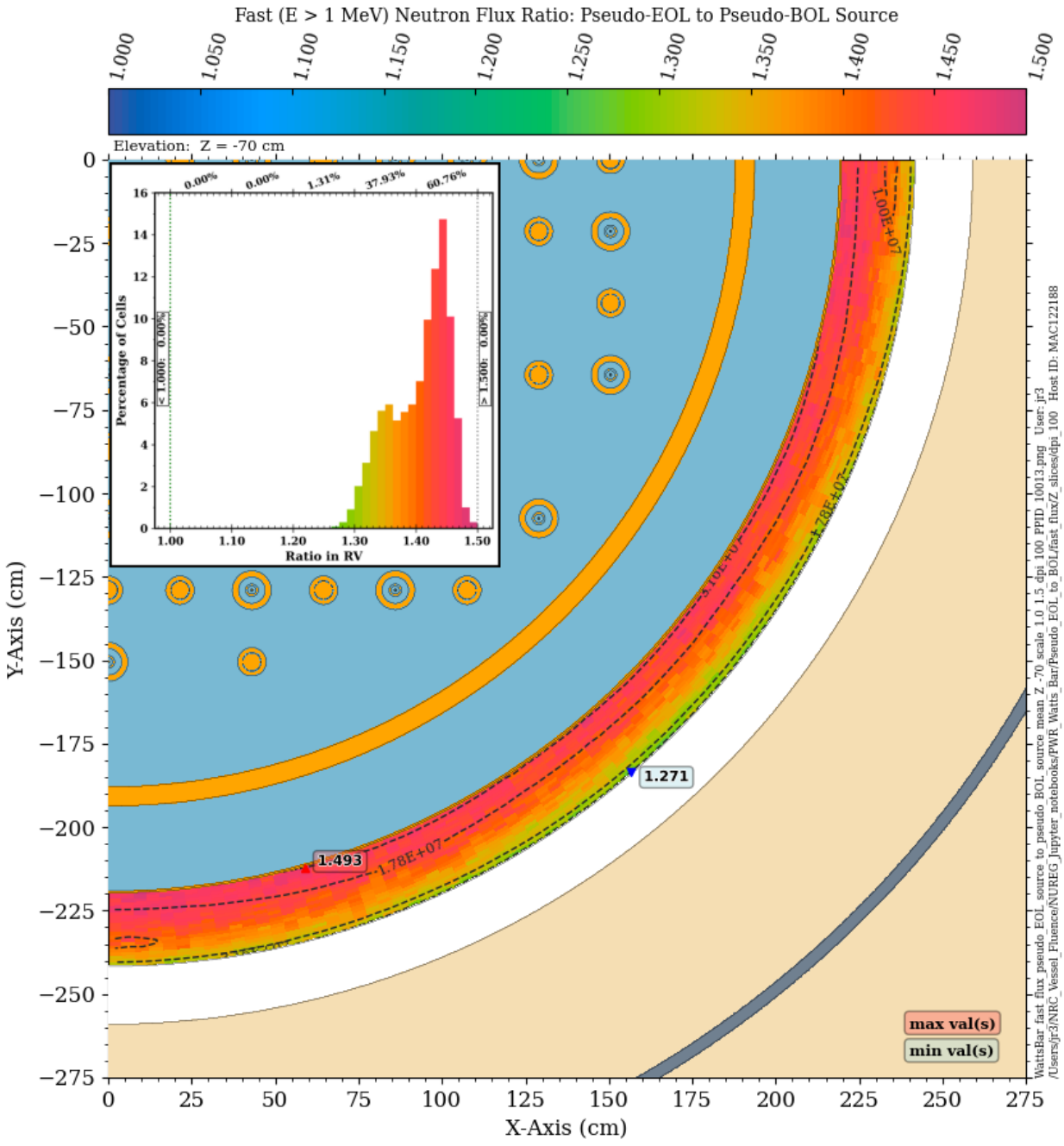

Figure 5-18 Fast neutron flux ratio for a pseudo EOL source relative to a pseudo BOL source in the PWR model. Elevation at Z = -70 cm *The dashed contour lines represent the fast flux with the pseudo-BOL source.*

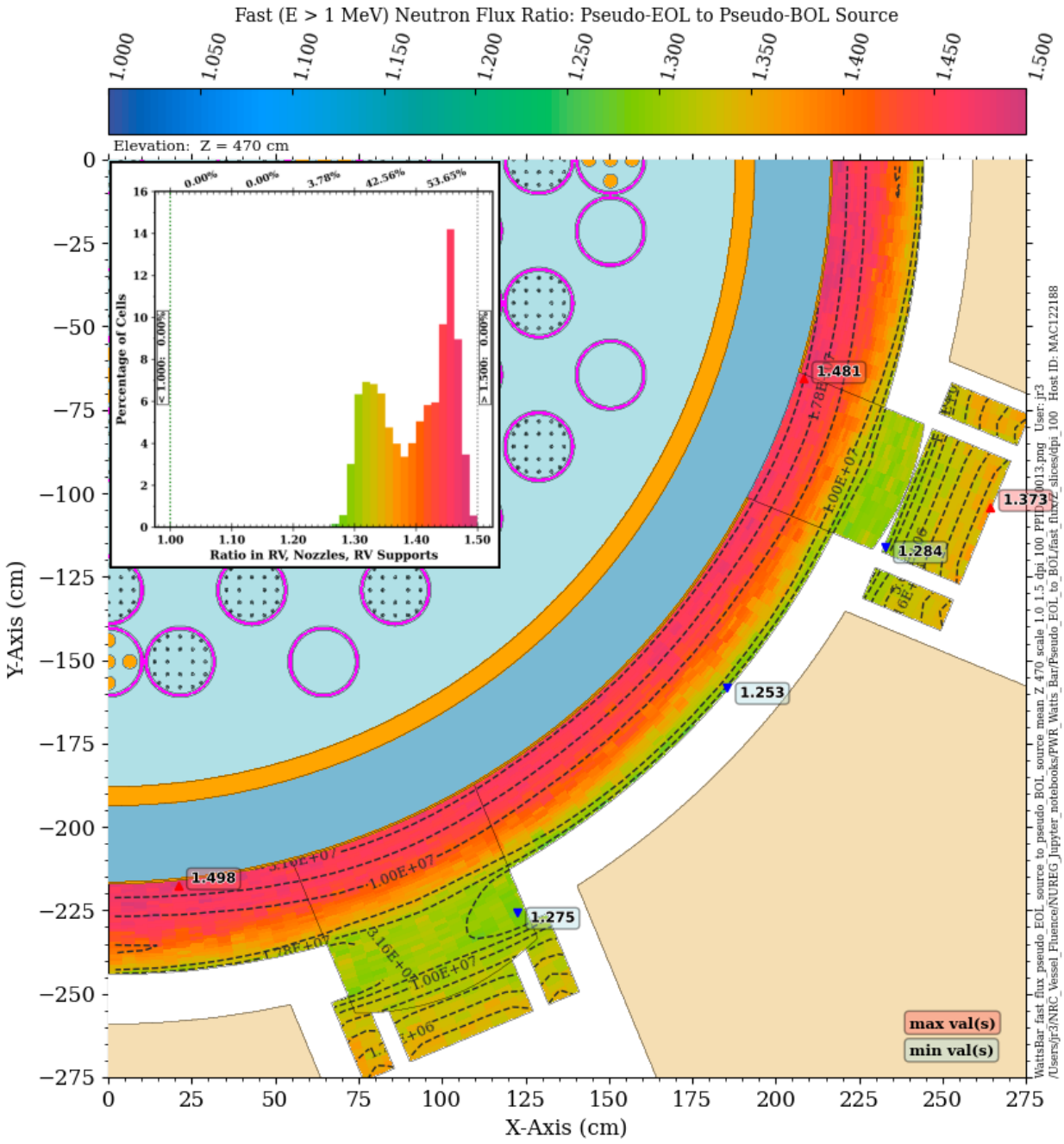

Figure 5-19 Fast neutron flux ratio for a pseudo EOL source relative to a pseudo BOL source in the PWR model. Elevation at Z = 470 cm *The dashed contour lines represent the fast flux with the pseudo-BOL source.*

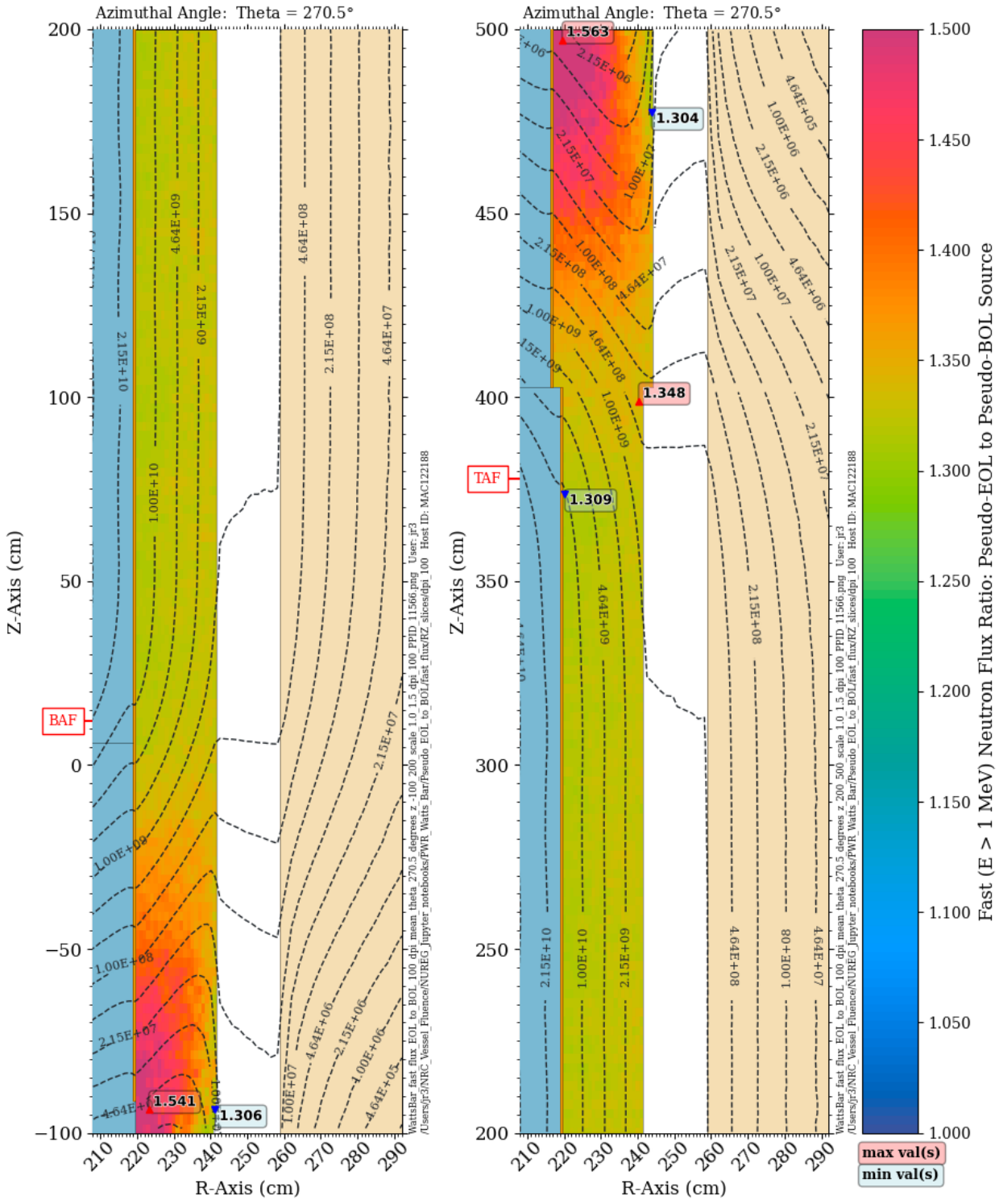

Figure 5-20 Fast neutron flux ratio for a pseudo EOL source relative to a pseudo BOL source in the PWR model. Elevation view at an azimuthal angle of 270.5° *The dashed contour lines represent the fast flux with the pseudo BOL source.*

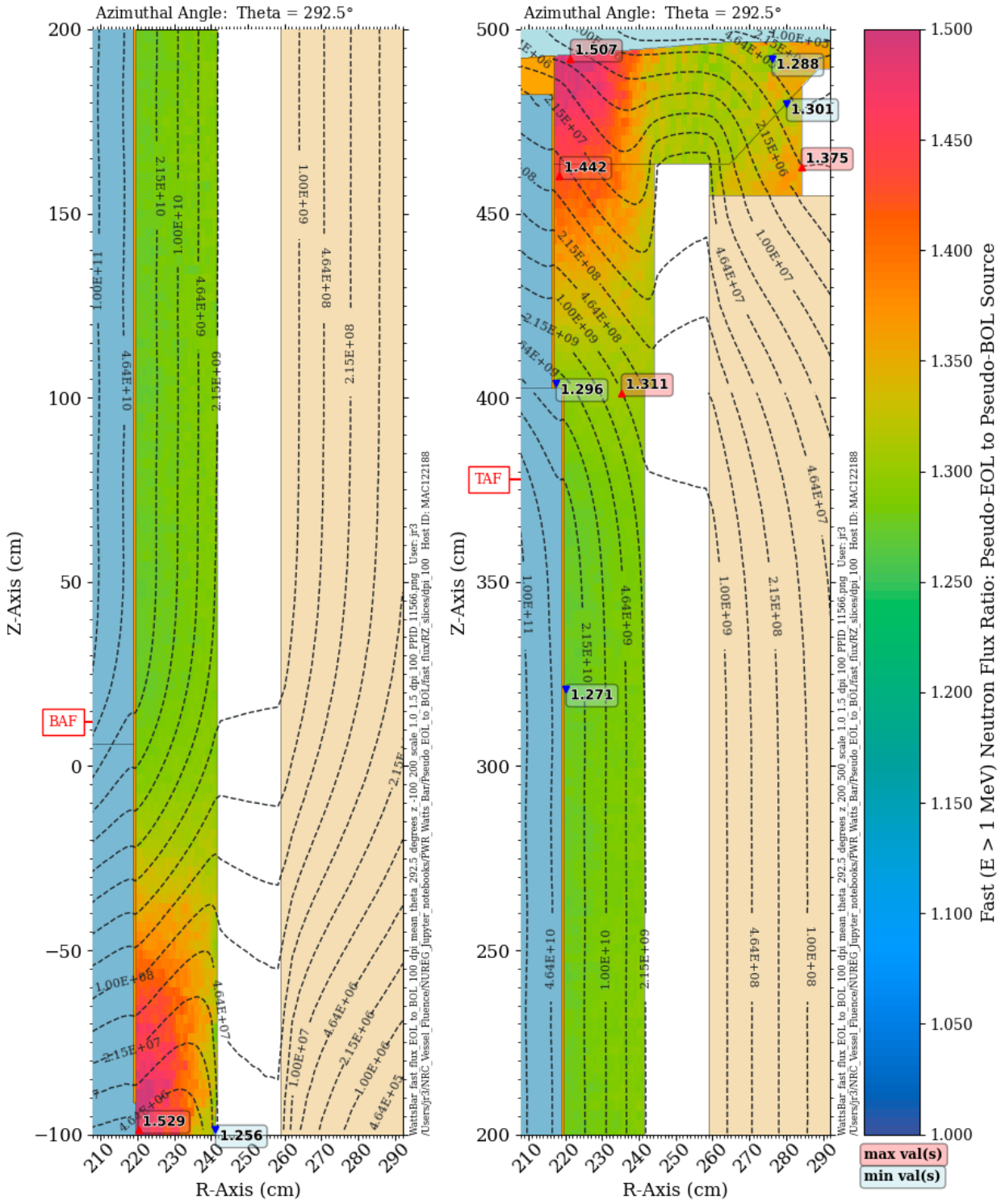

Figure 5-21 Fast neutron flux ratio for a pseudo EOL source relative to a pseudo BOL source in the PWR model. Elevation view at an azimuthal angle of 292.5° *The dashed contour lines represent the fast flux with the pseudo-BOL source.*

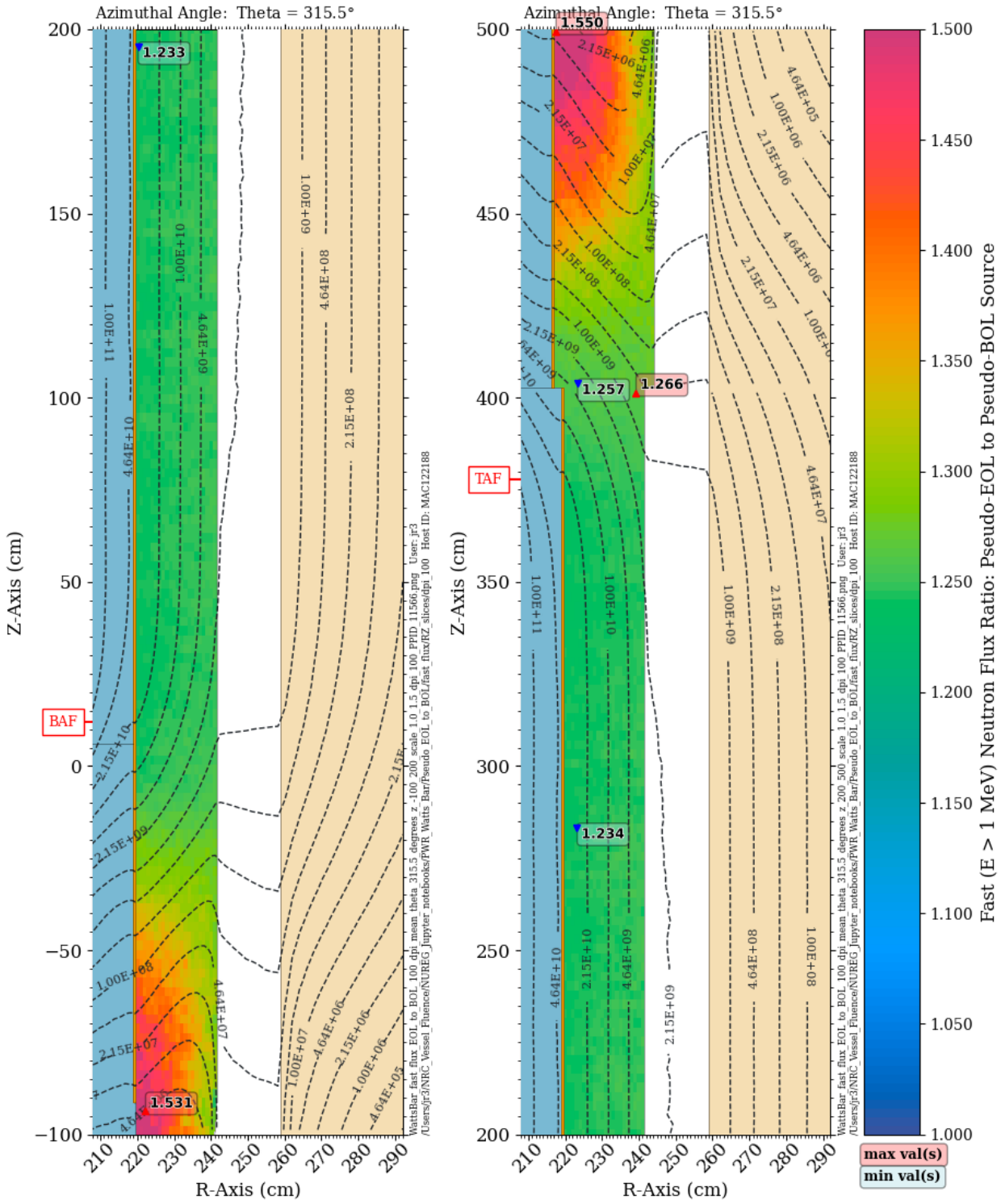

Figure 5-22 Fast neutron flux ratio for a pseudo EOL source relative to a pseudo BOL source in the PWR model. Elevation view at an azimuthal angle of 315.5° *The dashed contour lines represent the fast flux with the pseudo BOL source.*

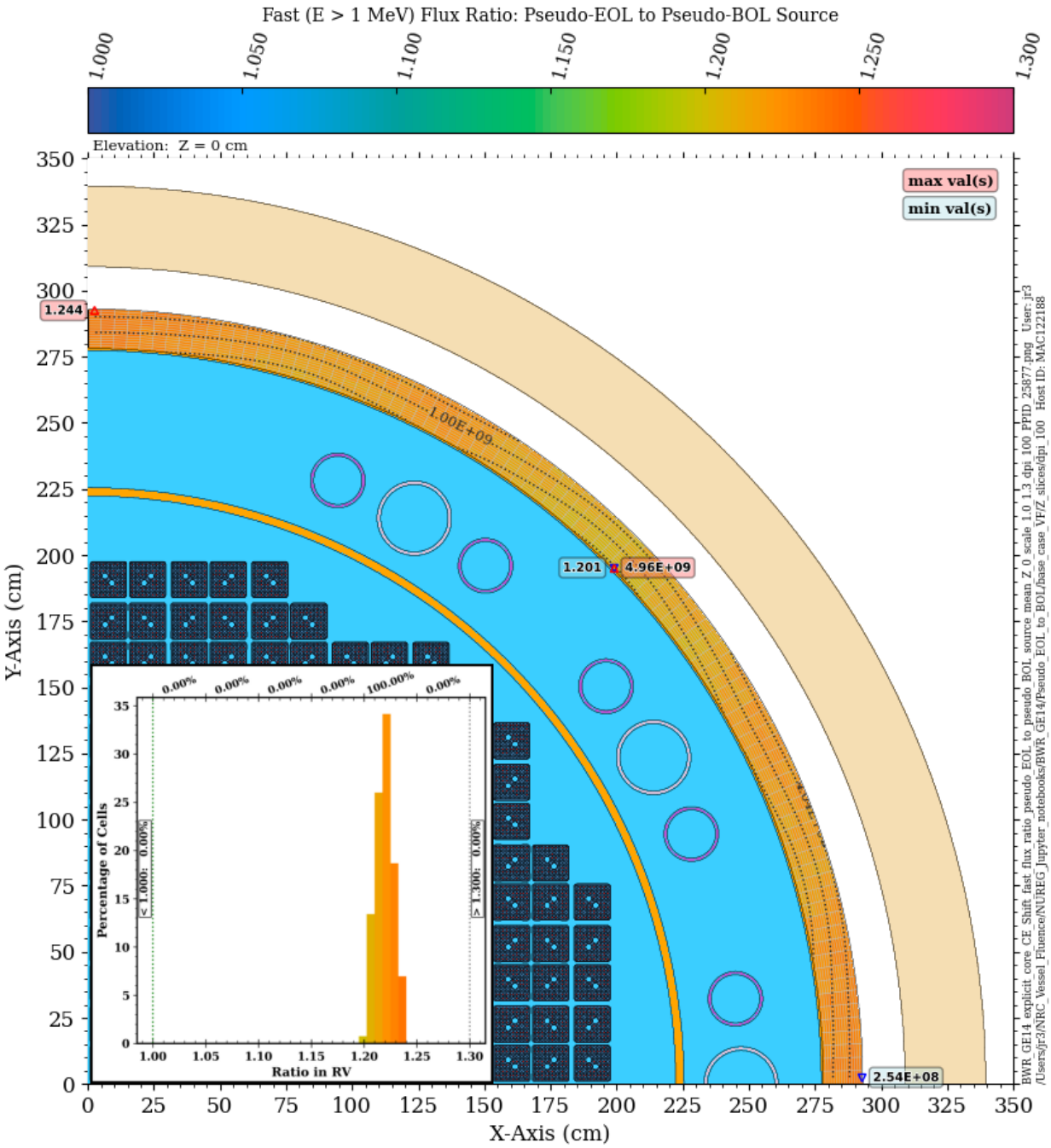

Figure 5-23 Fast neutron flux ratio for a pseudo EOL source relative to a pseudo BOL source in the BWR model. Plan view at the core midplane *The dashed contour lines represent the fast flux with the pseudo BOL source.*

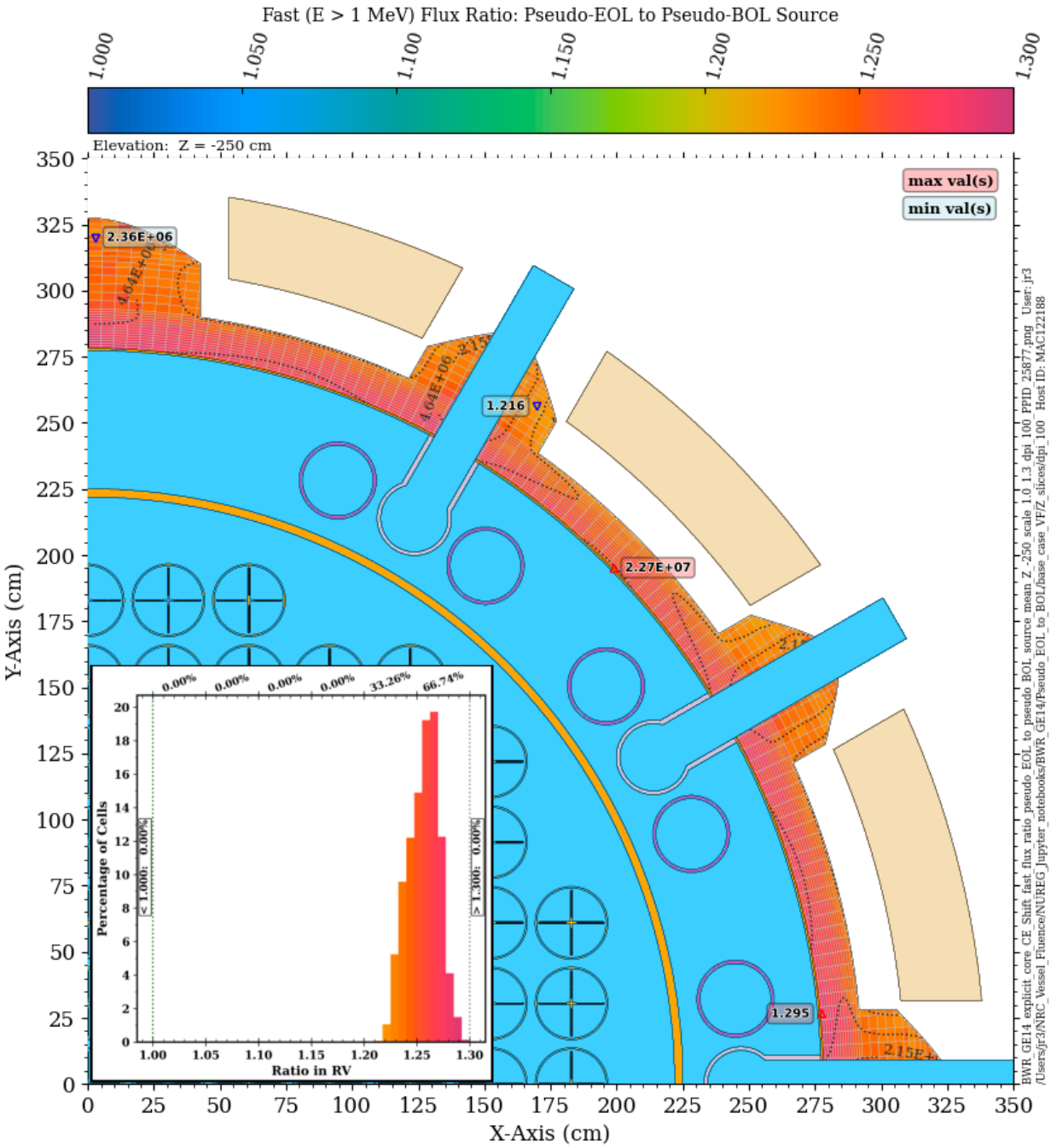

Figure 5-24 Fast neutron flux ratio for a pseudo EOL source relative to a pseudo BOL source in the BWR model. Plan view through the recirculation outlet nozzles at Z = -250 cm *The dashed contour lines represent the fast flux with the pseudo-BOL source.*

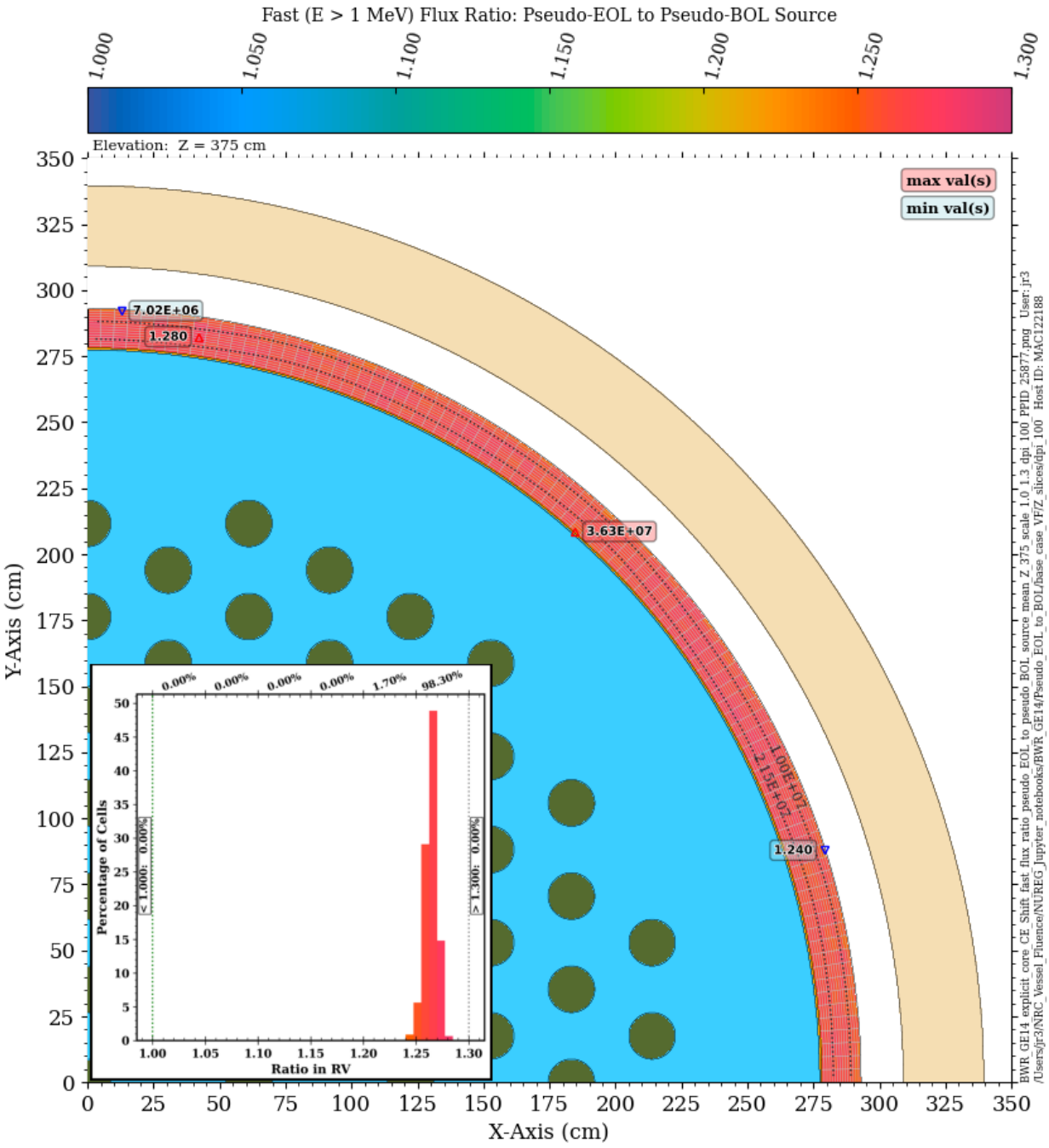

Figure 5-25 Fast neutron flux ratio for a pseudo EOL source relative to a pseudo BOL source in the BWR model. Plan view above the core shroud at Z = 375 cm *The dashed contour lines represent the fast flux with the pseudo BOL source.*

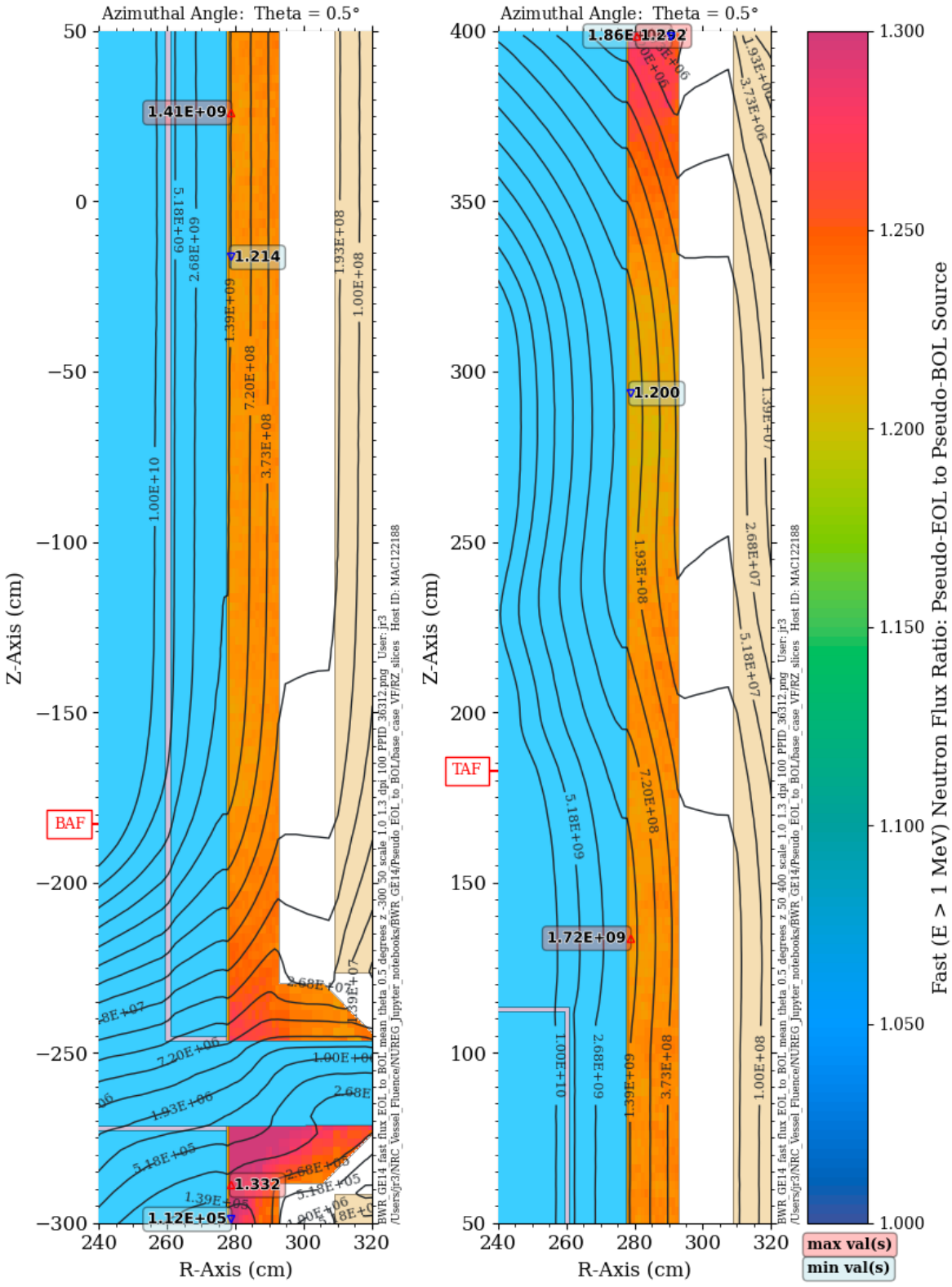

Figure 5-26 Fast neutron flux ratio for a pseudo EOL source relative to a pseudo BOL source in the BWR model. Elevation view at an azimuthal angle of 0.5° *The contour lines represent the fast flux with the pseudo BOL source.*

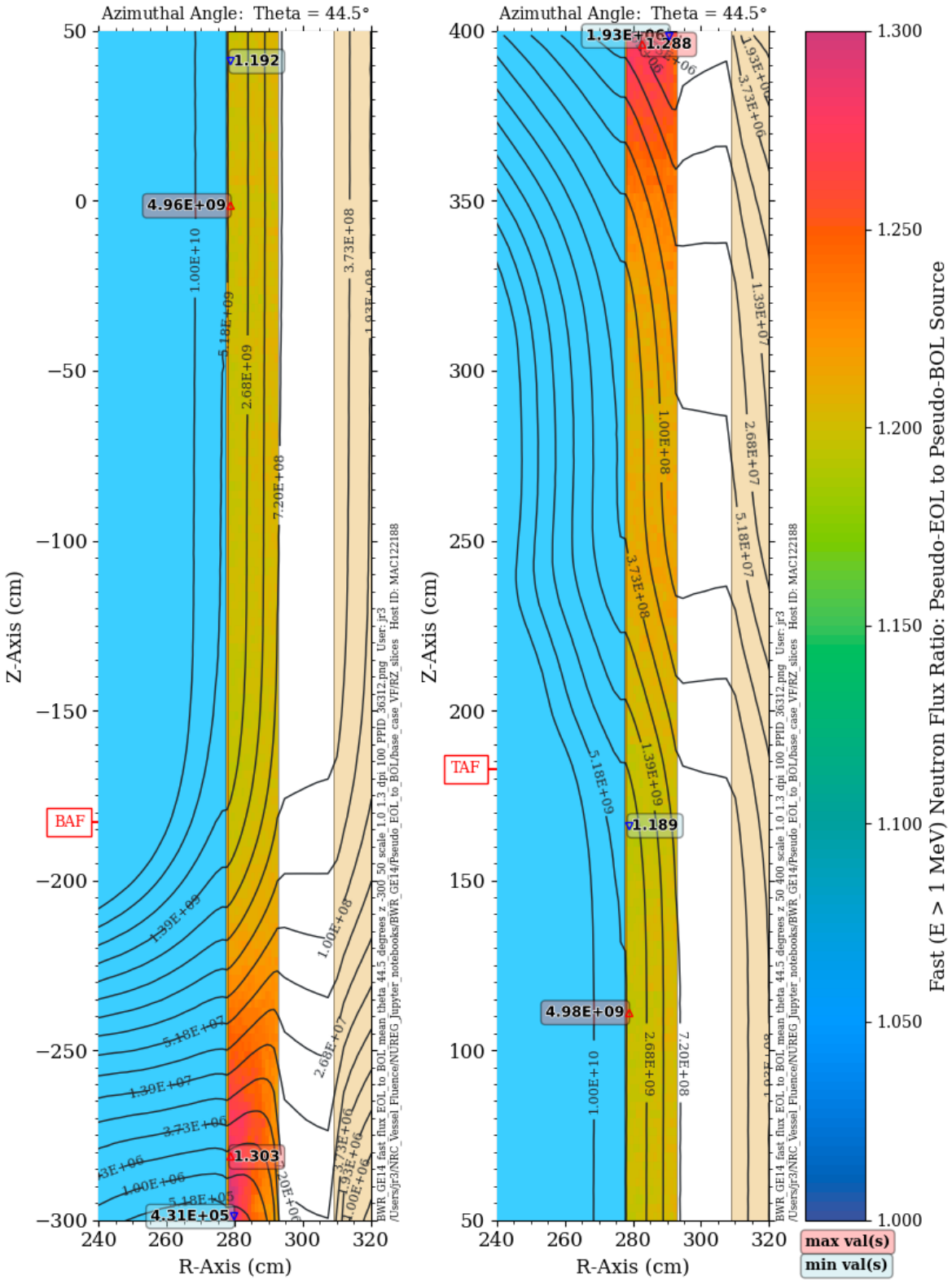

Figure 5-27 Fast neutron flux ratio for a pseudo EOL source relative to a pseudo BOL source in the BWR model. Elevation view at an azimuthal angle of 0.5° *The contour lines represent the fast flux with the pseudo BOL source.*

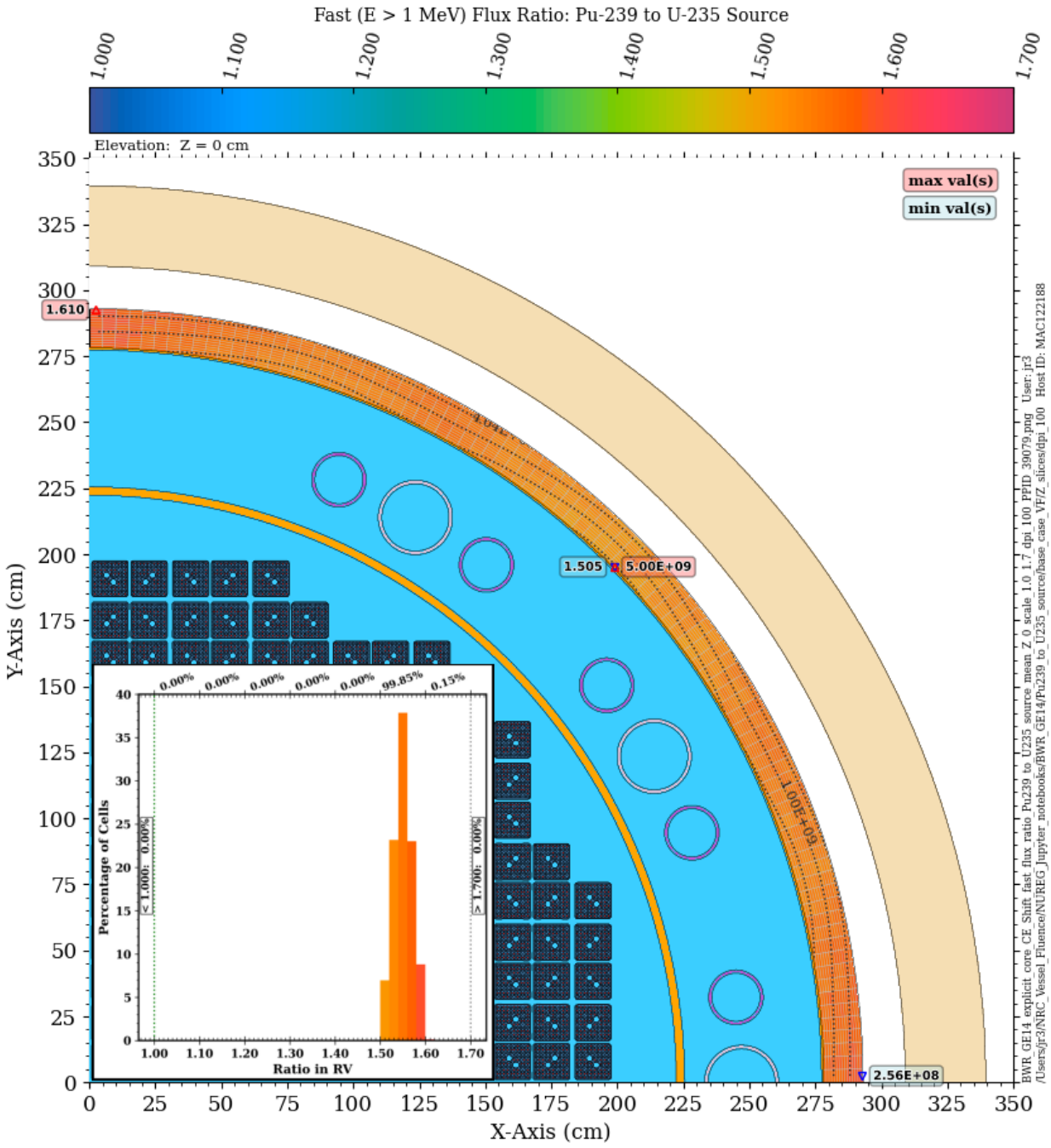

Figure 5-28 Fast neutron flux ratio for a ^{239}Pu source relative to a ^{235}U source in the BWR model. Plan view at the core midplane *The dashed contour lines represent the fast flux with a ^{235}U source.*

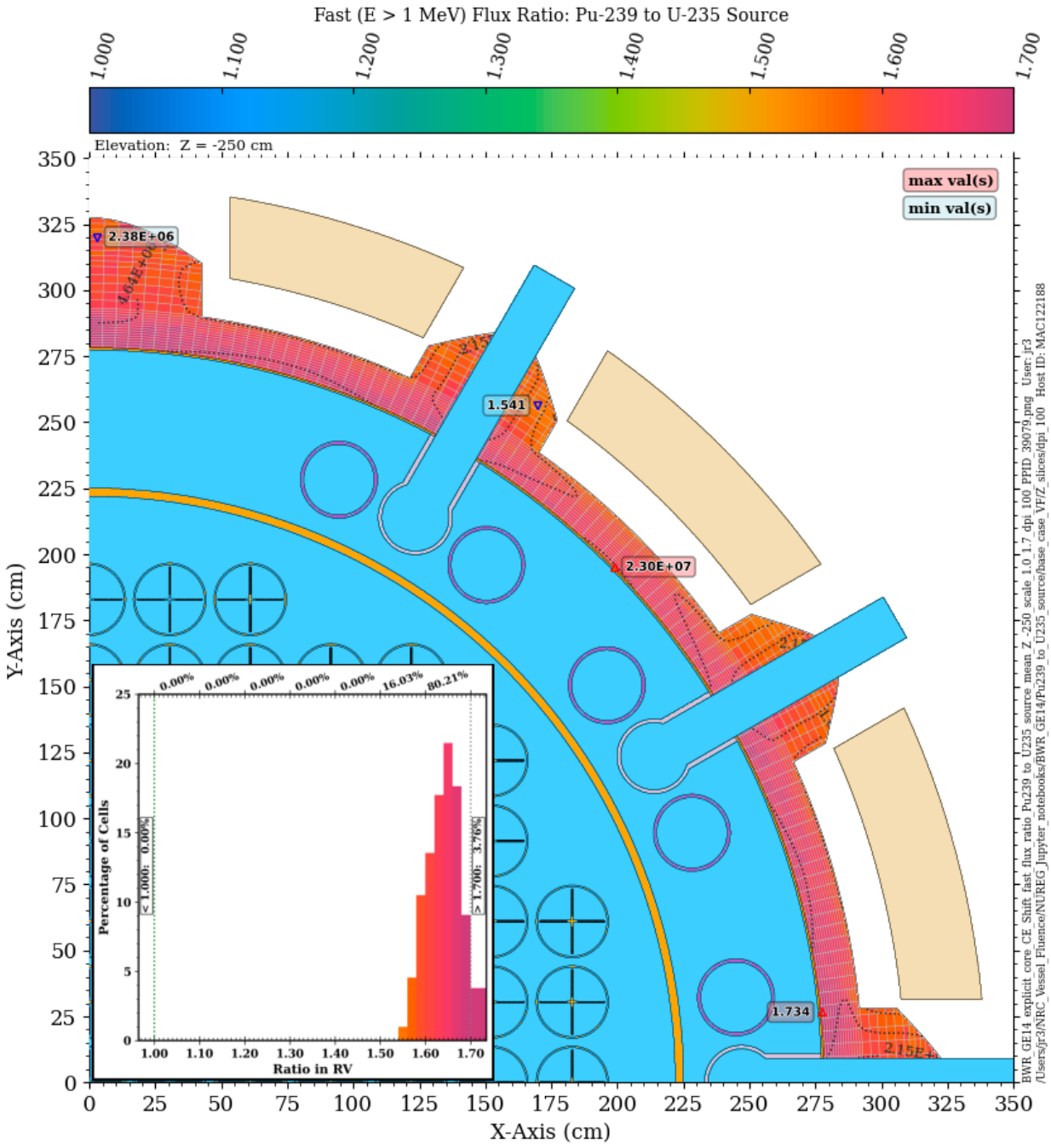

Figure 5-29 Fast neutron flux ratio for a ^{239}Pu source relative to a ^{235}U source in the BWR model. Plan view through the recirculation outlet nozzles at Z = -250 cm *The dashed contour lines represent the fast flux with a ^{235}U source.*

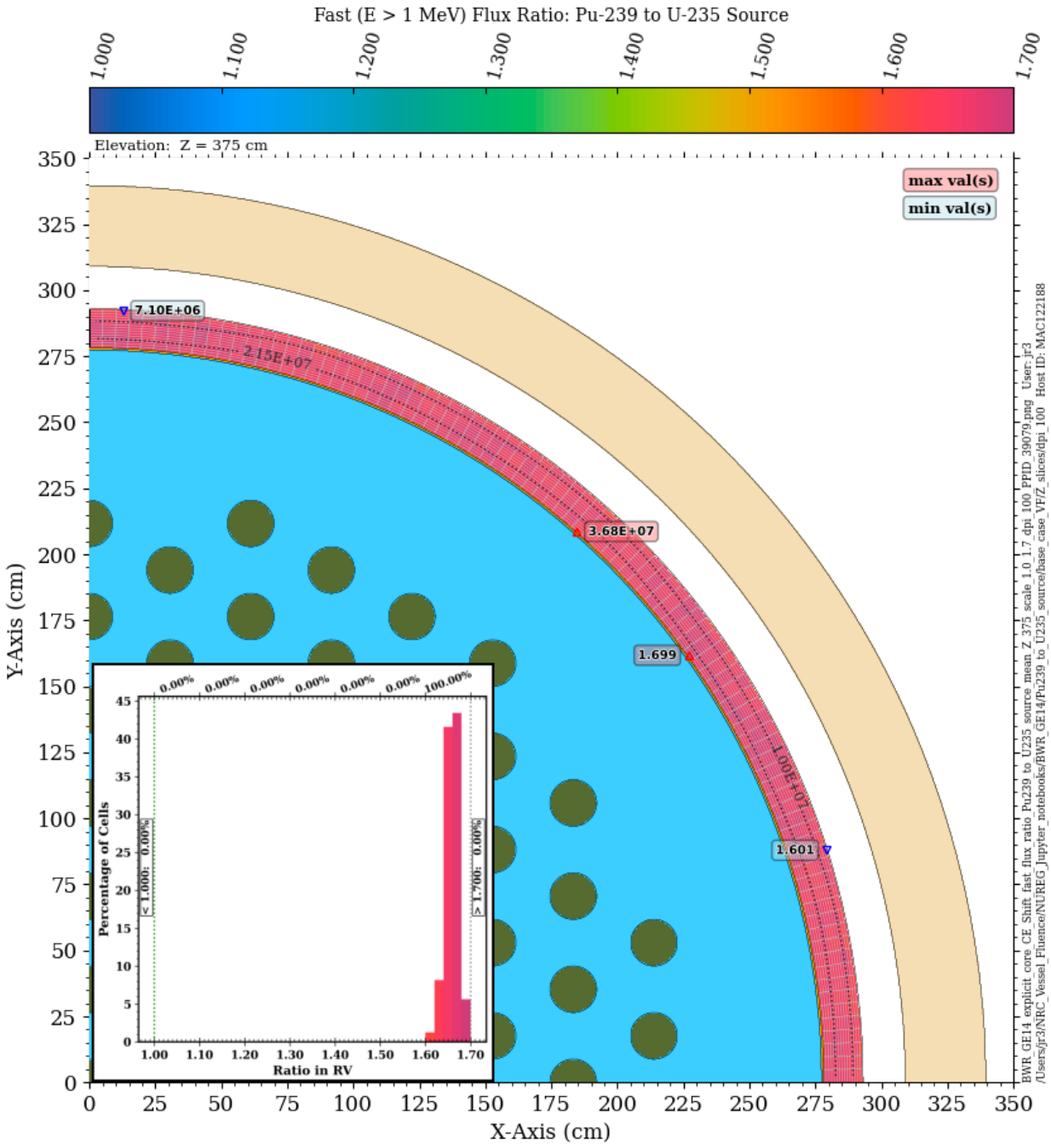

Figure 5-30 Fast neutron flux ratio for a ^{239}Pu source relative to a ^{235}U source in the BWR model. Plan view above the core shroud at Z = 375 cm *The dashed contour lines represent the fast flux with a ^{235}U source.*

5.3 Coolant Temperature Variations in the PWR Model

Changes in the coolant temperature at any location within the RPV will affect neutron attenuation due to changes in the density of the coolant and hence the macroscopic cross section. Coolant temperature increases lead to reduced attenuation and hence higher fast flux levels incident to the RPV; the reverse is true for reductions in temperature. The primary question with regard to fast fluence levels in the extended beltline region is this: are coolant temperature changes likely to affect fast fluence in the extended beltline region differently than they do within the traditional beltline region?

While an exact analysis would require detailed knowledge of the coolant temperature at numerous locations within the RPV, a reasonable assessment of temperature changes can be made by simply adjusting all coolant temperatures by a specified amount. Calculations with the PWR model were run with temperature changes of 5, 10, and 15 °F above and below the baseline temperature. The source in each case was a spatially uniform pinwise distribution with a ^{235}U fission spectrum. Results for the -10 °F and +10 °F models are presented in this section. Results for the 5 °F and 15 °F temperature changes show the same overall trend.

The effect of reducing the coolant temperatures by 10°F is shown in Figure 5-31, Figure 5-32, and Figure 5-33. Within the traditional beltline region, the fast neutron flux in the RPV has a reduction of ~5% to ~10%. In the extended beltline region there is a greater reduction in the fast flux in the inner portion of the RPV. This increased effect is due to the greater amount of water through which the neutrons are transported to reach the inner portion of the RPV in the extended beltline region. There is little change in the fast flux ratio in the outer portion of the RPV at all elevations, as the flux levels in the outer RPV in the extended beltline region are dominated by cavity streaming neutrons.

The effect of increasing the coolant temperatures by 10 °F is shown in Figure 5-34, Figure 5-35, and Figure 5-36. Here the behavior is essentially the inverse of that seen for the coolant temperature reduction. The fast neutron flux increases by ~5 to 10% through the thickness of the RPV in the traditional beltline region. In the extended beltline region, the increased amount of water through which the fast neutrons are transported to the inner surface of the RPV results in a greater increase in the fast neutron flux. In the outer portion of the RPV, the fast flux change is again nearly constant through the extended beltline region, as well as the traditional beltline region.

The results of the parametric water temperature study indicate that the impact of changes in coolant temperature with respect to RPV fluence levels is more significant for locations outside the traditional beltline region. This sensitivity suggests that accurate modeling of coolant temperatures throughout the RPV and the nozzles as a function of the plant operating history (including power uprates or other changes that may affect coolant pressure and temperature) is particularly important for extended beltline fluence calculations.

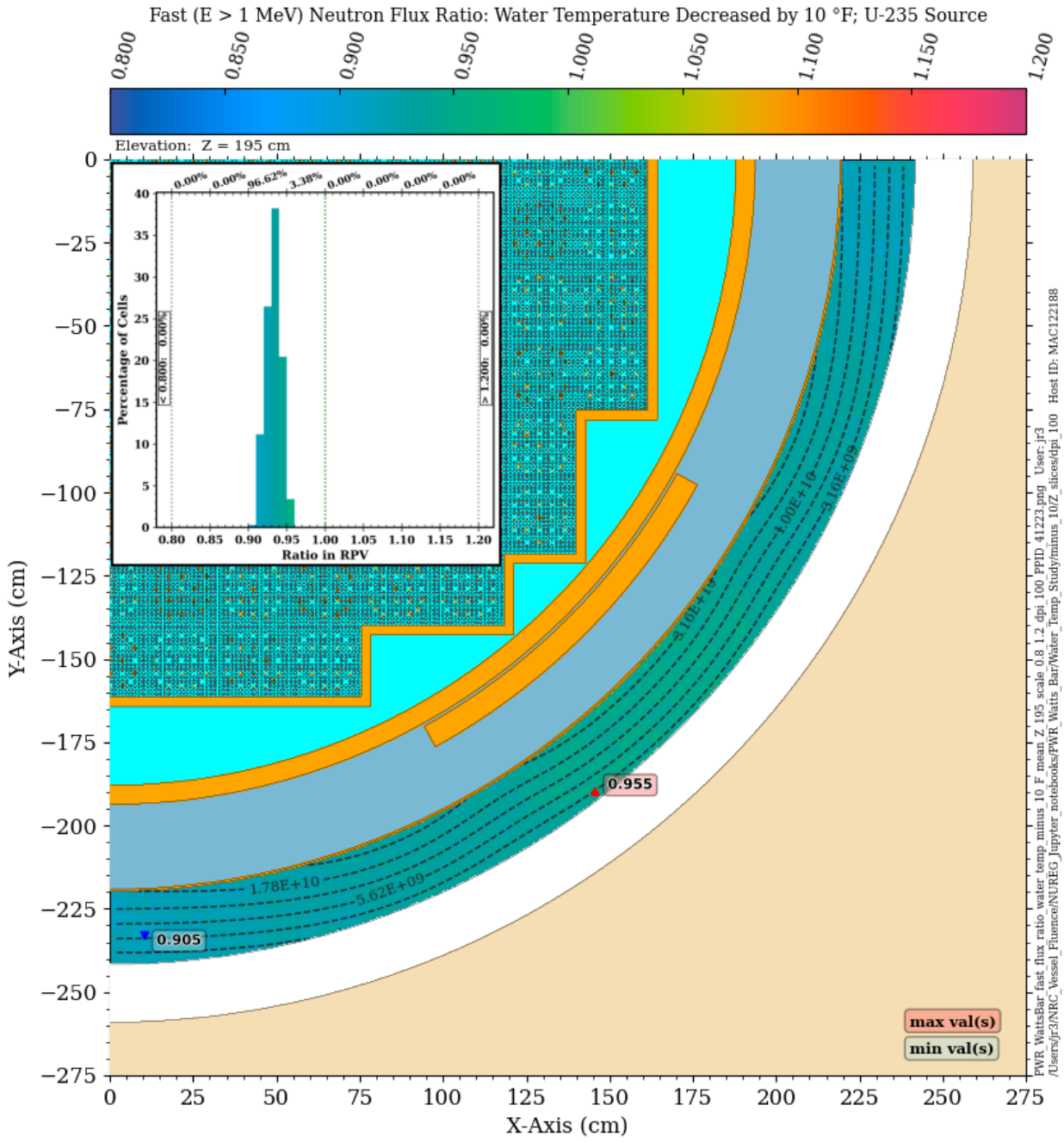

Figure 5-31 Ratio of the fast neutron flux in the RPV of the PWR when all water temperatures are decreased by 10°F relative to the base case model. Plan view at an elevation of Z = 195 cm *The contour lines show the fast neutron flux for the base case model.*

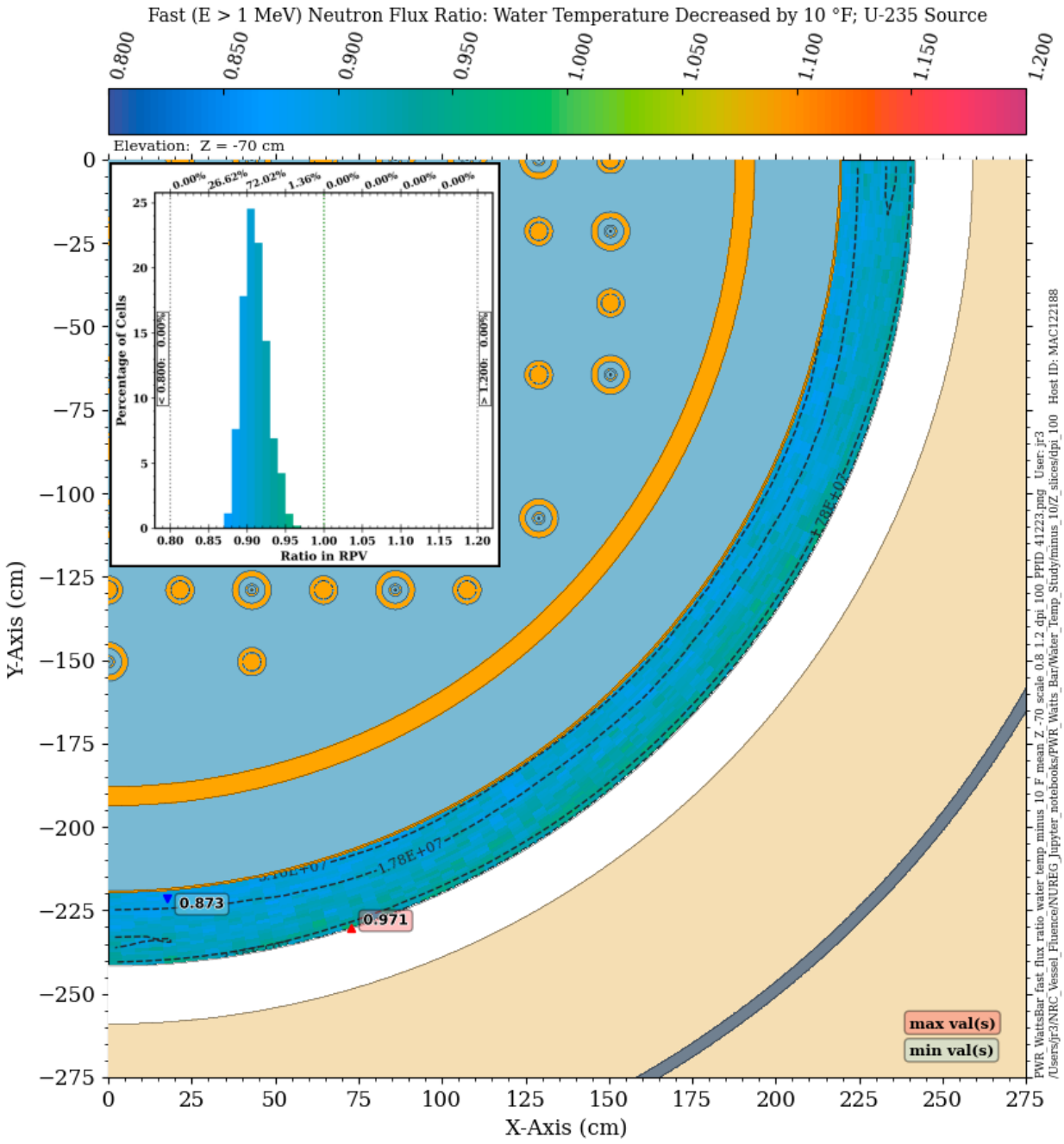

Figure 5-32 Ratio of the fast neutron flux in the RPV of the PWR when all water temperatures are decreased by 10°F relative to the base case model. Plan view at an elevation of Z = -70 cm *The contour lines show the fast neutron flux for the base case model.*

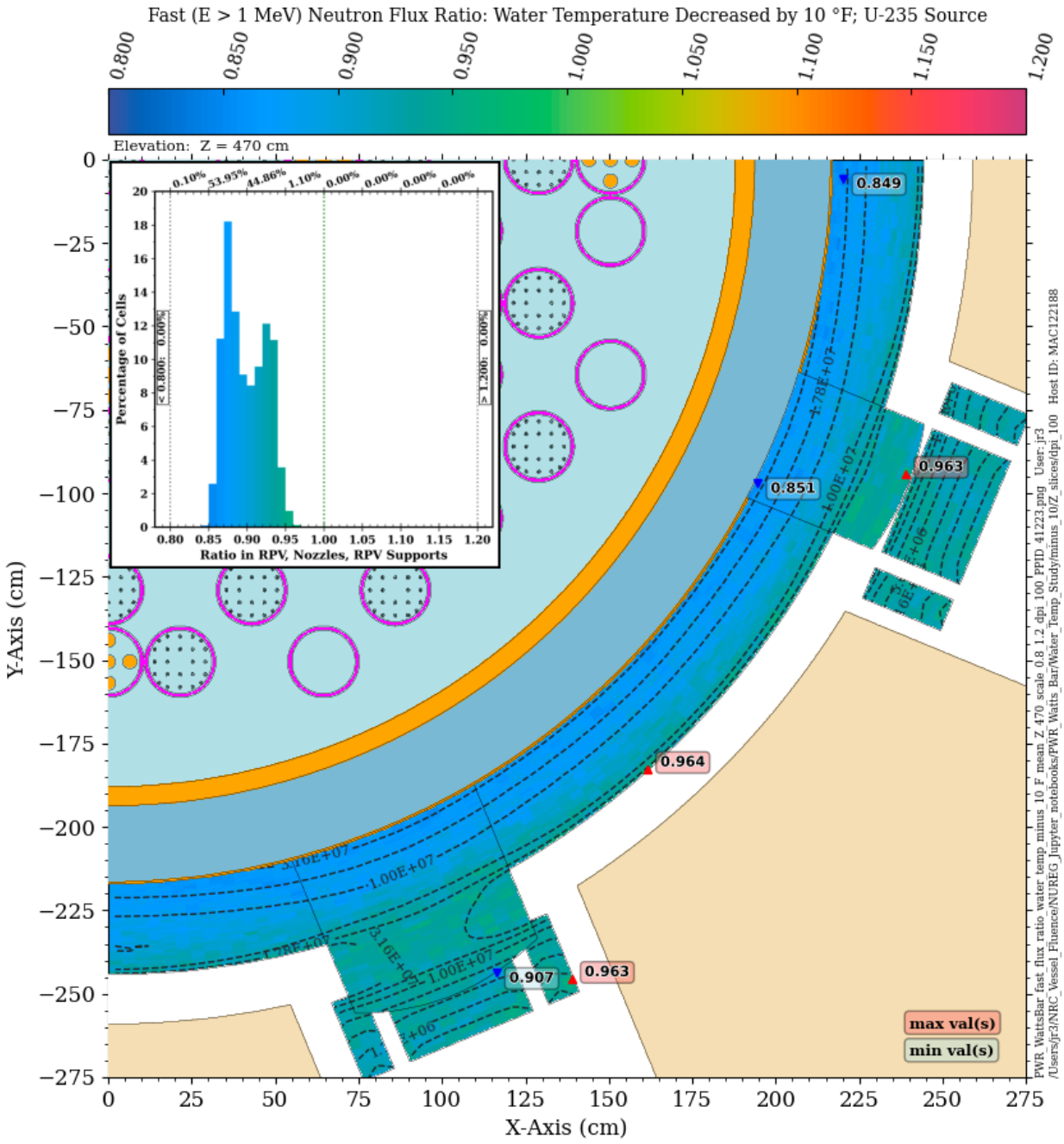

Figure 5-33 Ratio of the fast neutron flux in the RPV of the PWR when all water temperatures are decreased by 10°F relative to the base case model Plan view at an elevation of Z = 470 cm *The contour lines show the fast neutron flux for the base case model.*

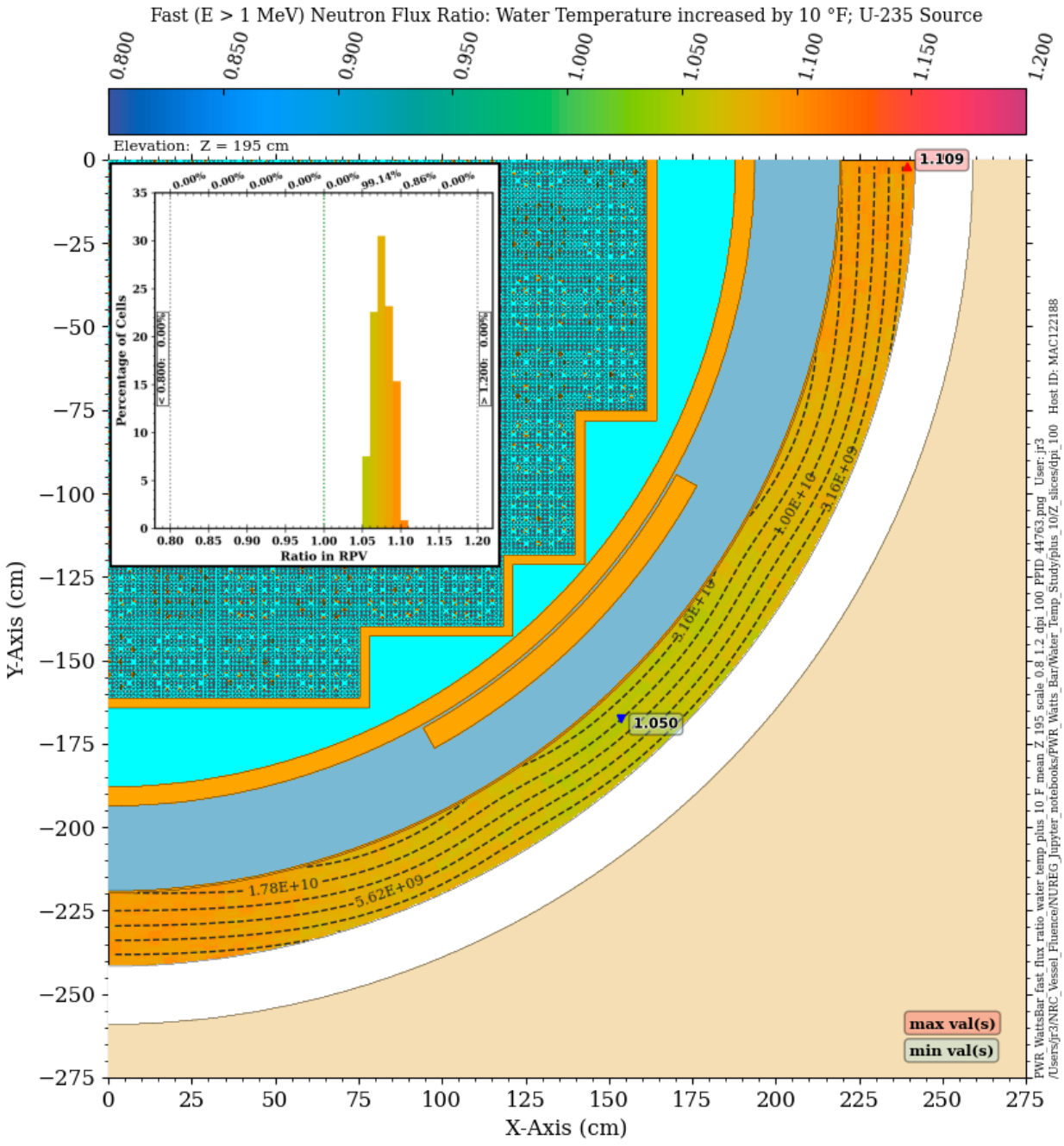

Figure 5-34 Ratio of the fast neutron flux in the RPV of the PWR when all water temperatures are increased by 10°F relative to the base case model Plan view at an elevation of Z = 195 cm *The contour lines show the fast neutron flux for the base case model.*

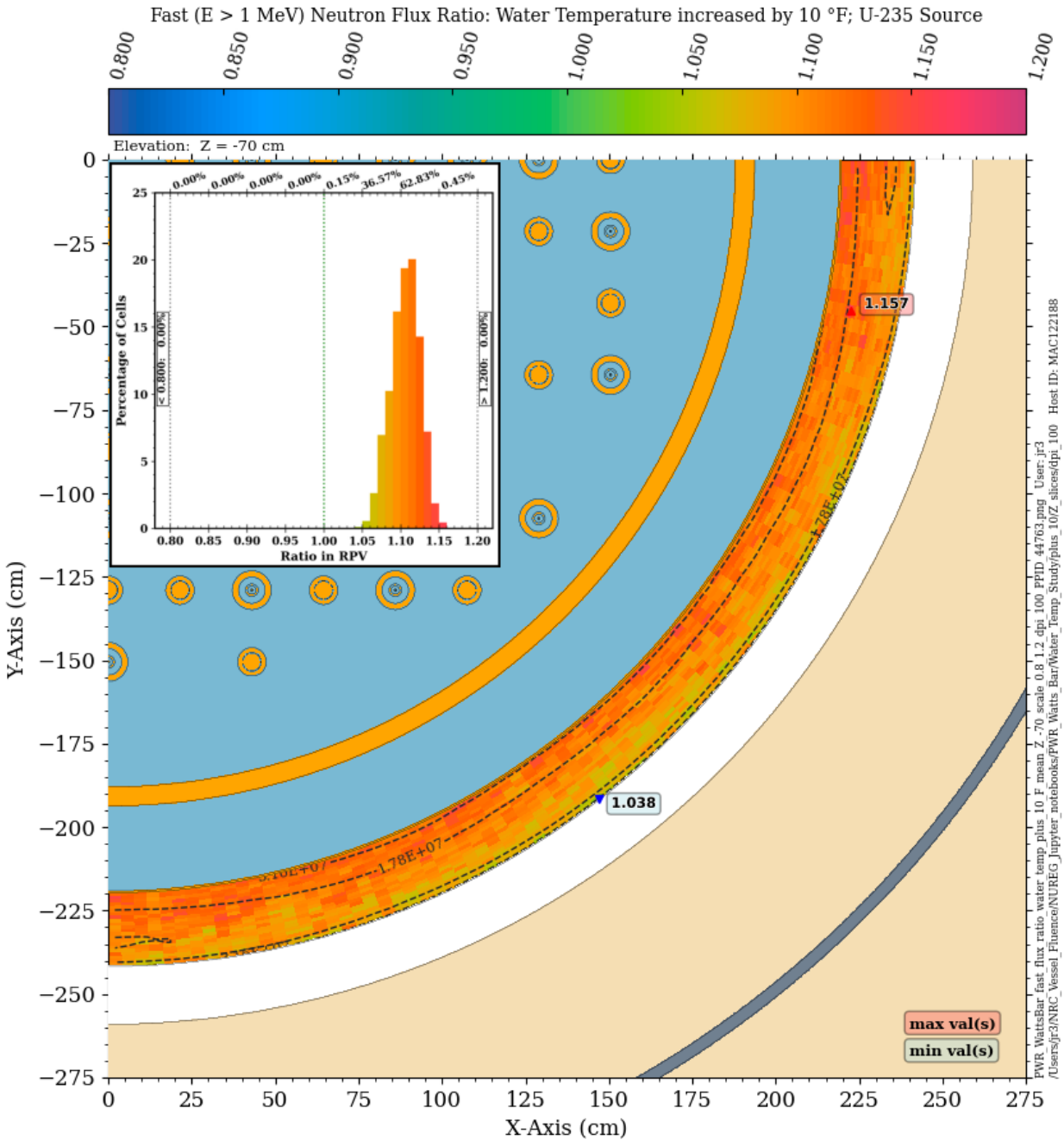

Figure 5-35 Ratio of the fast neutron flux in the RPV of the PWR when all water temperatures are increased by 10°F relative to the base case model. Plan view at an elevation of Z = -70 cm *The contour lines show the fast neutron flux for the base case model.*

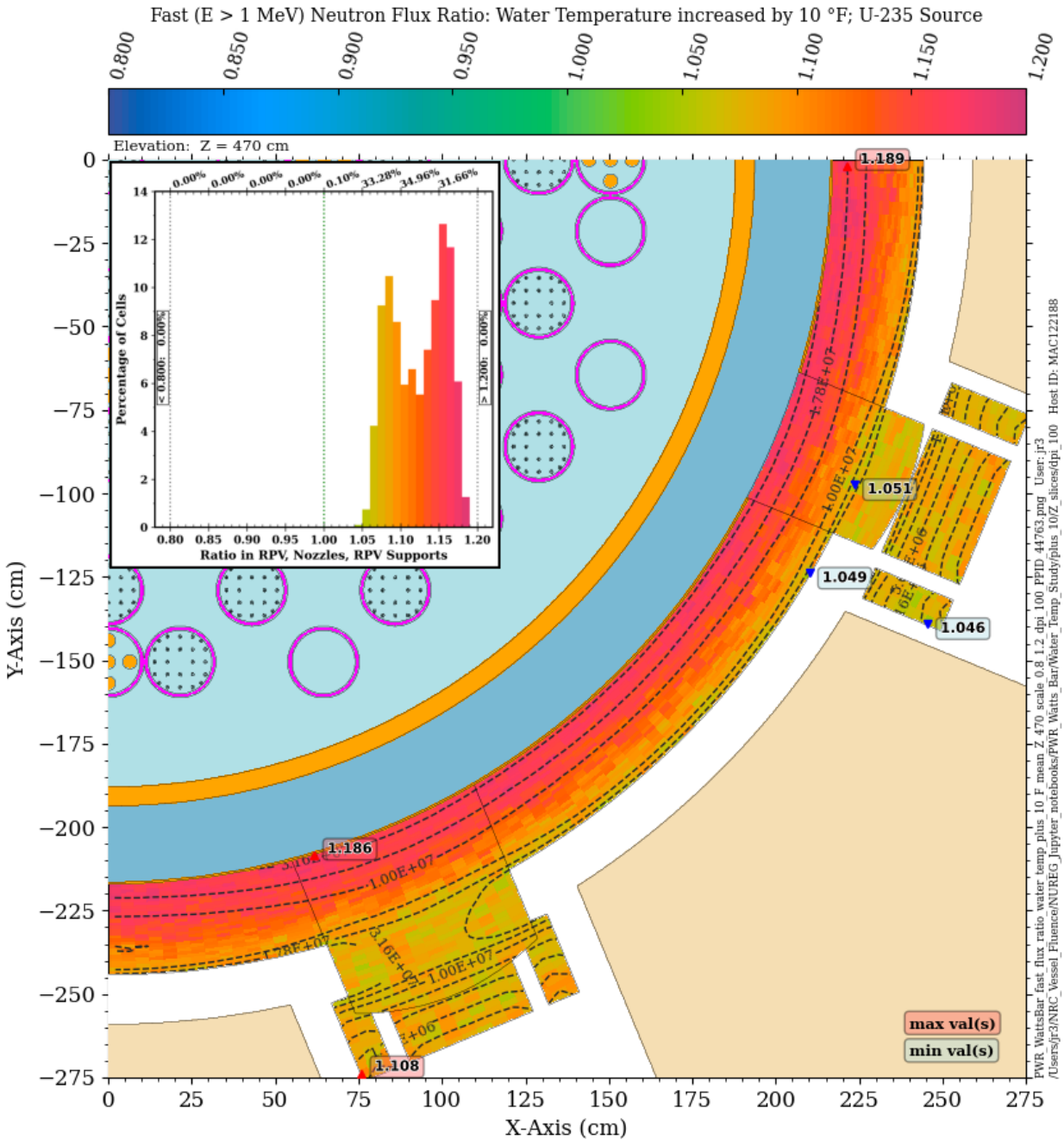

Figure 5-36 Ratio of the fast neutron flux in the RPV of the PWR when all water temperatures are increased by 10°F relative to the base case model. Plan view at an elevation of Z = 470 cm *The contour lines show the fast neutron flux for the base case model.*

5.4 Void Fractions in the BWR Model

Variations in the void fraction (VF) in a BWR core can affect the fast flux levels in the RPV due to two effects: changes in neutron attenuation within the fuel assemblies, and changes in the neutron spectrum as the isotopic fission fractions change due to hardening or softening of the neutron spectrum. In general, both of these effects will only be significant in the outer assemblies. Changes in the RPV fast flux levels due to fission spectrum changes are addressed in Section 5.2. The effects of VF changes are addressed in this section.

The VFs in each of the seven axial zones in the BWR model were obtained based on data in NUREG/CR-7224 [73]. In general, the VFs are highest near the center of the core and lower near the periphery. Data from NUREG/CR-7224, Figure 4.1 [73] were used to determine minimum, maximum, and average VF values based on assembly locations in the outermost part of the core. These values are shown in Table 5-5. The base case model has coolant densities based on the average VF values. Those densities are consistent with the BWR material data provided in Table 4-4 above. The source in each case was a spatially uniform pinwise distribution with a ^{235}U fission spectrum.

Table 5-5 VFs by axial zone in the BWR GE14 fuel assembly modeling

Axial zone (Figure 4-6)	Minimum VF (%)	Maximum VF (%)	Average VF (%)
NAT	2	2	2
PSZ	3	7	5
DOM	7	30	18.5
PLE	25	50	37.5
VAN	35	60	47.5
N-V	44	70	57
N-T	44	70	57

5.4.1 Minimum Void Fraction

Use of the minimum VF values by axial zone in place of the average values results in higher coolant densities for all zones above the NAT zone (Figure 4-6 and Table 5-5). Because the density differences in the NAT and PSZ zones are relatively small (or zero) when going from the average to the minimum VF, fast flux differences in the RPV at elevations near or below the lower portion of the core are likely to be small, whereas differences around the core midplane and above should be more pronounced.

This behavior can be seen in Figure 5-37 through Figure 5-40. At the core midplane, the reduction in the fast flux in the RPV is predominantly between 2.5 and 5%. At an elevation through the recirculation outlet nozzles at -250 cm, where the fast flux is approximately two orders of magnitude lower than at the core midplane, the differences in the fast flux are less than 2.5% in 98% of the mesh tally cells. At an elevation of 375 cm, where the fast flux is approximately two orders of magnitude lower than at the core midplane, the fast flux ratios are largely clustered between 0.925 and 0.95 (i.e., reductions of 5 to 7.5%). These results are consistent with expectations.

5.4.2 Maximum Void Fraction

Use of the maximum VF values results in coolant densities that are lower than the average case in all axial zones above the NAT zone. As with the minimum VF model, the density differences are minor in the two lower zones of the fuel assemblies, so fast flux differences in the RPV should be relatively minor for locations near or below the lower part of the core, and higher at the core midplane and above.

This behavior is confirmed in Figure 5-41 through Figure 5-44. At the core midplane, the fast flux in the RPV increases by 3–6%. At an elevation of -250 cm, the differences are less than 2.5% in nearly 99% of the mesh tally cells. At an elevation of 375 cm, the fast flux values in the RPV with the maximum VF model are 5–10% greater than the base case. As with the minimum VF case, these results are consistent with expectations.

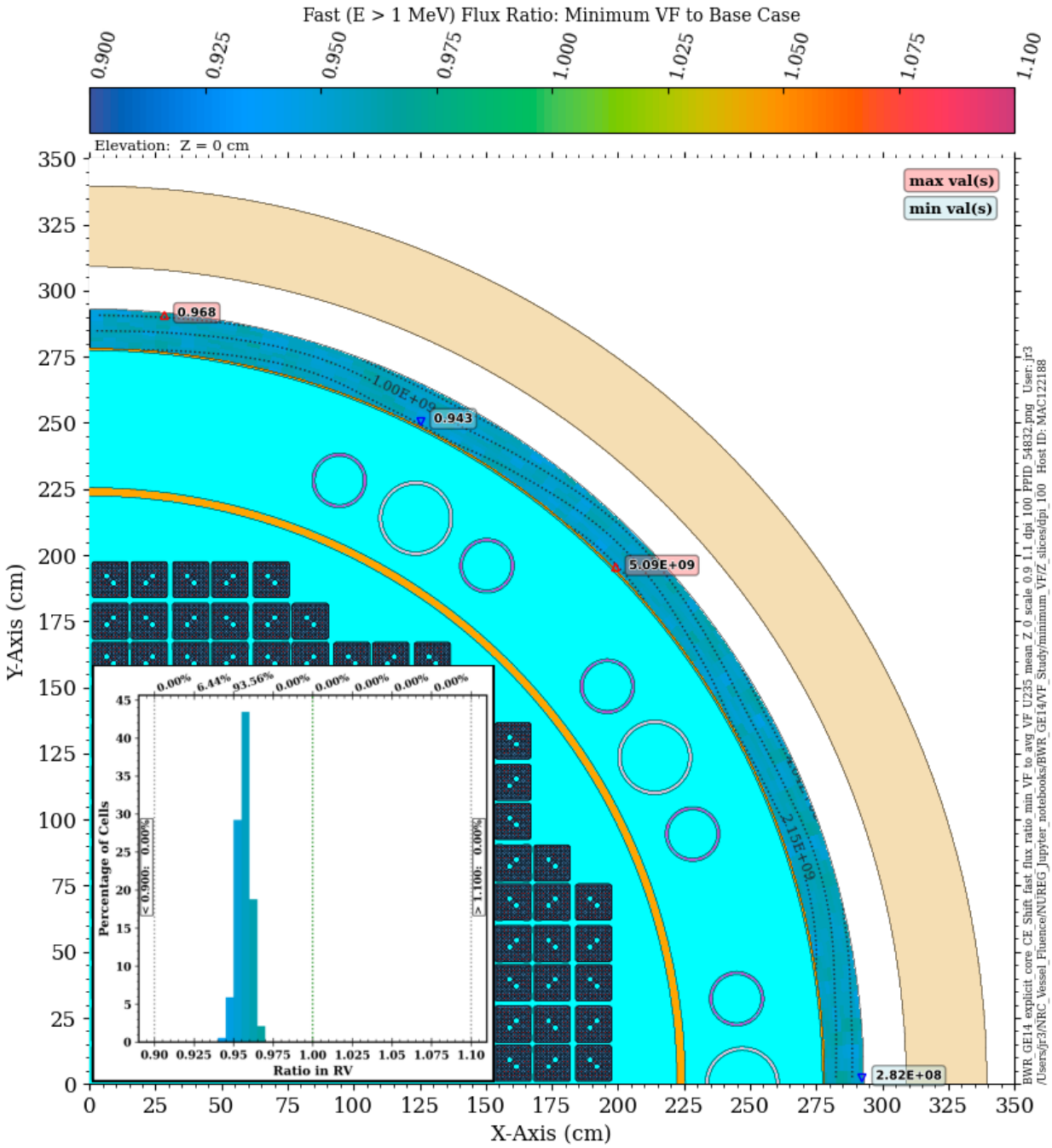

Figure 5-37 Fast neutron flux ratio for the minimum VF model to the base case BWR model. Plan view at the core midplane elevation

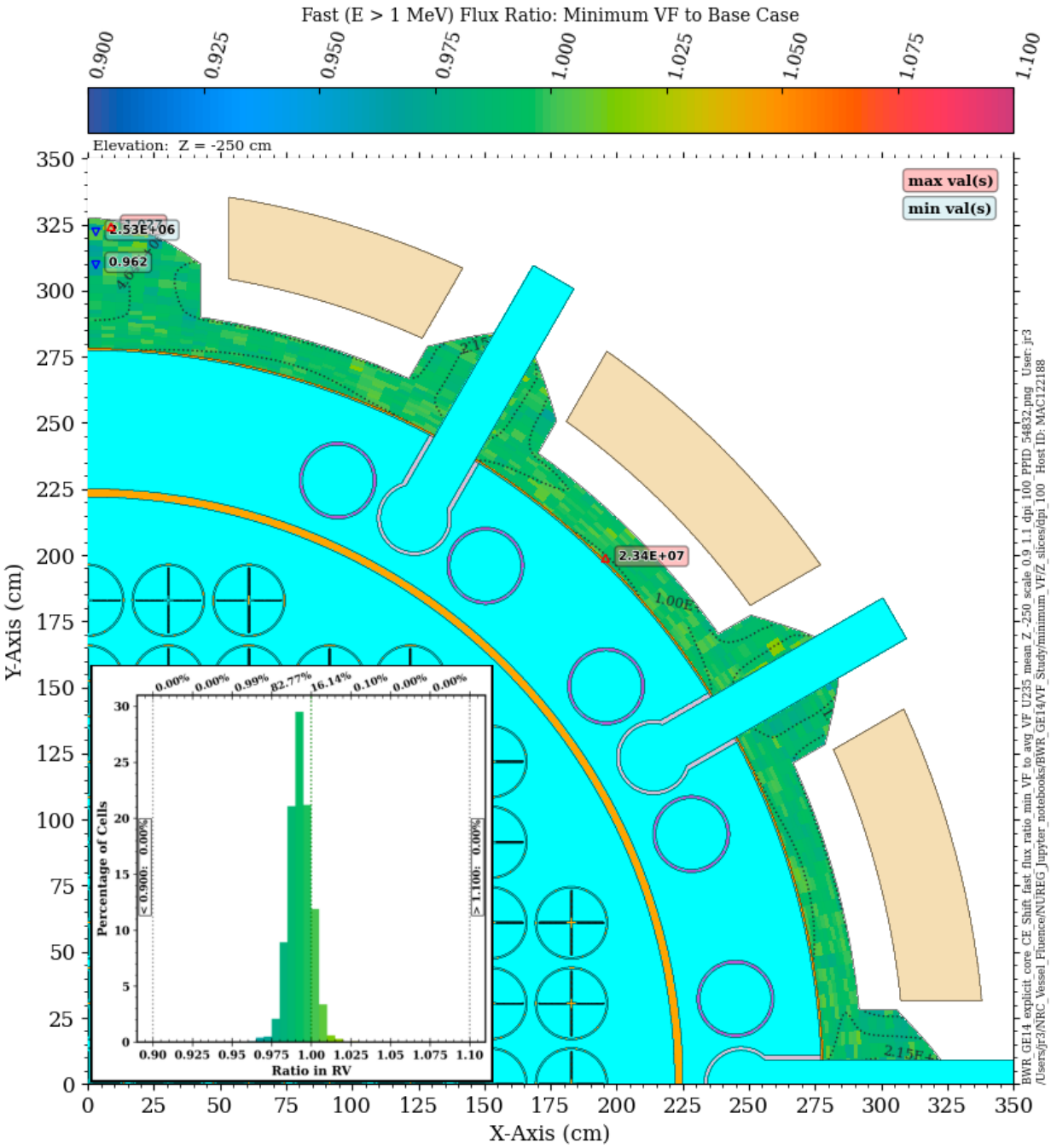

Figure 5-38 Fast neutron flux ratio for the minimum VF model to the base case BWR model. Plan view at an elevation through the recirculation outlet nozzles

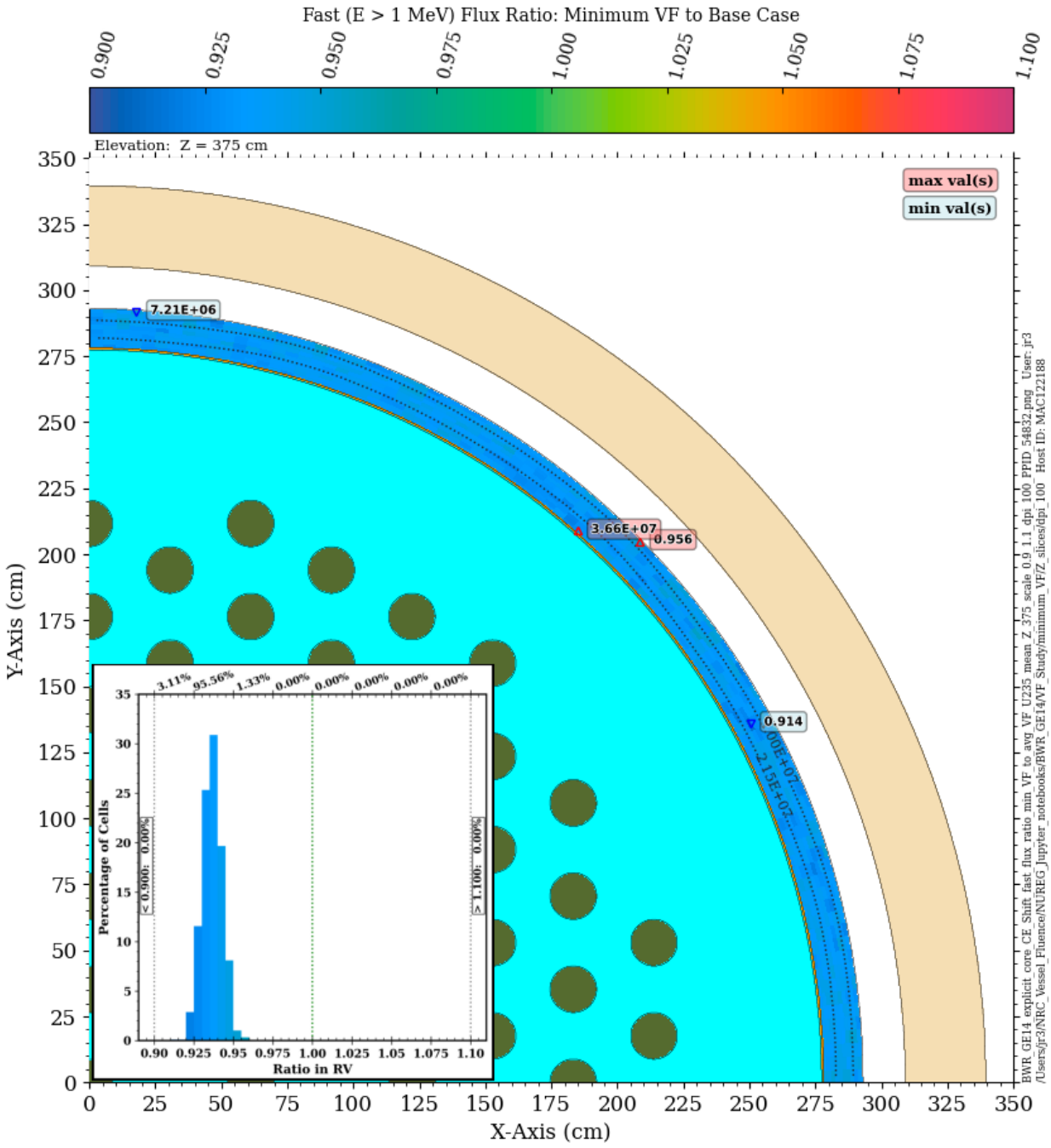

Figure 5-39 Fast neutron flux ratio for the minimum VF model to the base case BWR model. Plan view at an elevation above the core shroud

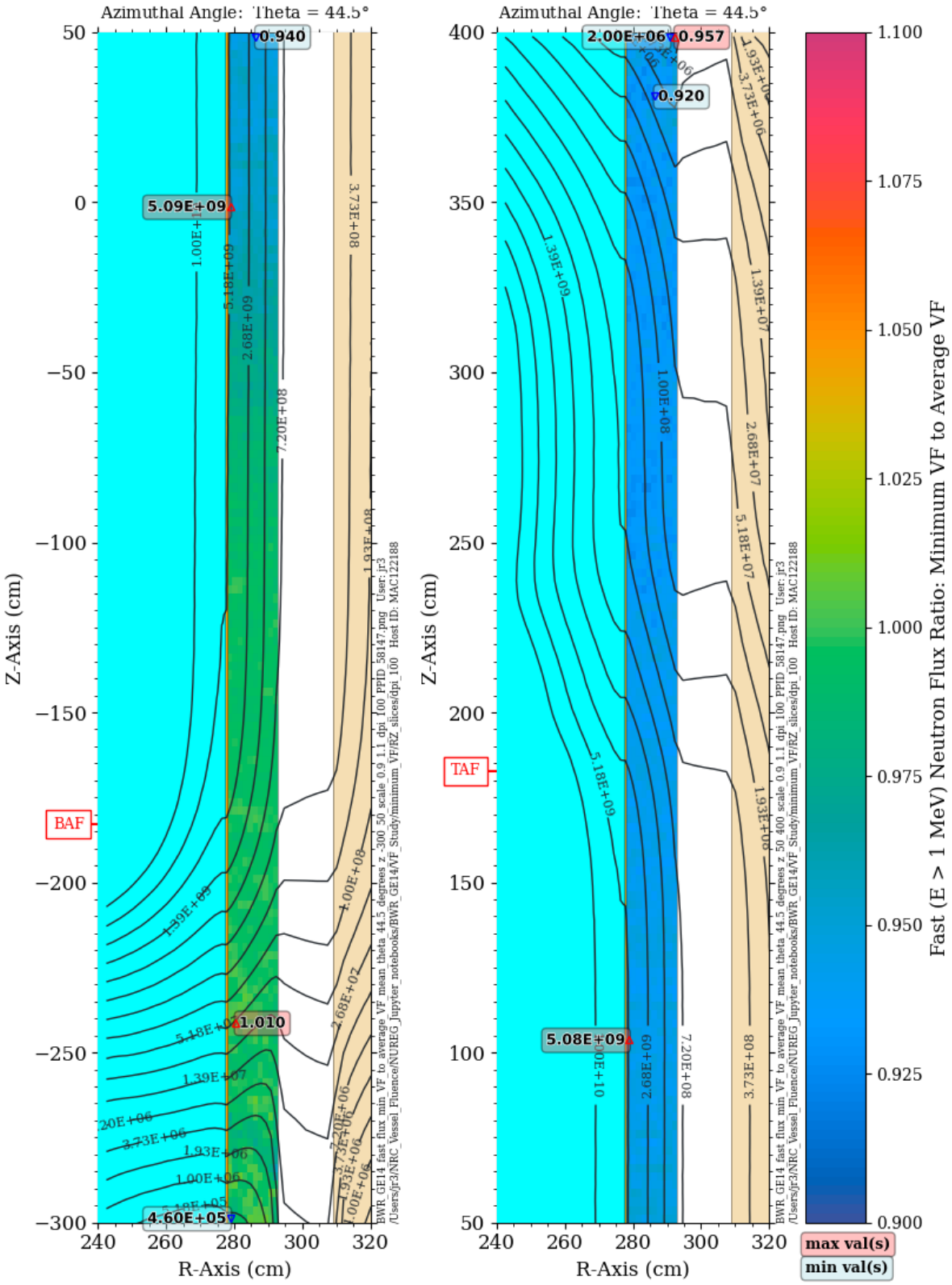

Figure 5-40 Fast neutron flux ratio for the minimum VF model to the base case BWR model at an azimuthal angle of 44.5°

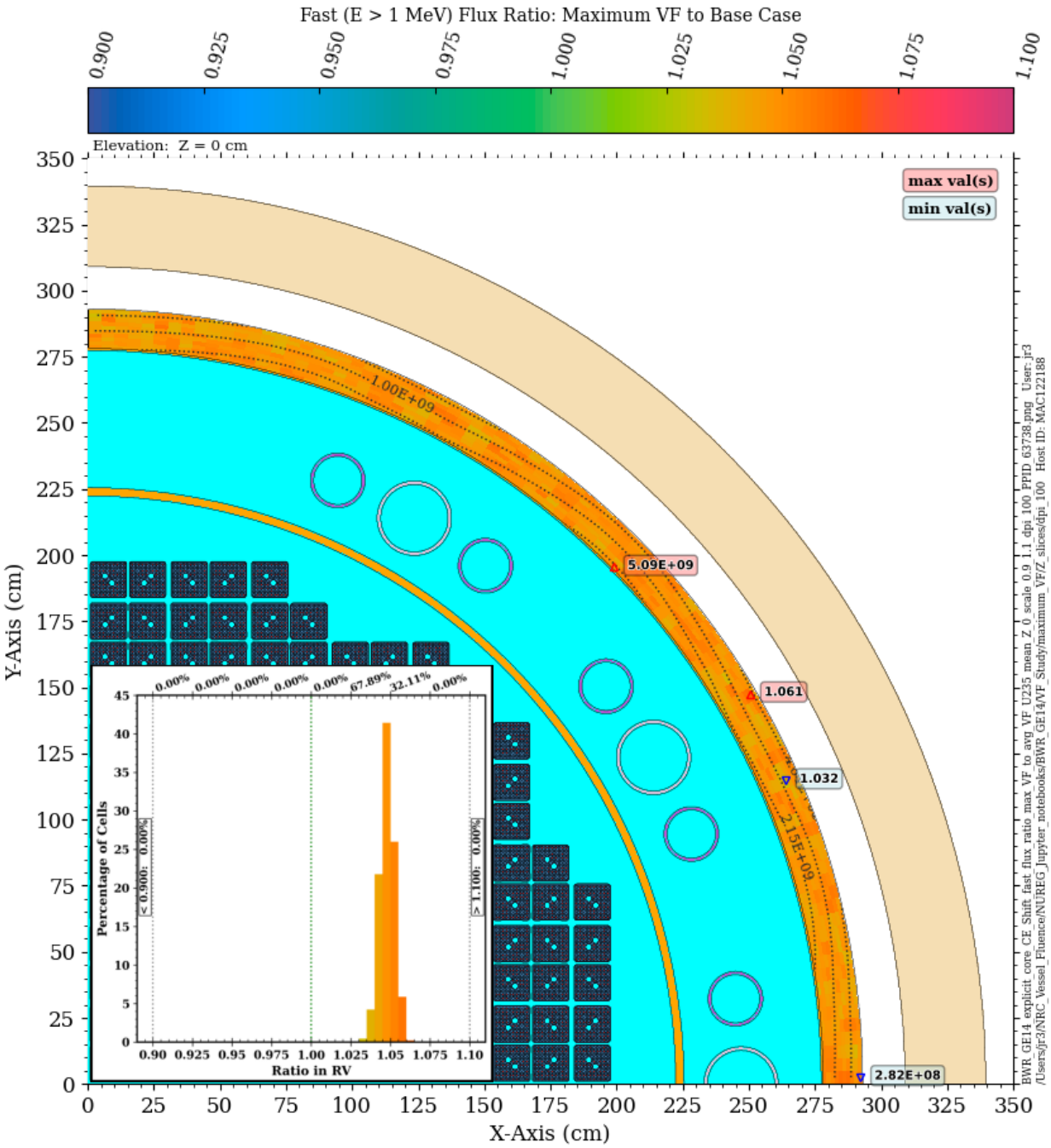

Figure 5-41 Fast neutron flux ratio for the maximum VF model to the base case BWR model at the core midplane elevation

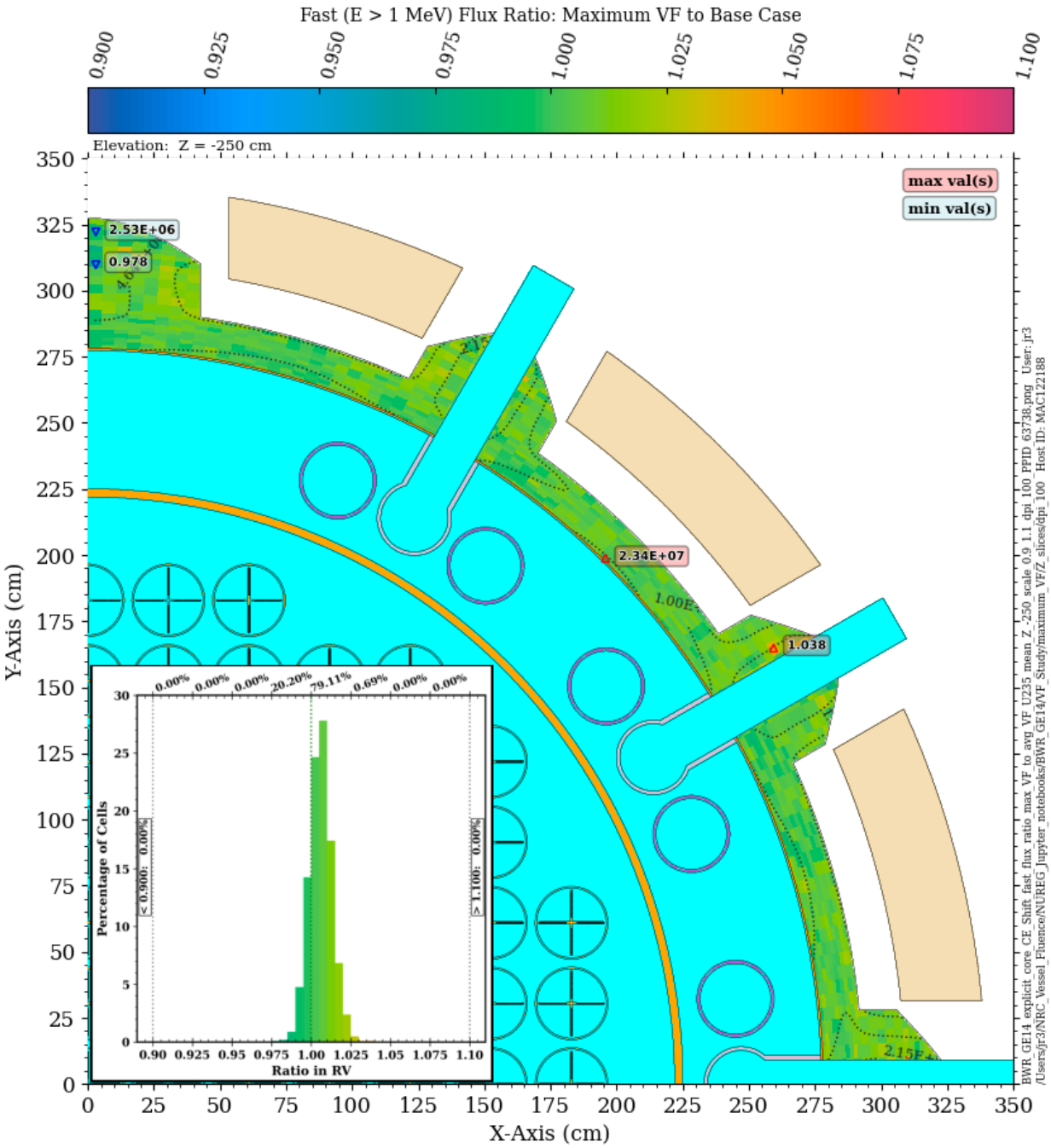

Figure 5-42 Fast neutron flux ratio for the maximum VF model to the base case BWR model. Plan view at an elevation through the recirculation outlet nozzles

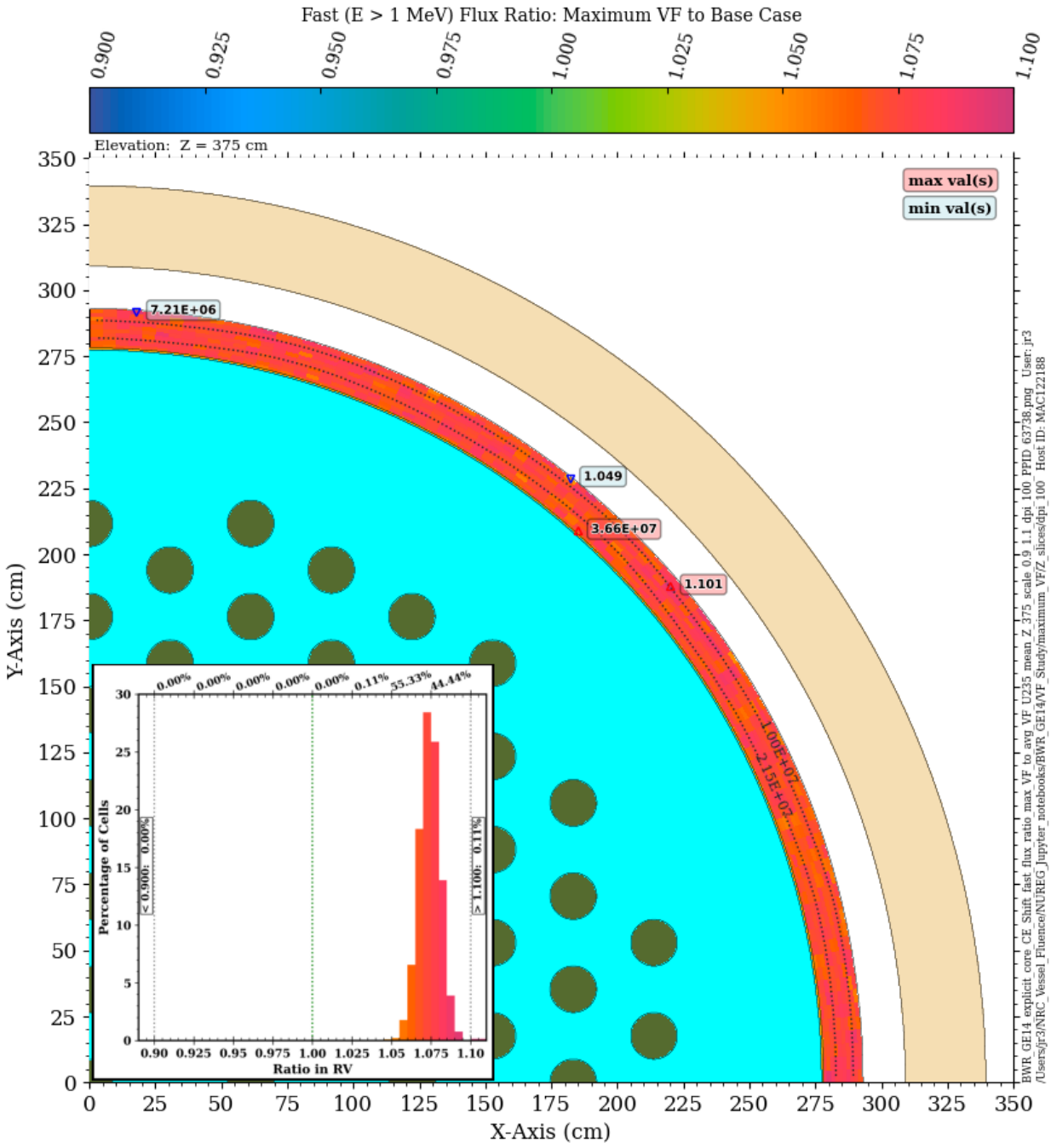

Figure 5-43 Fast neutron flux ratio for the maximum VF model to the base case BWR model. Plan view at an elevation above the core shroud

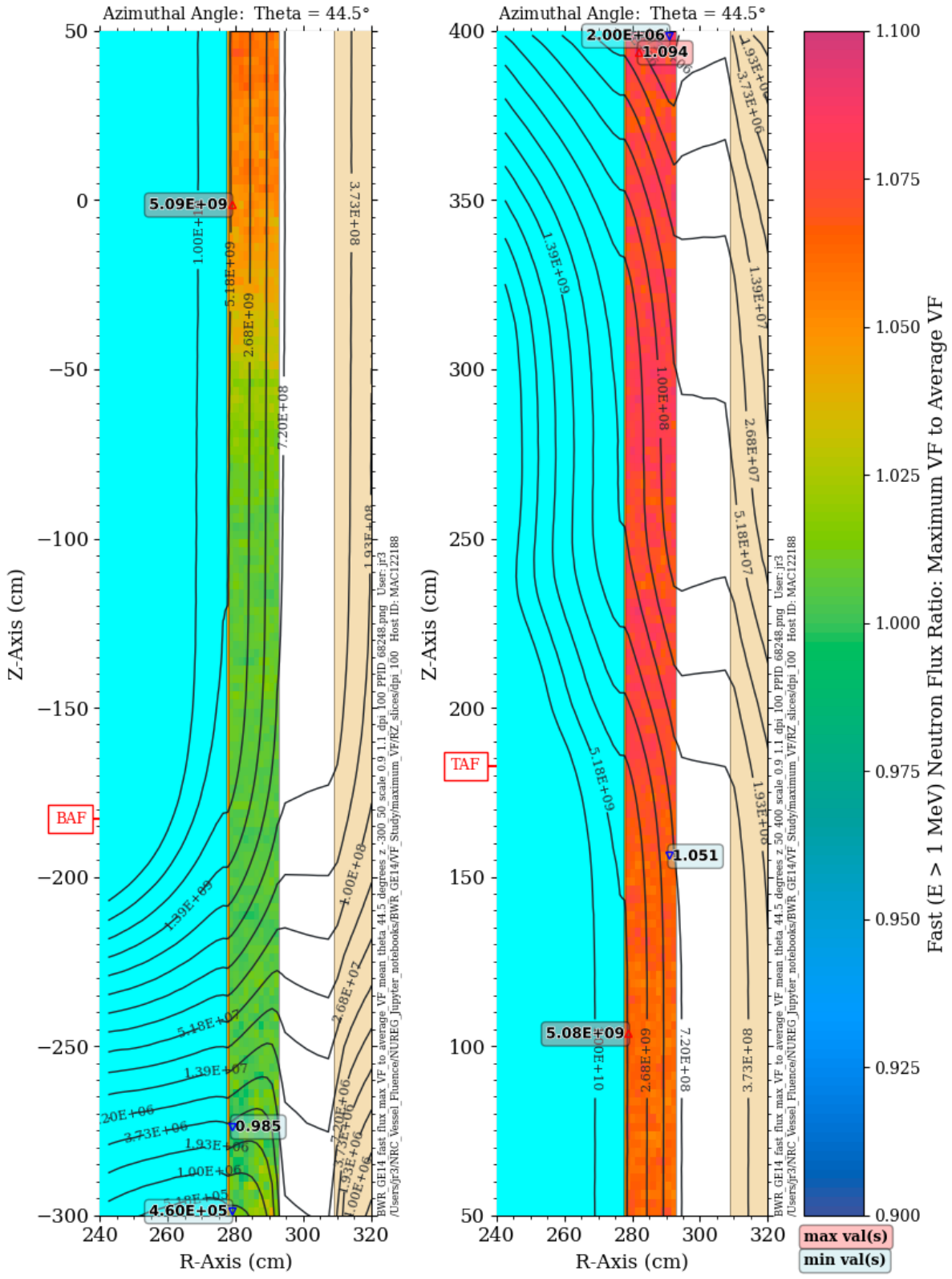

Figure 5-44 Fast neutron flux ratio for the maximum VF model to the base case BWR model. Elevation view at an azimuthal angle of 44.5°

5.5 Reactor Cavity Gap

For RPV locations above and below the traditional beltline region, the effect of neutrons that scatter in the bioshield and stream upwards and downwards in the gap between the RPV and the bioshield becomes progressively more important at increasing distances. As shown in Section 5.1, at sufficient distances from the core, these gap streaming neutrons are capable of not only reducing the rate of attenuation of the fast flux through the RPV, but they can also result in the peak flux being on the outer surface of the RPV. This behavior has been noted in previous studies, including work by Jones [76]. The effect of cavity streaming is particularly important with regard to the methods used for fluence predictions in the extended beltline region.

Because cavity gap streaming has been shown to be more significant in PWRs than BWRs in this work and in the work by Jones [76], the parametric study for the effect of the cavity gap width on fast neutron flux levels in the extended beltline region was carried out for the PWR model only. The cavity gap width in the baseline PWR model is 17.38 cm at elevations below Z = 402.59 cm, and the cavity gap width is 14.75 cm above 402.59 cm (Table 4-1). Three variant models were constructed having gap width increases of 10, 20, and 30 cm. The source in each case was a spatially uniform pinwise distribution with a ^{235}U fission spectrum.

No changes were made to the modeling of the nozzles or vessel supports. Consequently, flux levels in the vicinity of the nozzles and supports will not be realistic, as the bioshield inner surface is moved to radii beyond the location of the vessel supports. However, at an azimuthal angle of 315.5°, which is midway between the inlet and outlet nozzles, the fast flux levels are relatively unperturbed by the nozzle structures. This is also the azimuthal location where the fast flux levels in the RPV are greatest.

Ratio plots for the three increased-gap models at the azimuthal angle of 315.5° are shown in Figure 5-45 through Figure 5-50. The following observations can be made from these results:

1. Within the traditional beltline region, there is very little change in the fast flux in the RPV as the cavity width increases. The fast flux at the outer surface of the RPV shows a slight decrease (ranging from ~2.5% for the gap-plus-10-cm model to ~4.5% for the gap-plus-30-cm model) as the gap width increases. This is due to a decrease in the contribution of neutrons which scatter from the bioshield back to the RPV. As the gap width increases, the fast flux incident to the inner surface of the bioshield is reduced as a result of distance fall-off effects, so the contribution of neutrons that scatter from the bioshield back to the RPV diminishes.
2. At elevations in the extended beltline region, there is an increase in the fast flux level in the outer portion of the RPV as the cavity gap width is increased. The fast flux increase becomes greater with increasing distance from the core, and it also extends further into the RPV because of the dominant contribution of cavity streaming neutrons at these elevations.

Ratio plots for the increased gap models at an azimuthal angle of 270.5°—which is also midway between inlet and outlet nozzles—show behavior that is very similar to the results for the location at 315.5°. The magnitude of the fast flux is lower at 270.5° (Section 5.1.1), but the flux ratios for the increased gap cases are very similar.

A more comprehensive evaluation of differing cavity gaps would require plant-specific modeling to address the specific geometry of the RPV, nozzles, and vessel supports, as well as the cavity gap. However, this limited parametric study does confirm that the impact of changes in cavity gap width could be much more significant in the extended beltline region than the traditional beltline region.

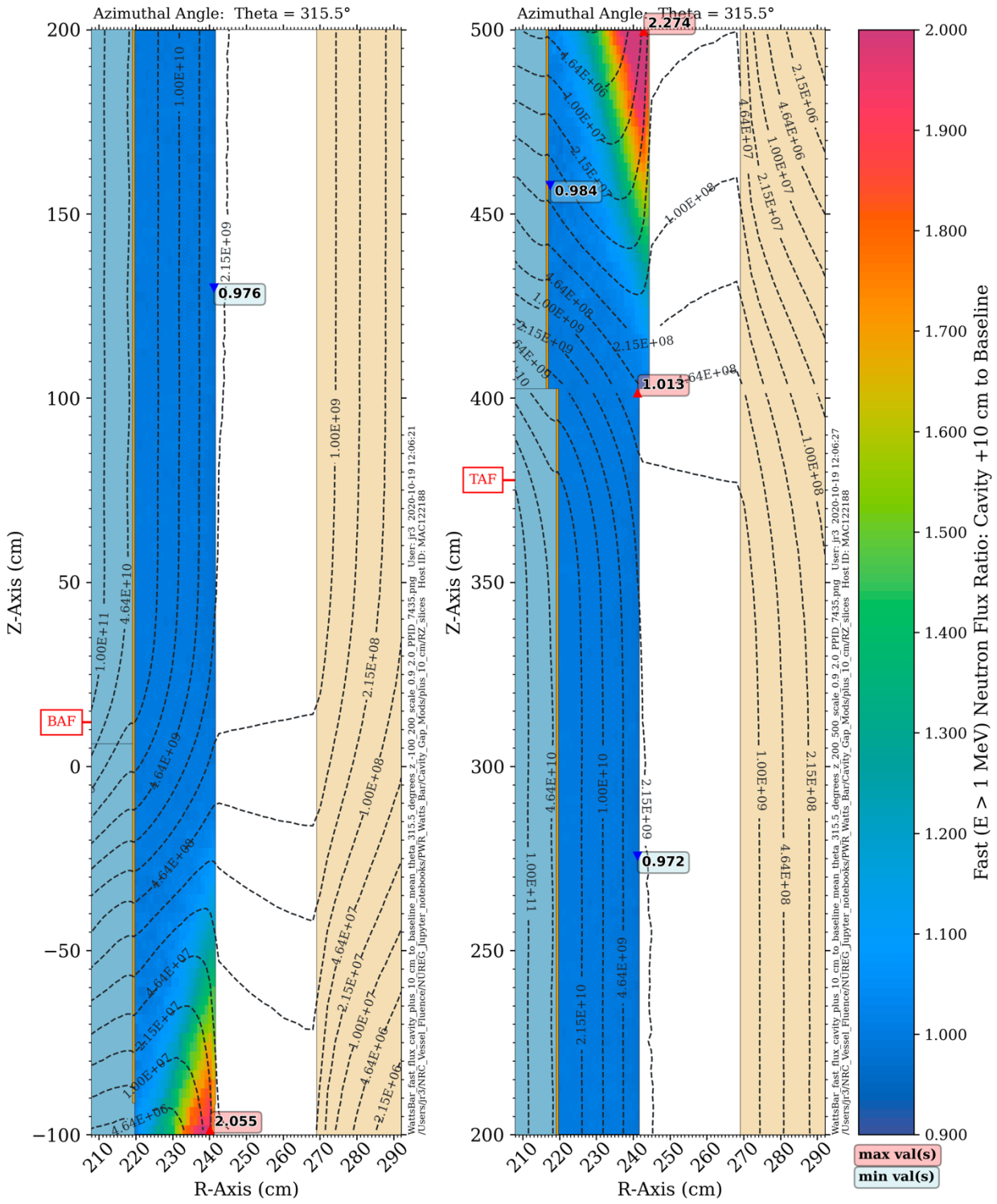

Figure 5-45 Fast neutron flux ratio in the PWR model with a cavity gap increase of 10 cm relative to the baseline gap width. Elevation view at an azimuthal angle of 315.5°
The contour lines represent the fast flux with the increased cavity gap.

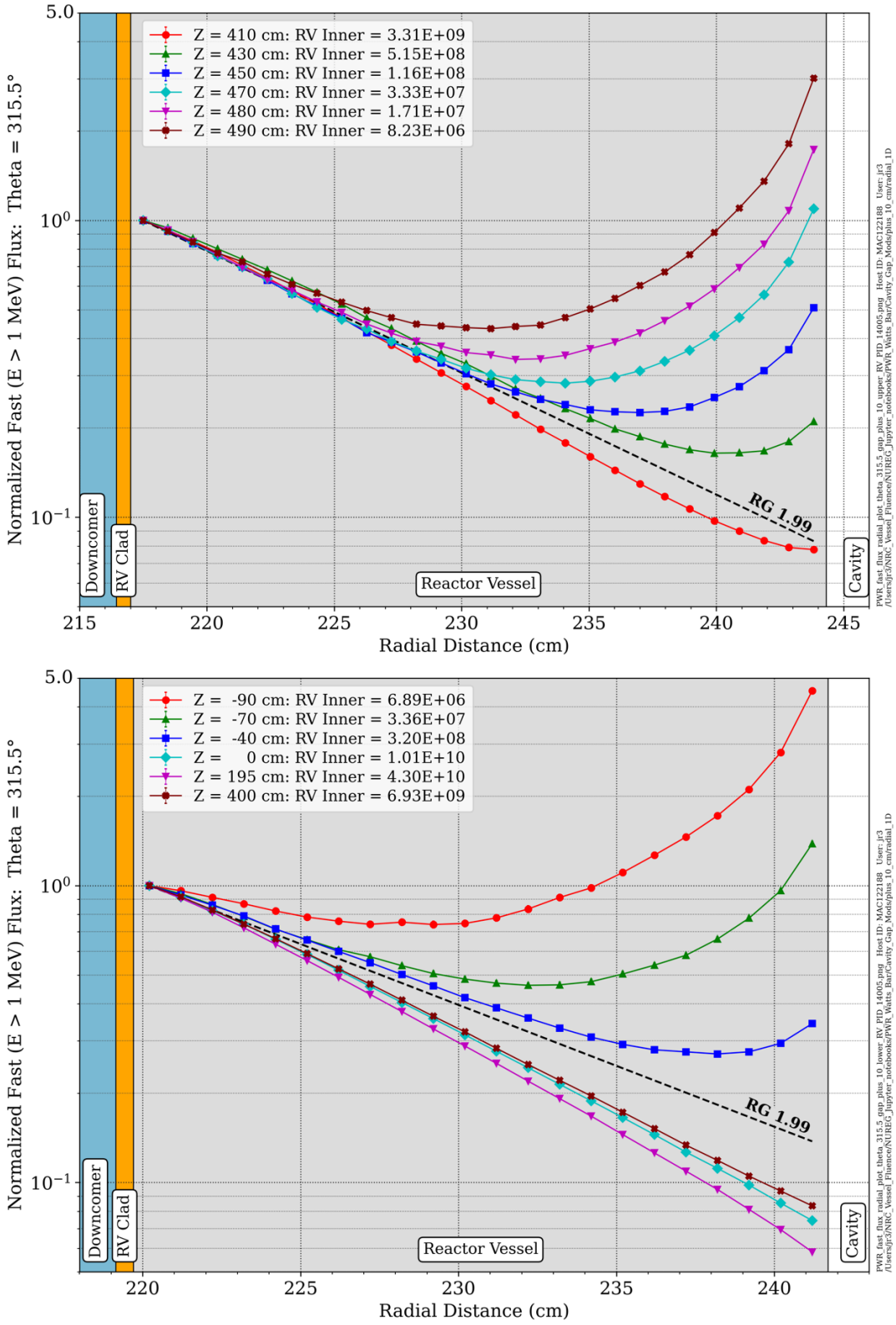

Figure 5-46 Normalized radial fast neutron flux profiles in the PWR model with a cavity gap increase of 10 cm Azimuthal angle of 315.5° *The profiles are normalized to the flux at the RPV inner diameter at each elevation.*

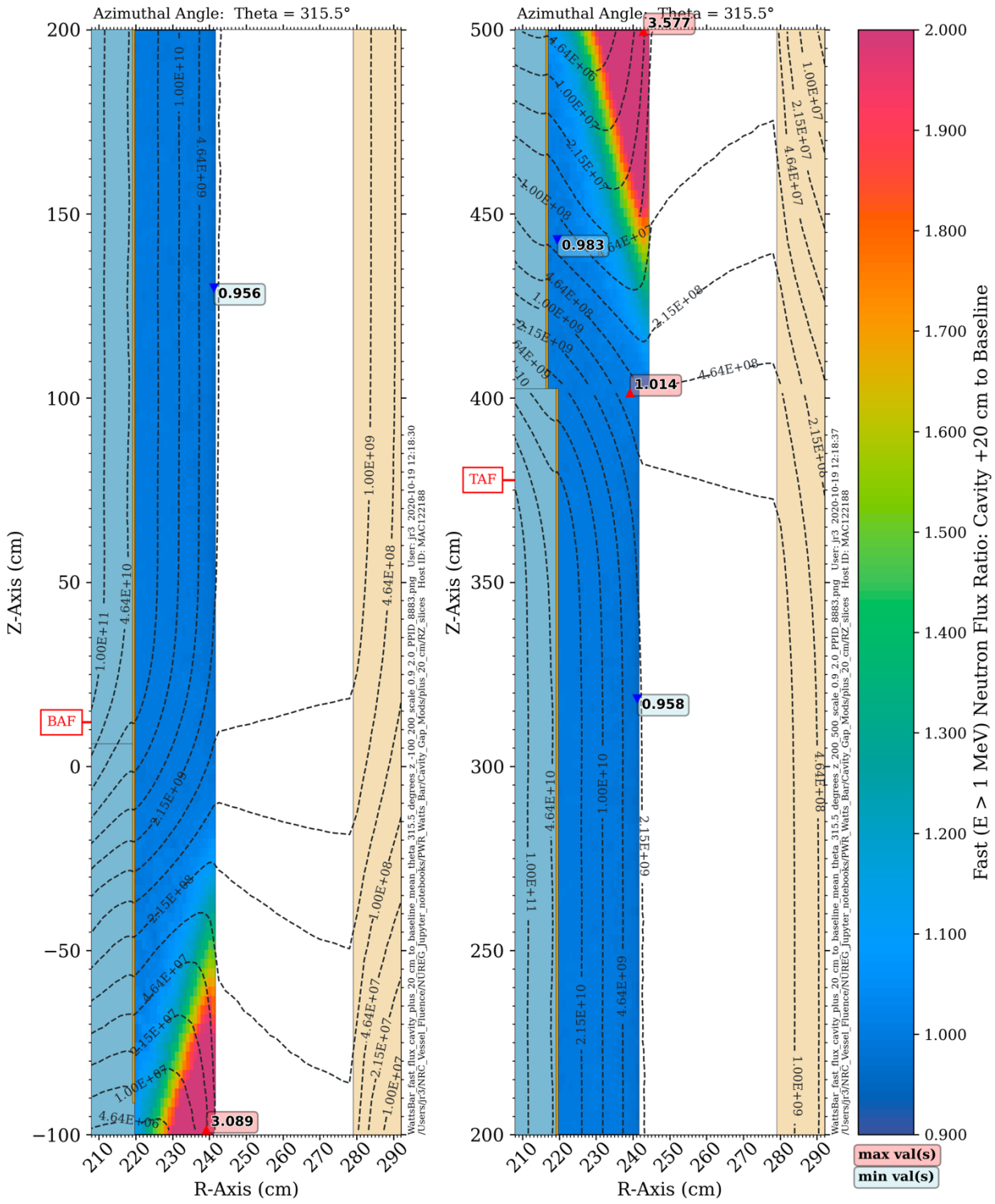

Figure 5-47 Fast neutron flux ratio in the PWR model with a cavity gap increase of 20 cm. Elevation view at an azimuthal angle of 315.5° *The contour lines represent the fast flux with the increased cavity gap.*

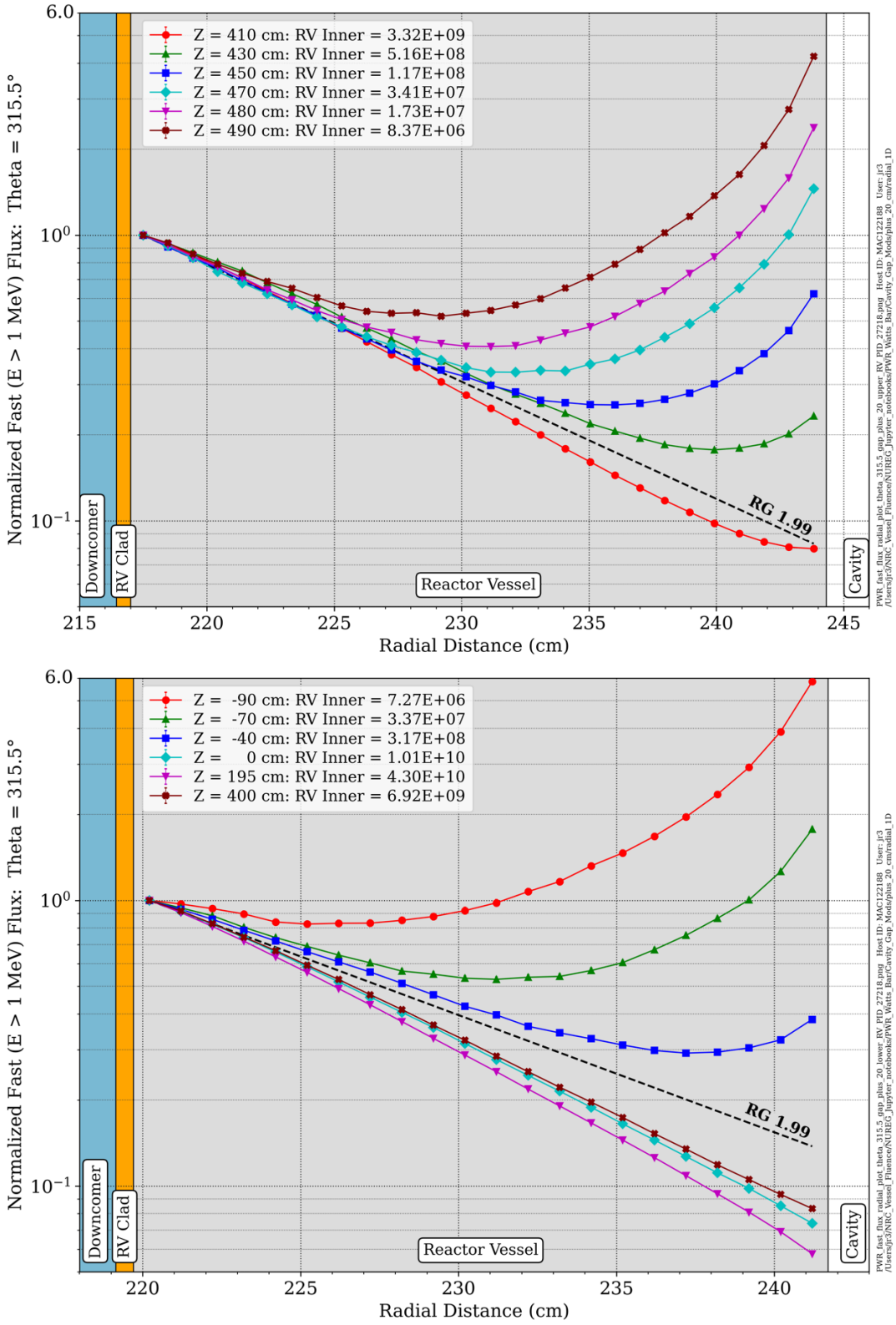

Figure 5-48 Normalized radial fast neutron flux profiles in the PWR model with a cavity gap increase of 20 cm. Azimuthal angle of 315.5° *The profiles are normalized to the flux at the RPV inner diameter at each elevation.*

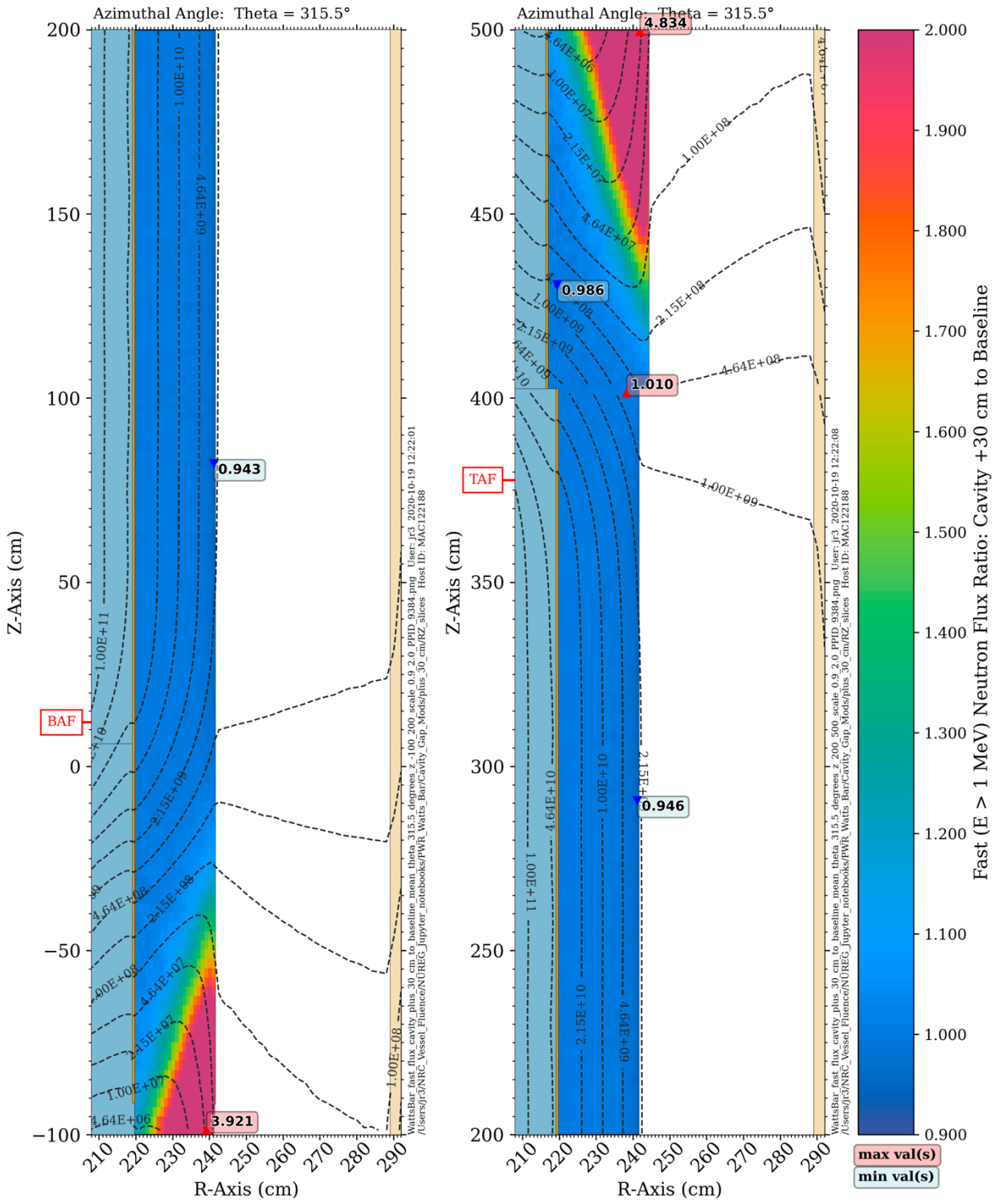

Figure 5-49 Fast neutron flux ratio in the PWR model with a cavity gap increase of 30 cm. Elevation view at an azimuthal angle of 315.5° *The contour lines represent the fast flux with the increased cavity gap.*

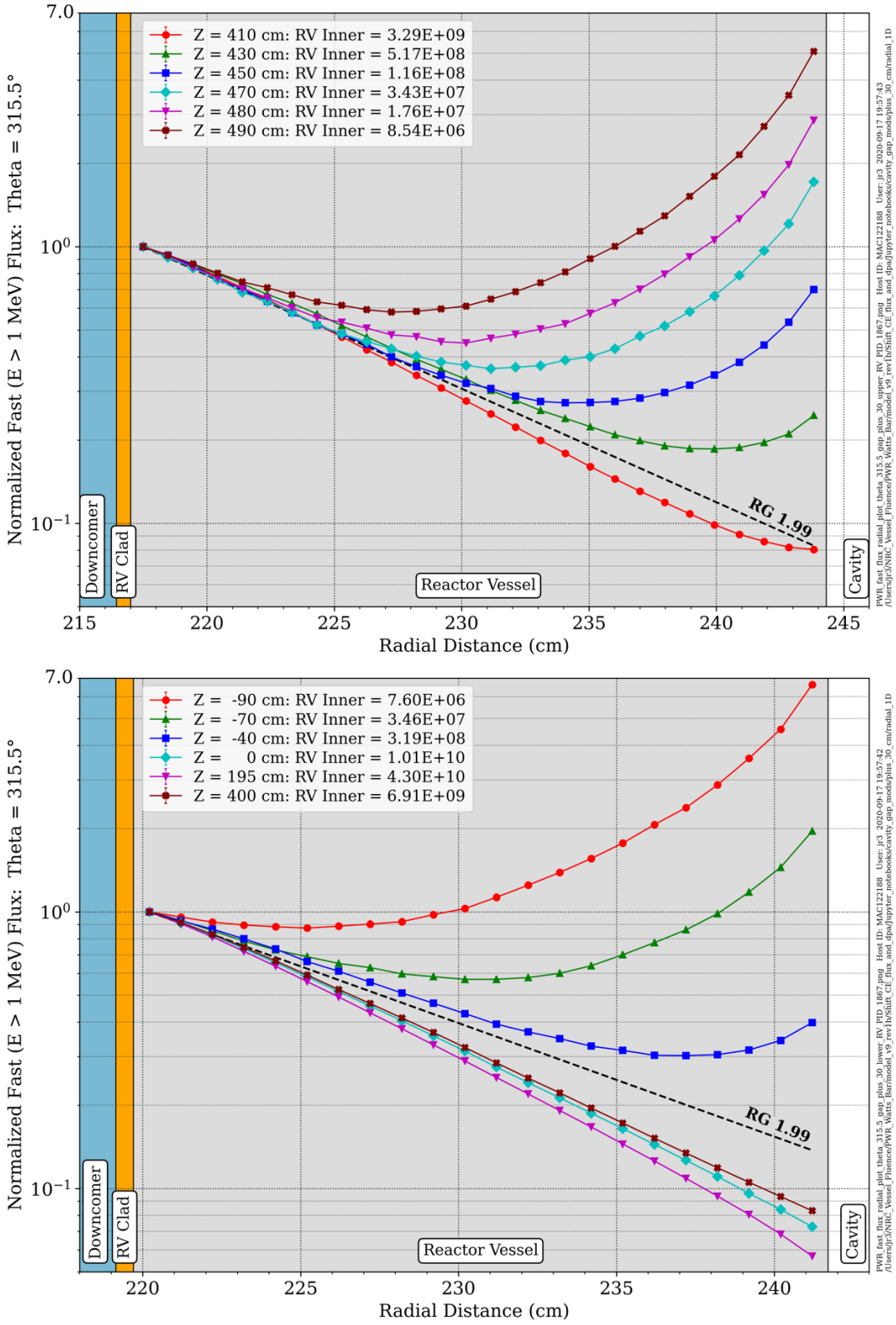

Figure 5-50 Normalized radial fast neutron flux profiles in the PWR model with a cavity gap increase of 30 cm. Azimuthal angle of 315.5° *The profiles are normalized to the flux at the RPV inner diameter at each elevation.*

5.6 Concrete Composition

The discussion in Section 5.1 shows that the effect of neutron scattering from the concrete bioshield into the cavity gap has a significant effect on RPV fast flux levels at some elevations in the extended beltline region. Although this effect is minor for the BWR model, it can be quite pronounced for the PWR model, as shown in Figure 5-7 and Figure 5-8.

Because the compositions of different types of concrete vary significantly, the type of concrete can have a noticeable effect on RPV fast flux levels in regions where gap streaming is important. Of particular importance is the amount of hydrogen present in the concrete. This importance is due to two primary effects:

1. High-energy neutrons scatter from hydrogen with a forward-peaked angular distribution.[7] Thus, neutrons entering the concrete bioshield and scattering from hydrogen are more likely to be scattered further into the bioshield rather than backscattered into the cavity gap.
2. As noted in Section 5.2, the average energy loss from elastic scattering of neutrons by hydrogen is greater than the average energy loss for elastic scattering by any other element, so those neutrons that do scatter from hydrogen into the cavity gap are more likely to have an energy below the 1 MeV cutoff than neutrons that scatter from other elements in the bioshield back into the cavity gap.

To assess the impact of variations in concrete composition on cavity streaming neutron flux levels, three variants of the PWR reference model were constructed using three different concrete compositions. (Recall that the baseline models for the PWR and BWR have Type 04 concrete.) The amount of hydrogen in Type 04 concrete can be considered to be a typical value. Concretes with minimum and maximum hydrogen densities were chosen for the parameter study, along with a variant of Type 04 concrete in which the water density was reduced by 50%. The four concretes used in this parameter study are listed in Table 5-6. The isotopic compositions are listed in Table 5-7.

Table 5-6 Concrete types used in the concrete parameter study

Concrete type	Reference	Hydrogen density (g/cm^3)	Concrete density (g/cm^3)	Note
Type 01	ANL-6443 [79]	0.00484	2.33	Minimum hydrogen density
Hanford wet	PNNL-15870, Rev. 1 [80]	0.029	2.35	Maximum hydrogen density
Type 04	ANS-6.4-2006 (R2016) [81]	0.013	2.35	ANS-6.4-2006 (R2016) recommendation
Type 04 with 50% water reduction (Type 04 Mod)	ISRD10 Proceedings [82]	0.0065	2.29	Evaluates the effect of reducing the water content of Type 04 concrete by 50% while leaving all other constituents unchanged.

[7] The scattering of neutrons from hydrogen is isotropic in the center-of-mass (CM) coordinate system, but forward peaked in the laboratory coordinate system.

Table 5-7 Composition of four concretes used in the PWR concrete parameter study

Isotopic number density (atoms/b cm)	Concrete type and density (g/cc)			
	Type 04 2.35	Type 04 Mod 2.29	Type 01 2.33	Hanford wet 2.35
1001	7.7679E-03	3.8840E-03	2.8936E-03	1.7284E-02
6000	----------	----------	6.5223E-03	----------
8016	4.4081E-02	4.2142E-02	4.3275E-02	4.5414E-02
11023	1.0479E-03	1.0479E-03	----------	1.2325E-04
12024	1.1744E-04	1.1744E-04	9.5178E-05	5.9842E-04
12025	1.4868E-05	1.4867E-05	1.2050E-05	7.5760E-05
12026	1.6370E-05	1.6370E-05	1.3266E-05	8.3412E-05
13027	2.3884E-03	2.3884E-03	2.6577E-04	3.3596E-03
14028	1.4675E-02	1.4674E-02	8.6667E-03	1.1906E-02
14029	7.4547E-04	7.4546E-04	4.4028E-04	6.0484E-04
14030	4.9199E-04	4.9199E-04	2.9057E-04	3.9918E-04
16032	5.3526E-05	5.3525E-05	3.4275E-05	----------
16033	4.2261E-07	4.2261E-07	2.7062E-07	----------
16034	2.3948E-06	2.3948E-06	1.5335E-06	----------
16036	5.6349E-09	5.6348E-09	3.6083E-09	----------
19039	6.4646E-04	6.4645E-04	----------	4.0538E-04
19040	8.1103E-08	8.1103E-08	----------	5.0859E-08
19041	4.6653E-05	4.6652E-05	----------	2.9256E-05
20040	2.8262E-03	2.8262E-03	8.4684E-03	2.5352E-03
20042	1.8862E-05	1.8862E-05	5.6519E-05	1.6920E-05
20043	3.9357E-06	3.9357E-06	1.1793E-05	3.5304E-06
20044	6.0814E-05	6.0814E-05	1.8222E-04	5.4552E-05
20046	1.1661E-07	1.1661E-07	3.4943E-07	1.0461E-07
20048	5.4518E-06	5.4517E-06	1.6335E-05	4.8904E-06
26054	1.8281E-05	1.8281E-05	----------	7.8567E-05
26056	2.8697E-04	2.8697E-04	----------	1.2333E-03
26057	6.6274E-06	6.6273E-06	----------	2.8483E-05
26058	8.8198E-07	8.8197E-07	----------	3.7906E-06
28058	----------	----------	5.0743E-05	4.0538E-04
28060	----------	----------	1.9546E-05	----------
28061	----------	----------	8.4964E-07	----------
28062	----------	----------	2.7090E-06	----------
28064	----------	----------	6.8991E-07	----------

Ratio plots showing the change in the fast neutron flux at elevations from Z = -100 cm to Z = 500 cm in the PWR model for Type 01, Type 04 Mod, and Hanford wet concrete are shown in Figure 5-51 through Figure 5-57.

For the Type 01 concrete, which has the minimum amount of hydrogen, there is essentially no change in the RPV fast flux in the traditional beltline region. At elevations beginning at about 25–30 cm below the bottom of the core and above the top of the core, the effect of the reduced hydrogen content in the Type 01 concrete results in increases of up to ~20% in the fast neutron flux in the RPV's outer portion.

At the azimuthal location of the outlet nozzle (Figure 5-52), there is an additional impact of the minimum hydrogen content in the Type 01 concrete. The fast neutron flux levels in the vessel support below the outlet nozzle increase by up to 55%. This increase is partially due to the increased contribution of cavity streaming with the Type 01 concrete. In addition, as a result of the lower hydrogen content, neutrons which enter the bioshield at locations below the vessel support experience less attenuation as they are transported through the Type 01 concrete. This is shown more clearly in Figure 5-53, in which the separation between the flux contours of the two solutions (Type 04 and Type 01) is relatively uniform in the nozzle region directly above the cavity gap, but it increases in the bioshield and in the lower part of the nozzle support. In these regions, the flux is dominated by fast neutrons that have penetrated the bioshield and entered the nozzle support.

While the EOL fluence at the vessel support locations will likely be well below the monitoring threshold of 1×10^{-17} n/cm^2, the dpa rate may exceed the monitoring requirement of 3×10^{-4} in ASTM E1035-18 [86]. (See Section 6 for further discussion of dpa rates in the vessel supports.) Consequently, the specific composition of the concrete may be important with regard to neutron exposure limits (fast fluence or dpa) in the vessel supports.

The differences in the fast flux levels with the Type 04 Mod concrete model (Figure 5-54 and Figure 5-55) are very similar to those for the Type 01 concrete. This behavior is of particular significance for potential changes in the concrete water content over the operating lifetime of an NPP. Radiation transport calculations that include evaluations of the neutron fluence in the extended beltline region, and in the nozzle support regions, in particular, may need to employ transport models in which the concrete composition is modified throughout the operating history.

The results with the Hanford wet concrete (Figure 5-56 and Figure 5-57) are consistent with expectations. For this concrete, which has a hydrogen content more than twice that of Type 04 concrete, cavity streaming effects are reduced. Because there is a higher probability of neutron scattering from hydrogen in the Hanford wet concrete, the level of backscattering from the bioshield into the cavity gap is reduced. In addition, neutrons which penetrate the bioshield before entering the vessel support experience more attenuation, resulting in further depression of the fast flux in the vessel supports.

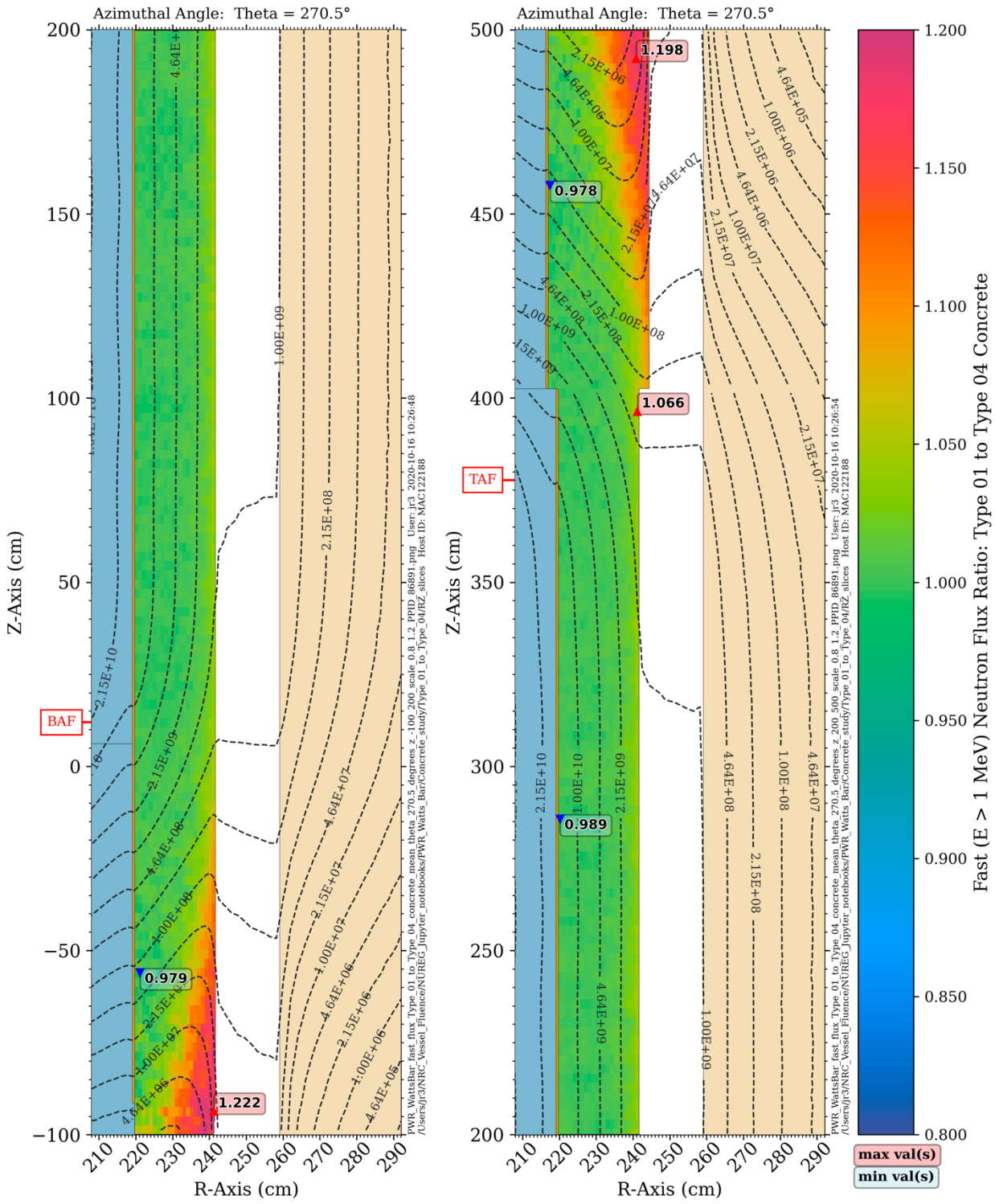

Figure 5-51 Fast neutron flux ratio in the PWR model with Type 01 concrete in the bioshield relative to Type 04 concrete. Elevation view at an azimuthal angle of 270.5° *The contour lines represent the fast flux for the Type 04 model. A spatially uniform pinwise ^{235}U source is used in both cases.*

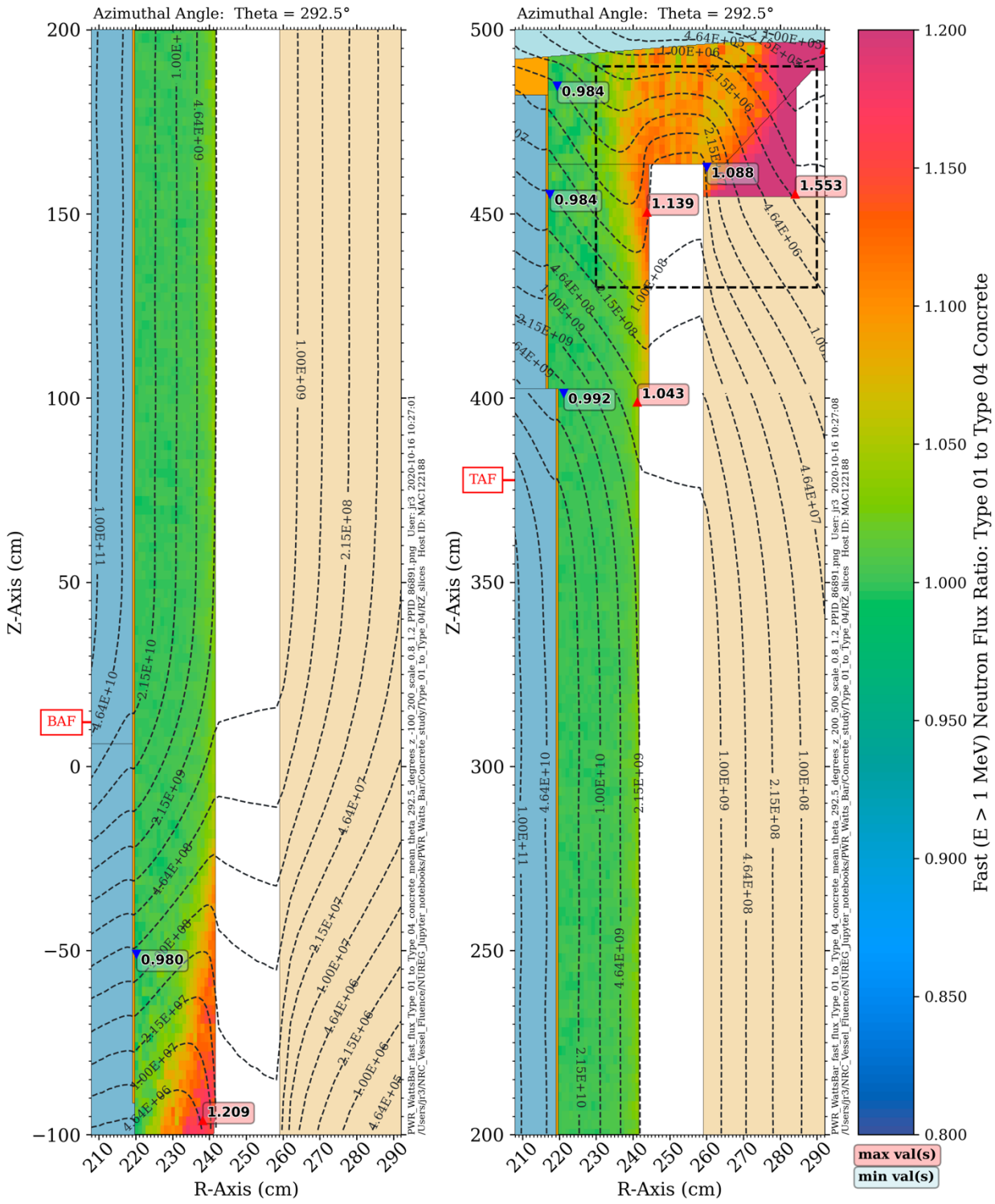

Figure 5-52 Fast neutron flux ratio in the PWR model with Type 01 concrete in the bioshield relative to Type 04 concrete. Elevation view at an azimuthal angle of 292.5° *The contour lines represent the fast flux for the Type 04 model. A spatially uniform pinwise ^{235}U source is used in both cases. The dashed box in the vicinity of the outlet nozzle vessel support corresponds to the plot area of Figure 5-53.*

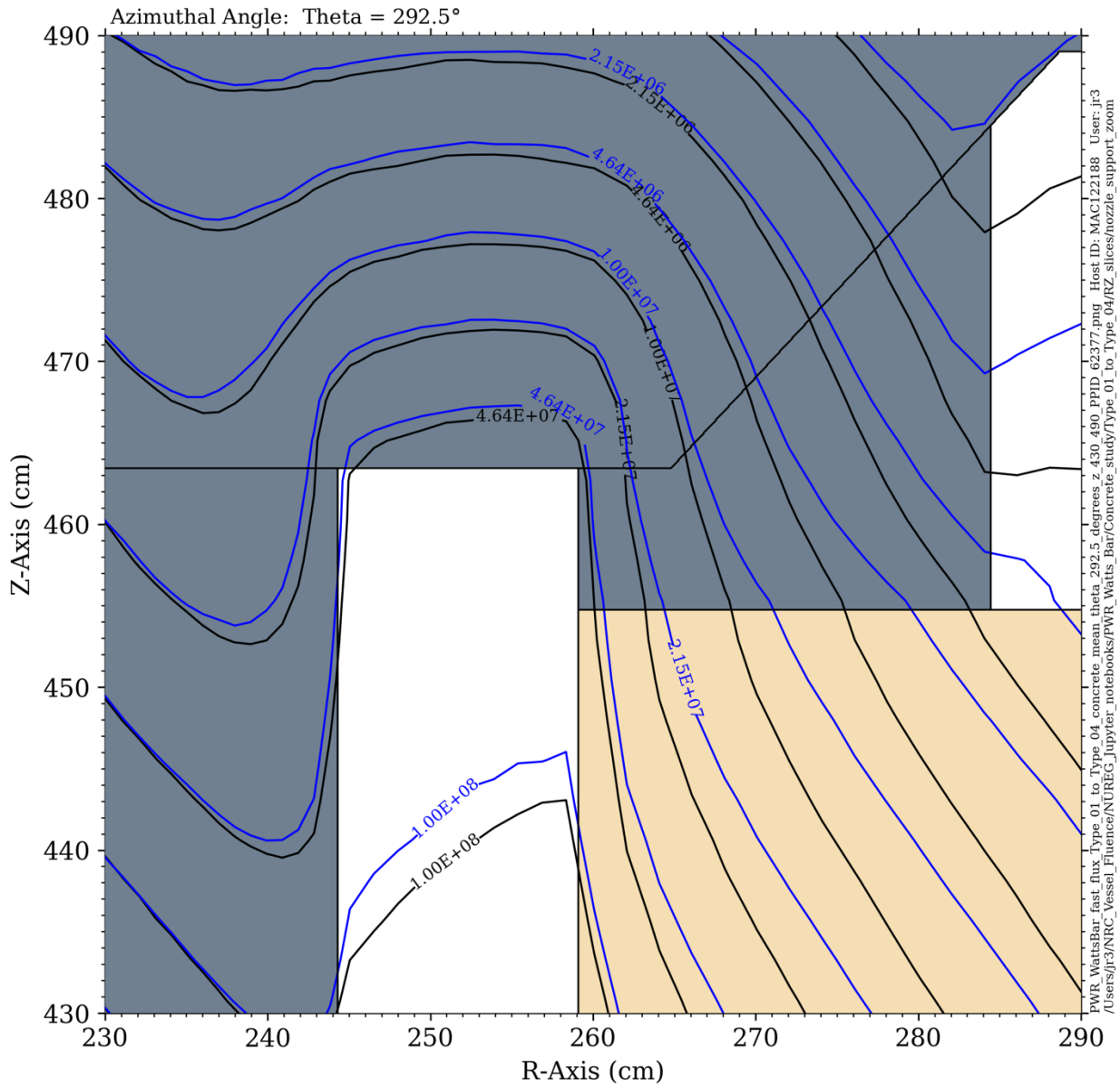

Figure 5-53 Fast neutron flux levels in the vicinity of the outlet nozzle vessel support. Elevation view at an azimuthal angle of 292.5° *The black contour lines represent the fast flux for the Type 04 concrete model, and the blue lines represent the fast flux for the Type 01 concrete model. Note the increasing separation in the two solutions that occurs with increasing depth into the concrete, with the Type 01 concrete providing less attenuation.*

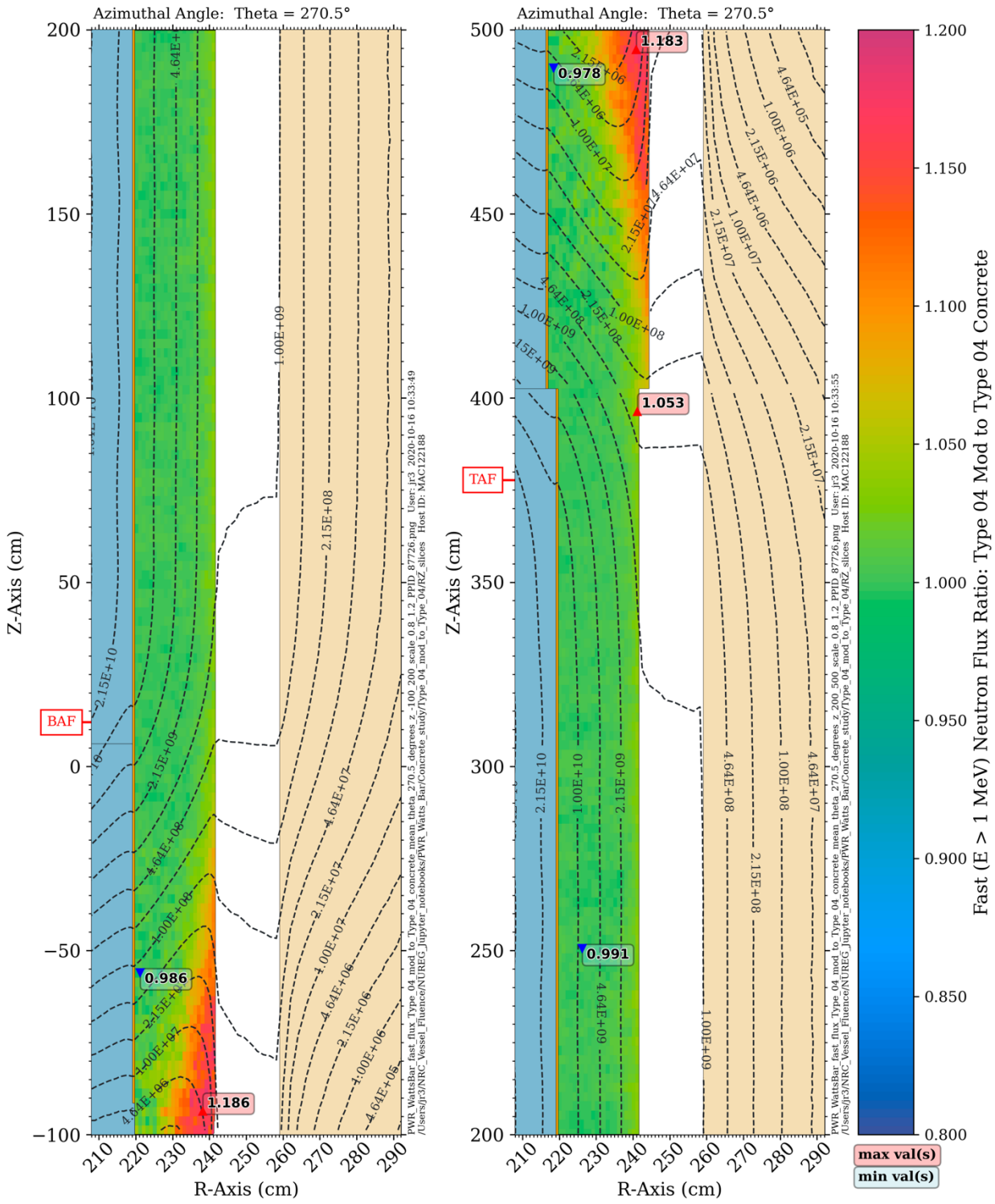

Figure 5-54 Fast neutron flux ratio in the PWR model with Type 04 Mod concrete in the bioshield relative to Type 04 concrete. Elevation view at an azimuthal angle of 270.5° *The contour lines represent the fast flux for the Type 04 model. A spatially uniform pinwise ^{235}U source was used in both cases.*

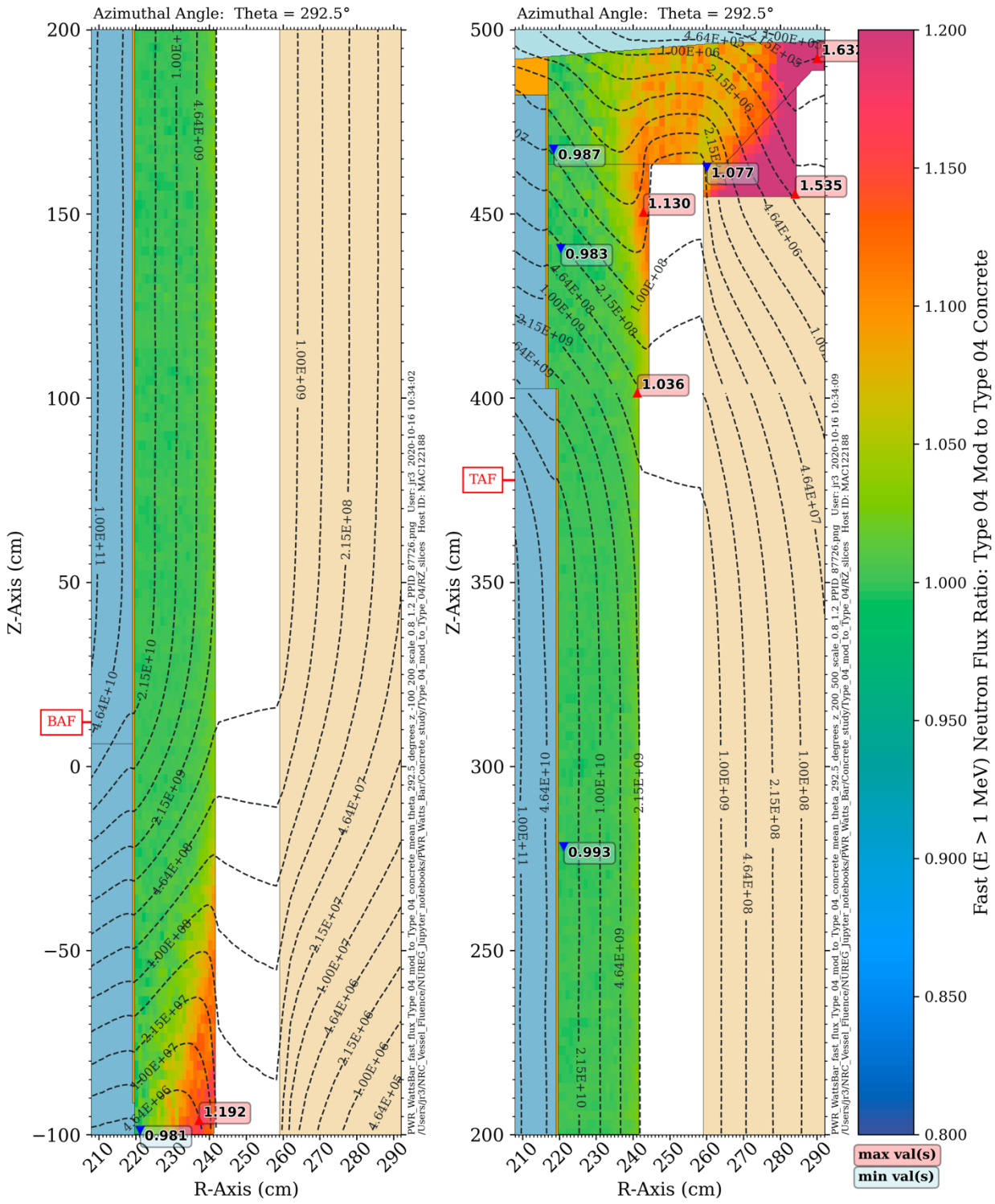

Figure 5-55 Fast neutron flux ratio in the PWR model with Type 04 Mod concrete in the bioshield instead of Type 04 concrete. Elevation view at an azimuthal angle of 292.5° *The contour lines represent the fast flux for the Type 04 model. A spatially uniform pinwise ^{235}U source was used in both cases.*

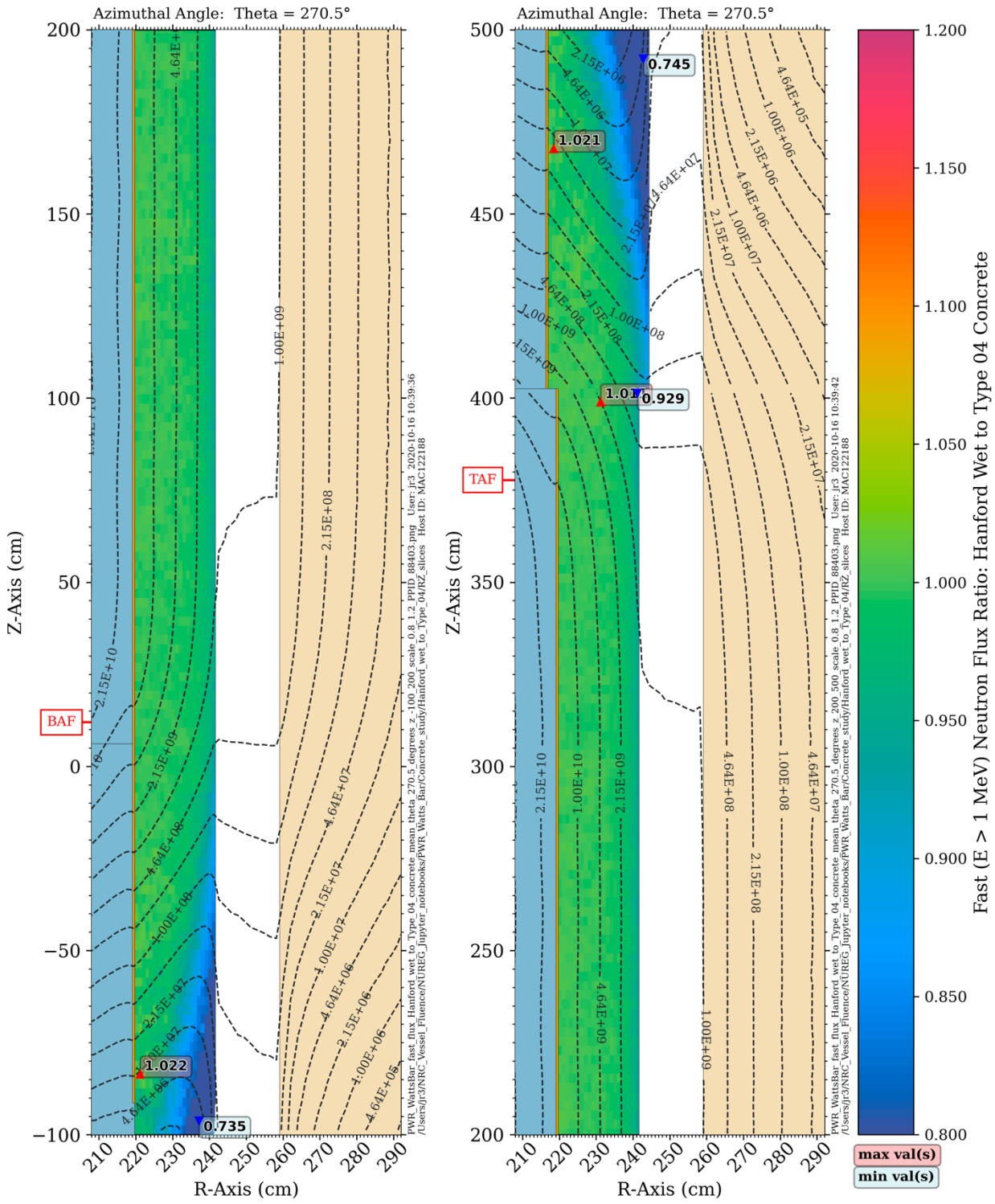

Figure 5-56 Fast neutron flux ratio in the PWR model with Hanford wet concrete in the bioshield relative to Type 04 concrete. Elevation view at an azimuthal angle of 270.5° *The contour lines represent the fast flux for the Type 04 model. A spatially uniform pinwise ^{235}U source was used in both cases.*

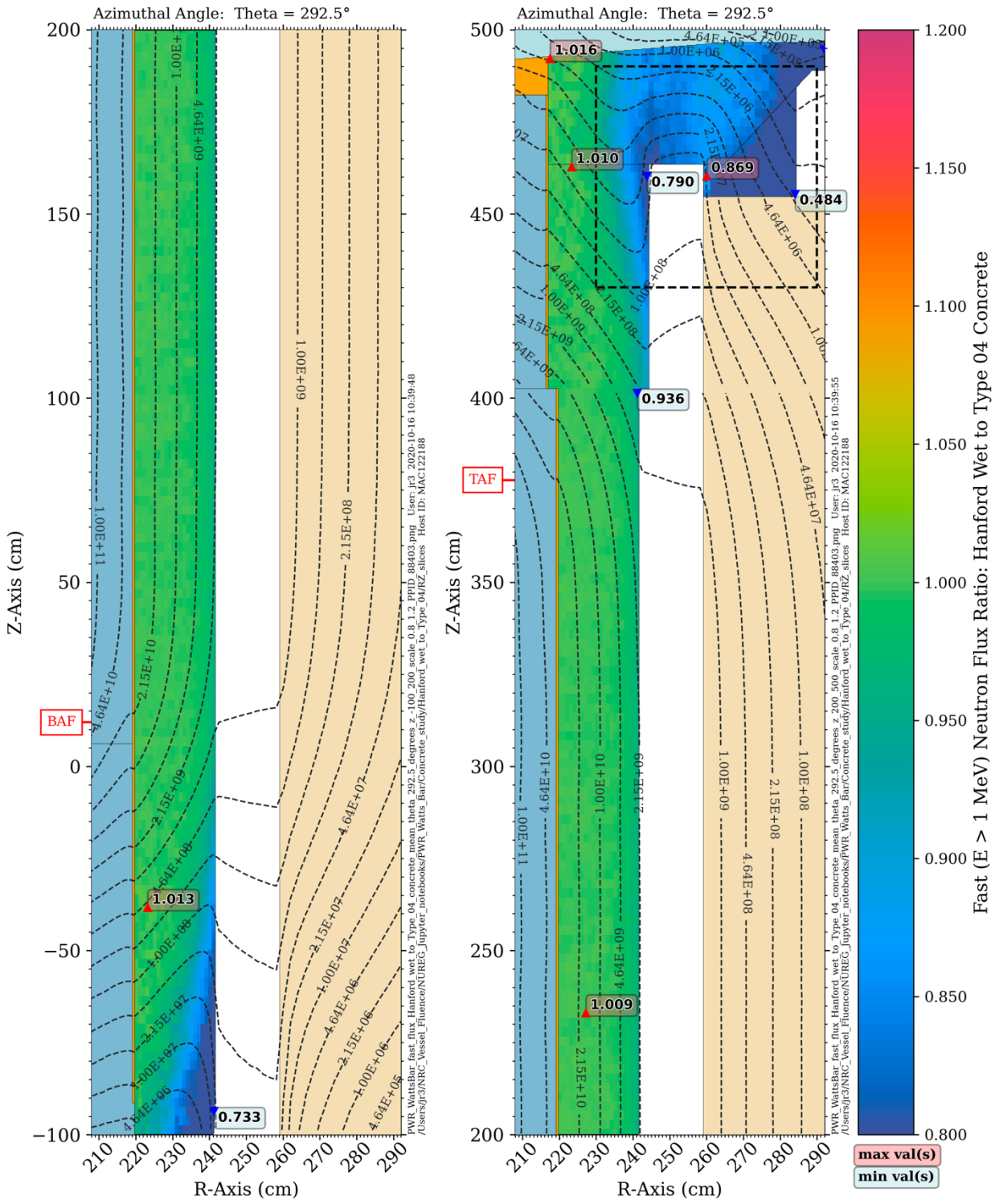

Figure 5-57 Fast neutron flux ratio in the PWR model with Hanford wet concrete in the bioshield relative to Type 04 concrete. Elevation view at an azimuthal angle of 292.5° *The contour lines represent the fast flux for the Type 04 model. The dashed box in the vicinity of the outlet nozzle vessel support corresponds to the plot area of Figure 5-58.*

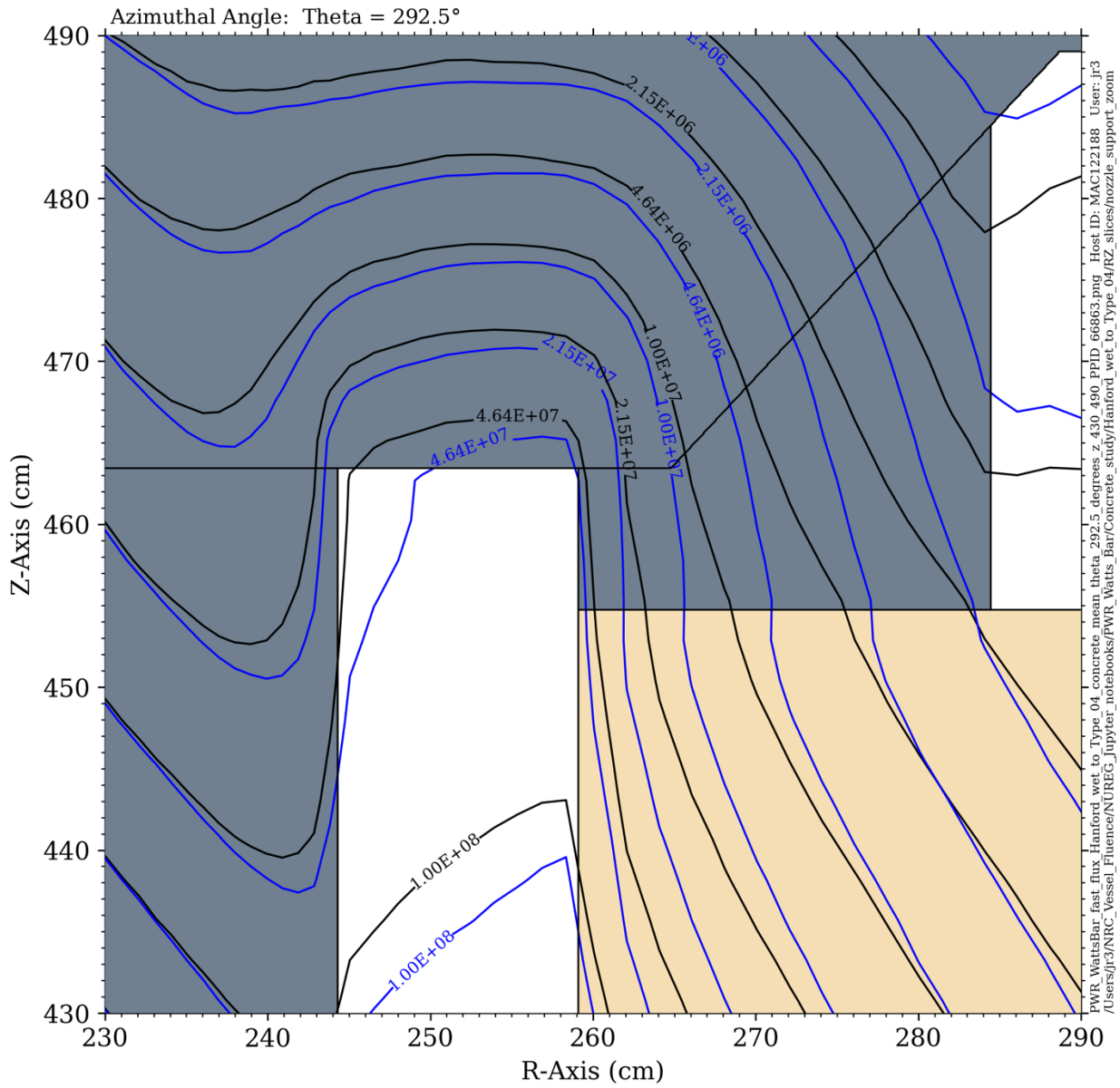

Figure 5-58 Fast neutron flux levels in the vicinity of the outlet nozzle vessel support. Elevation view at an azimuthal angle of 292.5° *The black contour lines represent the fast flux for the Type 04 concrete model; the blue lines represent the fast flux for the Hanford wet concrete model. Note the increasing separation in the two solutions with increasing depth into the concrete, with the Hanford wet concrete providing significantly more attenuation.*

5.7 Steel Bioshield Liner

The bioshield in the baseline PWR and BWR models is constructed of Type 04 concrete with no liner on the inner surface of the concrete, which is the cylindrical surface facing the RPV. Some reactor plant designs include a steel liner. The presence of a liner will have an effect on scattering from the bioshield into the cavity gap, as the angular distribution and average energy loss of scattered neutrons are different in steel than they are in the lighter elements that are the dominant constituents of the concrete.

Because the effect of a bioshield liner will primarily be on cavity-streaming neutrons, the PWR model was selected for a liner sensitivity study. (As shown in Section 5.1.2, cavity streaming neutrons in the BWR model are only significant at elevations where the magnitude of the fast flux is approximately three orders of magnitude lower than the peak fast flux in the beltline region.) To assess the impact of a steel liner on fluence levels in the reactor vessel, a 6.35 mm Type 304 stainless steel liner was added to the concrete bioshield in the PWR model below an elevation of 630.48 cm, where the inner radius of the concrete bioshield increases near the vessel flange (Figure 4-1).

The effect of the stainless steel liner is illustrated in Figure 5-59 through Figure 5-62. In Figure 5-59 and Figure 5-60 it can be seen that the effect of the liner on the fast neutron flux at the outer surface of the RPV is less than 3% at locations away from the nozzles.[8] The most notable effect is the reduction in the fast flux in the vessel support, which is also shown in Figure 5-61. Section 5.6 shows that the fast flux in the vessel support is dominated by neutrons that are transported through the concrete into the vessel support. This is also shown in Figure 5-62. At each location in the concrete region below the vessel support, the fast neutron flux when a stainless steel liner is present 'lags' the fast neutron flux with no liner. This difference is due to the reduced energy of fast neutrons that scatter in the liner before entering the concrete.

Calculations were also performed using a carbon steel liner with the same thickness (6.35 mm) as that of the stainless steel liner. The effect of a carbon steel liner is nearly equivalent to that of a stainless steel liner, although the changes in the fast flux (whether increases on the outer surface of the RPV or decreases in the vessel supports) are slightly less pronounced.

[8] Only the outlet nozzle location at an azimuthal angle of 292.5° is shown. The liner–to–no-liner ratio at the location of the inlet nozzle (337.5°) is consistent with that at the outlet nozzle.

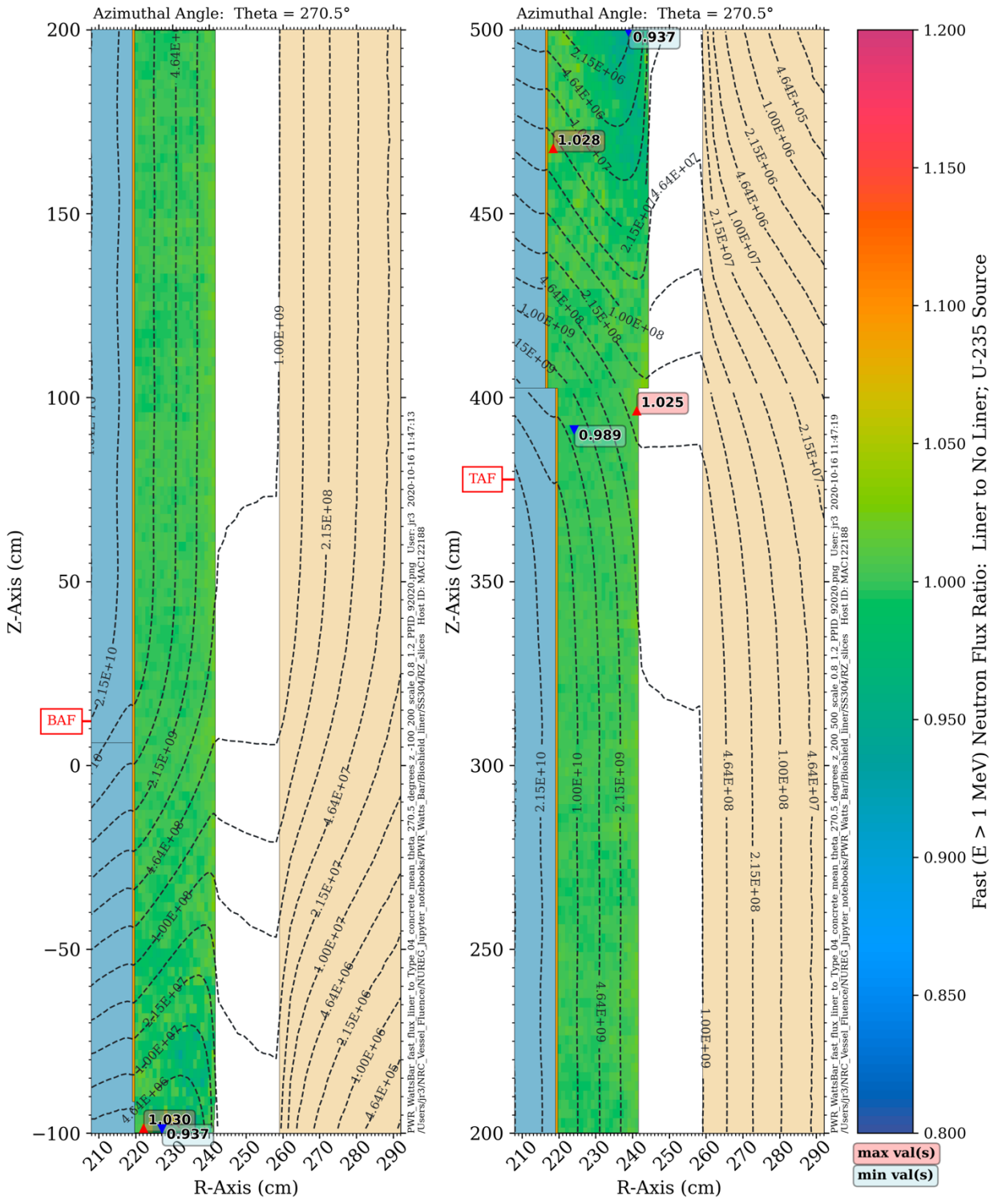

Figure 5-59 Ratio of the fast neutron flux in the RPV of the PWR model with a 6.35 mm stainless steel bioshield liner relative to the base case with no liner. Elevation view at an azimuthal location of 270.5° *The contour lines show the fast neutron flux for the base case model.*

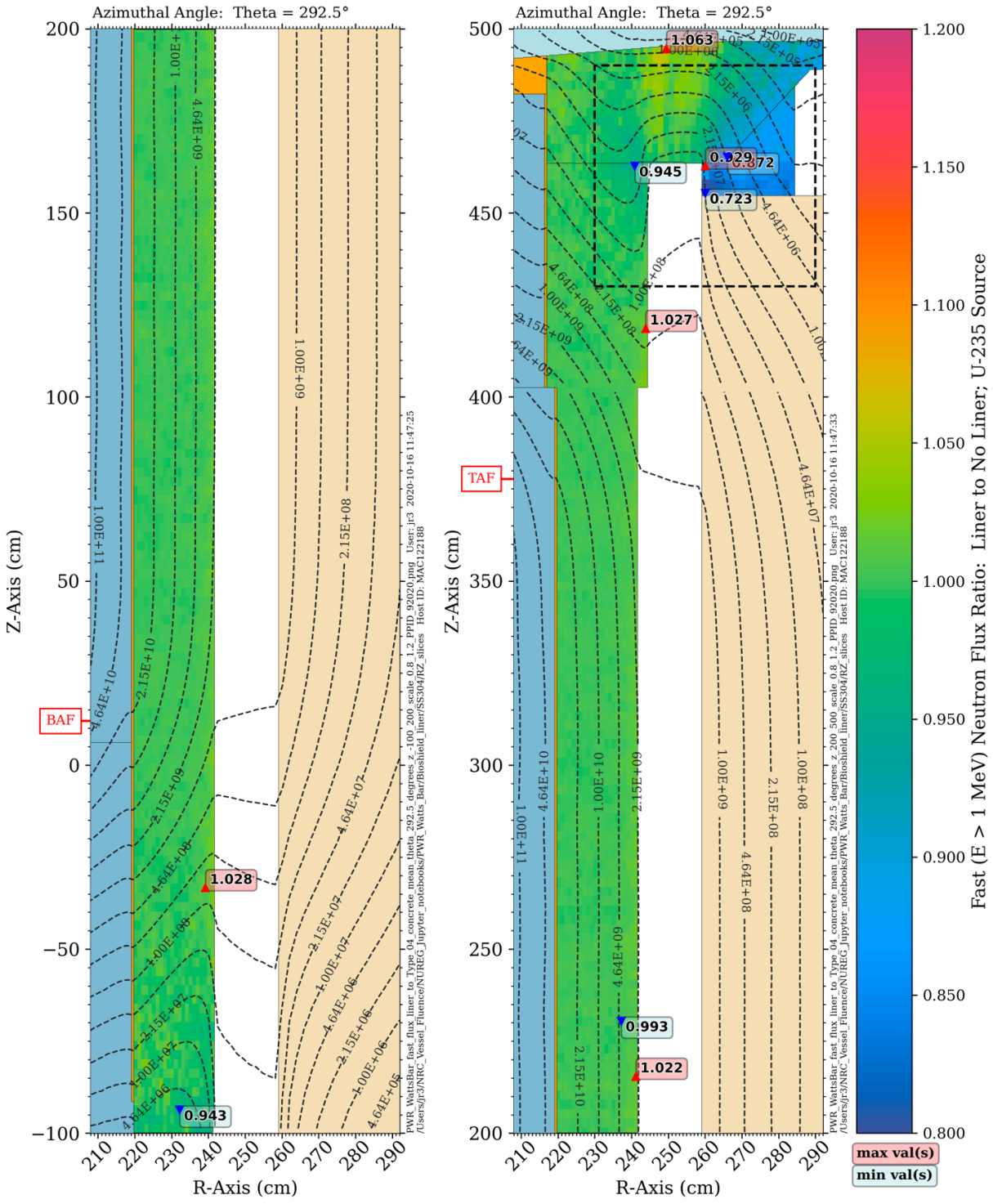

Figure 5-60 Ratio of the fast neutron flux in the RPV of the PWR model with a 6.35 mm stainless steel bioshield liner relative to the base case with no liner. Elevation view at an azimuthal location of 292.5° *The contour lines show the fast neutron flux for the base case model. The dashed box in the vicinity of the outlet nozzle vessel support corresponds to the plot area of Figure 5-61.*

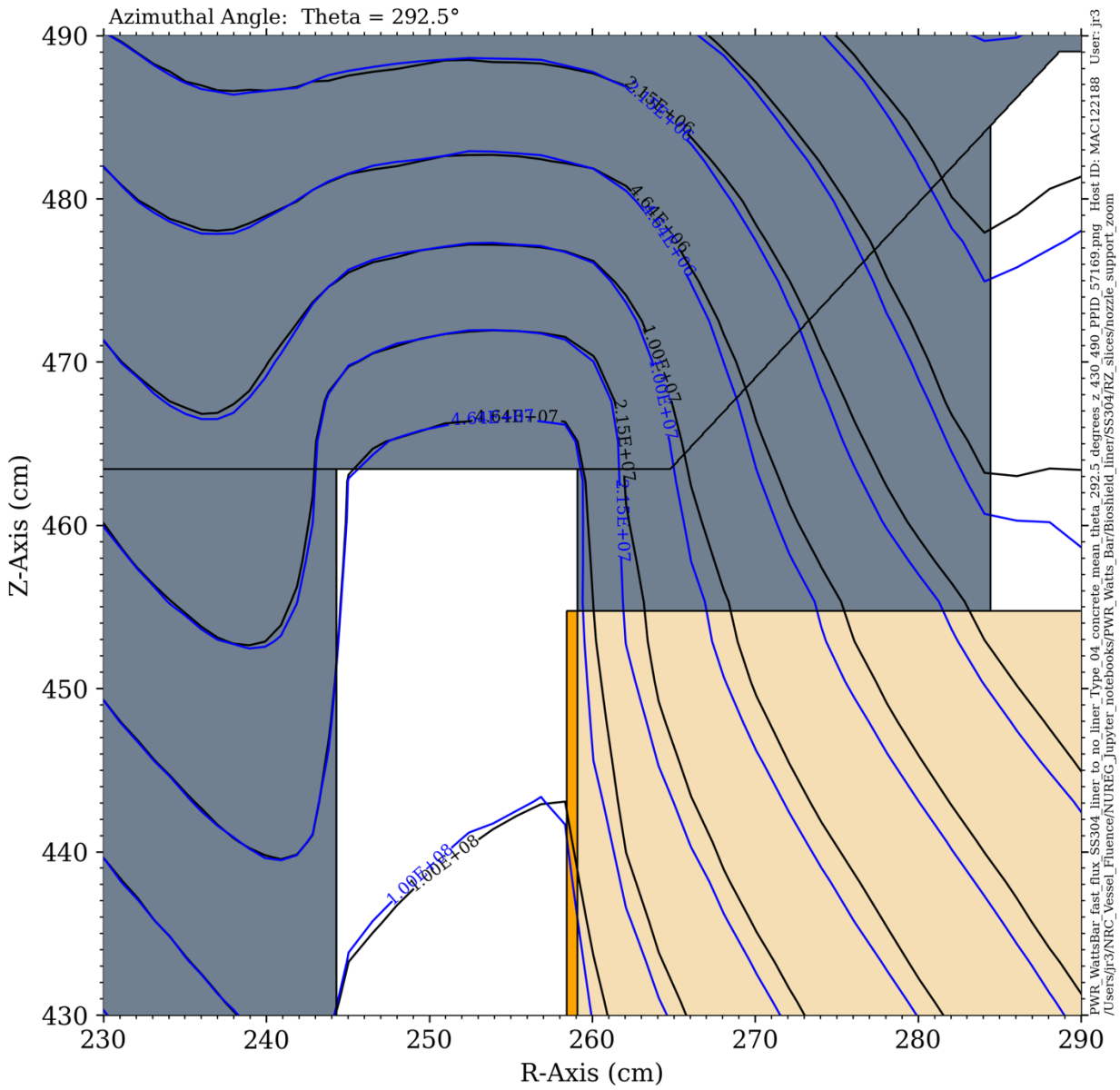

Figure 5-61 Fast neutron flux levels in the vicinity of the outlet nozzle vessel support. Elevation view at an azimuthal angle of 292.5° *The black contour lines represent the fast flux for the baseline model with no bioshield liner; the blue lines represent the fast flux for the model that includes at 6.35 mm SS304 bioshield liner.*

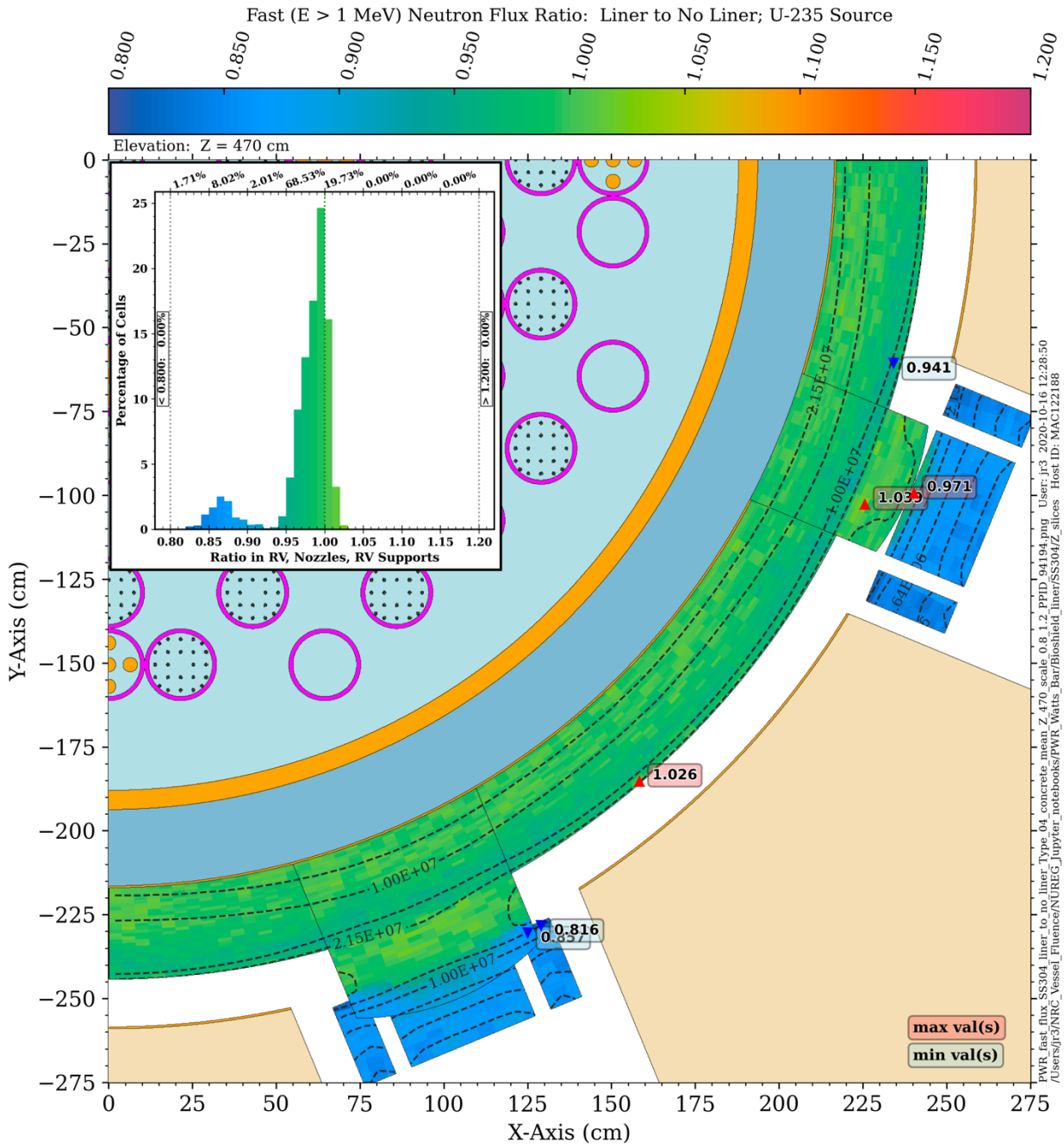

Figure 5-62 Ratio of the fast neutron flux in the RPV of the PWR model with a 6.35 mm stainless steel bioshield liner relative to the base case with no liner. Plan view at Z = 470 cm *The dashed contour lines show the fast neutron flux for the base case model.*

5.8 Thermal Insulation

RPVs for PWR and BWR designs typically have a layer of thermal insulation between the RPV's outer radius and the inner radius of the concrete bioshield. This insulation layer has a minor effect on fast flux levels in the RPV in the beltline region, where it can cause very slight increases in the fast flux levels at the outer surface of the RPV due to backscatter of neutrons from the insulation. At locations in the extended beltline region, the presence of thermal insulation can reduce fast flux levels in the RPV due to attenuation of the cavity-streaming neutron flux by the thermal insulation.

To assess the effect of insulation, a reflective metallic insulation layer was modeled using a 7.62 cm (3 in.) layer composed of air with a 3% volume fraction of stainless steel. The thickness and material composition are based on data provided in Table 1.1 of NUREG/CR-6453 [83]. The axial extent of the insulation is from the bottom of the lower cylindrical portion of the RPV to the elevation of the nozzle tunnels. Note that changes in the thickness, axial extent, and/or the insulation composition could affect the neutron transport behavior in the cavity gap.

The effect of the insulation is shown at two azimuthal locations in Figure 5-63 and Figure 5-64 and at an elevation of Z = 470 cm in Figure 5-65. While there is no significant effect within the traditional beltline region, the decreased cavity streaming due to the presence of the insulation leads to a reduction of up to ~15–20% in the fast flux in the RPV at locations where cavity streaming dominates the fast flux profile in the RPV.

It should be noted that even though the reflective metallic insulation has an effective density of only 0.24 g/cm^3, neutrons that scatter from the bioshield back into the cavity gap and subsequently enter the outer surface of the RPV will typically pass through the insulation twice (once before and once after scattering in the bioshield), and they may have steep, slanted paths through the insulation that further increase the attenuation provided by the insulation.

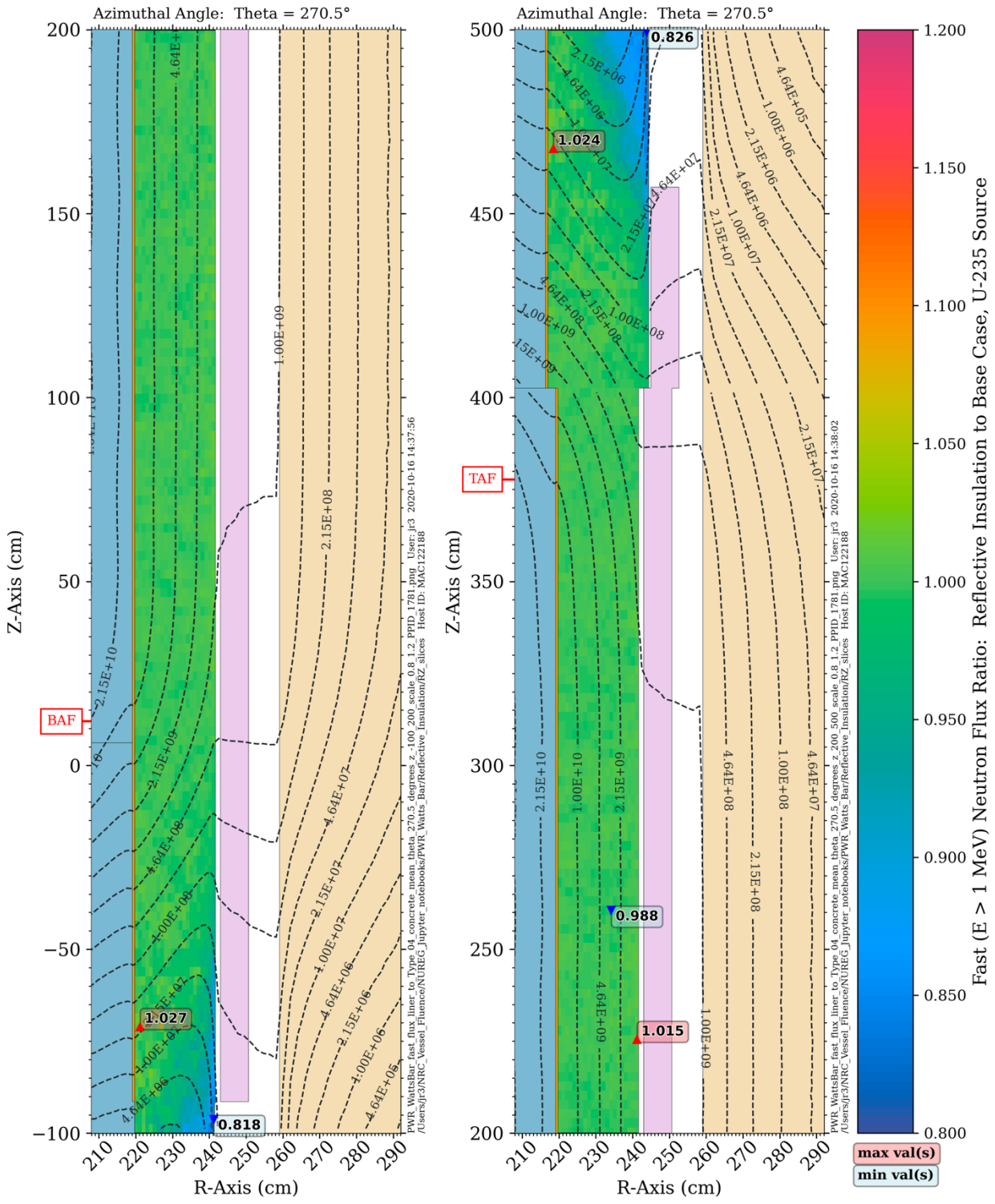

Figure 5-63 Fast neutron flux ratio for a PWR model with reflective metallic thermal insulation relative to the base case model with no thermal insulation. Elevation view at an azimuthal angle of 270.5° *The contour lines represent the fast flux for the base case model.*

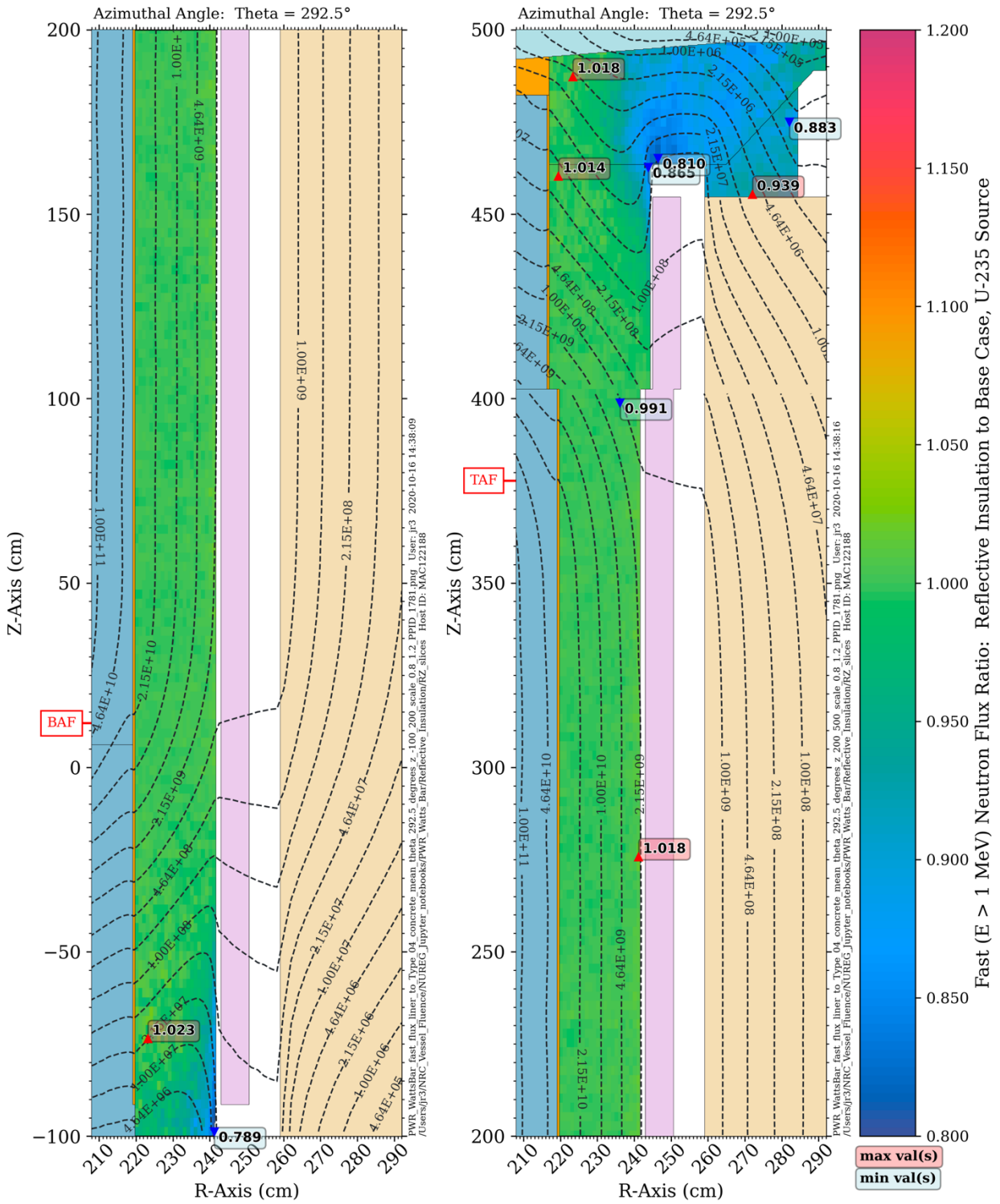

Figure 5-64 Fast neutron flux ratio for a PWR model with reflective metallic thermal insulation relative to the base case model with no thermal insulation. Elevation view at an azimuthal angle of 292.5° *The contour lines represent the fast flux for the base case model.*

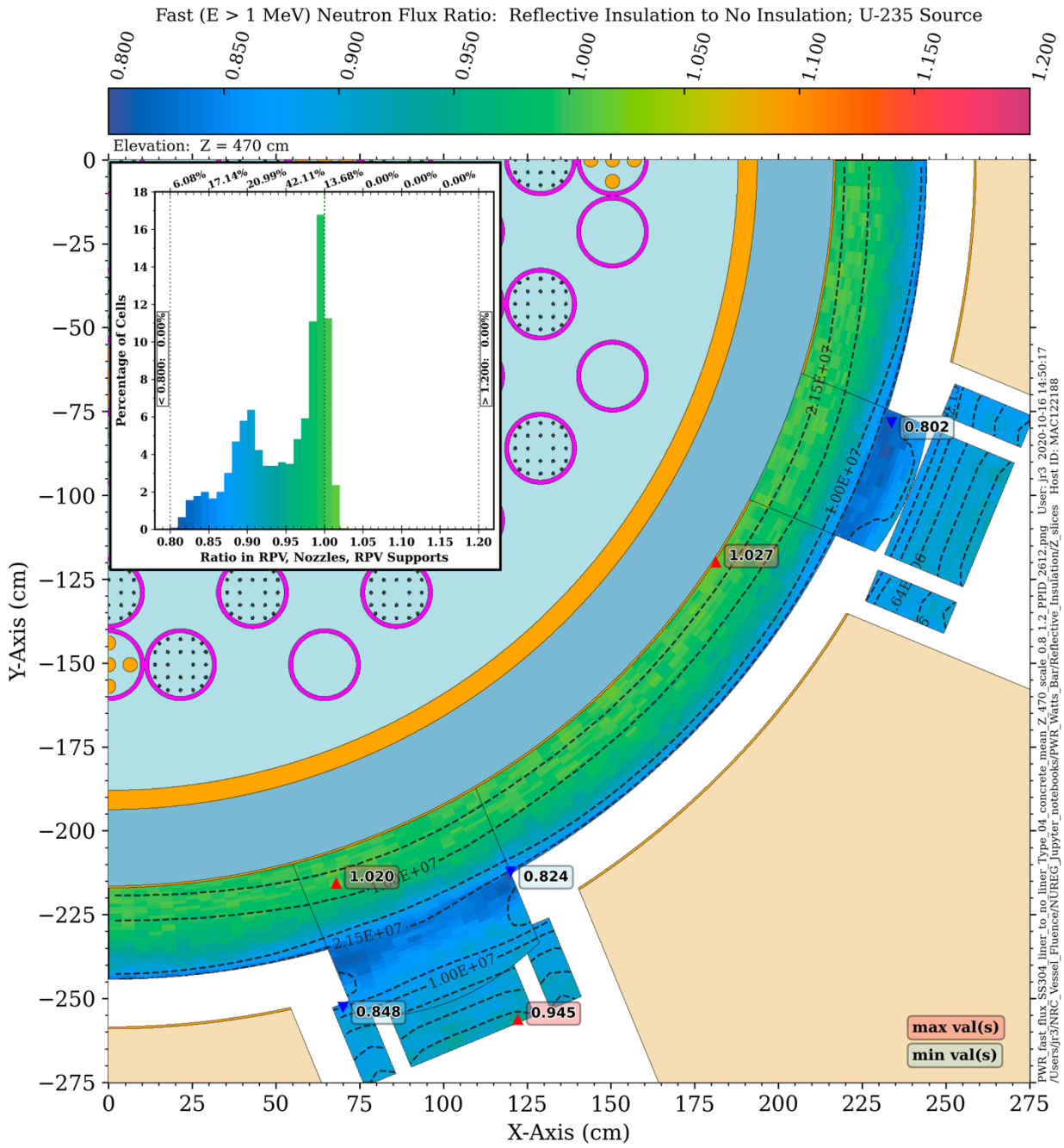

Figure 5-65 Fast neutron flux ratio for a PWR model with reflective metallic thermal insulation relative to the base case model with no thermal insulation. Plan view at an elevation of Z = 470 cm *The contour lines represent the fast flux for the base case model.*

5.9 Core Homogenization

A common approximation in RPV fluence calculations is to homogenize the materials within the fuel assemblies into a set of mixtures rather than having the explicit geometry representation of the fuel pins, control assemblies, guide tubes, and other components. This is a reasonable modeling approximation for fast neutron flux calculations, as the neutron transport characteristics of the homogenized fuel assemblies are essentially identical to those of explicitly modeled assemblies when calculating fast neutron flux levels in the RPV.

To verify the validity of this modeling approximation and assess whether it is appropriate for fluence calculations in the extended beltline region, homogenized versions of the PWR and BWR reference models were created by calculating the mass fractions of each element in specific axial regions of each assembly and creating homogenized assembly models in which a single mixed material fills each assembly region. These homogenized models are also used in the Denovo deterministic calculations discussed in Section 7. Using transport models with homogenized fuel assemblies for deterministic calculations with Denovo—or with any code that uses material mixing for spatially discretized models—is significantly more memory efficient. Using an explicit core model with Denovo would produce mixed materials for every spatial mesh cell that has a unique material mixture. This could result in a very large number of mixed materials, which would substantially increase the amount of memory needed to store the cross-section data.

5.9.1 PWR Model

Calculations of the fast flux levels in the RPV with the homogenized PWR model were compared with explicit core calculations for a spatially uniform ^{235}U source. Plan views of the fast flux ratio for the homogenized core model relative to the explicit core model are shown in Figure 5-66, Figure 5-67, and Figure 5-68. At the core midplane elevation (Figure 5-66), the fast flux with the homogenized core model agrees with the explicit core model within 1.5% in all mesh tally voxels. At an elevation ~80 cm below the bottom of the core (Figure 5-67), the fast flux in the RPV with the homogenized core is up to ~4% higher on average than the explicit core model. However, the maximum fast flux in the RPV at this elevation is more than three orders of magnitude lower than the core midplane value, so this difference is not significant. At an elevation ~90 cm above the top of the core (Figure 5-68), the homogenized core solution typically agrees with the explicit core solution within 2%.

5.9.2 BWR Model

Calculations of the fast flux levels in the RPV with the homogenized BWR model were compared with explicit core calculations for a spatially uniform ^{235}U source. Average VFs (Section 5.4) were used in both the explicit and homogenized models. Plan views of the fast flux ratio for the homogenized core model compared to the explicit core model are shown in Figure 5-69, Figure 5-70, and Figure 5-71. At the core midplane elevation, the fast flux with the homogenized core model agrees with the explicit core model within 2% in all mesh tally voxels. At the lower (Z = -250 cm) and upper (Z = 375 cm) elevations, the agreement is within 2% in nearly all the mesh tally voxels.

5.9.3 Summary

The results presented in Section 5.9.1 and Section 5.9.2 suggest that homogenization of the core in both the PWR and BWR models is appropriate not only for RPV fluence calculations

within the traditional beltline region, but also within the extended beltline region. The primary purpose of this parameter study is to confirm that the use of homogenized fuel assembly models is appropriate in discrete ordinates calculations of RPV vessel fluence.

There is little if any benefit to using a homogenized core model for Monte Carlo transport calculations. There may be a slight reduction in the average time per history because there are fewer surface crossings when transporting neutrons through a homogenized core, but those savings are typically not significant. Use of an explicit core model also provides the benefit of having a single model that can be used for core eigenvalue and power distribution calculations, as well as RPV fluence calculations.

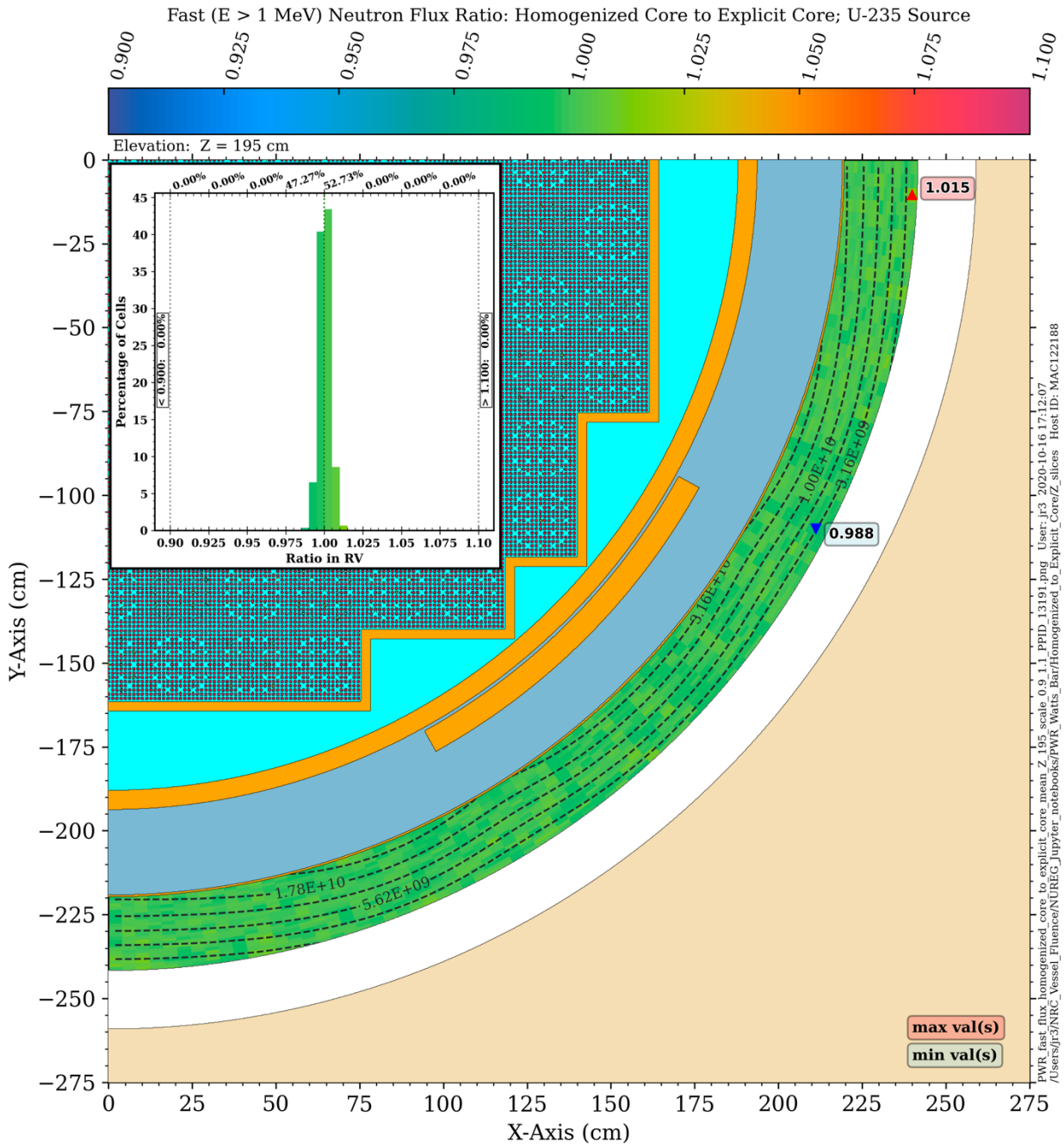

Figure 5-66 Fast neutron flux ratio for the homogenized PWR core model relative to the explicit core model. Plan view at Z = 195 cm *The source is spatially uniform with a ^{235}U fission spectrum. The contour lines represent the fast flux from the explicit core model.*

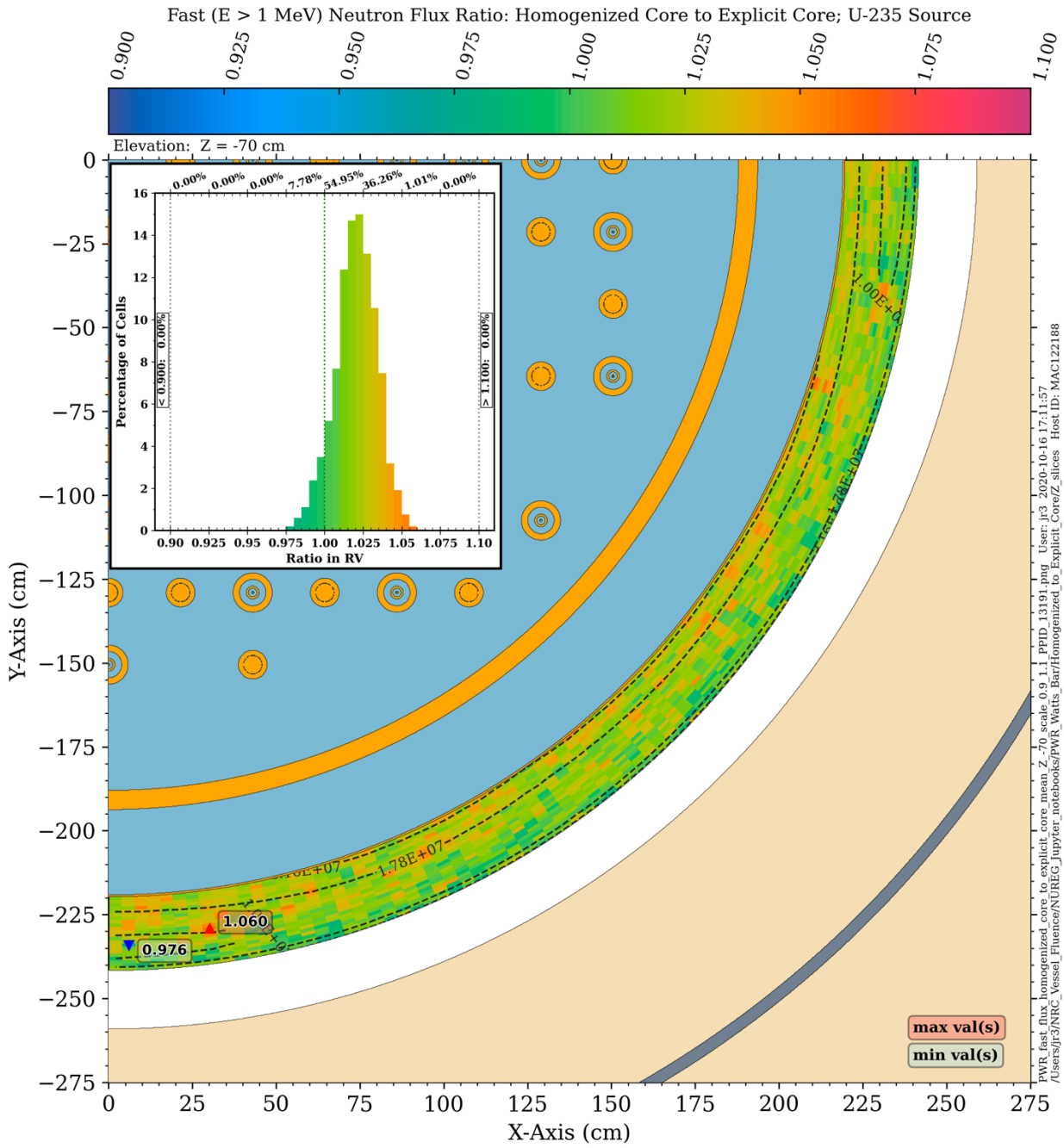

Figure 5-67 Fast neutron flux ratio for the homogenized PWR core model relative to the explicit core model Plan view at Z = -70 cm *The source is spatially uniform with a ^{235}U fission spectrum. The contour lines represent the fast flux from the explicit core model.*

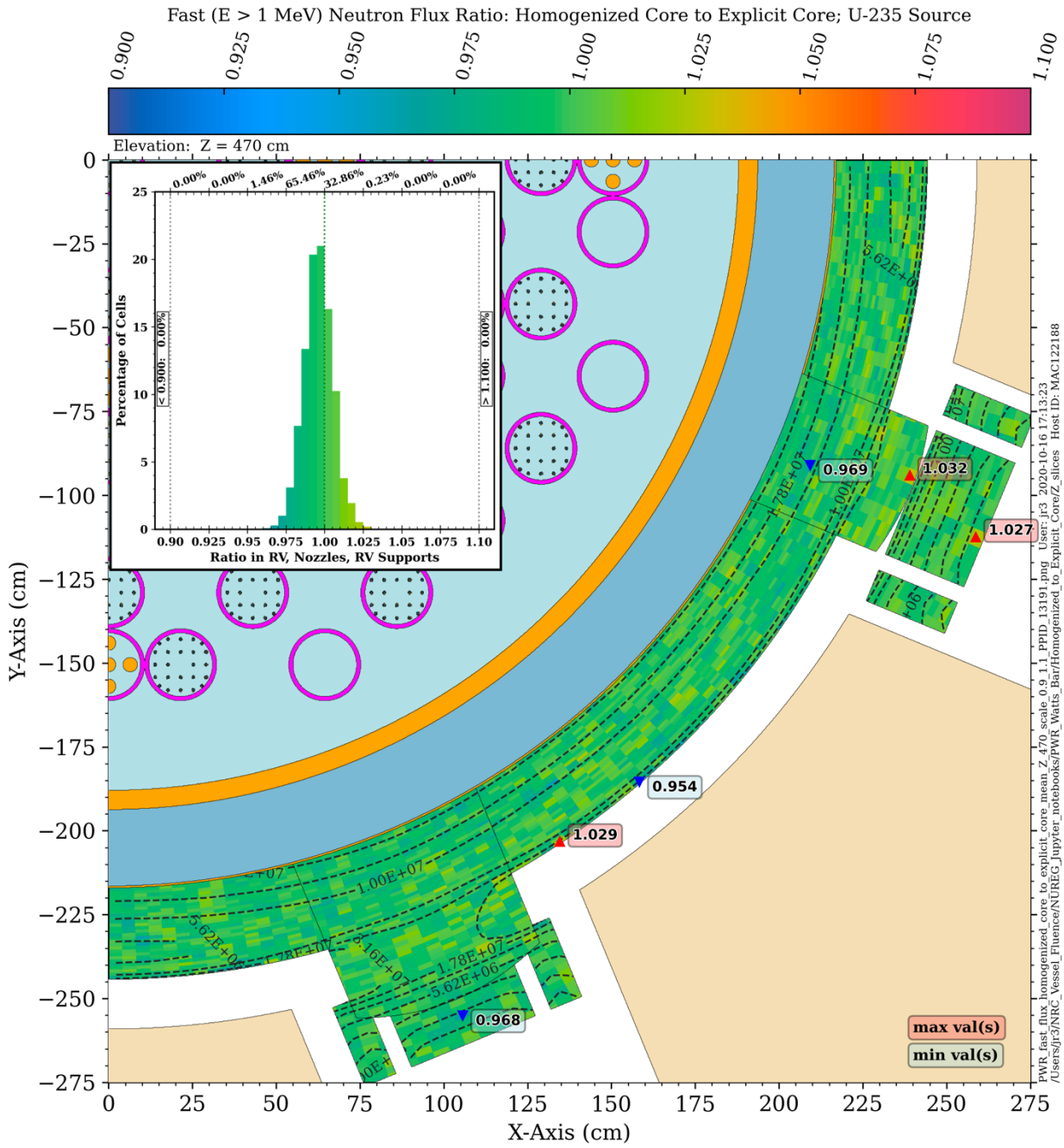

Figure 5-68 Fast neutron flux ratio for the homogenized PWR core model relative to the explicit core model. Plan view at Z = 470 cm *The source is spatially uniform with a ^{235}U fission spectrum. The contour lines represent the fast flux from the explicit core model.*

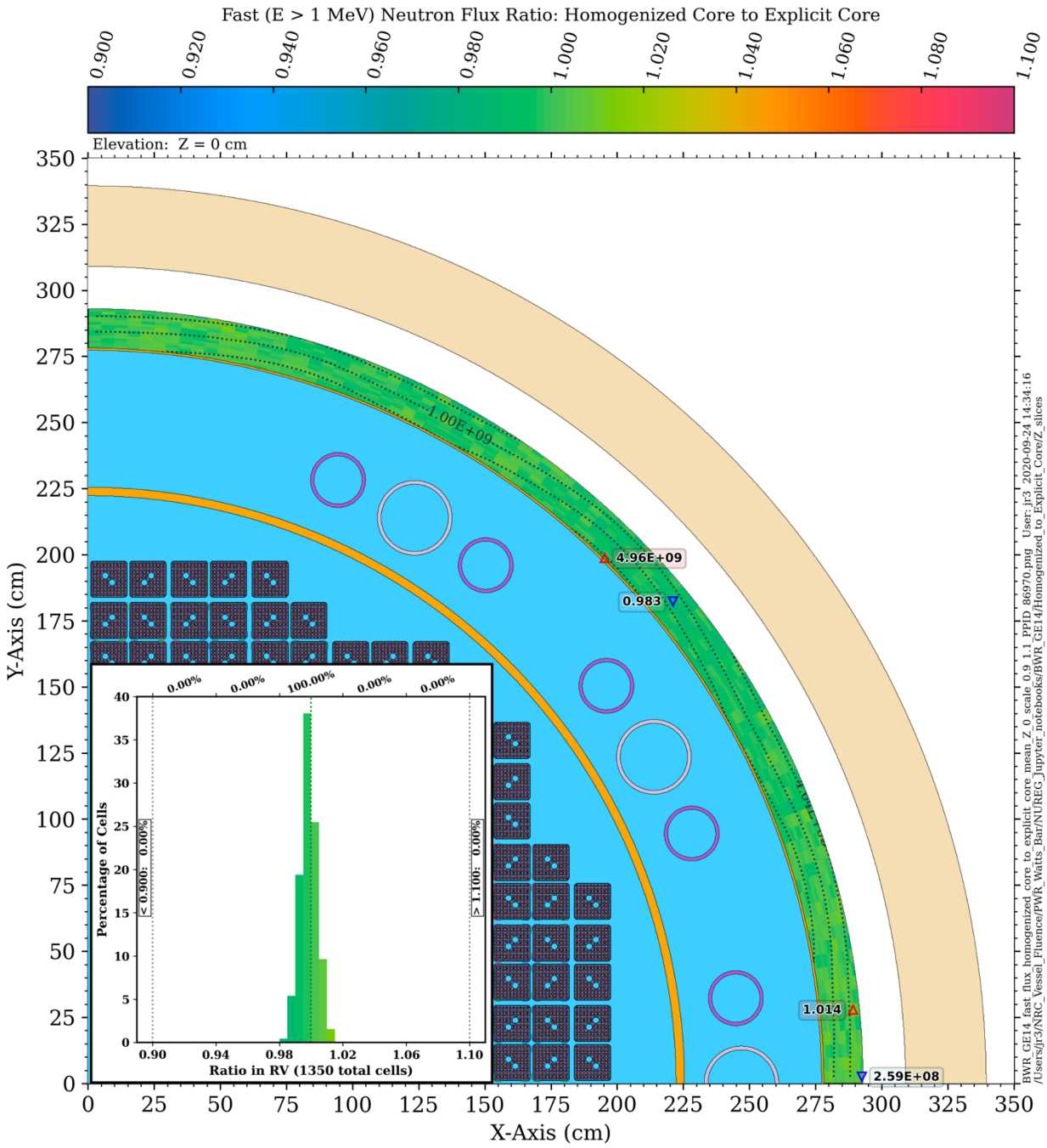

Figure 5-69 Fast neutron flux ratio for the homogenized BWR core model relative to the explicit core model. Plan view at Z = 195 cm *The source is spatially uniform with a ^{235}U fission spectrum. The contour lines represent the fast flux from the explicit core model.*

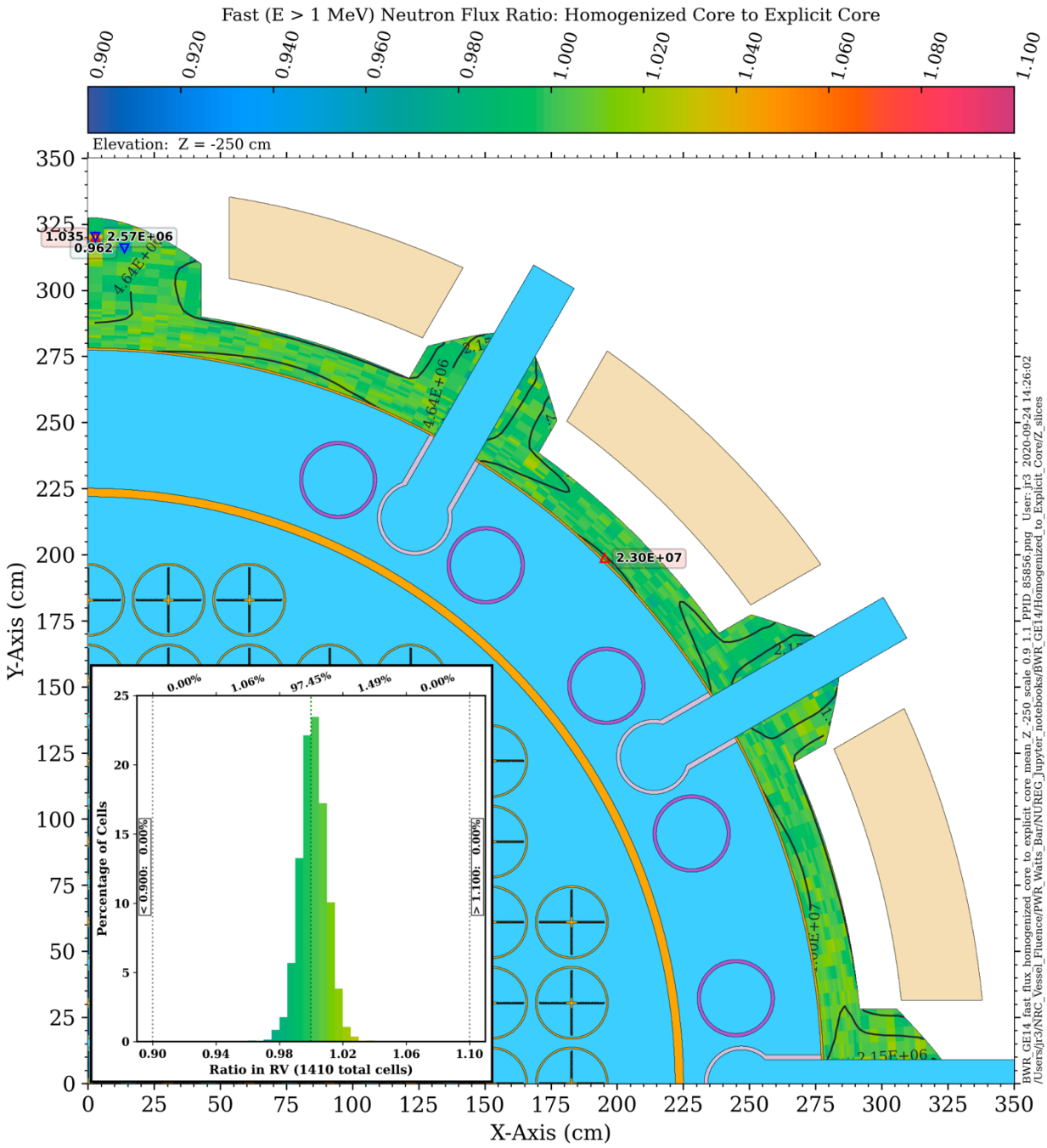

Figure 5-70 Fast neutron flux ratio for the homogenized BWR core model relative to the explicit core model. Plan view at Z = -250 cm *The source is spatially uniform with a ^{235}U fission spectrum. The contour lines represent the fast flux from the explicit core model.*

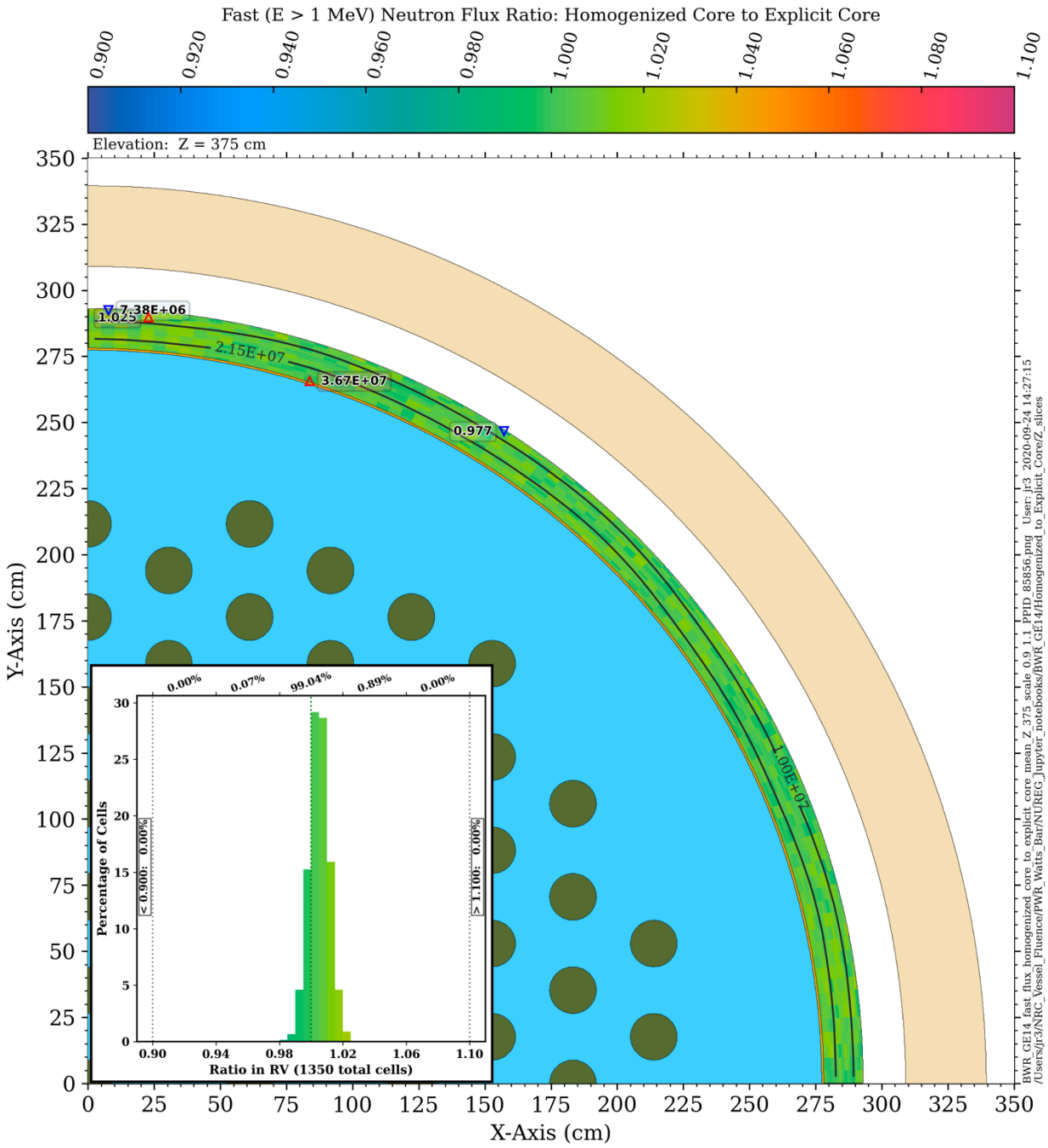

Figure 5-71 Fast neutron flux ratio for the homogenized BWR core model relative to the explicit core model. Plan view at Z = -250 cm *The source is spatially uniform with a ^{235}U fission spectrum. The contour lines represent the fast flux from the explicit core model.*

6 DPA CONSIDERATIONS

While Regulatory Guide 1.190 is primarily directed toward calculations and measurement procedures for RPV fluence, the procedures it establishes are also applicable to analyses of displacements per atom (dpa). Calculation of dpa is somewhat more complex than calculation of fast fluence, as knowledge of the total neutron fluence and flux spectrum is required [85].

For calculations of fast fluence and dpa in extended beltline regions, the following issues must be considered:

1. The relationship between dpa rates and fast flux in the RPV varies as a function of location. This suggests that using fast fluence as a surrogate for dpa may have limitations with respect to locations in the RPV.
2. The rates of attenuation for fast flux and dpa rates change due to elevation and, to a lesser extent, the azimuthal location in the RPV. At elevations sufficiently far above or below the active fuel, the maximum values of the fast flux and dpa rate can occur at the outer edge of the RPV due to cavity streaming effects.
3. While the effects of gamma-induced dpa are known to be much less than the effects of neutron dpa in the traditional beltline region, it may be possible for gamma dpa effects to become important contributors at locations within vessel support structures [86].

6.1 Relationship Between DPA and Fast Neutron Fluence in the PWR and BWR Models

Because the dpa cross section is a function of neutron energy, the relationship between dpa and fast fluence is inherently nonlinear. This nonlinearity can become problematic if fast neutron fluence is used as a surrogate for dpa in regions where the ratio of dpa to fast fluence deviates significantly from the ratio within the traditional beltline region.

In considering this effect, the fast flux and dpa rates are examined herein, as well as the ratio of the dpa rate to the fast flux at selected locations in the reference PWR and BWR models. Calculations of fast flux and dpa rates in both models were performed using the pseudo-BOL sources described in Section 5.1.

6.1.1 PWR Model

The fast (E > 1 MeV) neutron flux and total neutron dpa rate (i.e., the dpa rate integrated over all neutron energies) at the core midplane in the PWR model are shown in Figure 6-1 and Figure 6-2. In Figure 6-1 and all other 2D fast flux plots in Section 6, flooded contours are used for the flux in the RPV, vessel supports, and nozzles, while contour lines only are used in other materials (e.g., downcomer water, the cavity gap, and the bioshield). In Figure 6-2 and all other 2D dpa rate plots in Section 6, flooded contours are used for the dpa rate in the RPV, vessel supports, and nozzles. No contour lines are present in any material other than the carbon steel, as dpa rates based on the dpa cross-section data in [85] are valid only in carbon steel.

Based on these figures, it is immediately obvious that the relationship between fast fluence and dpa is not linear, as the variation (based on the ratio of the maximum to minimum flux or dpa rates in the RPV) is ~37 for the fast flux and ~16 for the dpa rate. This tendency of the dpa rate to attenuate less rapidly than the fast flux in the traditional beltline region has been shown in numerous studies [75], [76].

The slower attenuation of the dpa rate is due to the contribution of neutrons with energies below 1 MeV. As neutrons penetrate into the RPV, their energies rapidly decrease due to scattering. Figure 6-3 illustrates the attenuation of the neutron flux as a function of energy through the RPV in a 1D representation of the PWR model. In this 1D model, which has no azimuthal variation (unlike the 3D model results in Figure 6-1), the flux for neutron energies greater than 1.0026 MeV decreases by nearly a factor of 20 in the RPV. Neutrons with energies between 111.09 keV and 1.0026 MeV enter the RPV with nearly the same magnitude as the fast (E > 1.0026 MeV) flux.[9] There is an initial increase in the flux of neutrons with energies from 111.09 keV to 1.0026 MeV, as fast neutrons are scattered to lower energies. The increase is followed by a gradual decrease, with a reduction of only about a factor of 2 between the inner and outer surfaces of the RPV.

The increasing contribution of neutrons with energy less than 1 MeV to the total dpa rate is also seen in Figure 6-4, where neutrons with energies greater than 1 MeV are responsible for ~70% of the total dpa rate near the inner radius of the RPV, but only 20–25% at the outer surface of the RPV.

The net result of these effects is an increase of more than a factor of two in the ratio of the dpa rate to the fast flux, as shown in Figure 6-5.

At the elevation of the vessel supports, significant differences occur in the relationship between the fast flux and the dpa rate. This behavior is illustrated in Figure 6-6 through Figure 6-9. As shown in Figure 6-8, the fraction of the dpa rate due to neutrons with energies greater than 1 MeV decreases from a peak value of 56.1% at the inner surface of the RPV to minimum values of 4.4% in the outer portion of the RPV and to values as low as 2.2% in the nozzle supports. Because of this significant increase in the contribution of neutrons with energies below 1 MeV to the dpa rate, the ratio of the dpa rate to the fast flux increases by more than an order of magnitude for locations in the nozzle supports (Figure 6-9).

Figure 6-10 through Figure 6-13 provide additional insights into the behavior of the fast flux and dpa rates in the PWR RPV. In Figure 6-10, the dpa rate displays an exponential attenuation with an attenuation coefficient of -0.23/inch. This value is nearly identical to the attenuation coefficient of -0.24/inch in Regulatory Guide 1.99, Eq. (3) [78]. The fast flux experiences a more rapid attenuation rate, confirming that the use of the dpa-based attenuation presented in Regulatory Guide 1.99 is conservative for use with fast fluence levels through the RPV in the traditional beltline region. Figure 6-10 also shows the trend of neutrons with energies less than 1 MeV becoming the dominant contributors to the total dpa rate at increasing distances through the RPV.

At an elevation of approximately 10 cm above the top of the fuel (Figure 6-11), the general characteristics of the fast flux and dpa rate are similar to those at the core midplane, but the rates of attenuation of the fast flux and total dpa rate have decreased slightly. At an elevation of approximately 50 cm above the top of the fuel (Figure 6-12), the fast flux and dpa rate profiles cannot be reasonably represented by a simple exponential attenuation through the full depth of the RPV. At an elevation of 470 cm (Figure 6-13), the concept of an exponential attenuation of the dpa rate is completely meaningless. Figure 6-13 also demonstrates that the dpa rate profile reverses (i.e., has a peak level on the outer surface of the RPV) sooner than the fast flux profile.

[9] The energy boundaries used in the 1D model are based on multigroup boundaries to facilitate comparison of the 1D Monte Carlo results with 1D discrete ordinates calculations.

If the uniform power distribution used in this parameter study were realistic, then the peak neutron fluence in the vessel supports (Figure 6-6) for 80 years of operation with a capacity factor of 90% would be approximately 1.25×10^{17}, and the peak dpa value (Figure 6-7) would be approximately 9.7×10^{-4} dpa. The significance of these values lies in their relationship to the scope of ASTM E1035-18 [86], which is applicable to all PWRs with vessel supports that will experience a lifetime fluence (E > 1 MeV) exceeding 1×10^{17} n/cm^2, or a lifetime dpa exceeding 3.0×10^{-4} dpa. Based on the results of the calculations presented in this section, it is clear that the limiting dpa value from ASTM E1035-18 [86] may be more restrictive than the limiting fluence value for neutron exposure considerations in vessel supports.

6.1.2 BWR Model

The fast neutron flux and total neutron dpa rate at the core midplane in the BWR model are shown in Figure 6-14 and Figure 6-15. As with the PWR model results in the preceding subsection, there is less attenuation of the dpa rate through the RPV relative to the attenuation of the fast flux. However, the differences in these two quantities (based on the ratio of the maximum-to-minimum values in the RPV) is less pronounced than in the PWR model. This behavior is consistent with the differences in the thicknesses of the RPVs: 22 cm for the PWR model and 14.9 cm for the BWR model. Because the BWR RPV thickness is significantly less than the PWR RPV thickness, there is less overall attenuation through the BWR RPV. In addition, there is less impact from changes in the neutron energy spectrum through the thickness of the BWR RPV. This can be seen in Figure 6-16. The fraction of the dpa rate due to neutrons with energies greater than 1 MeV decreases by a factor of ~1.7, whereas the same fraction at the core midplane of the PWR model decreases by a factor of ~3.6 (Figure 6-4). Similarly, the ratio of the total dpa rate to the fast flux in the PWR RPV at the core midplane increases by a factor of ~2.6 (Figure 6-5), whereas the corresponding ratio in the BWR RPV increases by a factor of ~1.4 (Figure 6-17).

Similar trends can be seen in the extended beltline regions of the PWR model (Figure 6-6 through Figure 6-9) and the BWR model (Figure 6-18 through Figure 6-21). In particular, the variation in the ratio of the dpa rate to the fast flux in the BWR extended beltline location (Figure 6-21) is ~3.5, whereas in the extended beltline region of the PWR model (Figure 6-9), the variation in that ratio is nearly a factor of 14.

In summary, there is significantly less variation in the relationship between fast flux and dpa in the BWR model compared to the PWR model. Thus, the question of whether fast flux is an acceptable surrogate for dpa rate in RPVs, nozzles, and vessel supports may be a concern primarily for PWR neutron exposure analyses.

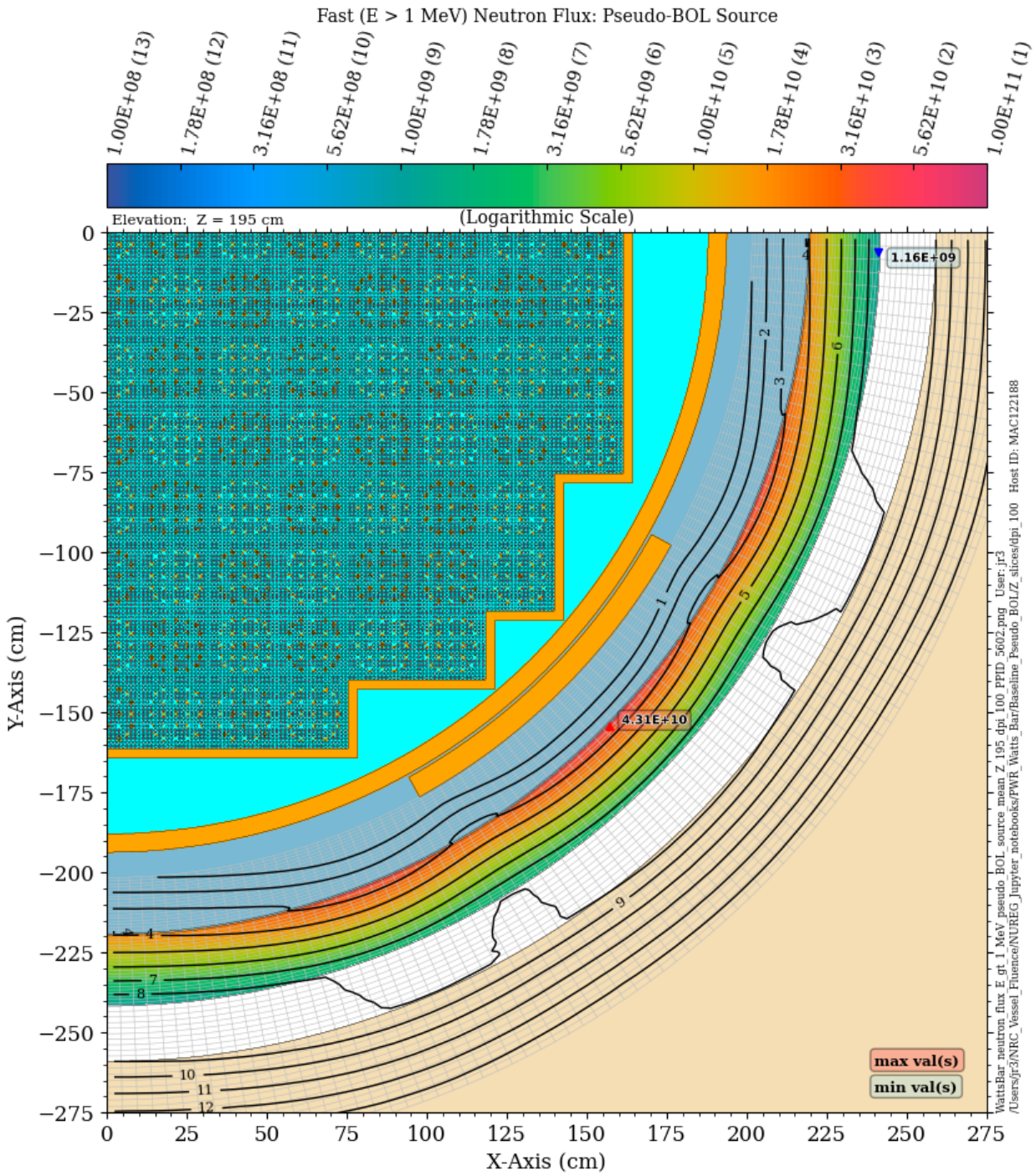

Figure 6-1 Fast neutron flux in the PWR model at the core midplane: pseudo-BOL source

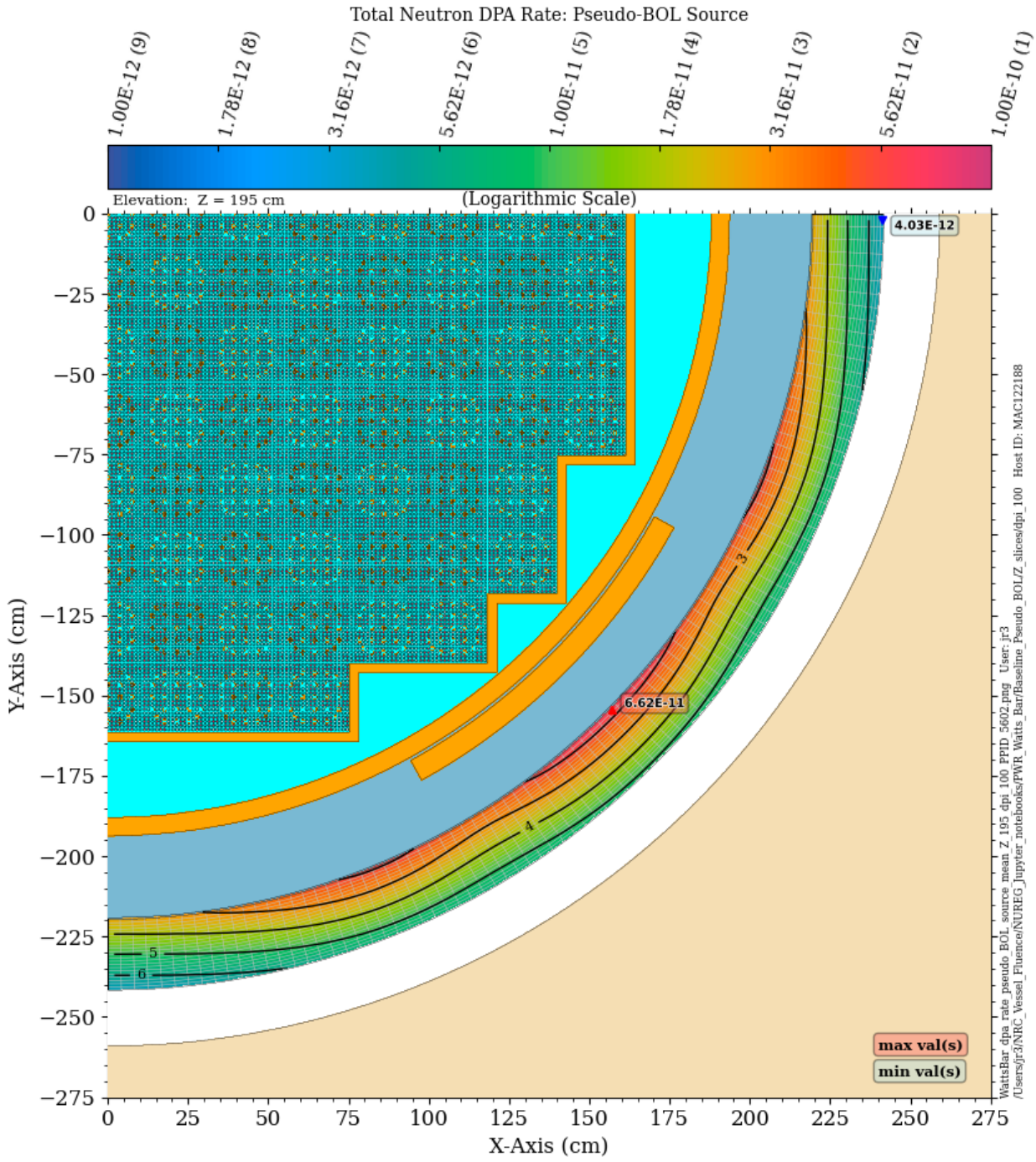

Figure 6-2 Total neutron dpa rate in the PWR model at the core midplane: pseudo-BOL source

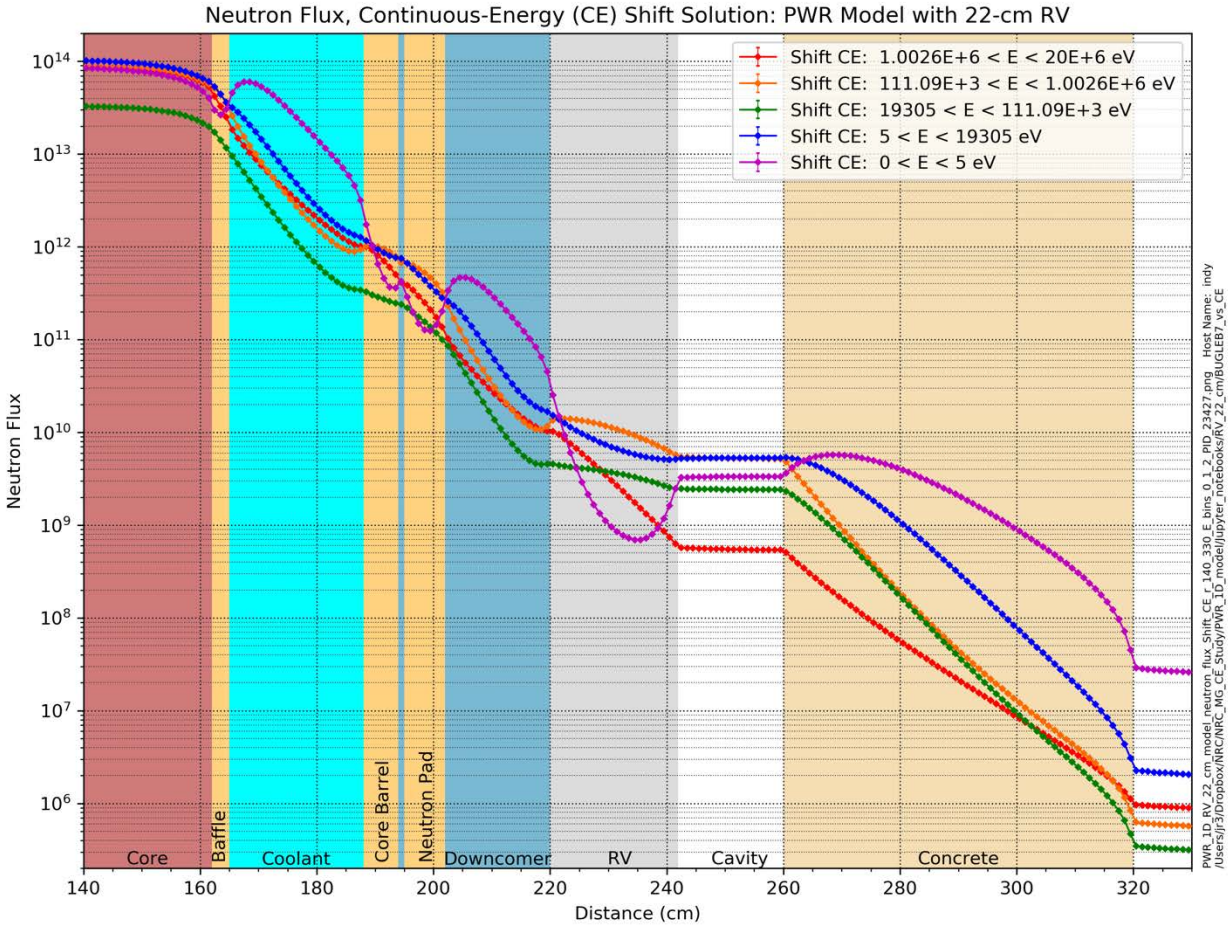

Figure 6-3 Neutron flux traverses for five energy ranges through a 1D mockup of the PWR reference model

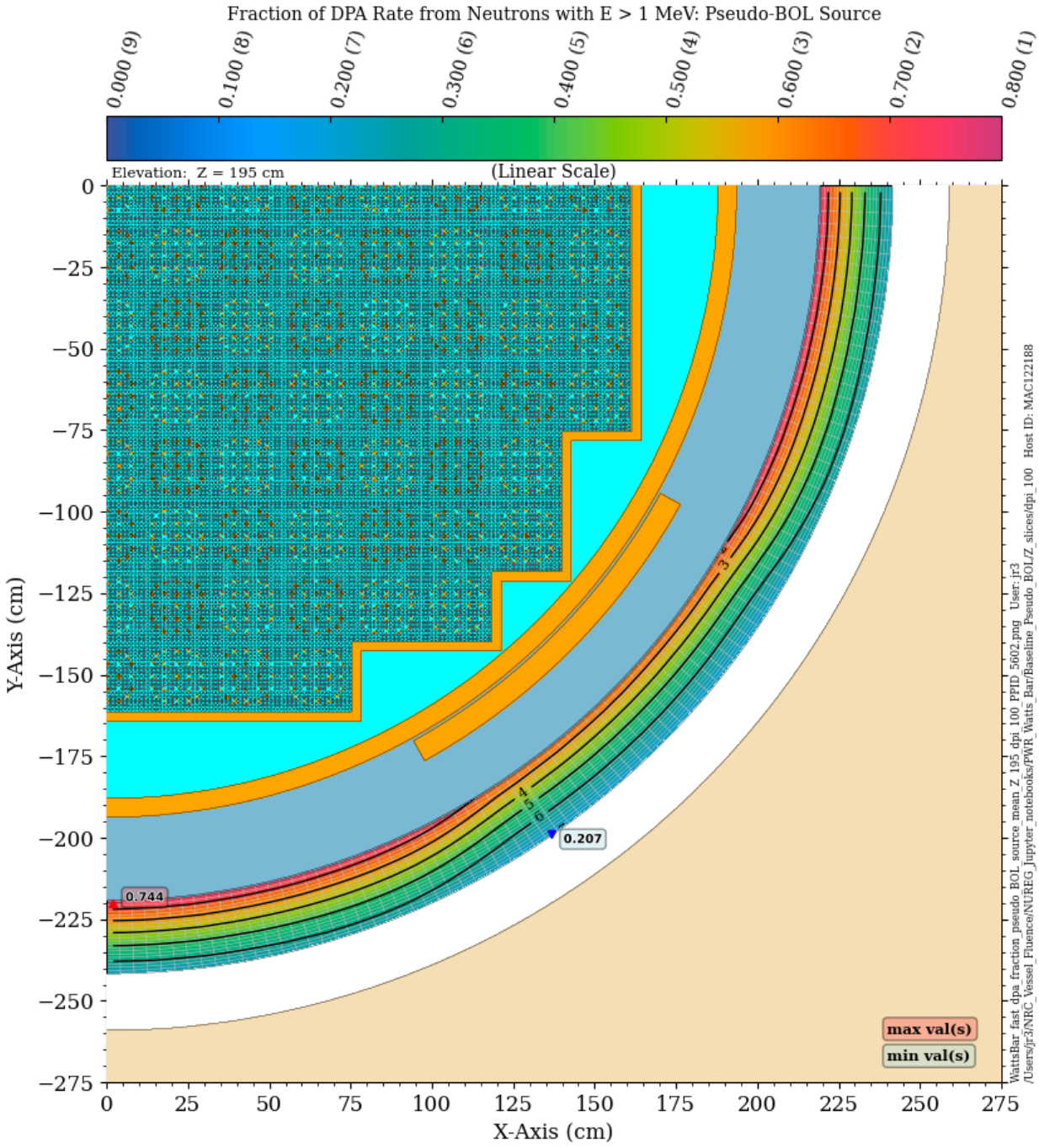

Figure 6-4 Fraction of the total neutron dpa rate due to neutrons with energy > 1 MeV in the PWR RPV. Plan view at the core midplane

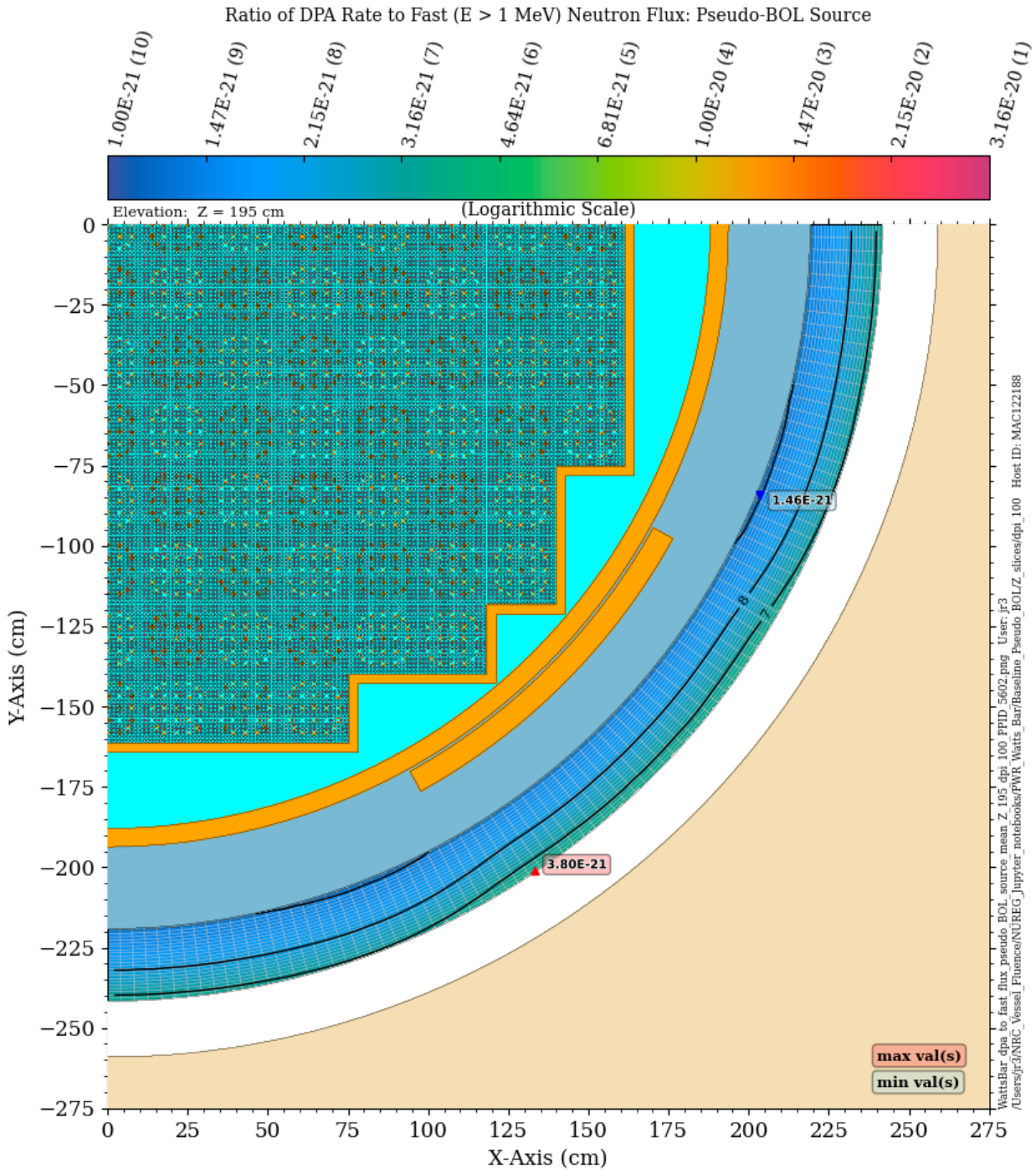

Figure 6-5 Ratio of the total neutron dpa rate to the fast (E > 1 MeV) neutron flux in the PWR RPV. Plan view at the core midplane

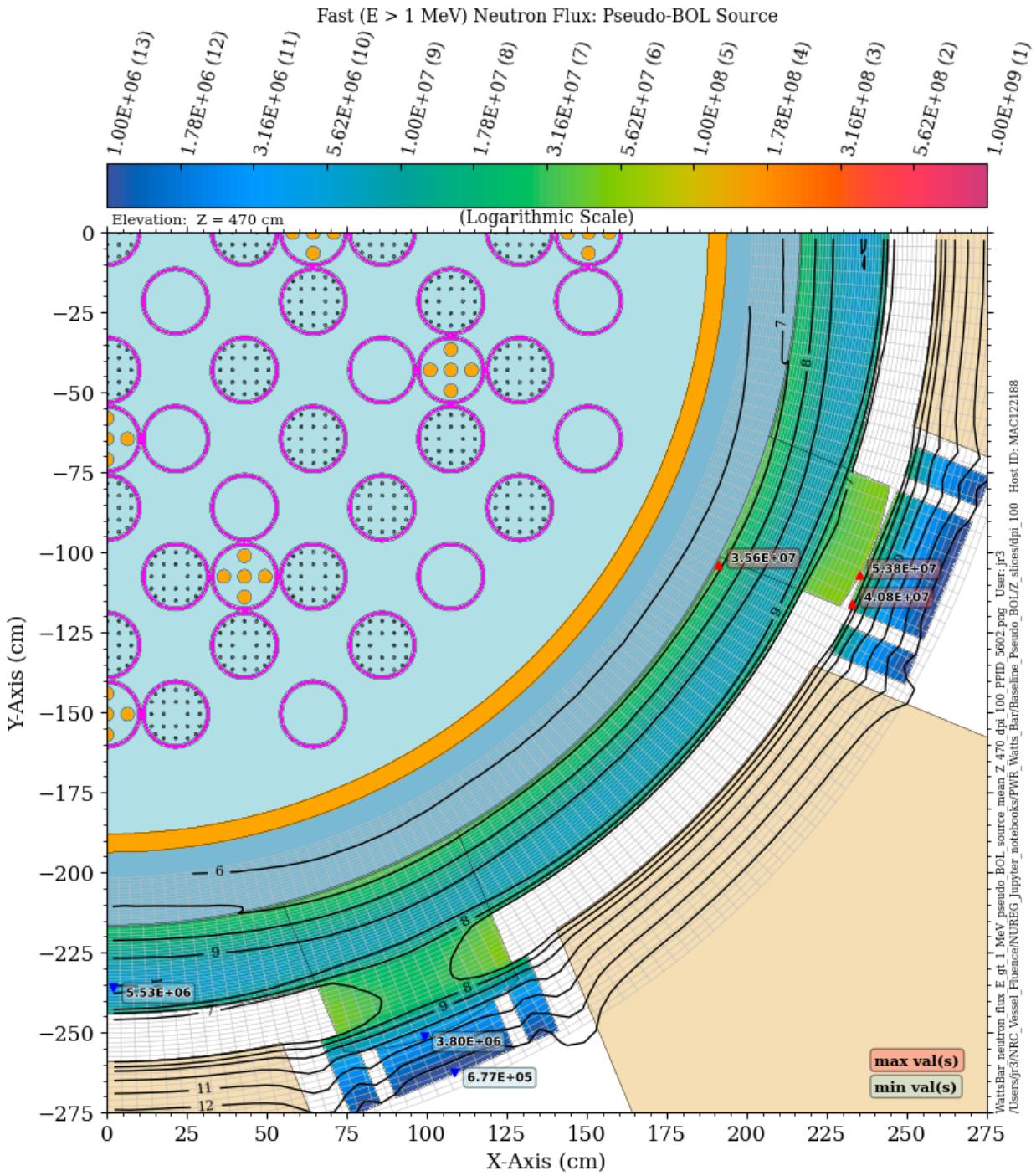

Figure 6-6 Fast neutron flux in the baseline PWR model at an elevation of Z = 470 cm

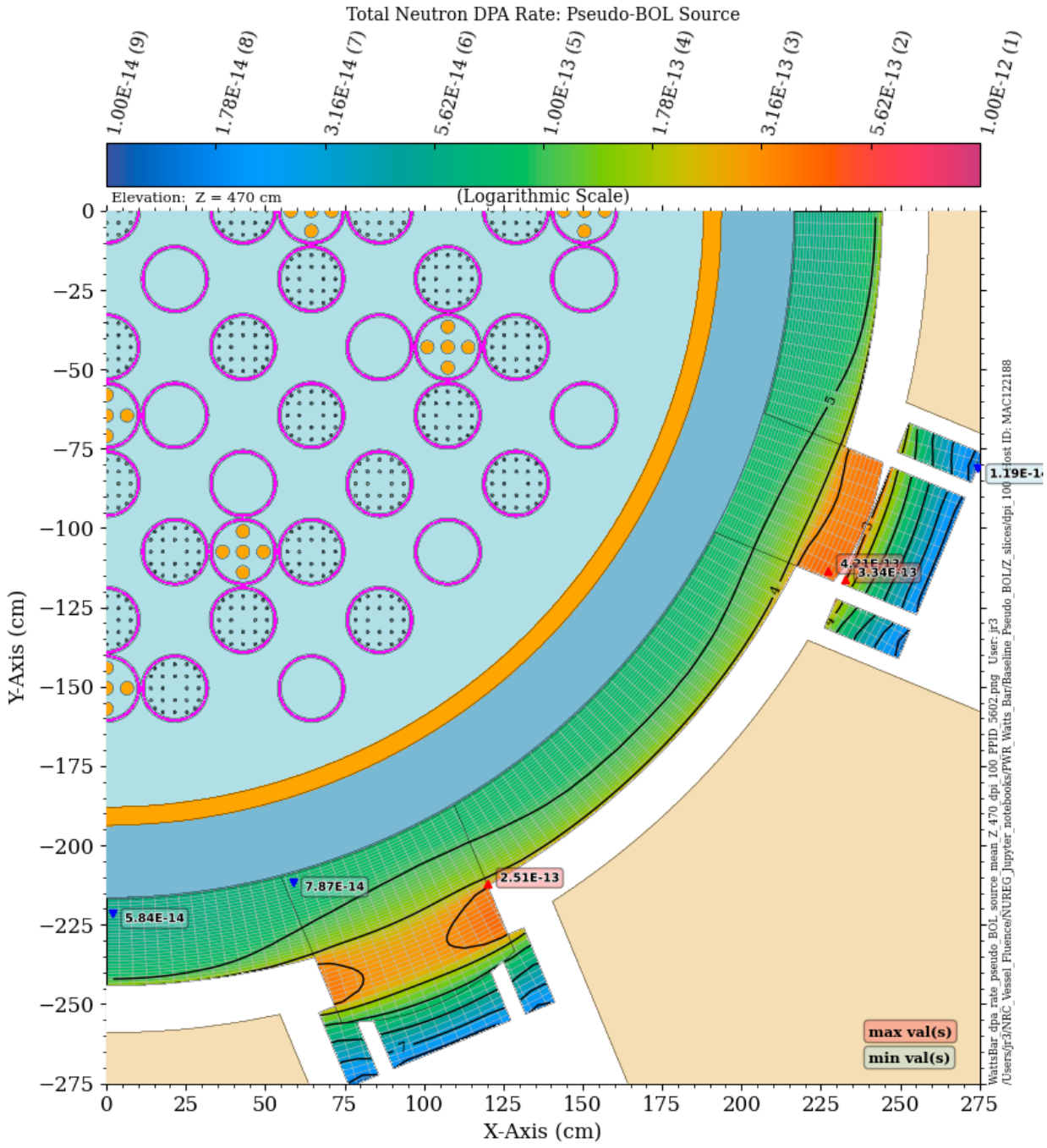

Figure 6-7 Total neutron dpa rate in the PWR RPV and vessel supports. Plan view at an elevation of 470 cm

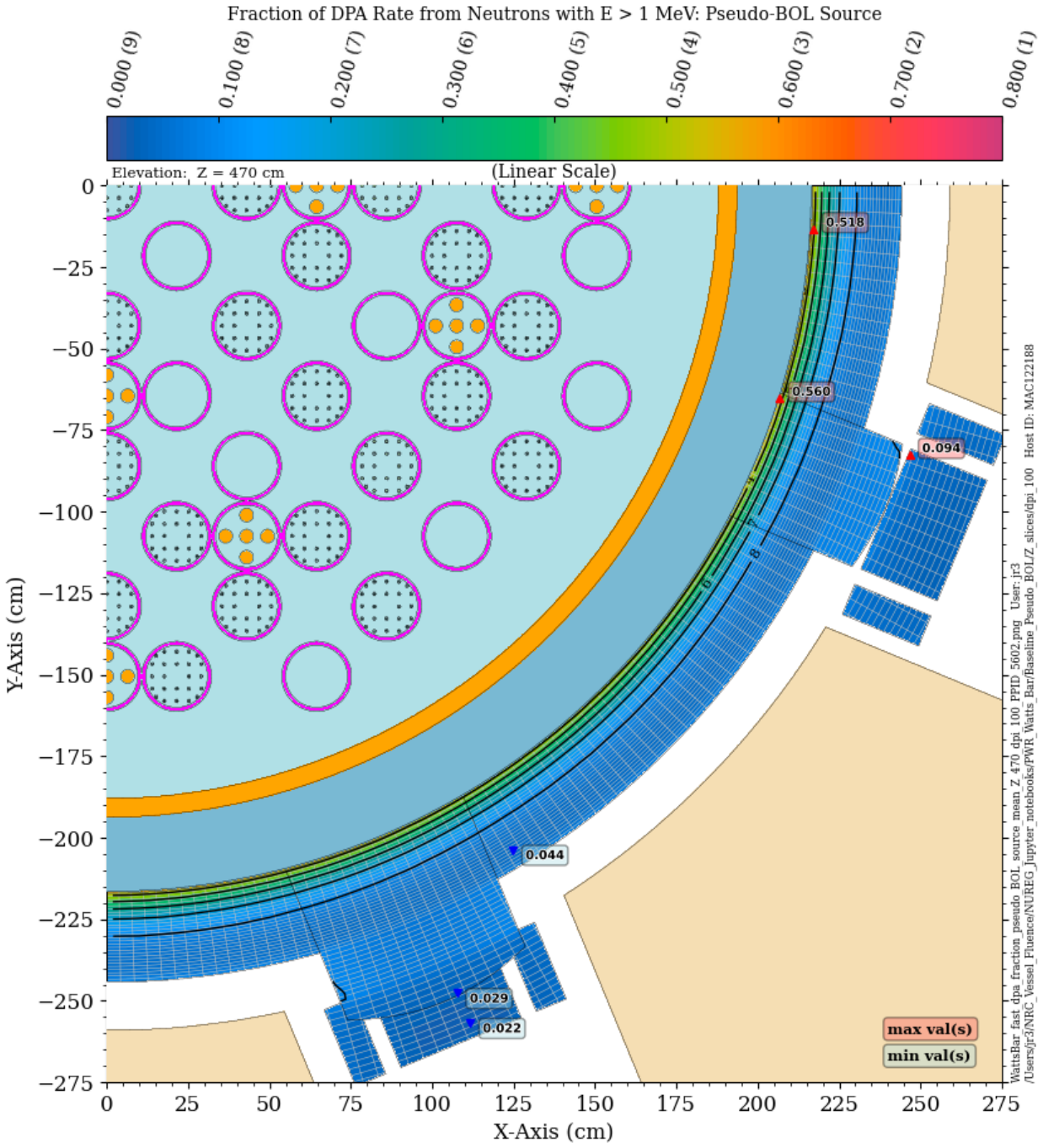

Figure 6-8 Fraction of the total neutron dpa rate due to neutrons with energy > 1 MeV in the PWR RPV, nozzles, and vessel supports. Plan view at an elevation of 470 cm

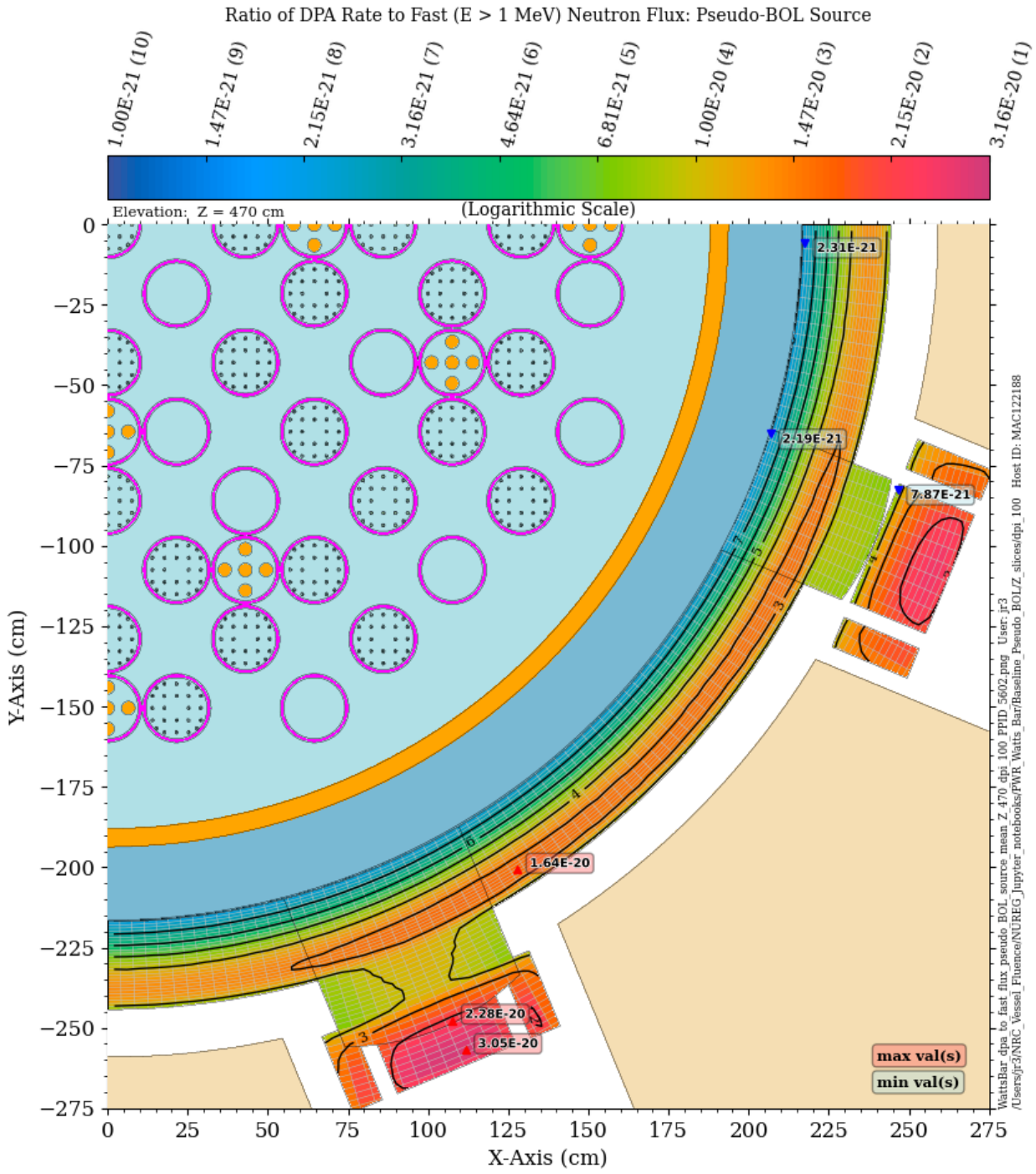

Figure 6-9 Ratio of the total neutron dpa rate to the fast (E > 1 MeV) neutron flux in the PWR RPV, nozzles, and vessel supports. Plan view at an elevation of 470 cm

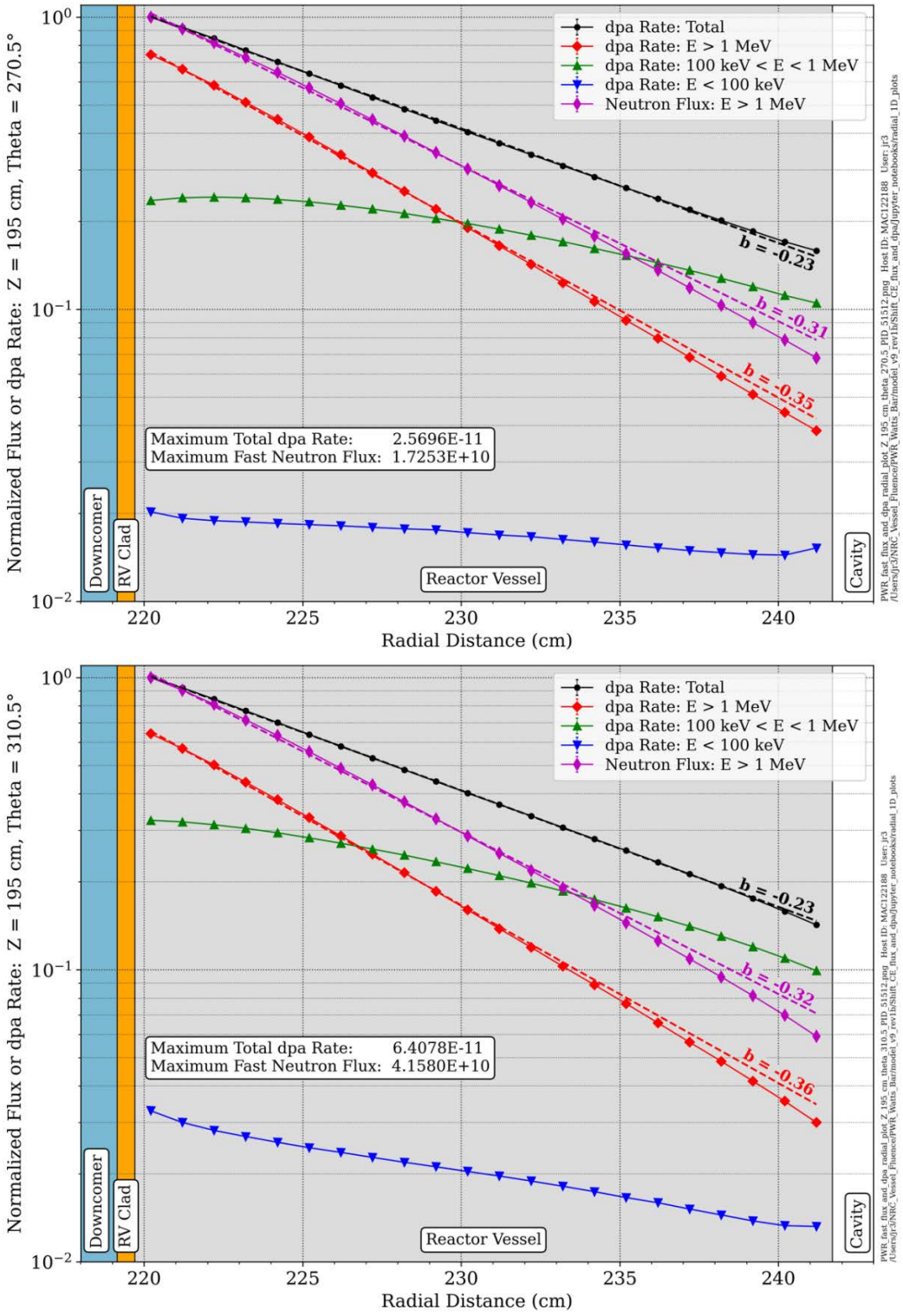

Figure 6-10 Normalized radial fast flux and dpa rate profiles in the PWR RPV at the core midplane *The dashed lines are exponential fits of the form e-bx, where x is the depth in the RPV in inches. The profiles are normalized to the flux and dpa rates at the RPV inner diameter at each azimuthal location.*

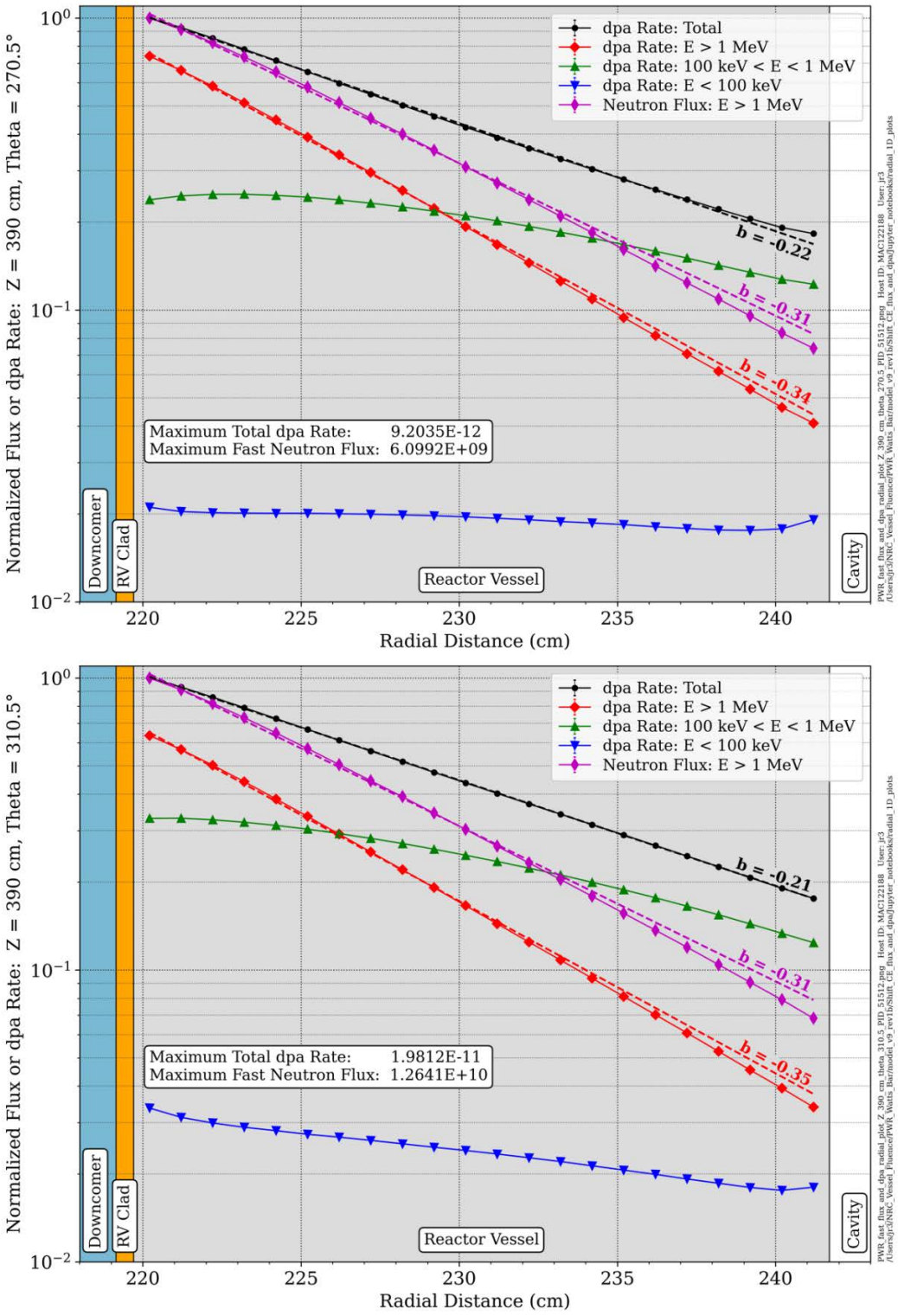

Figure 6-11 Normalized radial fast flux and dpa rate profiles in the PWR RPV at an elevation of 390 cm *The dashed lines are exponential fits of the form e-bx, where x is the depth in the RPV in inches. The profiles are normalized to the flux and dpa rates at the RPV inner diameter at each azimuthal location.*

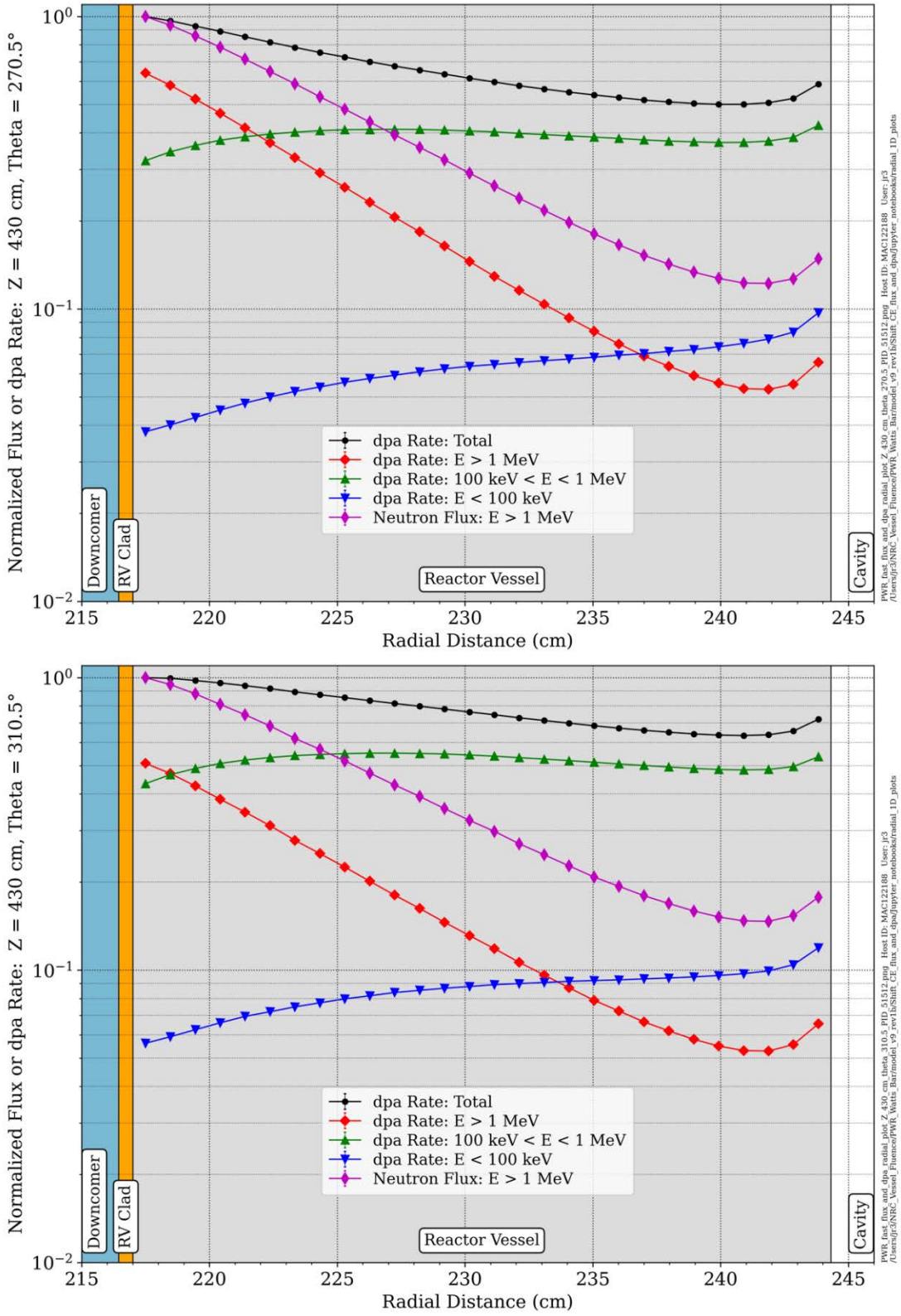

Figure 6-12 Normalized radial fast flux and dpa rate profiles in the PWR RPV at an elevation of 430 cm *The profiles are normalized to the flux and dpa rates at the RPV inner diameter at each azimuthal location.*

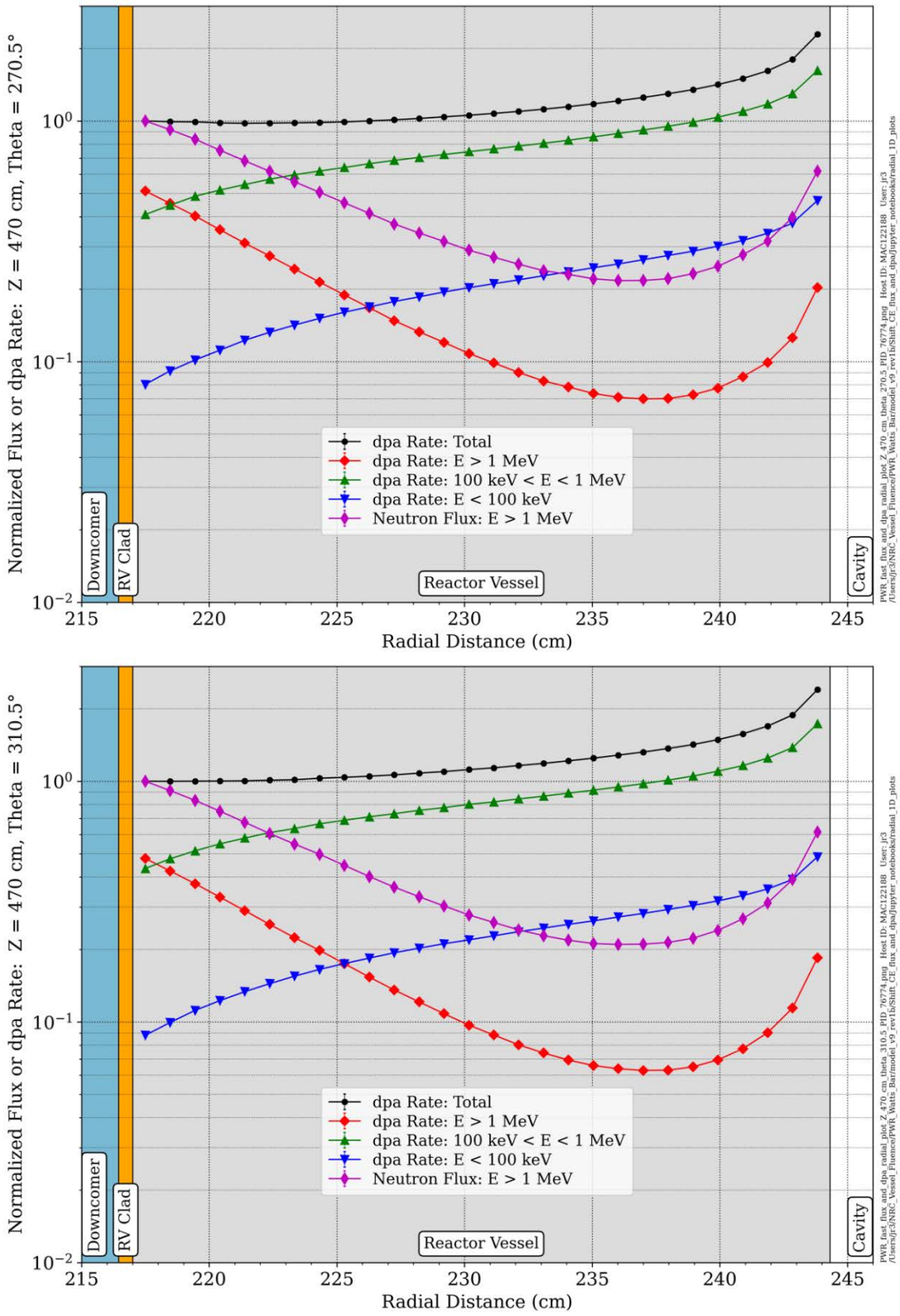

Figure 6-13 Normalized radial fast flux and dpa rate profiles in the PWR RPV at an elevation of 470 cm *The profiles are normalized to the flux and dpa rates at the RPV inner diameter at each azimuthal location.*

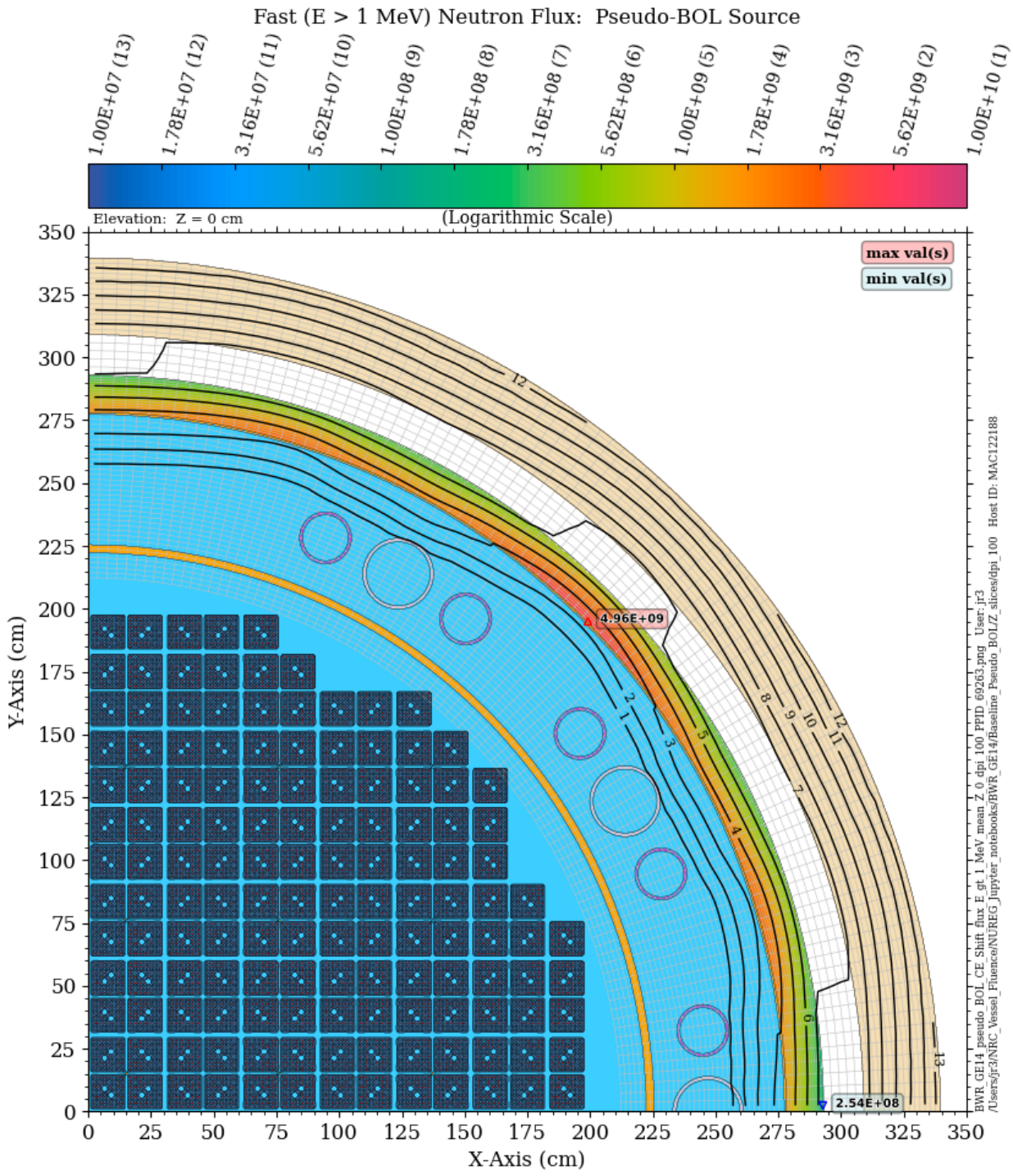

Figure 6-14 Fast neutron flux in the BWR model at the core midplane: pseudo-BOL source

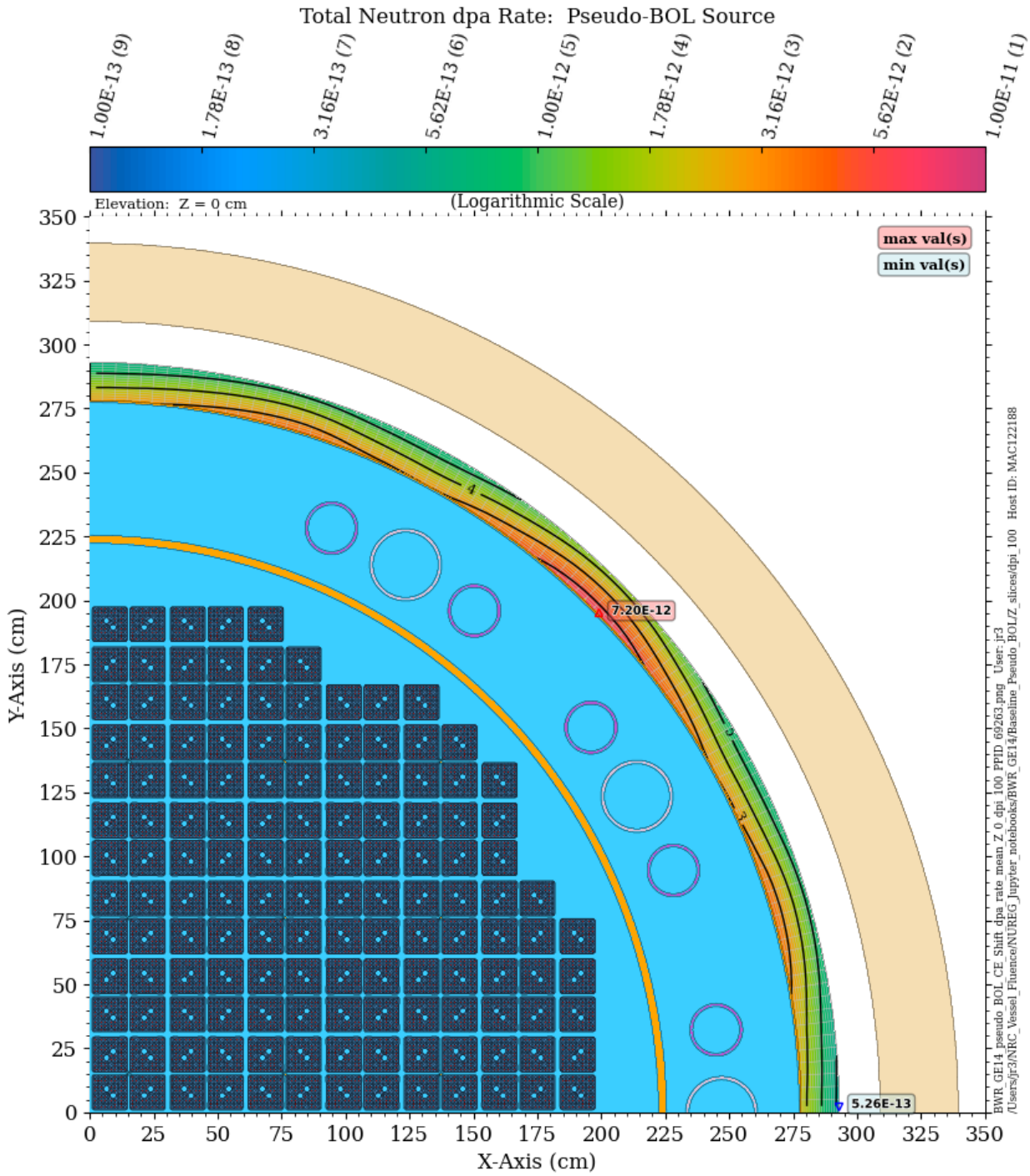

Figure 6-15 Total neutron dpa rate in the BWR model at the core midplane: pseudo-BOL source

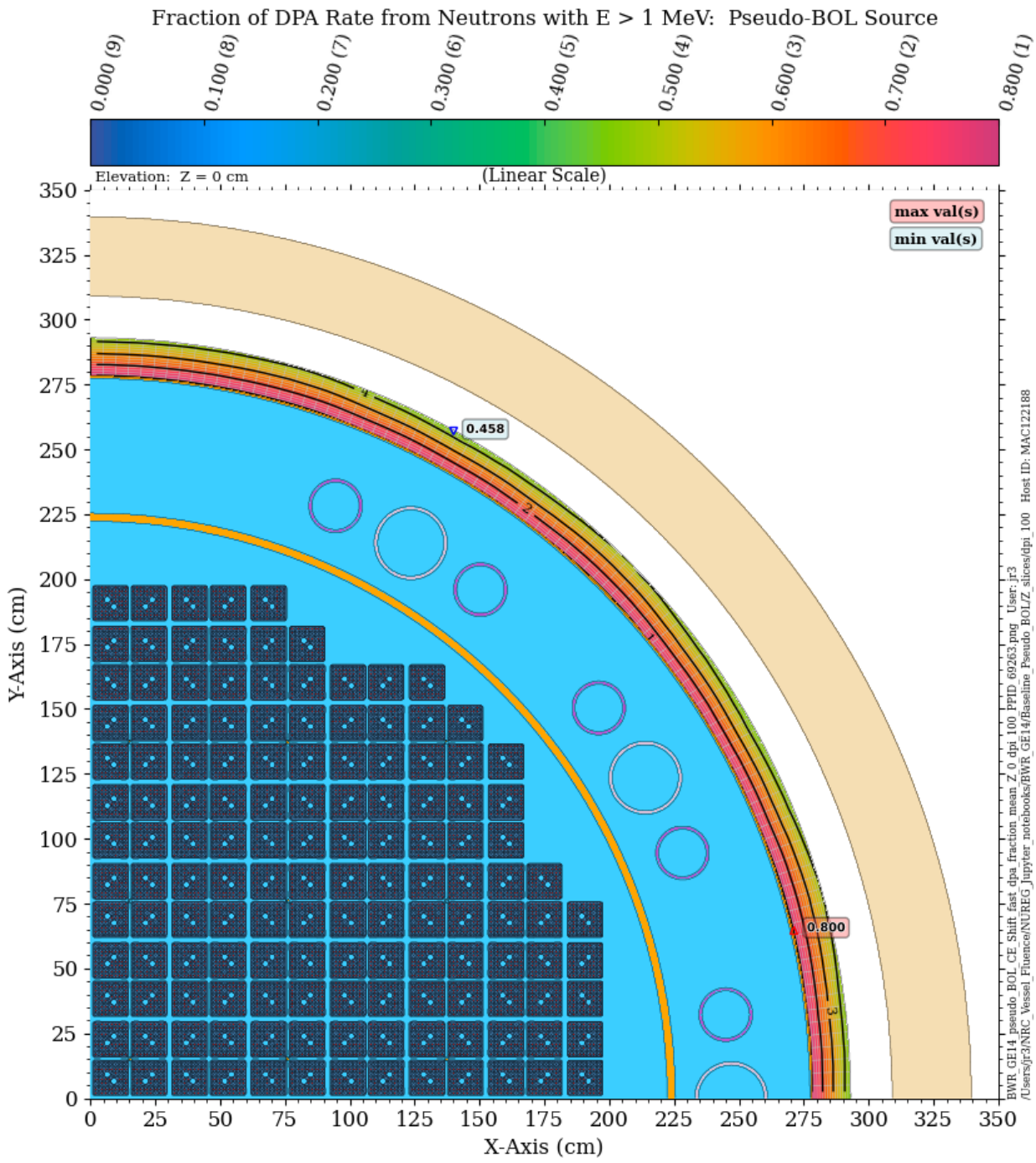

Figure 6-16 Fraction of the total neutron dpa rate due to neutrons with energy > 1 MeV in the BWR at the core midplane: pseudo-BOL source

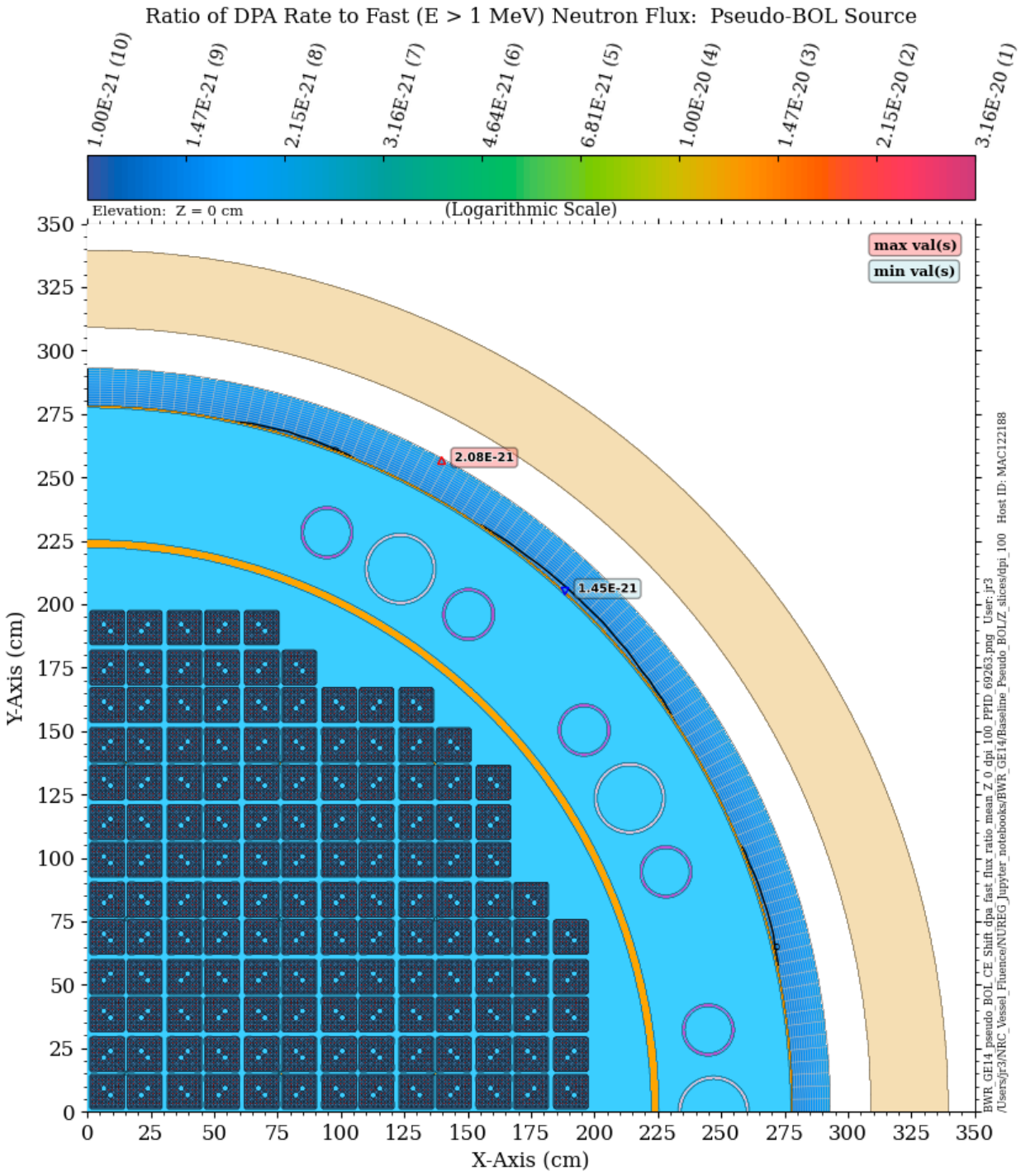

Figure 6-17 Ratio of the total neutron dpa rate to the fast (E > 1 MeV) neutron flux in the BWR RPV at the core midplane: pseudo-BOL source

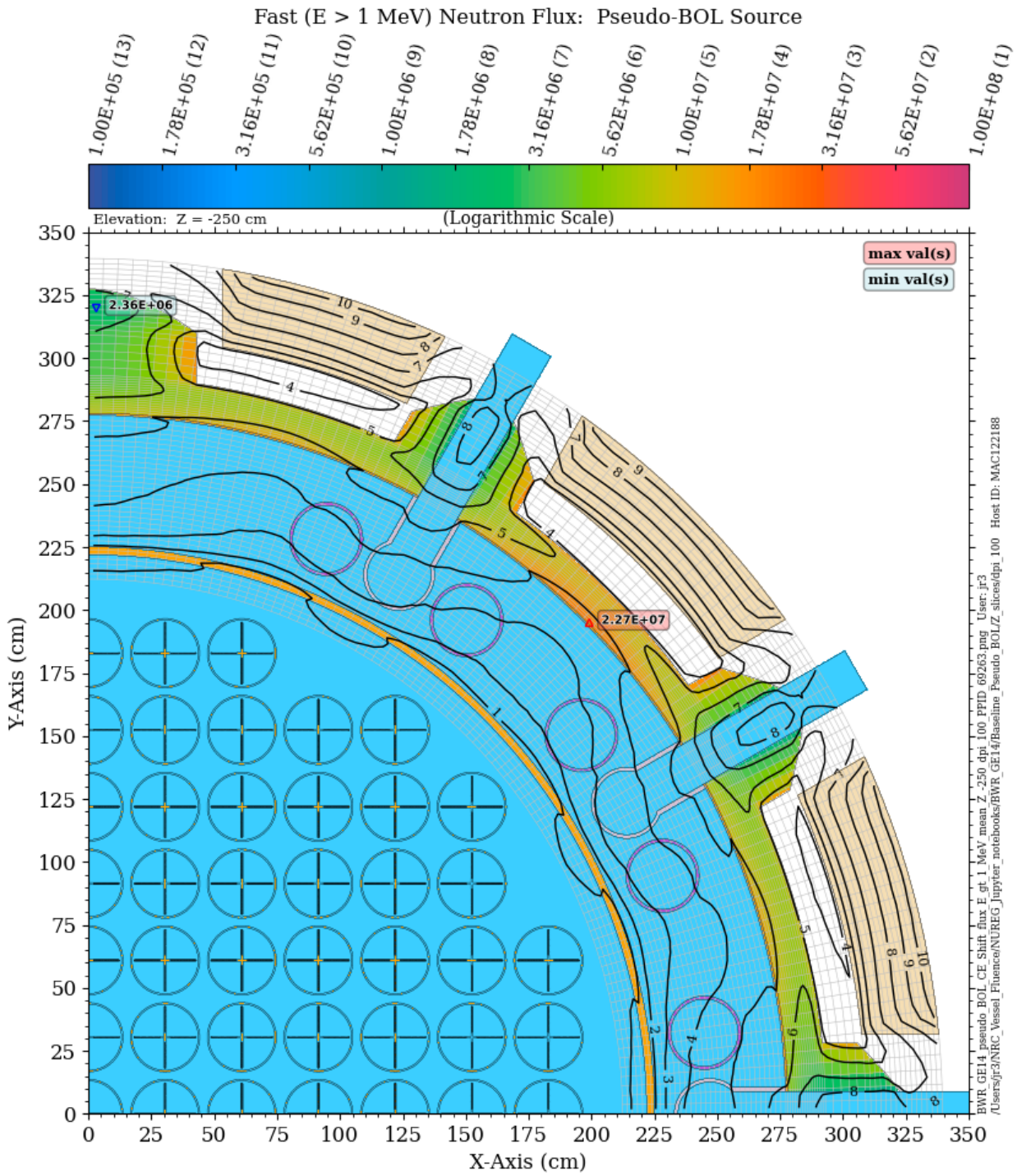

Figure 6-18 Fast neutron flux in the BWR model with a pseudo-BOL source. Plan view at an elevation of Z = -250 cm

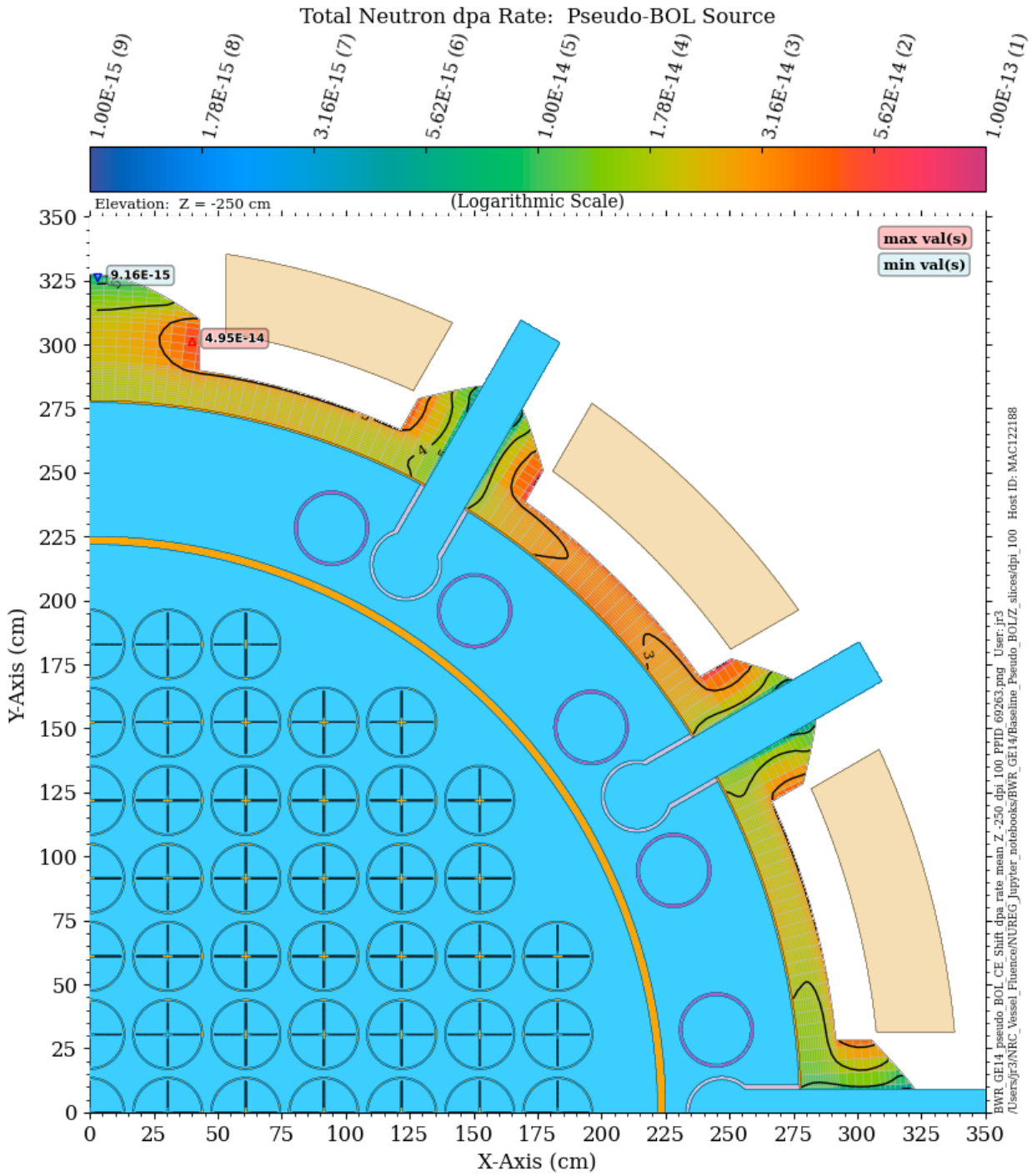

Figure 6-19 Total neutron dpa rate in the BWR model with a pseudo-BOL source. Plan view at an elevation of Z = -250 cm

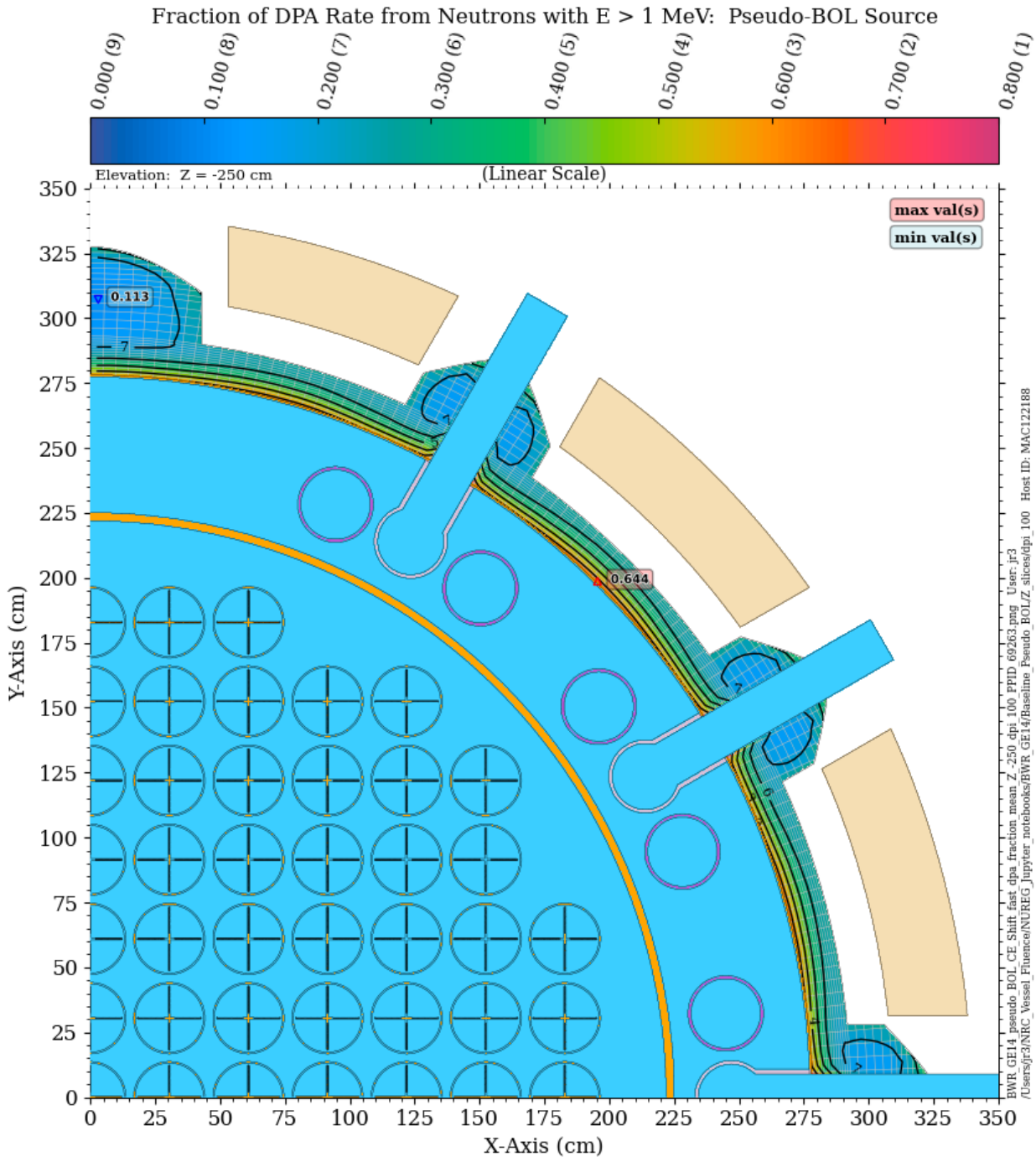

Figure 6-20 Fraction of the total neutron dpa rate due to neutrons with energy > 1 MeV in the BWR model with a pseudo-BOL source. Plan view at an elevation of Z = -250 cm

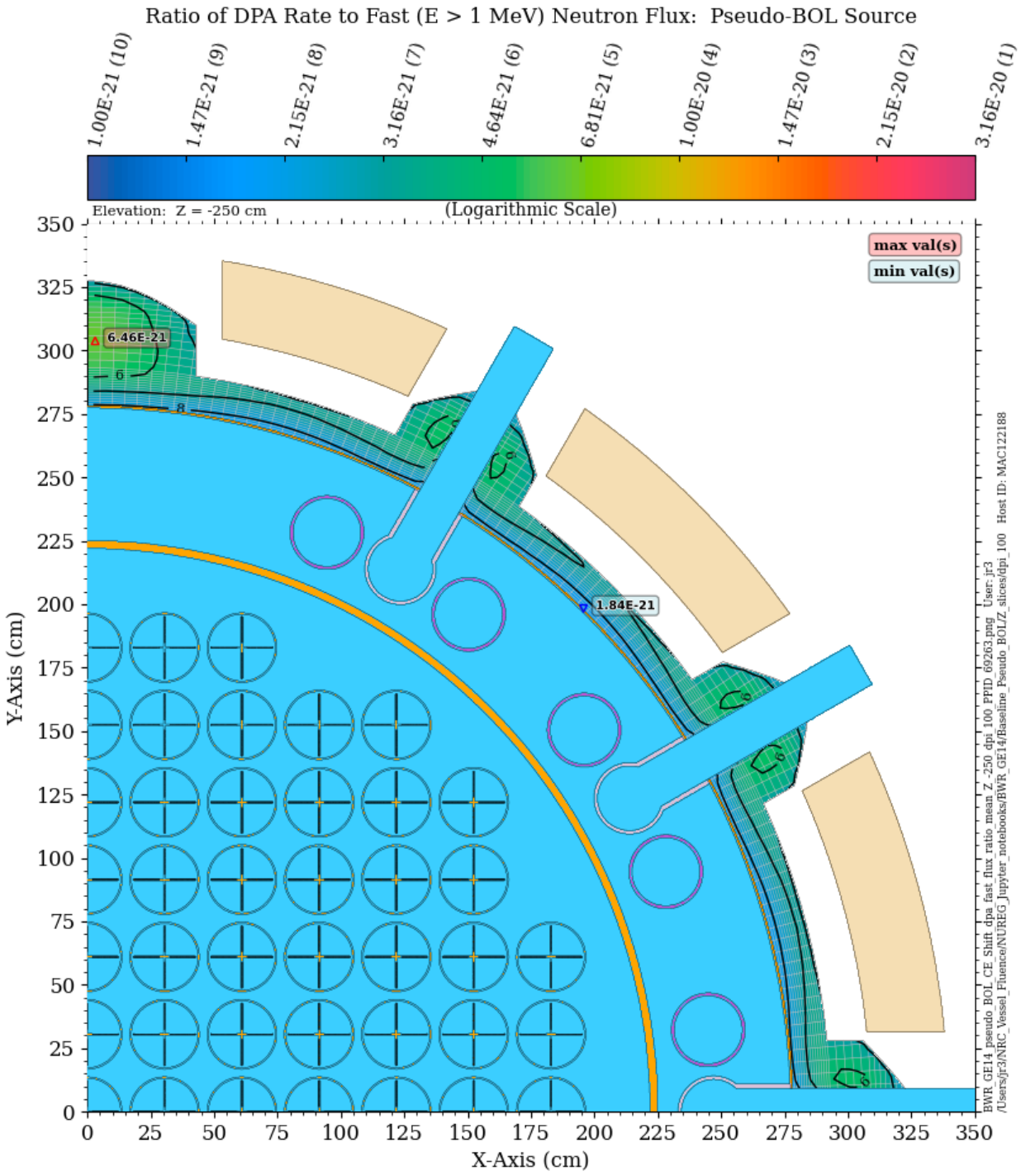

Figure 6-21 Ratio of the total neutron dpa rate to the fast (E > 1 MeV) neutron flux in the BWR model with a pseudo-BOL source. Plan view at an elevation of Z = -250 cm

6.2 Evaluation of Gamma DPA Rates in the Extended Beltline Region

Predictions of radiation-induced embrittlement in LWR RPVs are typically performed using correlations of damage to either fast neutron fluence or neutron-induced dpa. While gamma rays are capable of producing dpa, the contribution of the gamma-induced dpa to the total dpa (neutron plus gamma) is generally a very small fraction and is consequently ignored. ASTM E1035-18 [86] states that it may be prudent to calculate gamma-induced dpa in vessel support structures using coupled neutron-gamma radiation transport calculations with gamma dpa cross-section data.

Gamma dpa rates were calculated in the vessel supports for the PWR model. The gamma dpa cross sections were taken from the referenced work by Baumann [89]. While the fraction of the total dpa rate due to gamma-induced displacements does increase at the location of the vessel supports relative to the traditional beltline region, the increase is relatively minor, and the gamma dpa rate is significantly less than 1% of the neutron dpa rate.

Calculation of gamma dpa rates in the extended beltline region was also performed with the BWR model. As with the PWR model, the fraction of the total dpa rate due to gamma-induced displacements increases in the extended beltline region, but it is still well below 1% of the neutron dpa rate.

7 DISCRETE ORDINATES QUADRATURE SENSITIVITY IN THE EXTENDED BELTLINE REGION

As noted in Section 2.1.3, the accuracy that can be obtained with discrete ordinates transport calculations is dependent on the angular quadrature that is used, among other factors. In examining the effect of quadrature selection on RPV fluence calculations, three questions should be considered:

1. Are fluence calculations in the extended beltline region more sensitive to angular quadrature relative to calculations within the beltline region?
2. Ray effects tend to be more pronounced at high energies and to diminish at lower energies. Are discrete ordinates calculations of dosimetry reaction rates[10] for reactions with a high threshold energy, such as the ^{27}Al (n,α) reaction, more sensitive to quadrature than fast fluence calculations? This question is important with regard to calculations used to establish calculated-to-measured (C/M) ratios using measured dosimetry reaction data.
3. If there are significant solution differences with different quadrature sets, can one set be demonstrated to be more accurate than another?

The first and second questions are addressed in Sections 7.3 and 7.4 through comparisons of Denovo solutions in which the spatial mesh and MG libraries are kept constant and the quadrature set is changed. This type of comparison is often performed when demonstrating whether a discrete ordinates solution has converged with respect to quadrature (i.e., the point at which the solution changes by less than a specified amount as the quadrature is refined). Sections 7.3 and 7.4 also demonstrate that achieving convergence with respect to quadrature in the extended beltline region is very challenging.

The third question is considered in Section 7.5 by comparing Denovo calculations with Shift calculations that employ the same MG libraries as those used in Denovo. By using the same cross-section libraries and demonstrating that the Denovo solution has converged with respect to the mesh, it is possible to effectively isolate the effects of quadrature in the Denovo solutions and to demonstrate which quadratures are superior for a given application.

The observations and conclusions are summarized in Section 7.6.

7.1 Quadrature Sets Evaluated in this Study

The quadrature sets evaluated in this study included level symmetric sets and QR sets. A brief overview of these two quadrature types is provided in Section 2.1.3. The following quadrature sets were used in this study:

- Level symmetric: S8, S16
- Quadruple range: QR4T, QR6T, QR8T, QR8x8, QR10T, QR10x10, QR12T, QR12x12, and QR16T

[10] The threshold energies and energy response ranges for nine isotopes that are commonly used in dosimetry measurements are provided in APPENDIX C.

The notation QRnT refers to a QR set with n polar levels and a triangular arrangement of azimuthal angles (i.e., one angle on the polar level nearest the Z-axis, two angles on the next level, . . . , and n angles on the lowest level). The notation QRn×m refers to a QR set with n polar levels and m azimuthal angles on each level.

Figure 2-3 and Figure 2-4 show the quadrature ordinates and weights for the level symmetric S8 and S16 quadratures, which are widely used in RPV fluence calculations, and the QR8T set. Note that the QR8T quadrature has ordinates nearer each of the coordinate system axes, so it is likely to be more appropriate than S16 for problems in which particle streaming near the coordinate axes is a significant transport path.

Although many quadrature comparisons were performed, only selected results are presented in this section. Comments about additional quadrature sets (i.e., sets that are not included in the comparisons of Sections 7.3 and 7.4) are provided in Section 7.6.

7.2 Overview of Quadrature Sensitivity Plots

The quadrature sensitivity plots in Sections 7.3 through 7.5 include 2D and 3D ratio plots. The 3D plots illustrate the areas of the RPV (and the shroud for the BWR model) that are most susceptible to quadrature sensitivity. The 2D plots focus on specific elevations and azimuthal angles and provide a more quantitative assessment of the quadrature sensitivity in key locations.

In each of the 2D ratio plots, the maximum and minimum values are indicated for the RPV and for the nozzles and vessel supports where appropriate. Maximum and minimum values are also indicated in the cavity gap to show the quadrature sensitivity in locations where ex-vessel dosimetry may be used. The inset histogram plots show the magnitude of the solution differences in those regions, and they also indicate whether there is bias between the two solutions.

7.3 Denovo Quadrature Sensitivity: PWR Model

The sensitivity of discrete ordinates solutions to the angular quadrature selection was first examined using the PWR reference model with a homogenized core representation (Section 5.9.1). The discrete ordinates calculations were run using Denovo with the following parameters:

- BUGLE-B7 MG cross-section library with P_3 scattering expansions
- Uniform 1 cm mesh in X, Y, and Z with X- and Y-extents of 320 cm and a Z-extent of 750 cm (76.8 million cells)
- Linear discontinuous (LD) differencing scheme
- Source iteration (SI) solver with a convergence criterion of 1E-6

The mesh spacing was selected based on a parametric study which indicated that the Denovo solution converges with respect to mesh with 1 cm intervals in X, Y, and Z. The adequacy of this mesh is also confirmed using the Denovo/Shift comparisons presented in Section 7.5.

7.3.1 Denovo Solutions: S8 vs S16

The most commonly used quadratures for RPV fluence calculations are the level symmetric S8 and S16 sets. RG 1.190 prescribes a minimum quadrature order of S8 for RPV fluence calculations and notes that higher-order quadratures may be needed in reactor cavity fluence

calculations. This section considers the differences between S8 and S16 Denovo solutions in the extended beltline region of the PWR model, and it also address differences within the traditional beltline region, where S8 quadrature is routinely used.

Ratios of the PWR S8 Denovo solution to the S16 Denovo solution are shown in Figure 7-1 through Figure 7-10. Figure 7-1 illustrates the fast neutron flux ratio on the inner and outer surfaces of the RPV. The axial extent of these plots is from Z = -100 cm to Z = 650 cm. This axial range, which extends beyond the upper Z limit of 500 cm used in the 2D RZ plots in this and other sections, helps illustrate how quadrature sensitivity is particularly significant in the vicinity of the inlet and outlet nozzles. A notable feature of Figure 7-1 is the appearance of horizontal and vertical bands on the inner and (to a lesser extent) outer surfaces of the RPV. These bands are evidence of ray effects, which are an artifact of the discrete ordinates approximation in which the continuous angular variable is represented by a set of discrete directions.

Figure 7-2 shows the S8/S16 fast flux ratio at the core midplane. There is clear evidence of ray effects associated with the outer corners of the core and (to a lesser extent) the neutron pad. It is particularly noteworthy that the minimum and maximum values of the S8/S16 ratio in the RPV occur at locations separated by only ~2° in the azimuthal angle. (Because the model has octant symmetry over the height of the core, the flux solutions, and hence the ratios, are essentially identical at 292.5° and 337.5° and at 294.5° and 335.5°.) Over this narrow interval, the S8/S16 ratio changes by nearly 9%. This rapid variation over a small azimuthal extent suggests that S8 quadrature may not be appropriate for accurate calculations of fast fluence and dosimetry reaction rates, even within the traditional beltline region. A slight uncertainty in the azimuthal location of a surveillance capsule could result in significant changes in C/M values.

At elevations of Z = 390 cm (Figure 7-3) and Z = 400 cm (Figure 7-4), there are still indications of the assembly corner effects noted in Figure 7-2. There is also a significant change in the S8/S16 ratio throughout the RPV at these two elevations, with the general S8/S16 trend being greater than 1.0 at Z = 390 cm and less than 1.0 at Z = 400 cm. This can also be seen on the RPV inner surface in Figure 7-1.

At elevations of Z = -70 cm (Figure 7-5) and Z = 470 cm (Figure 7-6), there are significant differences in the S8/S16 fast flux ratio in the RPV, nozzles, and vessel supports. Of particular note are the locations in the nozzles and nozzle supports, where the S8 solution is lower than the S16 solution by 30% or more.

Figure 7-7 and Figure 7-8 provide insights into the horizontal bands seen on the inner surface of the RPV (Figure 7-1). Figure 7-7 is at an azimuthal angle, with the maximum distance between the former plates and the core barrel, and Figure 7-8 is at an azimuthal angle, with the minimum distance between the former plates and the core barrel. In Figure 7-7, pronounced ray effects originate near the former plates and propagate through the RPV. These ray effects correspond to the horizontal bands in Figure 7-1. In Figure 7-8, the effect of the former plates is very minor. As shown in Figure 7-1, the horizontal bands on the RPV inner surface at elevations within the height of the core are most prominent near 270° and 360° and are minimized near 310° and 320°.

Figure 7-9 and Figure 7-10 show the pronounced variation over a narrow azimuthal range (335.5° to 337.5°) in the S8/S16 fast flux ratio that was noted above in the discussion of Figure 7-2.

Further discussion of the S8 and S16 Denovo solutions is provided in Sections 7.5 and 7.6.

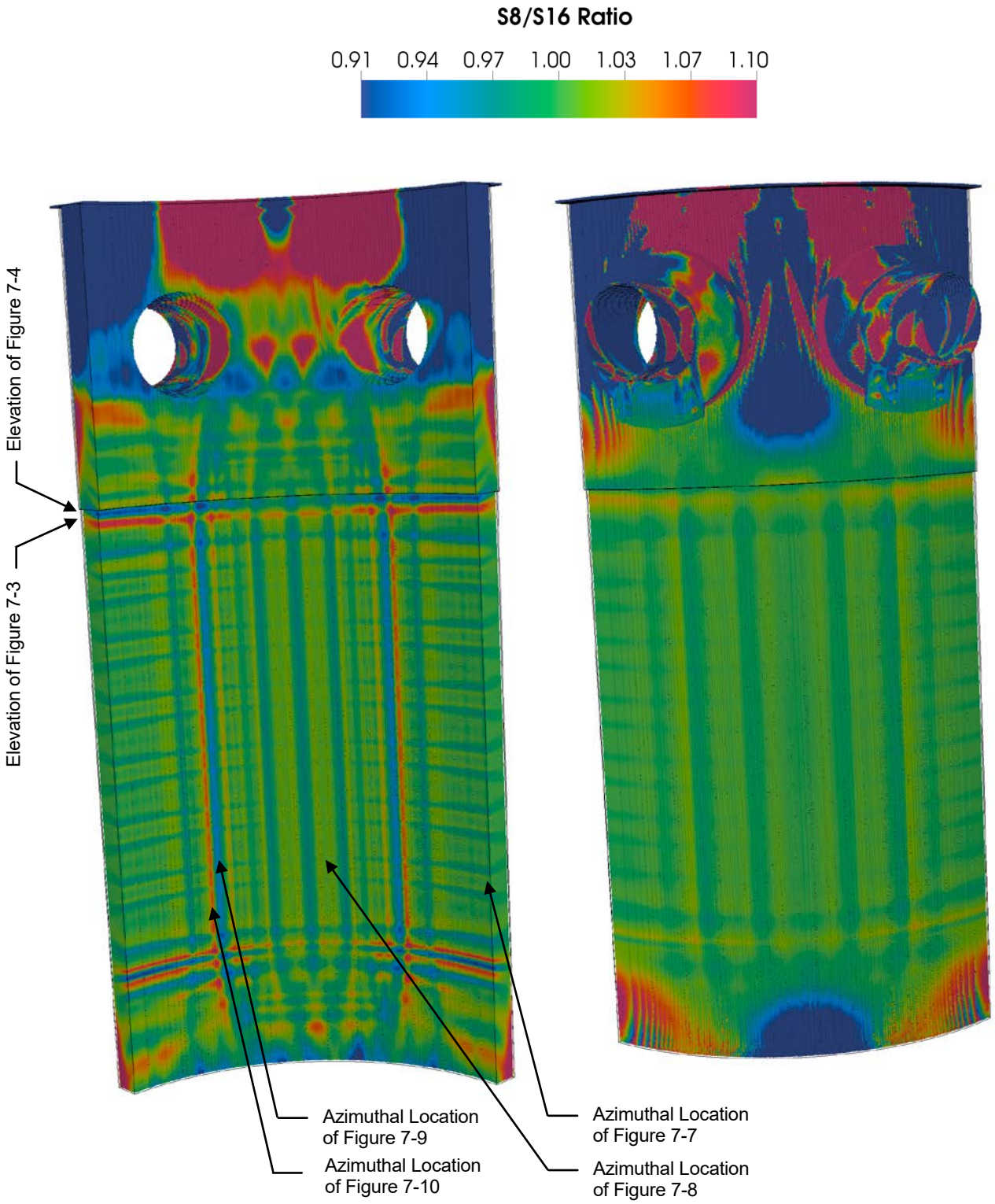

Figure 7-1 Fast neutron flux ratio on the inner and outer surfaces of the RPV for the PWR reference model: Denovo S8 solution relative to an S16 solution

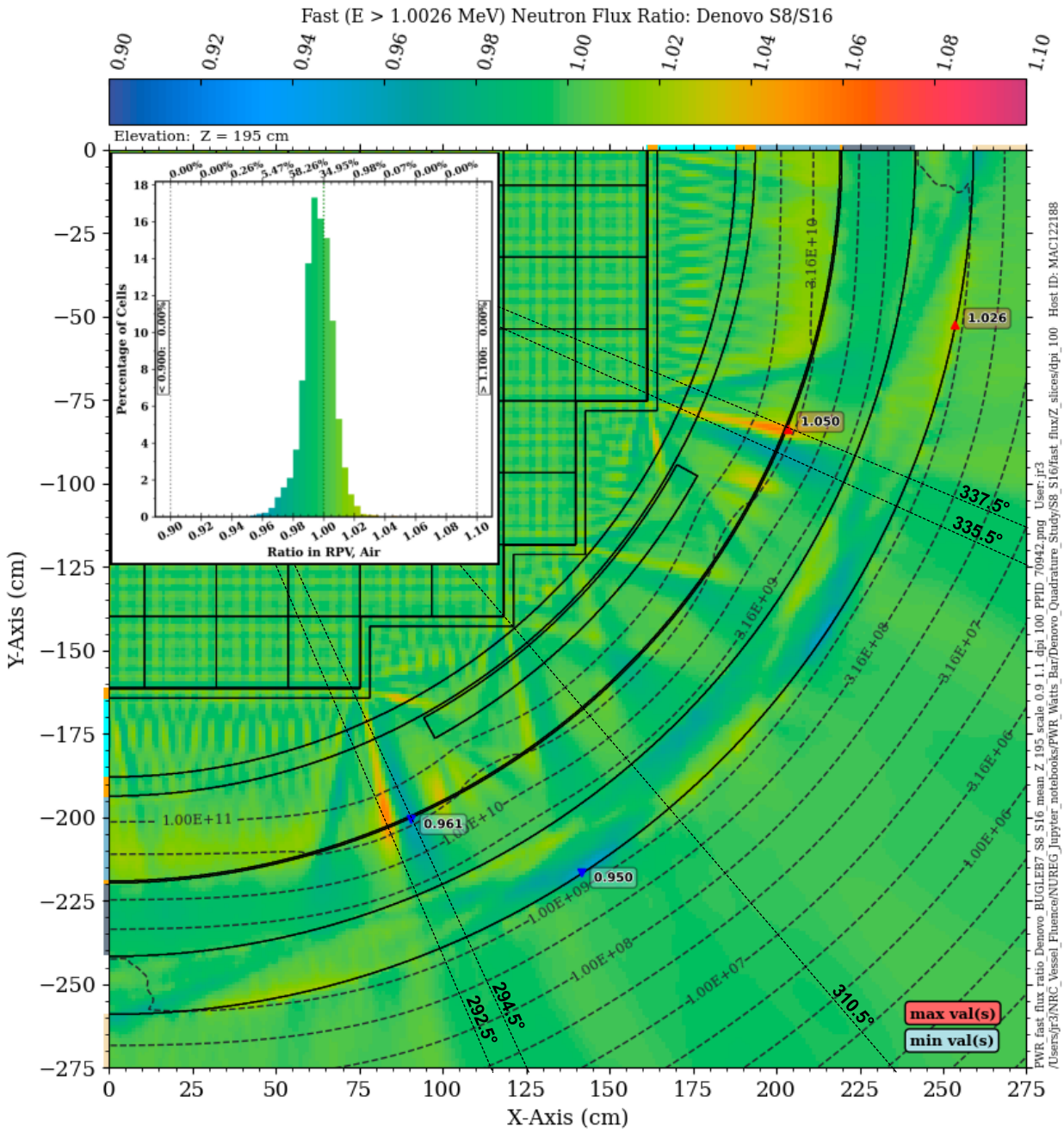

Figure 7-2 Fast neutron flux ratio in the PWR reference model: S8/S16 quadrature. Plan view at Z = 195 cm *The contour lines are the fast flux from the S16 solution. The azimuthal lines at 310.5°, 335.5°, and 337.5° are the locations for Figure 7-8, Figure 7-9, and Figure 7-10, respectively.*

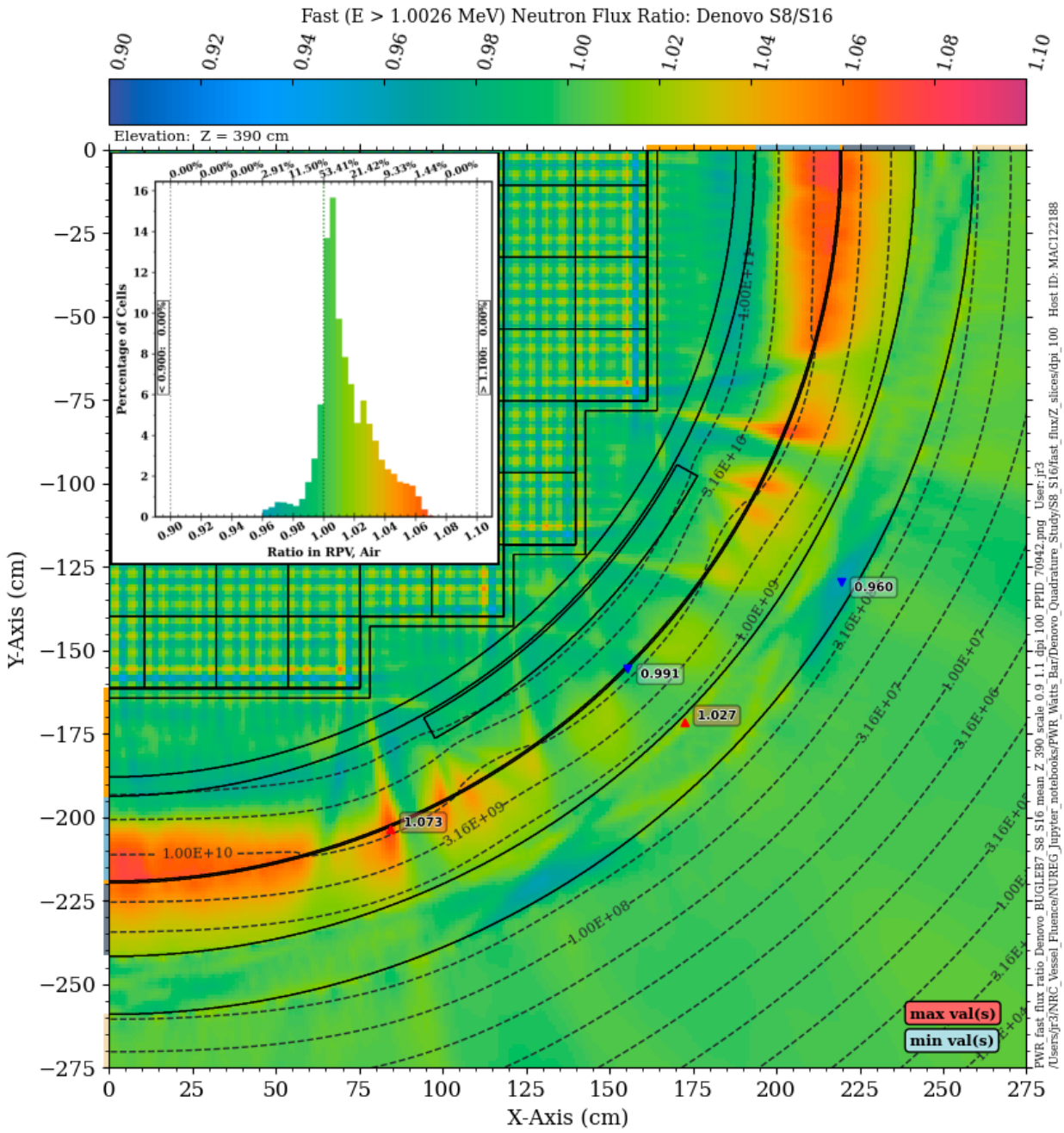

Figure 7-3 Fast neutron flux ratio in the PWR reference model: S8/S16 quadrature. Plan view at Z = 390 cm *The contour lines are the fast flux from the S16 solution.*

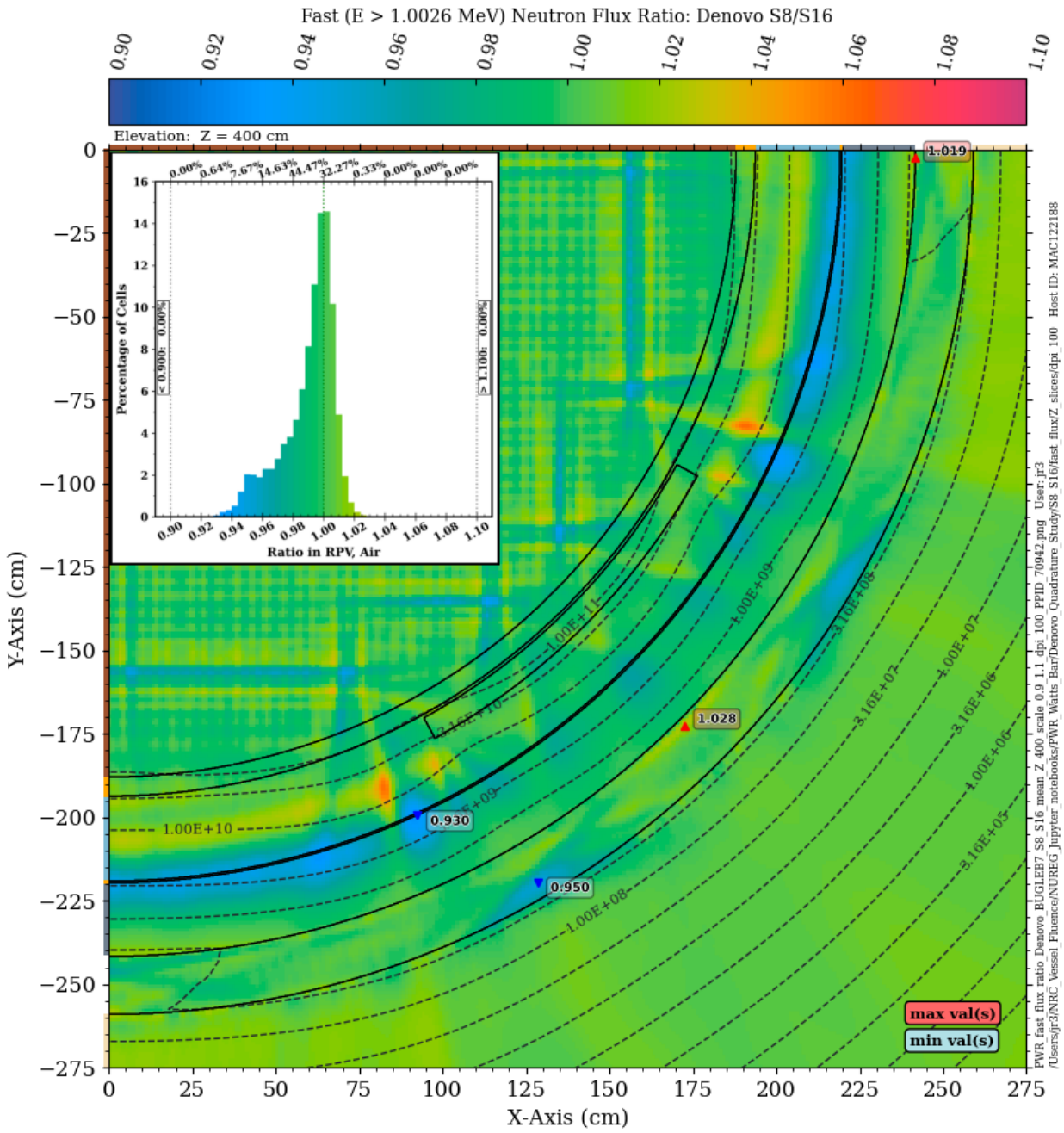

Figure 7-4 Fast neutron flux ratio in the PWR reference model: S8/S16 quadrature. Plan view at Z = 400 cm *The contour lines are the fast flux from the S16 solution.*

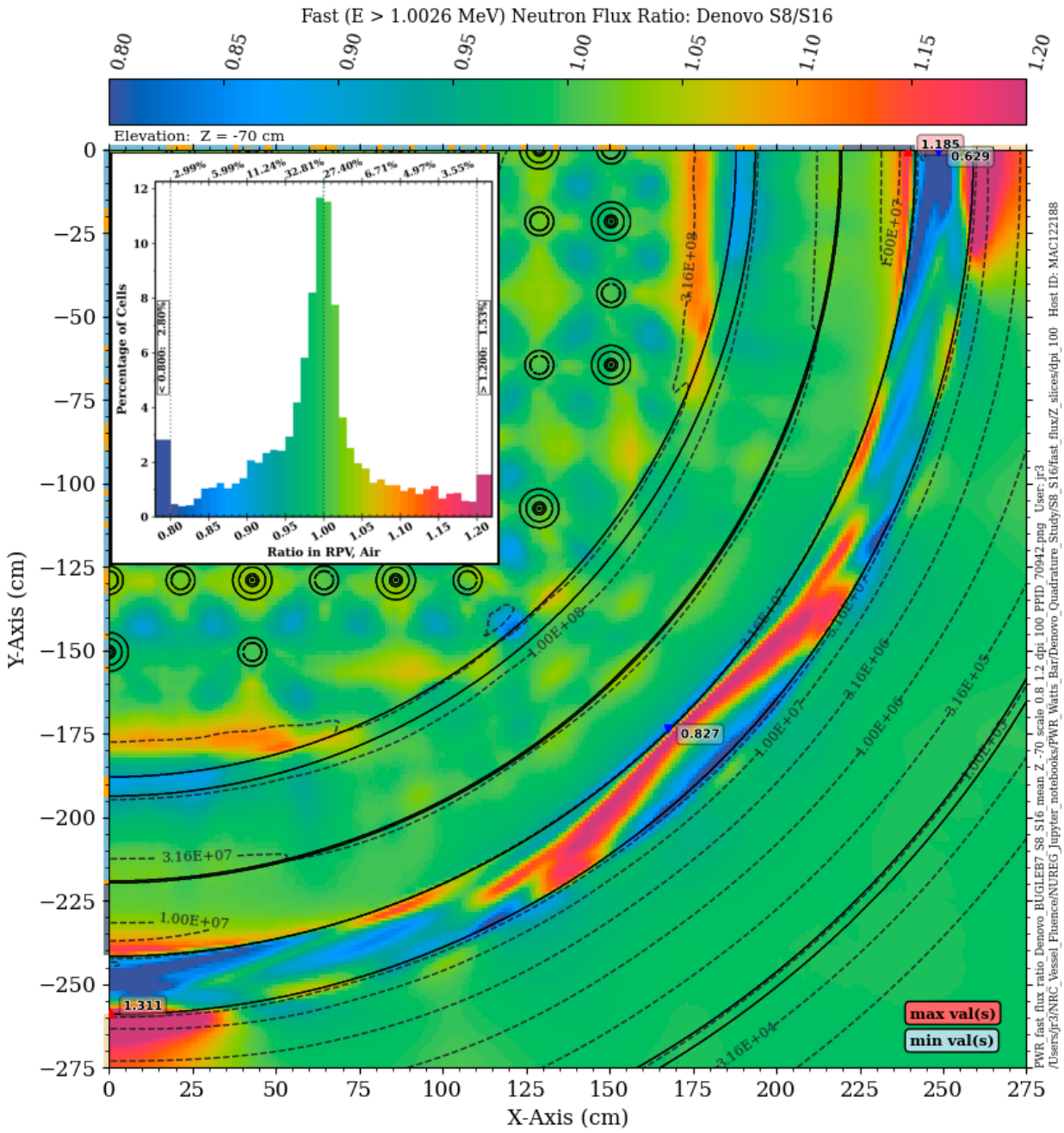

Figure 7-5 Fast neutron flux ratio in the PWR reference model: S8/S16 quadrature. Plan view at Z = -70 cm *The contour lines are the fast flux from the S16 solution. Note the change in scale relative to the previous three figures.*

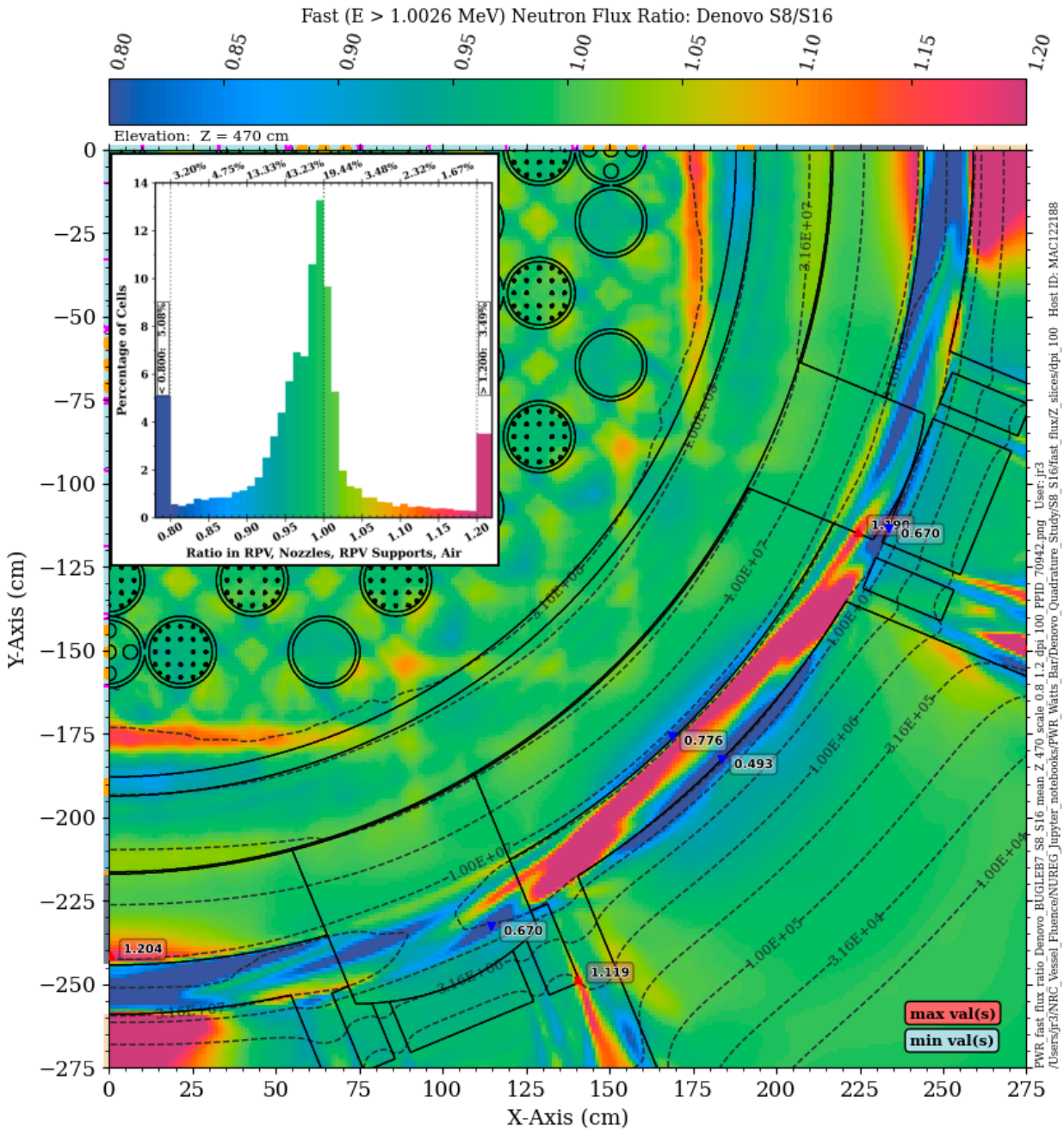

Figure 7-6 Fast neutron flux ratio in the PWR reference model: S8/S16 quadrature. Plan view at Z = 470 cm *The contour lines are the fast flux from the S16 solution.*

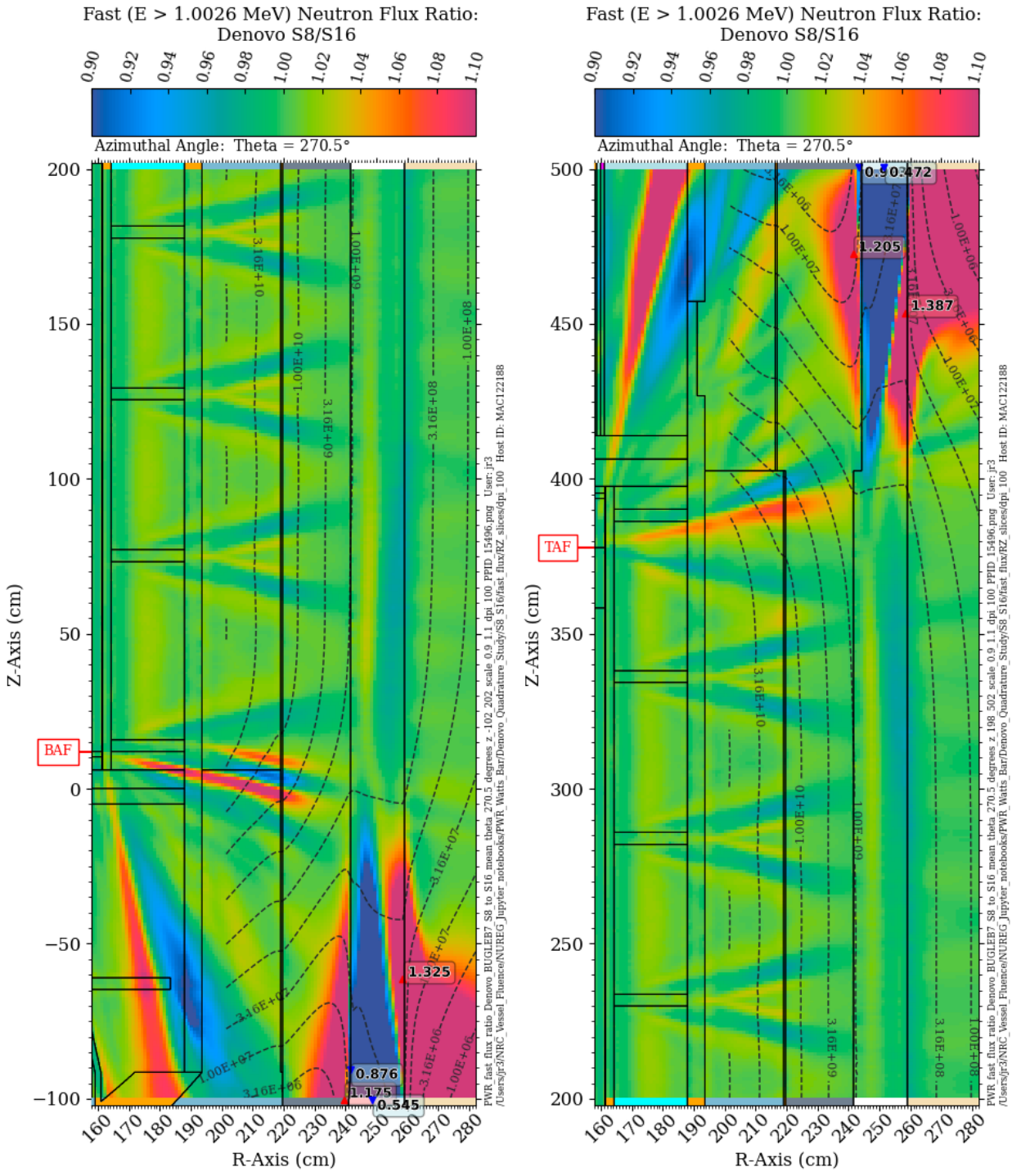

Figure 7-7 Fast neutron flux ratio in the PWR reference model: S8/S16 quadrature. Elevation view at an azimuthal angle of 270.5° *The contour lines are the fast flux from the S16 solution.*

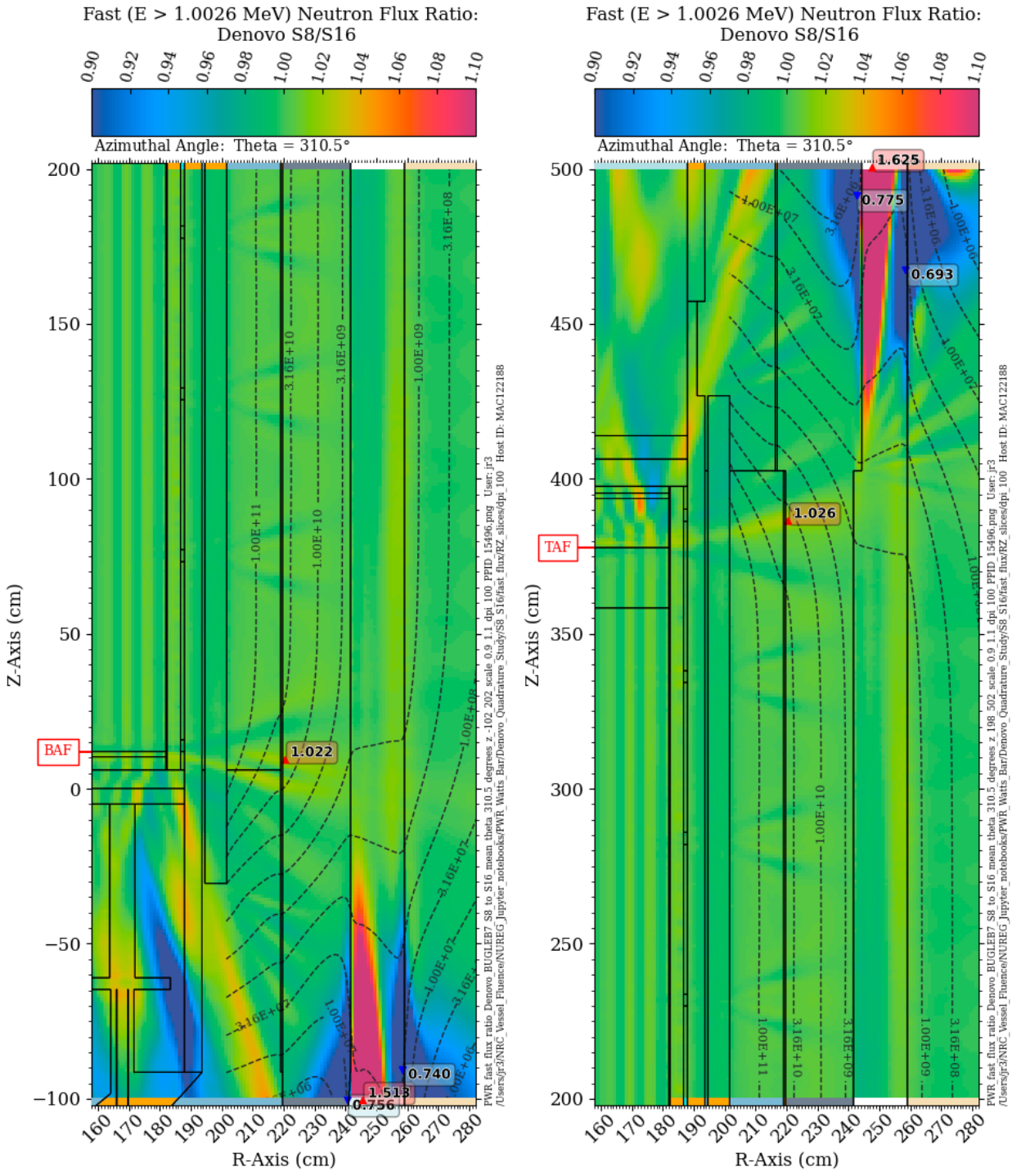

Figure 7-8 Fast neutron flux ratio in the PWR reference model: S8/S16 quadrature. Elevation view at an azimuthal angle of 310.5° *The contour lines are the fast flux from the S16 solution.*

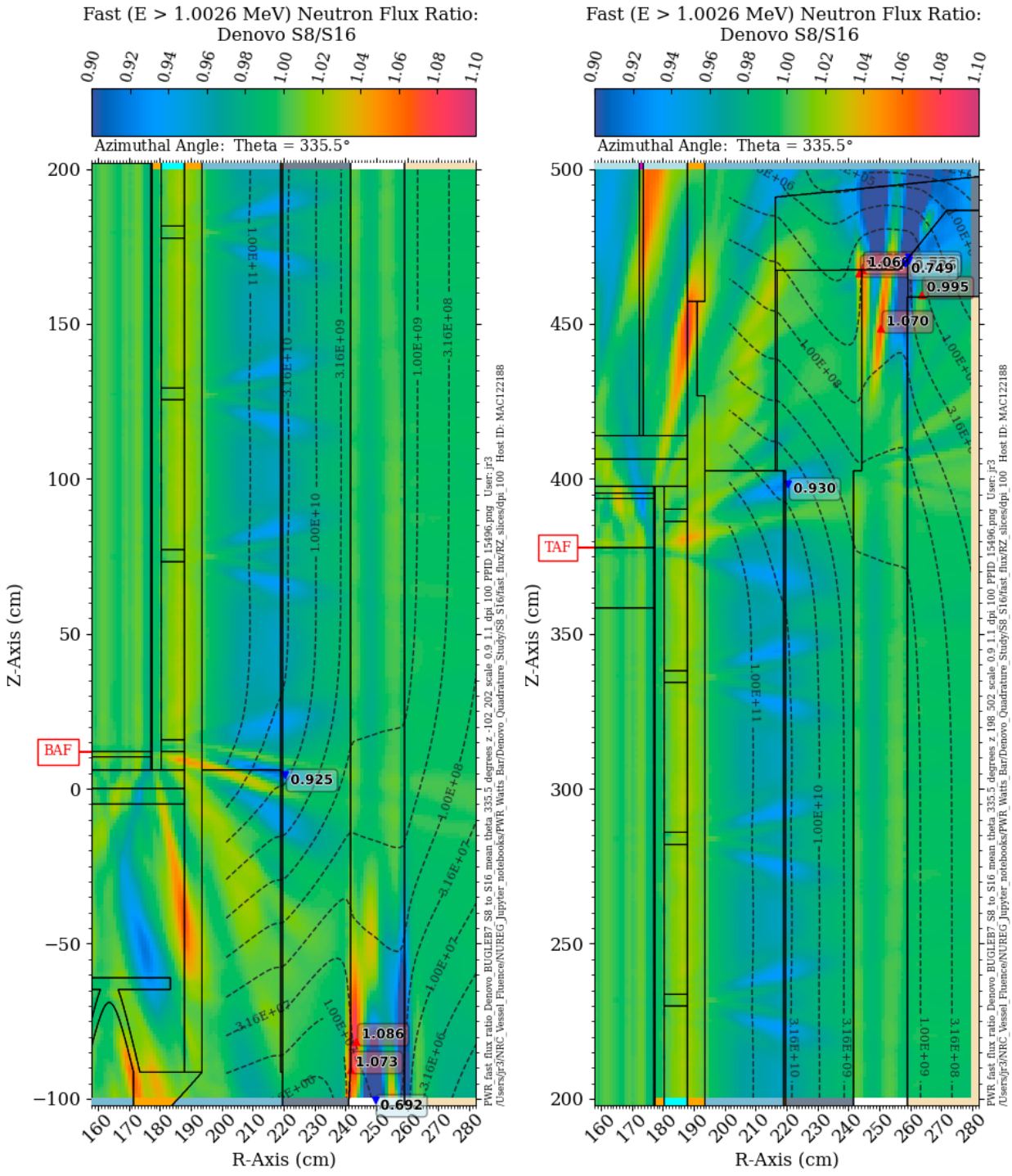

Figure 7-9 **Fast neutron flux ratio in the PWR reference model: S8/S16 quadrature. Elevation view at an azimuthal angle of 335.5°** *The contour lines are the fast flux from the S16 solution.*

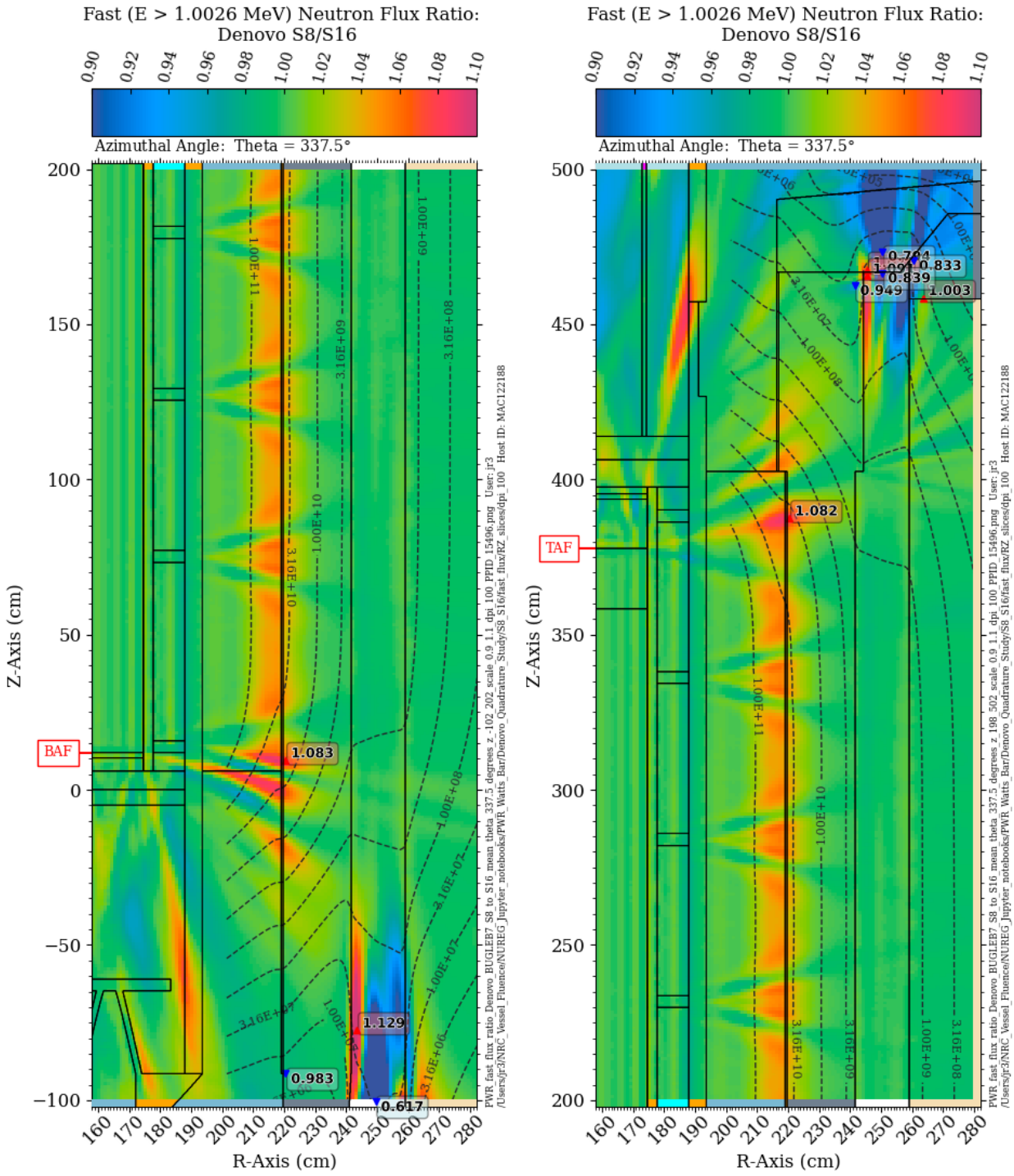

Figure 7-10 Fast neutron flux ratio in the PWR reference model: S8/S16 quadrature. Elevation view at an azimuthal angle of 337.5° *The contour lines are the fast flux from the S16 solution.*

7.3.2 Denovo Solutions: S16 vs QR8T

The S16 and QR8T quadratures each have 36 angles per octant on 8 polar levels with a triangular arrangement of azimuthal angles by polar level (Figure 2-4). As noted in Section 2.1.3, the QR8T set may be expected to provide more accurate discrete ordinates solutions for problems with material interfaces along any of the coordinate axes or with significant streaming paths along any of the coordinate axes.

Figure 7-11 through Figure 7-14 illustrate the S16/QR8T fast flux ratio on the inner and outer surfaces of the RPV and at elevations of Z = 195 cm, Z = -70 cm, and Z = 470 cm. The differences in the S16 and QR8T solutions at the core midplane are less than 2%, although there are still indications of ray effects. At the extended beltline elevations of Z = -70 cm and Z = 470 cm, differences between the S8 and QR16T solutions exceed 20% in some locations, particularly in the cavity gap region.

The question of which of these two quadrature sets provides a more accurate solution is addressed in Section 7.5.

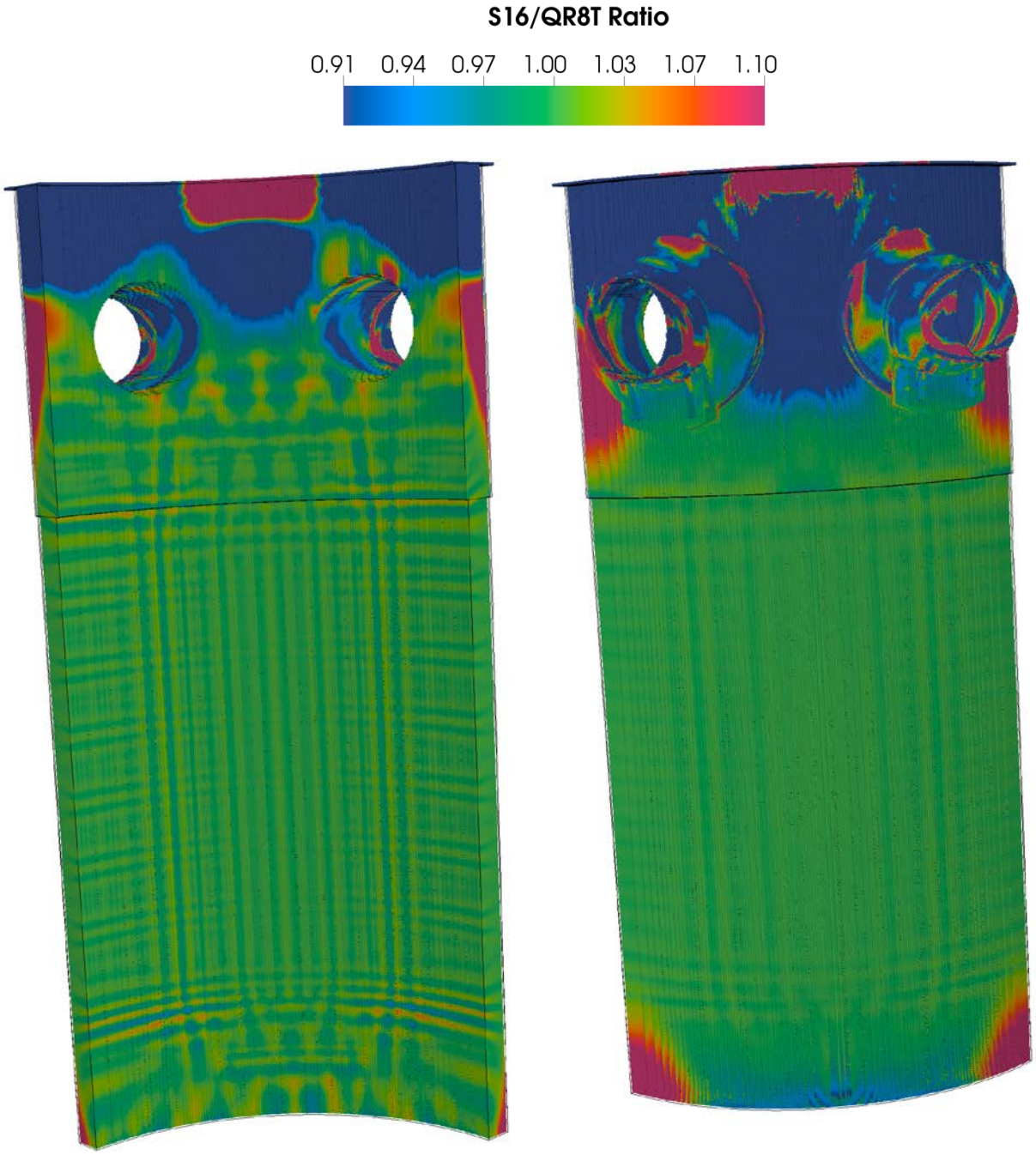

Figure 7-11 Fast neutron flux ratio on the inner and outer surfaces of the RPV for the PWR reference model *The ratio is for a Denovo S16 solution relative to a QR8T solution.*

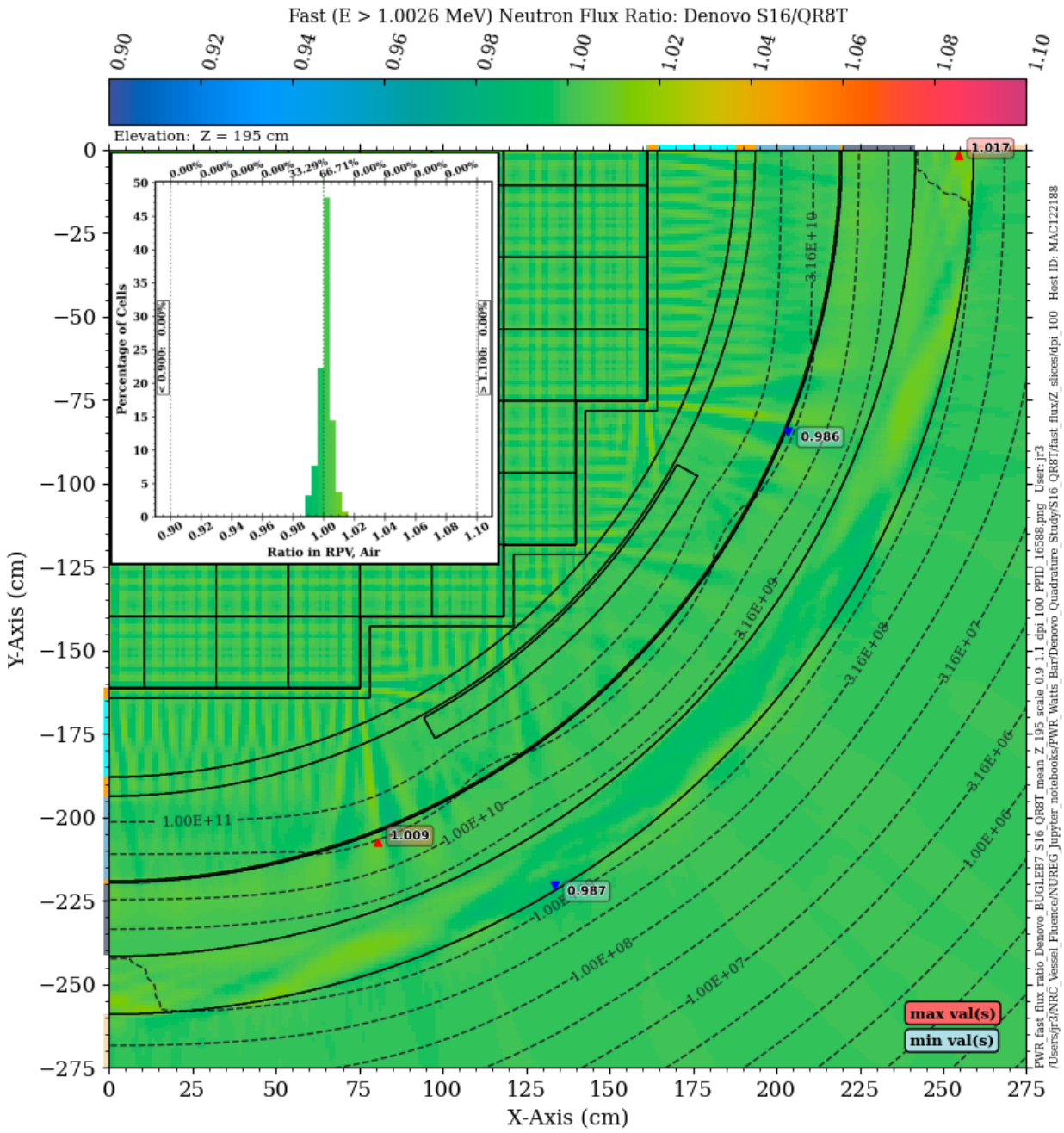

Figure 7-12 Fast neutron flux ratio in the PWR reference model: S16/QR8T quadrature. Plan view at Z = 195 cm *The contour lines are the fast flux from the QR8T solution.*

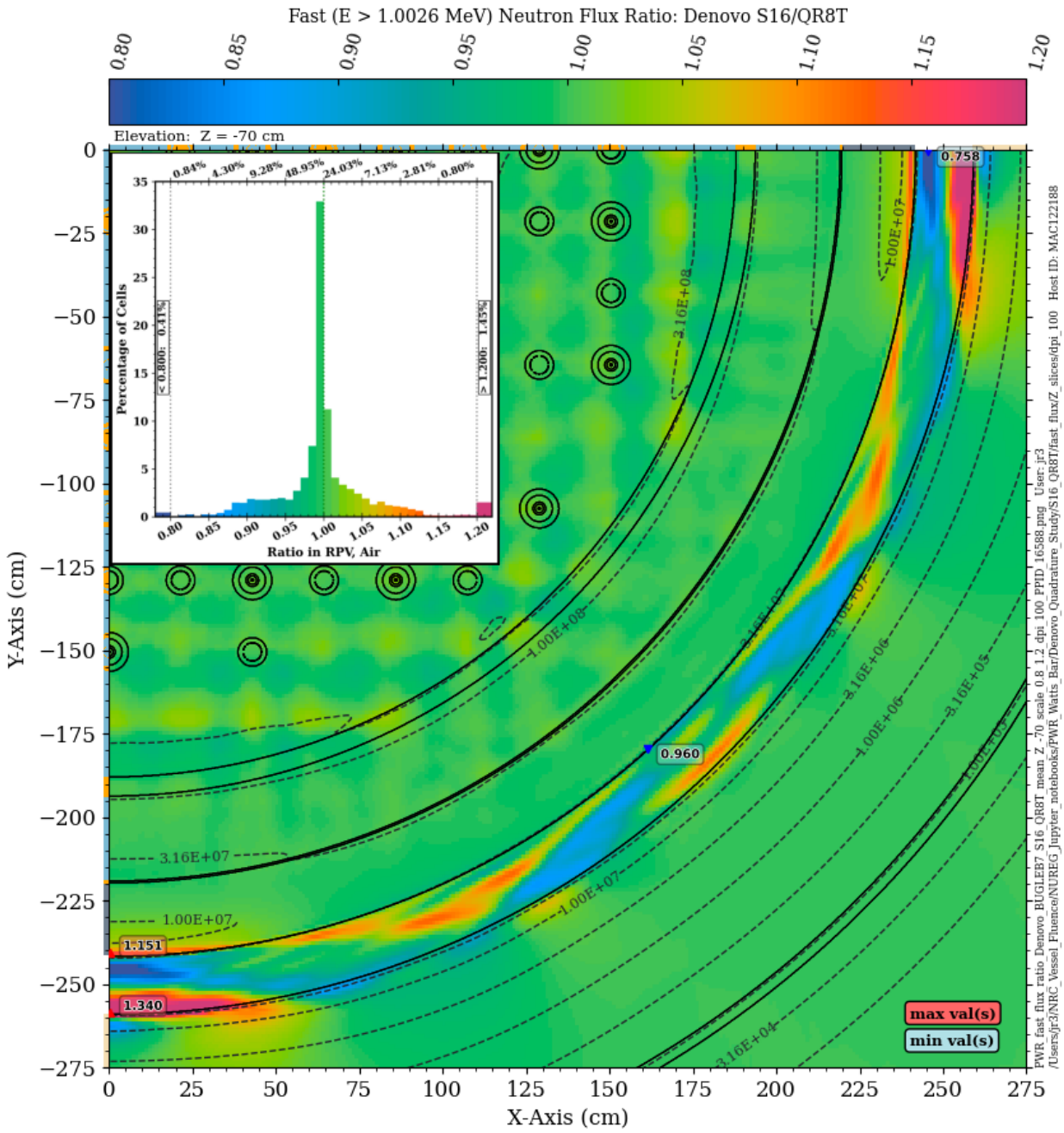

Figure 7-13 Fast neutron flux ratio in the PWR reference model: S16/QR8T quadrature. Plan view at Z = -70 cm *The contour lines are the fast flux from the QR8T solution. Note the change in scale relative to Figure 7-12.*

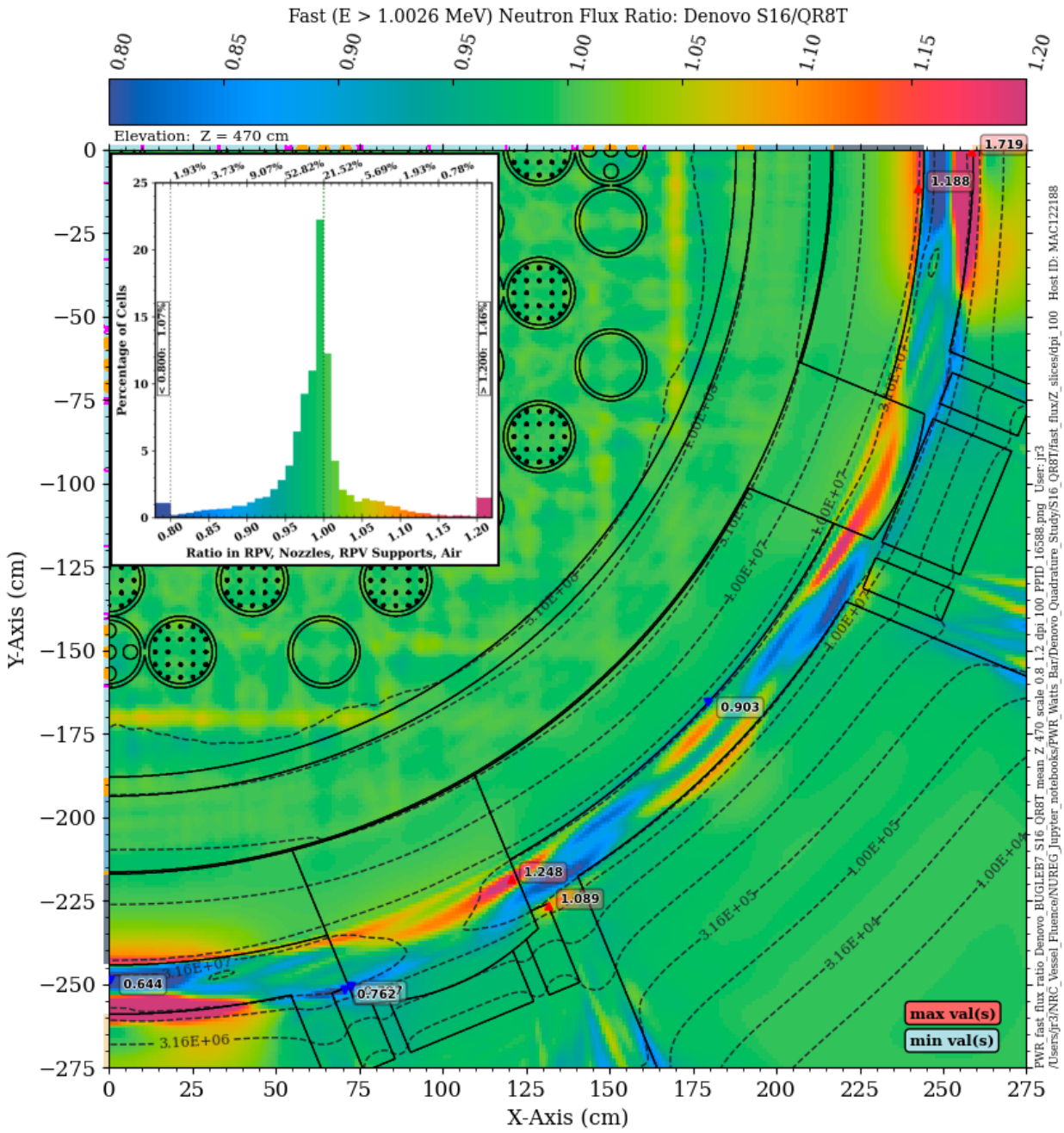

Figure 7-14 Fast neutron flux ratio in the PWR reference model: S16/QR8T quadrature. Plan view at Z = 470 cm *The contour lines are the fast flux from the QR8T solution.*

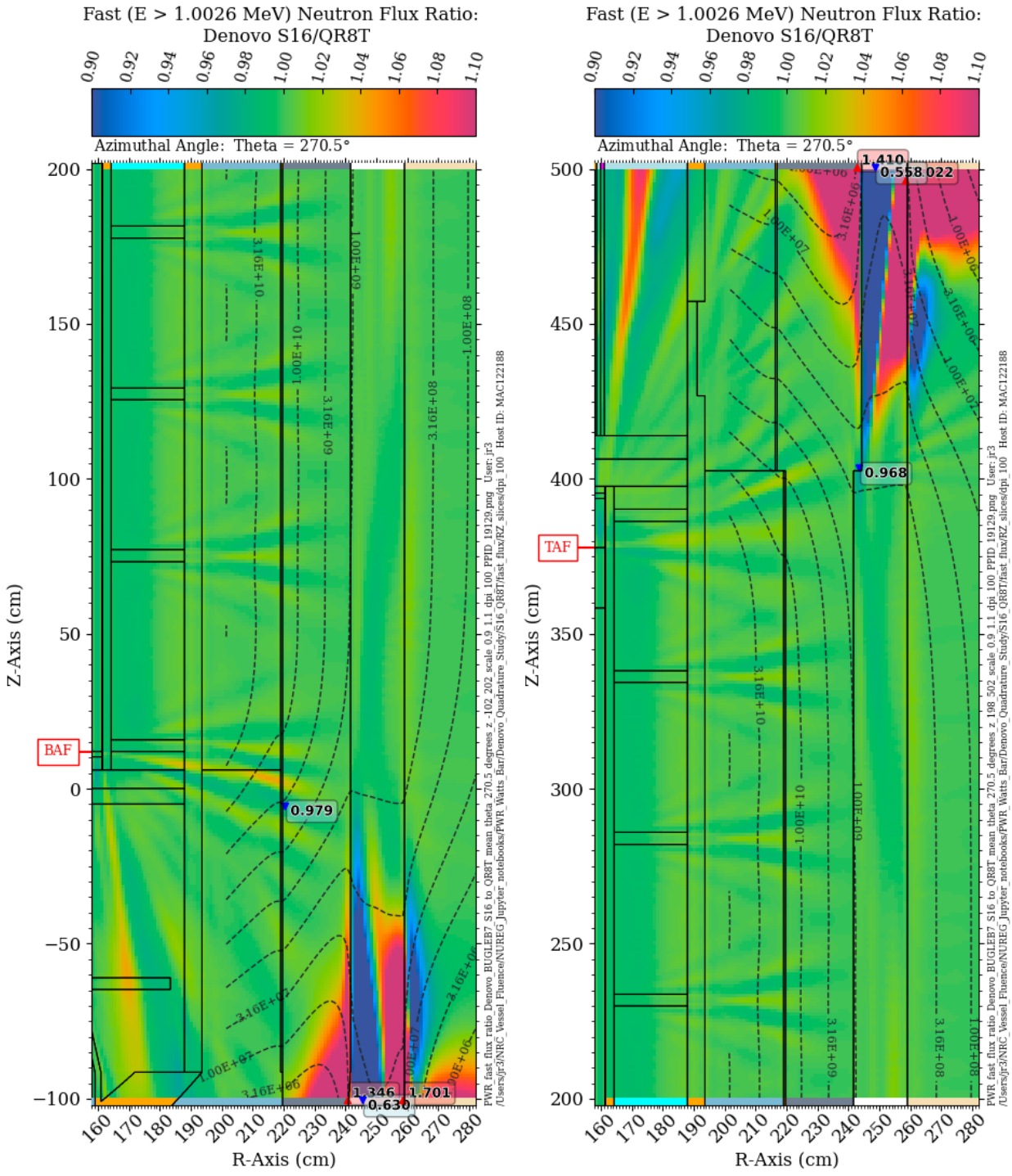

Figure 7-15 Fast neutron flux ratio in the PWR reference model: S16/QR8T quadrature. Elevation view at an azimuthal angle of 270.5° *The contour lines are the fast flux from the QR8T solution.*

7.3.3 Denovo Solutions: QR8T vs QR16T

It was noted in Section 2.1.3 that level symmetric SN quadrature sets have negative weights for orders greater than S20. The QR sets do not suffer from negative weights and allow higher-order quadratures to be used. The final Denovo solution comparison for the PWR model uses a QR8T solution and a QR16T solution. Note that a QR16T quadrature set has 136 angles per octant, which would be equivalent to an S32 set.

Figure 7-16 through Figure 7-19 illustrate the QR8T/QR16T fast flux ratio on the inner and outer surfaces of the RPV and at elevations of Z = 195 cm, Z = -70 cm, and Z = 470 cm. At the core midplane, the two solutions agree within 1% within the RPV and within less than 2% in the cavity gap. At the extended beltline elevations of Z = -70 cm (Figure 7-18) and Z = 470 cm (Figure 7-19), the differences are reduced relative to the S16/QR8T ratios in Figure 7-13 and Figure 7-14. While the QR8T and QR16T solutions at Z = -70 cm agree within 5% in the RPV and typically within 10% in the cavity gap, the differences are again more pronounced at Z = 470 cm, where differences can exceed 20% in the cavity gap.

Comparisons of the QR8T and QR16T with an MG Shift calculation using the BUGLE-B7 library are provided in Section 7.5.

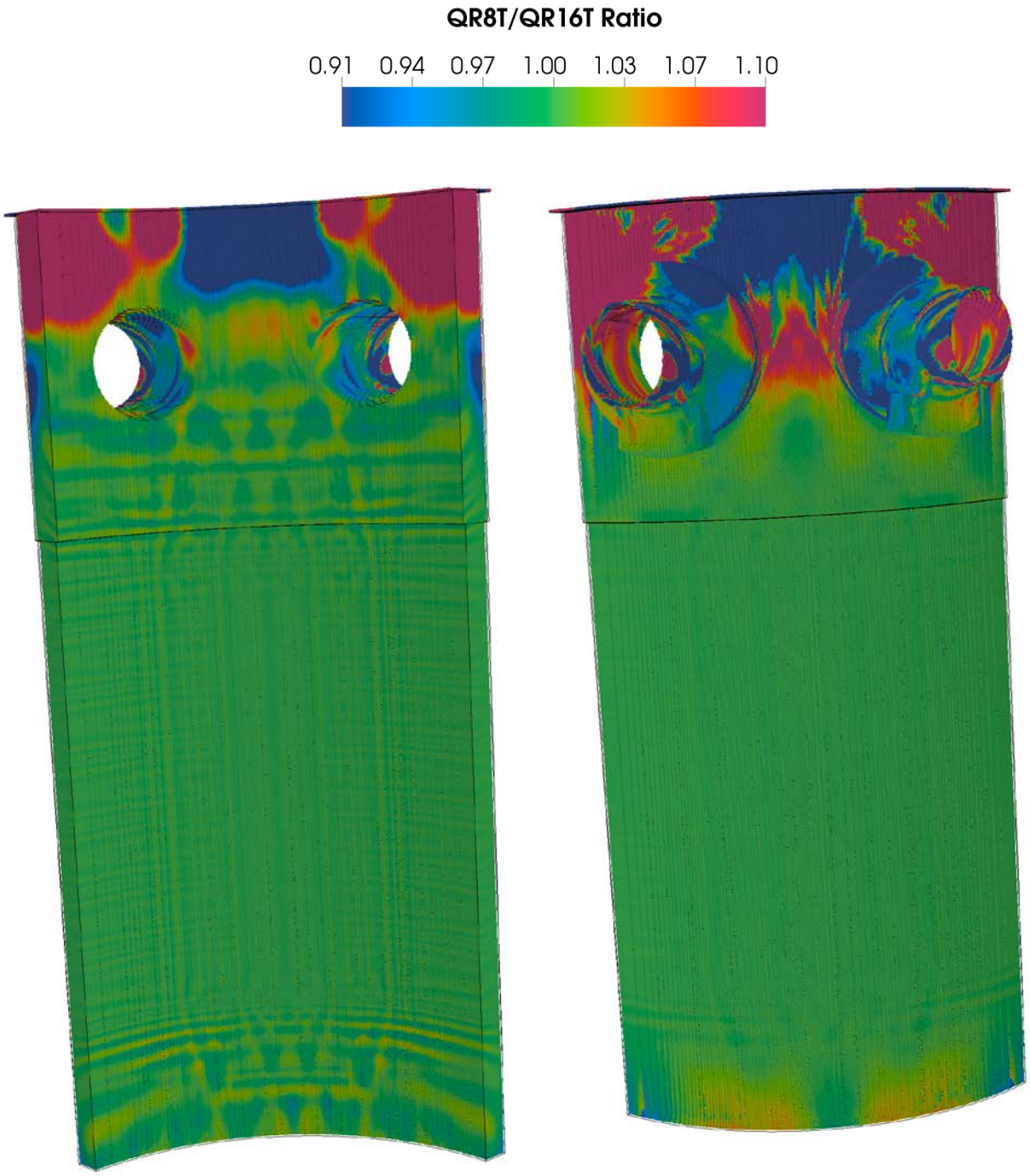

Figure 7-16 Fast neutron flux ratio on the inner and outer surfaces of the RPV for the PWR reference model: Denovo QR8T solution relative to a QR16T solution

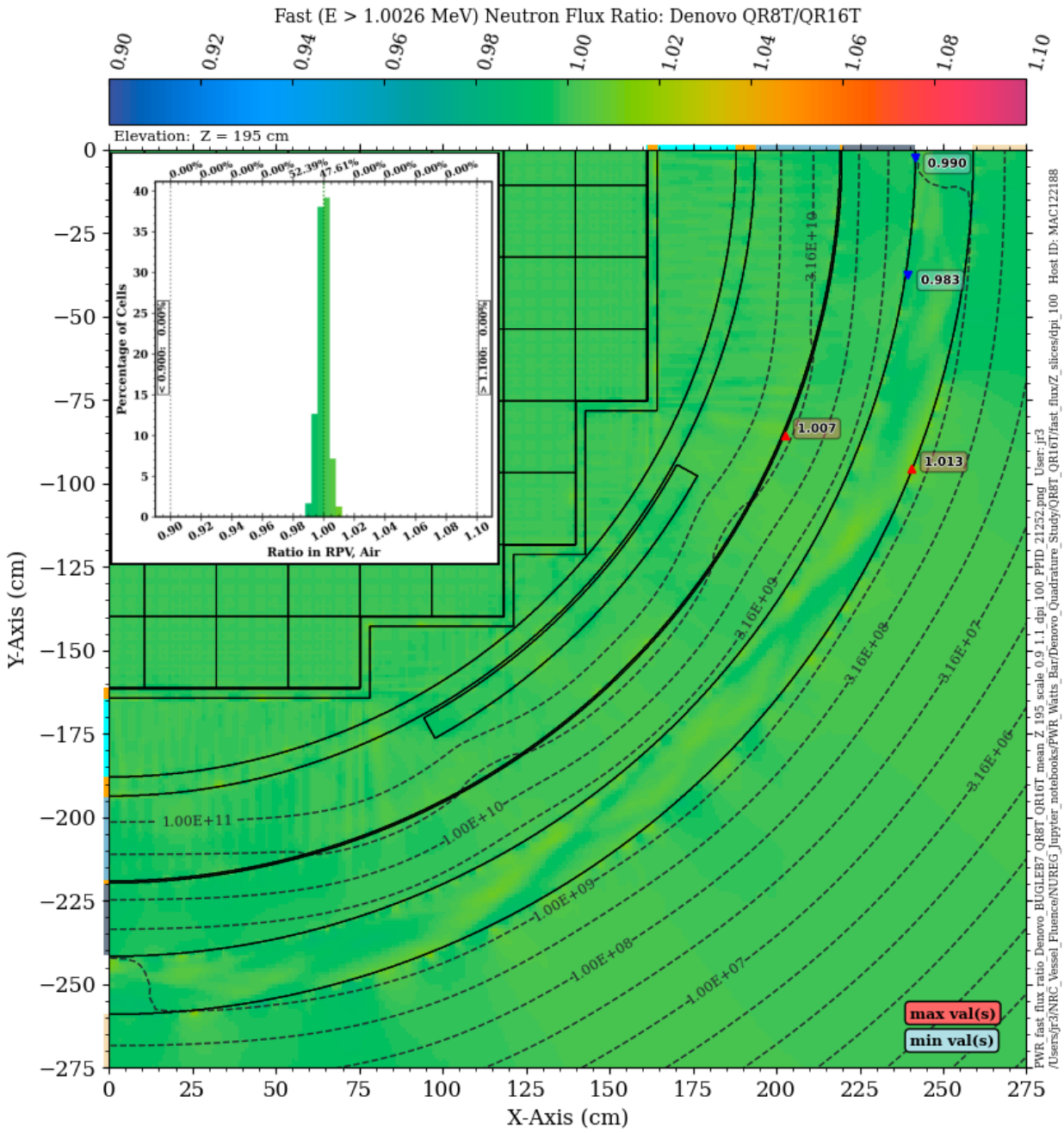

Figure 7-17 Fast neutron flux ratio in the PWR reference model: QR8T/QR16T quadrature. Plan view at Z = 195 cm *The contour lines are the fast flux from the QR16T solution.*

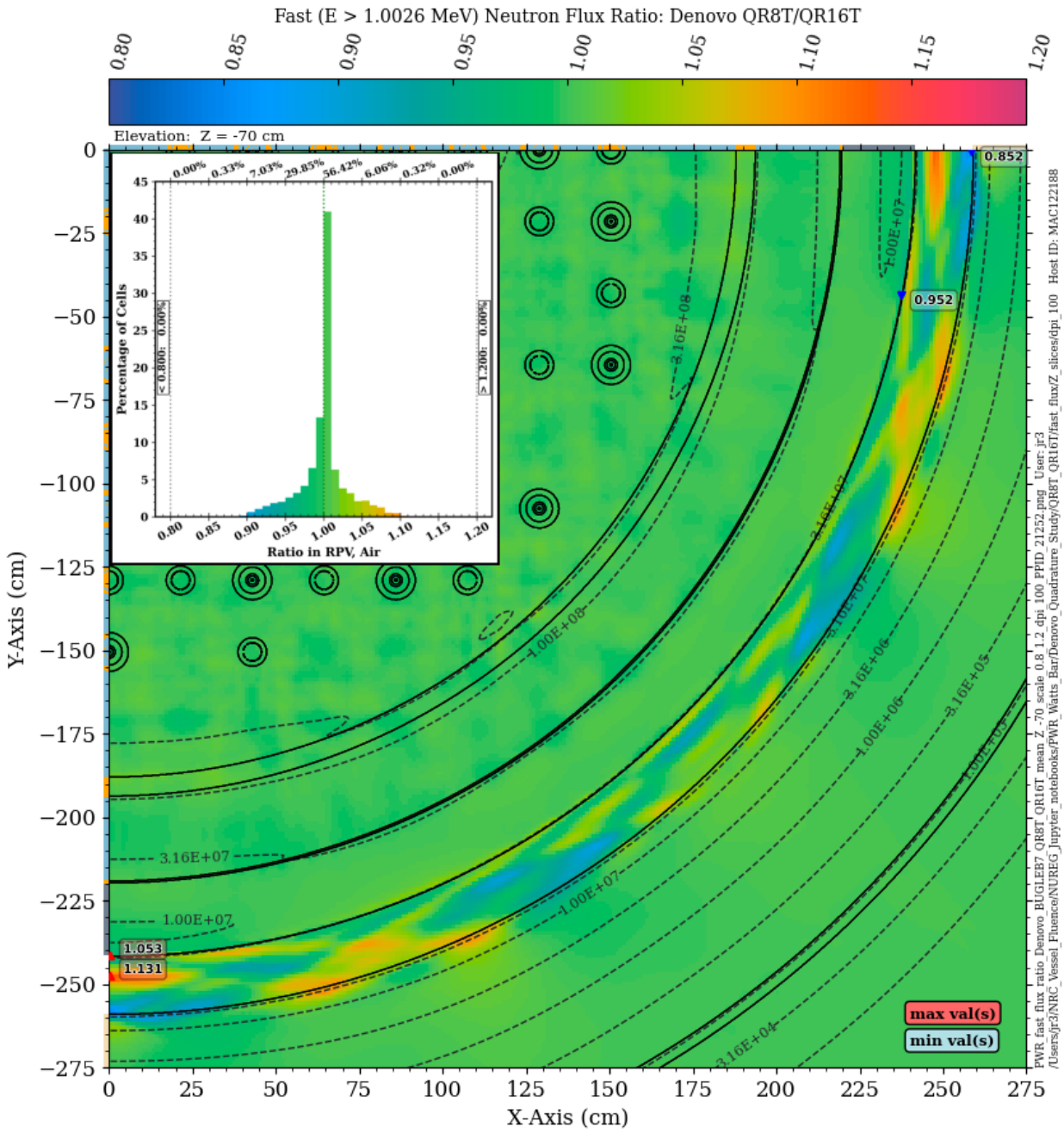

Figure 7-18 Fast neutron flux ratio in the PWR reference model: QR8T/QR16T quadrature. Plan view at Z = -70 cm *The contour lines are the fast flux from the QR16T solution. Note the change in scale relative to Figure 7-17.*

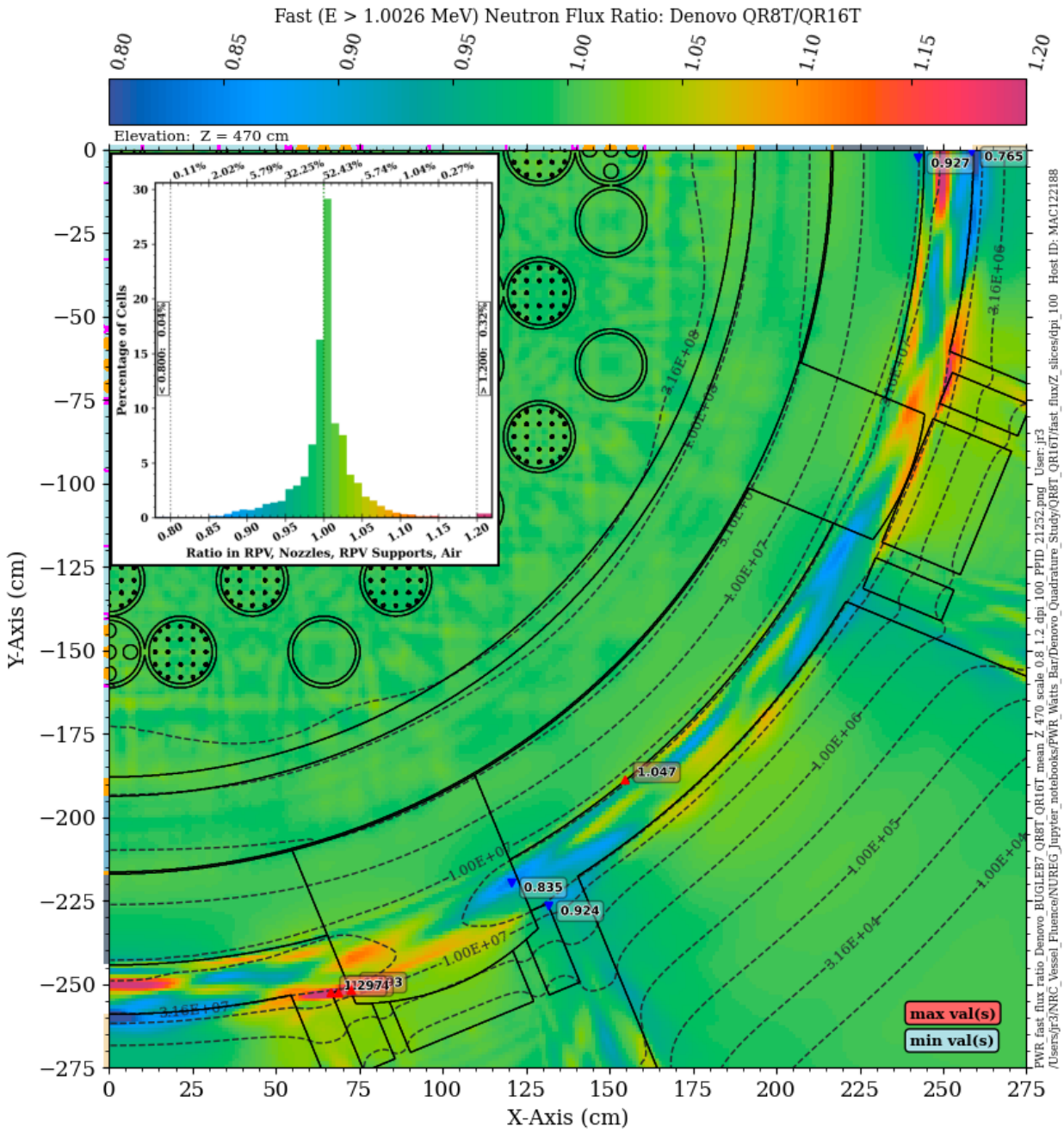

Figure 7-19 Fast neutron flux ratio in the PWR reference model: QR8T/QR16T quadrature. Plan view at Z = 470 cm *The contour lines are the fast flux from the QR16T solution.*

7.3.4 Quadrature Sensitivity for the ^{27}Al (n,α) Reaction Rate

Because ray effects tend to be more pronounced in high-energy groups in discrete ordinates calculations, the discrete ordinates solution sensitivity to quadrature order was examined for the ^{27}Al (n,α) dosimetry reaction. This reaction has a threshold energy (i.e., minimum neutron energy required for the reaction to occur) of 3.25 MeV and an energy response range (i.e., the energy range over which 90% of the response occurs in a ^{235}U fission spectrum) of 6.45–11.9 MeV. Quadrature comparisons were made for the ^{27}Al (n,α) reaction rate for the S8, S16, QR8T, and QR16T quadratures.

The S8/S16 quadrature sensitivity for the ^{27}Al (n,α) reaction rate at the core midplane (Figure 7-20) is significantly more pronounced than the S8/S16 fast flux ratio at the core midplane (Figure 7-2). Similarly, the S8/S16 ^{27}Al (n,α) reaction rate ratios at Z = 390 cm (Figure 7-21) and at Z = 400 cm (Figure 7-22) show substantially more variation than the S8/S16 fast flux ratios at those elevations (Figure 7-3 and Figure 7-4). Note that the ratio range extends from [0.9, 1.1] for the fast flux ratios and [0.8, 1.2] for the ^{27}Al (n,α) reaction rate ratios in those figures.

The ray effects that originate near the former plates and propagate through the RPV are also much more significant for the ^{27}Al (n,α) reaction rate than for the fast flux, as shown by a comparison of Figure 7-7 and Figure 7-25.

The differences in the ^{27}Al (n,α) reaction rates in the S16 and QR8T are substantially less than for the S8/S16 comparison, but they are still more pronounced than the S16/QR8T fast flux ratios. This can be seen by comparison of Figure 7-29 with Figure 7-12, and Figure 7-30 with Figure 7-15.

Differences between the QR8T and QR16T ^{27}Al (n,α) reaction rates (not shown) do not deviate significantly from the QR8T/QR16T fast flux ratios.

Further discussion of the increased quadrature sensitivity for high-energy threshold reactions is provided in Section 7.6.

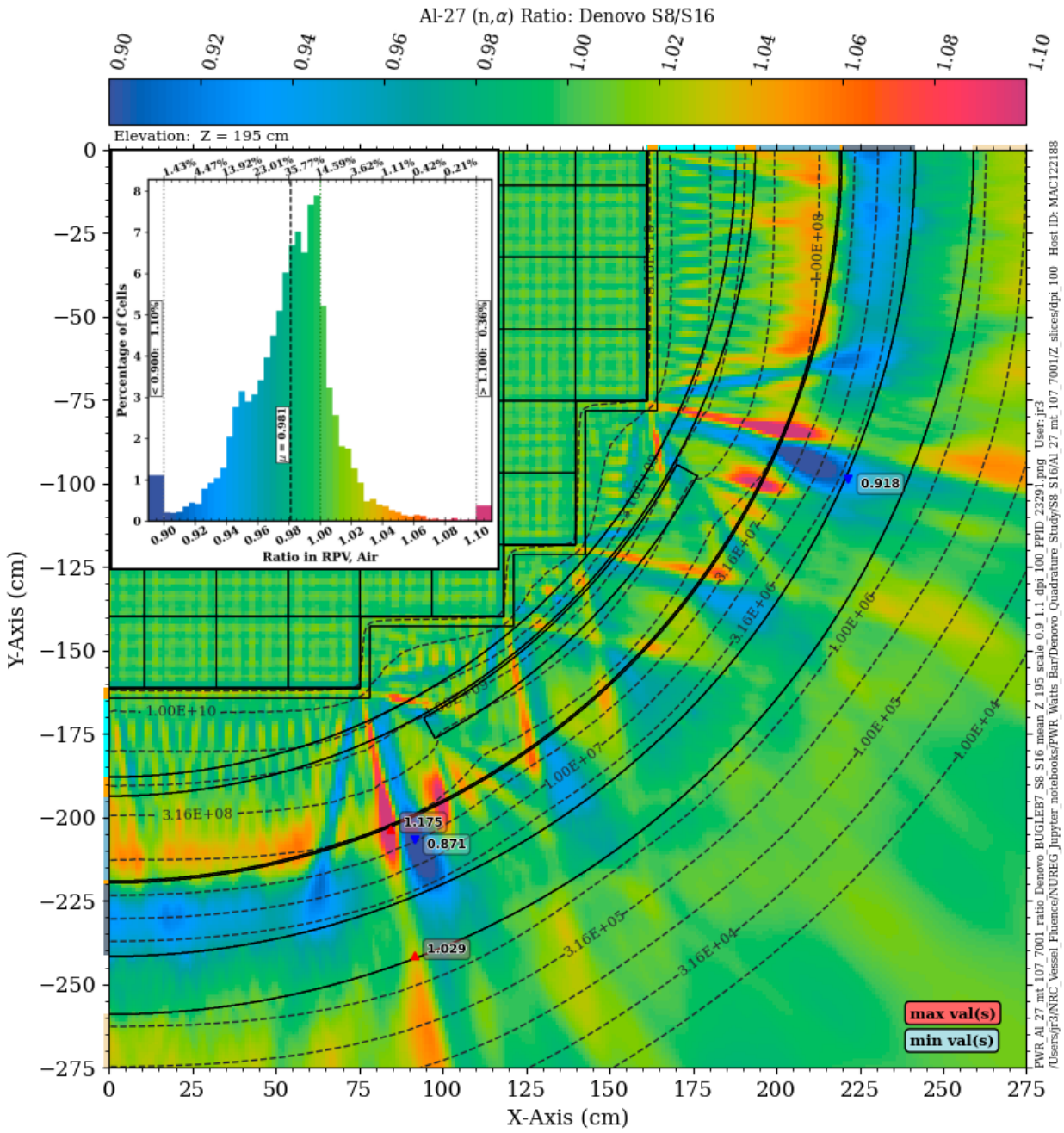

Figure 7-20 **^{27}Al (n,α) reaction rate ratio in the PWR reference model: S8/S16 quadrature. Plan view at Z = 195 cm** *The contour lines are the ^{27}Al (n,α) reaction rate from the S16 solution.*

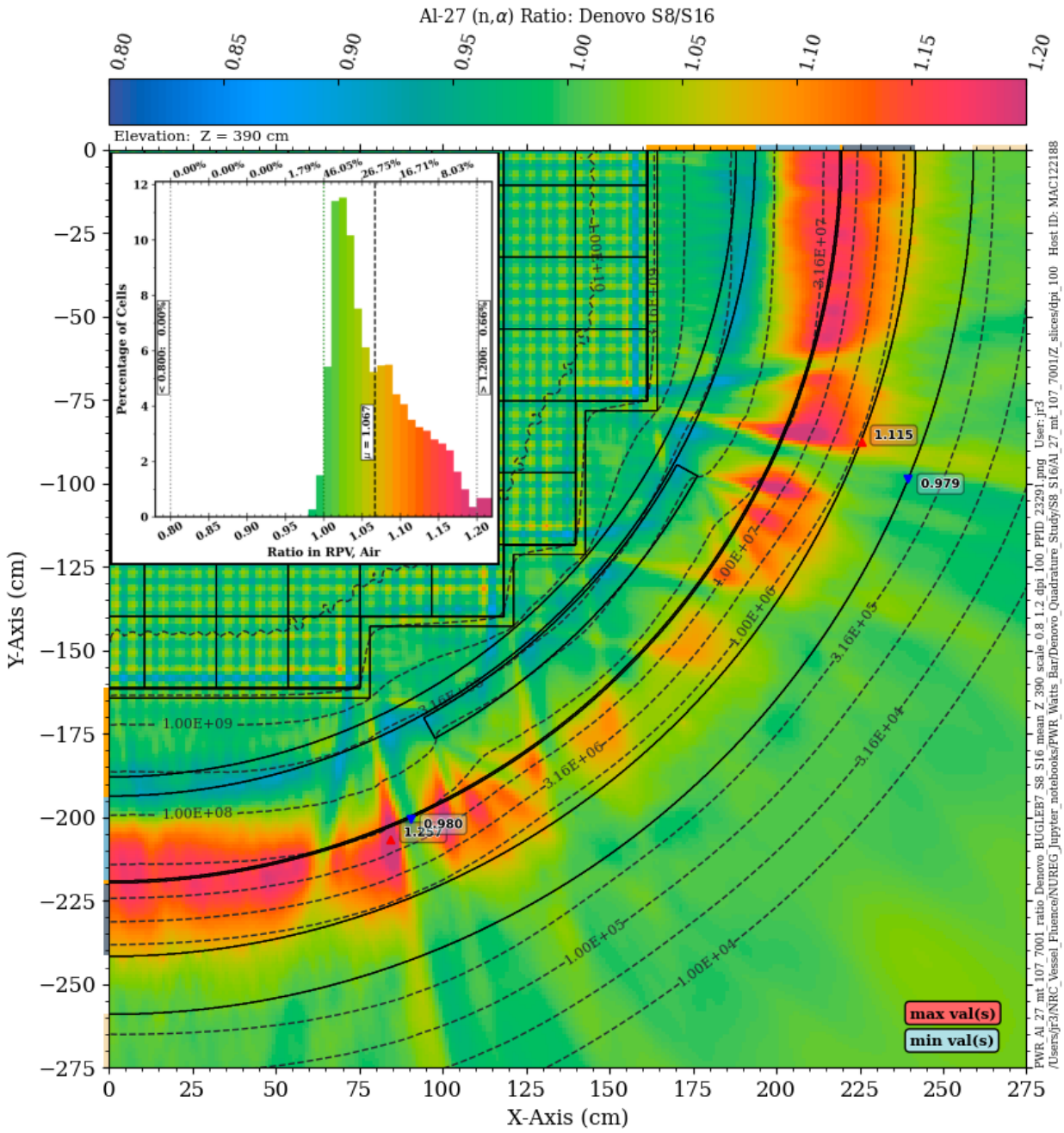

Figure 7-21 **^{27}Al (n,α) reaction rate ratio in the PWR reference model: S8/S16 quadrature. Plan view at Z = 390 cm** *The contour lines are the ^{27}Al (n,α) reaction rate from the S16 solution.*

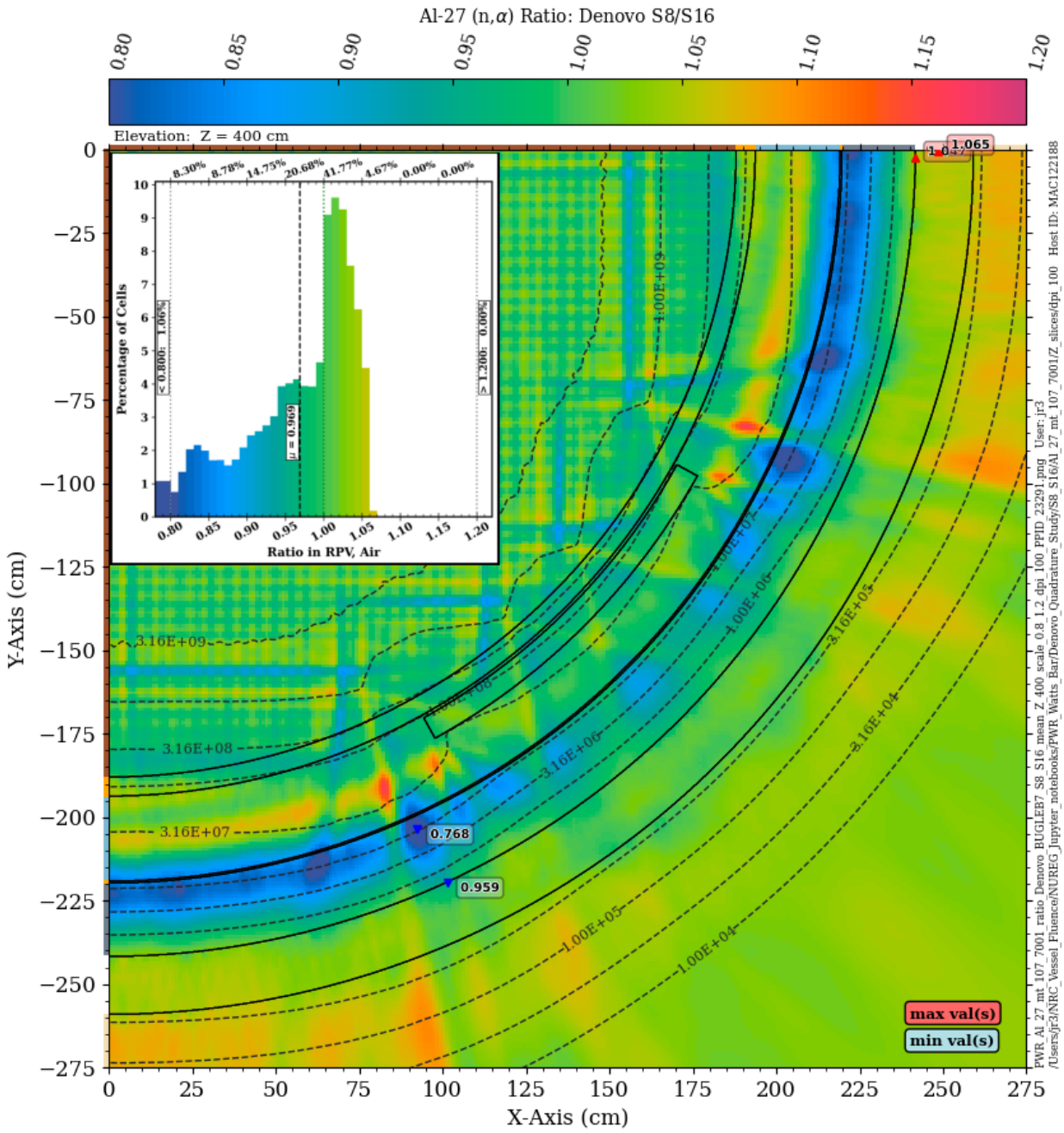

Figure 7-22 **^{27}Al (n,α) reaction rate ratio in the PWR reference model: S8/S16 quadrature. Plan view at Z = 400 cm** *The contour lines are the ^{27}Al (n,α) reaction rate from the S16 solution.*

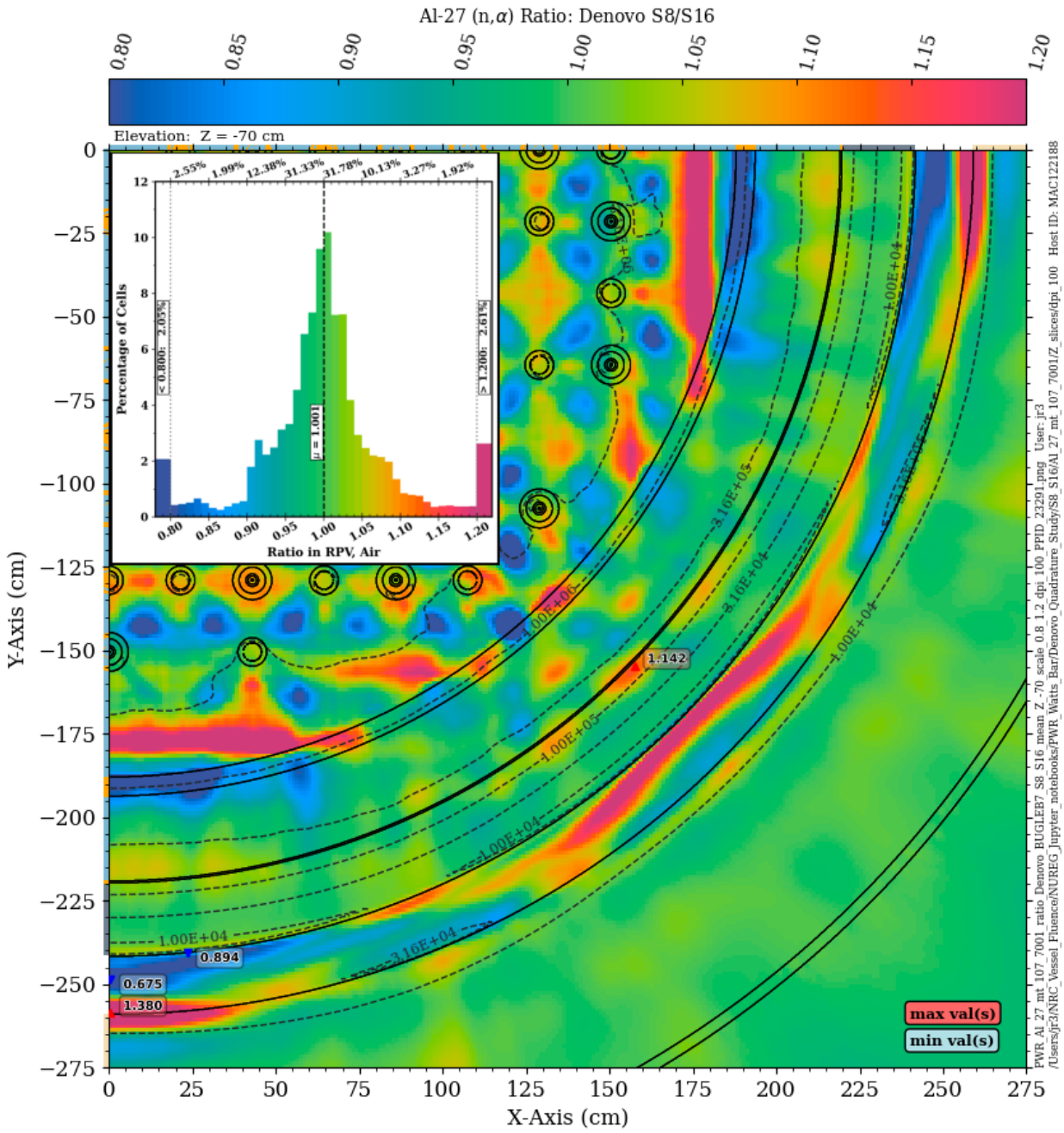

Figure 7-23 **^{27}Al (n,α) reaction rate ratio in the PWR reference model: S8/S16 quadrature. Plan view at Z = -70 cm** *The contour lines are the ^{27}Al (n,α) reaction rate from the S16 solution.*

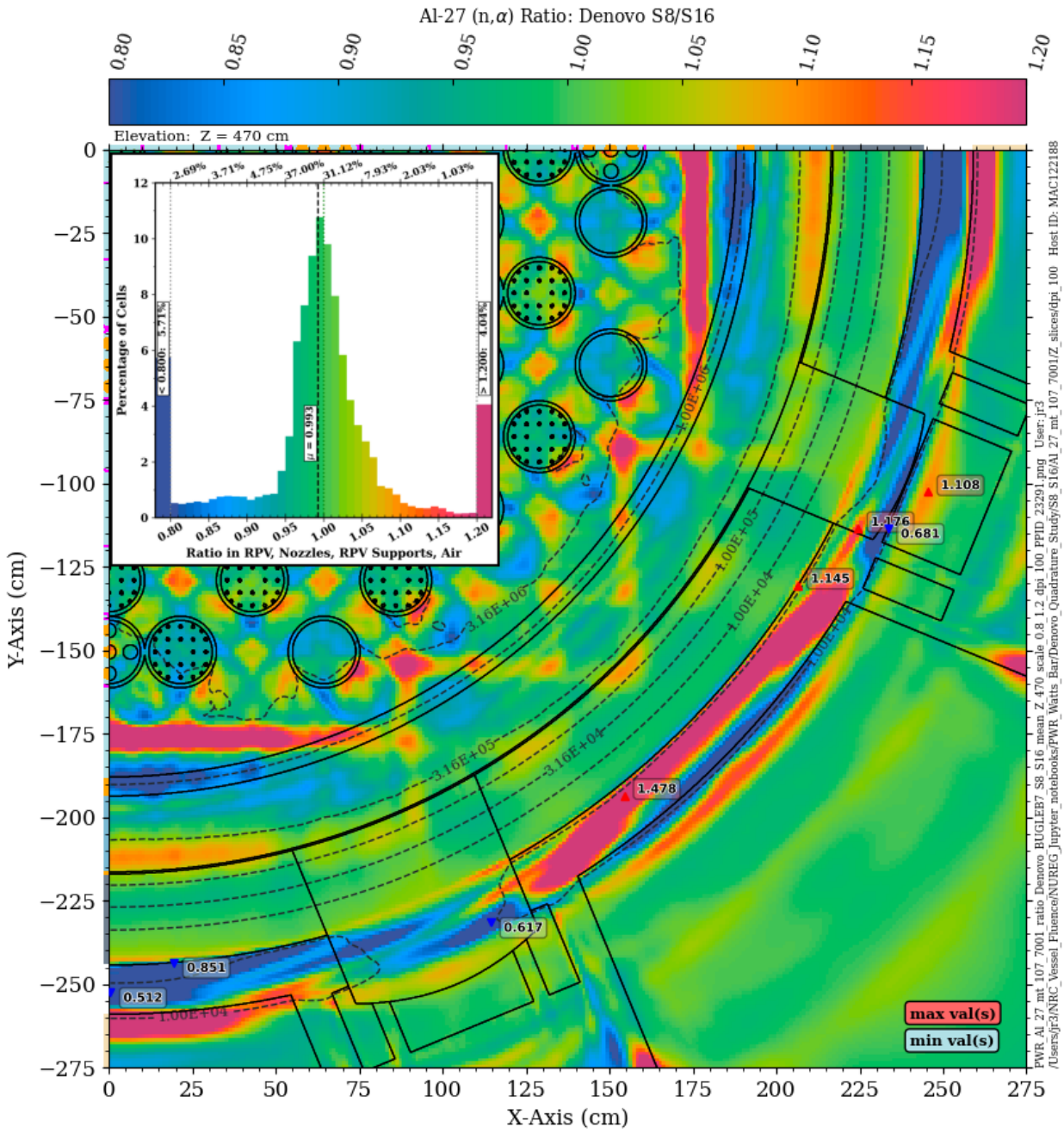

Figure 7-24 **^{27}Al (n,α) reaction rate ratio in the PWR reference model: S8/S16 quadrature. Plan view at Z = 470 cm** *The contour lines are the ^{27}Al (n,α) reaction rate from the S16 solution.*

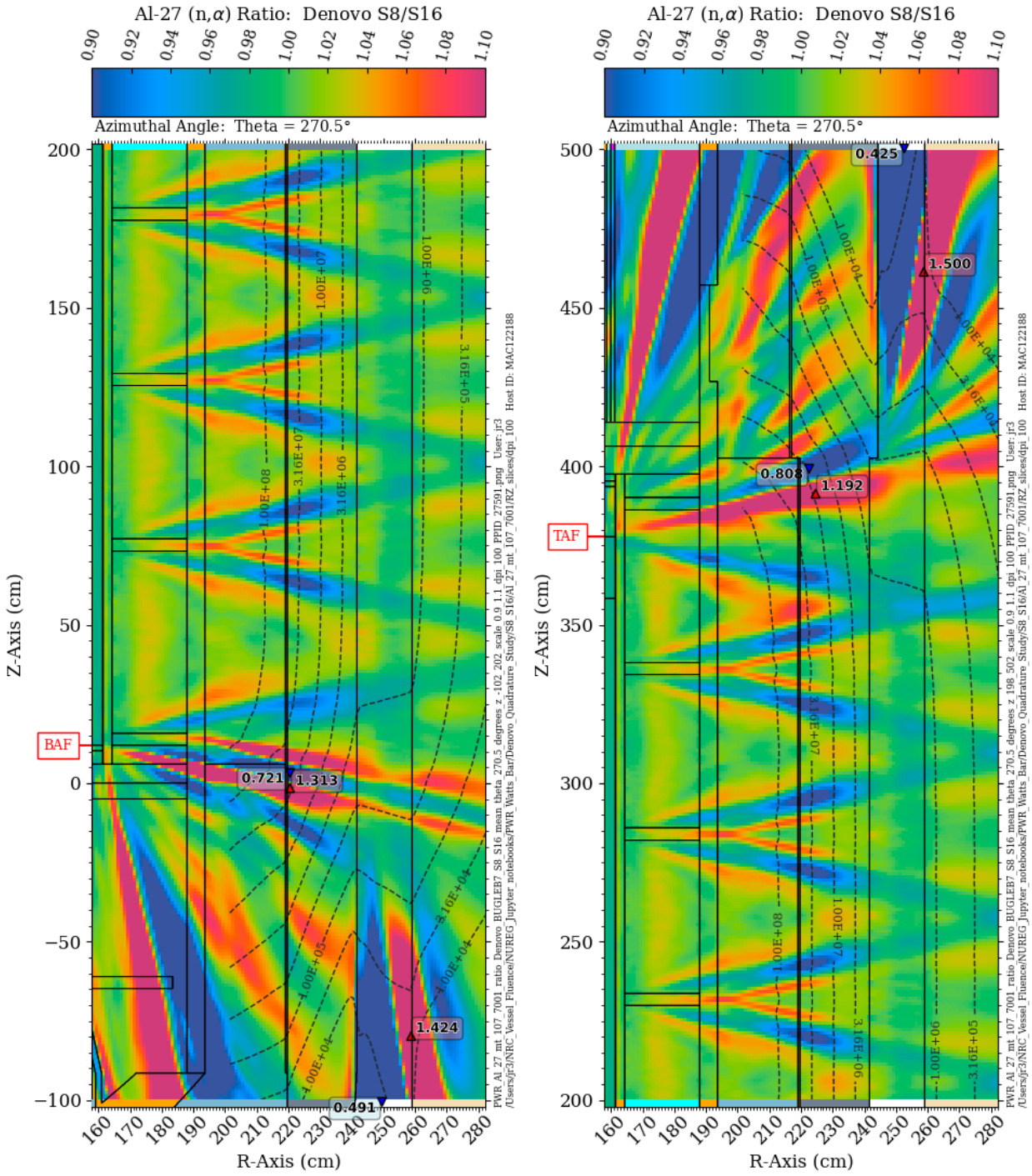

Figure 7-25 **^{27}Al (n,α) reaction rate ratio in the PWR reference model: S8/S16 quadrature. Elevation view at an azimuthal angle of 270.5°** *The contour lines are the ^{27}Al (n,α) reaction rate from the S16 solution.*

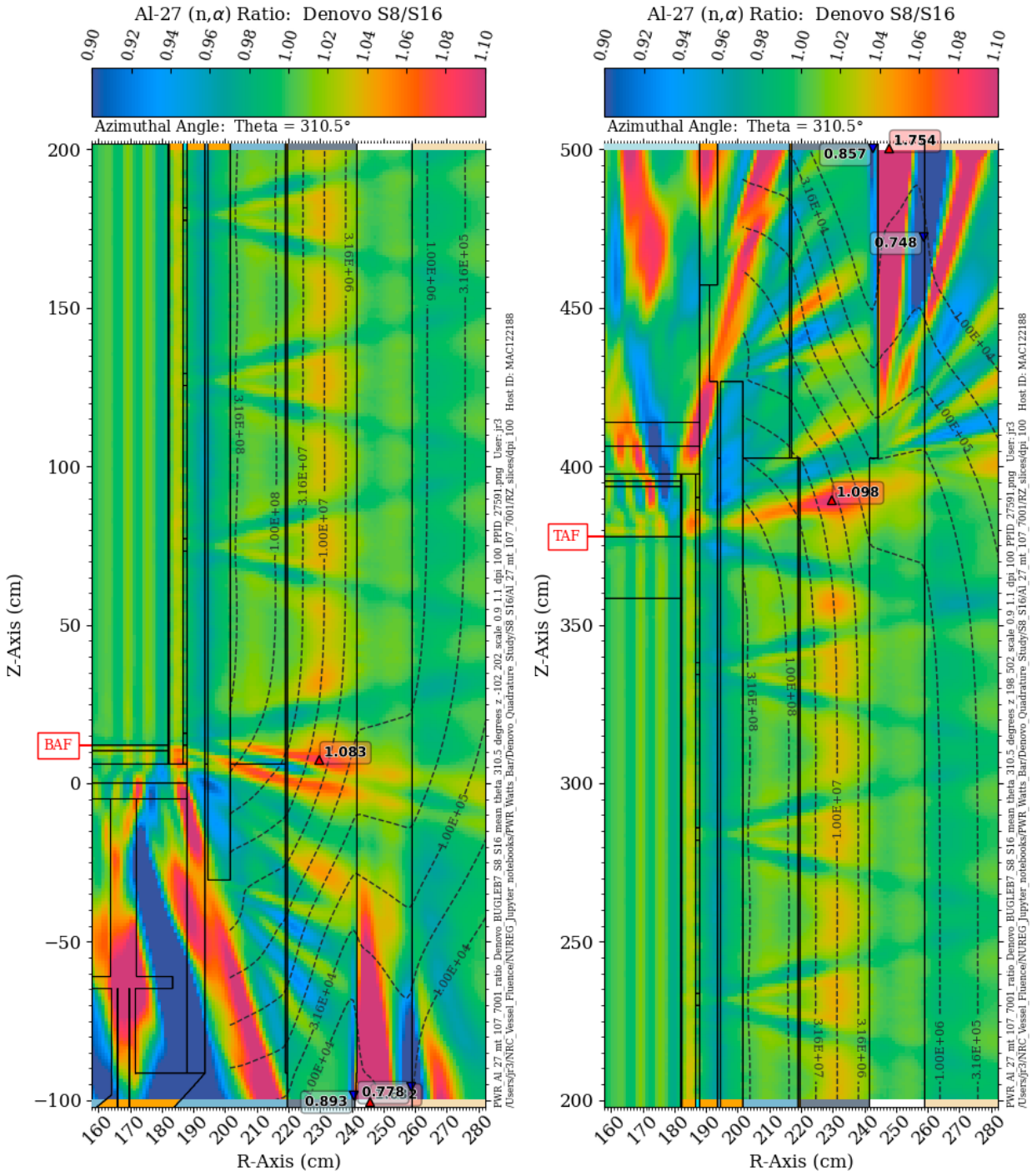

Figure 7-26 **^{27}Al (n,α) reaction rate ratio in the PWR reference model: S8/S16 quadrature. Elevation view at an azimuthal angle of 310.5°** *The contour lines are the ^{27}Al (n,α) reaction rate from the S16 solution.*

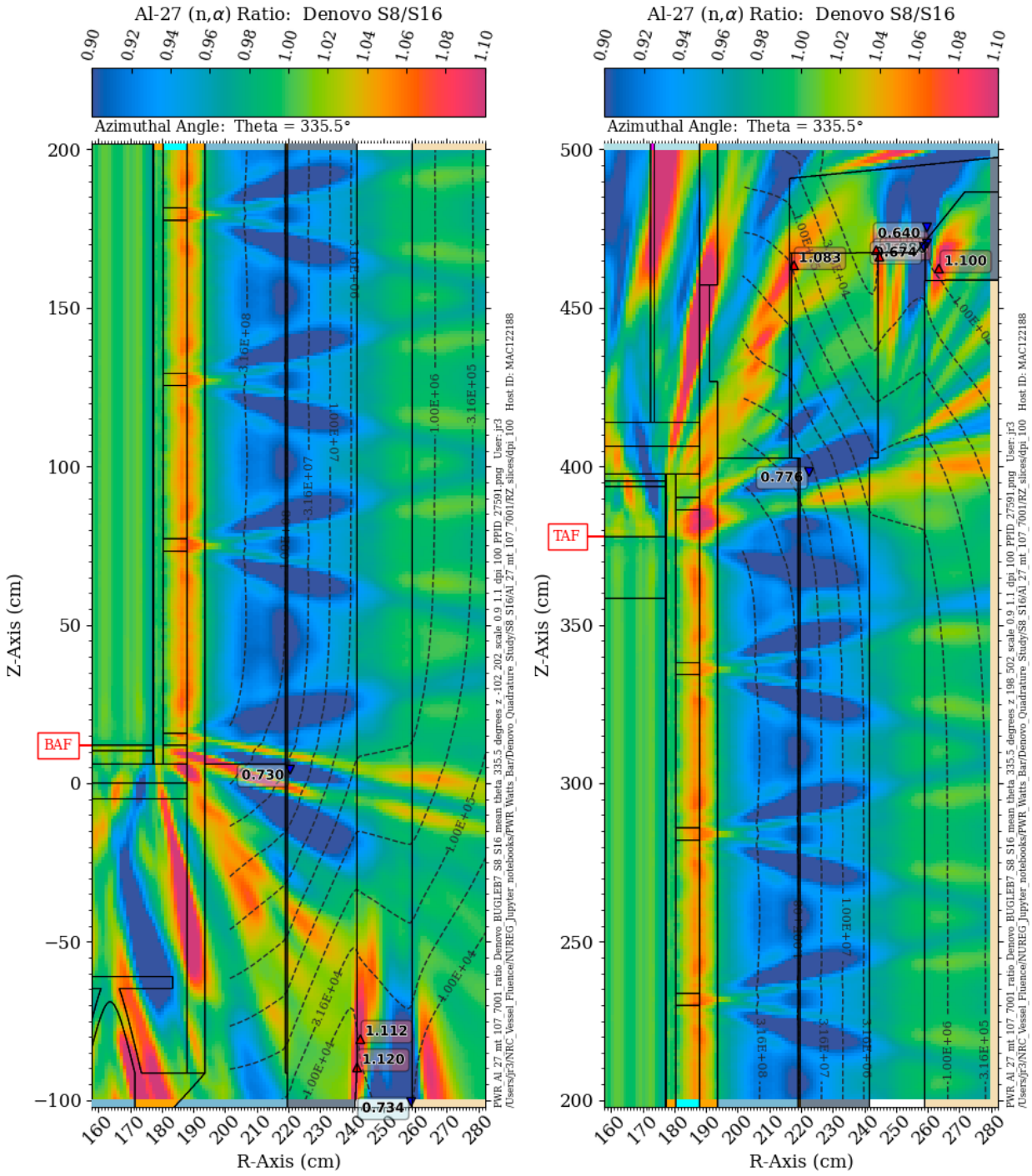

Figure 7-27 ^{27}Al (n,α) reaction rate ratio in the PWR reference model: S8/S16 quadrature. Elevation view at an azimuthal angle of 335.5° *The contour lines are the ^{27}Al (n,α) reaction rate from the S16 solution.*

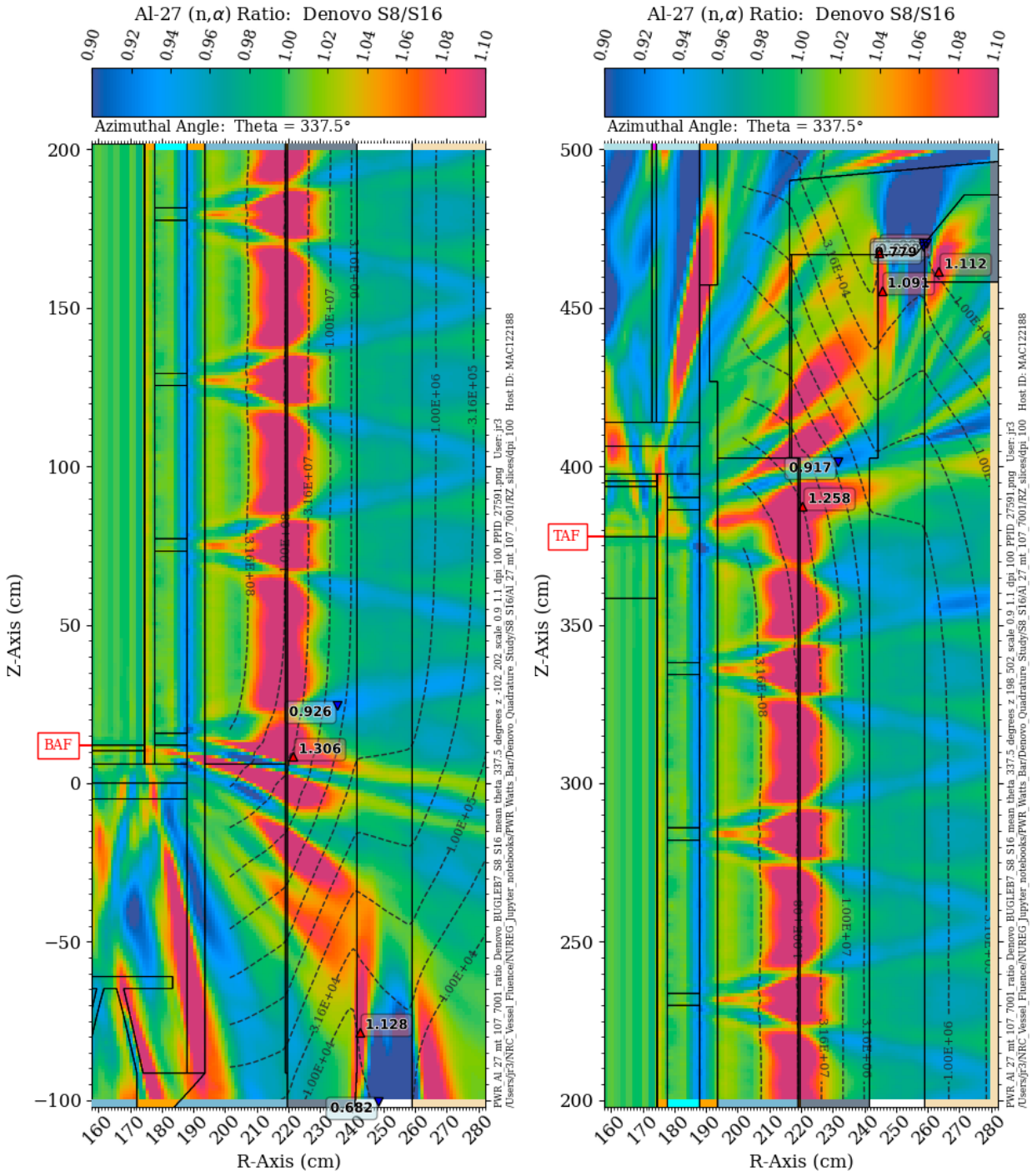

Figure 7-28 ^{27}Al (n,α) reaction rate ratio in the PWR reference model: S8/S16 quadrature. Elevation view at an azimuthal angle of 337.5° *The contour lines are the ^{27}Al (n,α) reaction rate from the S16 solution.*

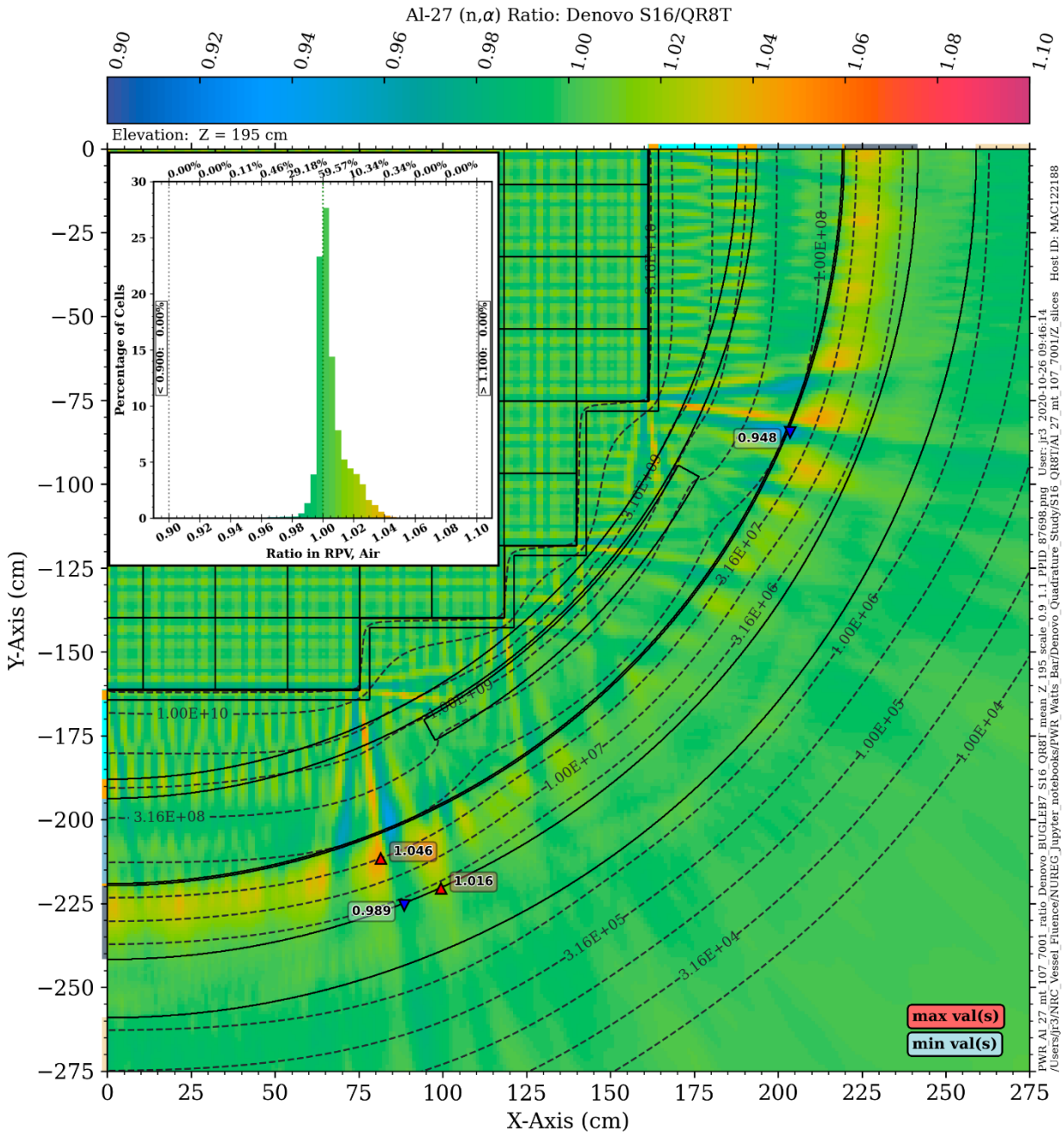

Figure 7-29 **^{27}Al (n,α) reaction rate ratio in the PWR reference model: S16/QR8T quadrature. Plan view at Z = 195 cm** *The contour lines are the ^{27}Al (n,α) reaction rate from the QR8T solution.*

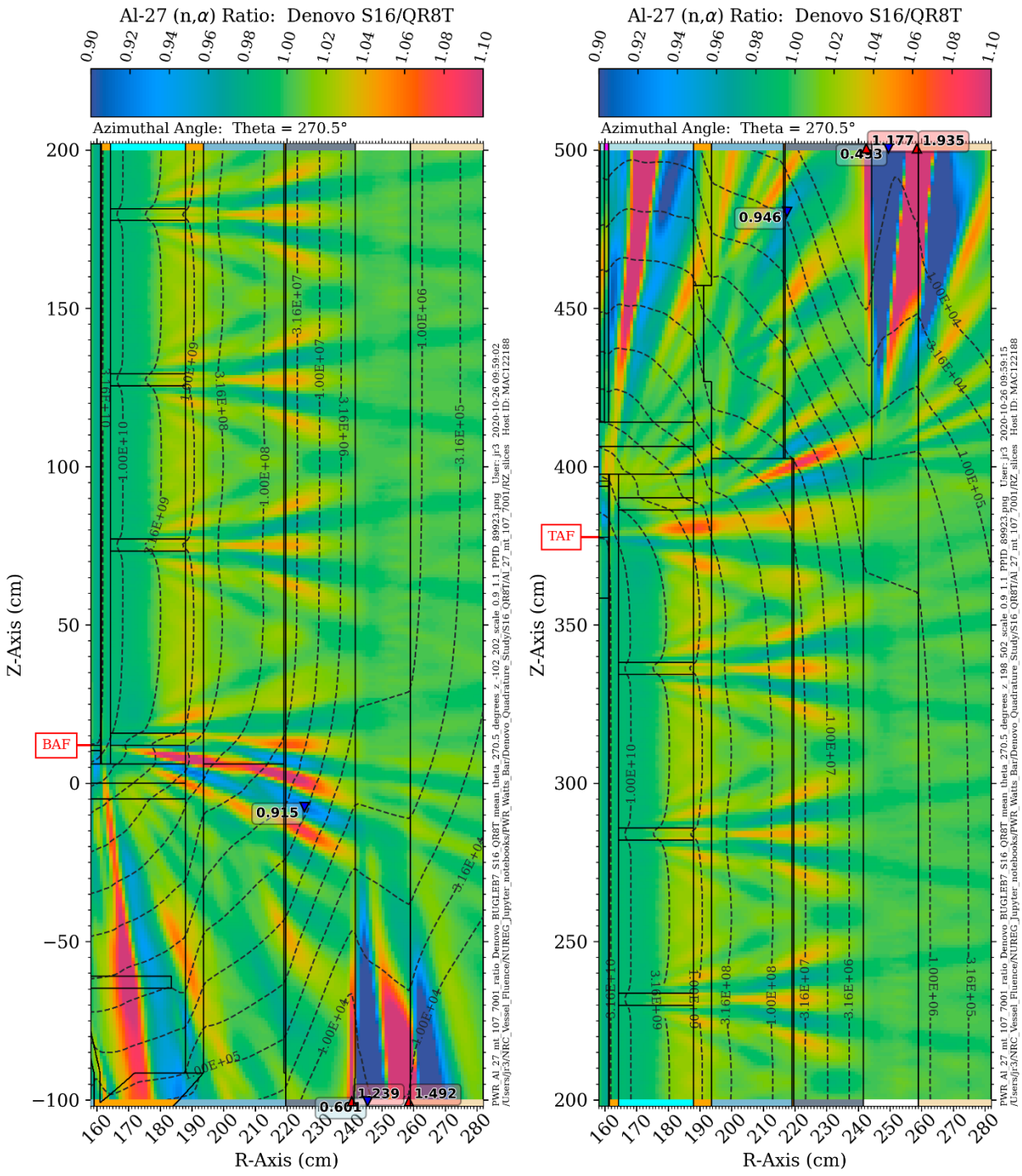

Figure 7-30 **^{27}Al (n,α) reaction rate ratio in the PWR reference model: S16/QR8T quadrature. Elevation view at an azimuthal angle of 270.5°** *The contour lines are the ^{27}Al (n,α) reaction rate from the QR8T solution.*

7.4 Denovo Quadrature Sensitivity: BWR Model

The sensitivity of discrete ordinates solutions to the angular quadrature selection for a BWR was examined using the BWR model with a homogenized core representation (Section 5.9.2). The discrete ordinates calculations were run using Denovo with the following parameters:

- BUGLE-B7 MG cross-section library with P_3 scattering expansions
- Uniform 1.25-cm mesh in X, Y, and Z with X- and Y-extents of 350 cm and a Z-extent of 800 cm (76.8 million cells)
- Linear discontinuous (LD) differencing scheme
- Source iteration (SI) solver with a convergence criterion of 1E-6

A parametric meshing study indicated that the Denovo solution converges with respect to mesh using the intervals noted above.

7.4.1 Denovo Solutions: S8 vs S16

Ratios of the BWR S8 Denovo fast (E > 1.0026 MeV) flux to the S16 Denovo fast flux are provided in Figure 7-31 through Figure 7-37. Figure 7-31 and Figure 7-32 illustrate the fast neutron flux ratio on the inner and outer surfaces of the RPV and shroud, respectively. There is evidence of ray effects within the core height in the shroud and the RPV. More notable ray effects are apparent in the upper portion of the shroud, and at elevations below the bottom of the fuel.

Figure 7-33 shows the S8/S16 fast flux ratio at the core midplane. As with the PWR model, ray effects originate at each corner fuel assembly on the periphery of the core. The jet pump risers also produce ray effects. The S8/S16 fast flux ratio in the RPV varies by nearly 20%, with a maximum value of 1.109 and a minimum value of 0.927. As with the PWR model, these changes occur over a relatively small spatial scale.

Figure 7-34 and Figure 7-35 show the S8/S16 fast flux ratio at elevations of Z = 210 cm and Z = 225 cm, respectively. These elevations correspond to the horizontal red and blue bands above the top of the core in Figure 7-31. These plots demonstrate significant variations in the fast flux ratio in the RPV as a function of elevation and of azimuthal angle.

Figure 7-36 and Figure 7-37 show the S8/S16 fast flux ratio at elevations of Z = -250 cm and Z = 375 cm, which correspond to the upper and lower plan view elevations for the BWR model in Section 5. Note that the scale on these two plots is expanded from a range of [0.9, 1.1] to [0.8, 1.2]. Also, as shown in the histograms, there is a significant bias at elevations outside of the traditional beltline.

As with the PWR results in Section 7.3.1, these results suggest that the S8 quadrature set may not be optimal for RPV fluence calculations even within the traditional beltline region.

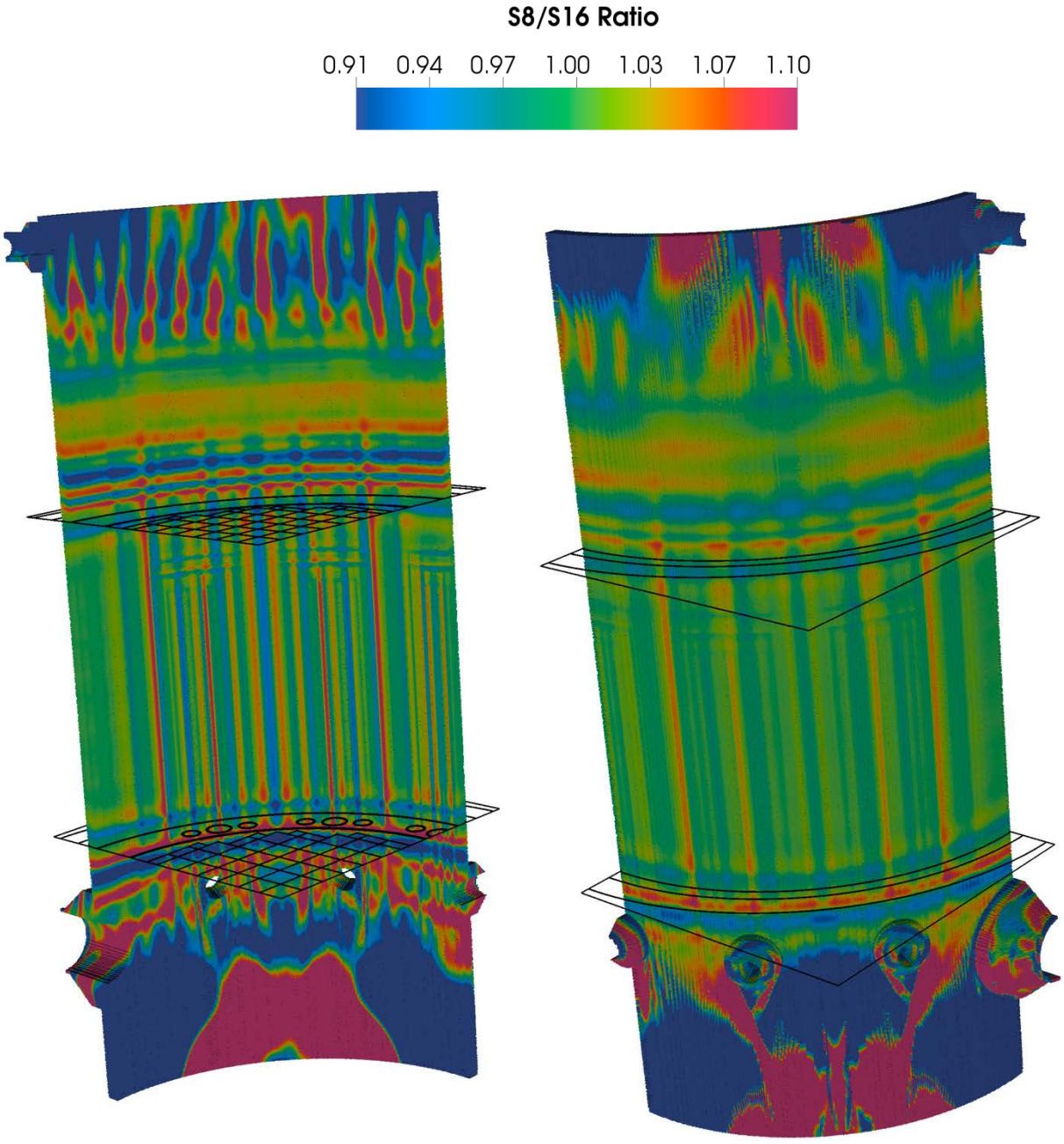

Figure 7-31 Fast neutron flux ratio on the inner and outer surfaces of the RPV for the BWR reference model: Denovo S8 solution relative to an S16 solution *The boundary planes show the extent of the fuel assemblies.*

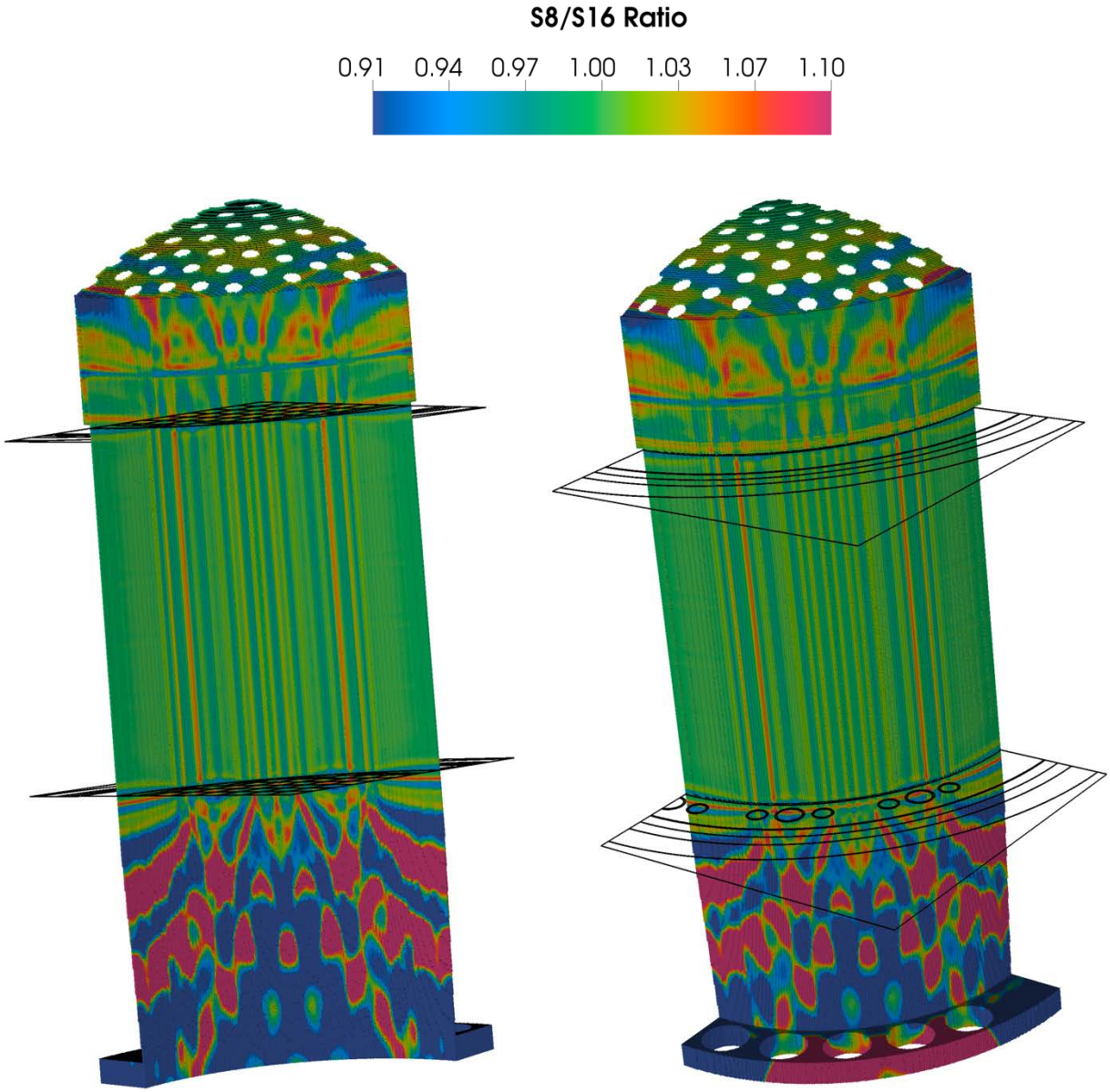

Figure 7-32 Fast neutron flux ratio on the inner and outer surfaces of the shroud for the BWR reference model: Denovo S8 solution relative to an S16 solution *The boundary planes show the extent of the fuel assemblies.*

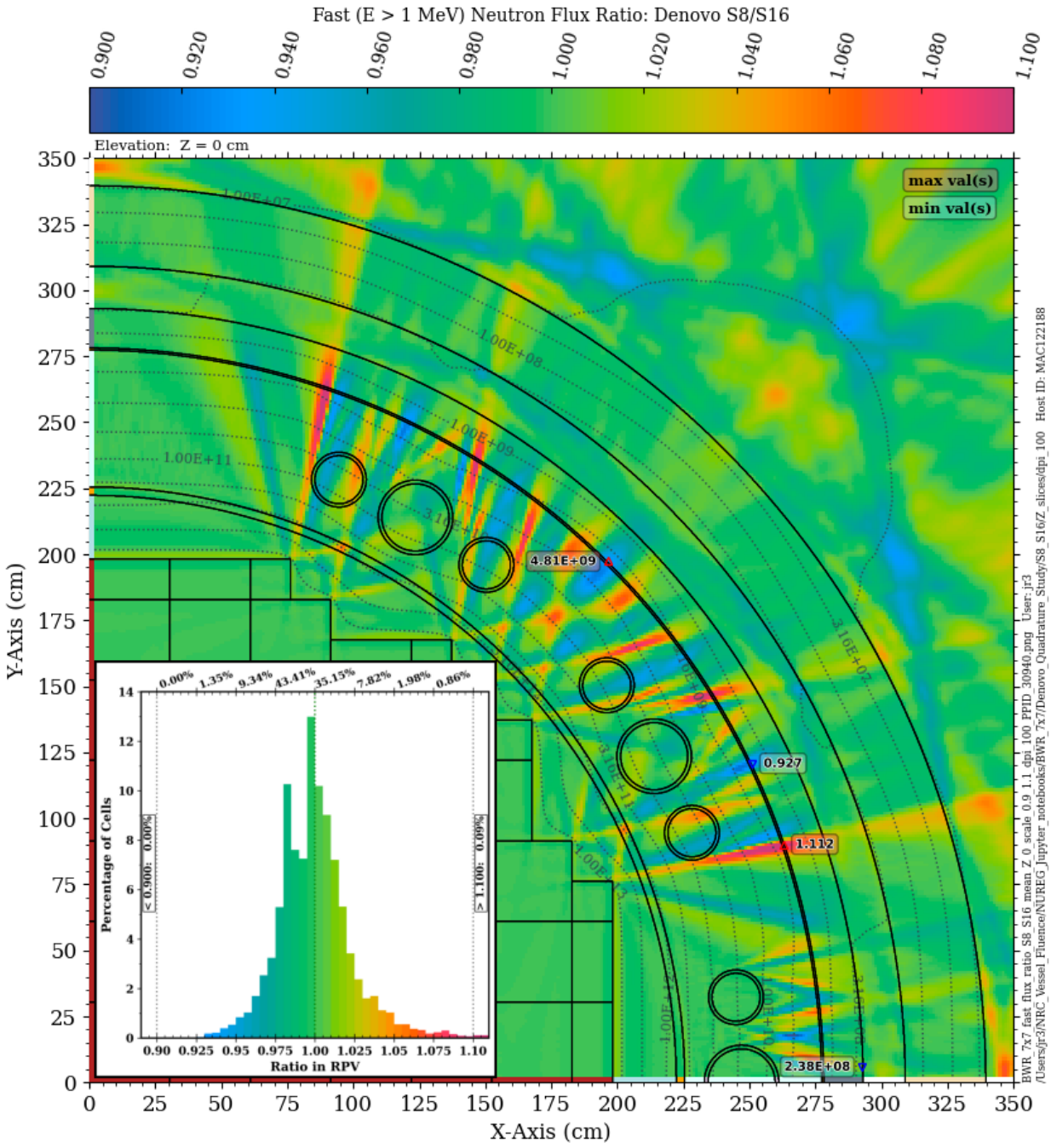

Figure 7-33 Fast neutron flux ratio in the BWR reference model: S8/S16 quadrature. Plan view at Z = 0 cm *The contour lines are the fast flux from the S16 solution. Minimum and maximum values within the RPV are shown for the S16 fast flux and the S8/S16 fast flux ratio.*

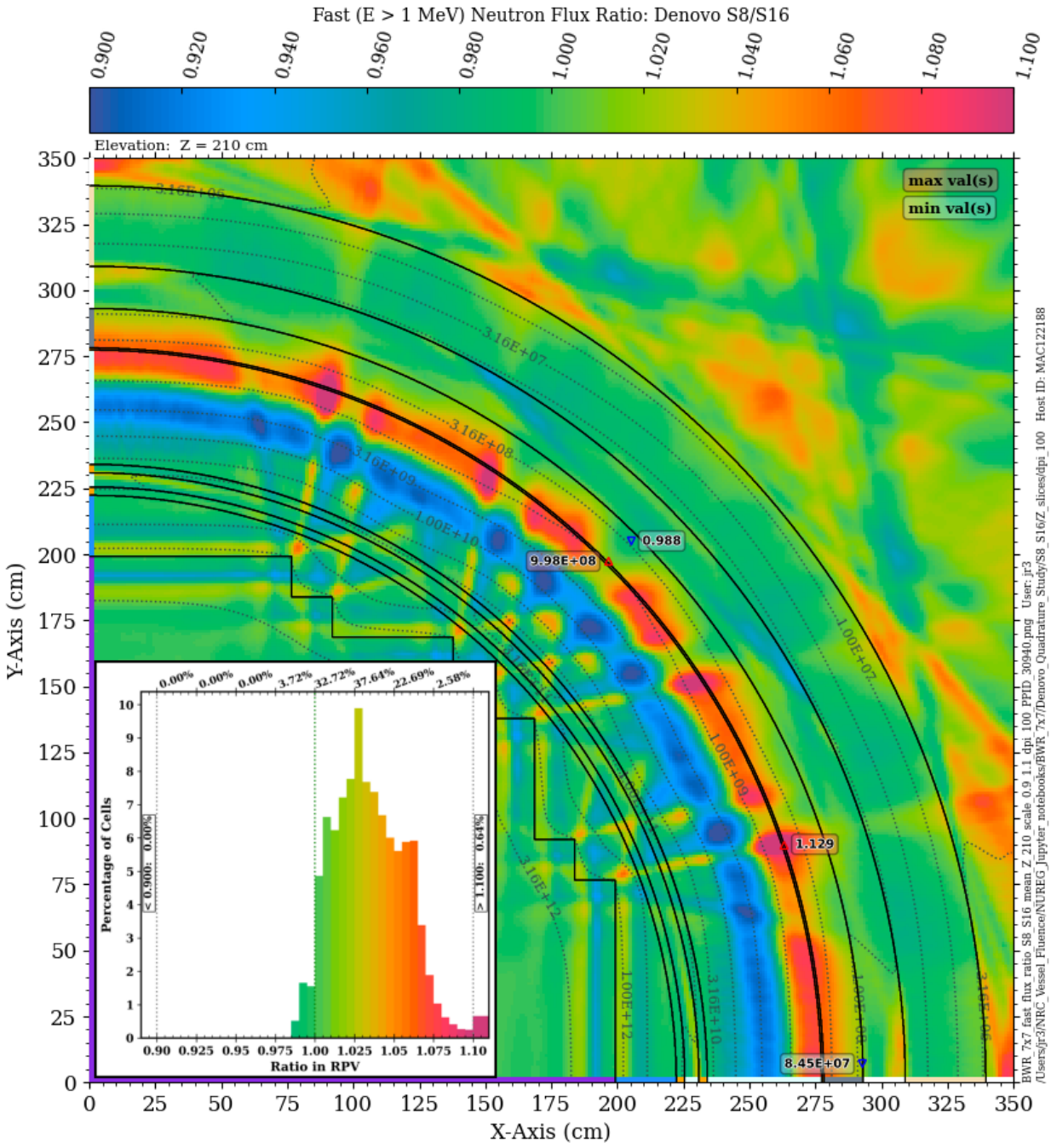

Figure 7-34 Fast neutron flux ratio in the BWR reference model: S8/S16 quadrature. Plan view at Z = 210 cm *The contour lines are the fast flux from the S16 solution. Minimum and maximum values within the RPV are shown for the S16 fast flux and the S8/S16 fast flux ratio.*

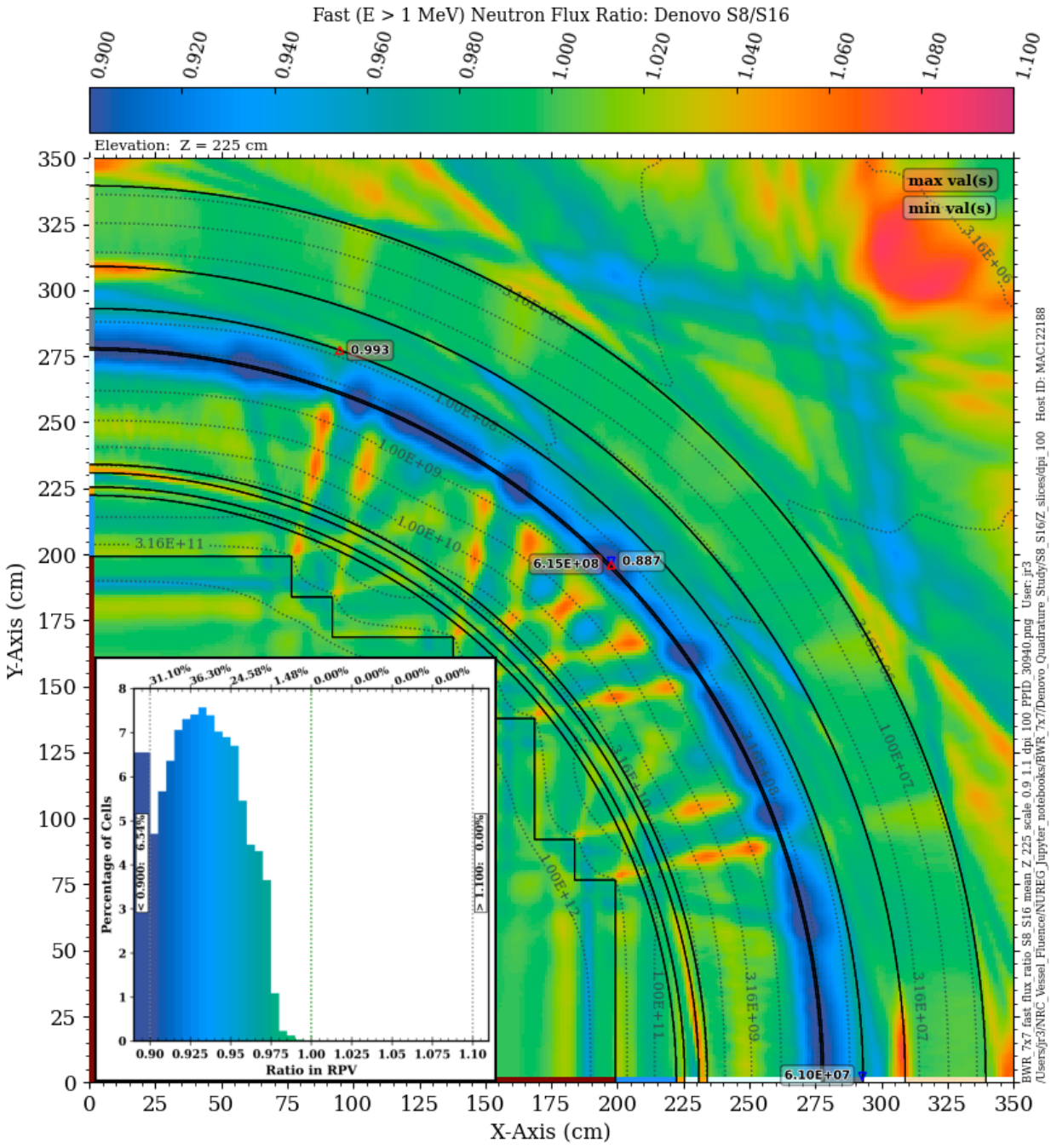

Figure 7-35 Fast neutron flux ratio in the BWR reference model: S8/S16 quadrature. Plan view at Z = 225 cm *The contour lines are the fast flux from the S16 solution. Minimum and maximum values within the RPV are shown for the S16 fast flux and the S8/S16 fast flux ratio.*

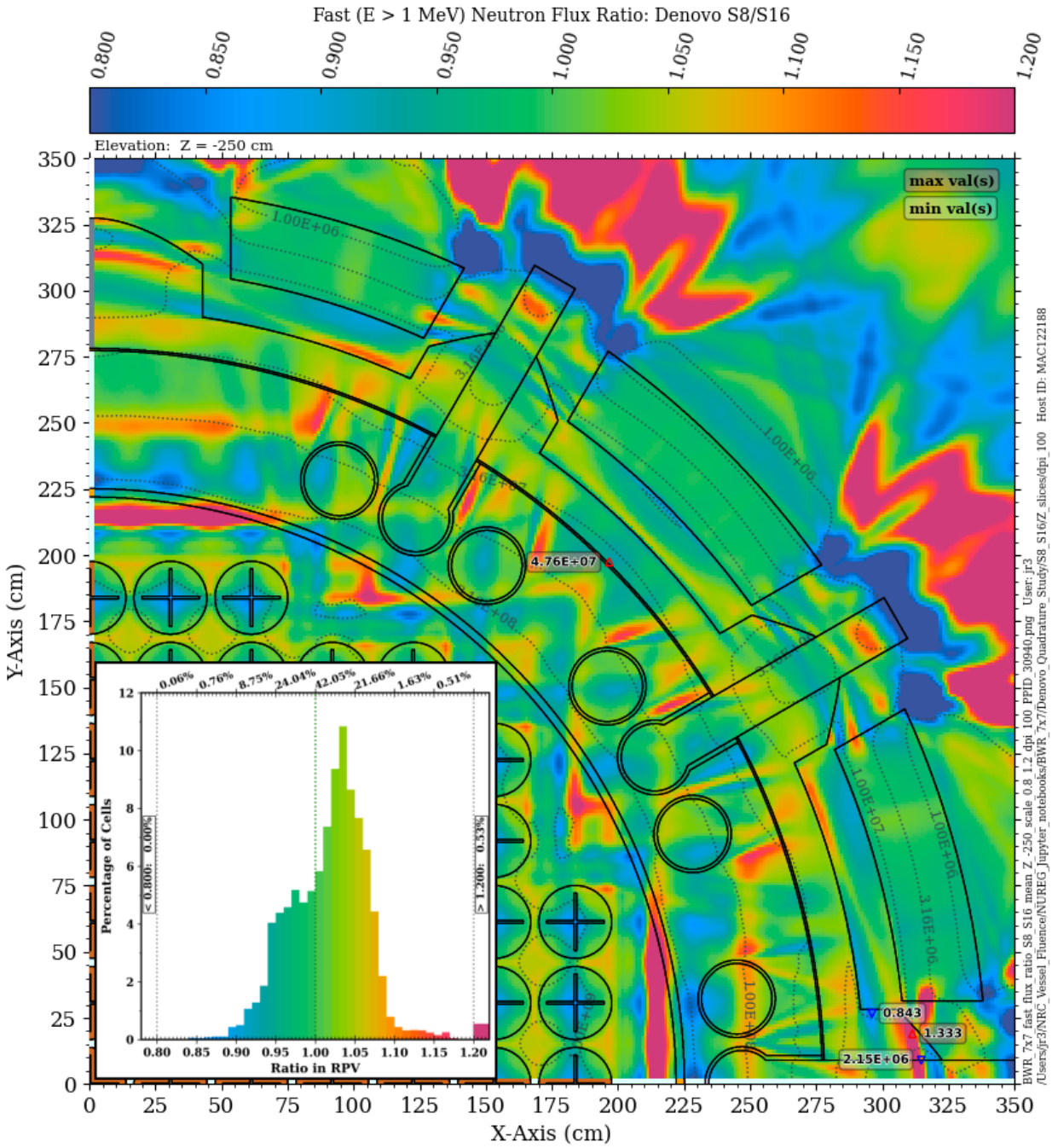

Figure 7-36 Fast neutron flux ratio in the BWR reference model: S8/S16 quadrature. Plan view at Z = -250 cm *The contour lines are the fast flux from the S16 solution. Minimum and maximum values within the RPV are shown for the S16 fast flux and the S8/S16 fast flux ratio. Note the change in scale relative to the three previous figures.*

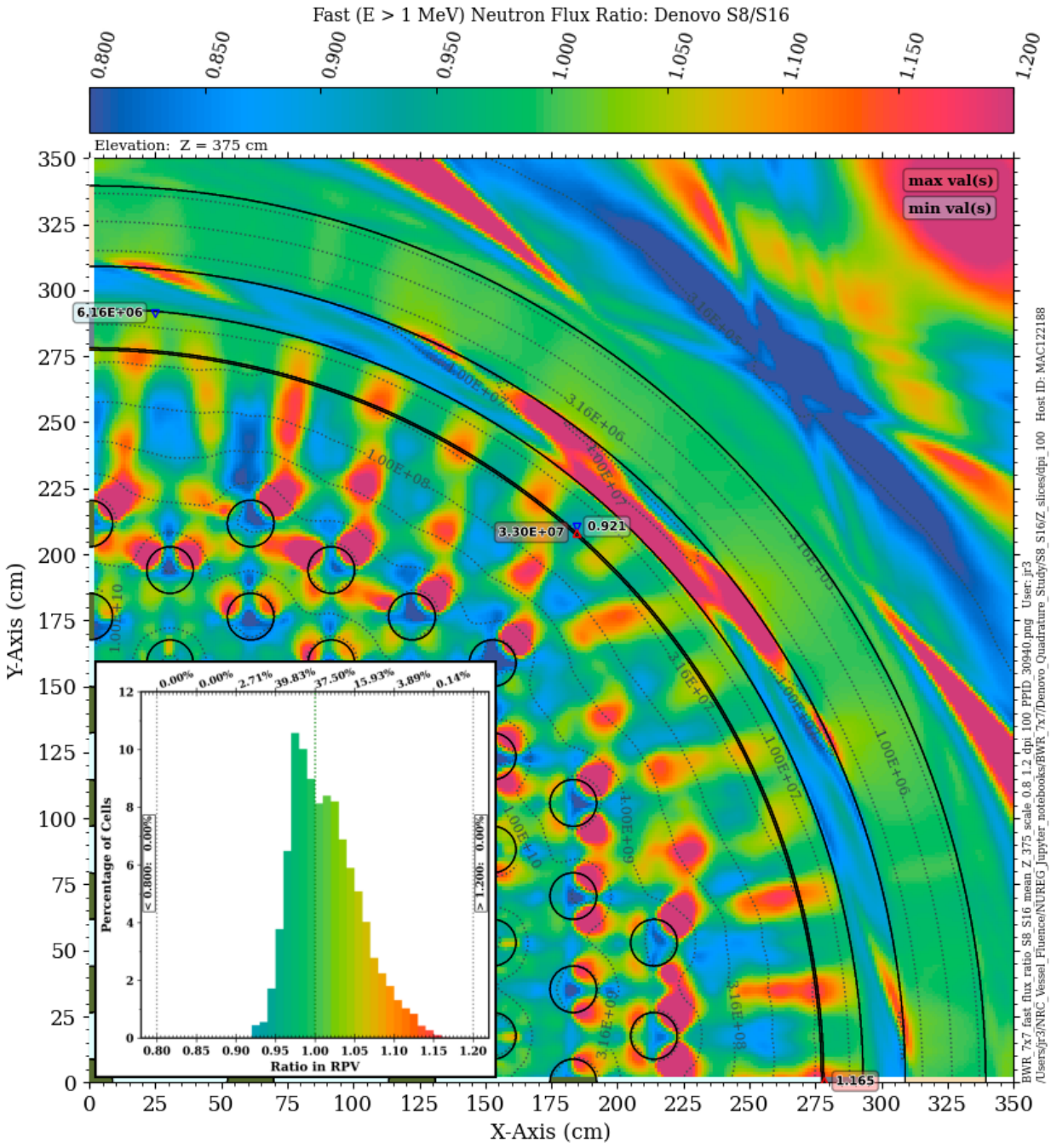

Figure 7-37 Fast neutron flux ratio in the BWR reference model: S8/S16 quadrature. Plan view at Z = 375 cm *The contour lines are the fast flux from the S16 solution. Minimum and maximum values within the RPV are shown for the S16 fast flux and the S8/S16 fast flux ratio.*

7.4.2 Denovo Solutions: S16 vs QR8T

Ratios of the BWR fast flux for S16 and QR8T Denovo solutions are provided in Figure 7-38 through Figure 7-44. The S16/QR8T fast flux ratios on the inner and outer surfaces of both the RPV and the shroud (Figure 7-38 and Figure 7-39, respectively) show much less variation than the S8/S16 ratios, as expected. At the core midplane (Figure 7-40), the two solutions differ by more than 2.5% in less than 2% of the RPV cells. The appearance of ray effects due to axial and azimuthal variations at Z = 210 cm and Z = 225 cm (Figure 7-41 and Figure 7-42) is still present, although their magnitude is substantially attenuated. At the elevations of Z = -250 cm (Figure 7-43)and Z = 375 cm (Figure 7-44), the solution agreement is also markedly improved relative to the S8/S16 ratios.

7.4.3 Denovo Solutions: QR8T vs QR16T

The final BWR comparison is between QR8T and QR16T solutions. The QR8T/QR16T fast flux ratios are plotted in Figure 7-45 through Figure 7-51. Within the axial range of interest (from Z = -250 cm to Z = 375 cm), the QR8T and QR16T solutions agree within 5% in nearly all the RPV cells.

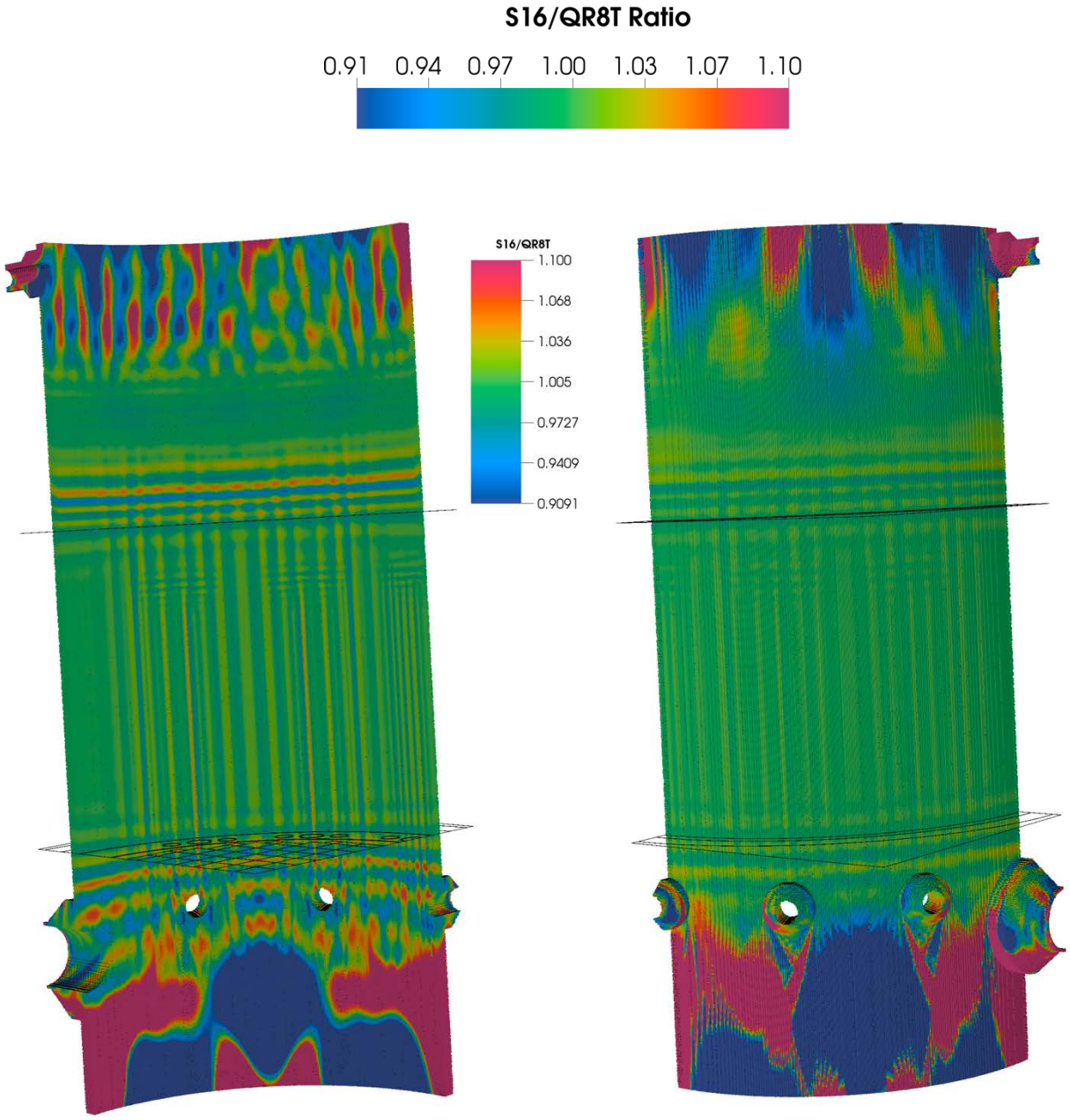

Figure 7-38 Fast neutron flux ratio on the inner and outer surfaces of the RPV for the BWR reference model: Denovo S16 solution relative to a QR8T solution *The boundary planes show the extent of the fuel assemblies.*

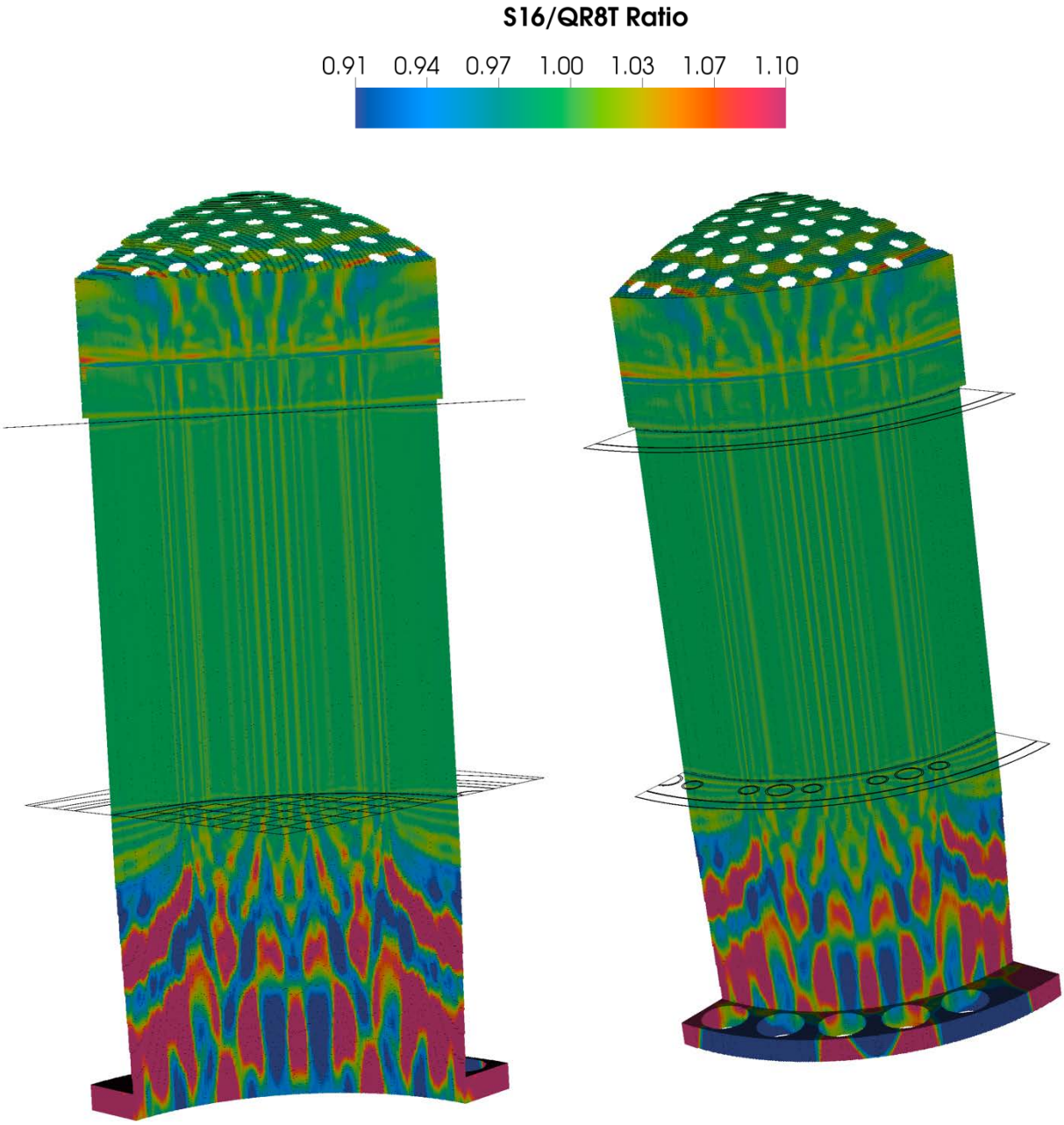

Figure 7-39 Fast neutron flux ratio on the inner and outer surfaces of the shroud for the BWR reference model: Denovo S16 solution relative to a QR8T solution *The boundary planes show the extent of the fuel assemblies.*

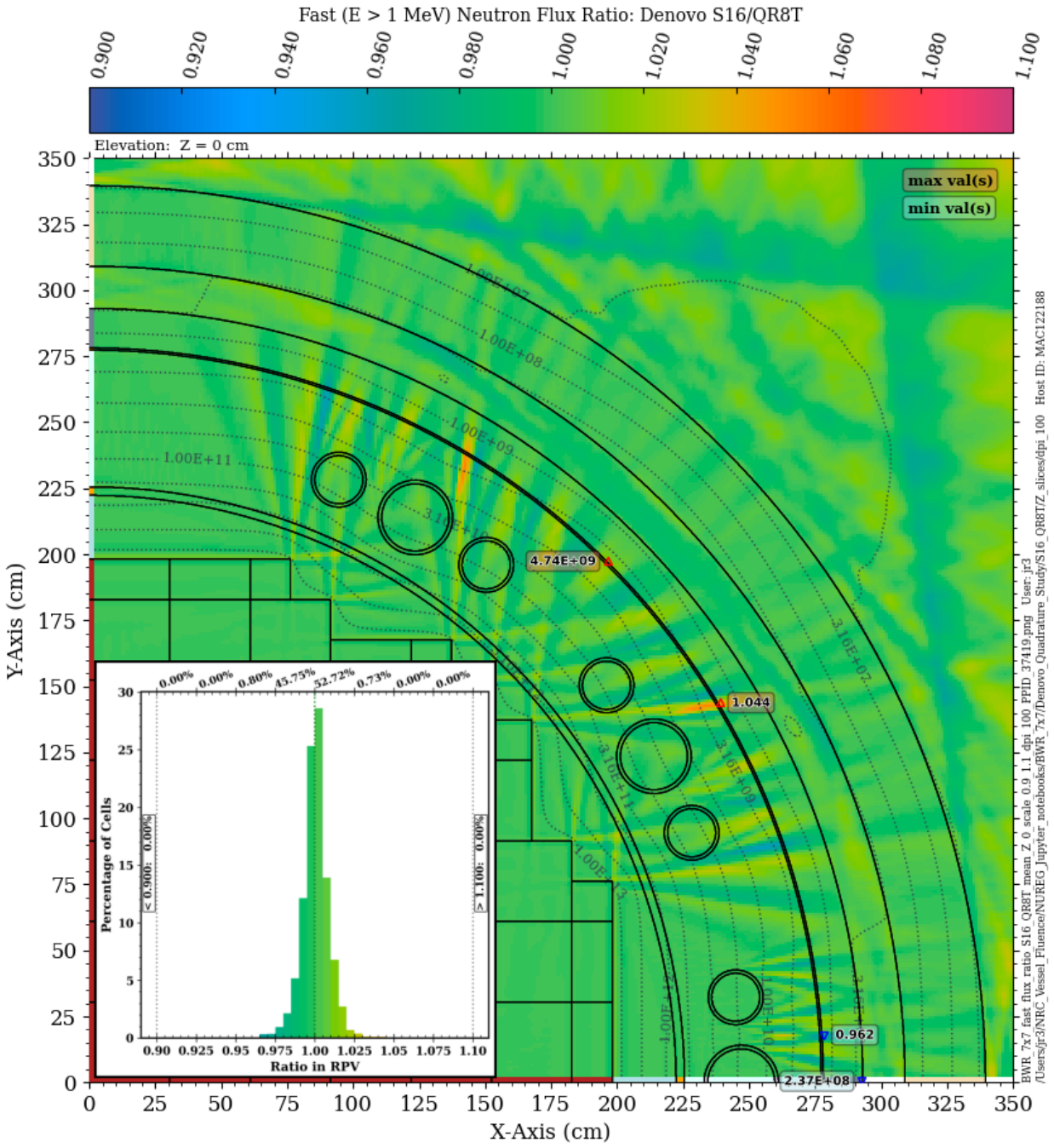

Figure 7-40 Fast neutron flux ratio in the BWR reference model: S16/QR8T quadrature. Plan view at Z = 0 cm *The contour lines are the fast flux from the QR8T solution. Minimum and maximum values within the RPV are shown for the QR8T fast flux and the S16/QR8T fast flux ratio.*

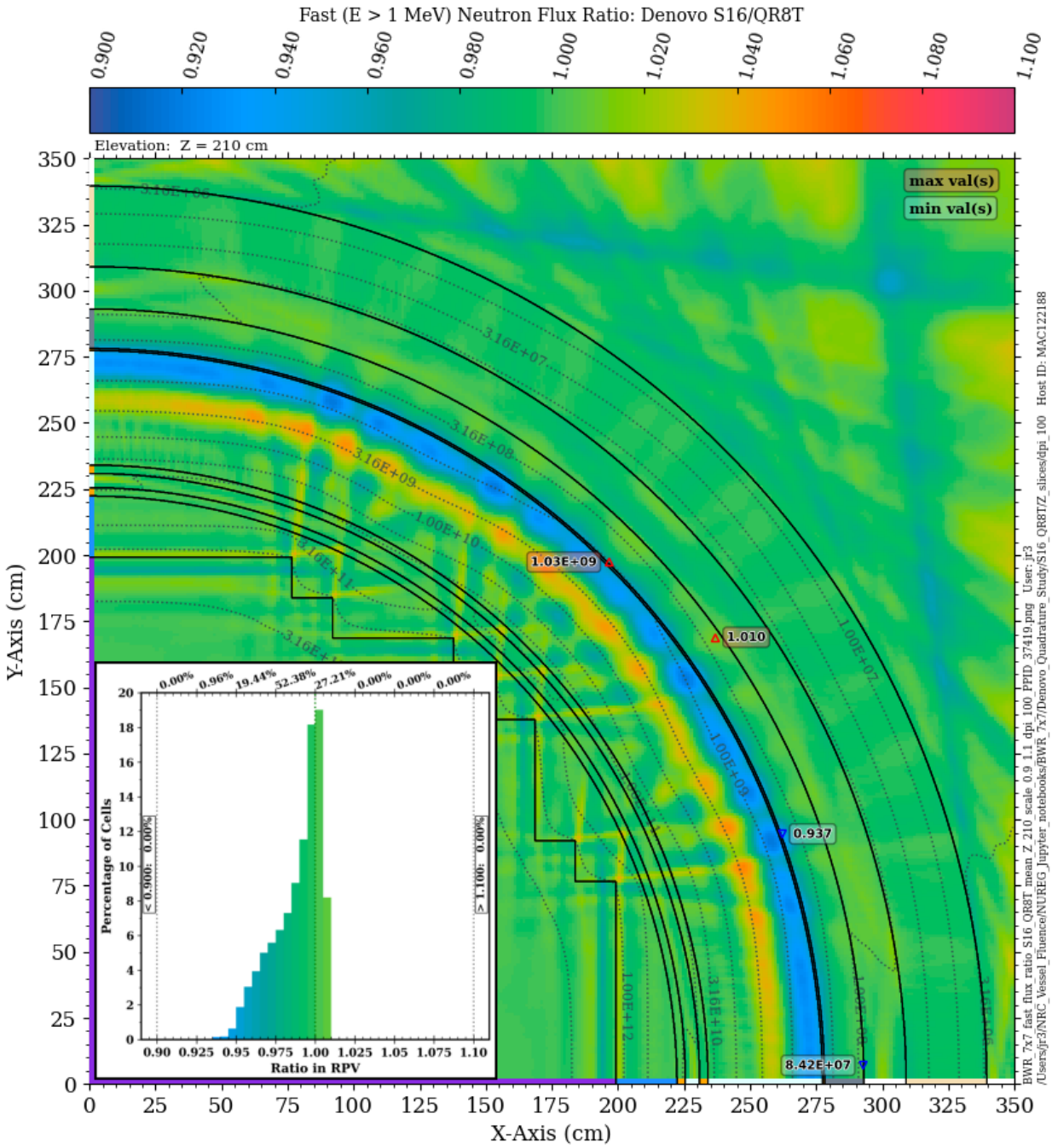

Figure 7-41 Fast neutron flux ratio in the BWR reference model: S16/QR8T quadrature. Plan view at Z = 210 cm *The contour lines are the fast flux from the QR8T solution. Minimum and maximum values within the RPV are shown for the QR8T fast flux and the S16/QR8T fast flux ratio.*

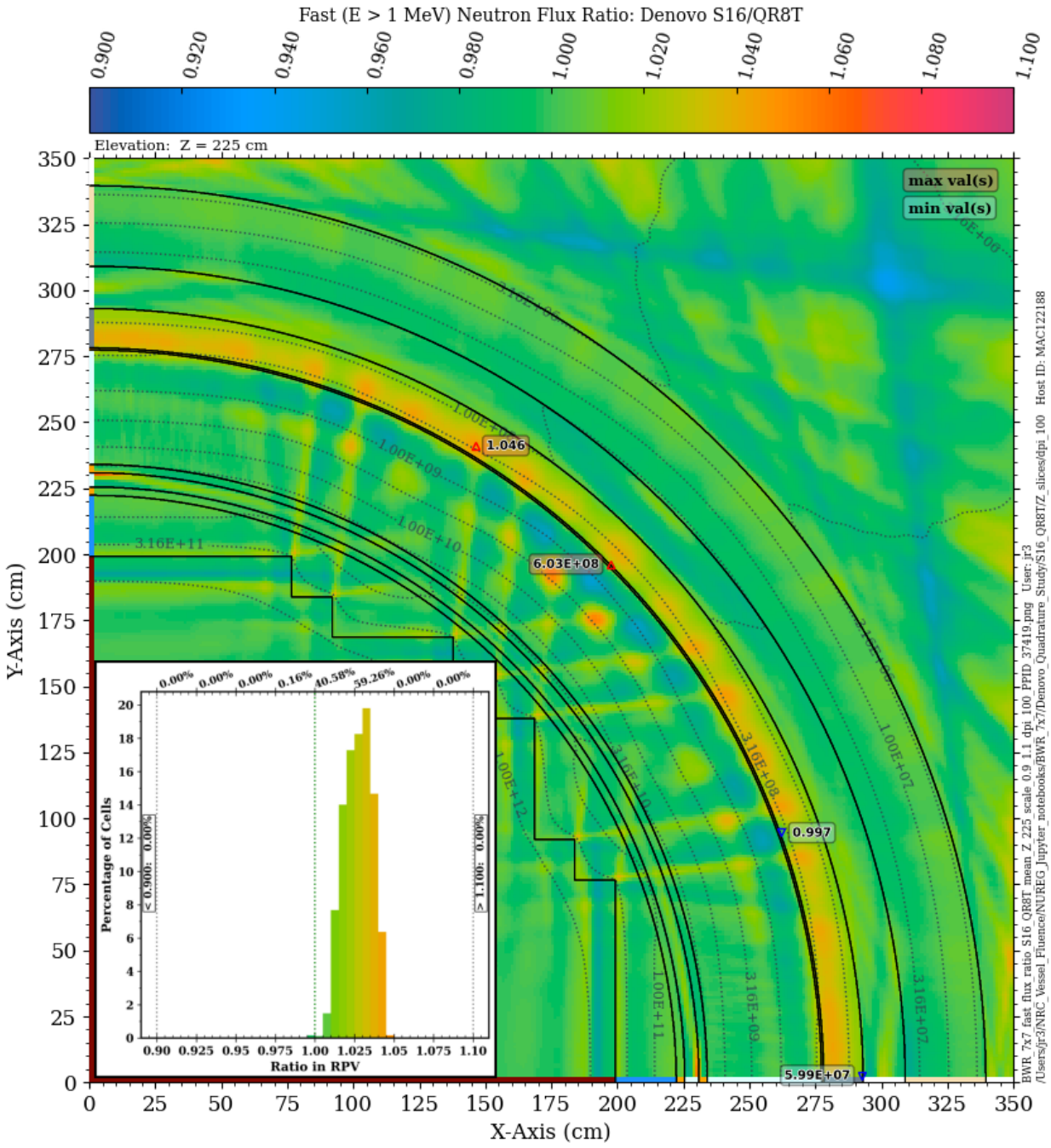

Figure 7-42 Fast neutron flux ratio in the BWR reference model: S16/QR8T quadrature. Plan view at Z = 225 cm *The contour lines are the fast flux from the QR8T solution. Minimum and maximum values within the RPV are shown for the QR8T fast flux and the S16/QR8T fast flux ratio.*

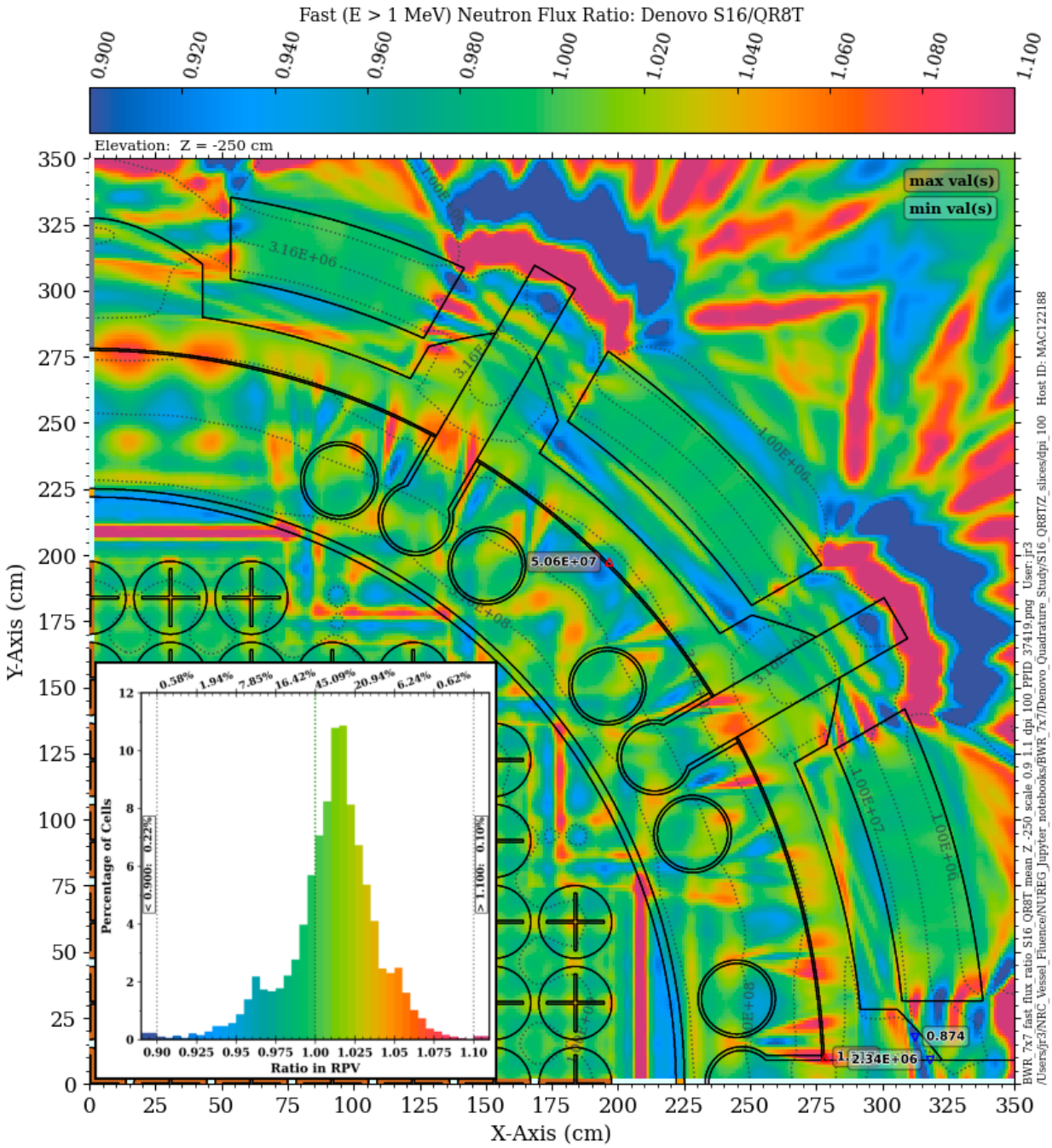

Figure 7-43 Fast neutron flux ratio in the BWR reference model: S16/QR8T quadrature. Plan view at Z = -250 cm *The contour lines are the fast flux from the QR8T solution. Minimum and maximum values within the RPV are shown for the QR8T fast flux and the S16/QR8T fast flux ratio.*

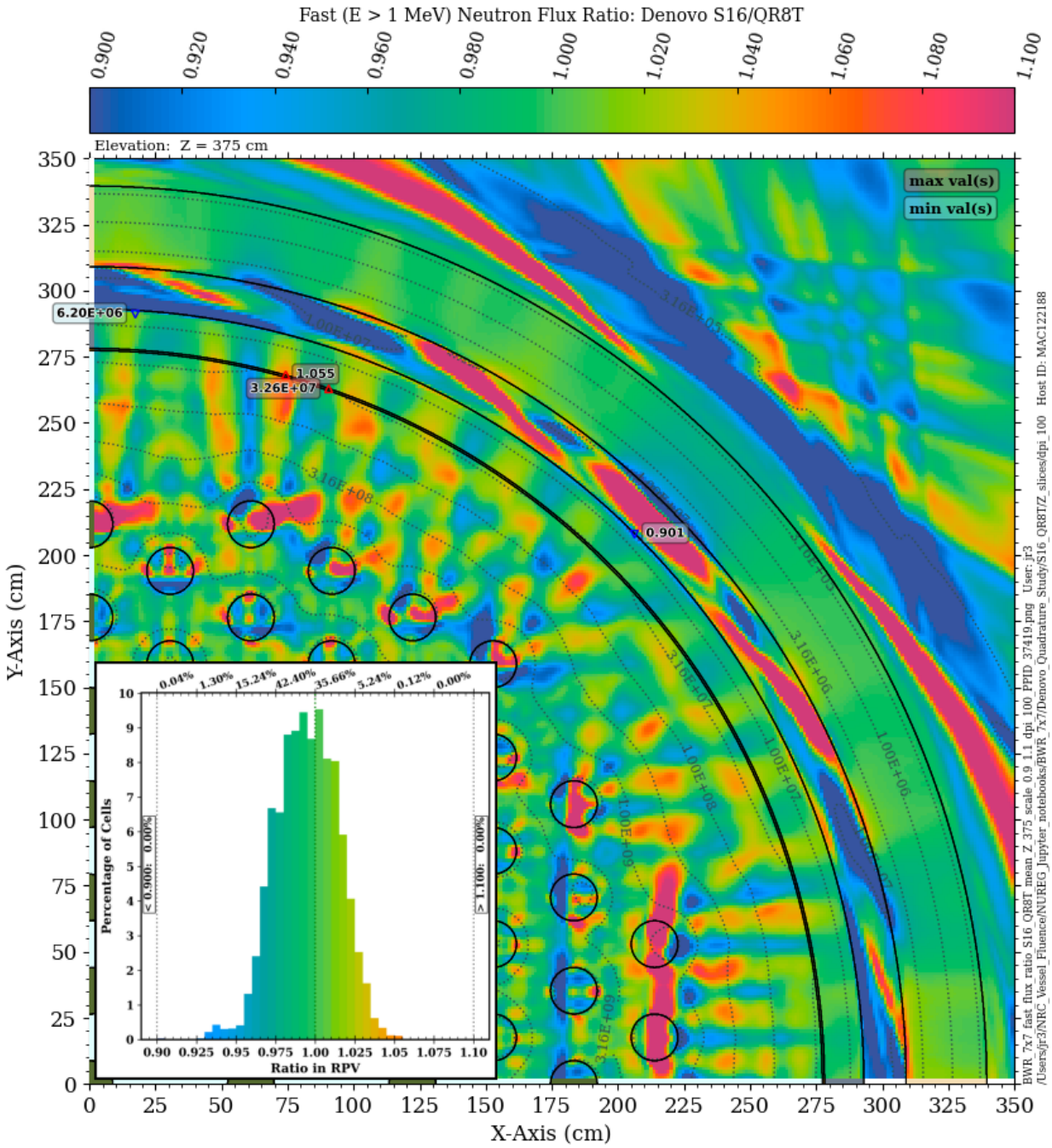

Figure 7-44 Fast neutron flux ratio in the BWR reference model: S16/QR8T quadrature. Plan view at Z = 375 cm *The contour lines are the fast flux from the QR8T solution. Minimum and maximum values within the RPV are shown for the QR8T fast flux and the S16/QR8T fast flux ratio.*

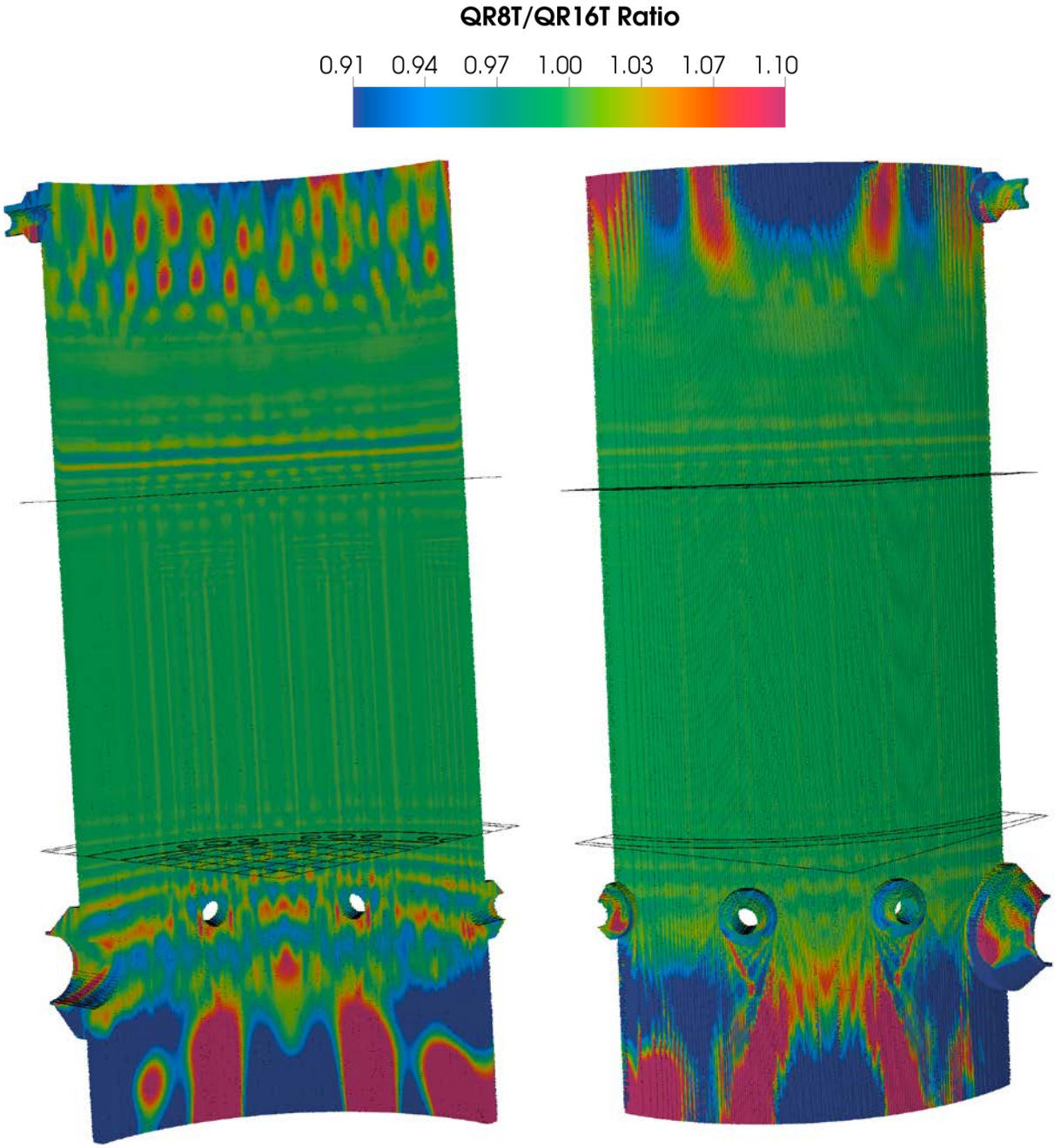

Figure 7-45 Fast neutron flux ratio on the inner and outer surfaces of the RPV for the BWR reference model: Denovo QR8T solution relative to a QR16T solution *The boundary planes show the extent of the fuel assemblies.*

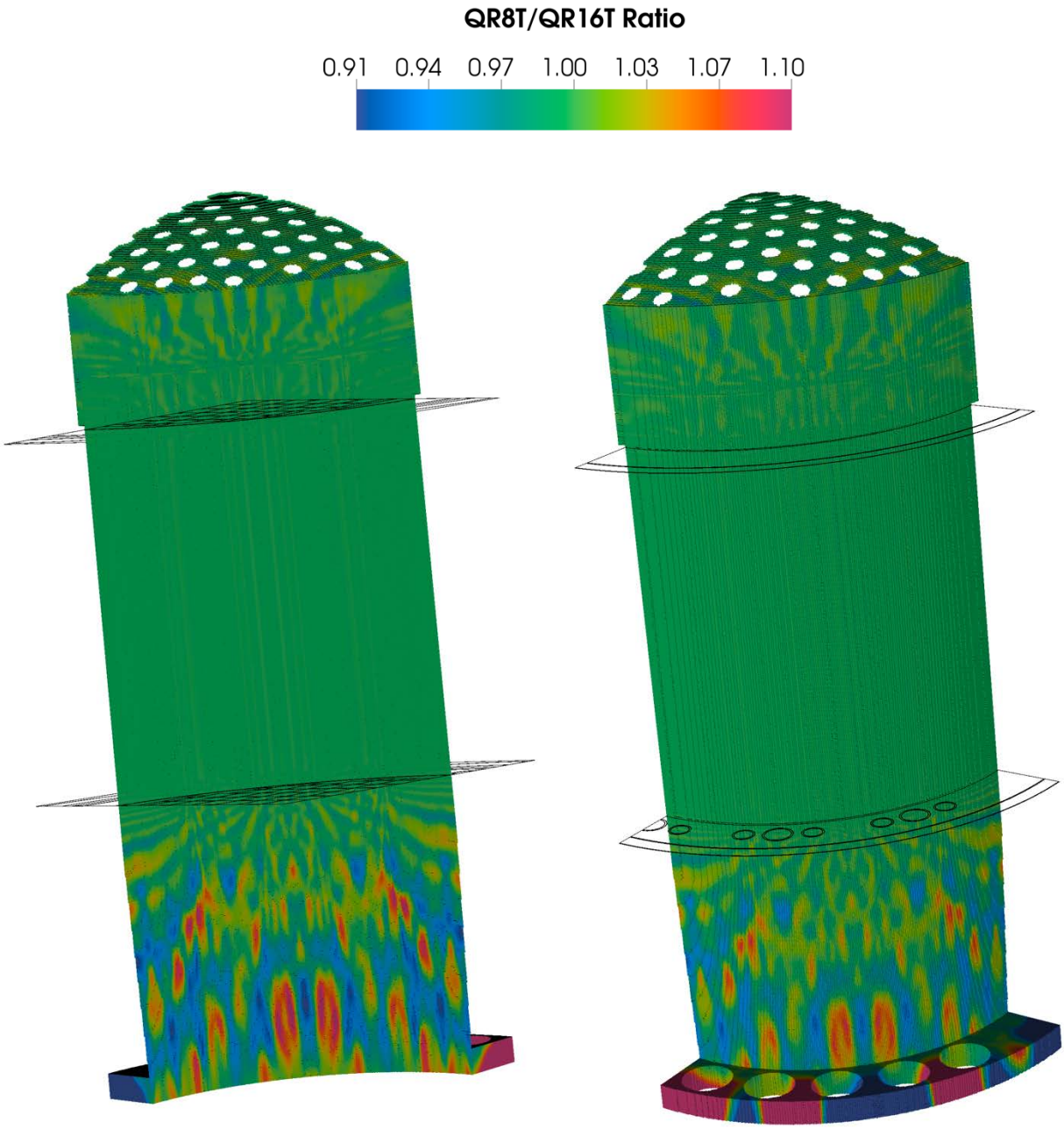

Figure 7-46 Fast neutron flux ratio on the inner and outer surfaces of the shroud for the BWR reference model: Denovo QR8T solution relative to a QR16T solution *The boundary planes show the extent of the fuel assemblies.*

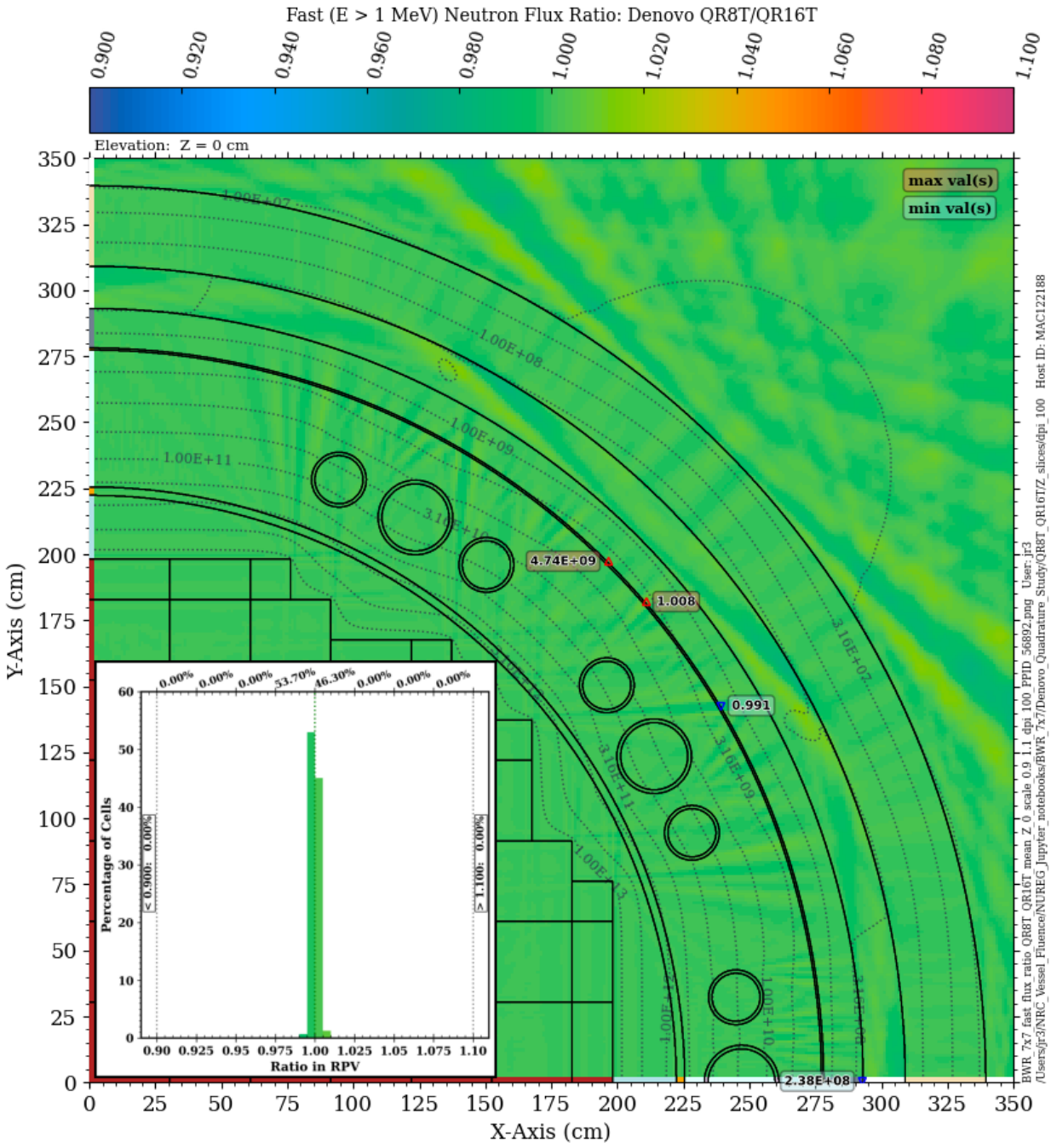

Figure 7-47 Fast neutron flux ratio in the BWR reference model: QR8T/QR16T quadrature. Plan view at Z = 0 cm *The contour lines are the fast flux from the QR16T solution. Minimum and maximum values within the RPV are shown for the QR16T fast flux and the QR8T/QR16T fast flux ratio.*

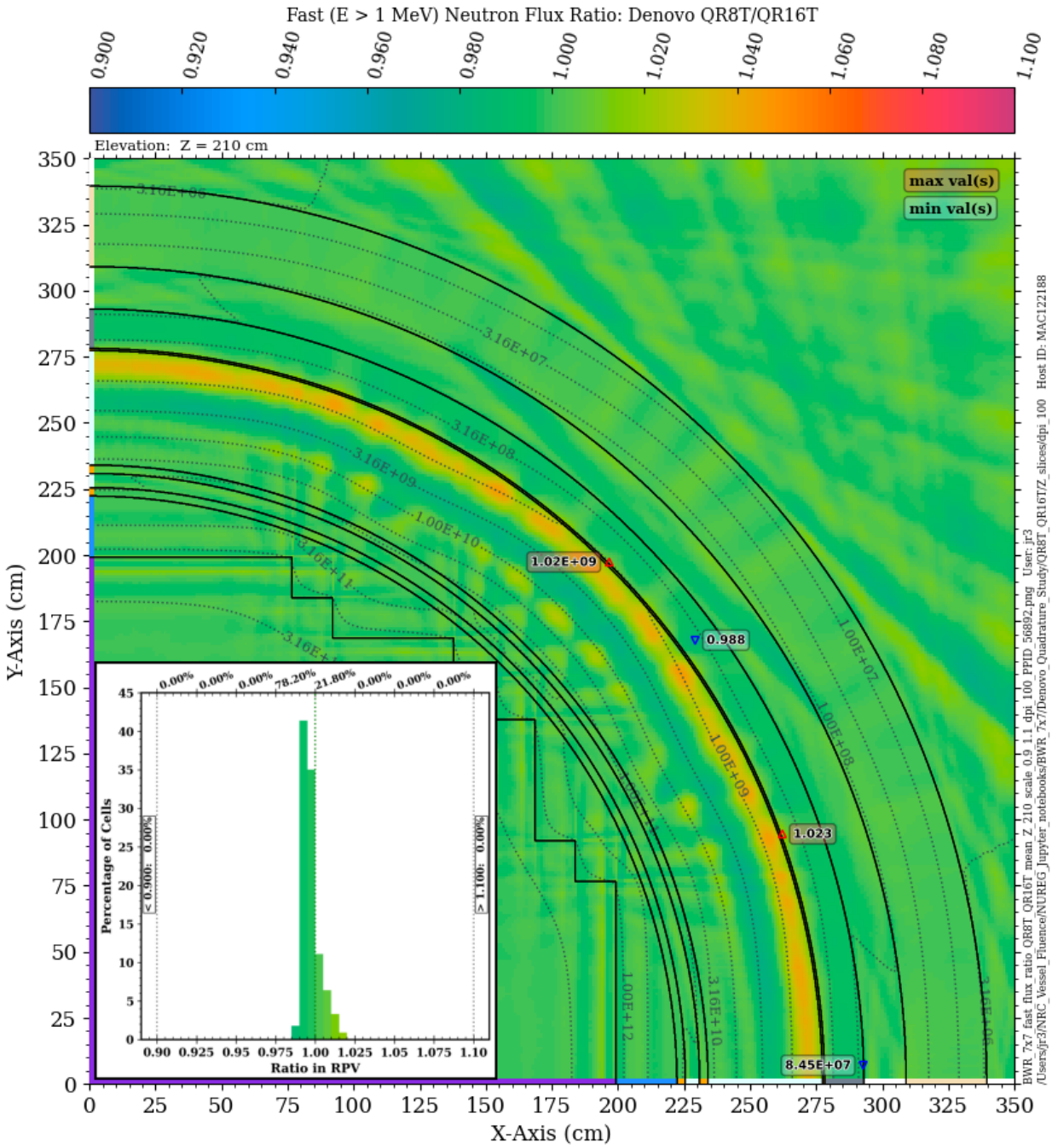

Figure 7-48 Fast neutron flux ratio in the BWR reference model: QR8T/QR16T quadrature. Plan view at Z = 210 cm *The contour lines are the fast flux from the QR16T solution. Minimum and maximum values within the RPV are shown for the QR16T fast flux and the QR8T/QR16T fast flux ratio.*

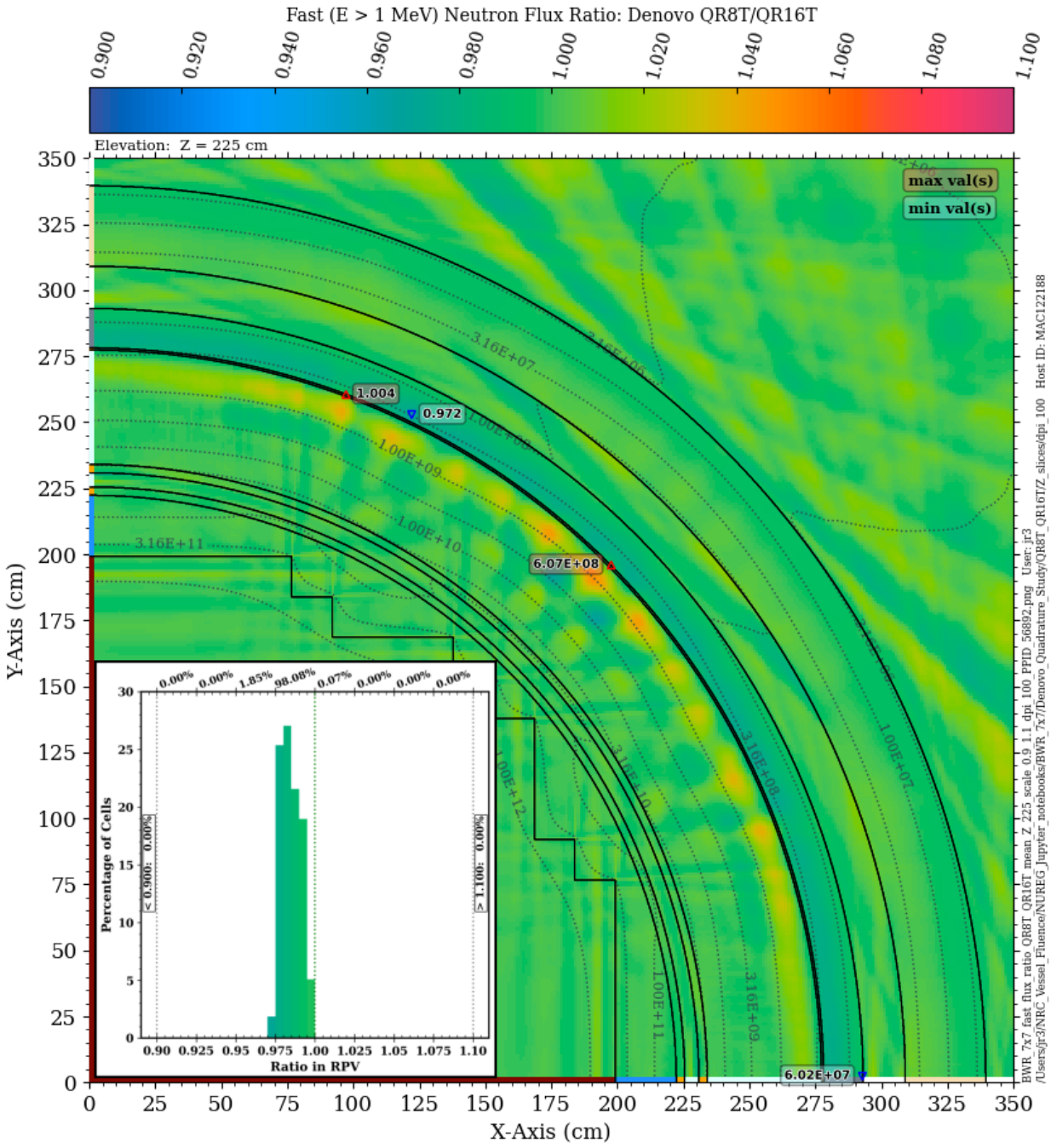

Figure 7-49 Fast neutron flux ratio in the BWR reference model: QR8T/QR16T quadrature. Plan view at Z = 225 cm *The contour lines are the fast flux from the QR16T solution. Minimum and maximum values within the RPV are shown for the QR16T fast flux and the QR8T/QR16T fast flux ratio.*

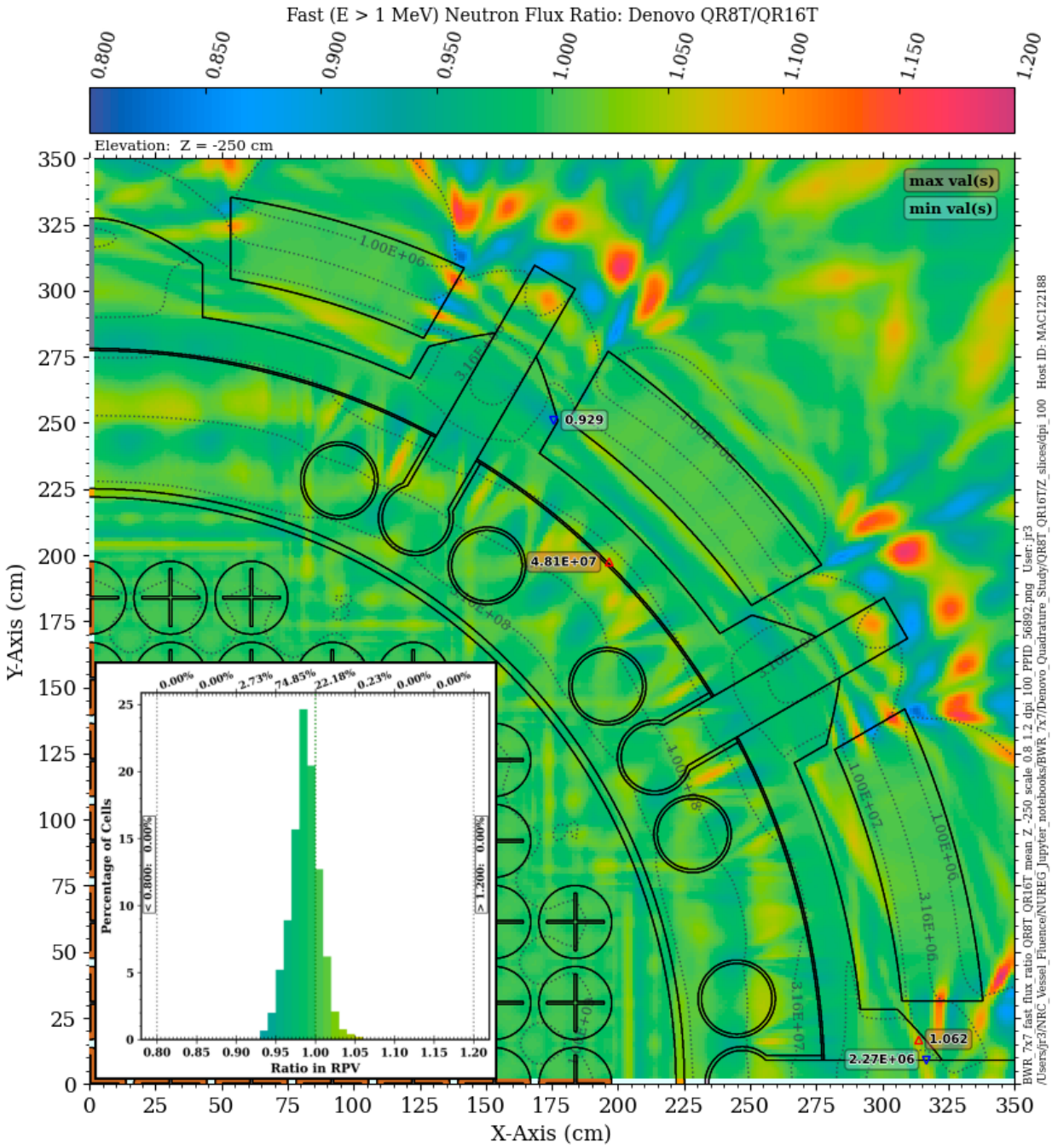

Figure 7-50 Fast neutron flux ratio in the BWR reference model: QR8T/QR16T quadrature. Plan view at Z = -250 cm *The contour lines are the fast flux from the QR16T solution. Minimum and maximum values within the RPV are shown for the QR16T fast flux and the QR8T/QR16T fast flux ratio. Note the change in scale relative to the three previous plots.*

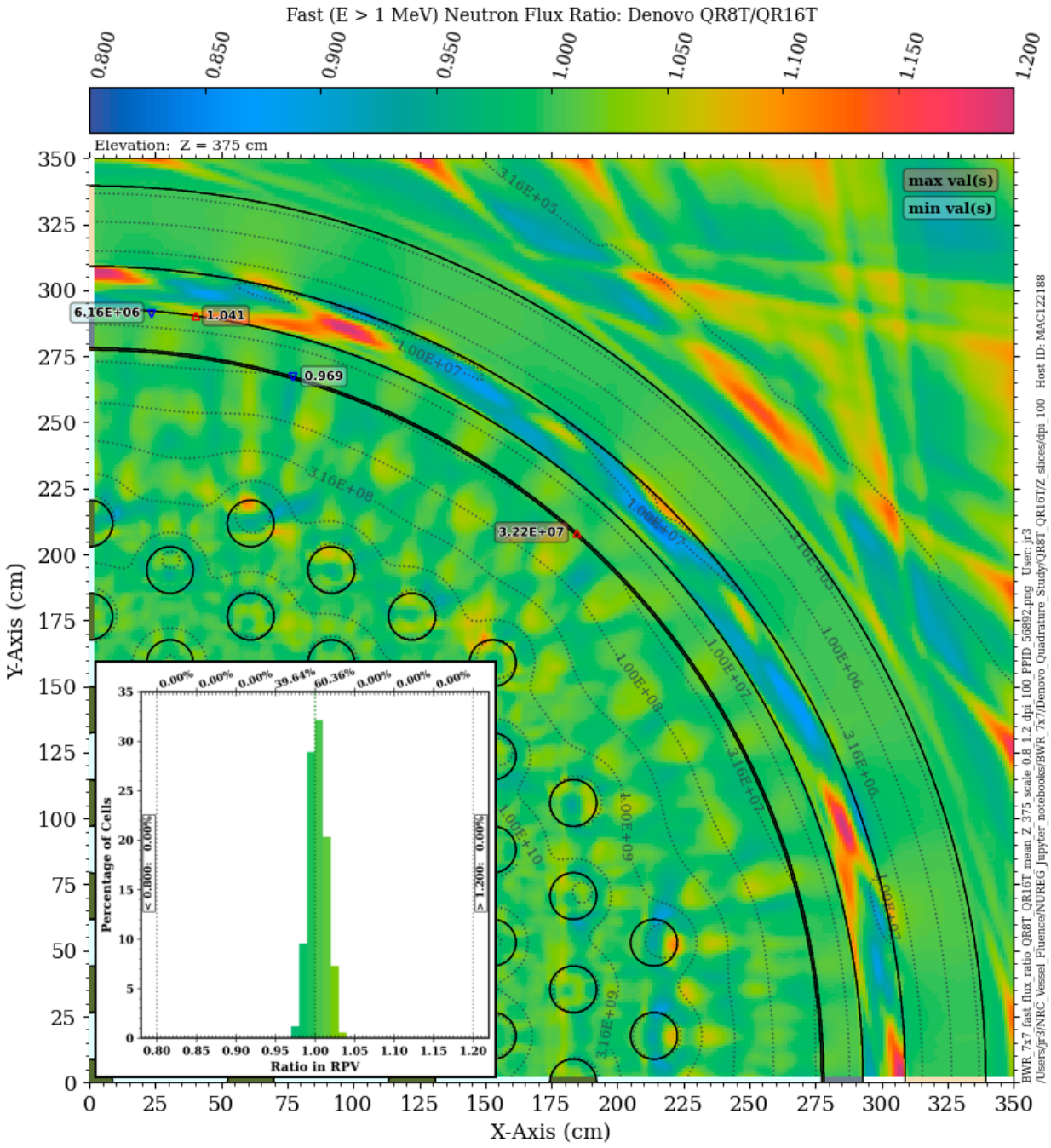

Figure 7-51 Fast neutron flux ratio in the BWR reference model: QR8T/QR16T quadrature. Plan view at Z = 375 cm *The contour lines are the fast flux from the QR16T solution. Minimum and maximum values within the RPV are shown for the QR16T fast flux and the QR8T/QR16T fast flux ratio.*

7.5 Comparison of Denovo Solutions to Multigroup Shift Solutions: PWR model

The comparisons presented in Section 7.3 and Section 7.4 demonstrate that quadrature sensitivity (i.e., the variation between two discrete ordinates calculations in which the only parameter that is modified is the quadrature set) for RPV fluence calculations is more pronounced in the extended beltline region compared to the traditional beltline region.

As a means of determining the effect of selection of quadrature sets on RPV fluence calculations, a Shift hybrid Monte Carlo calculation was performed using the homogenized core PWR model and the BUGLE-B7 MG library. The Shift fast flux was tallied using a mesh tally with the uniform 1 cm mesh that was used in the Denovo calculations. Because the Shift and Denovo calculations employ the same model and same MG cross sections, and the Denovo mesh was demonstrated to provide convergence of the Denovo solution with respect to mesh, the ratios of the Denovo calculations to the Shift solution provide a means of effectively isolating the quadrature effect in the Denovo calculations.

The Denovo S8, S16, QR8T, and QR16T solutions are compared to the Shift solution in Figure 7-52 through Figure 7-67. The results of these comparisons can be summarized as follows.

Comparison of Figure 7-52 with Figure 7-2 confirms that the ray effects seen in Figure 7-2 are indeed an indication of (minor) deficiencies in the S8 quadrature, even within the traditional beltline region. As noted in Section 7.3.1, these ray effects are associated with the corner fuel assemblies along the periphery of the core. Figure 7-53 and Figure 7-54 confirm the presence of significant ray effects for the S8 solution in the cavity gap and adjacent portions of the RPV and bioshield. Figure 7-55 confirms the presence of ray effects due to the former plate material interfaces, which is consistent with Figure 7-1 and Figure 7-2. However, as shown in the histograms, there is little indication of overall bias until the distance from the core midplane is large (Figure 7-54).

Comparison of the S16 and QR8T quadrature results is instructive, as both sets contain 36 angles per octant and thus have equivalent computational footprints. At the core midplane, both the S16 and QR8T solutions show excellent agreement with the BUGLE-B7 Shift solution, although the S16 solution (Figure 7-56) shows slightly more evidence of ray effects emanating from the corner fuel assemblies compared with the QR8T solution (Figure 7-60). At the extended beltline elevations of Z = -70 cm (Figure 7-57 and Figure 7-61) and Z = 470 cm (Figure 7-58 and Figure 7-62), both Denovo solutions exhibit ray effects in the cavity gap region. At both of these elevations, the QR8T solution provides better agreement than the S16 solution when compared to the Shift solution.

The same is true for elevation plots at an azimuthal angle of 270.5°, as shown in Figure 7-59 (S16) and Figure 7-63 (QR8T). While both solutions exhibit ray effects in the cavity gap, the QR8T solution does not have the ray effects that are seen in the S16 solution emanating from the former plates.

Denovo/Shift ratios for the QR16T solution are presented in Figure 7-64 through Figure 7-67. The QR16T quadrature, with 136 angles per octant, substantially reduces the ray effects in the cavity gap, although there are still locations in the extended beltline region where the QR16T Denovo solution differs from the Shift solution my 15% or more.

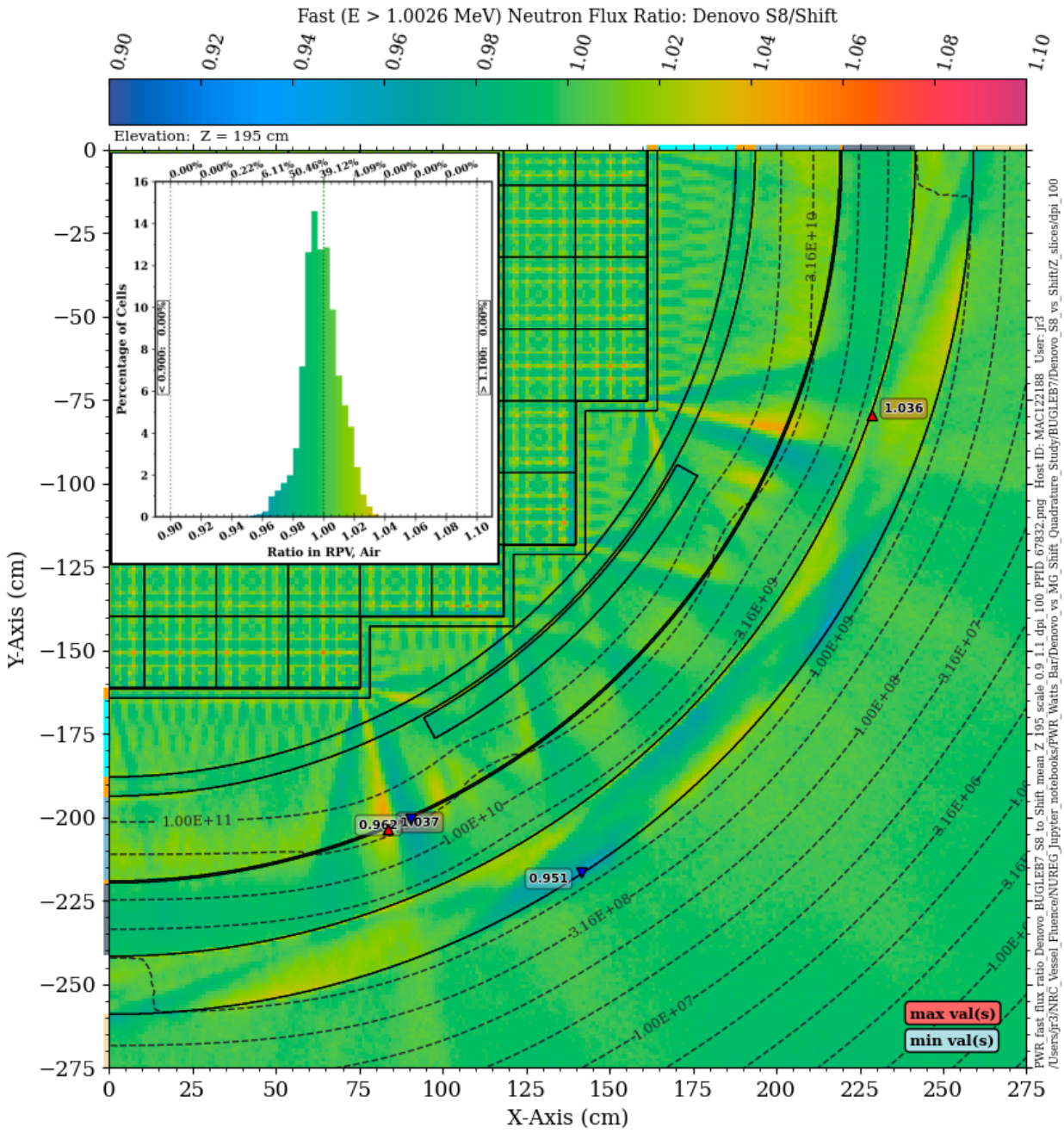

Figure 7-52 Ratio of the fast neutron flux from a BUGLE-B7 Denovo solution with S8 quadrature to a BUGLE-B7 Shift solution with the PWR model. Plan view at Z = 195 cm *The histogram plot shows the distribution of ratio values within the RPV and cavity gap.*

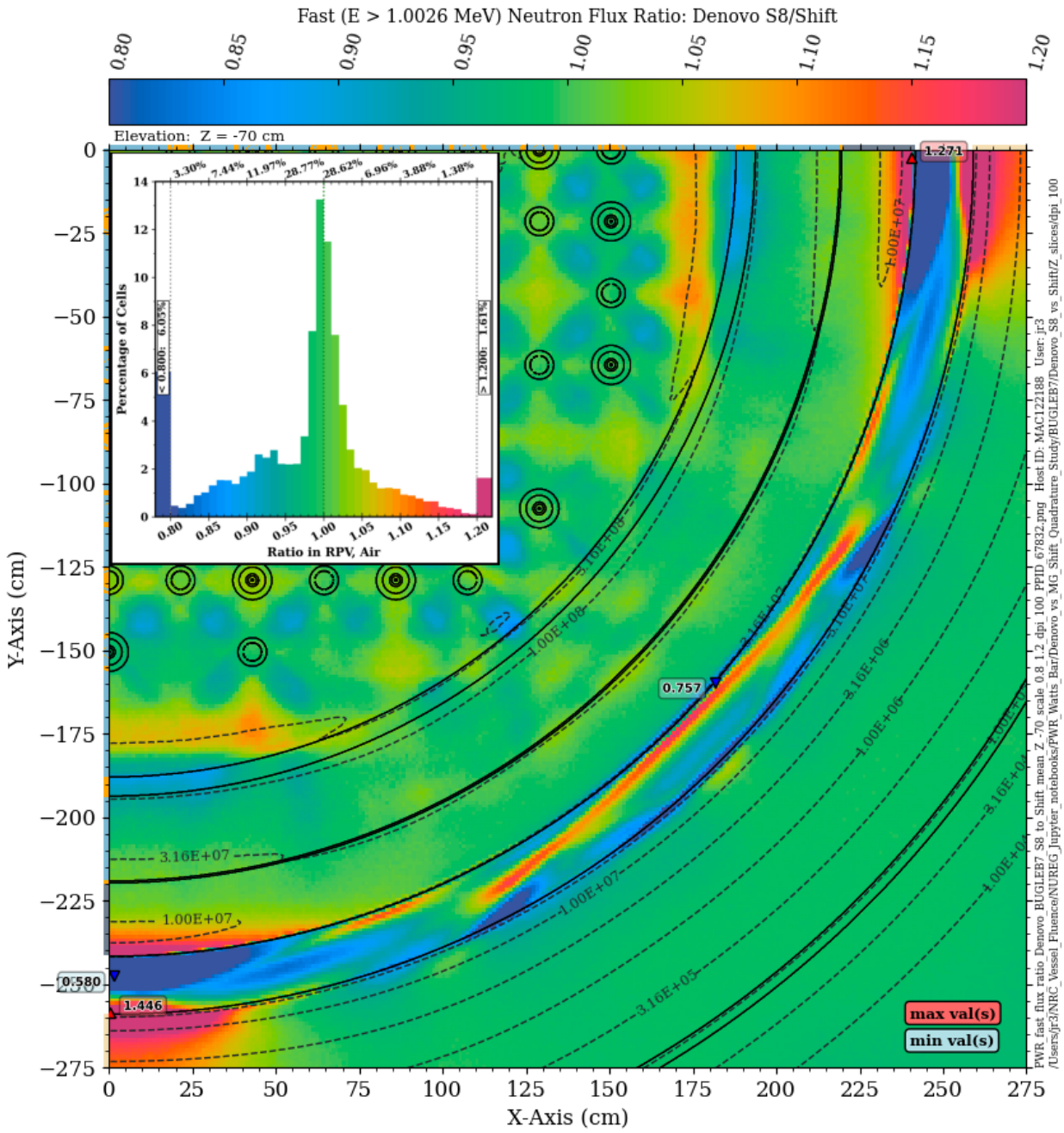

Figure 7-53 Ratio of the fast neutron flux from a BUGLE-B7 Denovo solution with S8 quadrature to a BUGLE-B7 Shift solution with the PWR model. Plan view at Z = -70 cm *The histogram plot shows the distribution of ratio values within the RPV and cavity gap. Note the change in scale relative to Figure 7-52.*

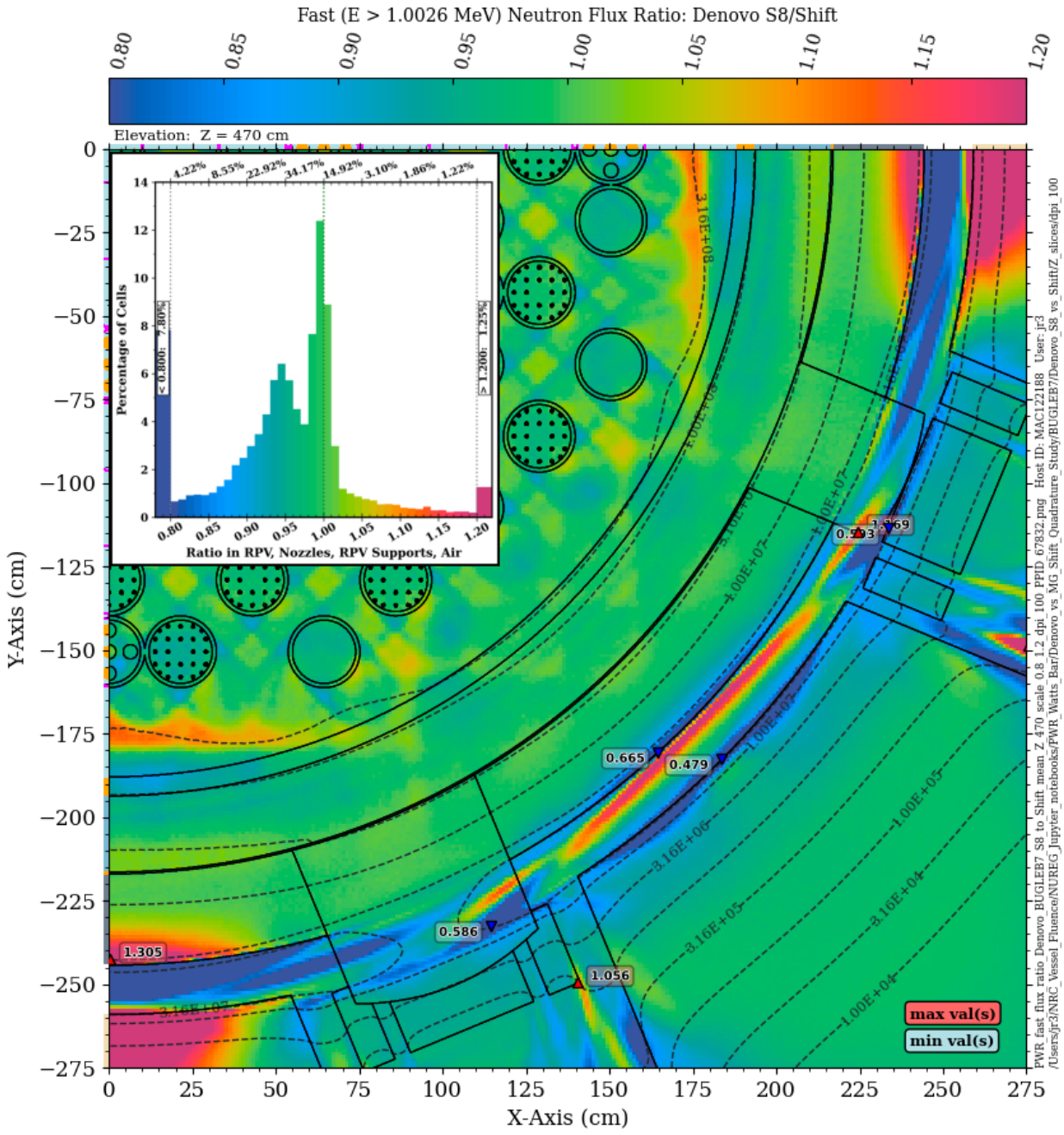

Figure 7-54 Ratio of the fast neutron flux from a BUGLE-B7 Denovo solution with S8 quadrature to a BUGLE-B7 Shift solution with the PWR model. Plan view at Z = 470 cm *The histogram plot shows the distribution of ratio values within the RPV, nozzle, vessel supports, and cavity gap.*

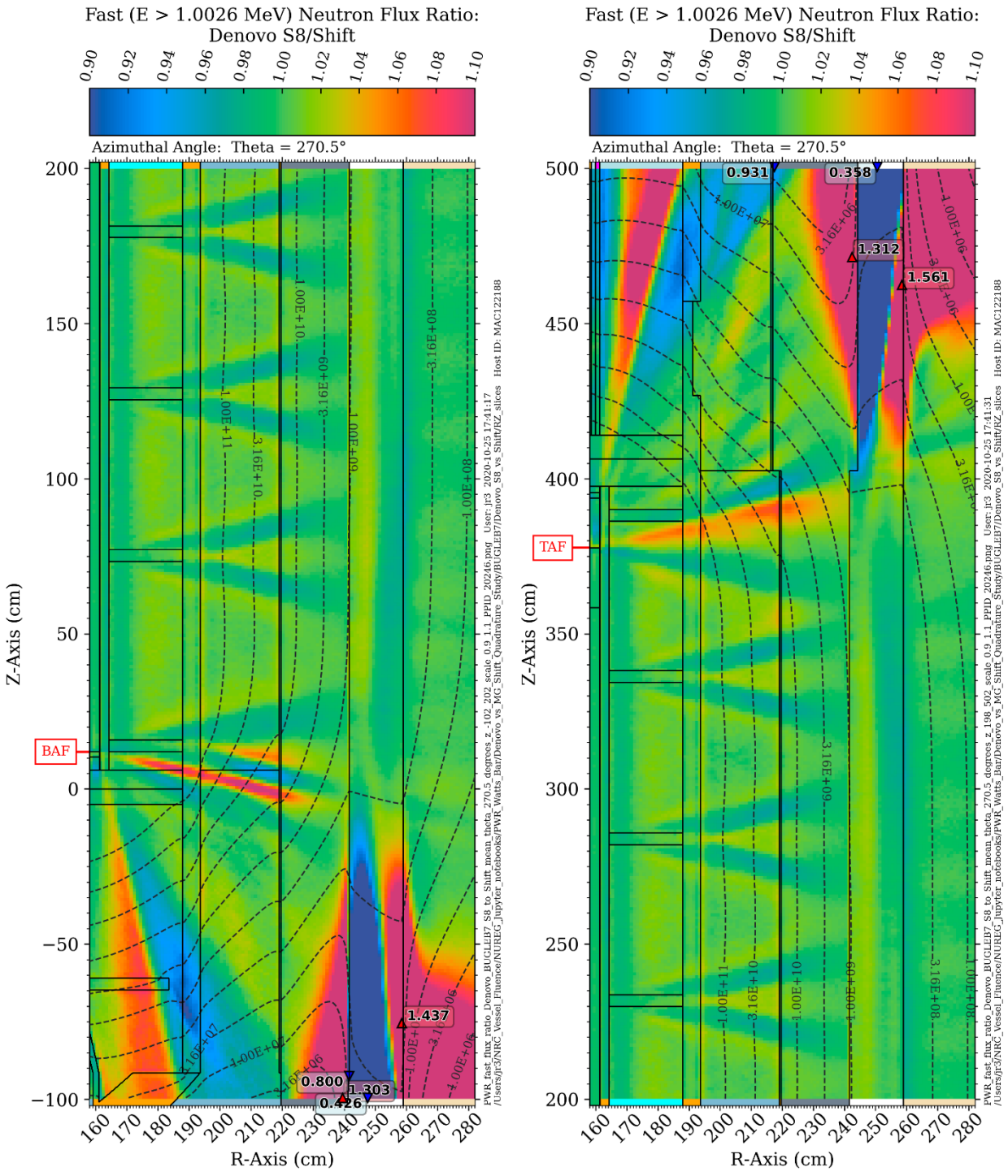

Figure 7-55 Ratio of the fast neutron flux from a BUGLE-B7 Denovo solution with S8 quadrature to a BUGLE-B7 Shift solution with the PWR model. Elevation view at an azimuthal angle of 270.5°

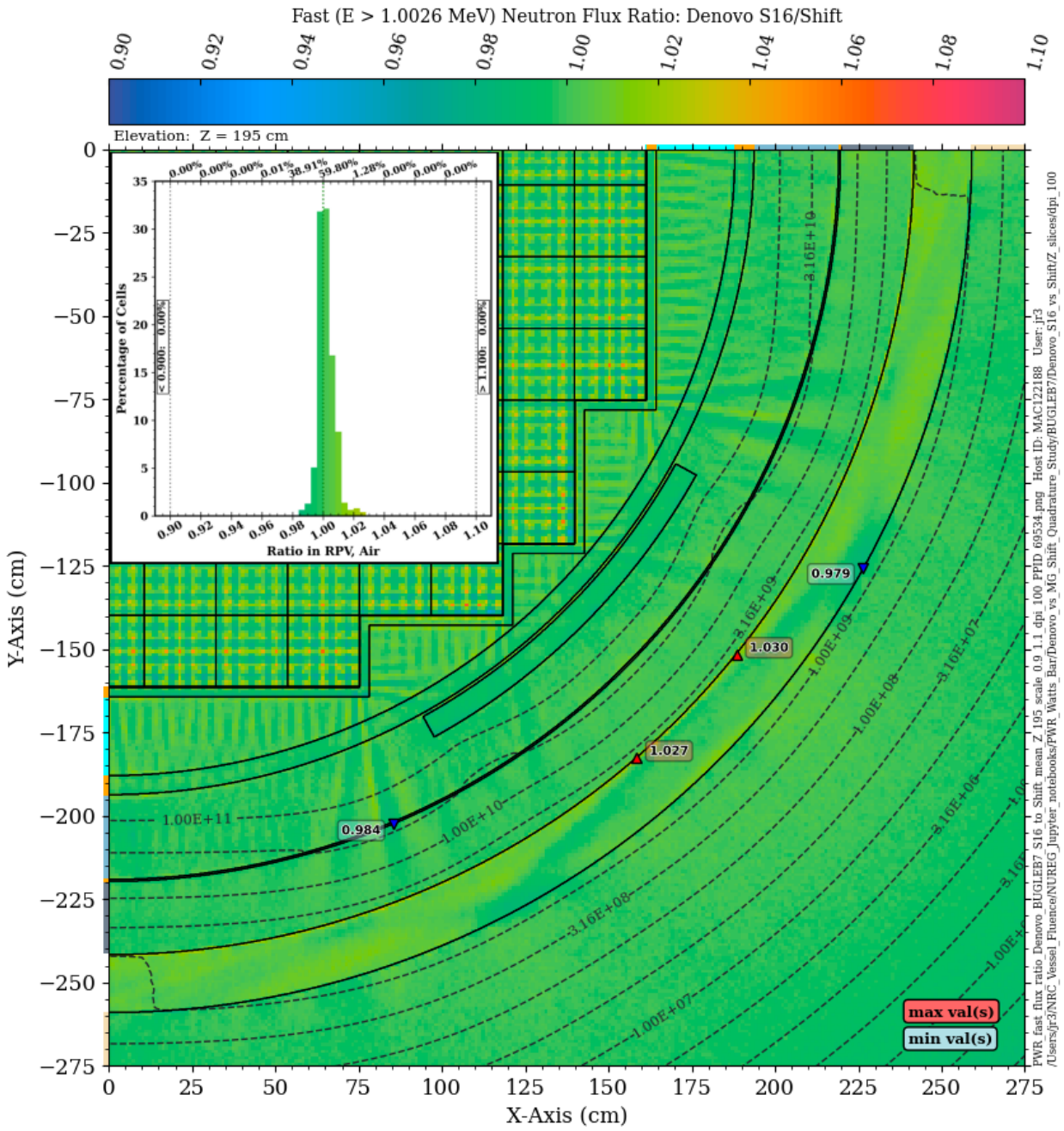

Figure 7-56 Ratio of the fast neutron flux from a BUGLE-B7 Denovo solution with S16 quadrature to a BUGLE-B7 Shift solution with the PWR model. Plan view at Z = 195 cm *The histogram plot shows the distribution of ratio values with the RPV and cavity gap.*

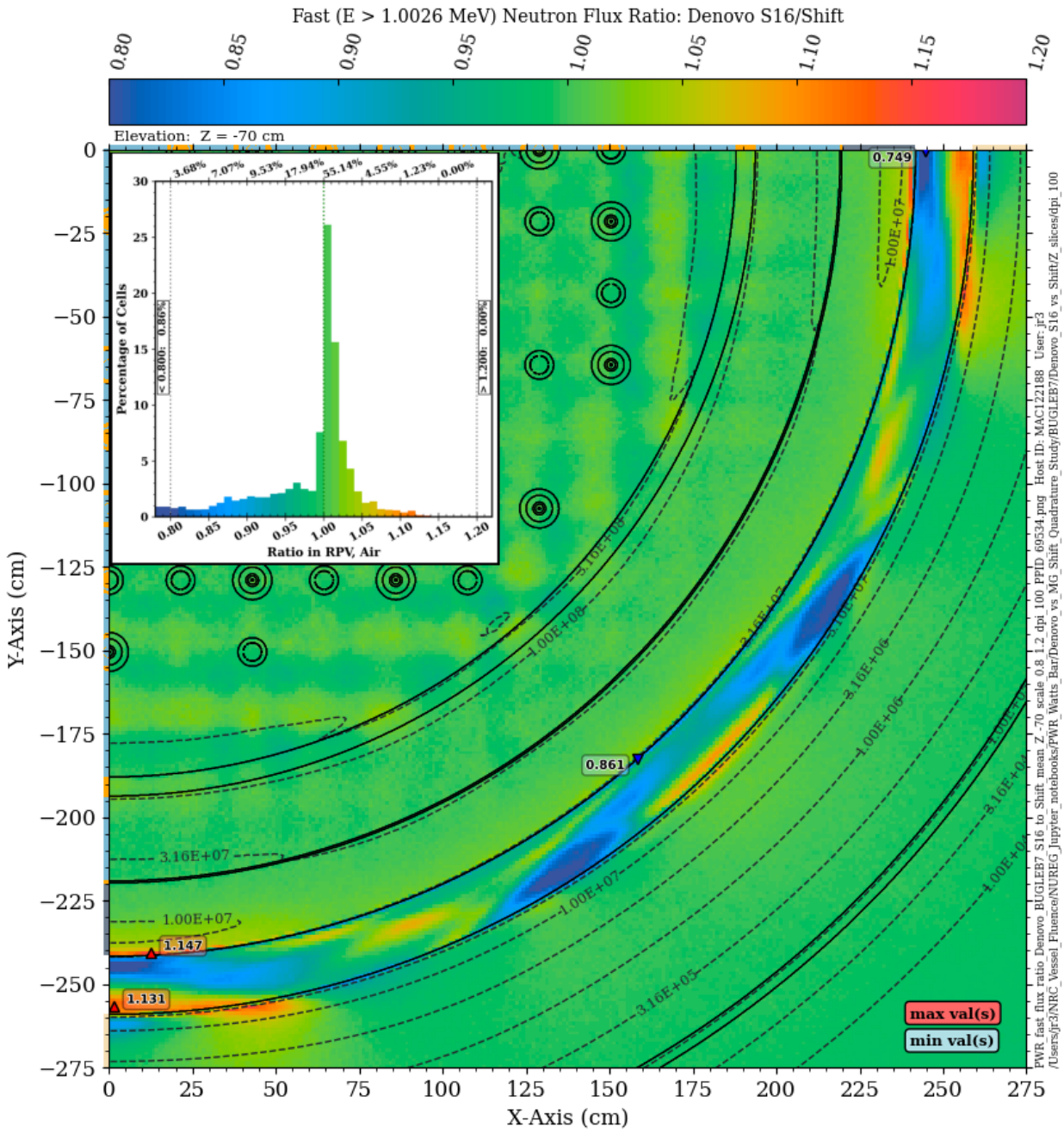

Figure 7-57 Ratio of the fast neutron flux from a BUGLE-B7 Denovo solution with S16 quadrature to a BUGLE-B7 Shift solution with the PWR model. Plan view at Z = -70 cm *The histogram plot shows the distribution of ratio values within the RPV and cavity gap. Note the change in scale relative to Figure 7-56.*

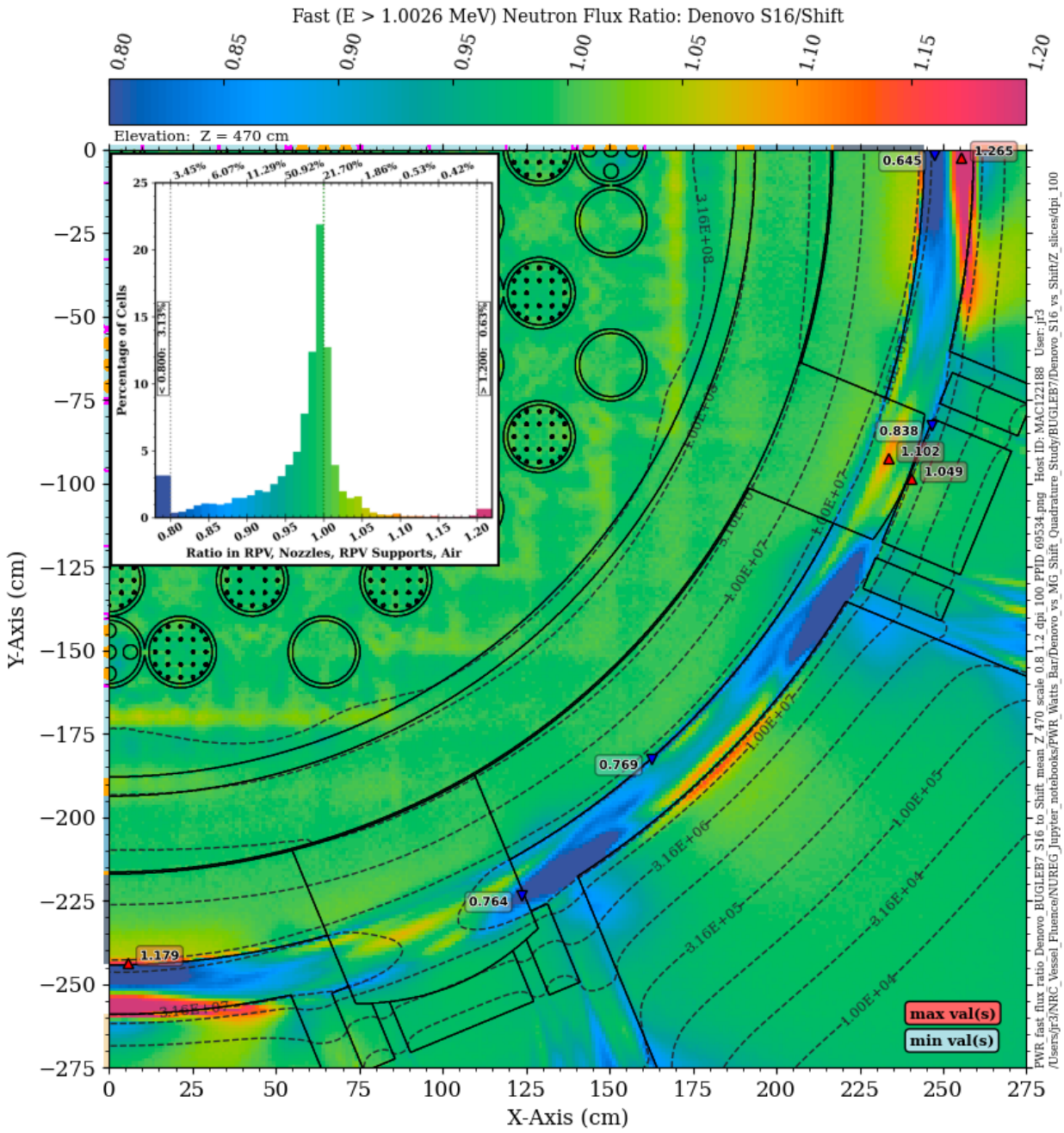

Figure 7-58 Ratio of the fast neutron flux from a BUGLE-B7 Denovo solution with S16 quadrature to a BUGLE-B7 Shift solution with the PWR model. Plan view at Z = 470 cm *The histogram plot shows the distribution of ratio values within the RPV, nozzle, vessel supports, and cavity gap.*

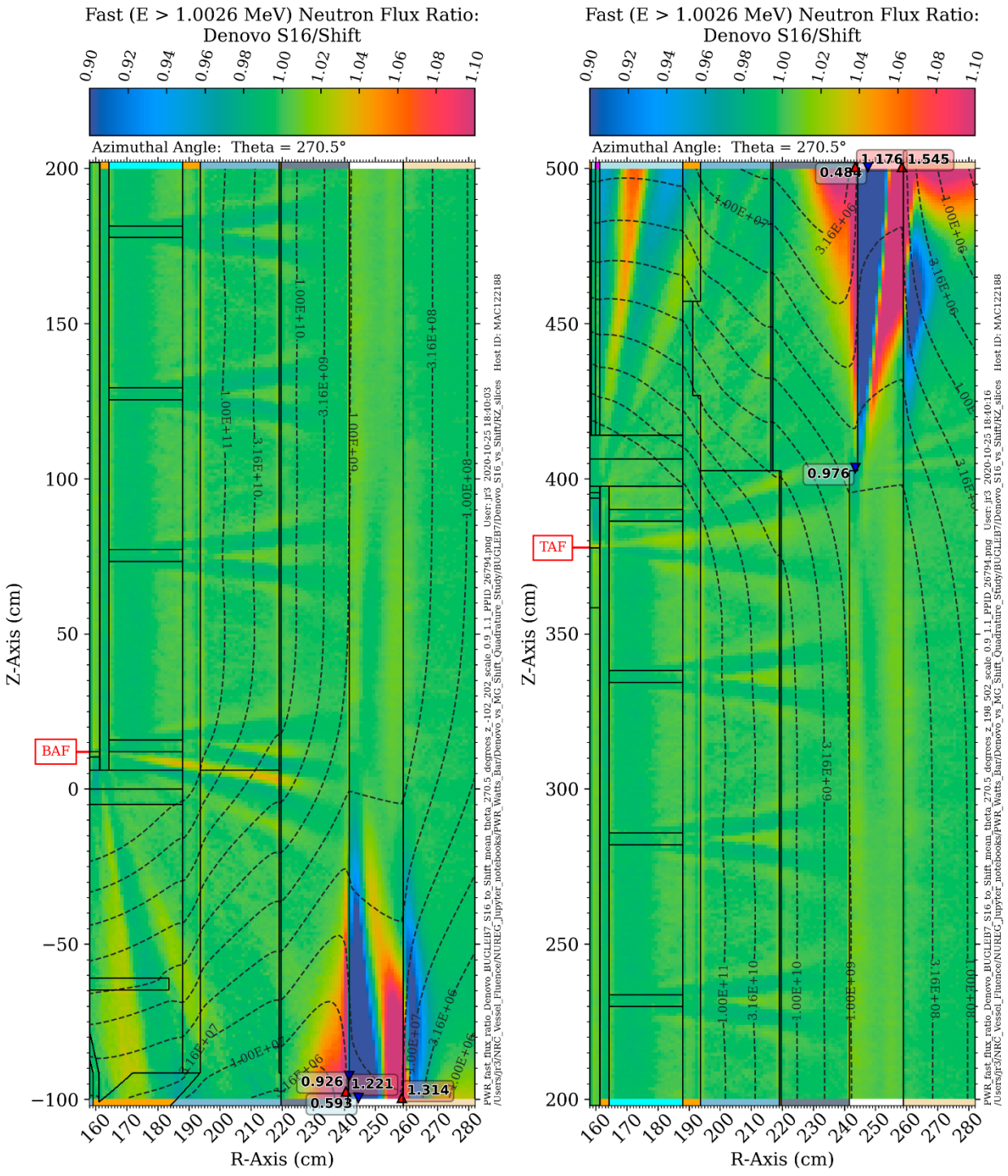

Figure 7-59 Ratio of the fast neutron flux from a BUGLE-B7 Denovo solution with S16 quadrature to a BUGLE-B7 Shift solution with the PWR model. Elevation view at an azimuthal angle of 270.5°

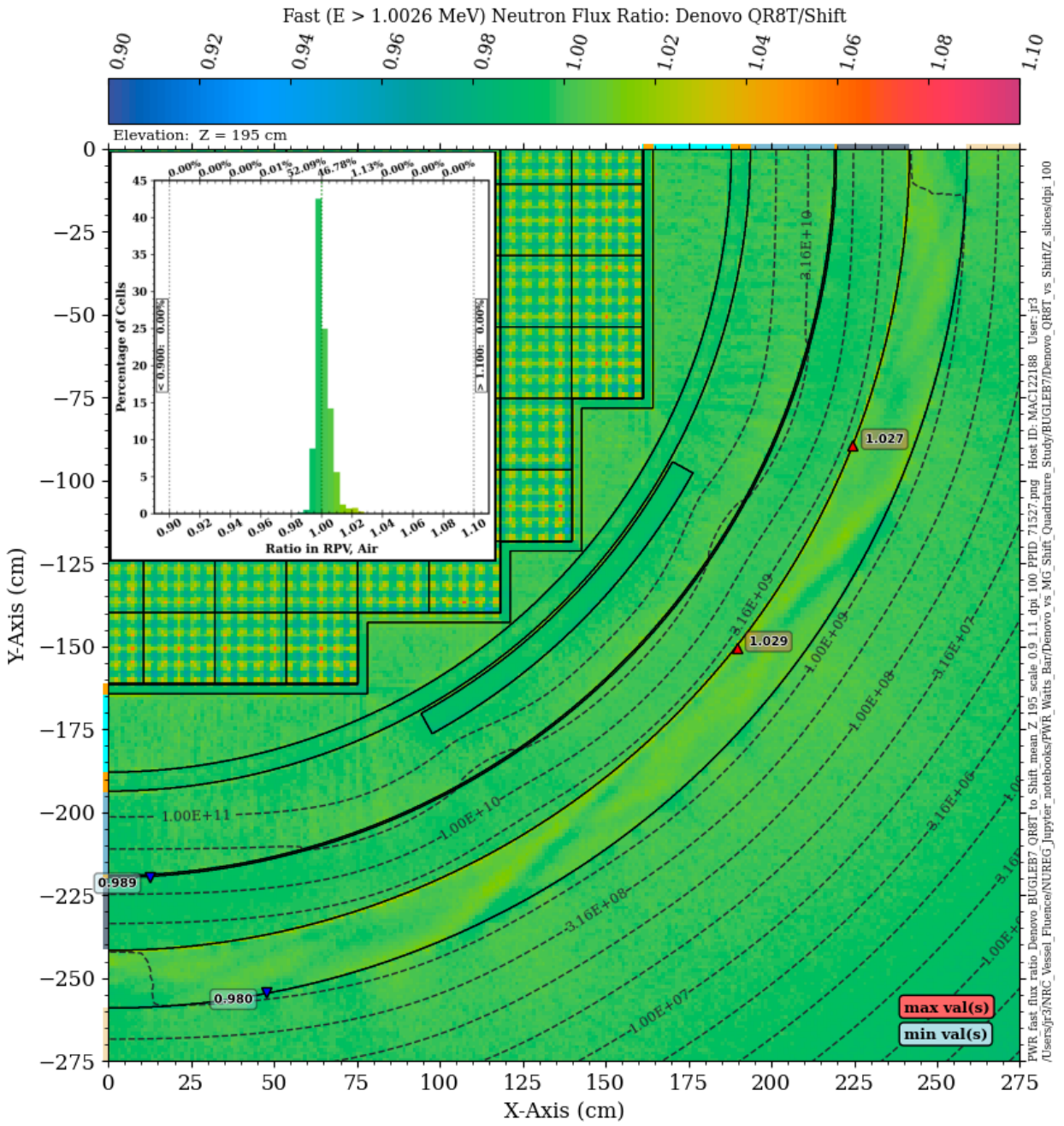

Figure 7-60 Ratio of the fast neutron flux from a BUGLE-B7 Denovo solution with QR8T quadrature to a BUGLE-B7 Shift solution with the PWR model. Plan view at Z = 195 cm *The histogram plot shows the distribution of ratio values with the RPV and cavity gap.*

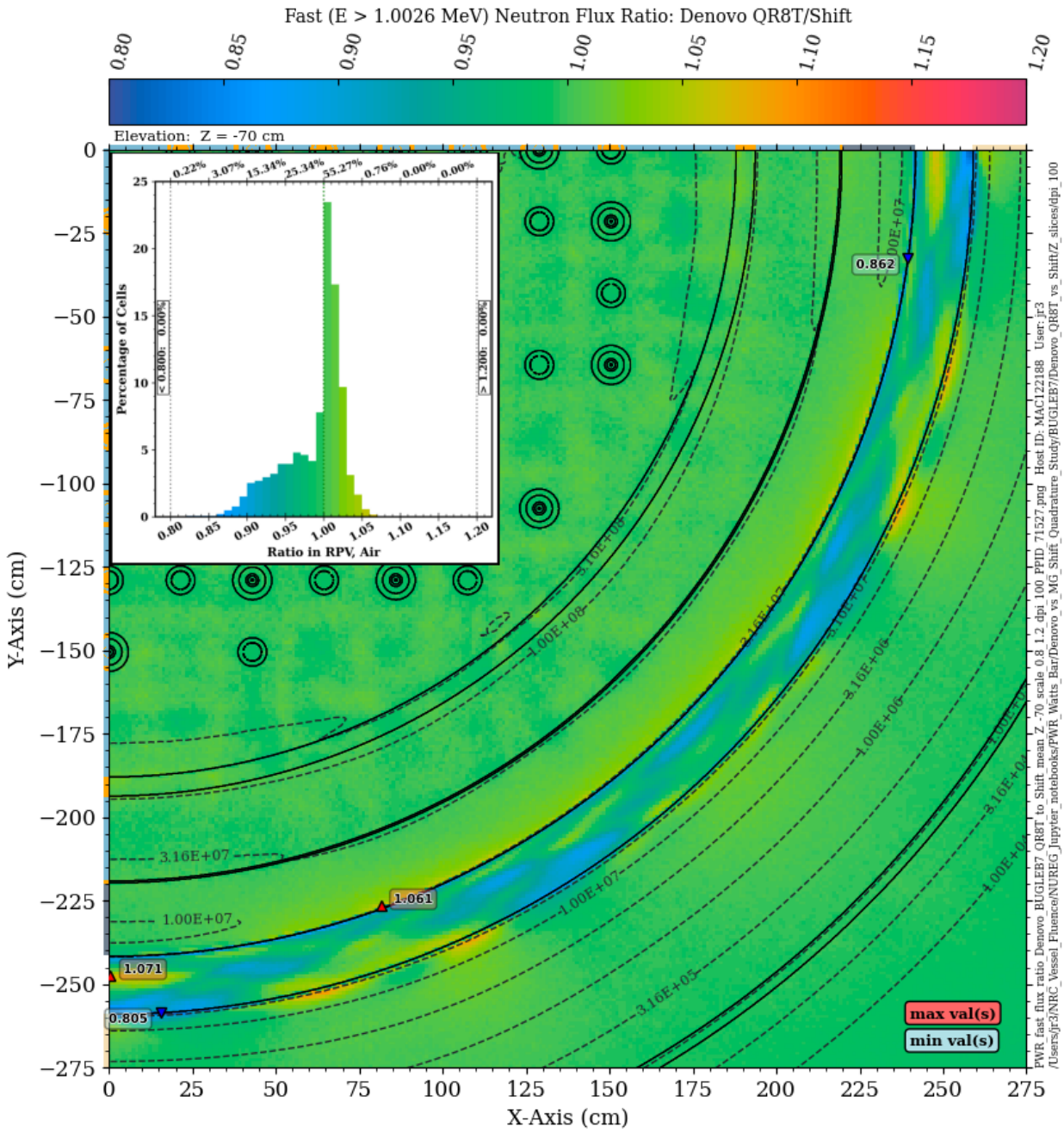

Figure 7-61 Ratio of the fast neutron flux from a BUGLE-B7 Denovo solution with QR8T quadrature to a BUGLE-B7 Shift solution with the PWR model. Plan view at Z = -70 cm *The histogram plot shows the distribution of ratio values within the RPV and cavity gap. Note the change in scale relative to Figure 7-60.*

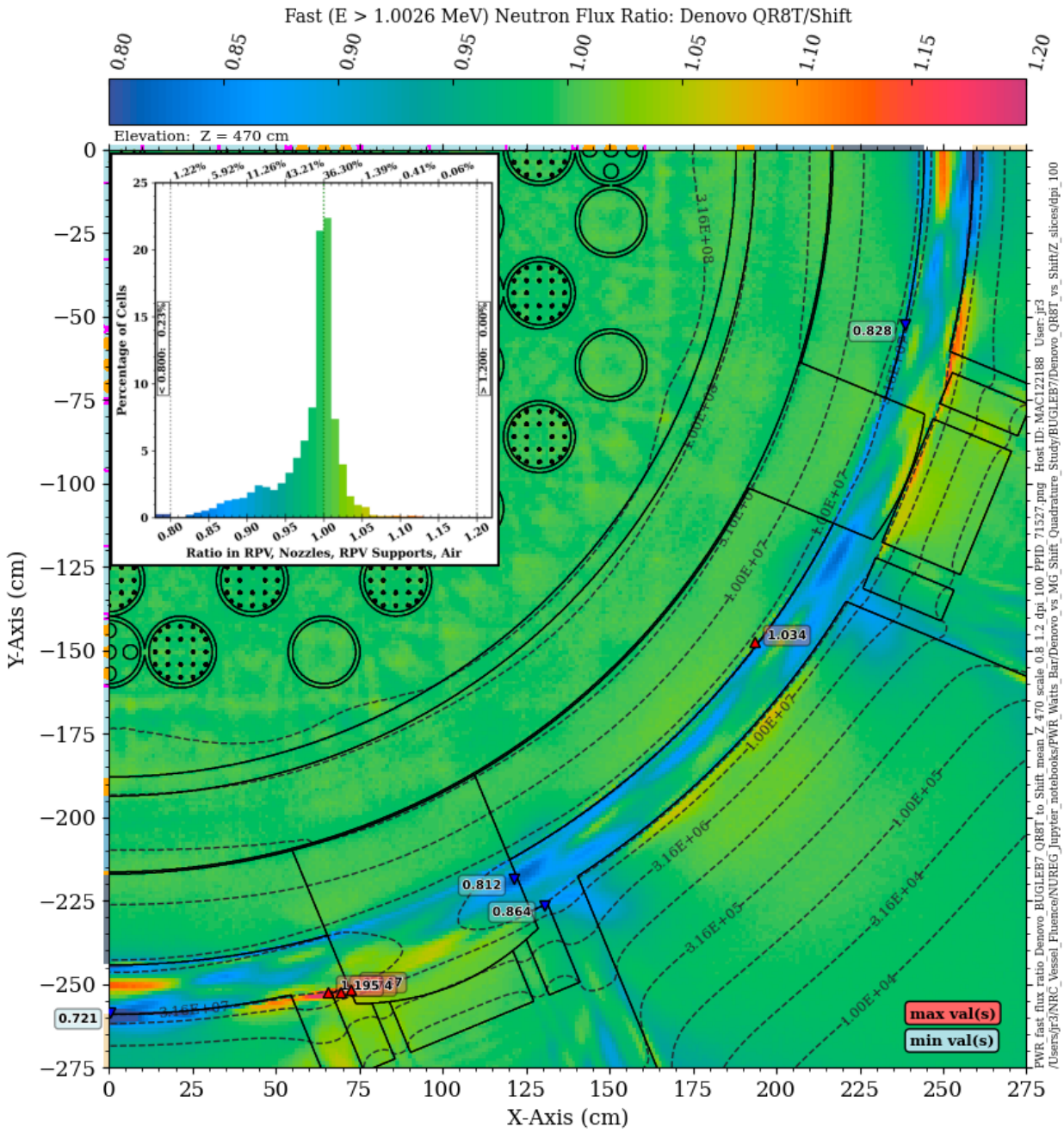

Figure 7-62 Ratio of the fast neutron flux from a BUGLE-B7 Denovo solution with QR8T quadrature to a BUGLE-B7 Shift solution with the PWR model. Plan view at Z = 470 cm *The histogram plot shows the distribution of ratio values within the RPV, nozzle, vessel supports, and cavity gap.*

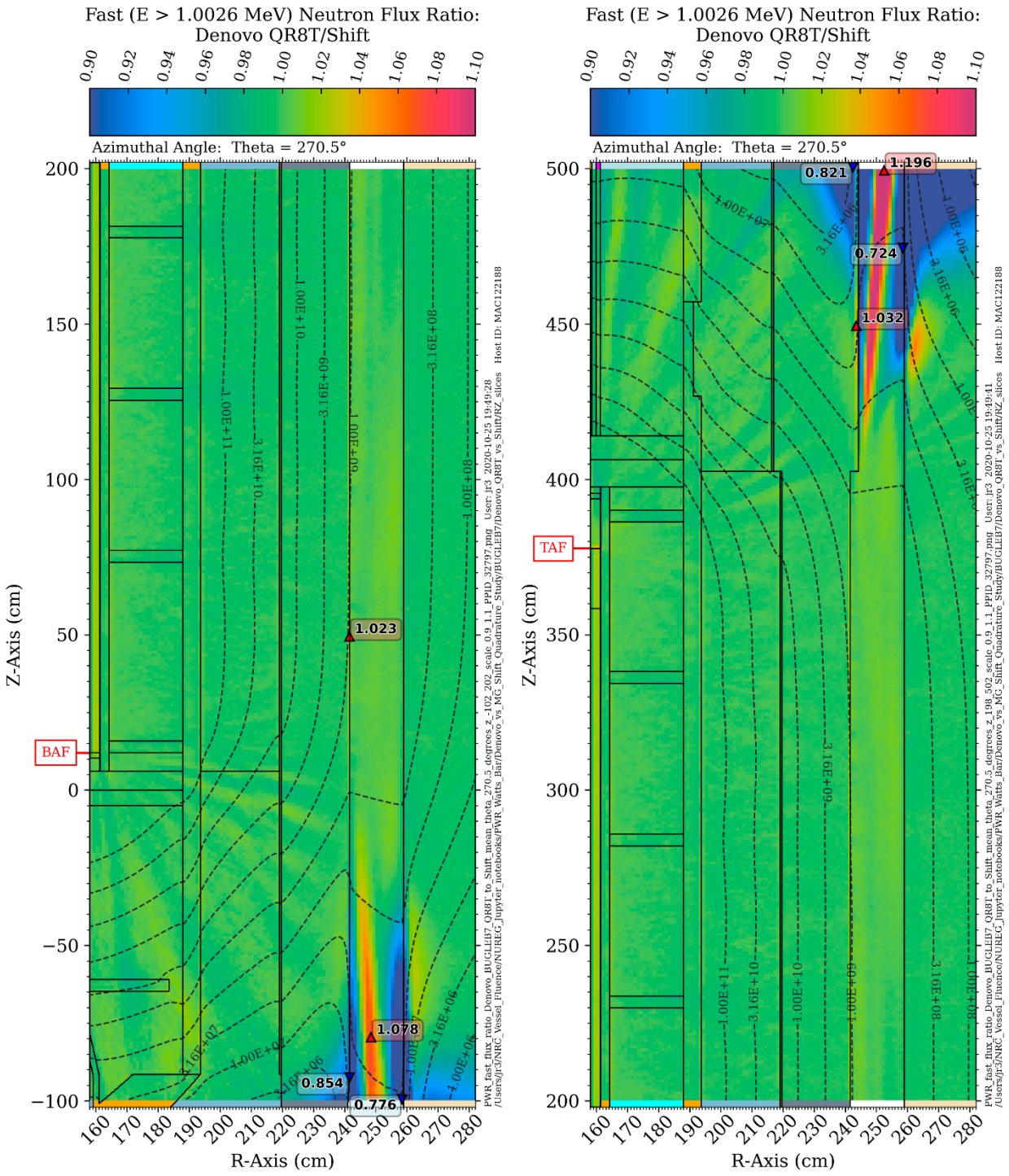

Figure 7-63 Ratio of the fast neutron flux from a BUGLE-B7 Denovo solution with QR8T quadrature to a BUGLE-B7 Shift solution with the PWR model. Elevation view at an azimuthal angle of 270.5°

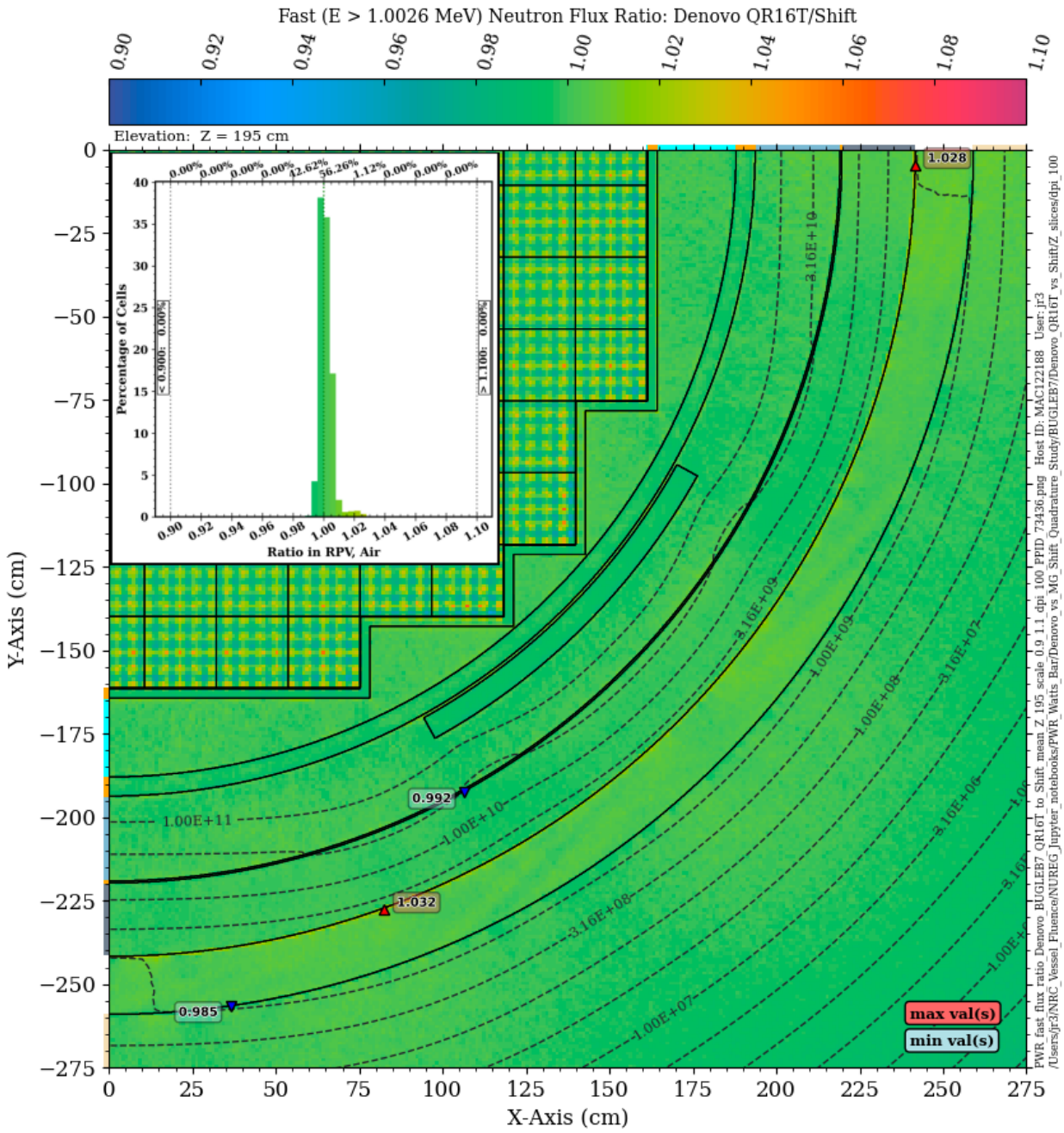

Figure 7-64 Ratio of the fast neutron flux from a BUGLE-B7 Denovo solution with QR16T quadrature to a BUGLE-B7 Shift solution with the PWR model. Plan view at Z = 195 cm *The histogram plot shows the distribution of ratio values within the RPV and cavity gap.*

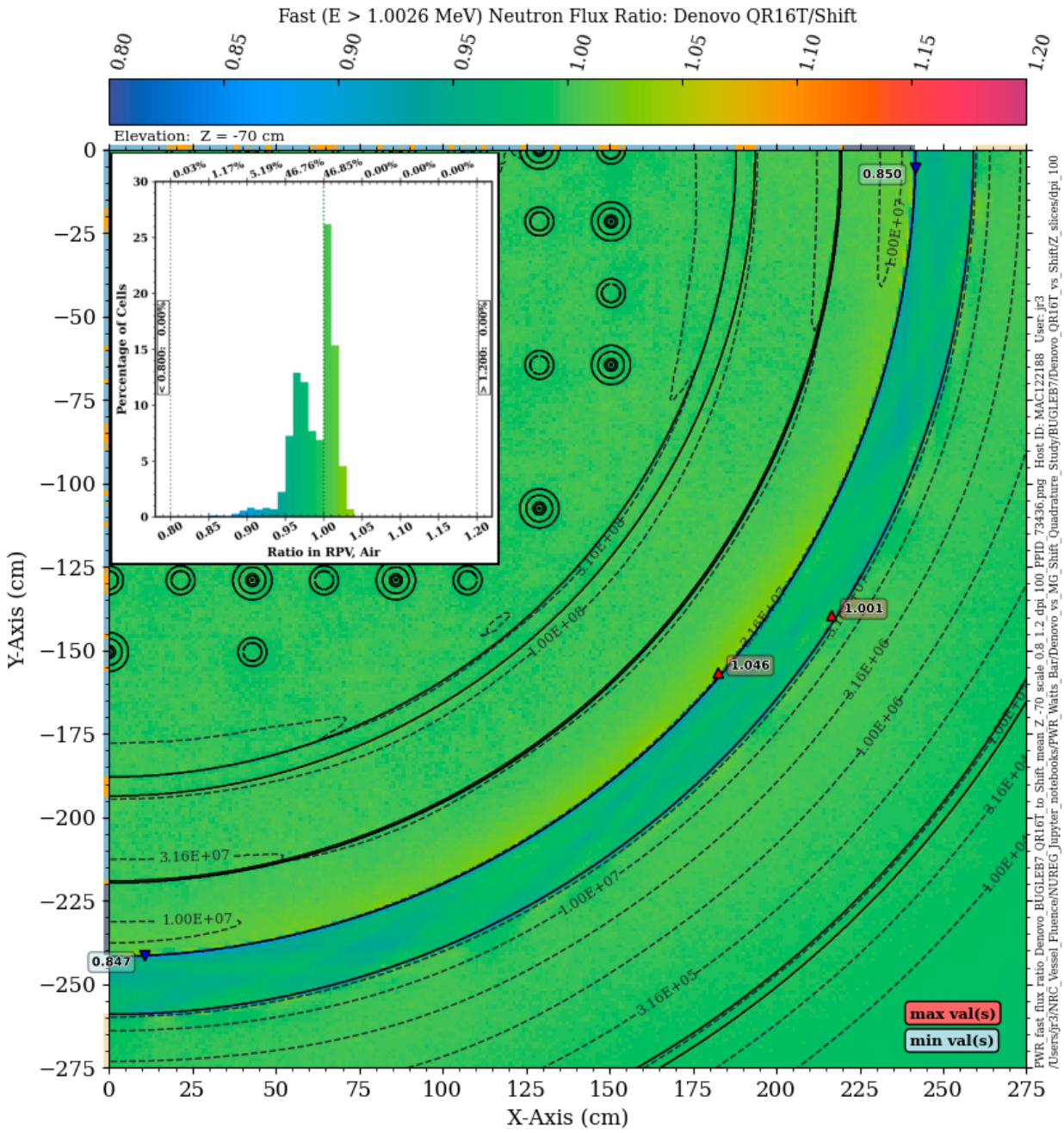

Figure 7-65 Ratio of the fast neutron flux from a BUGLE-B7 Denovo solution with QR16T quadrature to a BUGLE-B7 Shift solution with the PWR model. Plan view at Z = -70 cm *The histogram plot shows the distribution of ratio values within the RPV and cavity gap. Note the change in scale relative to Figure 7-64.*

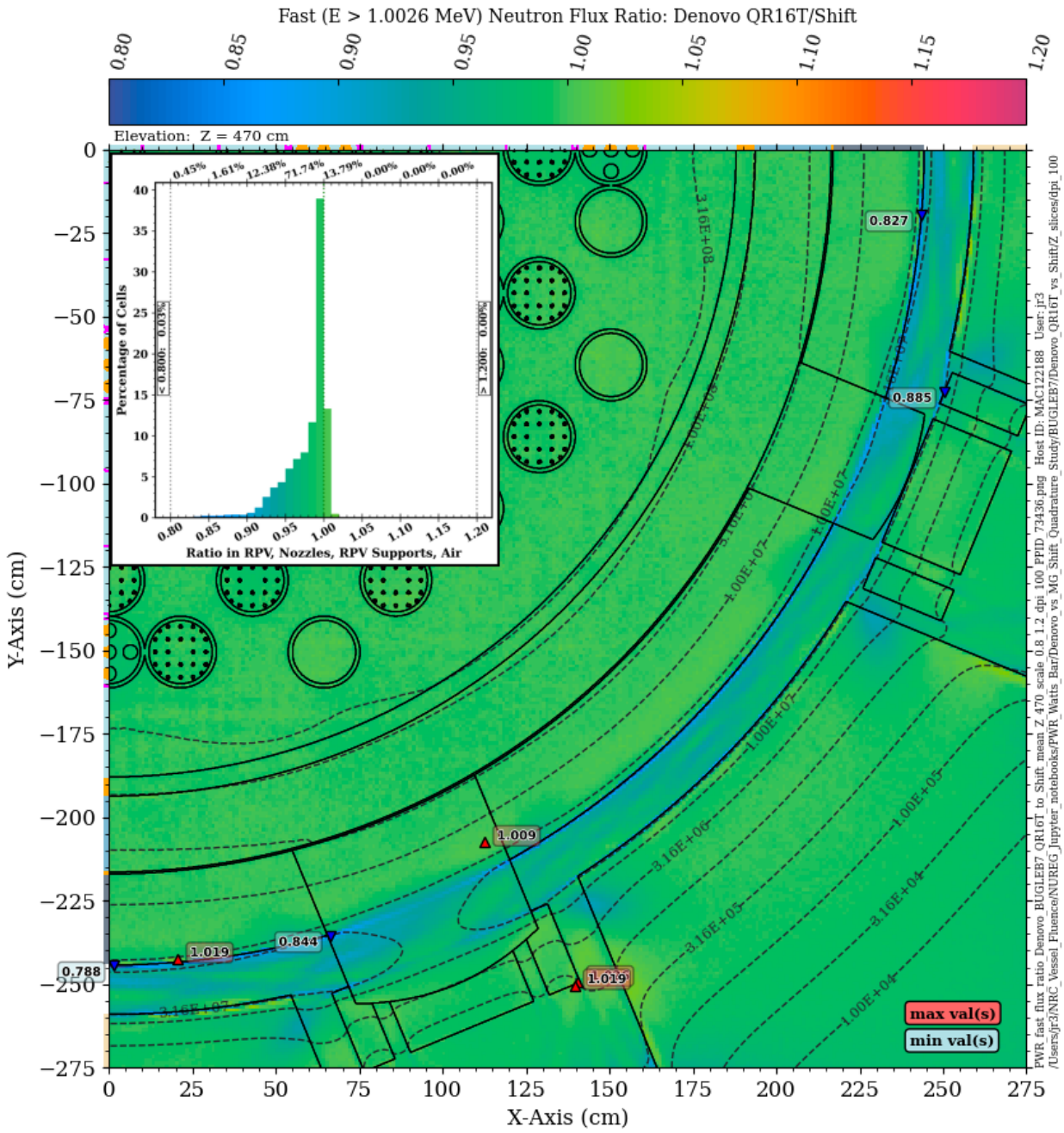

Figure 7-66 Ratio of the fast neutron flux from a BUGLE-B7 Denovo solution with QR16T quadrature to a BUGLE-B7 Shift solution with the PWR model. Plan view at Z = 470 cm *The histogram plot shows the distribution of ratio values within the RPV, nozzle, vessel supports, and cavity gap.*

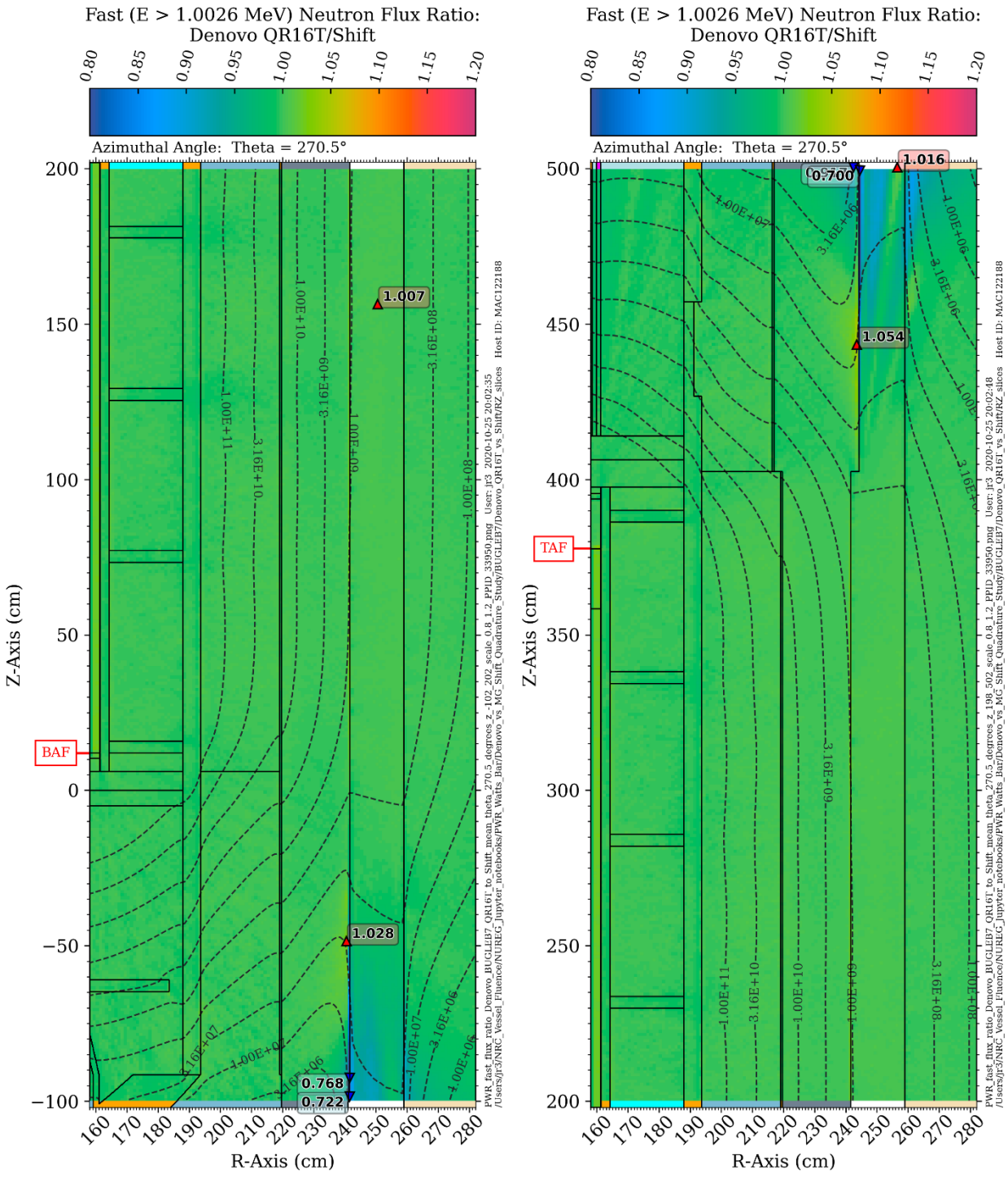

Figure 7-67 Ratio of the fast neutron flux from a BUGLE-B7 Denovo solution with QR16T quadrature to a BUGLE-B7 Shift solution with the PWR model. Elevation view at an azimuthal angle of 270.5°

7.6 Summary of Quadrature Studies

Angular quadrature sensitivity has long been a challenge in discrete ordinates radiation transport calculations, particularly with complex 3D models. Numerous studies have been performed over many years in attempts to provide optimal quadrature sets for RPV fluence calculations. The most widely used sets are still the level symmetric sets, particularly S8 and S16. However, their suitability for RPV fluence calculations in the extended beltline region has not been clearly established.

This section addresses three fundamental questions:

1. Are fluence calculations in the extended beltline region more sensitive to angular quadrature relative to calculations within the beltline region?
2. Are discrete ordinates calculations of dosimetry reaction rates for reactions with a high threshold energy, as in the ^{27}Al (n,α) reaction, more sensitive to quadrature than fast fluence calculations?
3. If there are significant solution differences with different quadrature sets, can one set be demonstrated to be more accurate than another?

The first two questions were addressed by performing parametric studies using Denovo PWR and BWR models. This approach is consistent with typical quadrature parameter studies that would be performed to determine whether a discrete ordinates solution has converged with respect to the angular quadrature.

The results of these studies demonstrate significant quadrature sensitivity in the extended beltline region of both models. In addition, they raise questions about the adequacy of the widely used S8 set for calculations, even within the traditional beltline region. The primary consideration with the S8 solutions may be with regard to benchmark calculations in which discrete ordinates calculations are compared to measured dosimetry data. Because of the azimuthal and axial sensitivity seen in portions of the S8 solutions, it is possible that a relatively minor shift in the location of a dosimetry capsule could have a nontrivial impact on the comparison of calculated and measured activities.

The question of sensitivity for high-energy threshold reactions was addressed by evaluating reaction rates for the ^{27}Al (n,α) reaction, which has a threshold energy of 3.25 MeV and an energy response range of 6.45–11.9 MeV. Results presented in Section 7.3.4 demonstrate that the calculation of this type of threshold reaction rate can be significantly more sensitive to quadrature effects compared with fast fluence calculations. Note that this is a concern not only in extended beltline locations, but even at locations well within the traditional beltline region.

The third question was addressed by comparing MG Shift calculations with Denovo calculations using the PWR model. These calculations used the same models and the same MG cross-section data (BUGLE-B7). Results of these calculations, which are presented in Section 7.5, suggest the following:

1. QR quadrature sets appear to be superior to level symmetric quadratures for RPV fluence calculations. A QR8T quadrature, which has the same number of angles as the high-order S16 level symmetric set, consistently provides closer agreement than S16 when compared with the Shift solution. This is not surprising, as at least some of the ray effects seen with the level symmetric sets are associated with material interfaces along a

coordinate axis or with streaming near the Z-axis. The QR quadrature sets were developed specifically to provide improved accuracy in those types of situations.

2. Given the increases in computing resources in recent years, it may be prudent to recommend a minimum quadrature order of QR8T. In the traditional beltline region, QR8T solutions provide generally good agreement with QR16T solutions, which have 136 angles per octant. However, in the extended beltline region, quadrature orders higher than QR8T should be considered.

8 ASSESSMENT OF MULTIGROUP CROSS-SECTION LIBRARIES FOR RADIATION TRANSPORT CALCULATIONS IN THE EXTENDED BELTLINE REGION

The majority of RPV fluence calculations have been and continue to be performed using discrete ordinates transport codes with MG cross-section libraries. The adequacy of an MG library for transport applications is dependent on, among other factors, the energy structure (i.e., the group boundaries) and the weighting spectrum used to collapse either pointwise data to a fine-group library or a fine-group library to a broad-group library (APPENDIX A).

The VITAMINB-B7 and BUGLE-B7 libraries [84] are widely used for LWR shielding analyses, with BUGLE-B7 being commonly used for RPV fluence applications. The VITAMIN-B7 library was created by collapsing pointwise ENDF/B-VII.0 data with (1) a weighting composed of a fission spectrum for neutron energies greater than 820.8 keV, (2) a 1/E slowing-down spectrum for energies between 0.125 eV and 820.8 keV, and (3) a Maxwellian spectrum for energies below 0.125 eV. For the BUGLE-B7 library, weighting spectra at several locations in representative 1D PWR and BWR models were calculated using the VITAMIN-B7 library. These spectra are shown in Figure 8-1.

The fine-group weighting spectrum used for generating the BUGLE-B7 library data for locations inside steel regions (especially the RPV) is taken at ¼ of the thickness of the RPV from a PWR model with an RPV thickness of 21.91 cm. As neutrons travel through the RPV, the spectrum changes substantially. Figure 8-2 shows how the neutron flux as a function of five energy ranges changes from the core radially outward through the concrete bioshield for a 1D mockup of the PWR reference model at the core midplane. Note that the flux for energies above 1 MeV is attenuated by a factor of ~20 from the inner surface of the RPV to the outer surface. In contrast, the flux profiles in the lower energy ranges (excluding the profile for $E < 5$ eV) decrease more slowly because high-energy neutrons are scattered into lower energy ranges. As a result of the down-scattering of high-energy neutrons (i.e., neutrons scattering to lower energies), the flux profile for neutron energies between 111.09 keV and 1.0026 MeV has a slight increase near the inner surface of the RPV before decreasing. This behavior is also shown in Figure 8-3, which illustrates how the neutron flux spectrum undergoes a significant change as neutrons are transported from the inner surface of the RPV to the outer surface.

In addition to the variation in the neutron spectrum as a function of radial distance into the RPV, significant changes also occur as a function of elevation. As a result, in an MG library such as BUGLE-B7, the data that are collapsed using the neutron spectrum from a single location may not be appropriate for use in other locations, even though the material composition (e.g., steel) may be identical.

Furthermore, the appropriateness of an MG library depends on the specific neutron response (e.g. flux, dpa rate, reaction rate) being considered in an analysis. For example, calculation of the rate of a neutron dosimetry reaction with a high threshold energy is likely to be less sensitive to MG structures compared to a reaction that occurs primarily at lower energies, when neutron transport through energy ranges with significant resonance regions is important.

The calculations presented in this section were performed with the objective of comparing neutron fluxes, dpa rates, and dosimetry reaction rates calculated using the Shift Monte Carlo code with both CE and MG physics treatments. The aim of this study is not to compare

calculated and measured data (which is difficult to do due to the lack of adequate measurement data in the extended beltline region), but rather to assess how well a given MG library performs compared to the more exact CE cross sections. For this purpose, the following neutron responses are considered:

1. Fast neutron flux (E > 1 MeV)
2. Neutron dpa rate using dpa cross-section data from ASTM E693-17 [85]
3. ^{27}Al (n,α) reaction rate
4. ^{63}Cu-63 (n,α) reaction rate
5. ^{46}Ti (n,p) reaction rate
6. ^{54}Fe (n,p) reaction rate
7. ^{58}Ni (n,p) reaction rate
8. ^{115}In (n,n′) ^{103m}In reaction rate
9. ^{103}Rh (n,n′) ^{103m}Rh reaction rate
10. ^{237}Np (n,f) reaction rate
11. ^{238}U (n,f) reaction rate

The (n,α), (n,p), and (n,n′) reactions have threshold energies ranging from 3.25 MeV to 40.14 keV. They are listed in decreasing order of the threshold energy. The cross-section data for these reactions are shown in Figure C-1 and Figure C-2 of APPENDIX C.

8.1 Selection of Multigroup Cross-Section Libraries

For the purposes of this study, seven MG libraries were evaluated. Scoping studies were performed using XSDRNPM [42] 1D deterministic calculations based on the PWR reference model. Based on the results of the 1D studies, 3D Shift calculations were performed using selected MG libraries for comparison to Shift CE solutions. The CE calculations were all run using Shift with the SCALE [42] ENDF/B-VII.1 CE library.

The following MG libraries were considered in the 1D calculations:

1. VITAMIN-B7: a fine-group library with 197 neutron energy groups.
2. BUGLE-B7: a broad-group library with 47 neutron energy groups which was created by collapsing the VITAMIN-B7 library using representative weighting spectra from 1D PWR and BWR models; widely used in LWR shielding applications.
3. X200N47G: One of two fine-group shielding libraries with energy structures identical to VITAMIN-B7, except for an additional group from 19.64 to 20.0 MeV. There are X200N47G libraries based on ENDF/B-VII.0 and ENDF/B-VII.1.
4. X999N: an experimental SCALE MG library with 999 neutron groups; developed primarily for reactor physics applications.
5. X1597N: an experimental SCALE MG library with 1,597 neutron energy groups; developed primarily for reactor physics applications.
6. X642N: a library with 642 neutron groups. For energies below 1.0026 MeV, the groups are identical to the SCALE X200N47G structure. There are 440 equal-lethargy groups from 1.0026 to 3.0119 MeV. The intent of these fine groups is to provide improved MG accuracy over an energy range that is particularly significant for neutron transport through thick iron regions. There are 48 equal-lethargy groups from 3.0119 to 10.0 MeV. Above 10.0 MeV, the groups are identical to the SCALE X200N47G structure.
7. X956N: a library with 956 neutron groups that is a refinement of the X642N library. This library has 100 equal-lethargy groups for the energy range from 3.0119 to 10.0 MeV. For

energies from 10.595 keV to 1.0026 MeV, the group structure of the X999N library is used.

The energy group structures for these libraries are shown in Figure 8-4.

Results of the 1D calculations showed that the X642N and X956N libraries, which were developed specifically for modeling neutron transport through iron, are superior to the X999N and X1597N libraries for LWR shielding applications. Consequently, the X999N and X1597N libraries were used only on a limited basis for the 3D calculations.

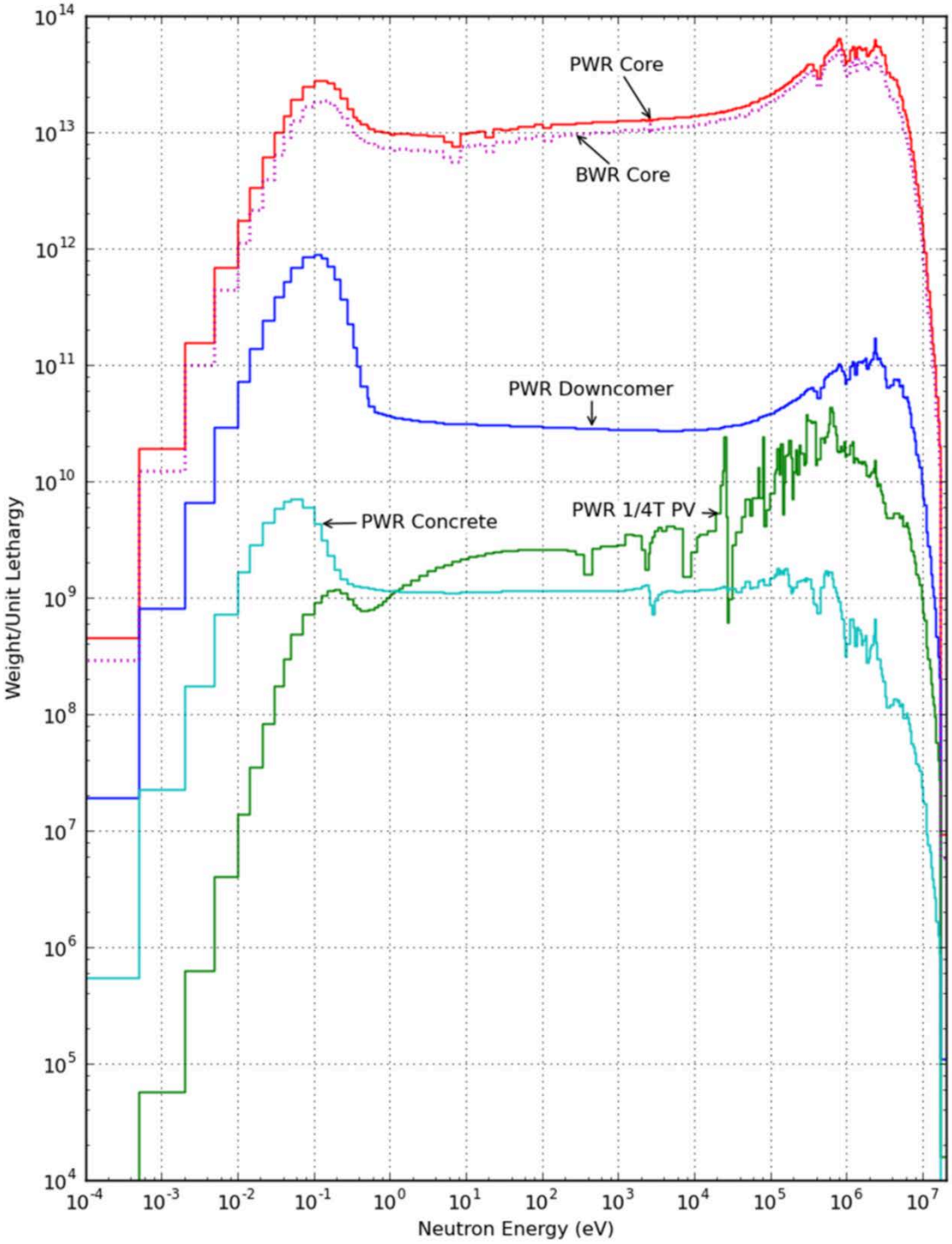

Figure 8-1 Weighting spectra used to generate the BUGLE-B7 MG library for LWR shielding analyses

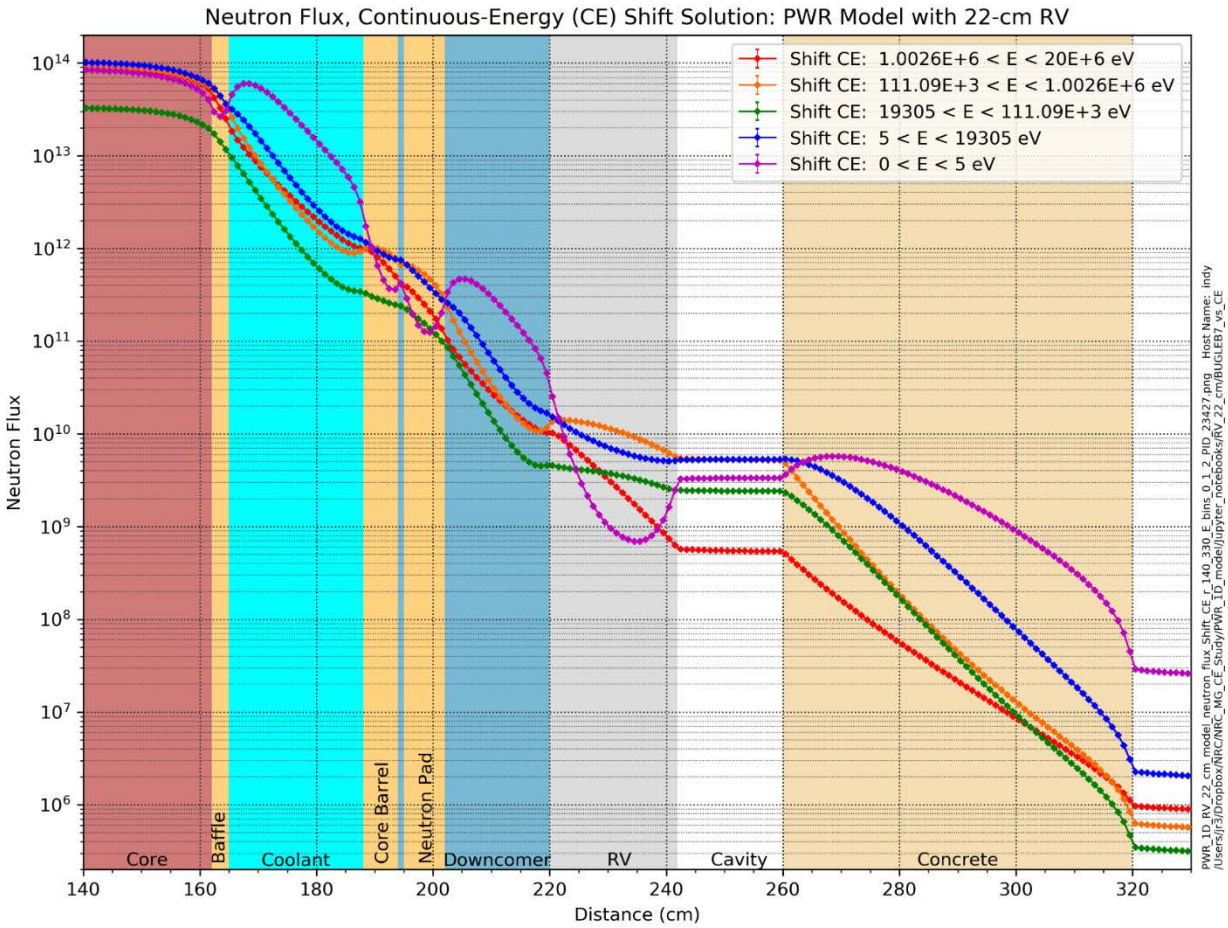

Figure 8-2 Neutron flux traverses for five energy ranges in a 1D mockup of the PWR reference model at the core midplane

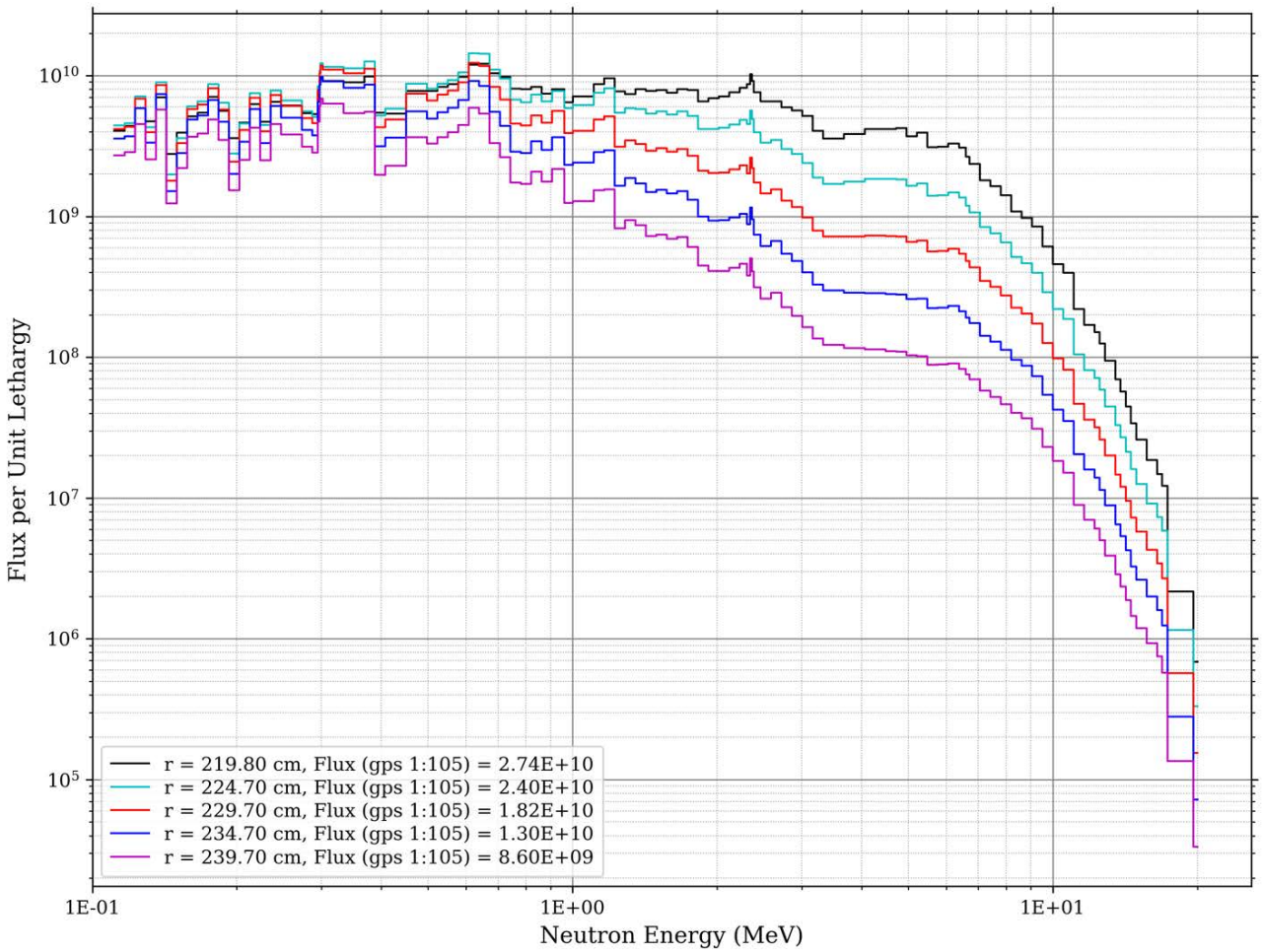

Figure 8-3 Neutron spectra for groups 1 to 105 (111.09 keV < E < 20 MeV) of the VITAMIN-B7 library at five locations through the thickness of the RPV for the 1D mockup of the PWR reference model

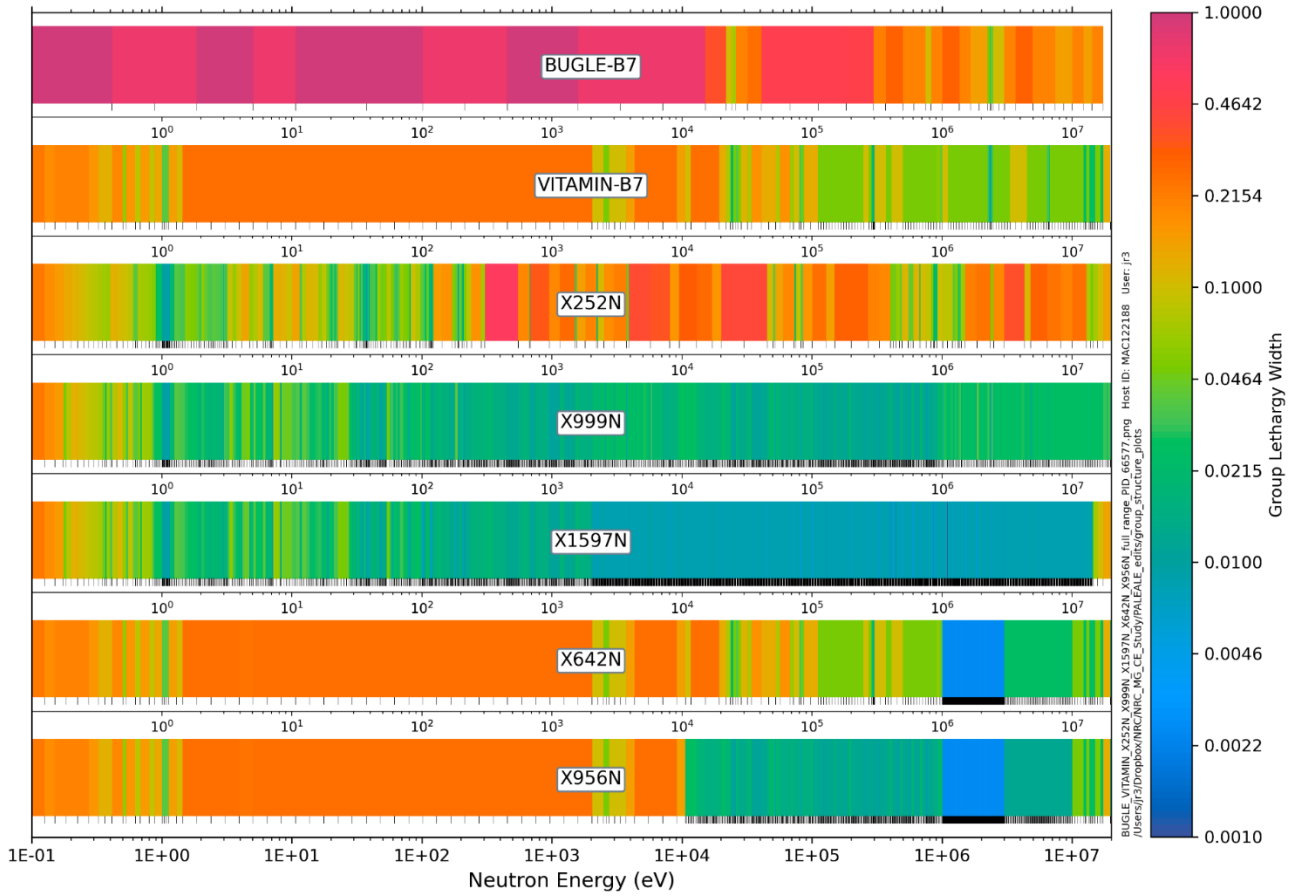

Figure 8-4 Group lethargy widths for the BUGLE-B7, VITAMIN-B7, X999N, X642N, X956N, and X1597N cross-section libraries

8.2 Fast Flux Calculations

Because the fast neutron fluence is a widely used metric for correlations of radiation damage in carbon steel RPVs, the first set of Shift MG/CE comparisons addresses how well an MG calculation can match a CE calculation of the neutron fast flux at locations in the traditional and extended beltline regions for a ^{235}U source. For calculational consistency, an energy cutoff of 1.0026 MeV was used in the CE calculations, as that is the nearest group boundary in each of the MG libraries considered in this analysis.

The results in this section demonstrate the performance of several MG libraries for fast neutron flux calculations at two elevations in the PWR reference model: at the core midplane at Z = 195 cm, and at an elevation of Z = 470 cm. These elevations are representative of the traditional beltline region and an extended beltline location near the RPV nozzles and vessel supports.

Figure 8-5 and Figure 8-6 show the MG/CE fast flux ratios when the BUGLE-B7 library is used with Shift. While the solutions agree well near the maximum flux in the RPV at the core midplane, they deviate more at azimuthal locations where the distance between the outer edge of the core and the RPV is maximized. At the outer edge of the RPV, the BUGLE-B7 solution underpredicts the CE solution by up to 10%. This is not significant for fast fluence in the traditional beltline region, where the peak fast flux levels occur at the inner surface of the RPV, but it suggests that cavity streaming neutron flux levels in extended beltline regions may be underpredicted using the BUGLE-B7 library, as the cavity streaming flux is driven by neutrons that escape the RPV and scatter from the bioshield back into the cavity gap. At the extended beltline elevation of 470 cm, the fast flux is underpredicted by ~5–14% throughout the RPV, and by as much as nearly 18% in the vessel supports. As noted in Section 5.6, at this location the EOL fast fluence is likely to be below 1×10^{17} n/cm^2, but the dpa rate may exceed the monitoring standard practice of 3×10^{-4} from ASTM E1035-18 [86]. Consequently, underprediction of the fast flux using the BUGLE-B7 library may be significant for vessel supports.

Figure 8-7 and Figure 8-8 show the MG/CE fast flux ratios when the VITAMIN-B7 library is used with Shift. It is somewhat surprising that the VITAMIN-B7/CE agreement is not noticeably improved compared to the BUGLE-B7/CE ratios. Use of the SCALE X200N47Gv71 MG library, which has the same group structure as the VITAMIN-B7 library, with the exception of an added group for energies between 19.64 MeV (the upper limit of the VITAMIN-B7 library), provides a slightly improved agreement relative to VITAMIN-B7 (Figure 8-9 and Figure 8-10). However, there is still an underprediction of ~9% at the outer surface of the RPV at the core midplane, and fast flux levels in the vessel support are underpredicted by up to nearly 20%.

Use of the Shift X999N library (Figure 8-11 and Figure 8-12), which was developed for reactor physics applications, yields an MG Shift solution that offers essentially no improvement, although the number of groups is increased by a factor of five. In contrast to the X999N library, the X956N library, which was developed specifically to improve MG accuracy over the energy range above 1 MeV, where there is resolved resonance data in the iron isotope cross sections, provides significantly improved solutions at the core midplane (Figure 8-13) and in the extended beltline region (Figure 8-14). At the core midplane, the X956N solution agrees with the CE solution within 2.5% at all mesh tally voxels. At the extended midplane elevation, the differences in the X956N and CE solutions are less than 5% in over 99% of the mesh tally voxels.

The final MG/CE fast flux comparison was made using the X642N library. Like the X956N library, it was developed to improve MG accuracy over the energy range above 1 MeV. The differences between the X642N and X956N libraries are primarily at energies below 1.0026 MeV, so they are likely to produce very similar results for fast flux calculations. This is shown in Figure 8-15 and Figure 8-16.

In summary, MG flux solutions obtained with today's commonly used libraries—BUGLE-B7, VITAMIN-B7, and Shift X200N47Gv71—tend to systematically underpredict fast flux levels in the outer portion of the RPV within the traditional beltline region and at all locations in the extended beltline region at the elevation of the vessel supports.

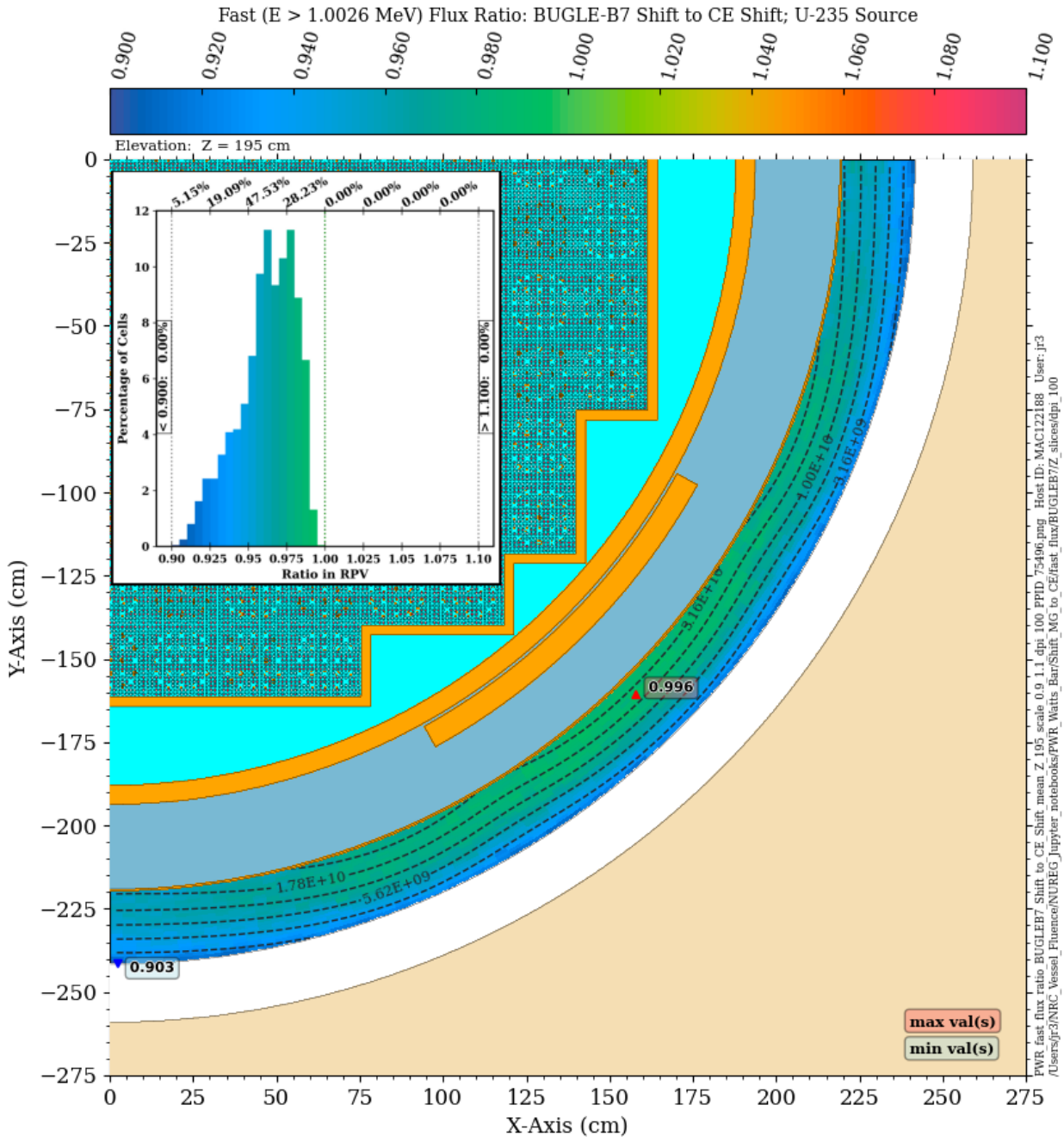

Figure 8-5 Fast neutron flux ratio in the PWR RPV: BUGLE-B7 Shift/CE Shift. Plan view at Z = 195 cm *The contour lines are the fast flux from the CE solution.*

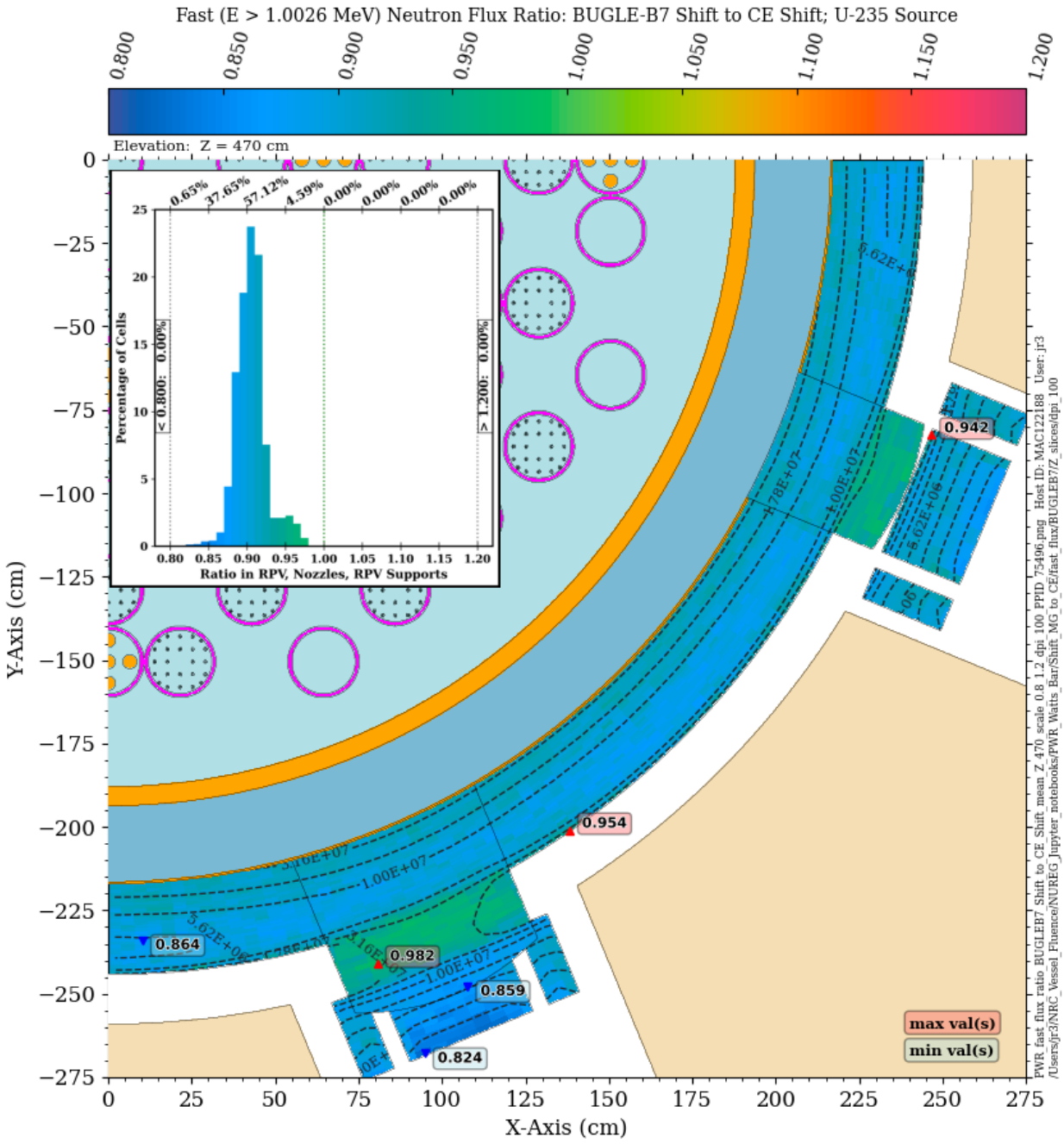

Figure 8-6 **Fast neutron flux ratio in the PWR RPV: BUGLE-B7 Shift/CE Shift. Plan view at Z = 470 cm** *The contour lines are the fast flux from the CE solution. Note the change in scale relative to Figure 8-5.*

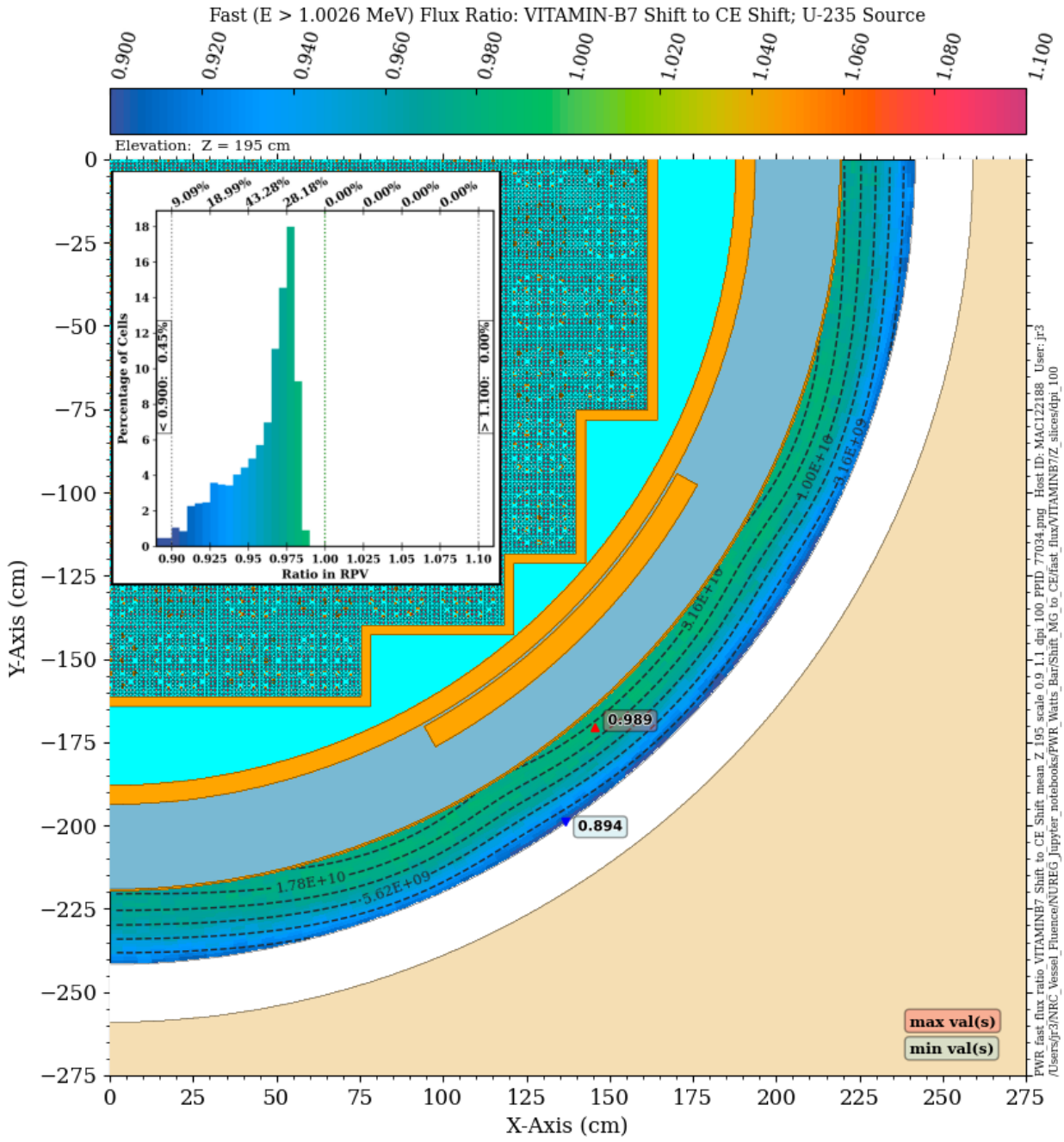

Figure 8-7 Fast neutron flux ratio in the PWR RPV: VITAMIN-B7 Shift/CE Shift. Plan view at Z = 195 cm *The contour lines are the fast flux from the CE solution.*

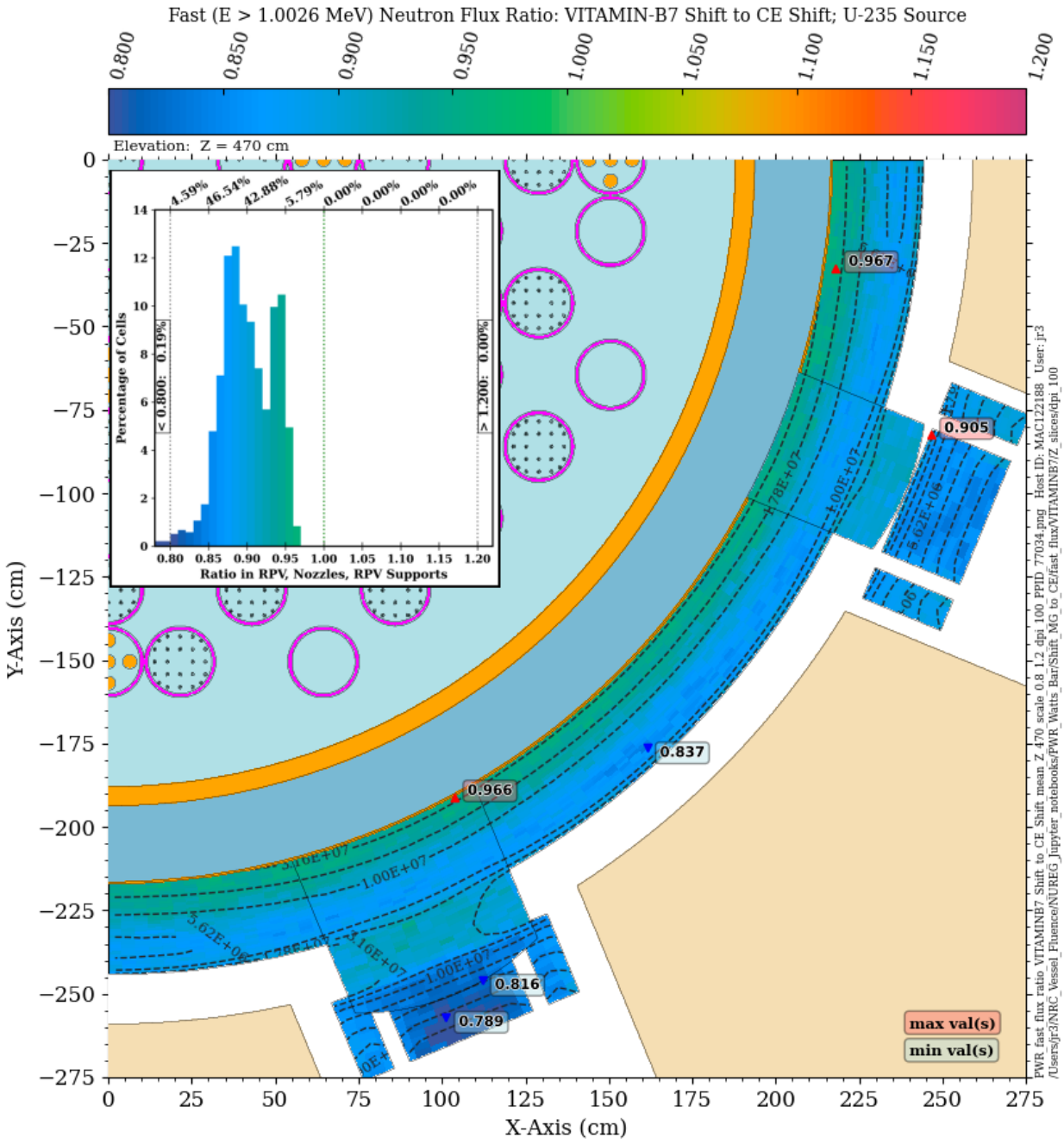

Figure 8-8 Fast neutron flux ratio in the PWR RPV: VITAMIN-B7 Shift/CE Shift. Plan view at Z = 470 cm *The contour lines are the fast flux from the CE solution. Note the change in scale relative to Figure 8-7.*

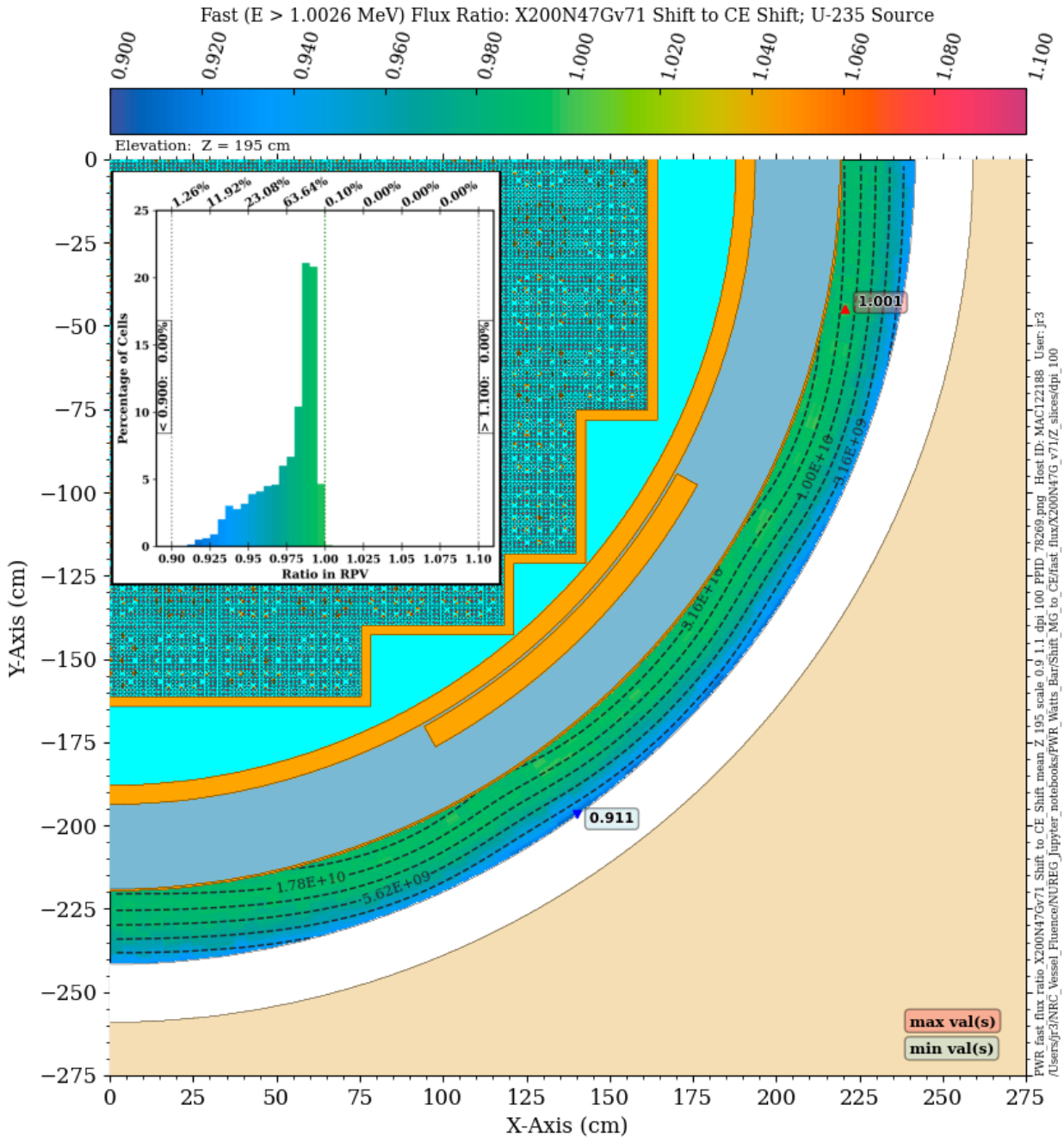

Figure 8-9 Fast neutron flux ratio in the PWR RPV: X200N47Gv71 Shift/CE Shift. Plan view at Z = 195 cm *The contour lines are the fast flux from the CE solution.*

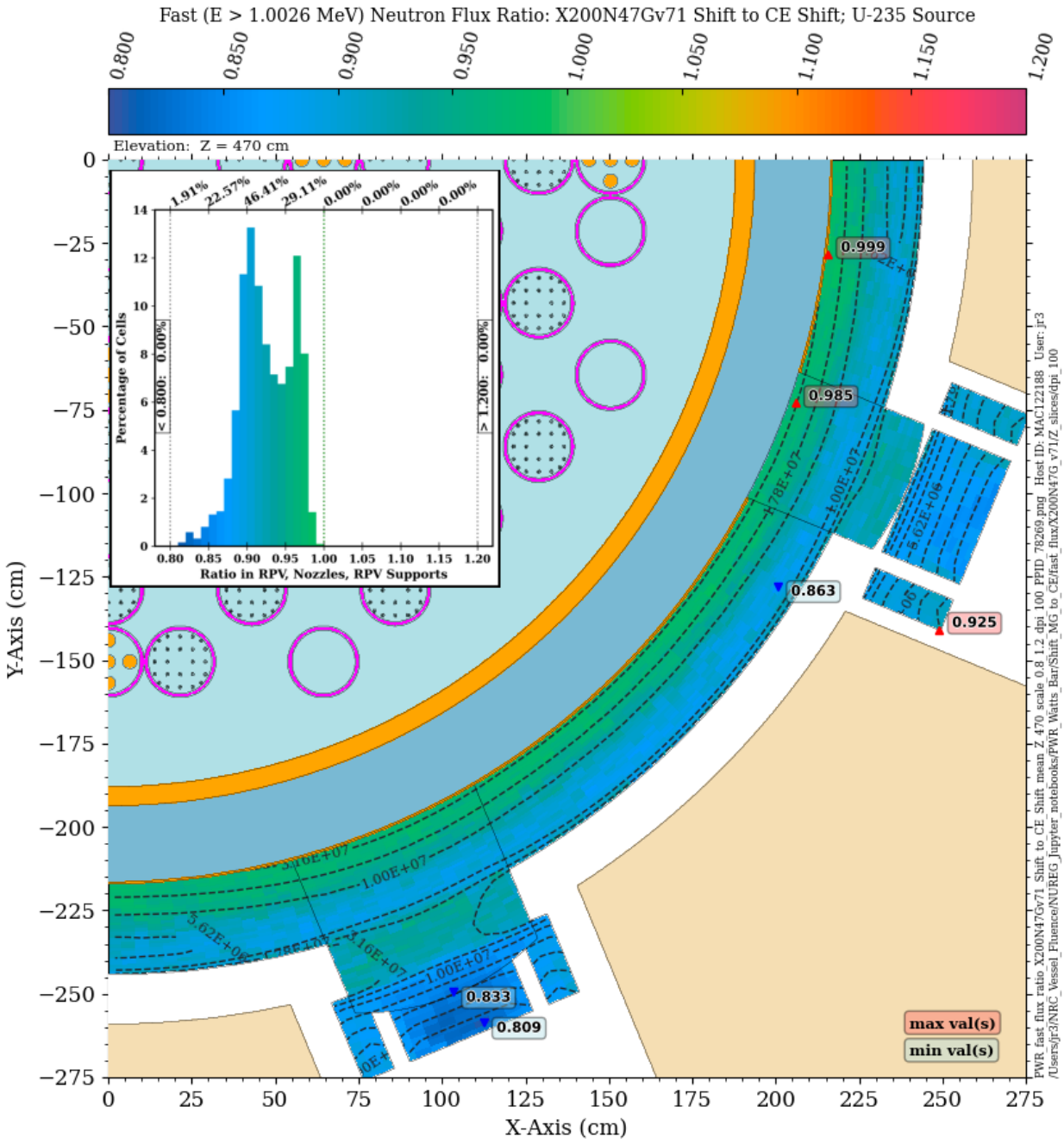

Figure 8-10 Fast neutron flux ratio in the PWR RPV: X200N47Gv71 Shift/CE Shift. Plan view at Z = 470 cm *The contour lines are the fast flux from the CE solution. Note the change in scale relative to Figure 8-9.*

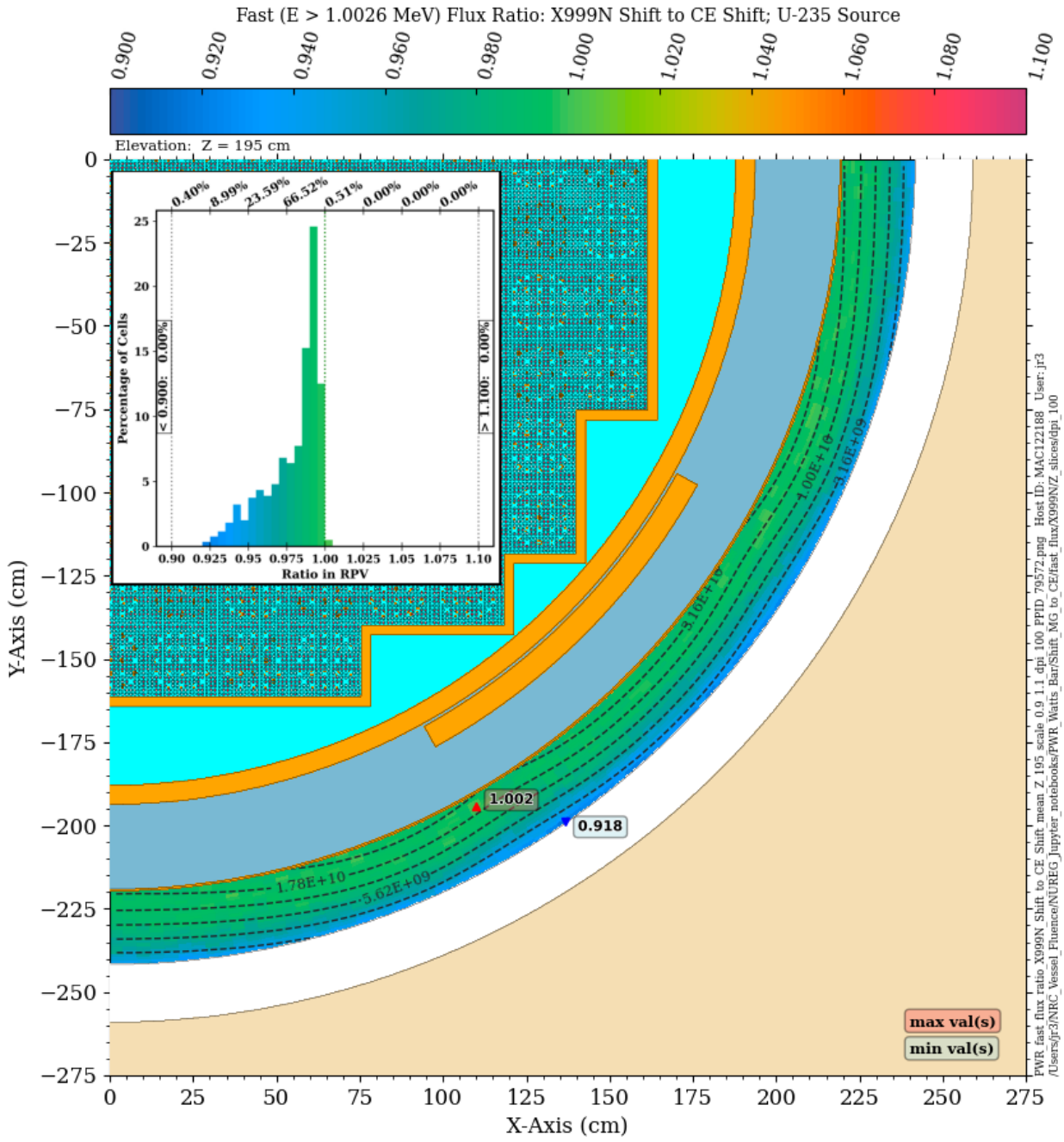

Figure 8-11 Fast neutron flux ratio in the PWR RPV: X999N Shift/CE Shift. Plan view at Z = 195 cm *The contour lines are the fast flux from the CE solution.*

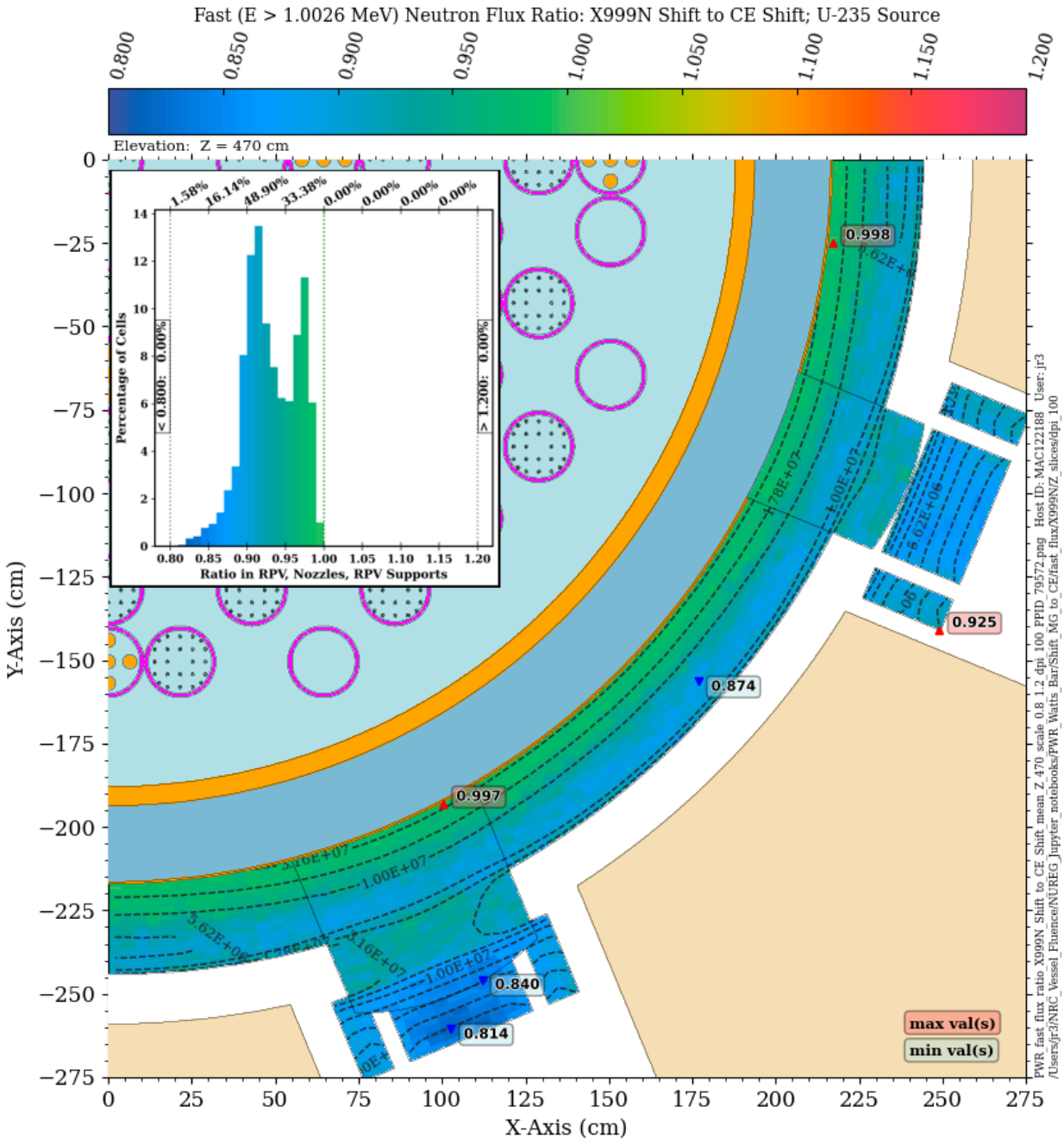

Figure 8-12 Fast neutron flux ratio in the PWR RPV: X999N Shift/CE Shift. Plan view at Z = 470 cm *The contour lines are the fast flux from the CE solution. Note the change in scale relative to Figure 8-11.*

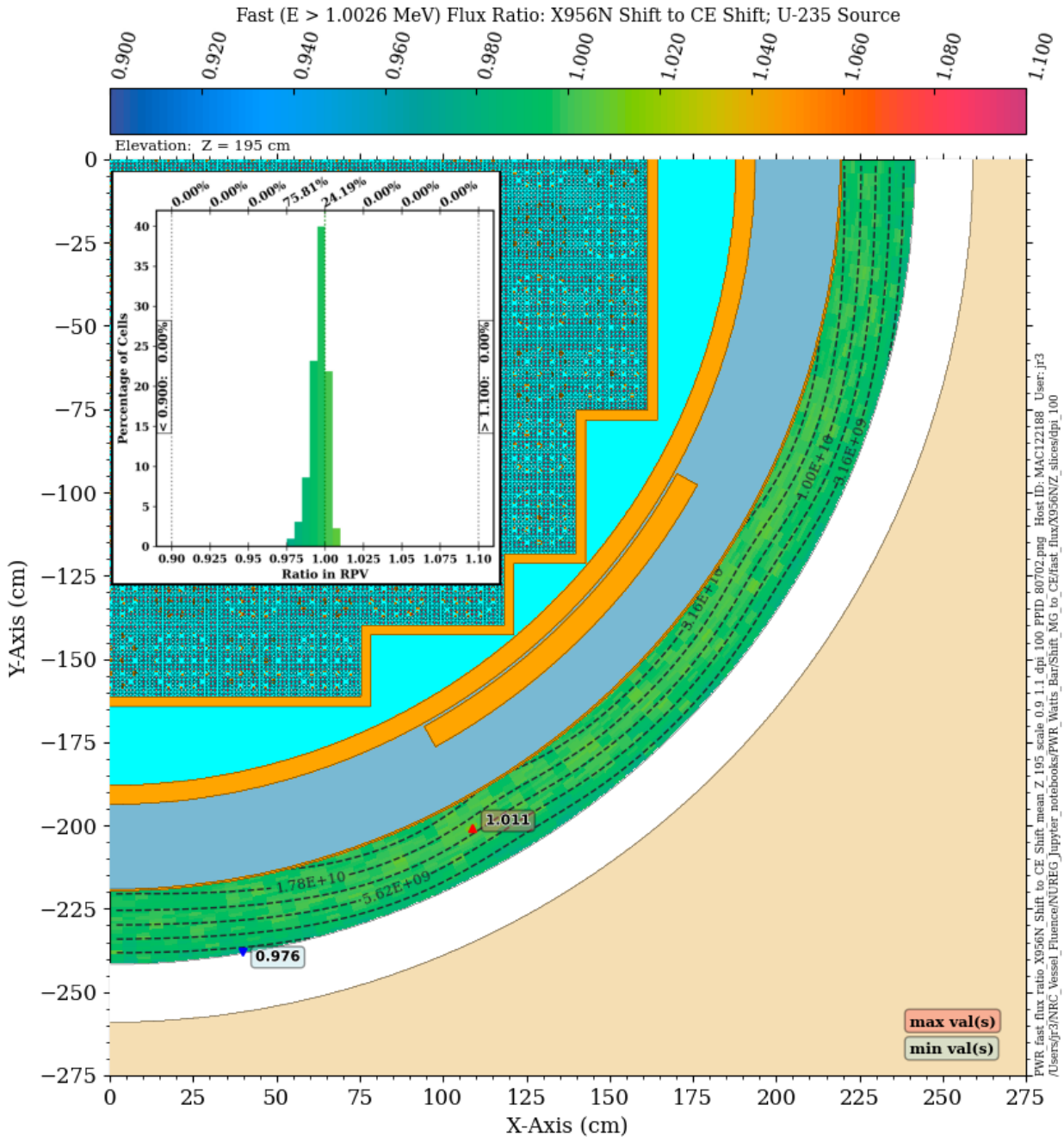

Figure 8-13 Fast neutron flux ratio in the PWR RPV: X956N Shift/CE Shift. Plan view at Z = 195 cm *The contour lines are the fast flux from the CE solution.*

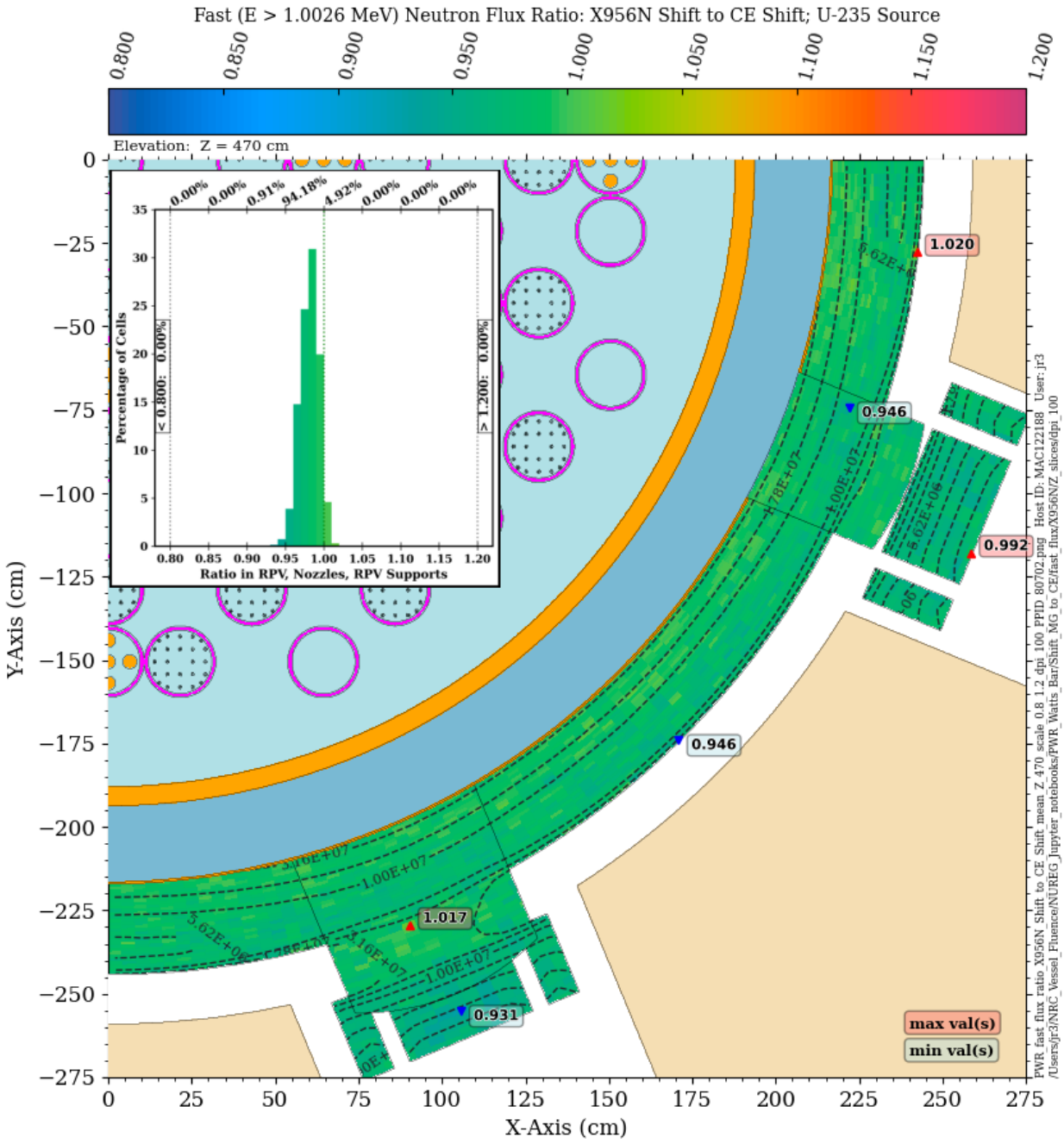

Figure 8-14 Fast neutron flux ratio in the PWR RPV: X956N Shift/CE Shift. Plan view at Z = 470 cm *The contour lines are the fast flux from the CE solution. Note the change in scale relative to Figure 8-13.*

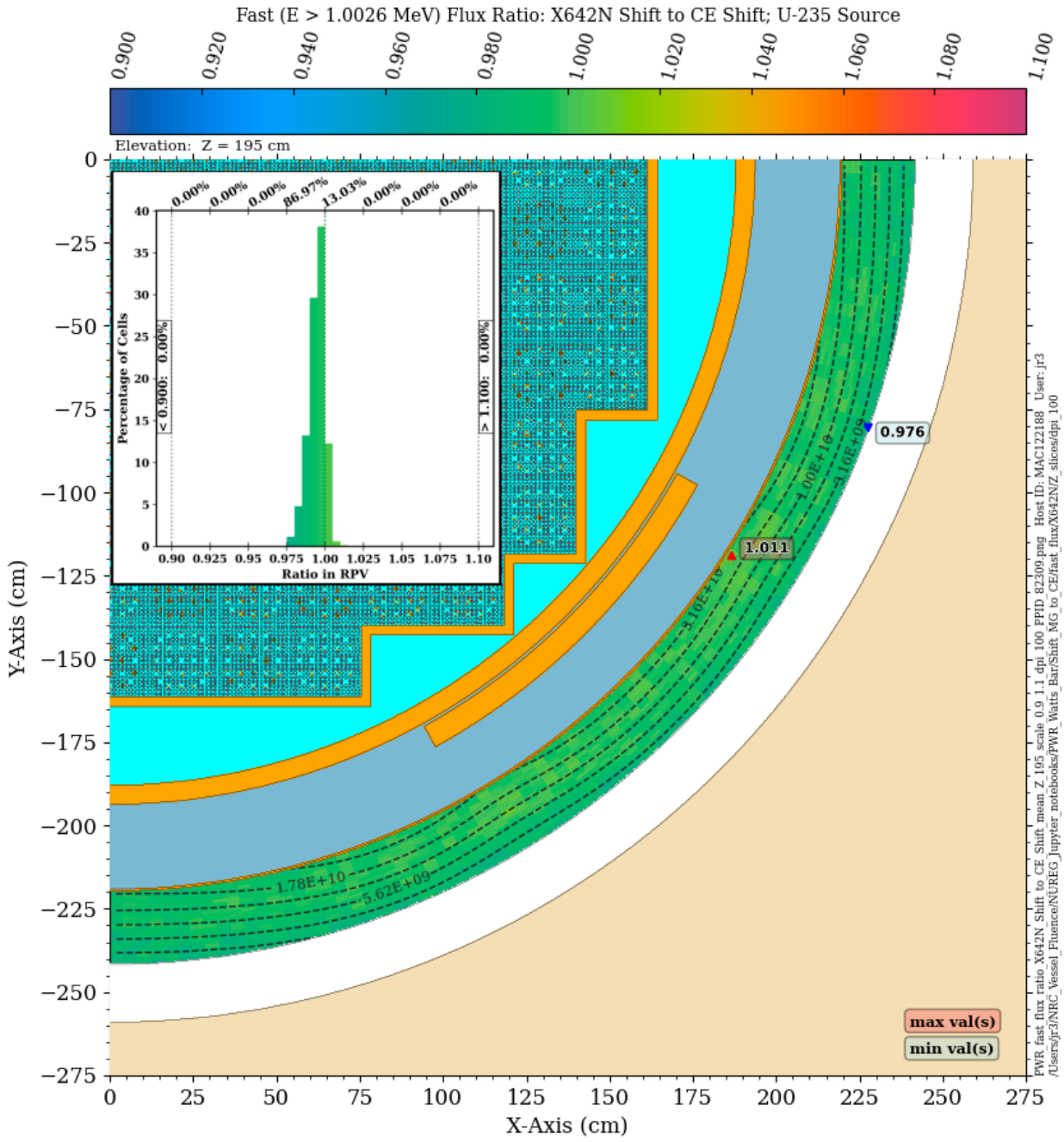

Figure 8-15 Fast neutron flux ratio in the PWR RPV: X642N Shift/CE Shift. Plan view at Z = 195 cm *The contour lines are the fast flux from the CE solution.*

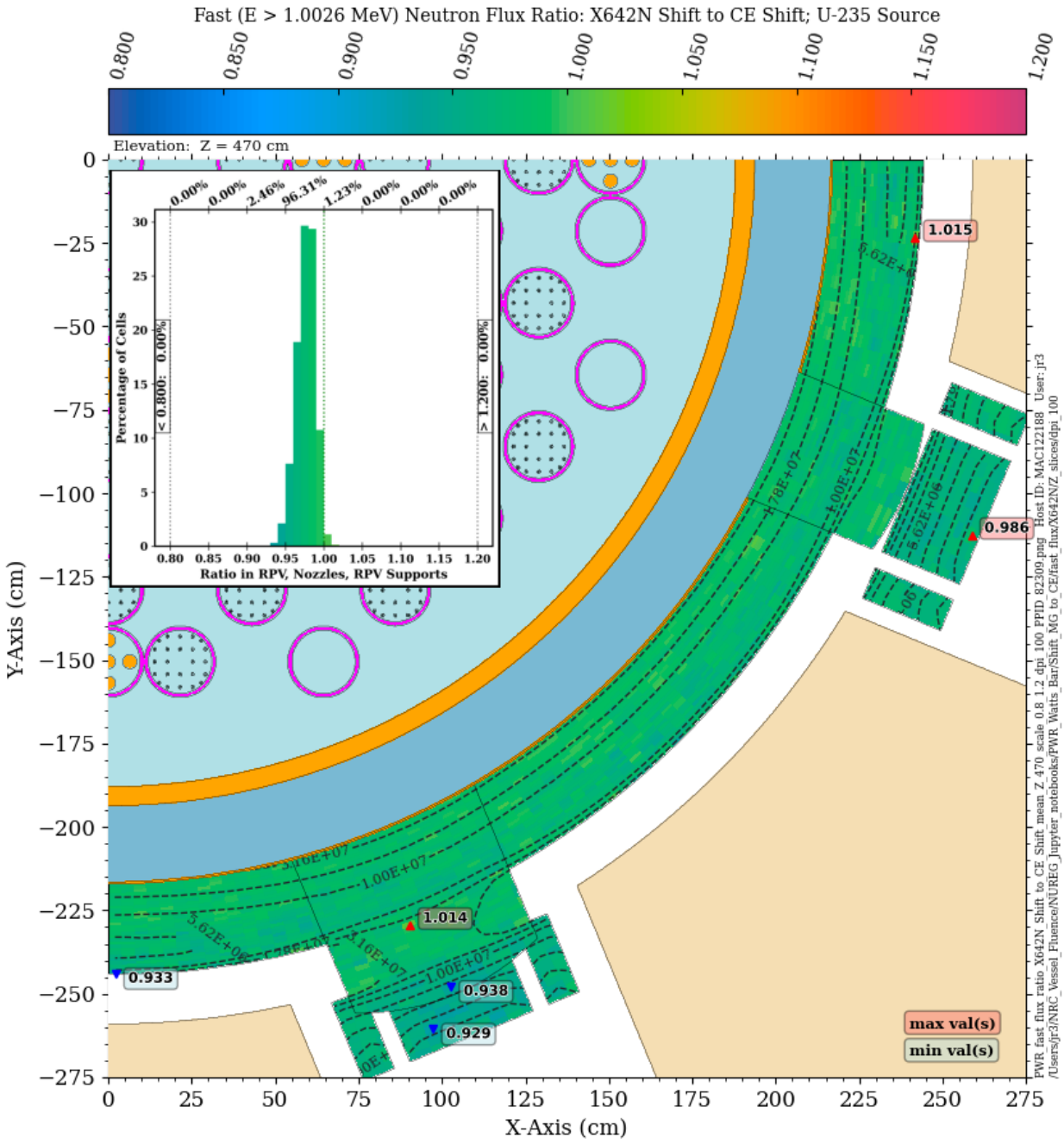

Figure 8-16 Fast neutron flux ratio in the PWR RPV: X642N Shift/CE Shift. Plan view at Z = 470 cm *The contour lines are the fast flux from the CE solution. Note the change in scale relative to Figure 8-15.*

8.3 DPA Rate Calculations

While the fast neutron fluence is often used for neutron damage estimates in RPVs, the accumulated dpa metric is often considered to be a more physically justified for neutron radiation damage effects [90],[91]. Unlike the fast neutron flux, the dpa rate is sensitive to spatial variations of the neutron energy spectrum over the entire neutron energy range. The dpa cross-section data [85] are shown in Figure 8-17. Because of variations in the neutron energy spectrum at different RPV locations (Figure 8-3), the fraction of the dpa rate due to neutrons in a specified energy interval will change as a function of location, as shown in Section 6.1.

As a result of these spectral effects, the difference in dpa rates calculated using MG and CE cross-section data will not mirror the difference in fast flux levels. For the BUGLE-B7 library, the difference in dpa rates compared to a CE solution is significantly greater than the difference in fast neutron flux rates. This can be seen when comparing Figure 8-5 with Figure 8-18 and Figure 8-6 with Figure 8-19. Even at the inner surface of the RPV near the core midplane, the BUGLE-B7 dpa rate is more than 5% lower than the dpa rate from a CE solution. At the outer surface of the RPV at the same elevation, the BUGLE-B7 solution underpredicts the CE solution by 20%. At the elevation of the vessel supports, the BUGLE-B7 solution is more than 20% lower than the CE solution in nearly all mesh tally voxels in the RPV, nozzle, and nozzle supports, with differences of more than 35% at some locations in the nozzle supports. As noted previously, this is an area where the EOL dpa in the nozzle supports could exceed the dpa monitoring threshold given in ASTM E1035-18 [86], even though the EOL fluence is likely to be below the neutron fluence monitoring threshold.

The MG/CE dpa rate ratios for calculations using the VITAMIN-B7 and X200N47Gv71 libraries are shown in Figure 8-20 through Figure 8-23. The MG/CE agreement with these libraries is significantly improved at the core midplane elevation relative to the BUGLE-B7 comparisons, but there are still substantial differences at Z = 470 cm, particularly in nozzle supports. The improvement relative to the BUGLE-B7 solution is likely due in part to the much finer energy-group widths for neutron energies below 1.0026 MeV in the VITAMIN-B7 and X200N47G libraries compared to the BUGLE-B7 library (Figure 8-4). The finer group structure at these energies is important because of the increasing contribution to the dpa rate from neutrons with energies below 1.0026 MeV in the outer part of the RPV, and especially at the elevation of the vessel supports.

The Shift solution with the X999N library shows further improvements at the core midplane (Figure 8-24) and the vessel support elevation (Figure 8-25). Results for the X956N and X642N libraries are shown in Figure 8-26 through Figure 8-29. The X956N library provides excellent agreement with the CE solution at the core midplane, with nearly all mesh tally voxels agreeing within 2.5%. At the elevation of the vessel supports, the deviation is greater, but all mesh tally voxels are within 10% of the CE solution, even in the vessel supports. The accuracy of the X642N solution is degraded relative to the X956N solution, likely due to the coarser group structure of the X642N library for energies below 1.0026 MeV.

Results of these comparisons suggest that dpa rates calculated using the BUGLE-B7 library may be slightly nonconservative in the beltline region and substantially nonconservative in the extended beltline region. Even the VITAMIN-B7 and X200N47Gv71 libraries tend to underpredict the dpa rate (by factors of up to 20% or more) at the elevation of the vessel supports. Only the X956N library provides solutions that agree within 10% of the CE solution at both elevations.

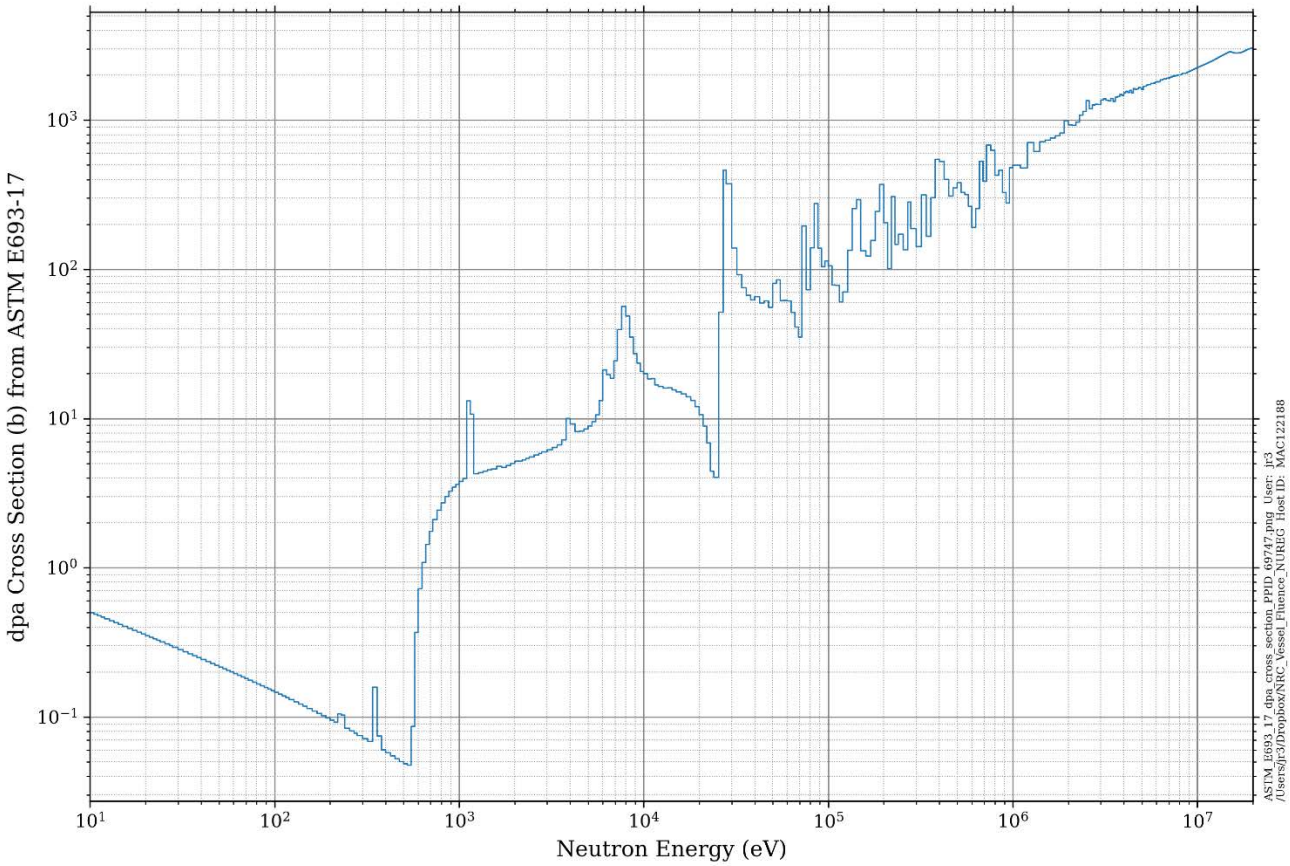

Figure 8-17 Neutron dpa cross section from ASTM E693-17 (reproduced with permission ASTM E693-17, copyright ASTM International, 100 Barr Harbor Drive, West Conshohocken, PA 19428)

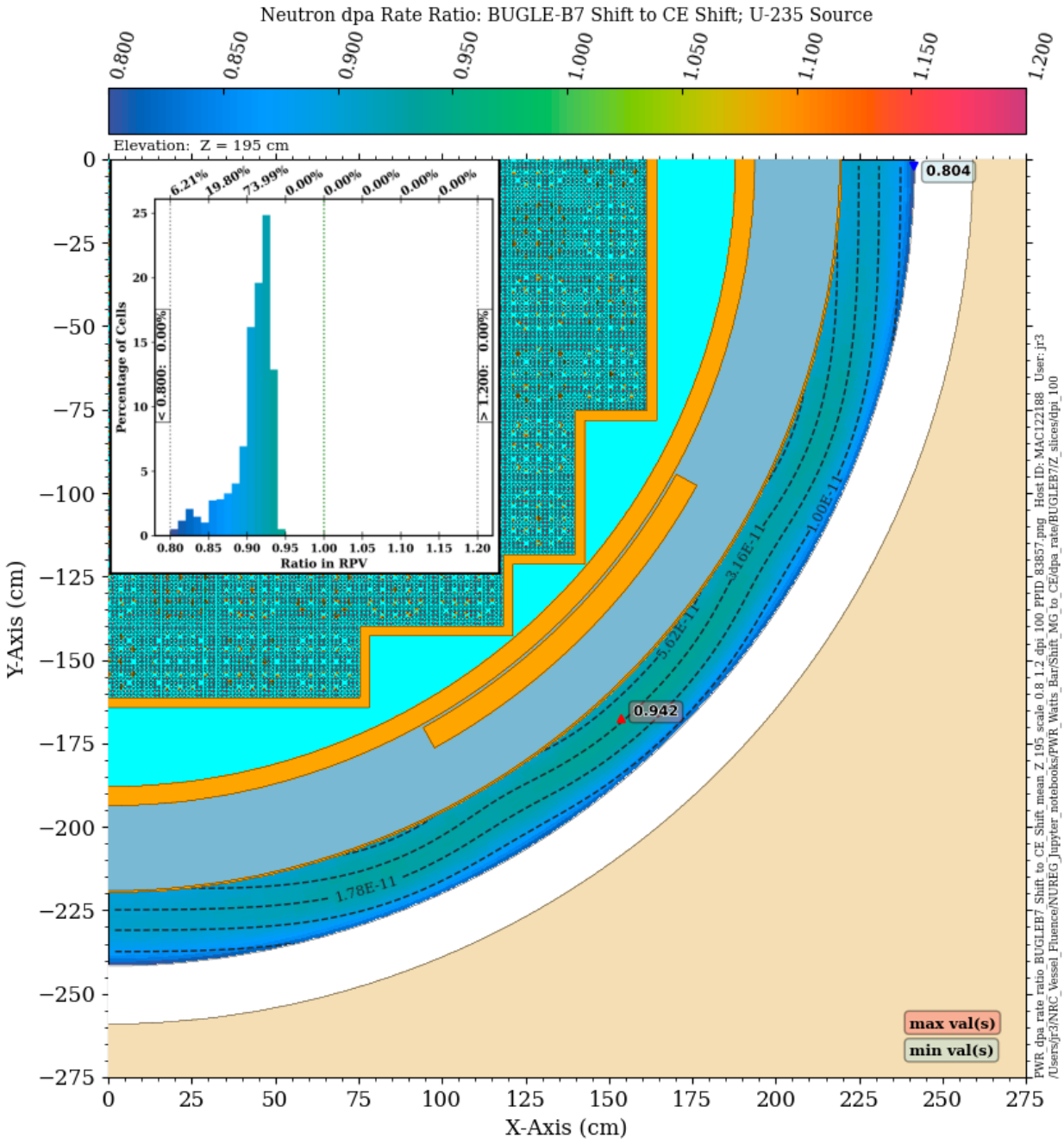

Figure 8-18 DPA rate ratio in the PWR model: BUGLE-B7 Shift/CE Shift. Plan view at Z = 195 cm *The contour lines are the dpa rate from the CE solution.*

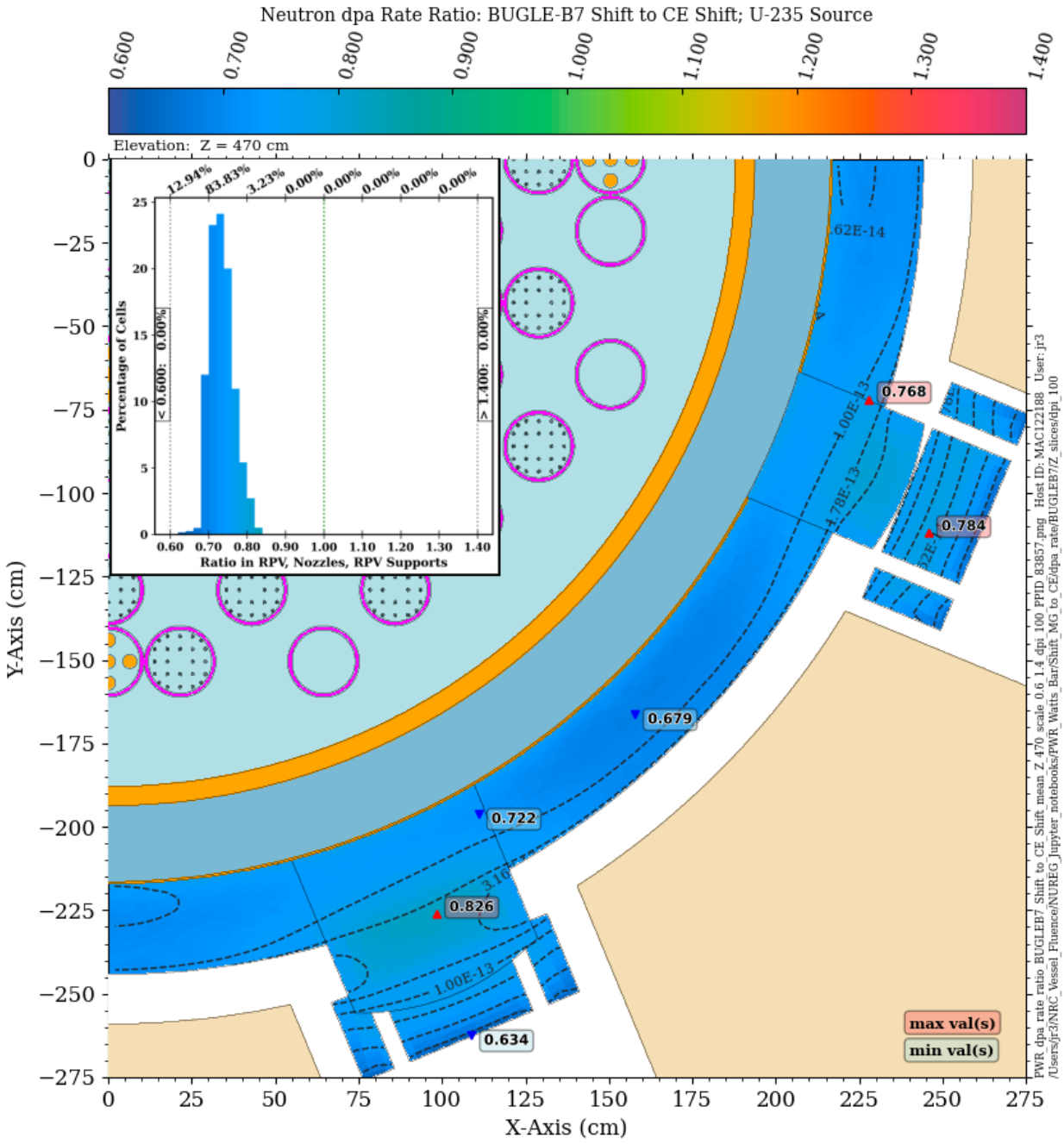

Figure 8-19 DPA rate ratio in the PWR model: BUGLE-B7 Shift/CE Shift. Plan view at Z = 470 cm *The contour lines are the dpa rate from the CE solution. Note the change in scale relative to Figure 8-18.*

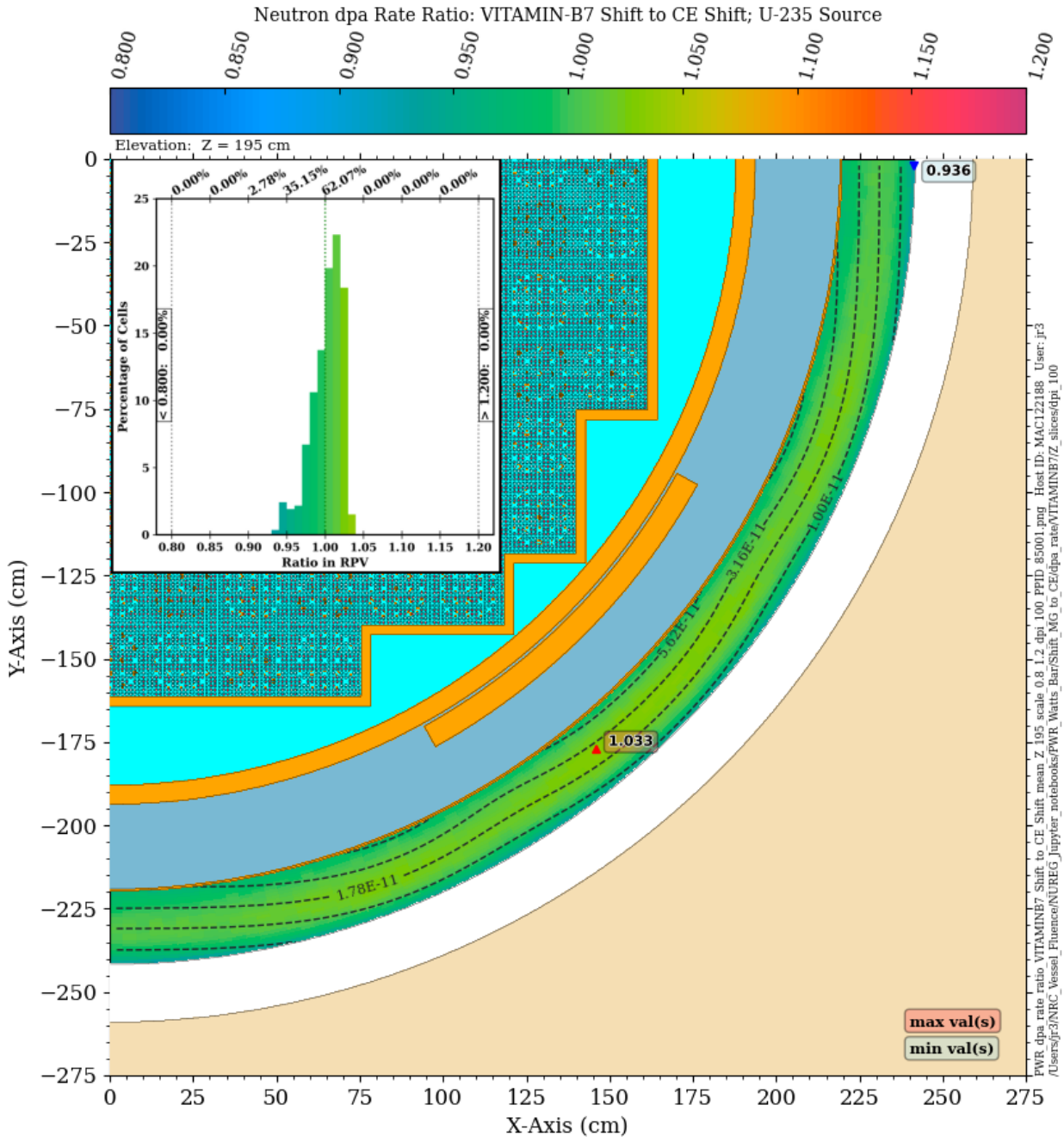

Figure 8-20 DPA rate ratio in the PWR model: VITAMIN-B7 Shift/CE Shift. Plan view at Z = 195 cm *The contour lines are the dpa rate from the CE solution*

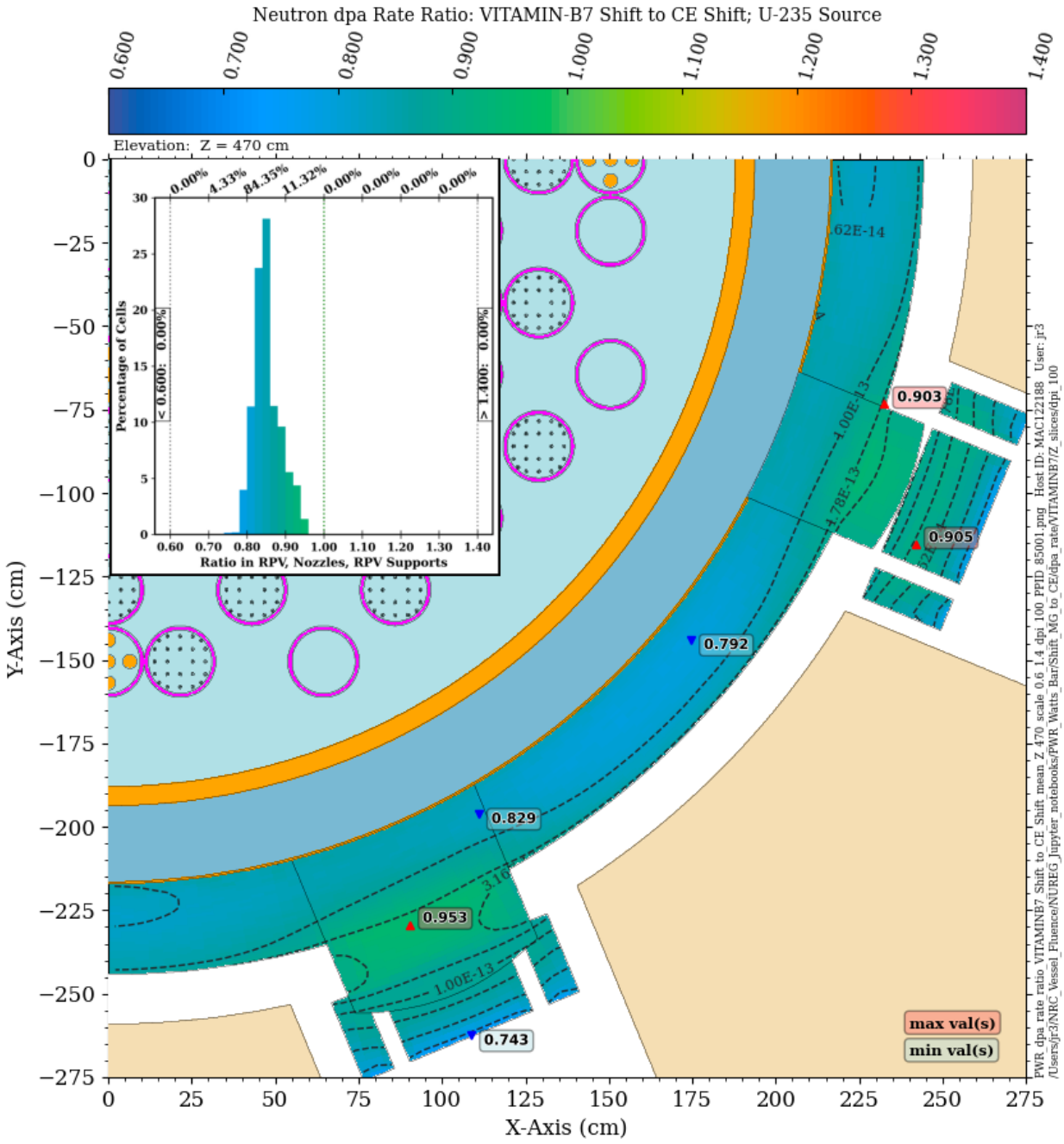

Figure 8-21 DPA rate ratio in the PWR model: VITAMIN-B7 Shift/CE Shift. Plan view at Z = 470 cm *The contour lines are the dpa rate from the CE solution. Note the change in scale relative to Figure 8-20.*

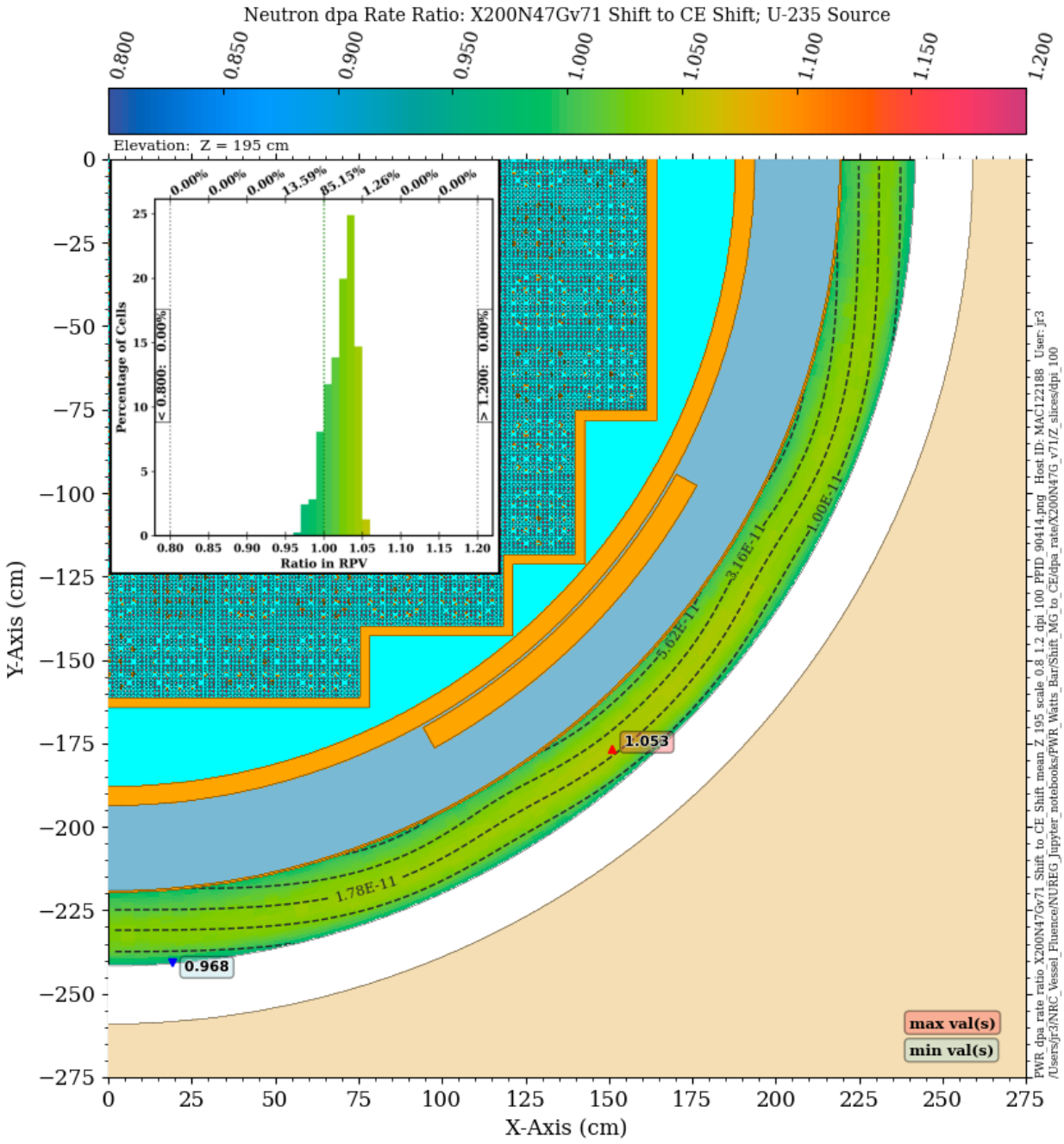

Figure 8-22 DPA rate ratio in the PWR model: X200N47Gv71 Shift/CE Shift. Plan view at Z = 195 cm *The contour lines are the dpa rate from the CE solution.*

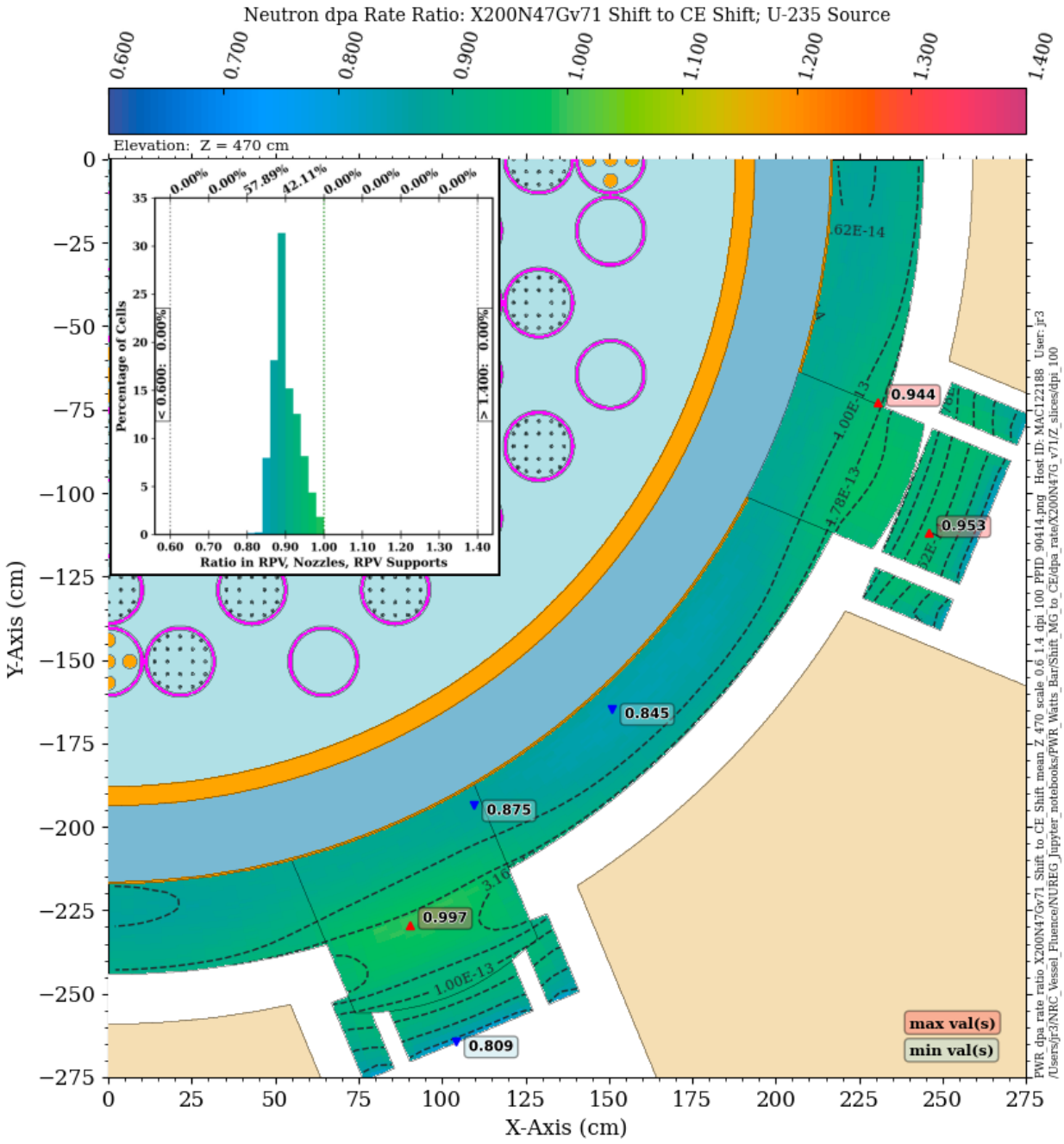

Figure 8-23 DPA rate ratio in the PWR model: X200N47Gv71 Shift/CE Shift. Plan view at Z = 470 cm *The contour lines are the dpa rate from the CE solution. Note the change in scale relative to Figure 8-22.*

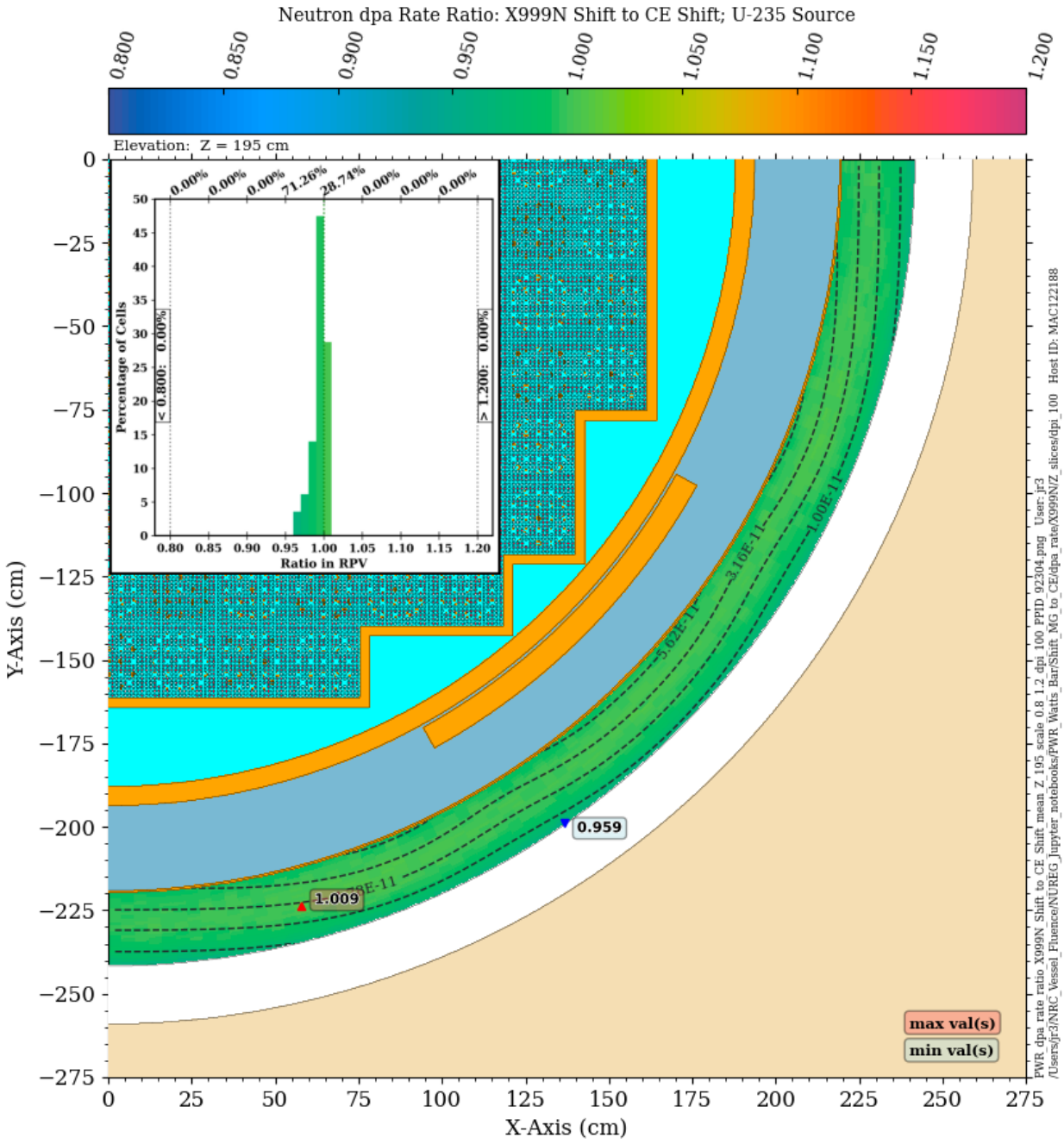

Figure 8-24 DPA rate ratio in the PWR model: X999N Shift/CE Shift. Plan view at Z = 195 cm
The contour lines are the dpa rate from the CE solution.

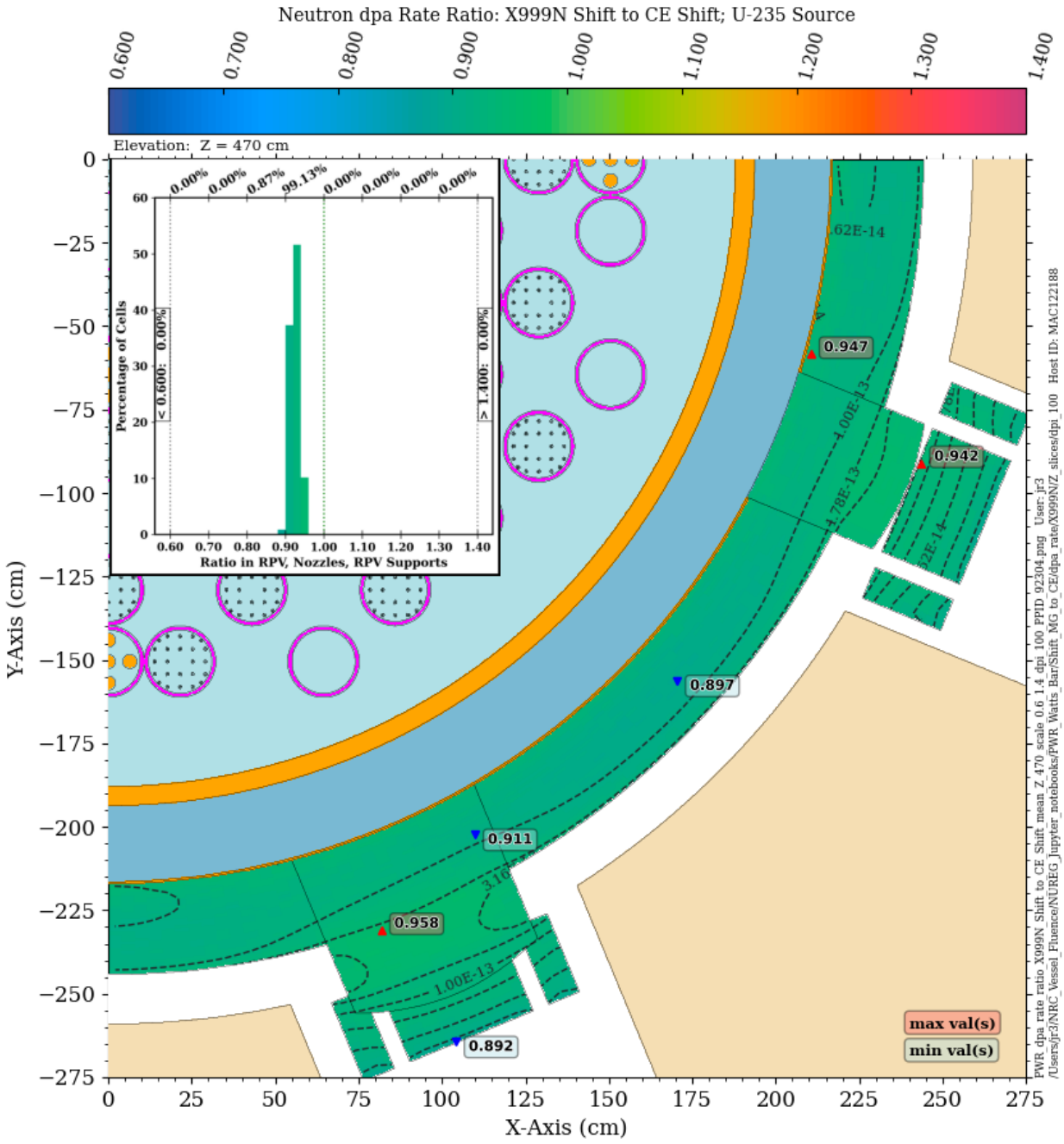

Figure 8-25 DPA rate ratio in the PWR model: X999N Shift/CE Shift. Plan view at Z = 470 cm
The contour lines are the dpa rate from the CE solution. Note the change in scale relative to Figure 8-24.

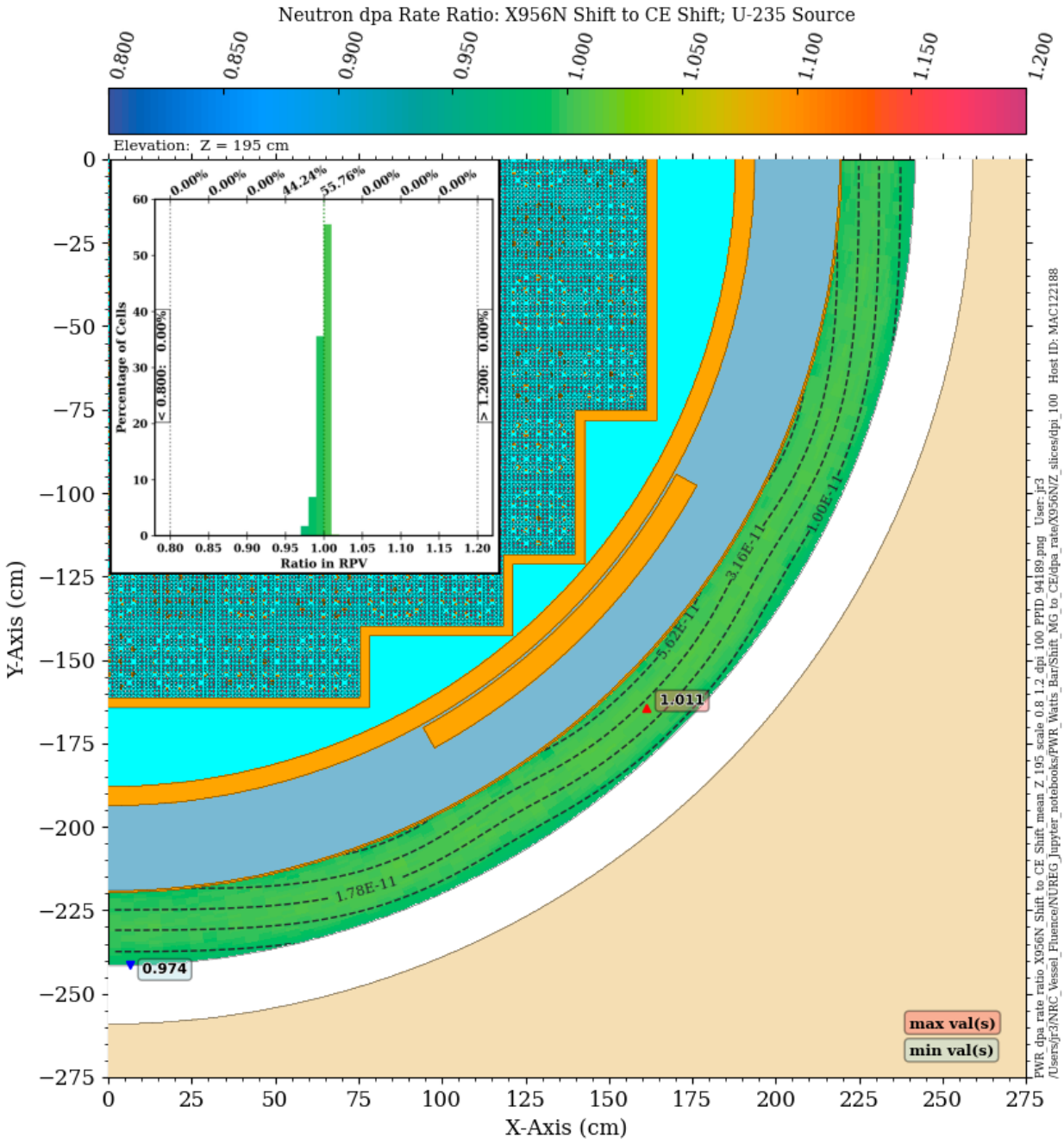

Figure 8-26 DPA rate ratio in the PWR model: X956N Shift/CE Shift. Plan view at Z = 195 cm
The contour lines are the dpa rate from the CE solution.

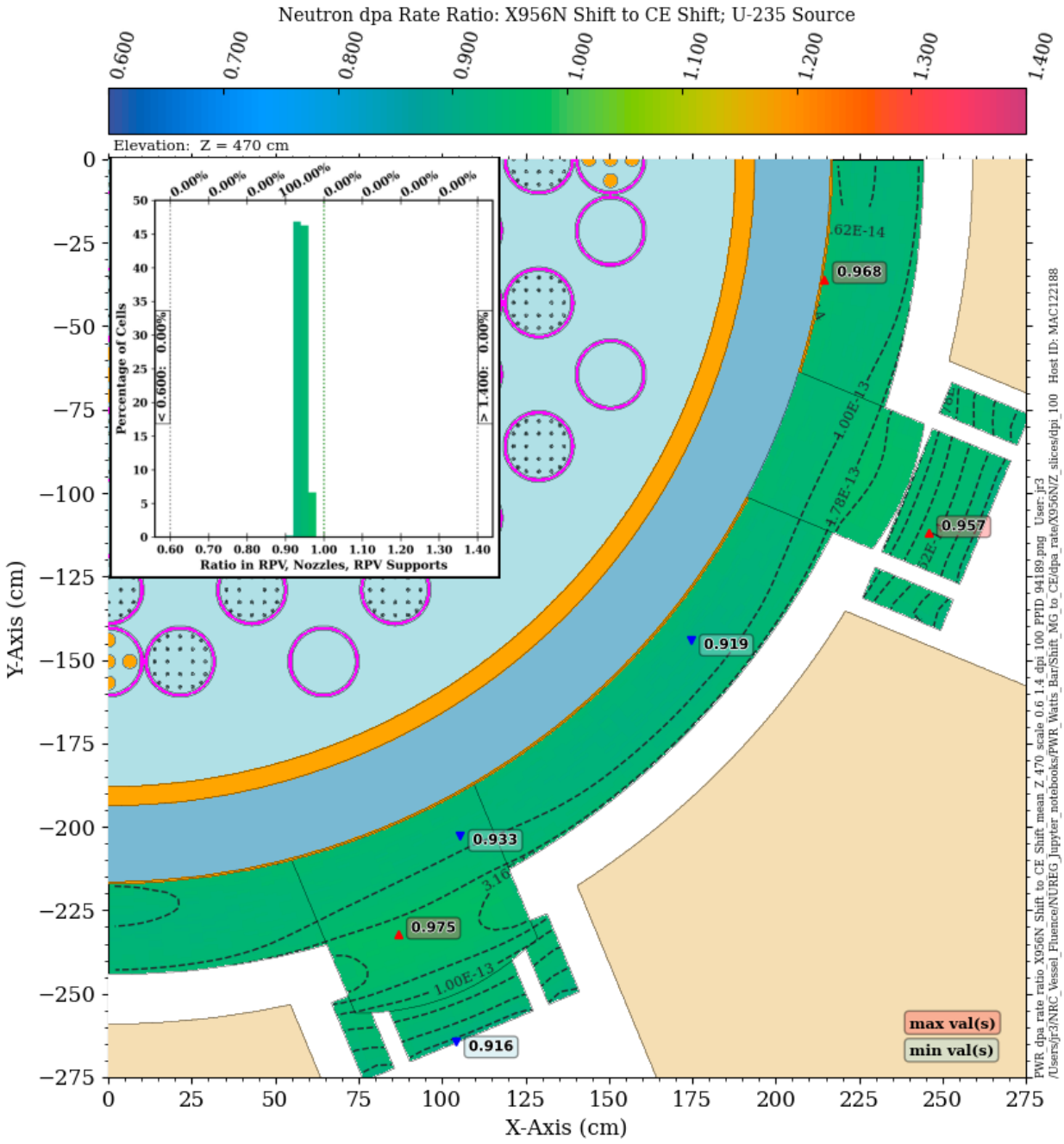

Figure 8-27 DPA rate ratio in the PWR model: X956N Shift/CE Shift. Plan view at Z = 470 cm
The contour lines are the dpa rate from the CE solution. Note the change in scale relative to Figure 8-26.

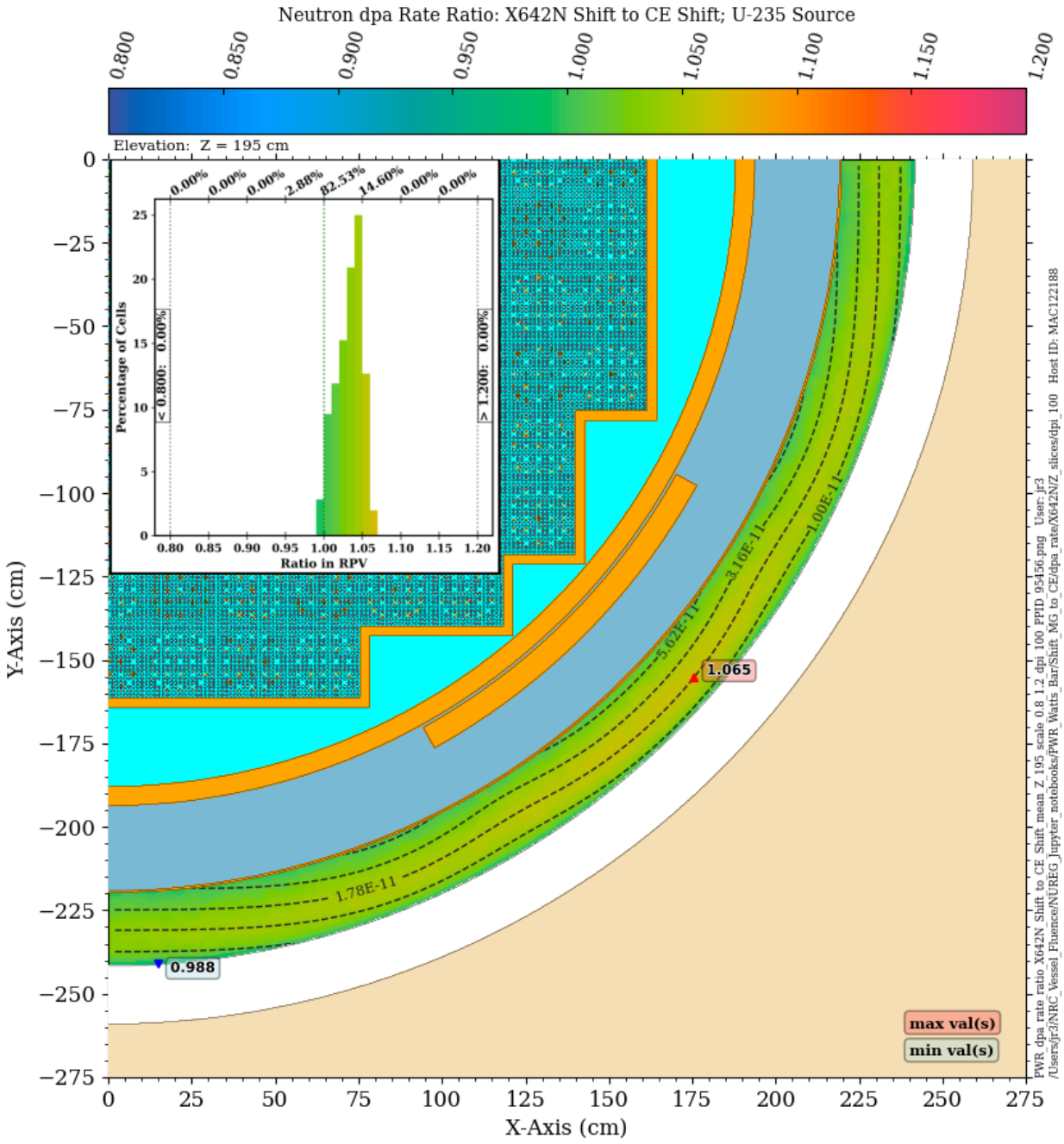

Figure 8-28 DPA rate ratio in the PWR model: X642N Shift/CE Shift. Plan view at Z = 195 cm
The contour lines are the dpa rate from the CE solution.

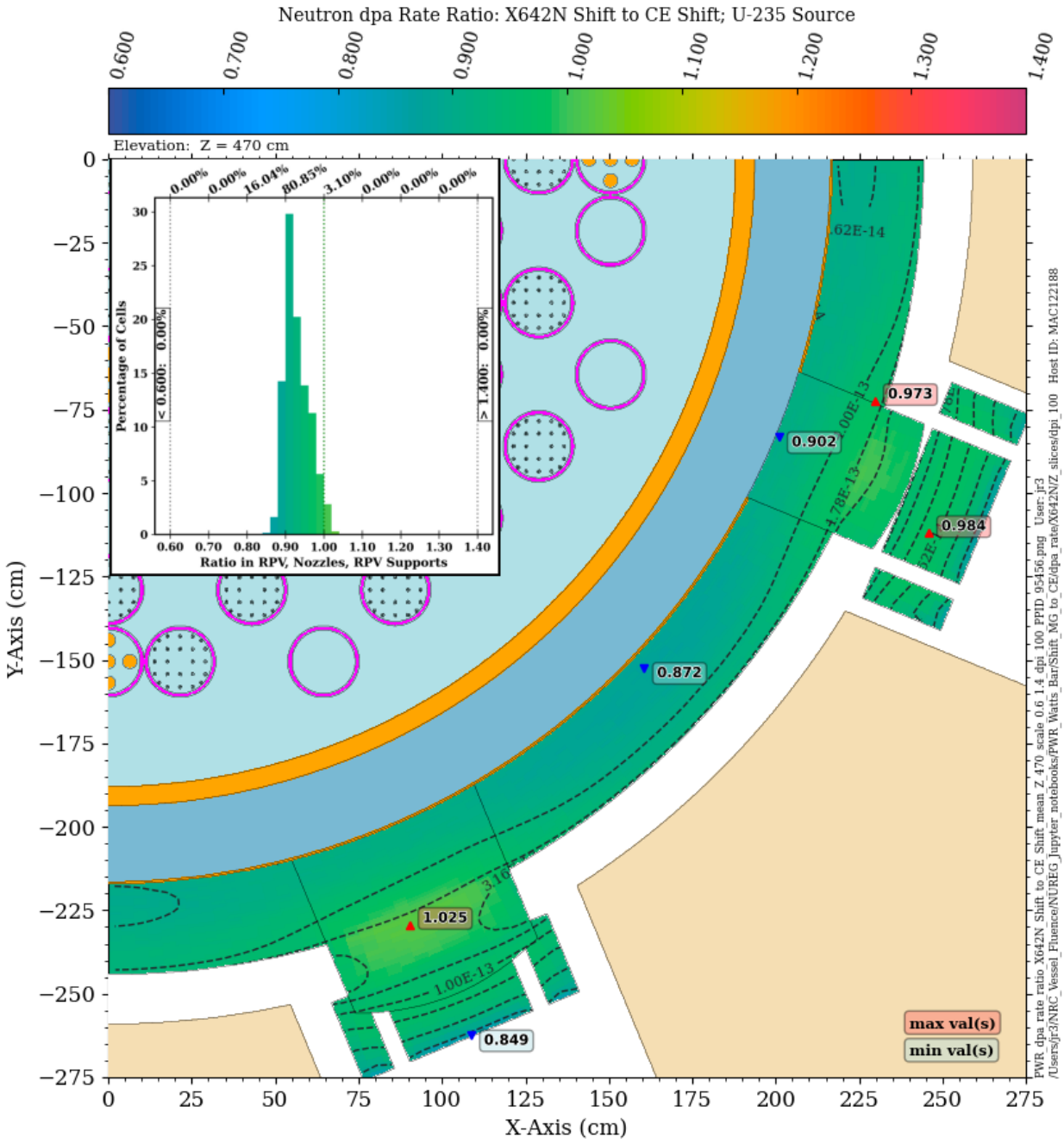

Figure 8-29 DPA rate ratio in the PWR model: X642N Shift/CE Shift. Plan view at Z = 470 cm
The contour lines are the dpa rate from the CE solution. Note the change in scale relative to Figure 8-28.

8.4 Dosimetry Reaction Rates

The dosimetry reaction rates considered in this study are based on dosimetry measurements that were used in the validation of the VITAMIN-B7 and BUGLE-B7 libraries for locations within the traditional beltline region. These reactions have a broad range of threshold energies, and consequently can be used to assess the ability of radiation transport calculations to accurately model neutron transport over the energies of concern for radiation damage. Cross sections for the dosimetry reactions are shown in Figure C-1 and Figure C-2 of APPENDIX C.

For all of the MG/CE ratio plots in this section, ratio values are shown in the cavity gap as well as in the RPV, nozzles, and nozzle supports. The cavity gap is included in the ratios because any ex-vessel dosimetry measurements would be made within the gap.

8.4.1 ^{27}Al (n,α)

The ^{27}Al (n,α) reaction has a threshold energy of 3.25 MeV and a 90% energy response range of 6.45 to11.9 MeV (Table C-1). For this dosimetry reaction, the Shift solution using the BUGLE-B7 library is in relatively good agreement with the CE Shift solution. At the core midplane elevation (Figure 8-30), all of the mesh tally voxels from the BUGLE-B7 solution are within 5% of the CE solution, and over 93% are within 2.5%. At an elevation of 470 cm (Figure 8-31), the BUGLE-B7 solution appears to have a bias of ~3.5% below the CE solution.

The Shift solution using the VITAMIN-B7 (Figure 8-32 and Figure 8-33) library shows no significant differences relative to the BUGLE-B7 solution.

The Shift solution using the X200N47G library is in excellent agreement with the CE solution. Nearly 98% of the ratio values at the core midplane (Figure 8-34) are within 2.5% of unity. At Z = 470 cm (Figure 8-35) nearly 95% of the X200N47G values are within 5% of the CE solution. Results using the X956N library (not shown) are very consistent with those using the X200N47G library.

The relatively good agreement between the MG and CE Shift solutions may not be surprising, as the majority of the ^{27}Al (n,α) reaction rate occurs at energies where the iron cross section is slowing varying (Figure A-1), so energy groups can be relatively broad compared to lower neutron energies where resonance effects are important and finer group widths are needed.

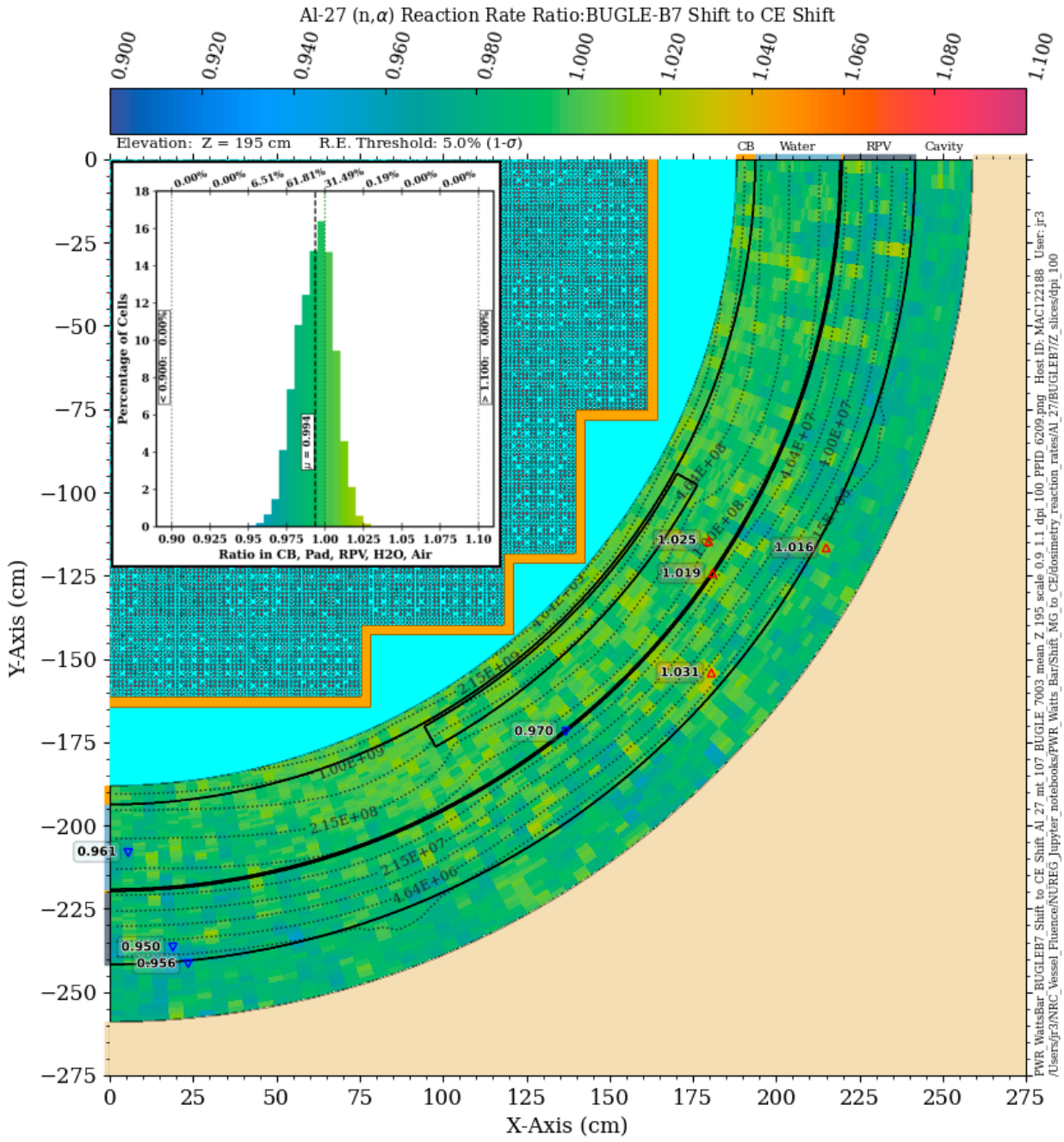

Figure 8-30 **^{27}Al (n,α) reaction rate ratio in the PWR model: BUGLE-B7 Shift/CE Shift. Plan view at Z = 195 cm** *The contour lines are the reaction rate values from the CE solution.*

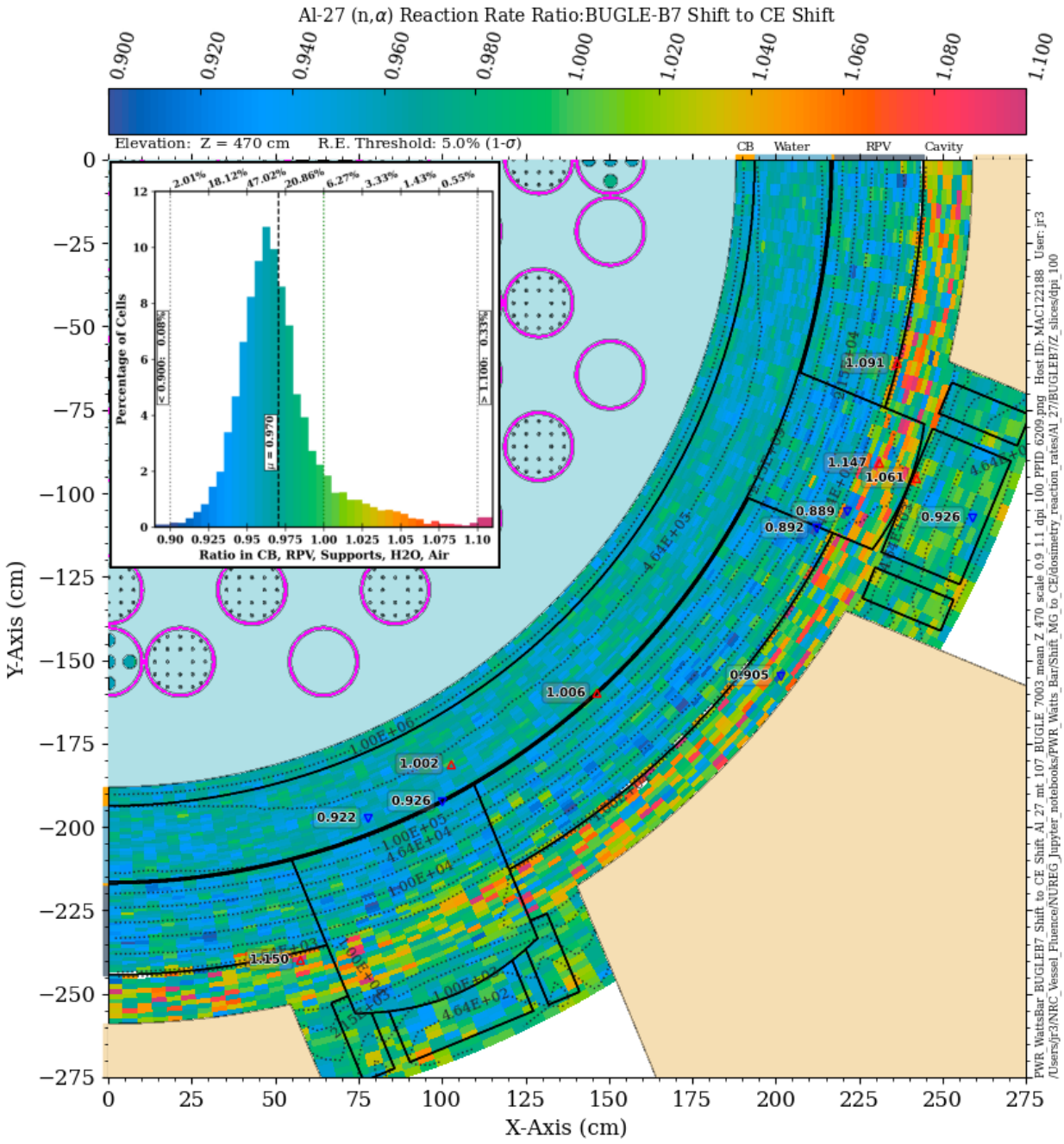

Figure 8-31 **^{27}Al (n,α) reaction rate ratio in the PWR model: BUGLE-B7 Shift/CE Shift. Plan view at Z = 470 cm** *The contour lines are the reaction rate values from the CE solution. Note the change in scale relative to Figure 8-30.*

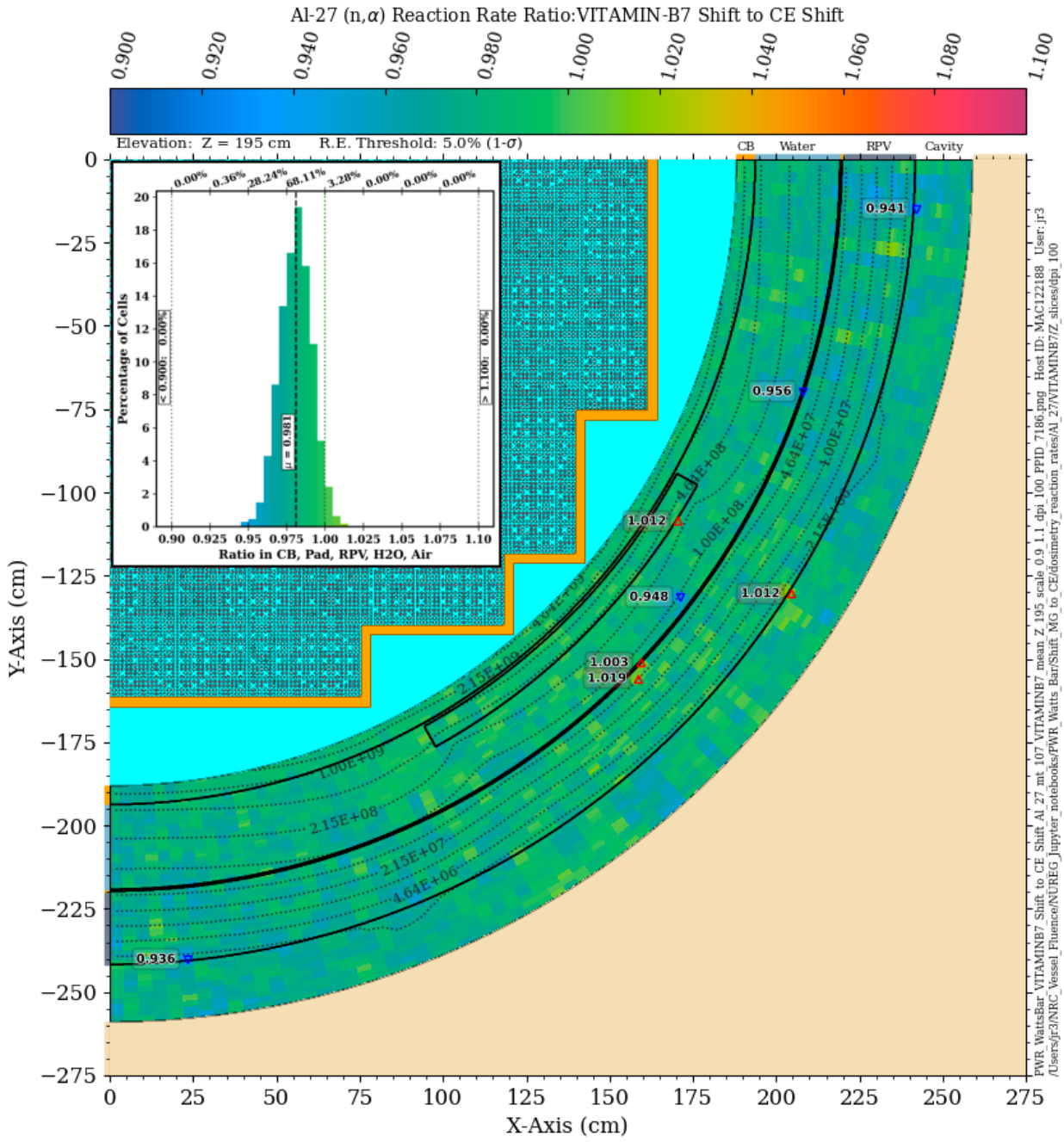

Figure 8-32 **^{27}Al (n,α) reaction rate ratio in the PWR model: VITAMIN-B7 Shift/CE Shift. Plan view at Z = 195 cm** *The contour lines are the reaction rate values from the CE solution.*

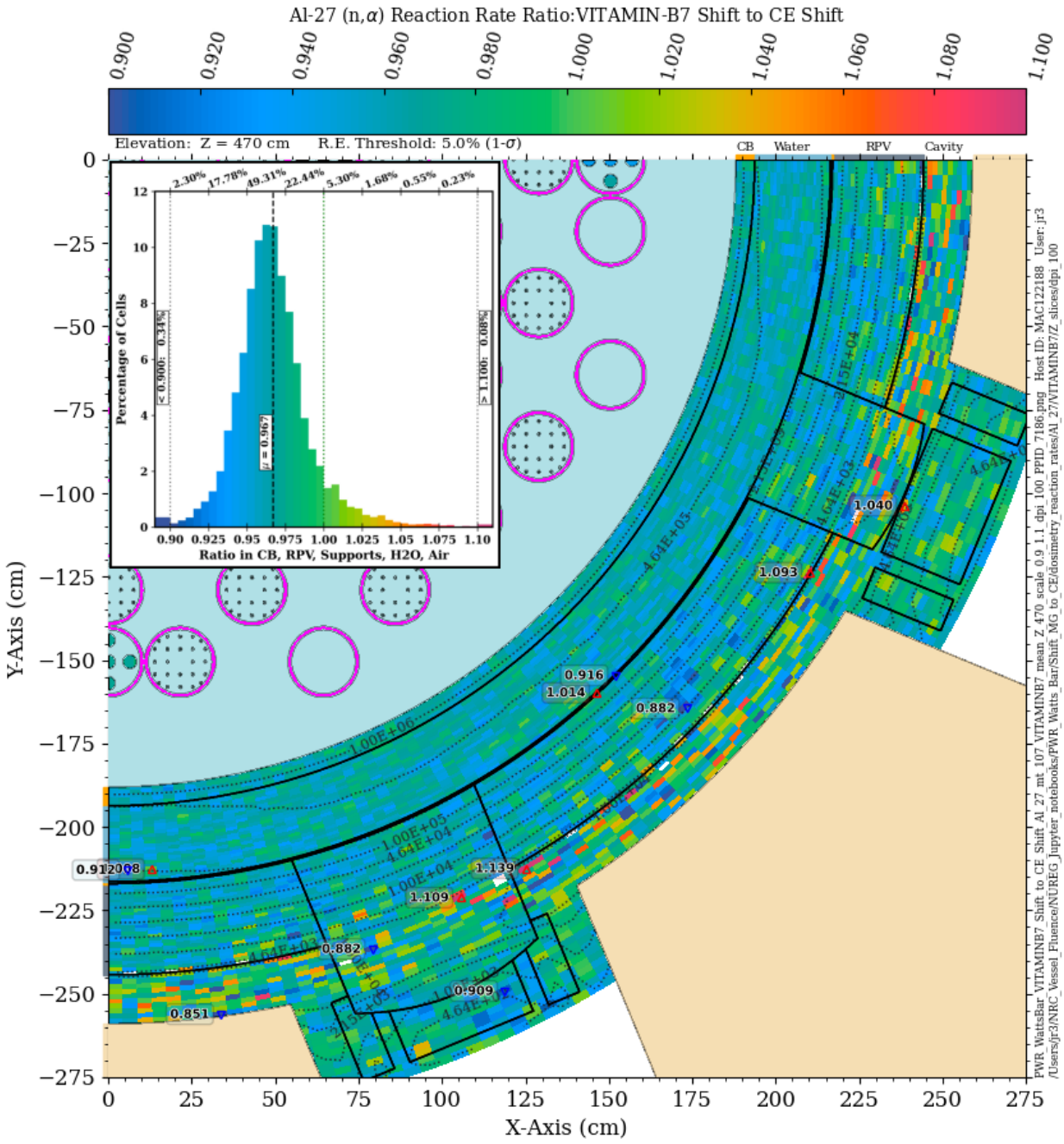

Figure 8-33 **^{27}Al (n,α) reaction rate ratio in the PWR model: VITAMIN-B7 Shift/CE Shift. Plan view at Z = 470 cm** *The contour lines are the reaction rate values from the CE solution.*

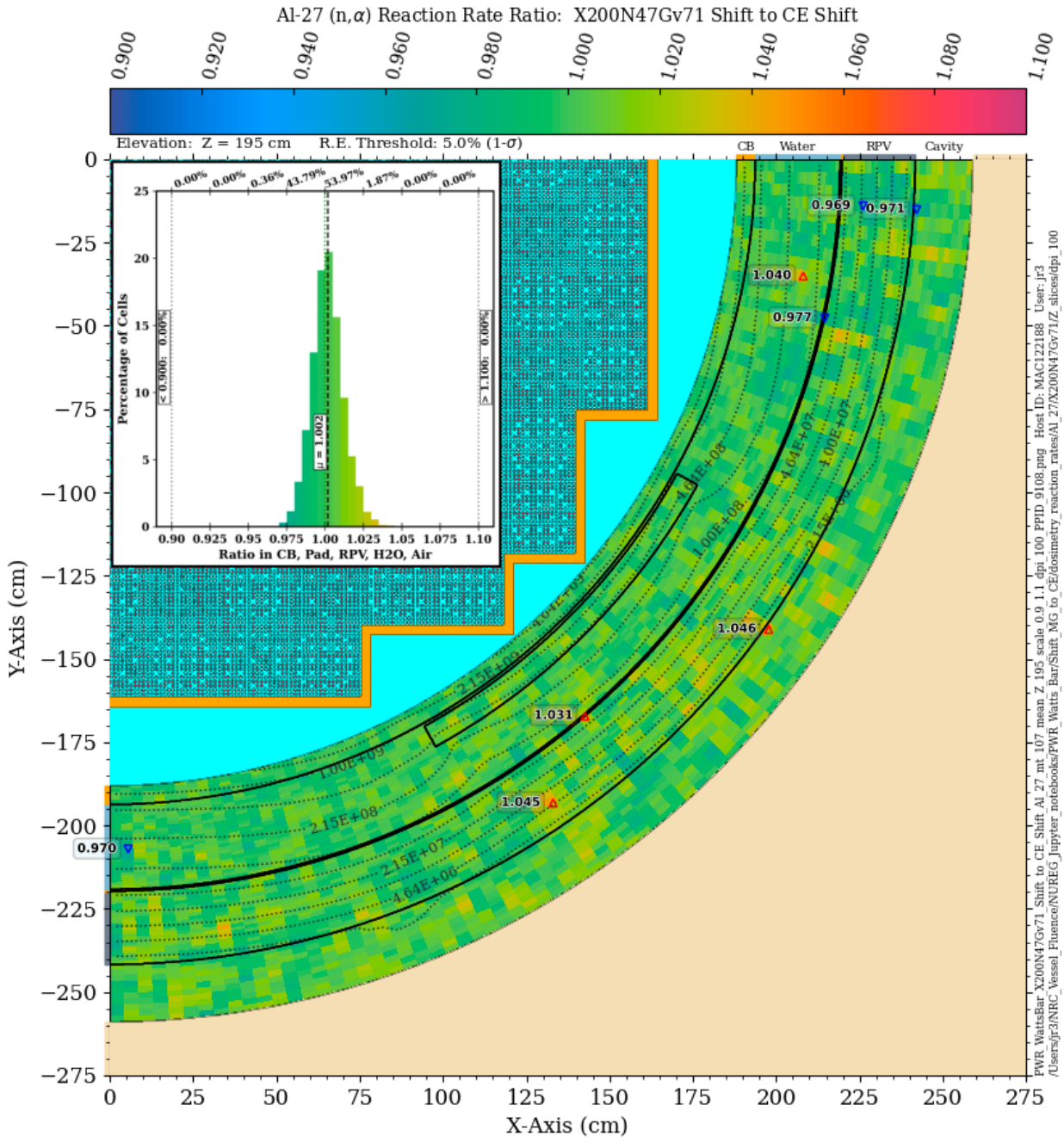

Figure 8-34 **^{27}Al (n,α) reaction rate ratio in the PWR model: X200N47Gv71 Shift/CE Shift. Plan view at Z = 195 cm** *The contour lines are the reaction rate values from the CE solution.*

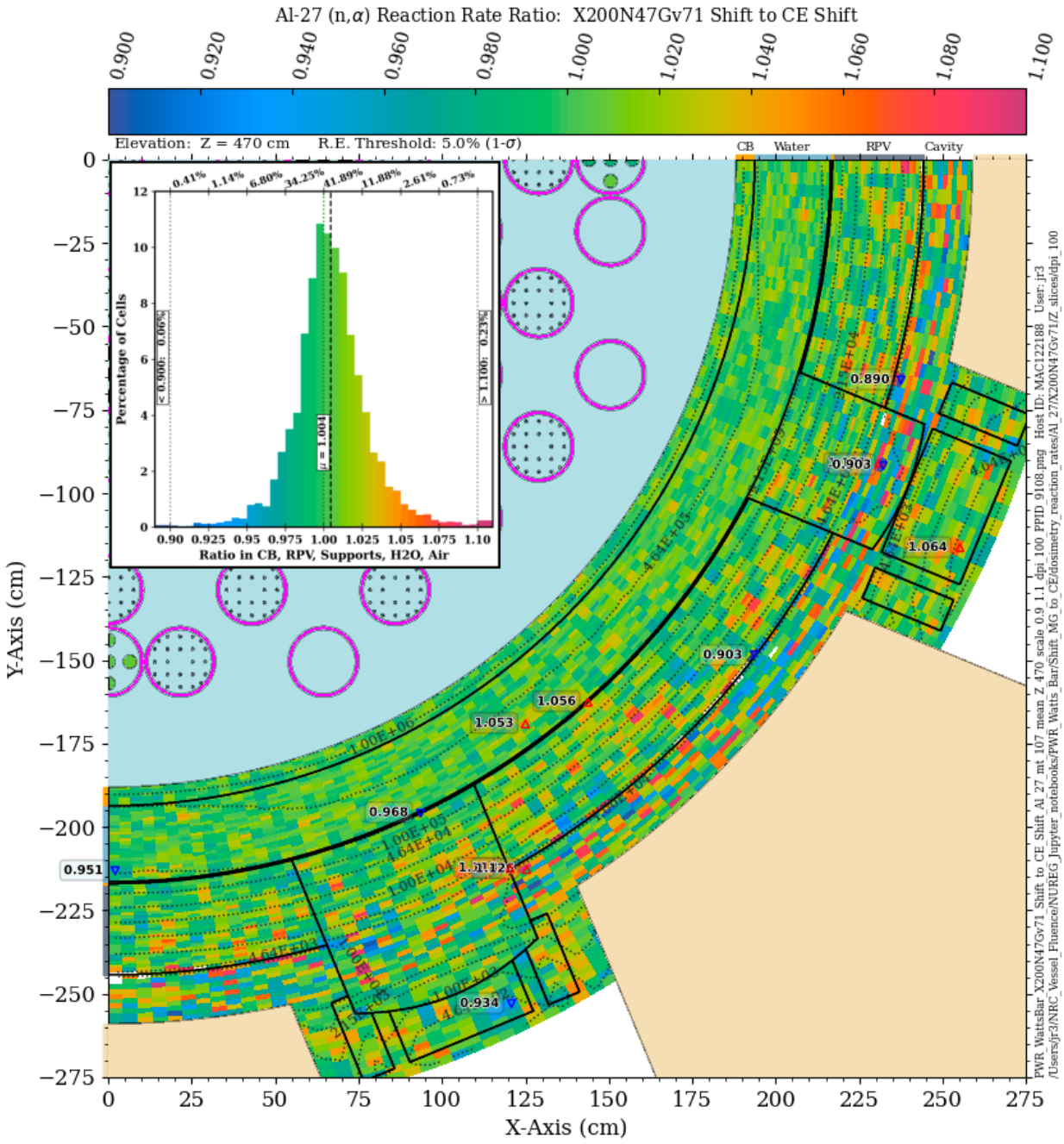

Figure 8-35 **^{27}Al (n,α) reaction rate ratio in the PWR model: X200N47Gv71 Shift/CE Shift. Plan view at Z = 470 cm** *The contour lines are the reaction rate values from the CE solution.*

8.4.2 ^{63}Cu (n,α)

The ^{63}Cu (n,α) reaction has a threshold energy of 2.25 MeV and a 90% energy response range of 4.53 to 11.0 MeV (Table C-1). For this dosimetry reaction, the Shift solution using the BUGLE-B7 library is in relatively good agreement with the CE Shift solution. At the core midplane elevation (Figure 8-36), over 99% of the mesh tally voxels from the BUGLE-B7 solution are within 5% of the CE solution, and nearly 90% are within 2.5%. At Z = 470 cm (Figure 8-37), the BUGLE-B7 solution appears to have a bias of ~5% below the CE solution.

As was the case with the ^{27}Al (n,α) reaction, the Shift solution using the VITAMIN-B7 library (Figure 8-38 and Figure 8-39) library shows no significant differences relative to the BUGLE-B7 solution.

The Shift MG solution using the X200N47G library is in excellent agreement with the CE solution at both elevations. At the core midplane (Figure 8-40), the X200N47G solution is within 2.5% of the CE solution in nearly 99% of the mesh tally voxels. At Z = 470 cm (Figure 8-41), the agreement is slightly degraded, but the solutions agree within 5% in over 94% of the mesh tally voxels. Results using the X956N library (not shown) are very consistent with those using the X200N47G library.

As with the ^{27}Al MG/CE comparisons (Section 8.4.1), the generally good agreement between the MG and CE solutions is likely due to the fact that the majority of the ^{63}Cu (n,α) reaction rate occurs at energies in which the iron cross section is slowly varying.

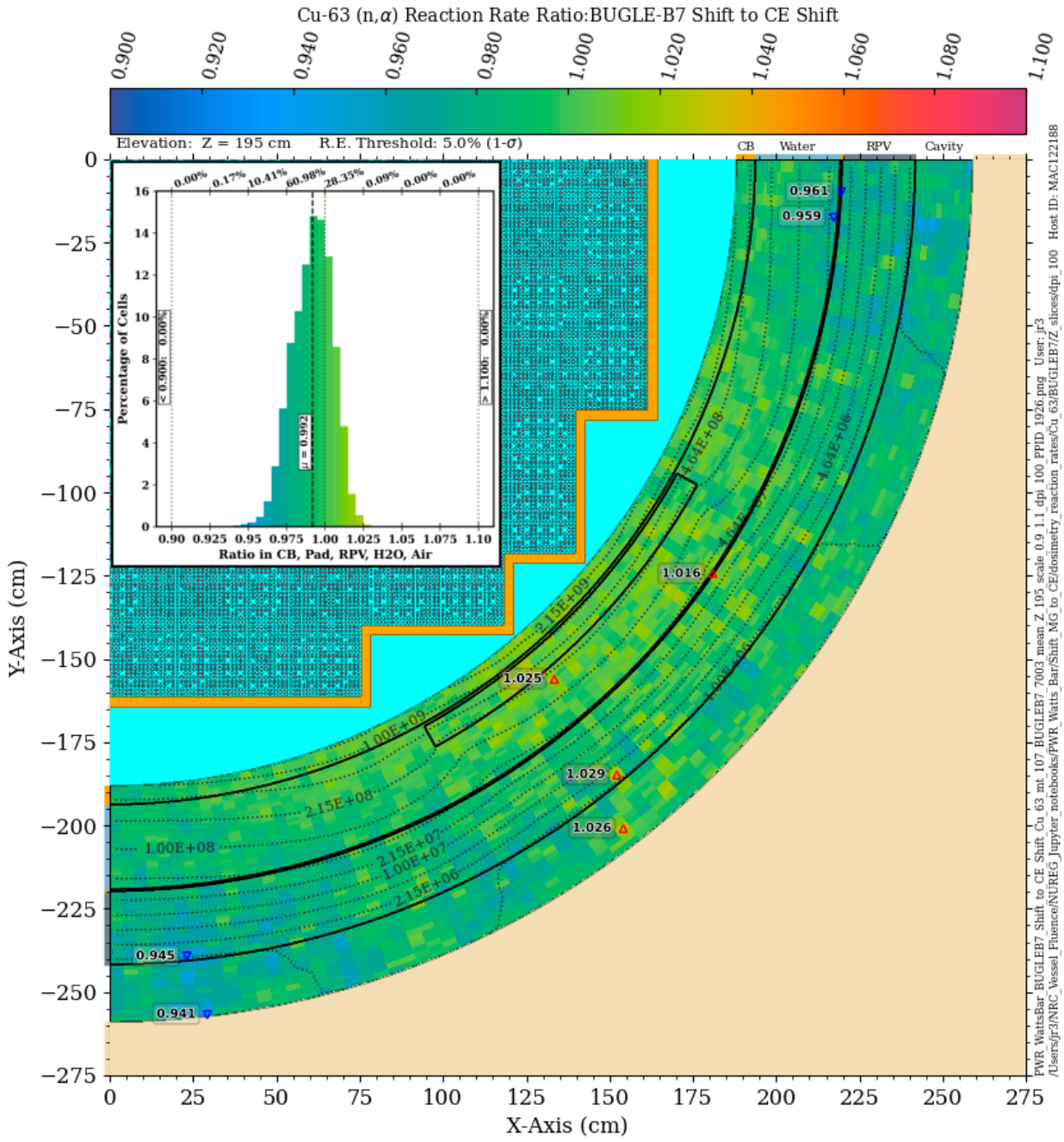

Figure 8-36 **^{63}Cu (n,α) reaction rate ratio in the PWR model: BUGLE-B7 Shift/CE Shift. Plan view at Z = 195 cm** *The contour lines are the reaction rate values from the CE solution.*

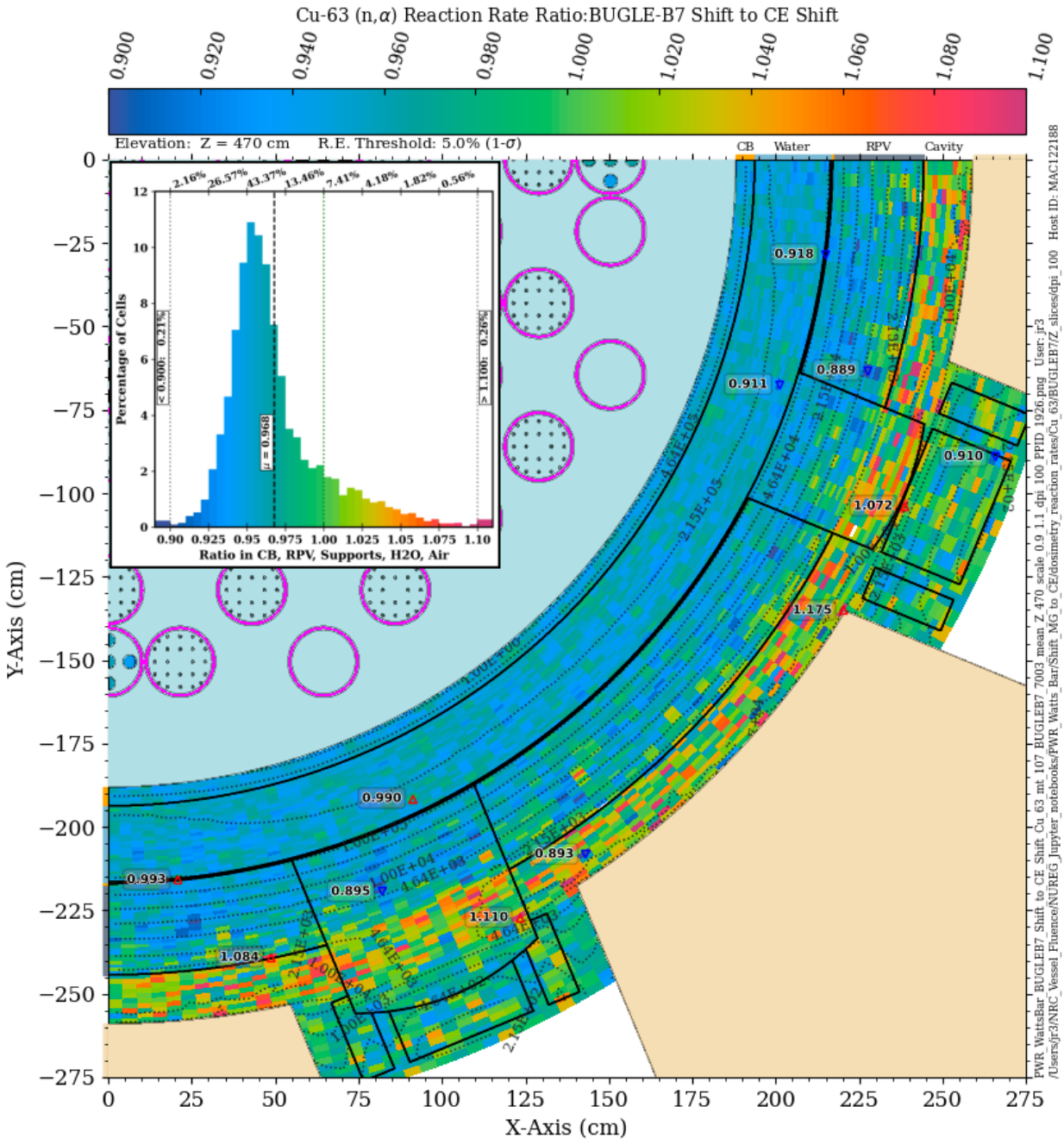

Figure 8-37 **^{63}Cu (n,α) reaction rate ratio in the PWR model: BUGLE-B7 Shift/CE Shift. Plan view at Z = 470 cm** *The contour lines are the reaction rate values from the CE solution.*

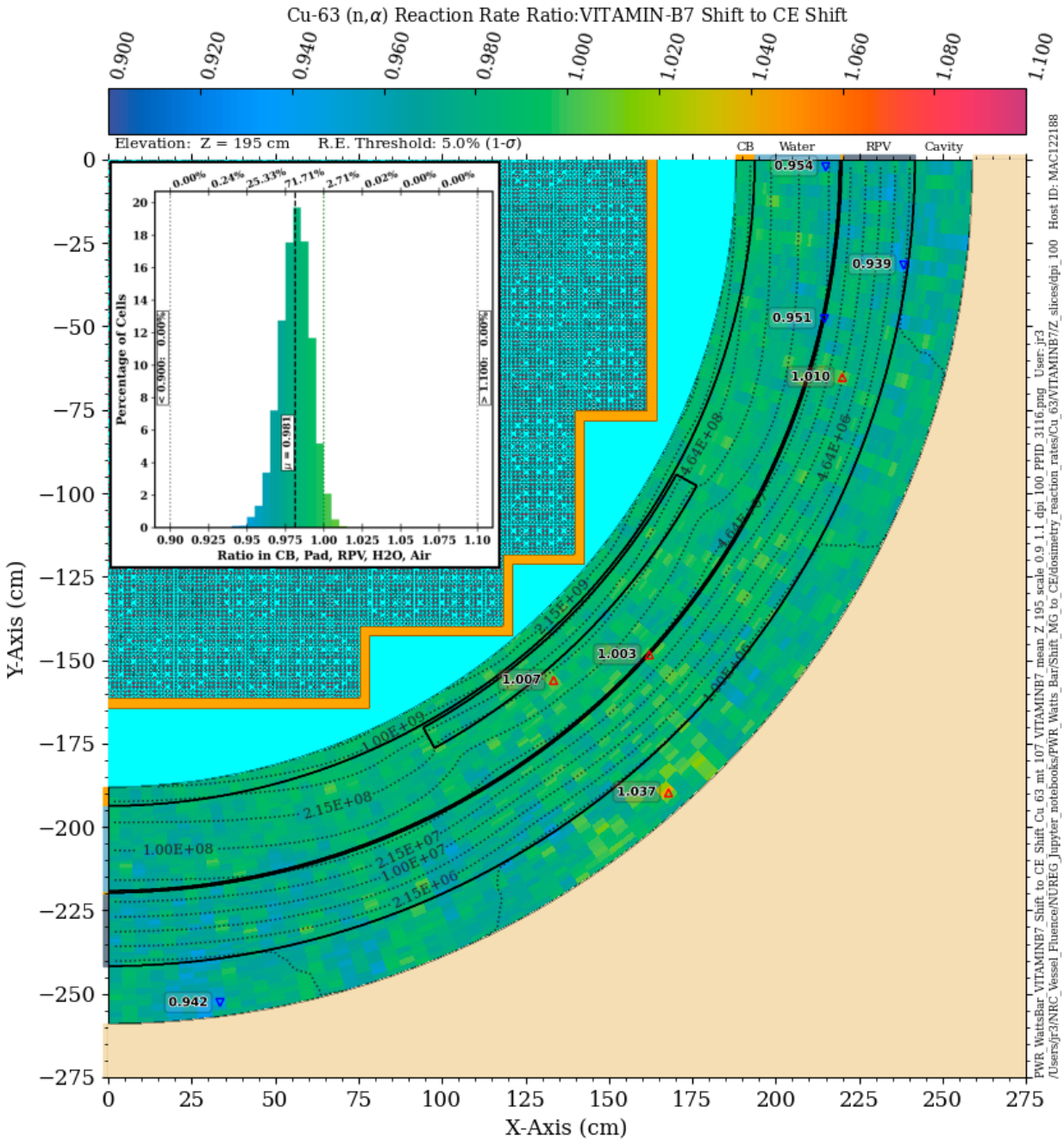

Figure 8-38 **^{63}Cu (n,α) reaction rate ratio in the PWR model: VITAMIN-B7 Shift/CE Shift. Plan view at Z = 195 cm** *The contour lines are the reaction rate values from the CE solution.*

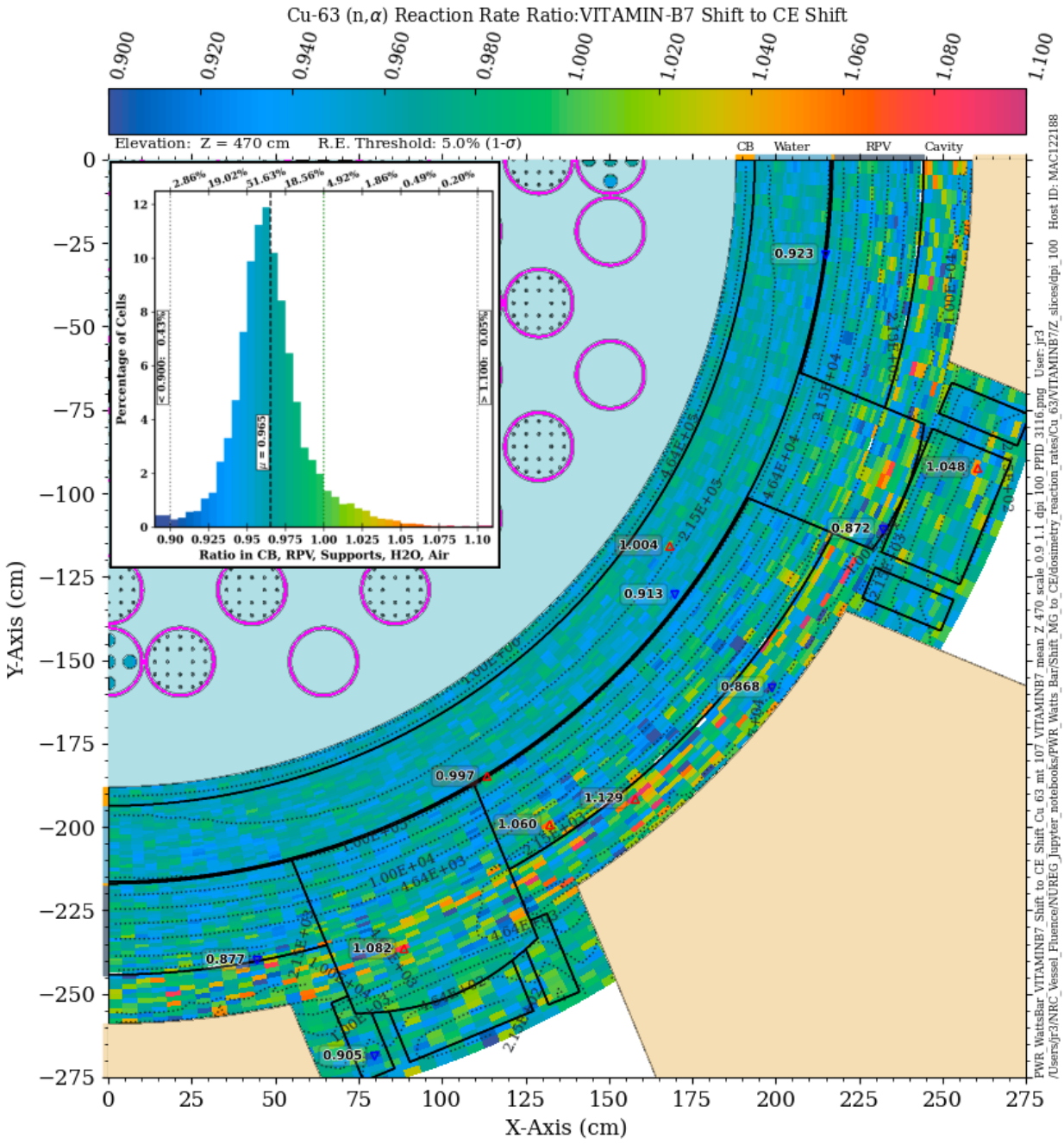

Figure 8-39 **^{63}Cu (n,α) reaction rate ratio in the PWR model: VITAMIN-B7 Shift/CE Shift. Plan view at Z = 470 cm** *The contour lines are the reaction rate values from the CE solution.*

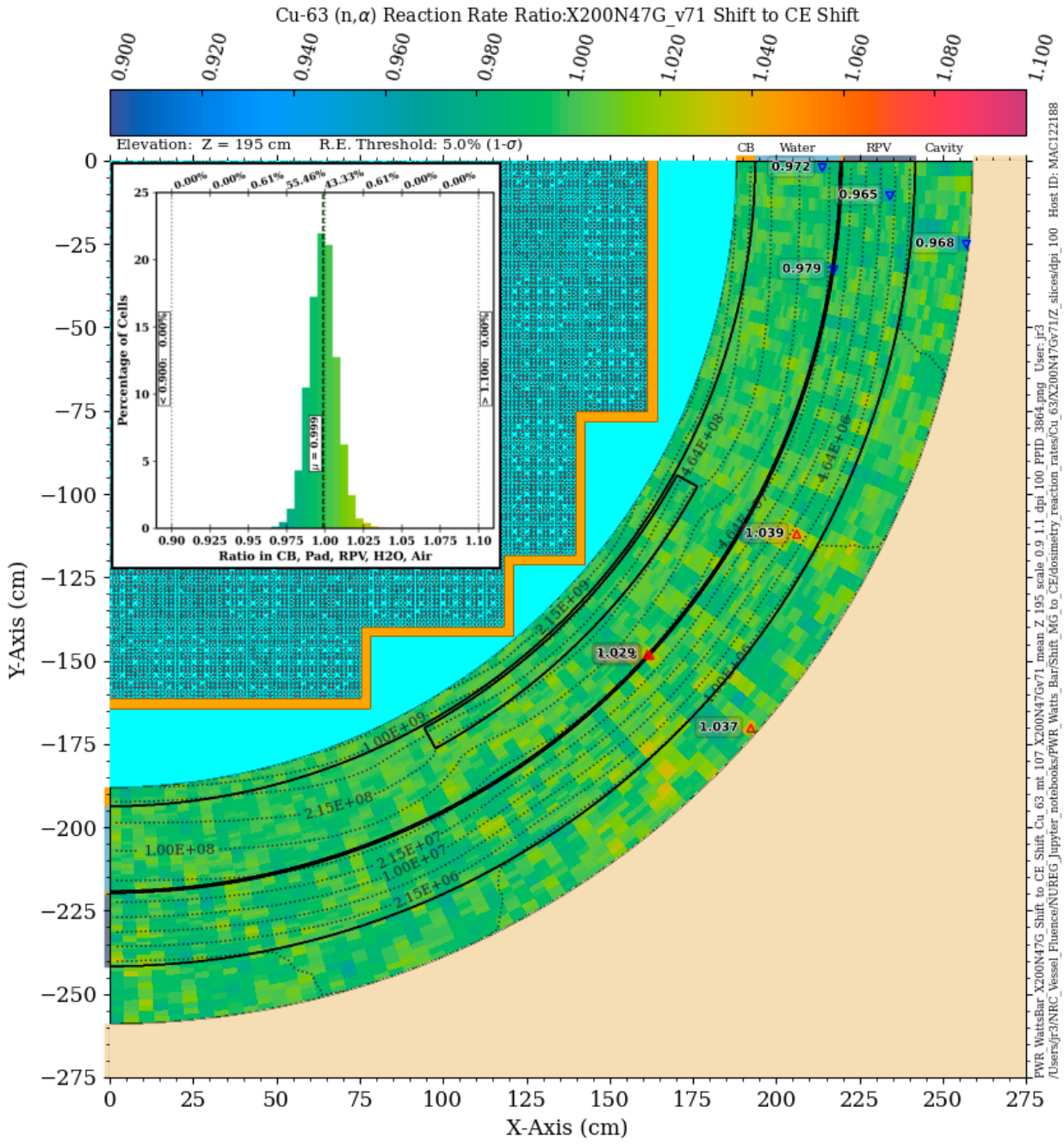

Figure 8-40 **^{63}Cu (n,α) reaction rate ratio in the PWR model: X200N47Gv71 Shift/CE Shift. Plan view at Z = 195 cm** *The contour lines are the reaction rate values from the CE solution*

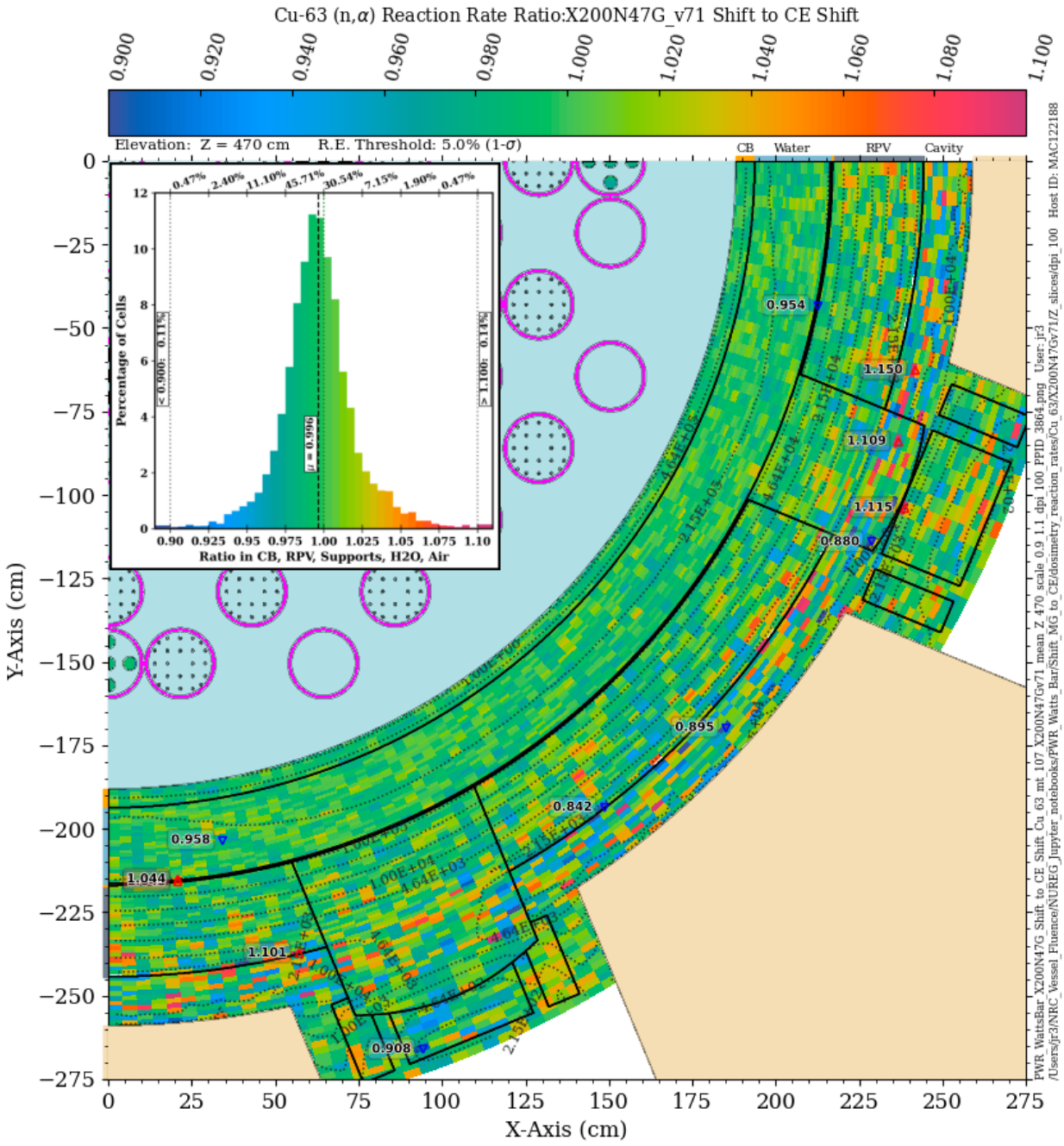

Figure 8-41 **^{63}Cu (n,α) reaction rate ratio in the PWR model: X200N47G Shift/CE Shift. Plan view at Z = 470 cm** *The contour lines are the reaction rate values from the CE solution.*

8.4.3 ^{46}Ti (n,p)

The ^{46}Ti (n,p) reaction has a threshold energy of 2.10 MeV and a 90% energy response range of 3.70 to 9.43 MeV (Table C-1). The agreement between a Shift solution with BUGLE-B7 cross-section data and a Shift solution with CE data for this reaction is poor. At the core midplane (Figure 8-42), the BUGLE-B7 solution is uniformly higher, with a bias centered at ~15%. At Z = 470 cm (Figure 8-43), the BUGLE-B7/CE agreement at locations within the outer radius of the RPV is improved, but agreement is very poor outside the RPV, where flux levels are dominated by cavity streaming. MG/CE ratios with the VITAMIN-B7 library (Figure 8-44 and Figure 8-45) are very similar to those for the BUGLE-B7 library.

An MG solution with the X200N47G library shows substantially improved agreement with the CE solution. At the core midplane (Figure 8-46), the solutions agree to within 2.5% in over 99% of the mesh tally voxels. At Z = 470 cm (Figure 8-47), the solutions agree to within 5% in over 98% of the mesh tally voxels. Results using the X956N library (not shown) are very consistent with those using the X200N47G library.

The marked difference between the VITAMIN-B7 and X200N47G results suggests that the difference in the reaction rates calculated using these two libraries is not in the transport cross sections but rather in the ^{46}Ti (n,p) dosimetry cross-section data from these two libraries. Figure 8-48 shows the cross-section data for this reaction from several CE and MG libraries, as well as the ratio of the VITAMIN-B7 data to the X200N47G data. This comparison is consistent with the behavior seen in the reaction rates and indicates that the (n,p) cross-section data for this reaction should be carefully examined when performing MG calculations.

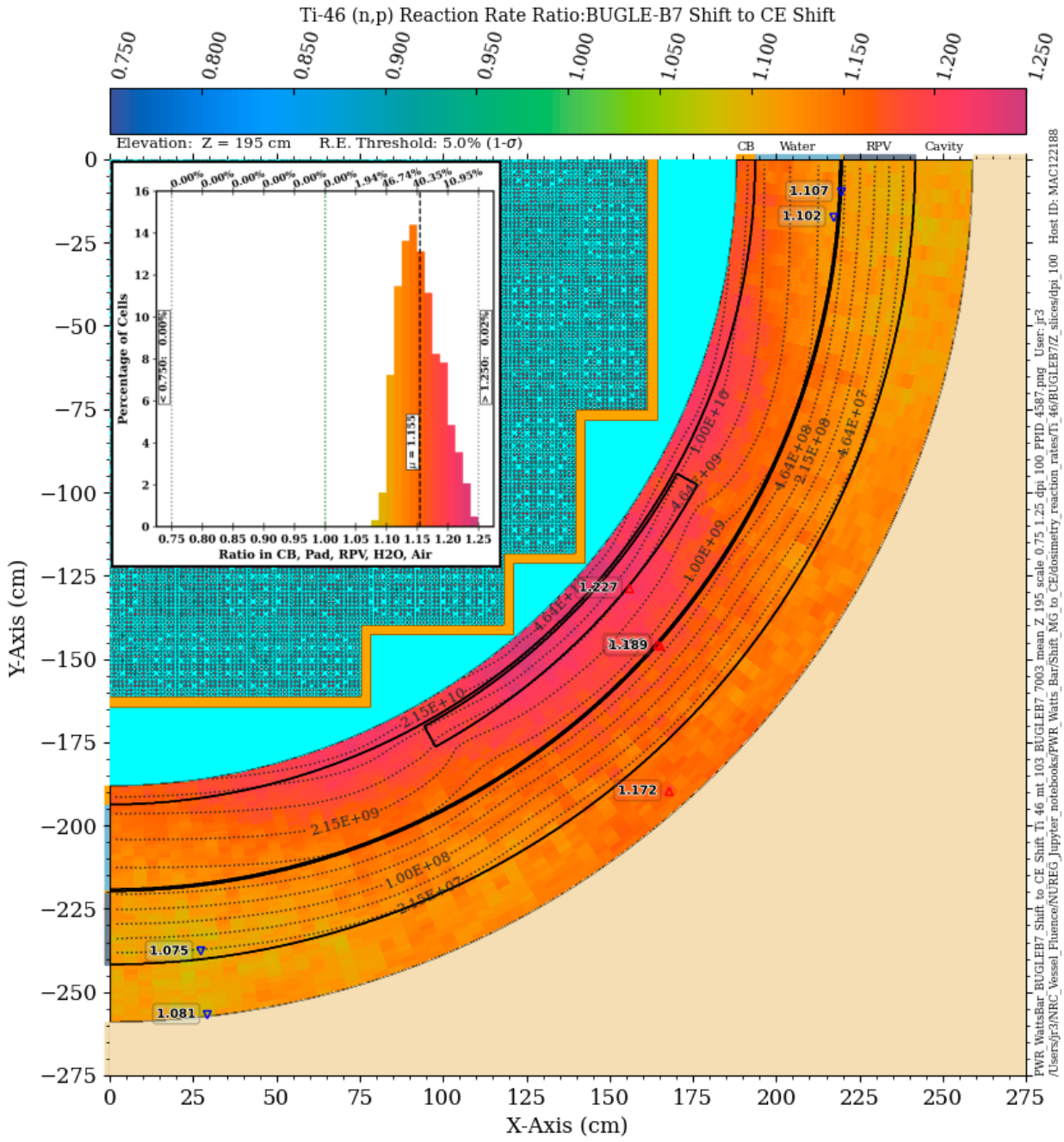

Figure 8-42 **^{46}Ti (n,p) reaction rate ratio in the PWR model: BUGLE-B7 Shift/CE Shift. Plan view at Z = 195 cm** *The contour lines are the reaction rate values from the CE solution.*

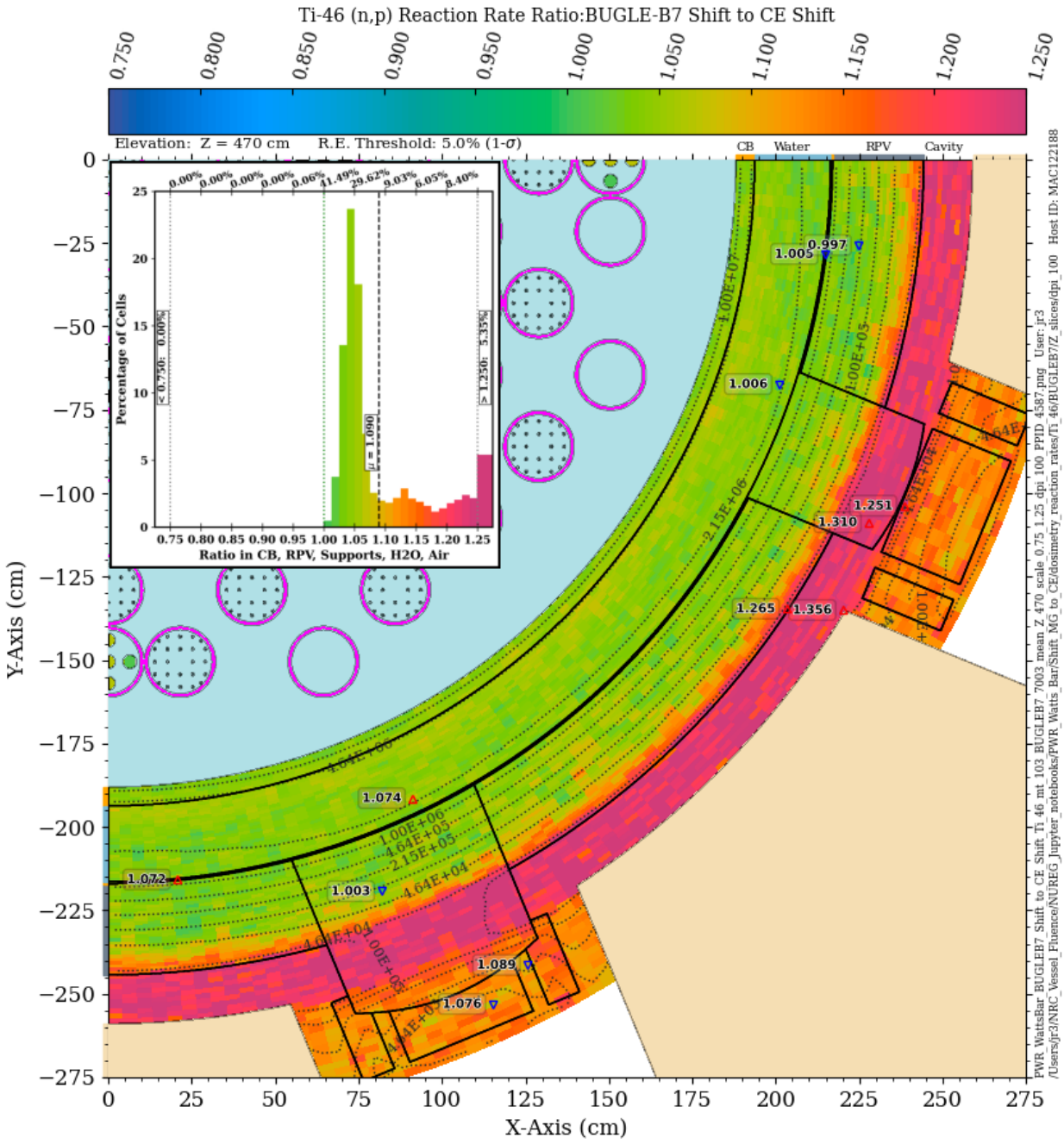

Figure 8-43 **^{46}Ti (n,p) reaction rate ratio in the PWR model: BUGLE-B7 Shift/CE Shift. Plan view at Z = 470 cm** *The contour lines are the reaction rate values from the CE solution.*

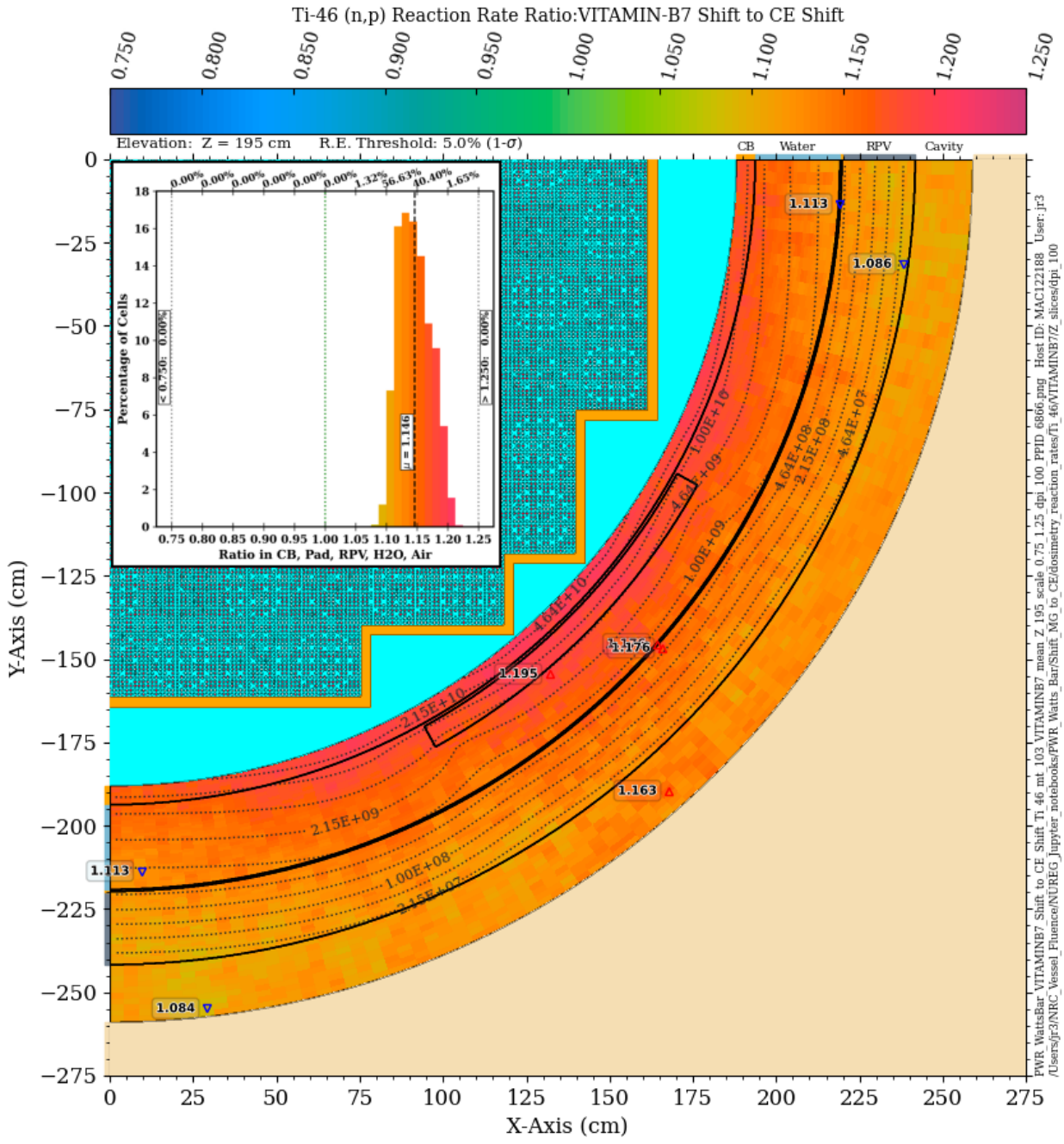

Figure 8-44 **^{46}Ti (n,p) reaction rate ratio in the PWR model: VITAMIN-B7 Shift/CE Shift. Plan view at Z = 195 cm** *The contour lines are the reaction rate values from the CE solution.*

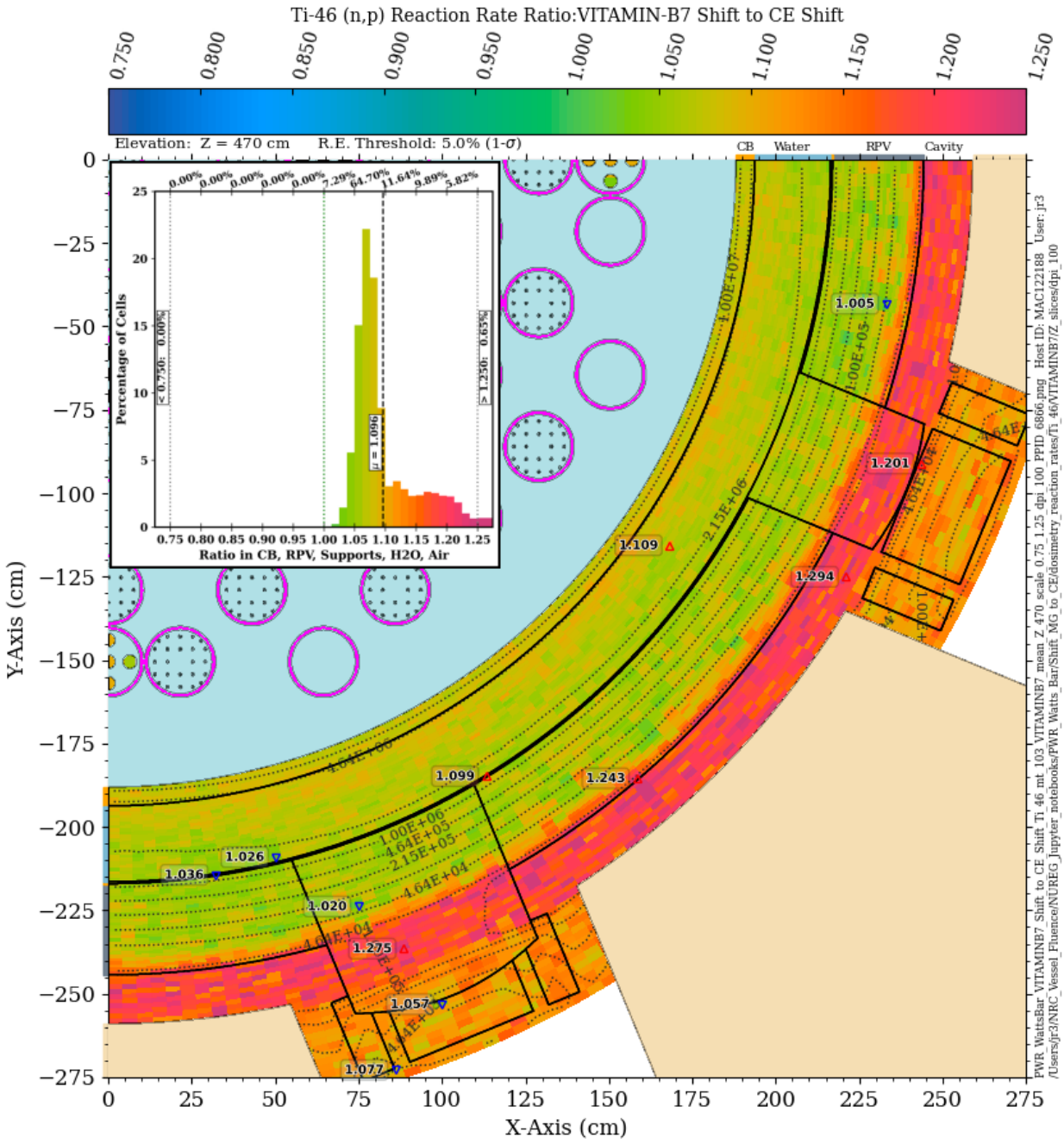

Figure 8-45 **^{46}Ti (n,p) reaction rate ratio in the PWR model: VITAMIN-B7 Shift/CE Shift. Plan view at Z = 470 cm** *The contour lines are the reaction rate values from the CE solution.*

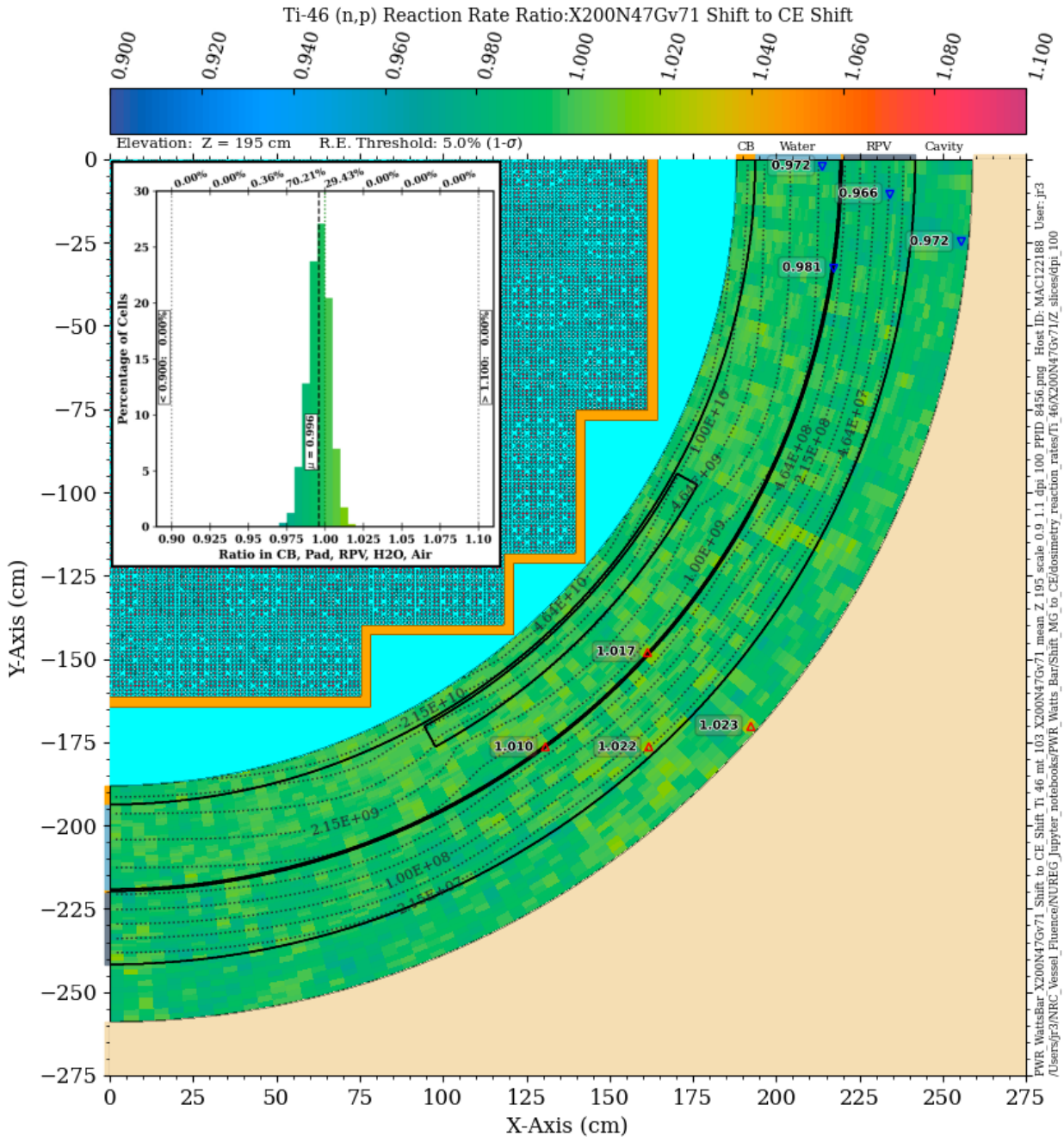

Figure 8-46 ^{46}Ti (n,p) reaction rate ratio in the PWR model: X200N47Gv71 Shift/CE Shift. Plan view at Z = 195 cm *The contour lines are the reaction rate values from the CE solution.*

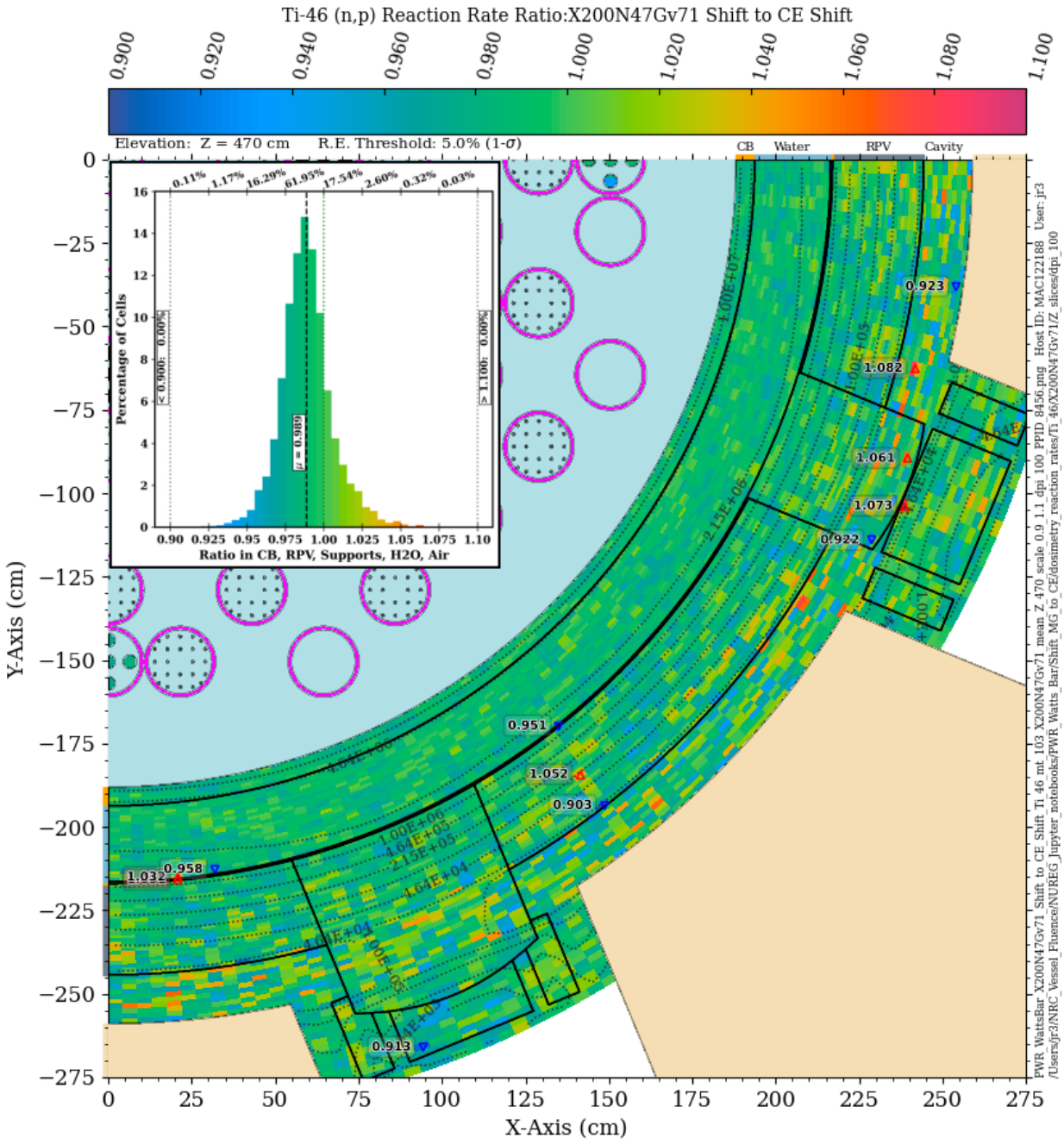

Figure 8-47 **^{46}Ti (n,p) reaction rate ratio in the PWR model: X200N47Gv71 Shift/CE Shift. Plan view at Z = 470 cm** *The contour lines are the reaction rate values from the CE solution.*

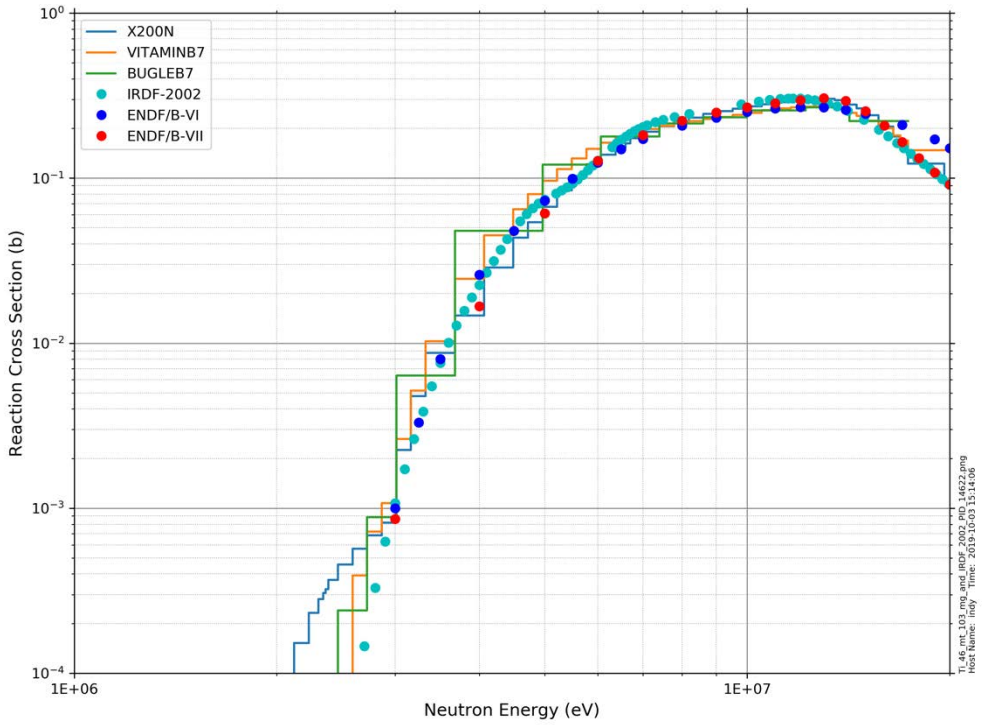

(a) Multigroup and CE cross-section data for the ^{46}Ti (n,p) reaction

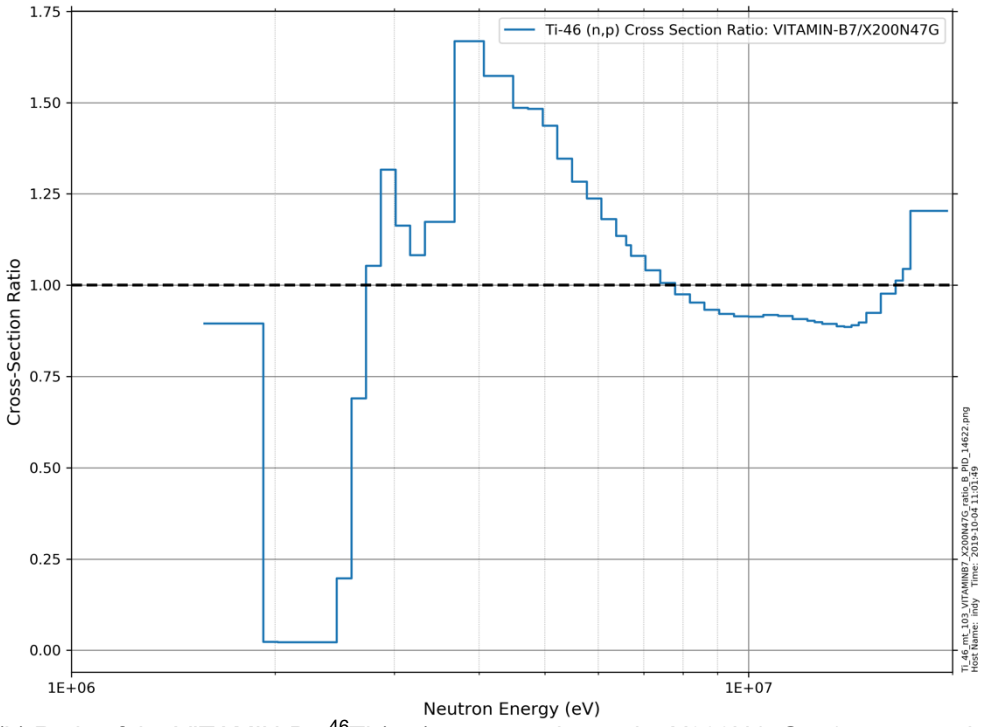

(b) Ratio of the VITAMIN-B7 ^{46}Ti (n,p) cross section to the X200N47Gv71 cross section

Figure 8-48 Cross-section data for the ^{46}Ti (n,p) reaction from MG and CE cross-section libraries and the ratio of the VITAMIN-B7 data to the X200N47G data

8.4.4 ^{54}Fe (n,p)

The ^{54}Fe (n,p) reaction has a threshold energy of 700 keV and a 90% energy response range of 2.27 to 7.54 MeV (Table C-1). For this dosimetry reaction, the Shift solution using the BUGLE-B7 library is in relatively good agreement with the CE Shift solution. At the core midplane (Figure 8-49), over 99% of the mesh tally voxels from the BUGLE-B7 solution are within 5% of the CE solution. It is also apparent that the MG/CE agreement is better at azimuthal locations which have the minimum amount of water between the baffle plates and the RPV. At an elevation of 470 cm (Figure 8-50), the BUGLE-B7 solution is lower than the CE solution in nearly 95% of the mesh tally voxels, with the majority of those locations have MG/CE ratios between 0.9 and 0.95.

Shift solutions using the VITAMIN-B7 library (Figure 8-51 and Figure 8-52) and the X200N47Gv71 library (Figure 8-53 and Figure 8-54) provide improved MG/CE ratios, with the X200N47Gv71 solution again showing better agreement than the VITAMIN-B7 solution. The distribution of ratio values at the core midplane with the X200N47G solution is centered at approximately 0.99, and over 99% of the X200N47G values are within 2.5% of the CE solution. At Z = 470 cm, the distribution is shifted slightly (~2%) below unity, and nearly 98% of the X200N47Gv71 values are within 5% of the CE solution. Results using the X956N library (not shown) are slightly improved relative to those using the X200N47Gv71 library.

8.4.5 ^{58}Ni (n,p)

The ^{58}Ni (n,p) reaction has a threshold energy of 400 keV and a 90% energy response range of 1.98–7.51 MeV (Table C-1). The MG/CE comparisons for this reaction (Figure 8-55 through Figure 8-60) are very similar to those for the ^{54}Fe (n,p) reaction. This consistency is likely due to the similarity in the energy thresholds and shapes of these two reaction cross sections (Figure C-2).

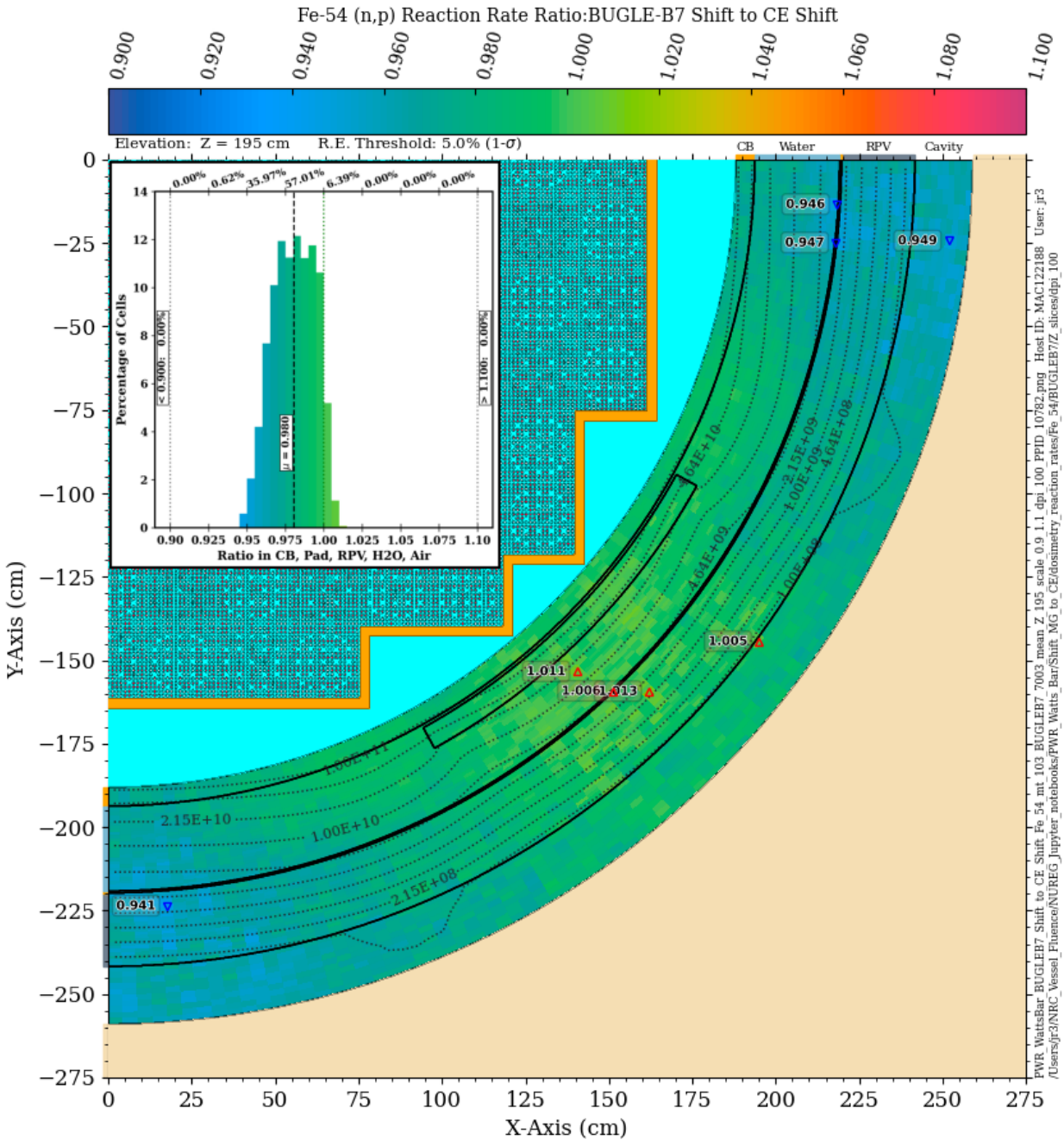

Figure 8-49 **^{54}Fe (n,p) reaction rate ratio in the PWR model: BUGLE-B7 Shift/CE Shift. Plan view at Z = 195 cm** *The contour lines are the reaction rate values from the CE solution.*

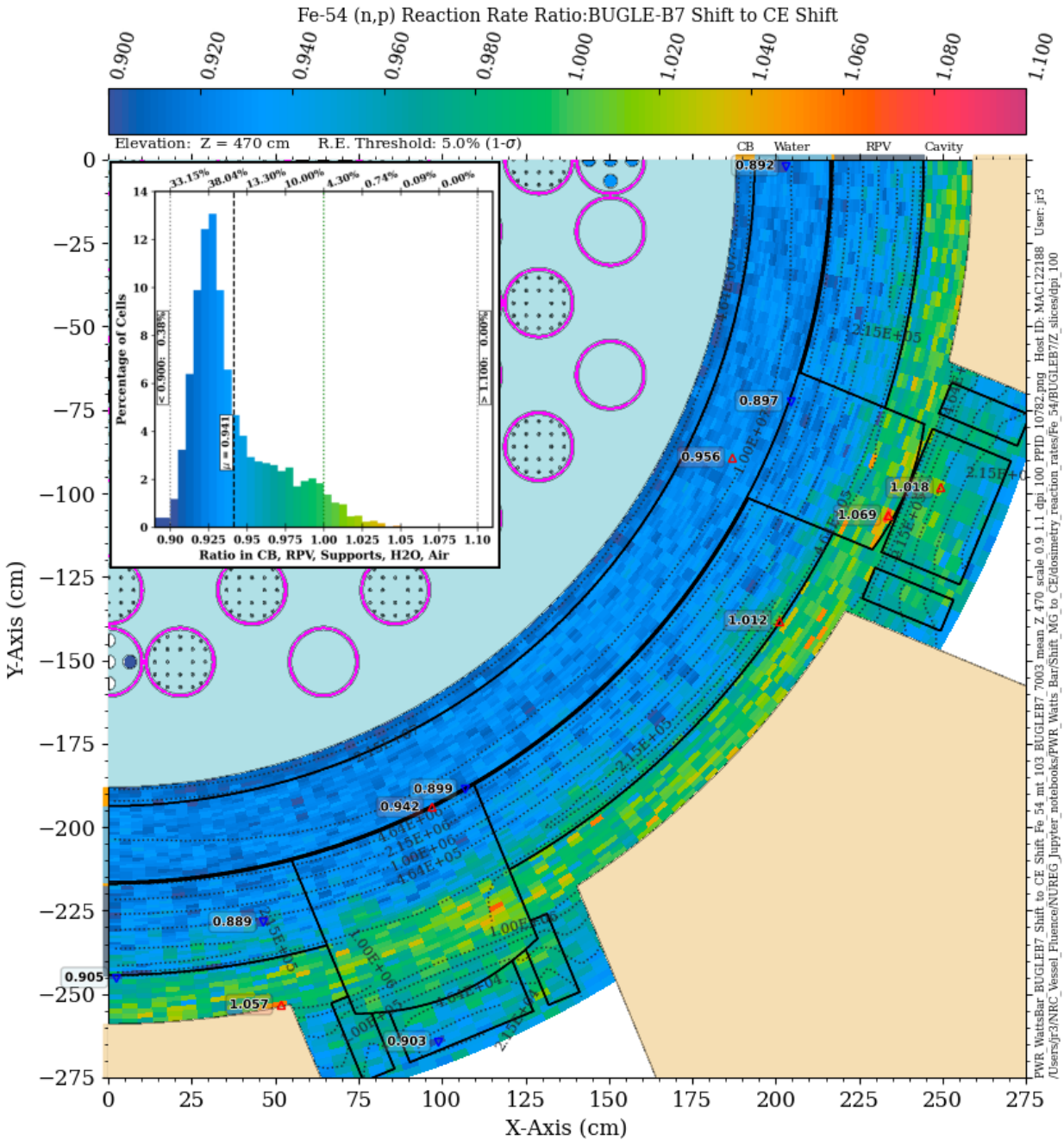

Figure 8-50 **^{54}Fe (n,p) reaction rate ratio in the PWR model: BUGLE-B7 Shift/CE Shift. Plan view at Z = 470 cm** *The contour lines are the reaction rate values from the CE solution.*

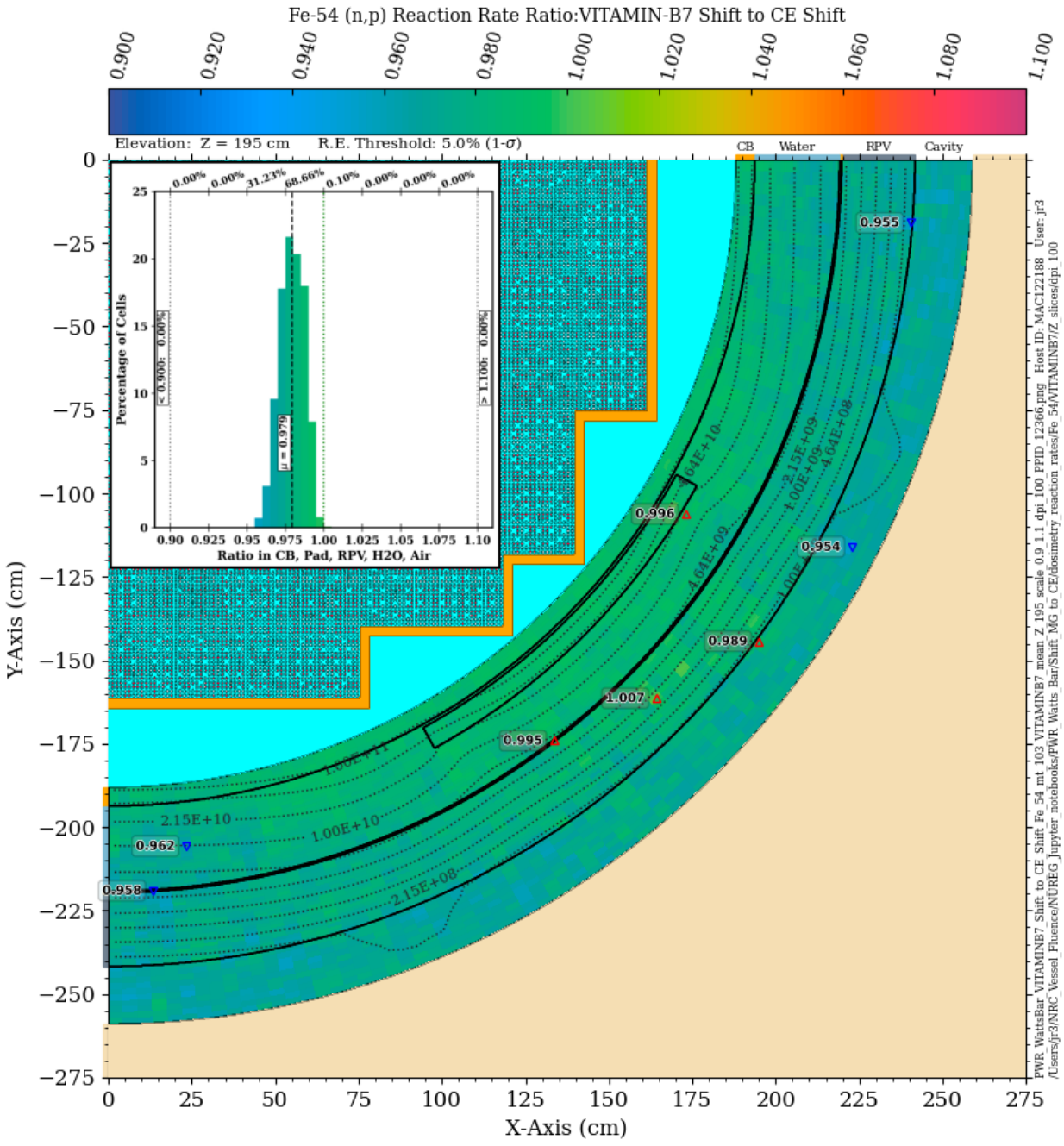

Figure 8-51 **^{54}Fe (n,p) reaction rate ratio in the PWR model: VITAMIN-B7 Shift/CE Shift. Plan view at Z = 195 cm** *The contour lines are the reaction rate values from the CE solution.*

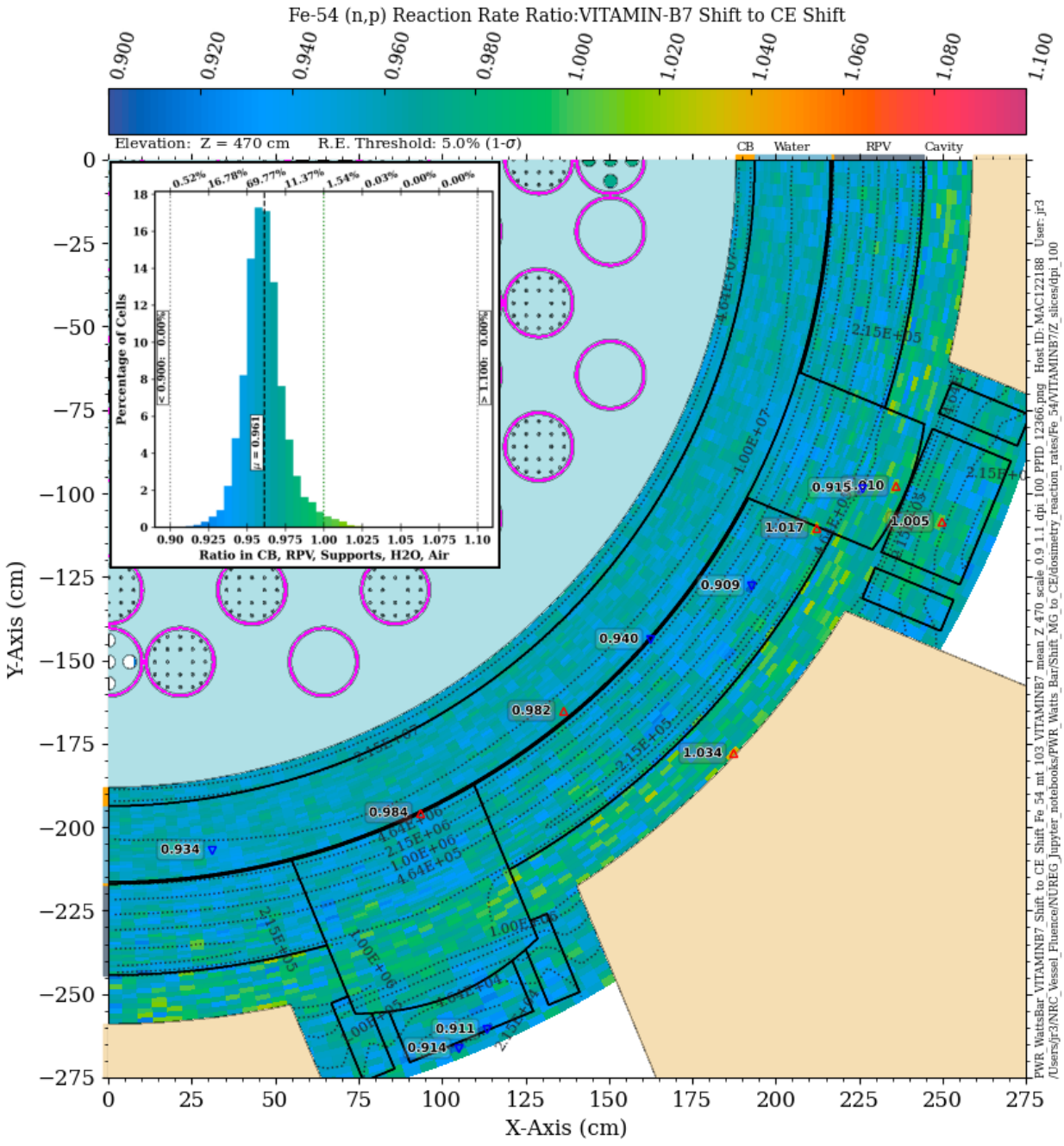

Figure 8-52 **^{54}Fe (n,p) reaction rate ratio in the PWR model: VITAMIN-B7 Shift/CE Shift. Plan view at Z = 470 cm** *The contour lines are the reaction rate values from the CE solution.*

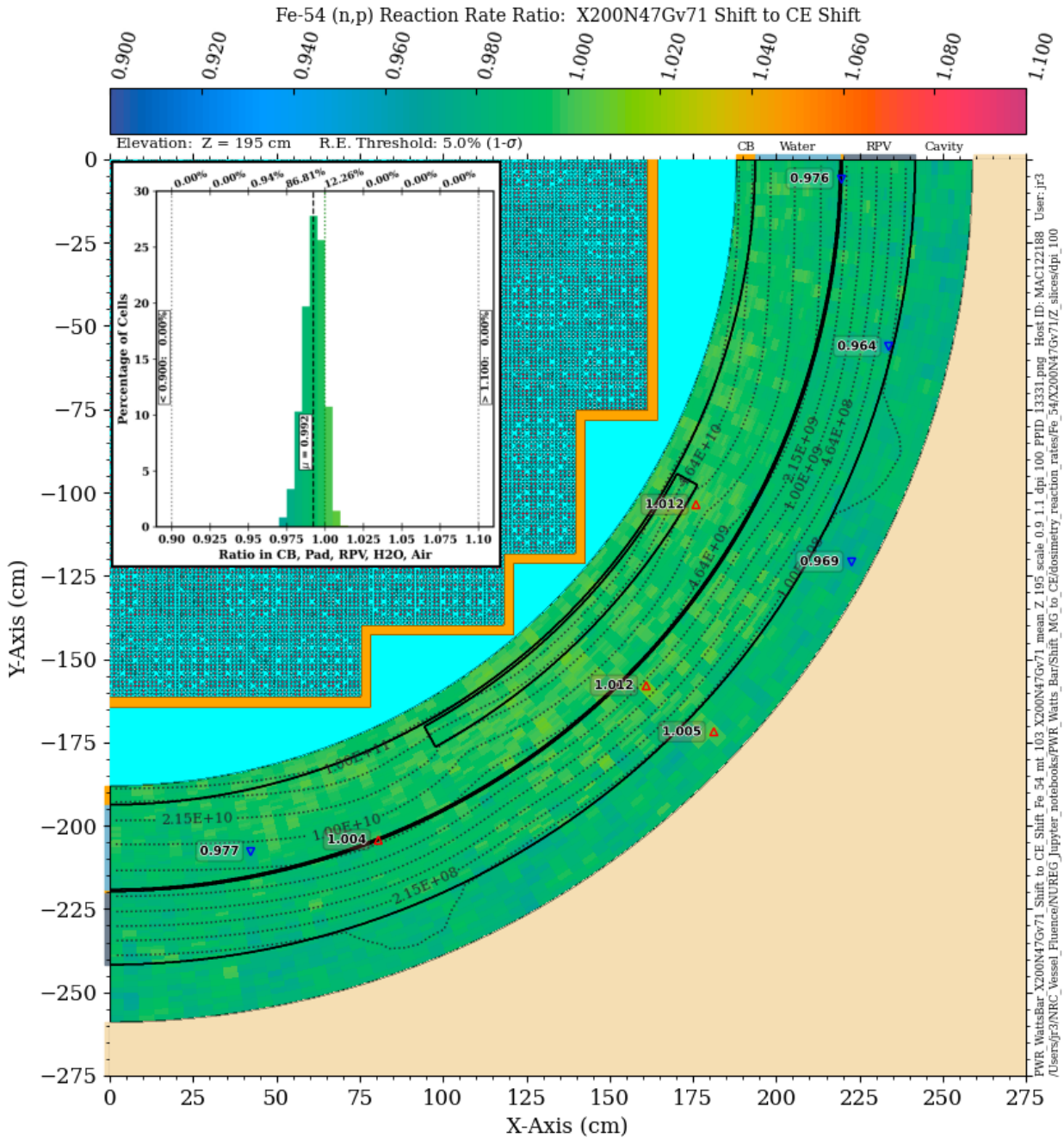

Figure 8-53 **^{54}Fe (n,p) reaction rate ratio in the PWR model: X200N47Gv71 Shift/CE Shift. Plan view at Z = 195 cm** *The contour lines are the reaction rate values from the CE solution.*

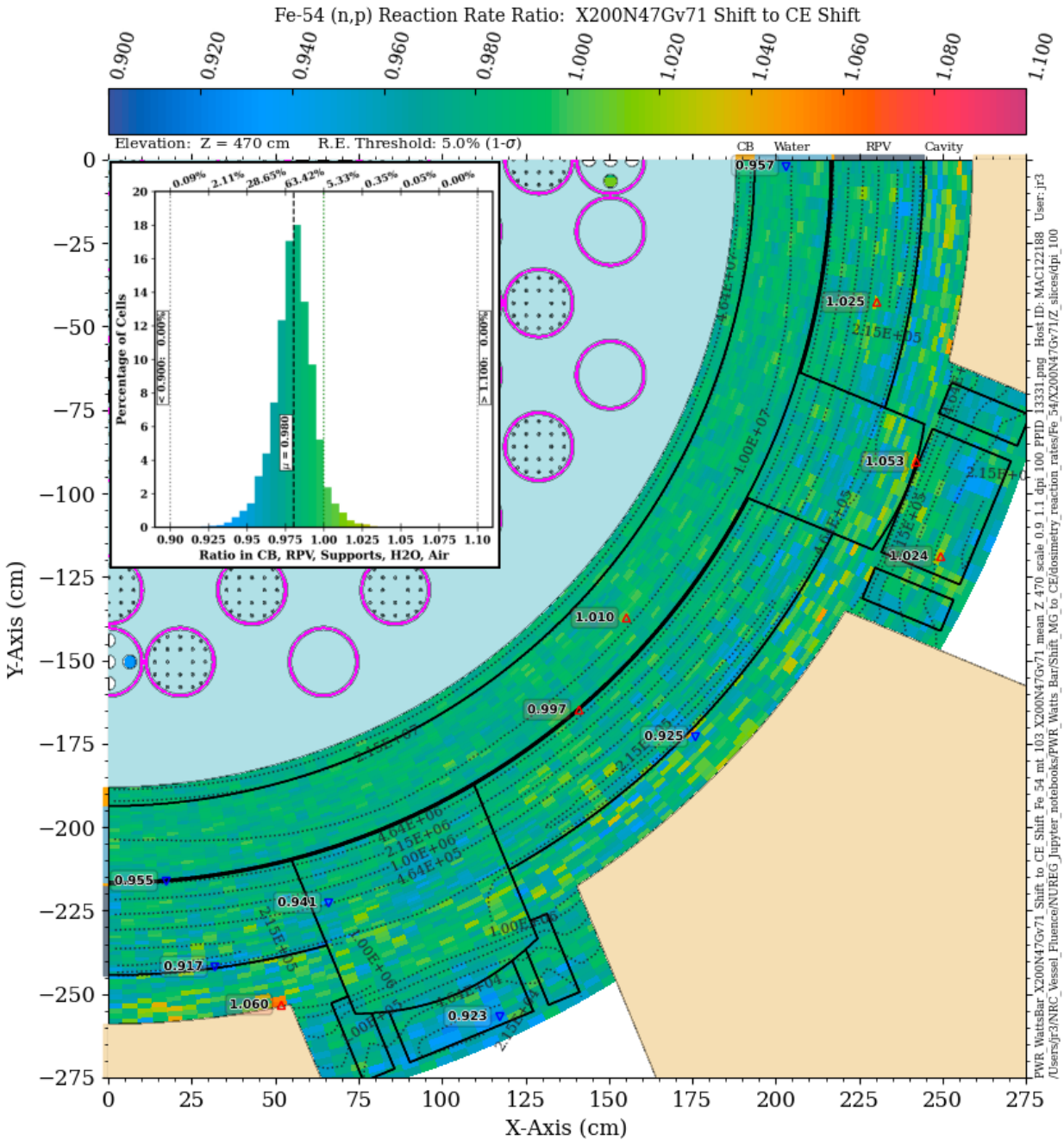

Figure 8-54 **^{54}Fe (n,p) reaction rate ratio in the PWR model: X200N47Gv71 Shift/CE Shift. Plan view at Z = 470 cm** *The contour lines are the reaction rate values from the CE solution.*

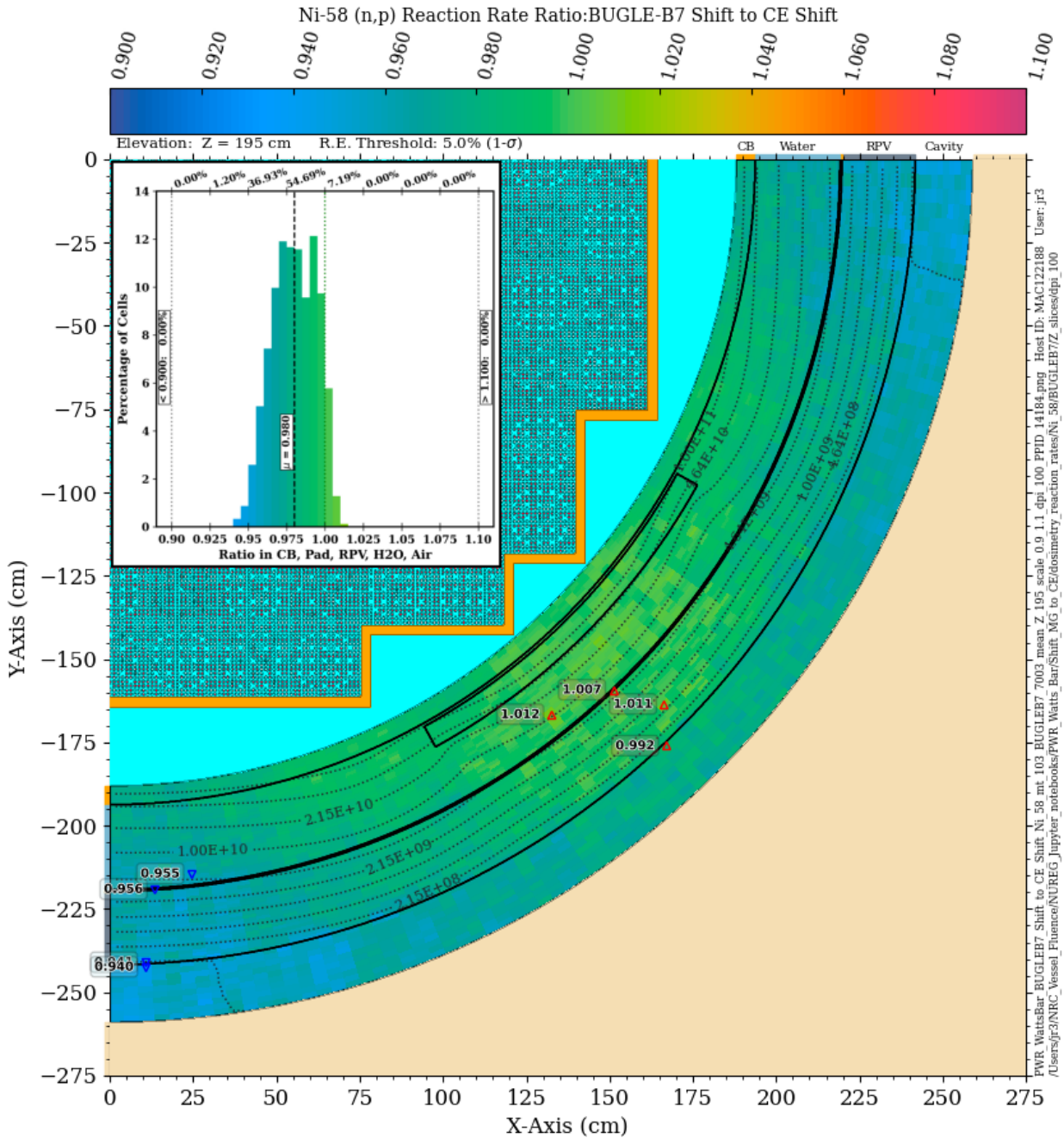

Figure 8-55 **^{58}Ni (n,p) reaction rate ratio in the PWR model: BUGLE-B7 Shift/CE Shift. Plan view at Z = 195 cm** *The contour lines are the reaction rate values from the CE solution.*

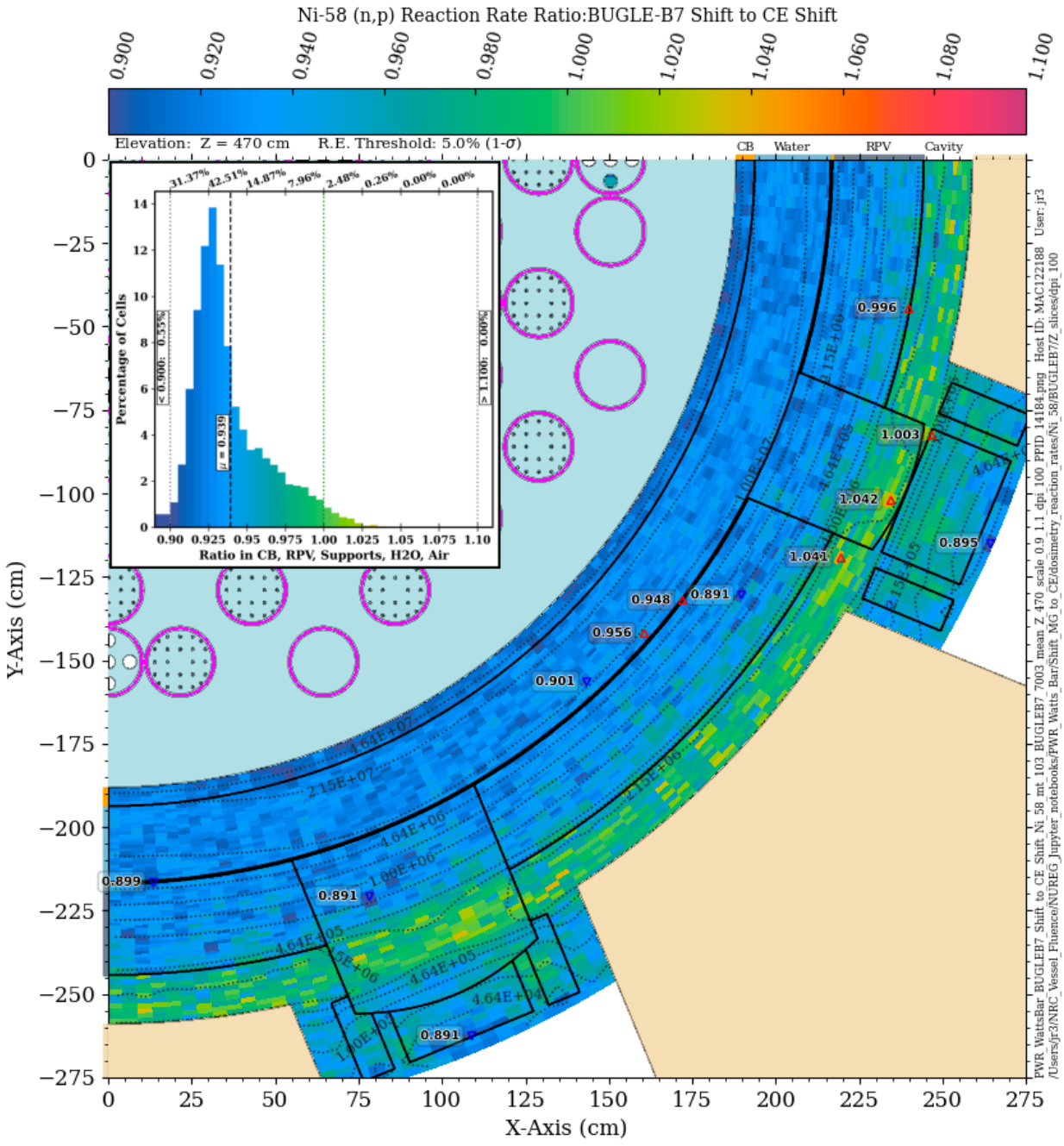

Figure 8-56 **^{58}Ni (n,p) reaction rate ratio in the PWR model: BUGLE-B7 Shift/CE Shift. Plan view at Z = 470 cm** *The contour lines are the reaction rate values from the CE solution.*

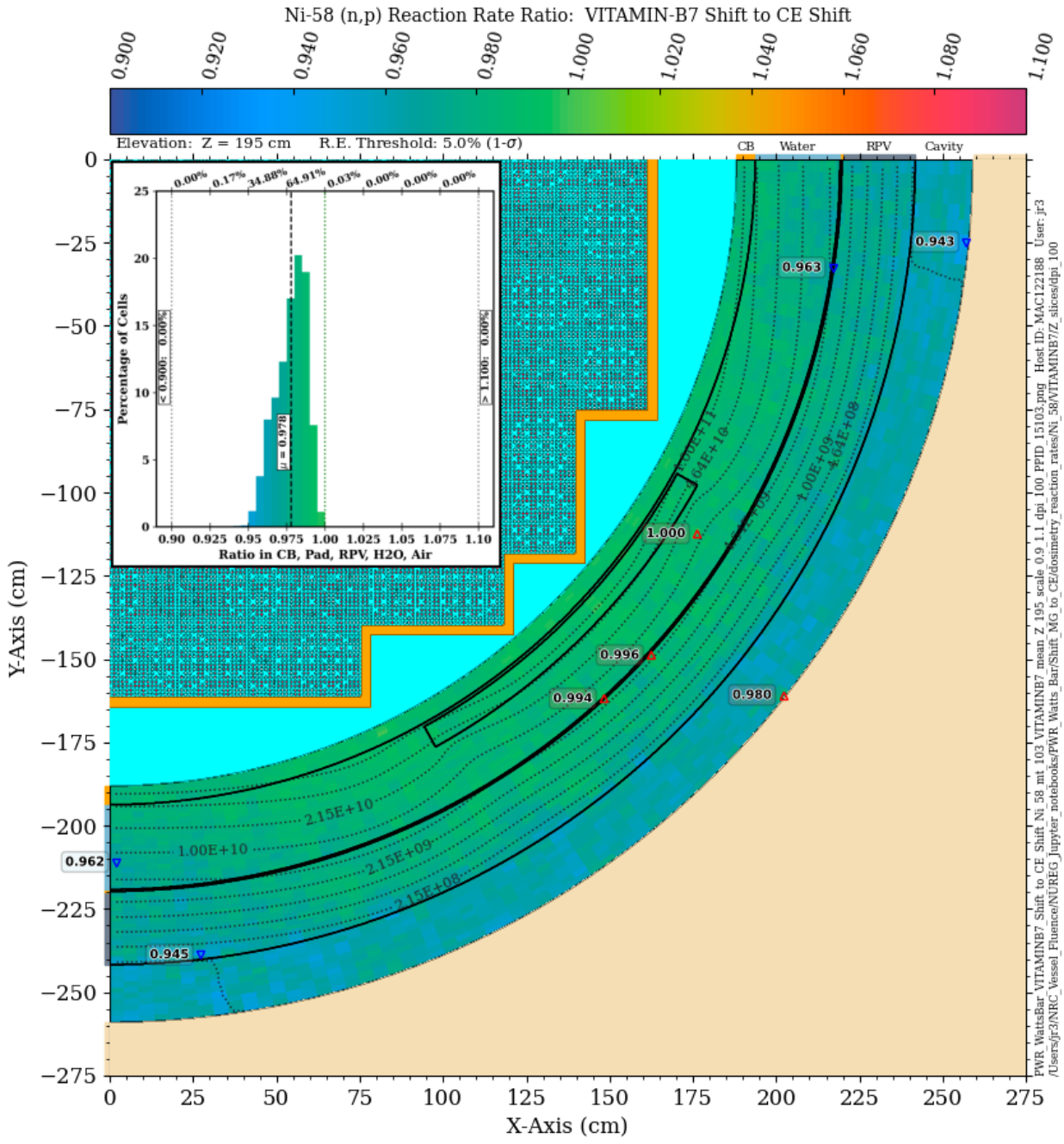

Figure 8-57 **^{58}Ni (n,p) reaction rate ratio in the PWR model: VITAMIN-B7 Shift/CE Shift. Plan view at Z = 195 cm** *The contour lines are the reaction rate values from the CE solution.*

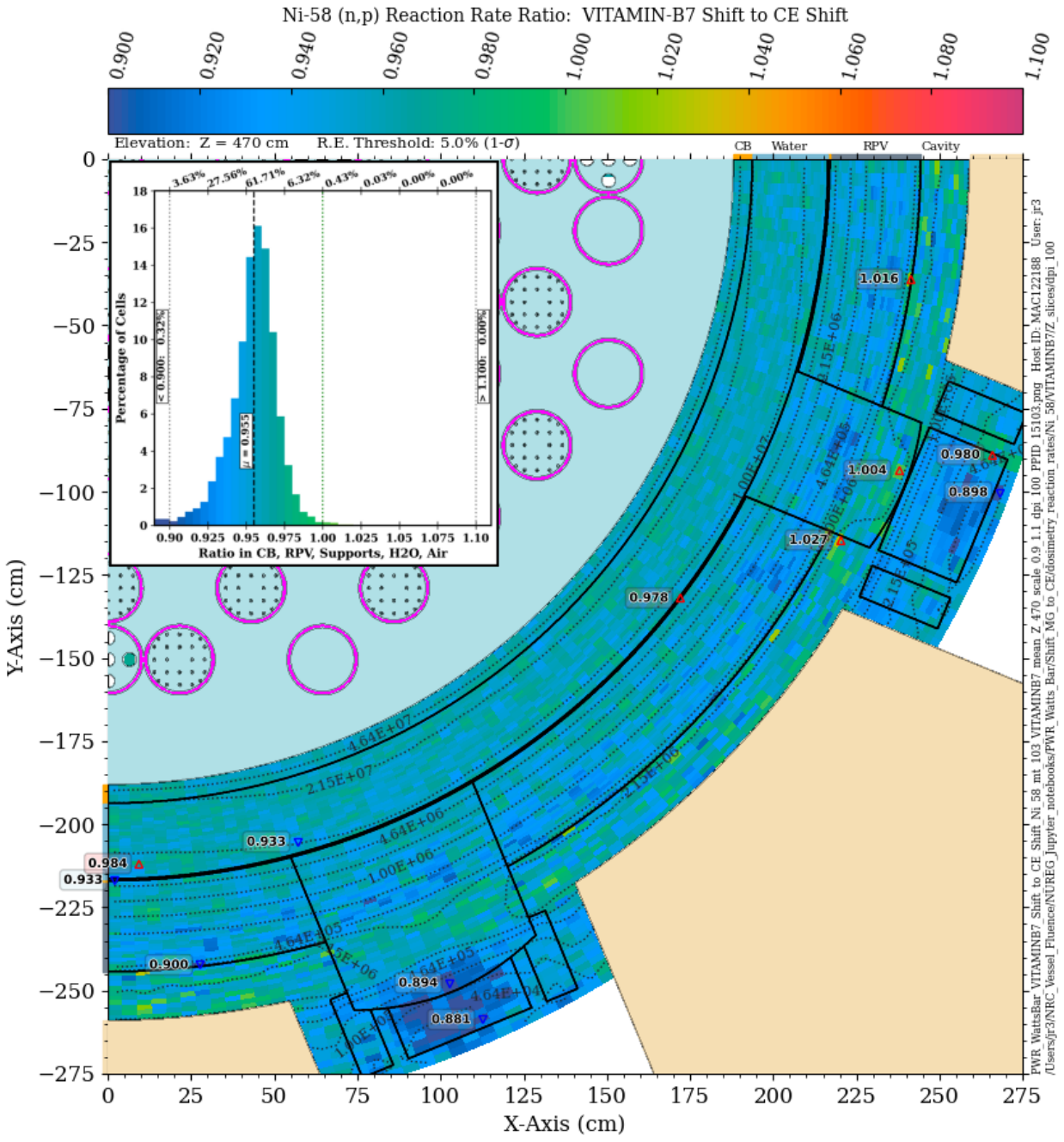

Figure 8-58 **^{58}Ni (n,p) reaction rate ratio in the PWR model: VITAMIN-B7 Shift/CE Shift. Plan view at Z = 470 cm** *The contour lines are the reaction rate values from the CE solution.*

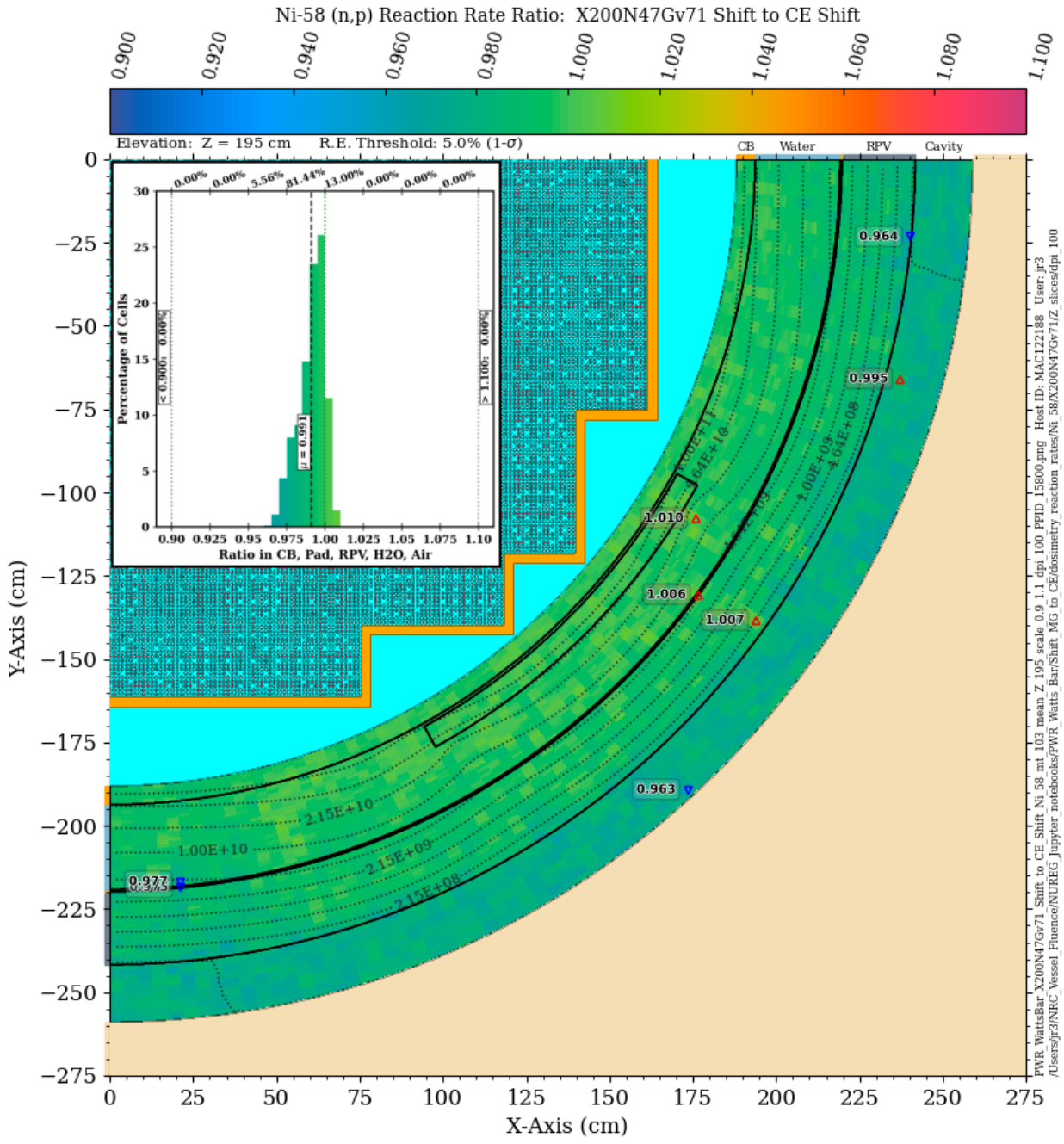

Figure 8-59 **^{58}Ni (n,p) reaction rate ratio in the PWR model: X200N47Gv71 Shift/CE Shift. Plan view at Z = 195 cm** *The contour lines are the reaction rate values from the CE solution.*

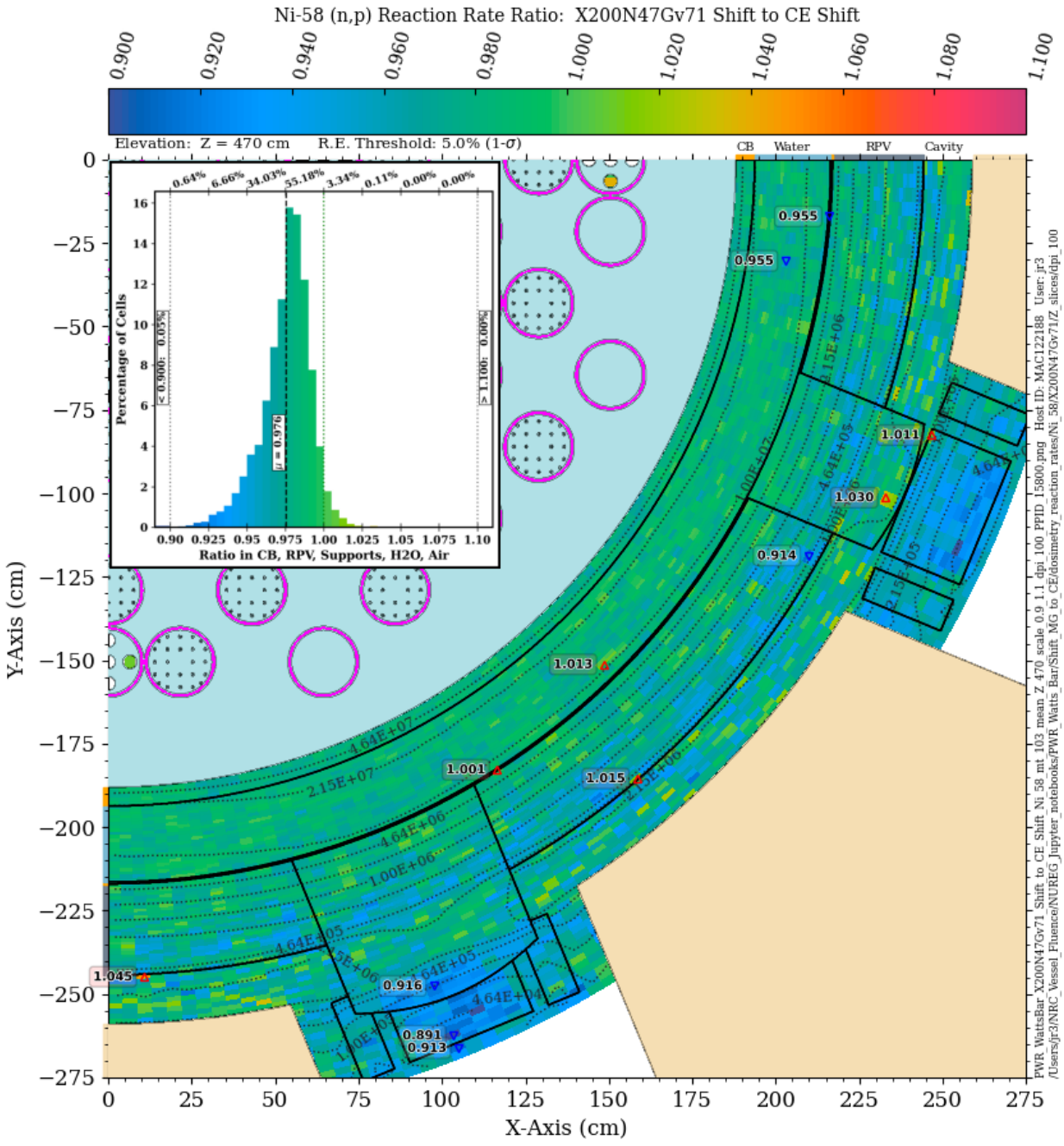

Figure 8-60 **^{58}Ni (n,p) reaction rate ratio in the PWR model: X200N47Gv71 Shift/CE Shift. Plan view at Z = 470 cm** *The contour lines are the reaction rate values from the CE solution.*

8.4.6 ^{115}In (n,n′) ^{115m}In

The ^{115}In (n,n′) ^{115m}In reaction has a threshold energy of 339.2 keV and a 90% energy response range of 1.12 to 5.86 MeV (Table C-1). Note that the cross-section data for this reaction is based on the International Reactor Dosimetry File 2002 (IRDF-2002) [87]. There is no single ENDF reaction type (MT value) that can be used to compute the production rate of the metastable isomer. The BUGLE-B7 library contains response function data for this reaction, but the remainder of the MG libraries considered in this study do not. A comparison of the X956N solution to the CE solution was made based on convolving the X956N flux with the pointwise IRDF-2002 cross-section data. While a similar approach could have been taken with the remaining MG libraries, it was not because of the way in which Shift applies a pointwise response function to a MG flux solution. The flux in each group is treated as though it is all at the group lower energy bound when interpolating a value of the pointwise cross-section data. This approximation has a minor effect for very fine group structures (such as the X956N library), but it can have a substantial effect on the calculated reaction rate when a relatively coarse MG library is used.

The BUGLE-B7 solution agrees well with the CE solution near the core midplane (Figure 8-61) from the core barrel radially out through the inner portion of the RPV. However, at the outer edge of the RPV and in the cavity gap, the BUGLE-B7 solution is 5–10% lower than the CE solution. At the elevation of the vessel supports (Figure 8-62), the BUGLE-B7 solution underpredicts the CE solution at all locations, with an apparent bias of 8–9%. The BUGLE-B7 reaction rate underpredicts the CE solution by more than 20% in some vessel support mesh tally voxels.

The MG solution with the X956N library is in excellent agreement with the CE solution near the core midplane (Figure 8-63), with MG/CE agreement within 5% in 99.9% of the mesh tally voxels. At the elevation of the vessel supports (Figure 8-64), the agreement between the X956N and CE solutions is somewhat degraded, but the solutions agree to within 10% in more than 99% of the mesh tally voxels.

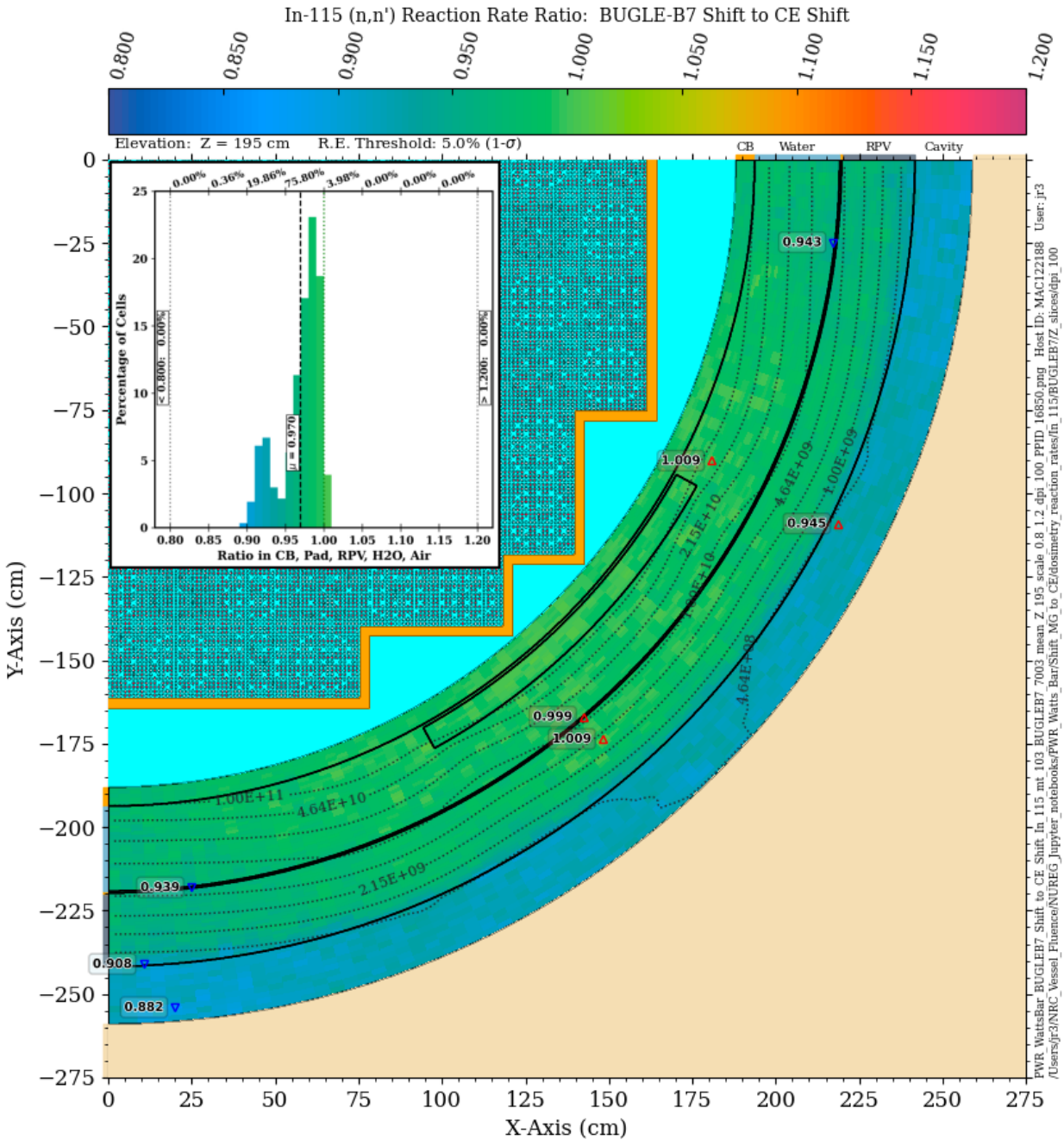

Figure 8-61 **^{115}In (n,n′) ^{115m}In reaction rate ratio in the PWR model: BUGLE-B7 Shift/CE Shift. Plan view at Z = 195 cm** *The contour lines are the reaction rate values from the CE solution.*

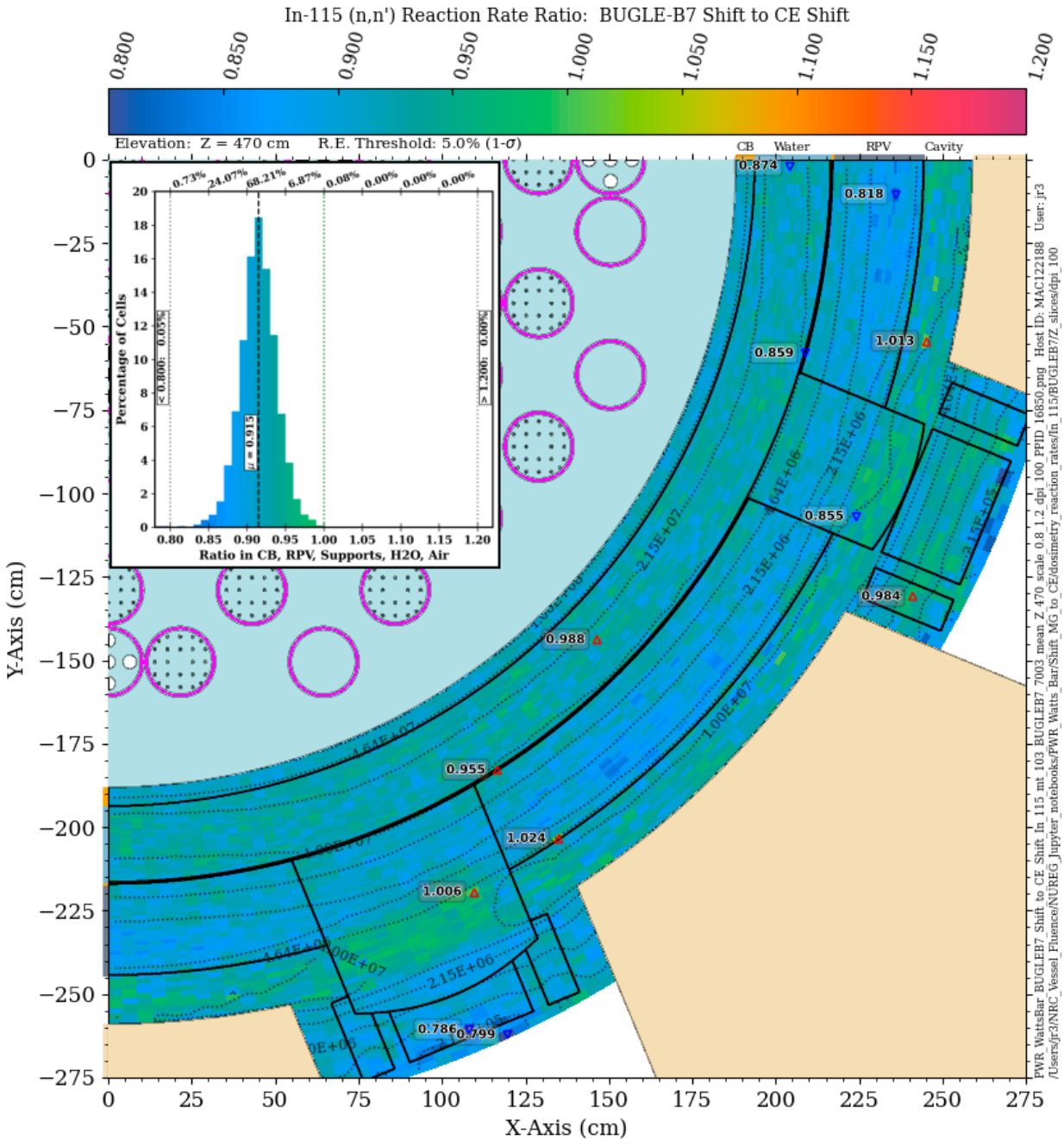

Figure 8-62 **^{115}In (n,n′) ^{115m}In reaction rate ratio in the PWR model: BUGLE-B7 Shift/CE Shift. Plan view at Z = 470 cm** *The contour lines are the reaction rate values from the CE solution.*

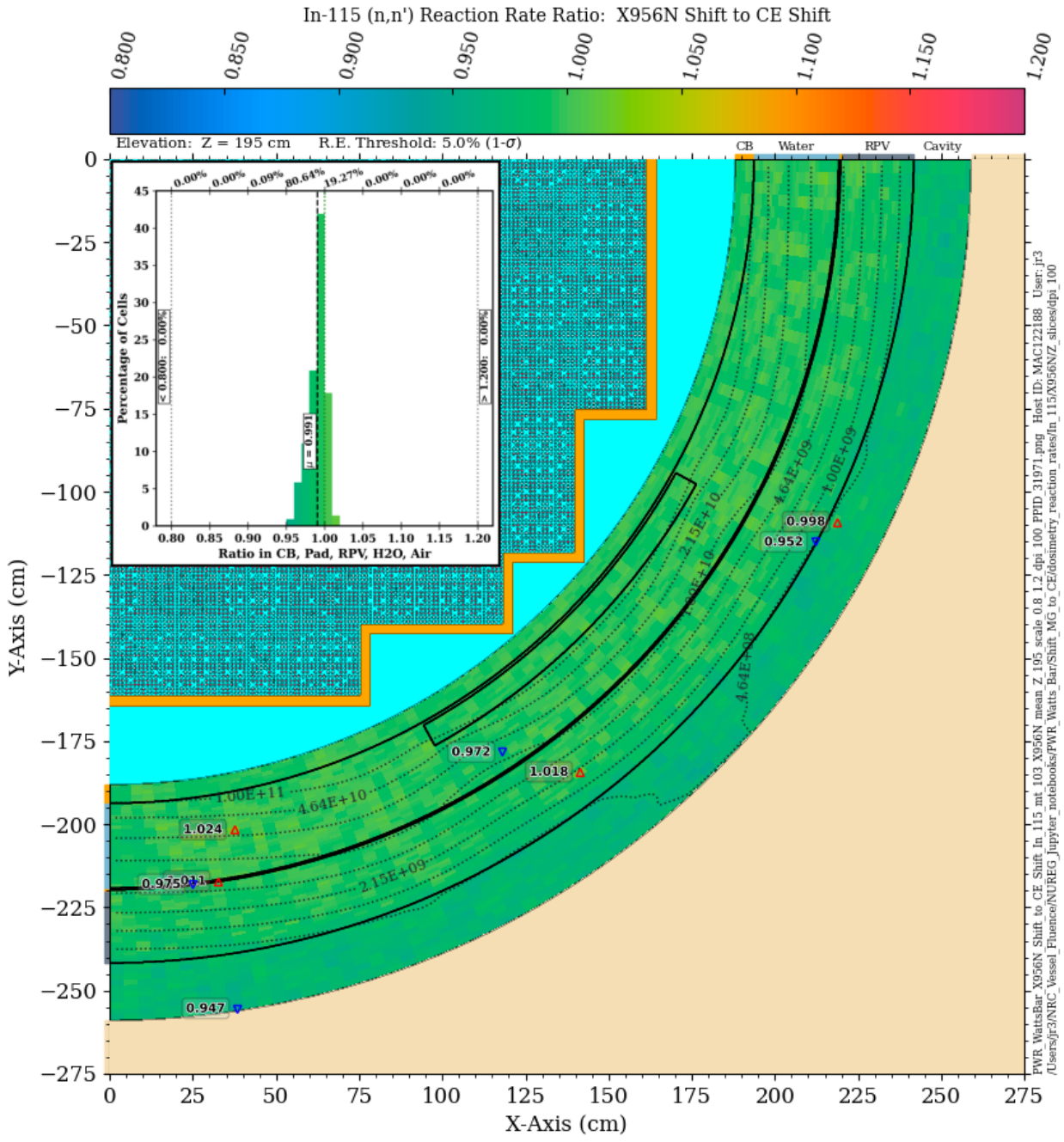

Figure 8-63 **^{115}In (n,n′) ^{115m}In reaction rate ratio in the PWR model: X956N Shift/CE Shift. Plan view at Z = 195 cm** *The contour lines are the reaction rate values from the CE solution.*

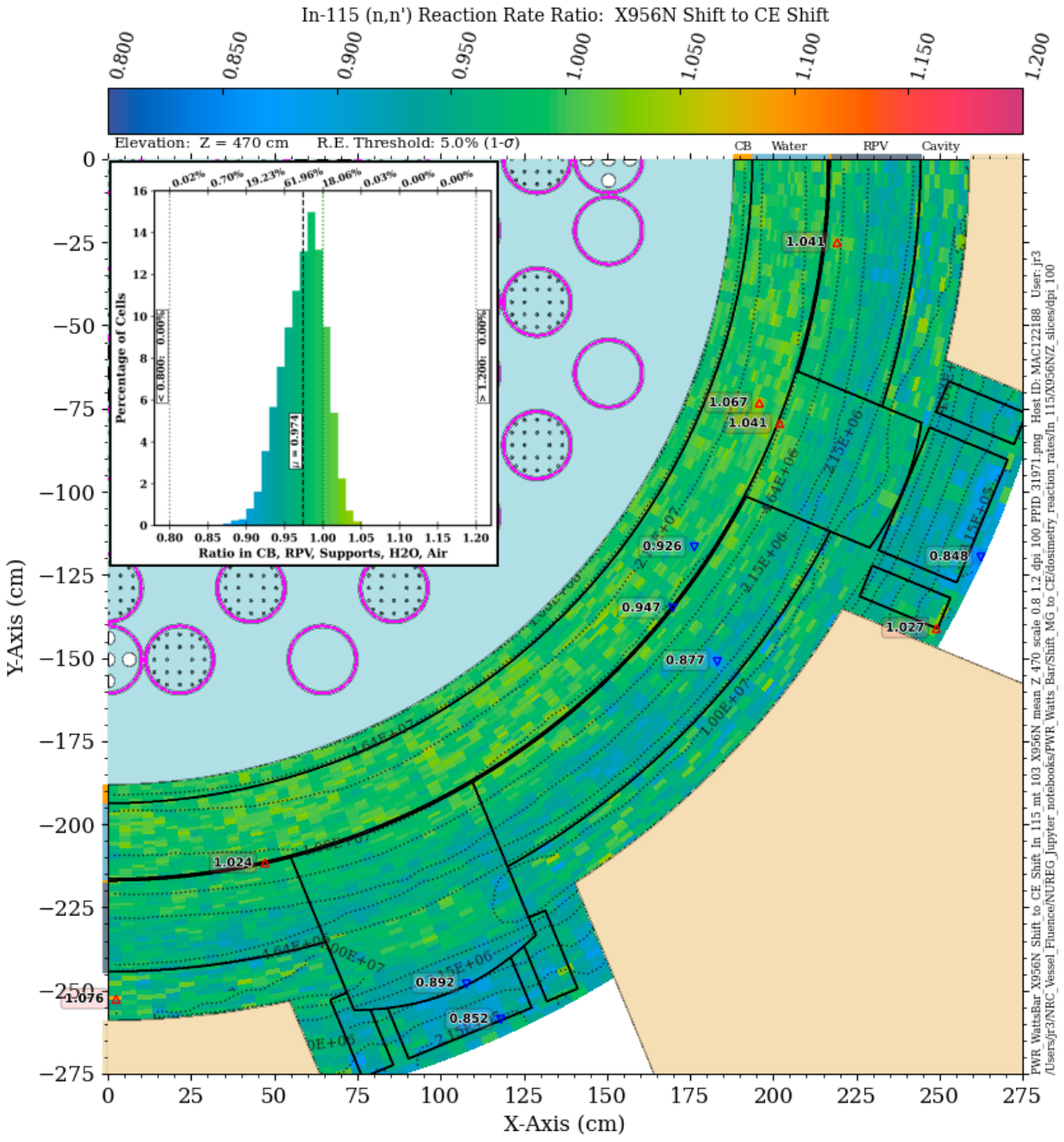

Figure 8-64 **^{115}In (n,n') ^{115m}In reaction rate ratio in the PWR model: X956N Shift/CE Shift. Plan view at Z = 470 cm** *The contour lines are the reaction rate values from the CE solution.*

8.4.7 ^{103}Rh (n,n′) ^{103m}Rh

The ^{103}Rh (n,n′) ^{103m}Rh reaction has a threshold energy of 40.14 keV and a 90% energy response range of 0.731 to 5.73 MeV (Table C-1). As with the ^{115}In (n,n′) ^{115m}In reaction, there is no single ENDF reaction type (MT value) which can be used to compute the production rate of the metastable isomer, and IRDF-2002 cross-section data are used. Consistent with the discussion in Section 8.4.6, only the BUGLE-B7 and X956N MG libraries were used.

The BUGLE-B7 solution agrees well with the CE solution at the core midplane (Figure 8-65) from the core barrel radially out through much of the RPV. At the outer edge of the RPV and in the cavity gap, though, the BUGLE-B7 solution underpredicts the CE solution by ~10–12%. At the elevation of the vessel supports (Figure 8-66), the BUGLE-B7 solution underpredicts the CE solution at all locations, with the difference exceeding 10% in ~55% of the mesh tally voxels, and differences exceeding 20% in some vessel support locations.

The MG solution with the X956N library is in excellent agreement with the CE solution near the core midplane (Figure 8-67), with nearly 100% of the mesh tally voxels agreeing within 5%. At Z = 470 cm, the agreement between the X956N and CE solutions is degraded (Figure 8-68), with differences of up to ~10% in the RPV, cavity gap, and vessel supports.

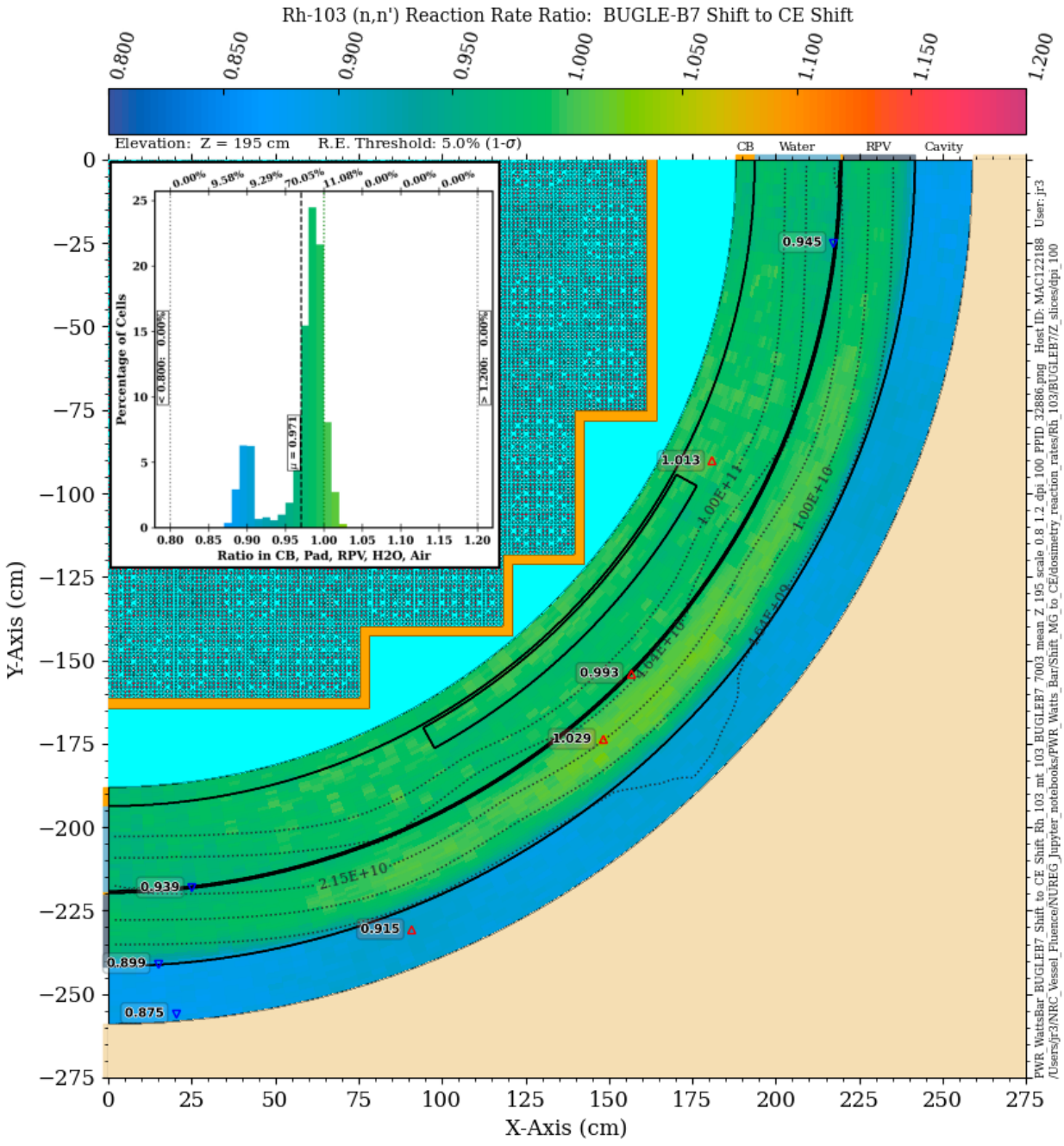

Figure 8-65 **^{103}Rh (n,n') ^{103m}Rh reaction rate ratio in the PWR model: BUGLE-B7 Shift/CE Shift. Plan view at Z = 195 cm** *The contour lines are the reaction rate values from the CE solution.*

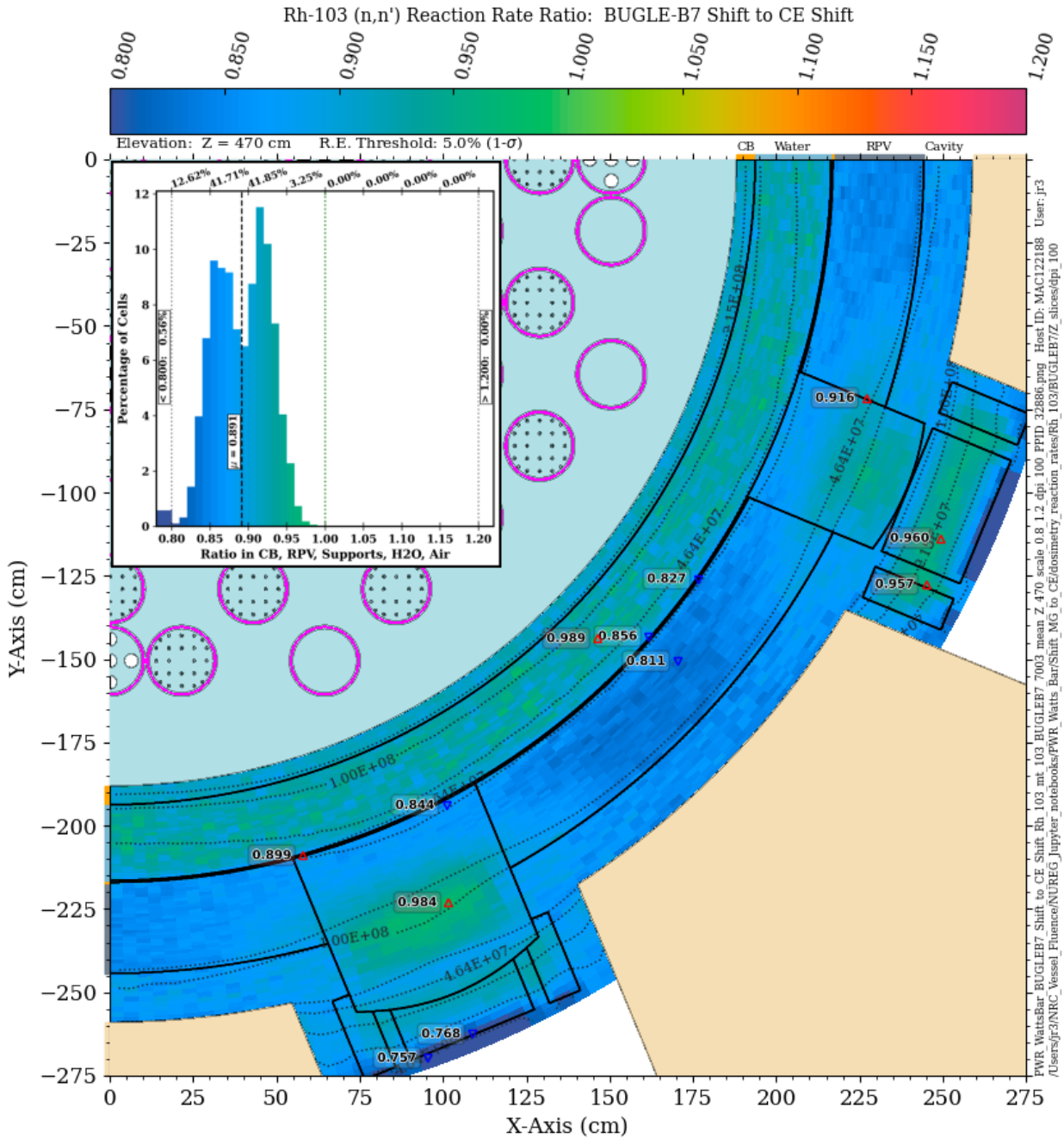

Figure 8-66 **^{103}Rh (n,n′) ^{103m}Rh reaction rate ratio in the PWR model: BUGLE-B7 Shift/CE Shift. Plan view at Z = 470 cm** *The contour lines are the reaction rate values from the CE solution.*

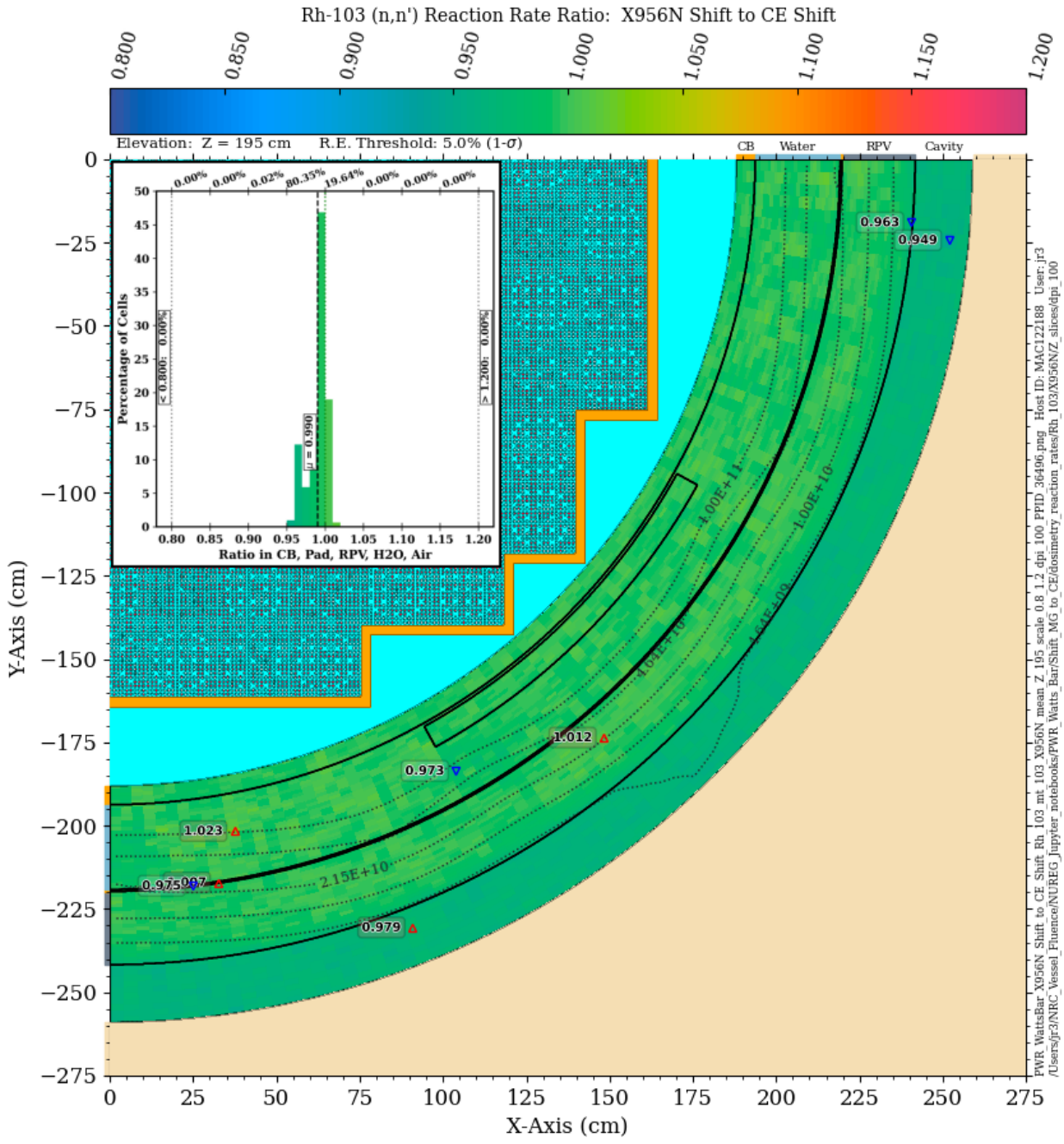

Figure 8-67 **^{103}Rh (n,n') ^{103m}Rh reaction rate ratio in the PWR model: X956N Shift/CE Shift. Plan view at Z = 195 cm** *The contour lines are the reaction rate values from the CE solution.*

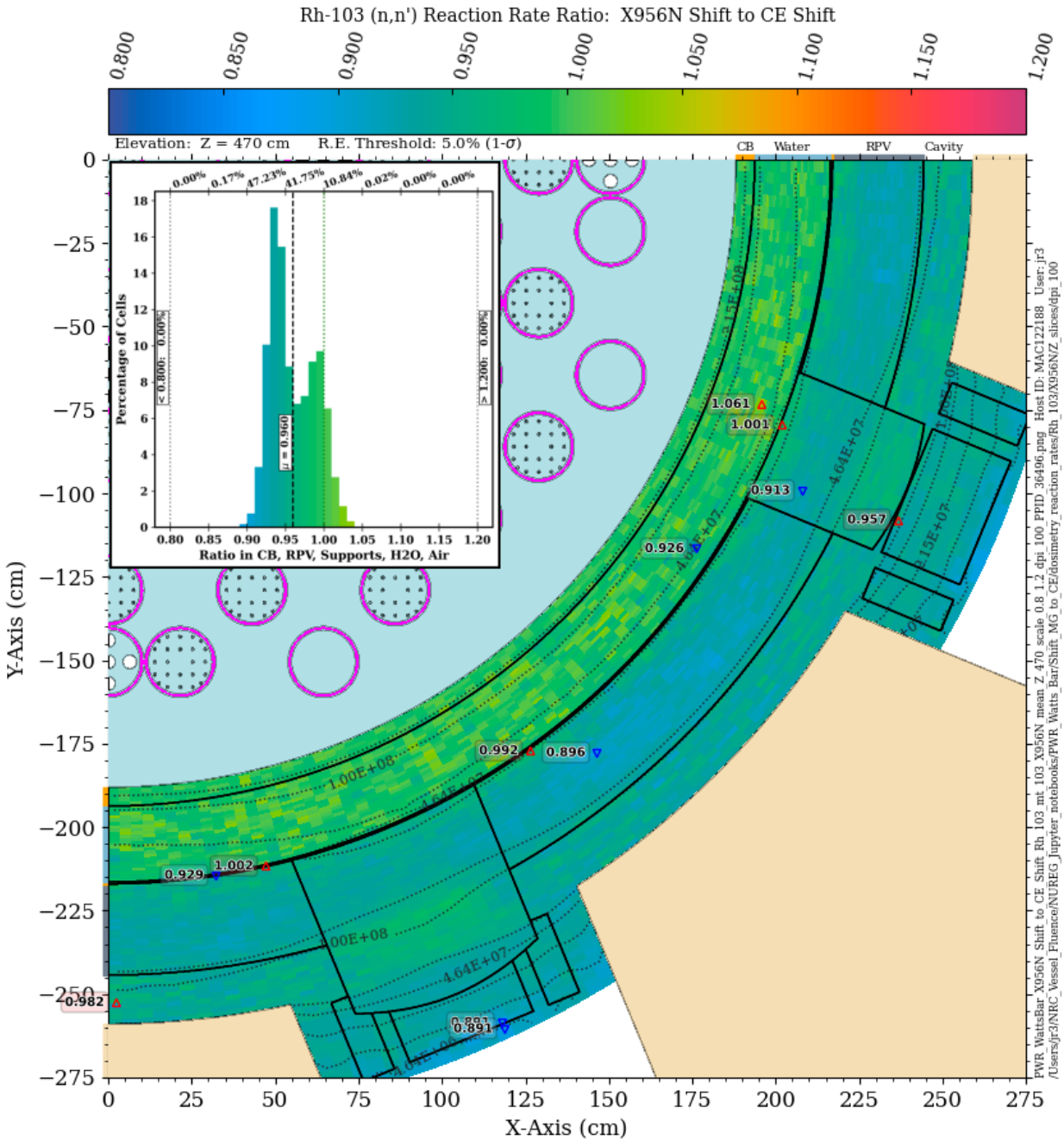

Figure 8-68 **^{103}Rh (n,n') ^{103m}Rh reaction rate ratio in the PWR model: X956N Shift/CE Shift. Plan view at Z = 470 cm** *The contour lines are the reaction rate values from the CE solution.*

8.4.8 ^{238}U (n,f)

The ^{238}U (n,f) reaction has no threshold energy and a 90% energy response range of 1.44 to 6.69 MeV (Table C-1). The fission rates calculated at the core midplane using the BUGLE-B7 library generally agree well with the CE solution at locations within the outer radius of the RPV, but they underpredict the CE values by up to 10% and more in the cavity gap (Figure 8-69). At Z = 470 cm (Figure 8-70), the BUGLE-B7 solution is almost uniformly lower than the CE solution in all locations other than the cavity gap, with an apparent bias of ~7–8%.

At the core midplane elevation, the X200N47G solution agrees well with the CE solution (typically within 5%) except for in the cavity gap, where the X200N47Gv71 solution underpredicts the CE solution by up to nearly 10% (Figure 8-71). At Z = 470 cm, the agreement is degraded, particularly in the outer portion of the RPV and the vessel supports, where the underprediction can reach 20% (Figure 8-72).

An MG calculation with the X956N library shows significant improvement in the MG/CE ratios. At the core midplane, the X956N solution and the CE solution agree, with the MG and CE solutions agreeing within 3% in over 98% of the mesh tally voxels (Figure 8-73). At Z = 470 cm, the MG/CE agreement is still very good, with more than 99% of the mesh tally voxels agreeing within 10%, and nearly 91% agreeing within 5%.

8.4.9 ^{237}Np (n,f)

The ^{237}Np (n,f) reaction has no threshold energy and a 90% energy response range of 0.684 to 5.61 MeV (Table C-1). The fission rates calculated using the BUGLE-B7 library agree with the CE solution within ~10% from the core barrel through the RPV (Figure 8-75), but they underpredict the CE solution by ~10–13% in the cavity gap. At Z = 470 cm (Figure 8-76), the differences between the BUGLE-B7 and CE solutions are substantially greater, with differences from 10–20% in the RPV, nozzles, and cavity gap, as well as locations in the vessel supports where the MG/CE ratio differs by more than 20%.

The Shift solution using the X200N47Gv71 library has better CE agreement than the BUGLE-B7 solution, but there are still differences of ~10% in the cavity gap at the core midplane elevation (Figure 8-77). At an elevation of 470 cm, the MG/CE differences are substantially larger (Figure 8-78), with differences of up to 20% and more in portions of the RPV, cavity gap, and vessel supports.

An MG calculation with the X956N library shows excellent agreement at the core midplane (Figure 8-79), with approximately 94% of the mesh tally voxels agreeing with the CE solution within 2.5%. At the elevation of the vessel supports (Figure 8-80), there are differences of 10–15% at locations in the RPV, cavity gap, and vessel supports.

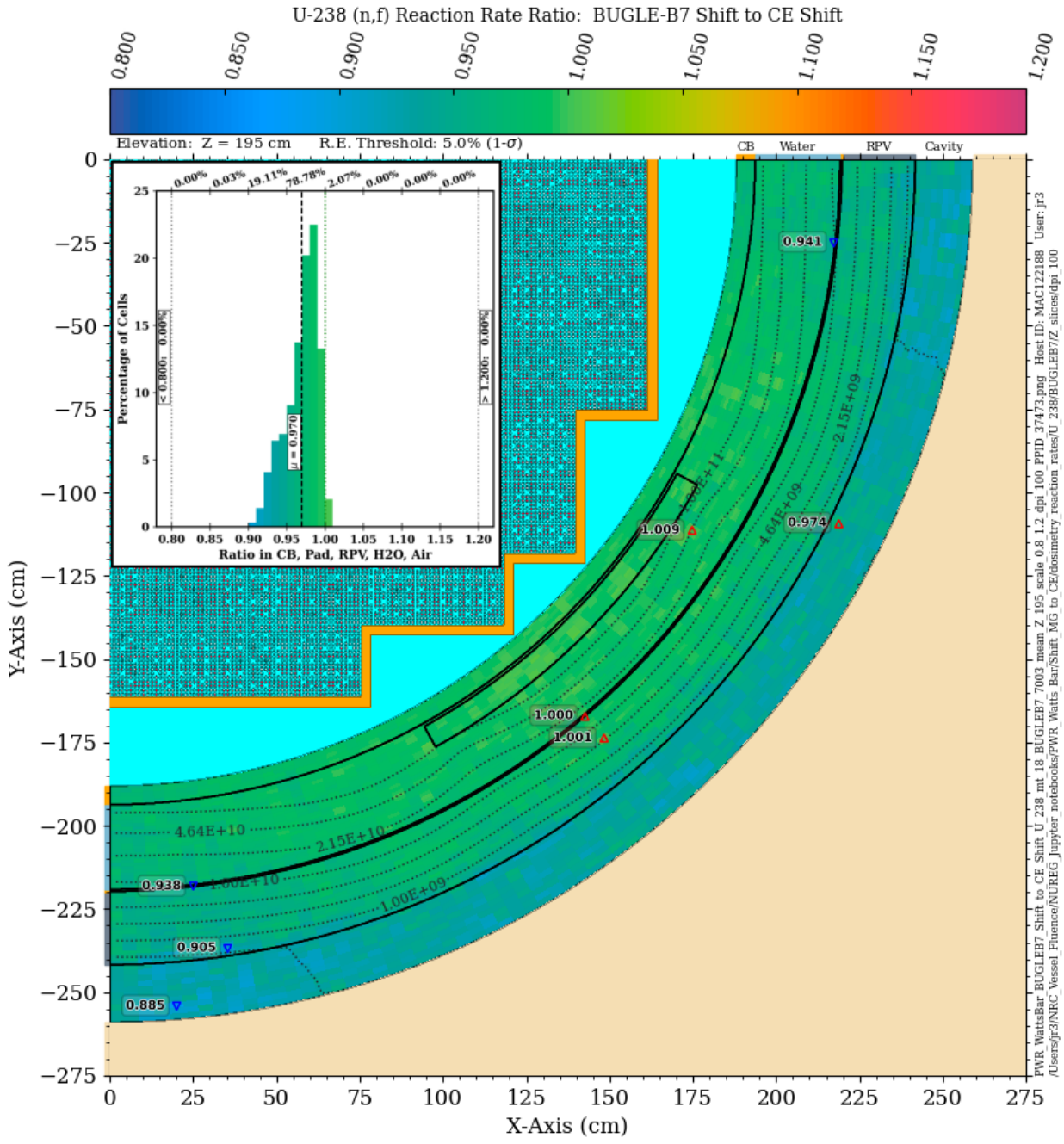

Figure 8-69 **^{238}U (n,f) reaction rate ratio in the PWR model: BUGLE-B7 Shift/CE Shift. Plan view at Z = 195 cm** *The contour lines are the reaction rate values from the CE solution.*

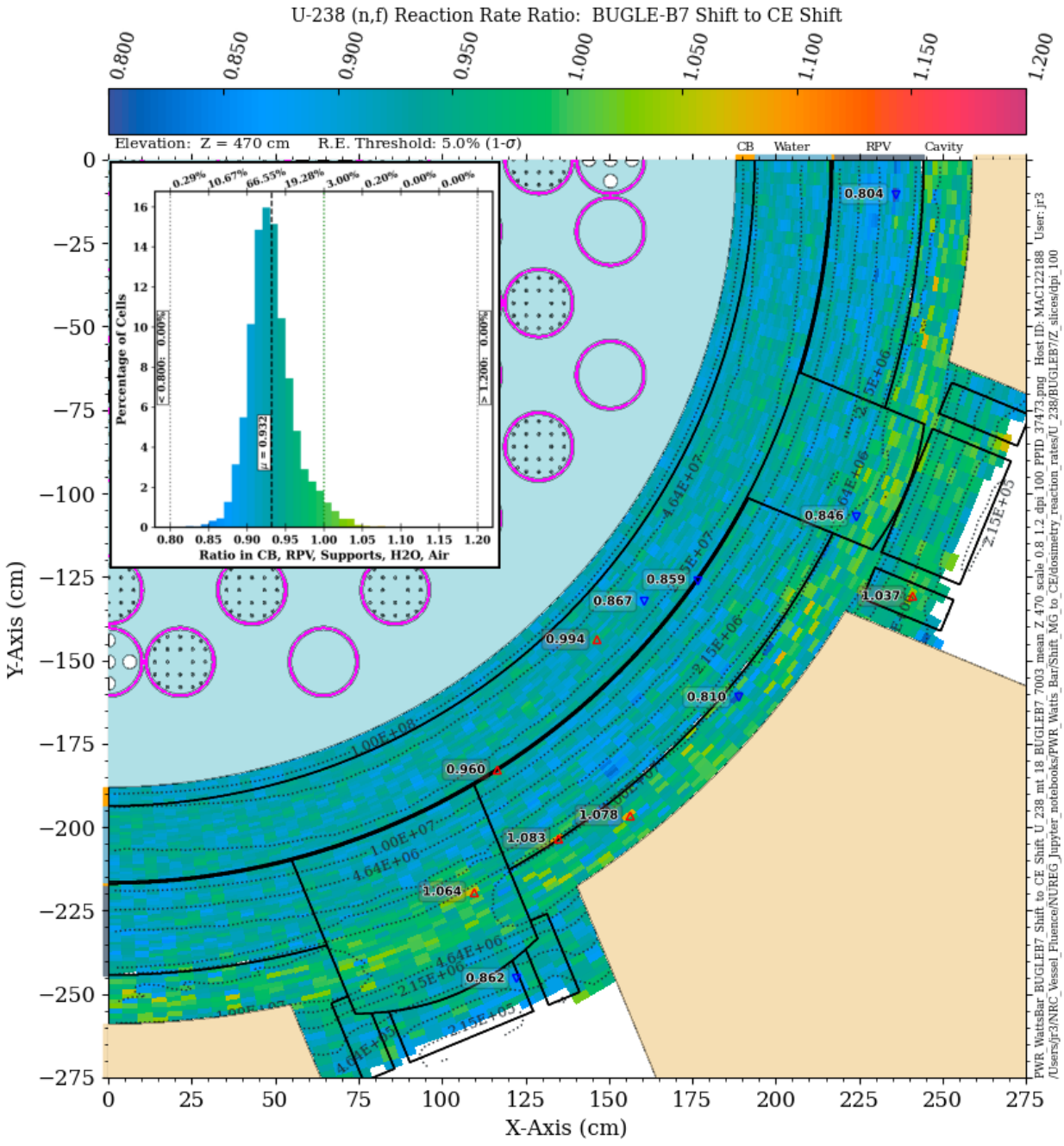

Figure 8-70 **^{238}U (n,f) reaction rate ratio in the PWR model: BUGLE-B7 Shift/CE Shift. Plan view at Z = 470 cm** *The contour lines are the reaction rate values from the CE solution.*

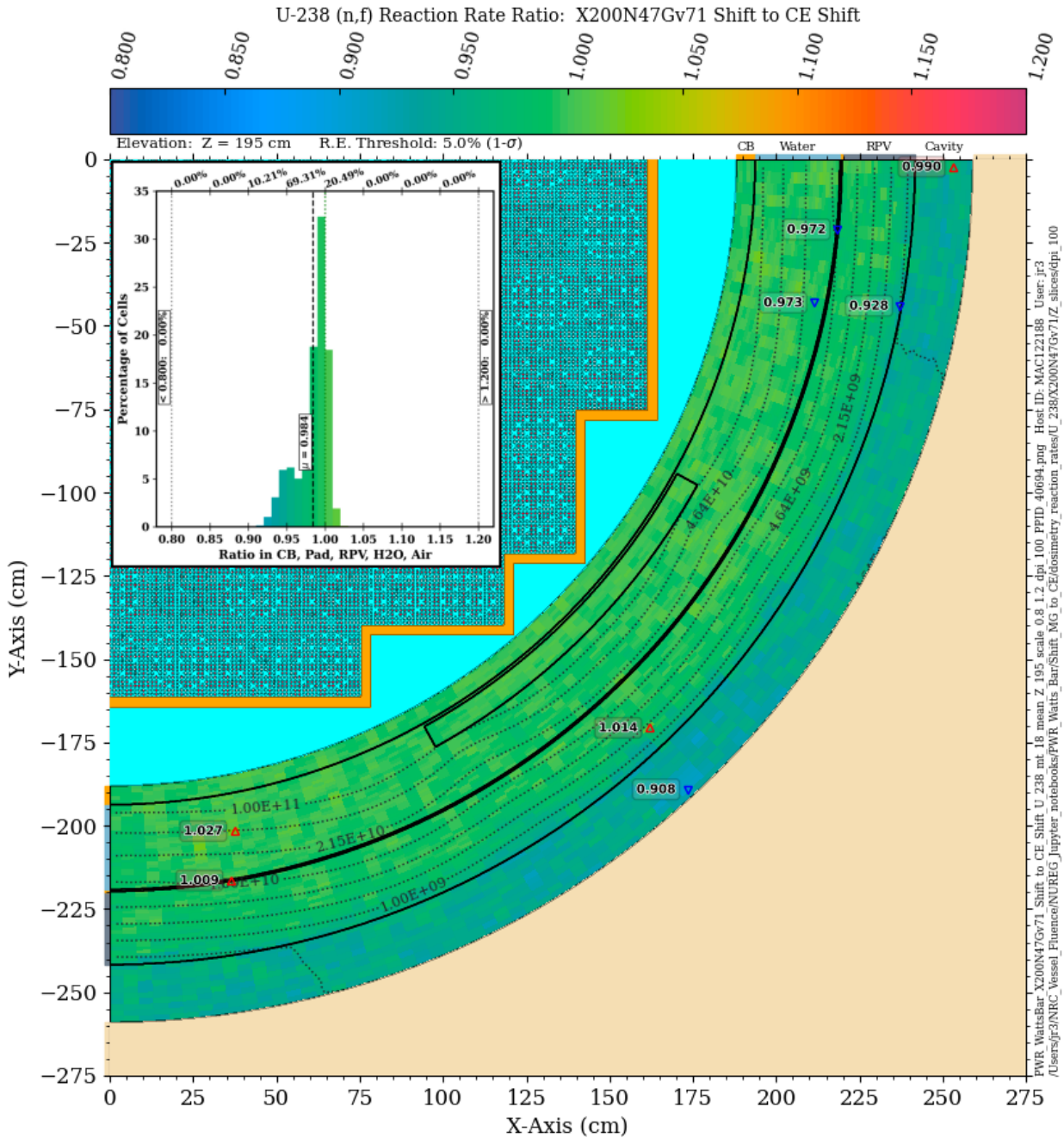

Figure 8-71 **^{238}U (n,f) reaction rate ratio in the PWR model: X200N47Gv71 Shift/CE Shift. Plan view at Z = 195 cm** *The contour lines are the reaction rate values from the CE solution.*

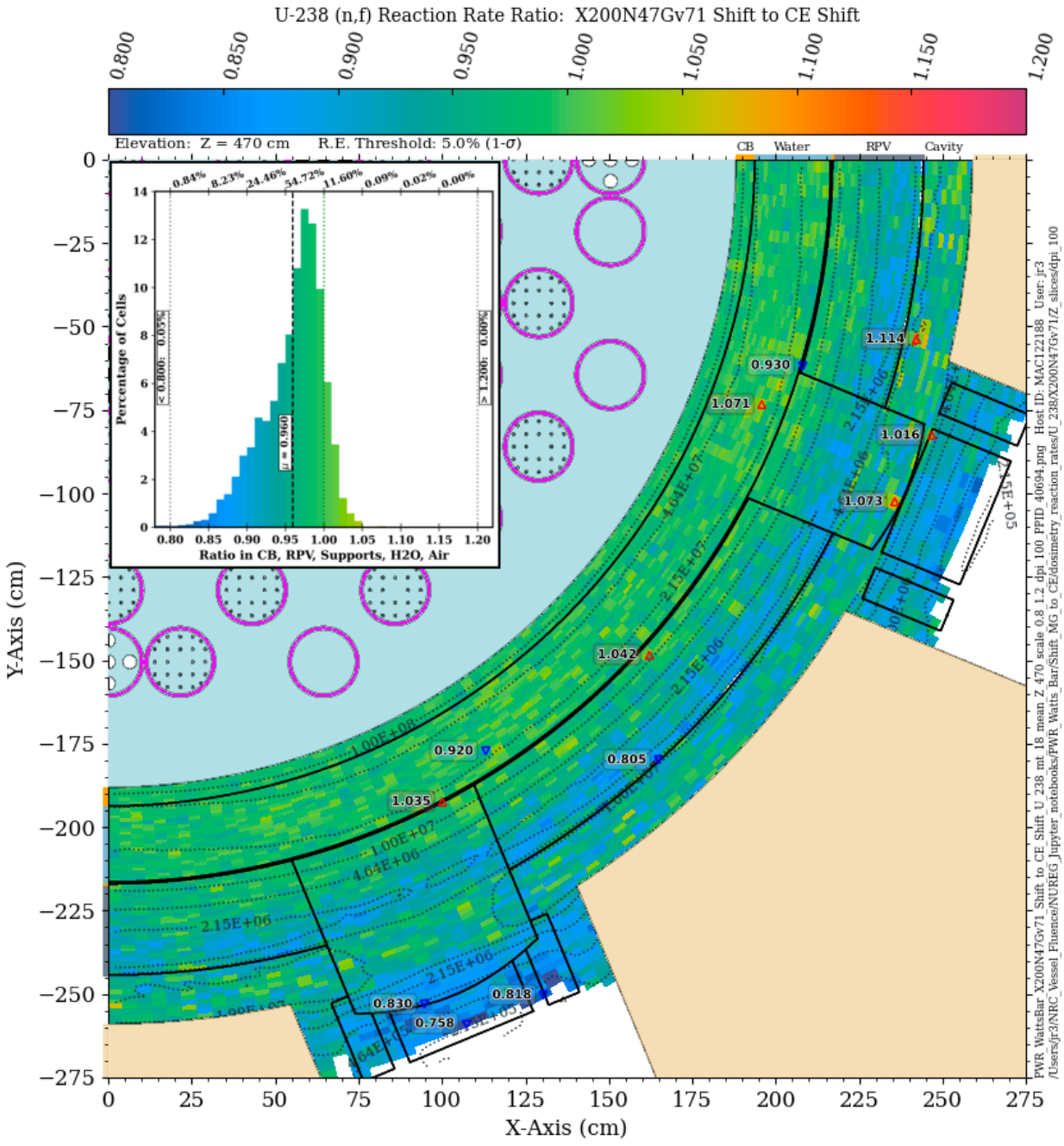

Figure 8-72 **^{238}U (n,f) reaction rate ratio in the PWR model: X200N47Gv71 Shift/CE Shift. Plan view at Z = 470 cm** *The contour lines are the reaction rate values from the CE solution.*

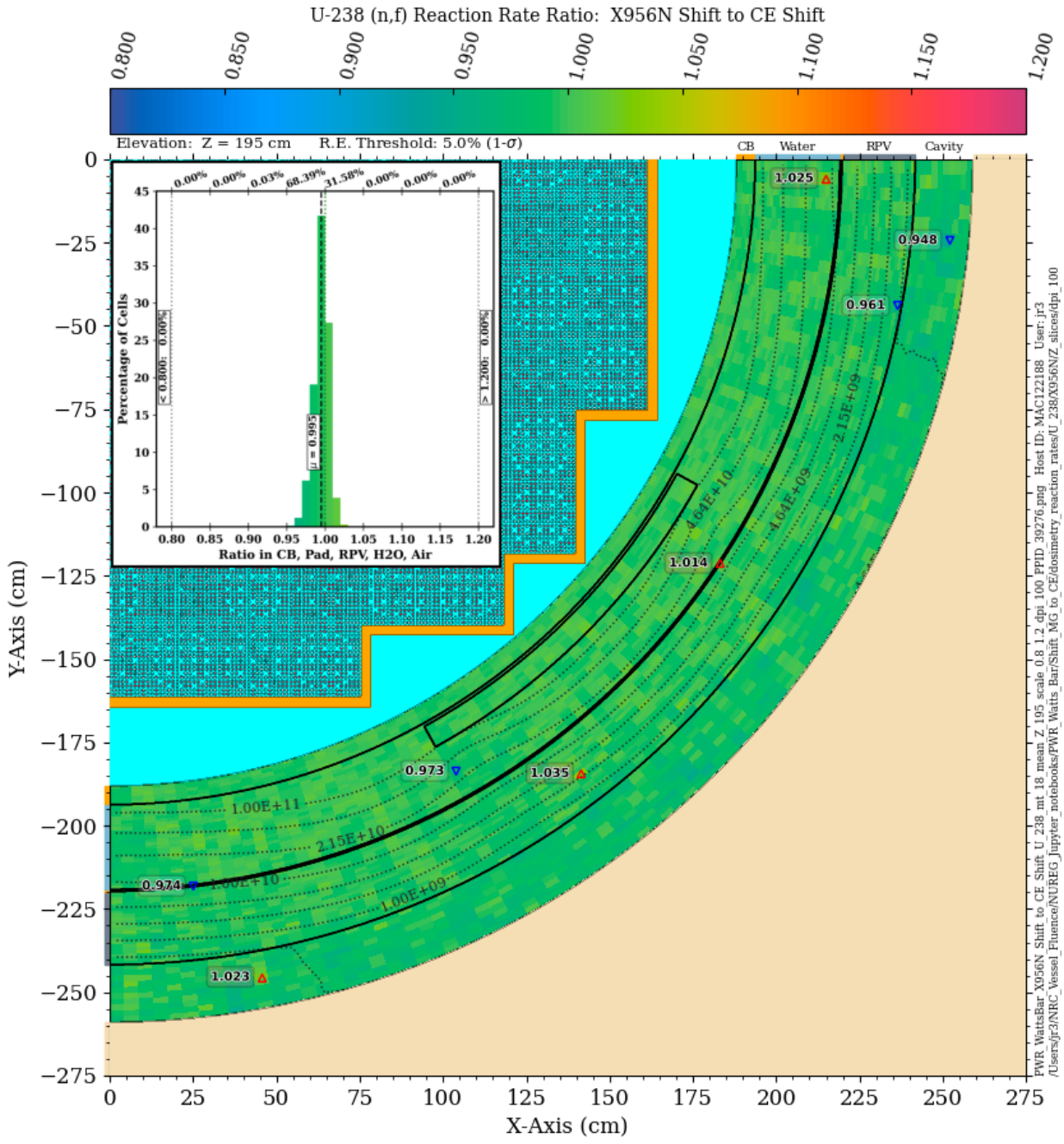

Figure 8-73 **^{238}U (n,f) reaction rate ratio in the PWR model: X956N Shift/CE Shift. Plan view at Z = 195 cm** *The contour lines are the reaction rate values from the CE solution.*

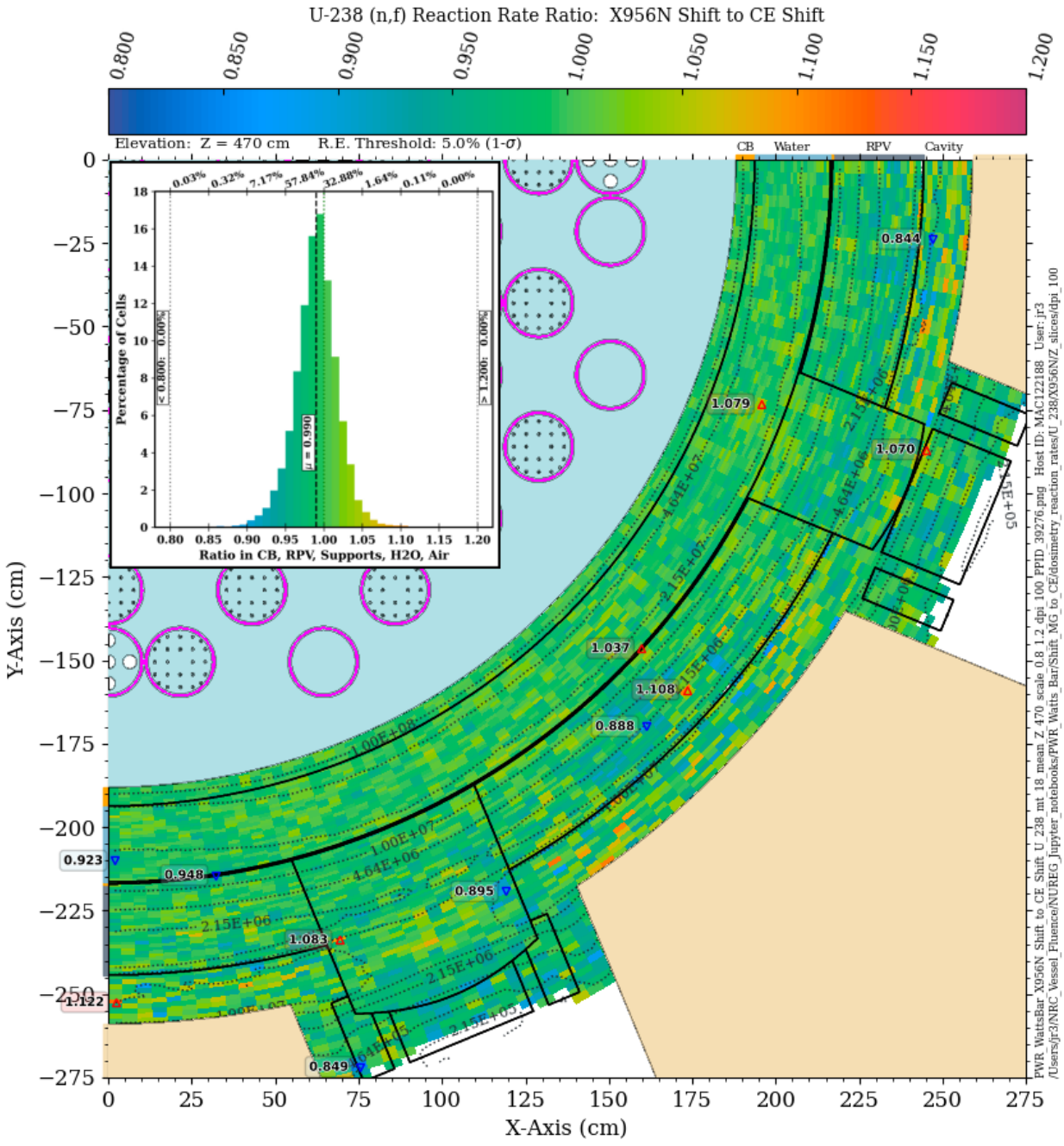

Figure 8-74 **^{238}U (n,f) reaction rate ratio in the PWR model: X956N Shift/CE Shift. Plan view at Z = 470 cm** *The contour lines are the reaction rate values from the CE solution.*

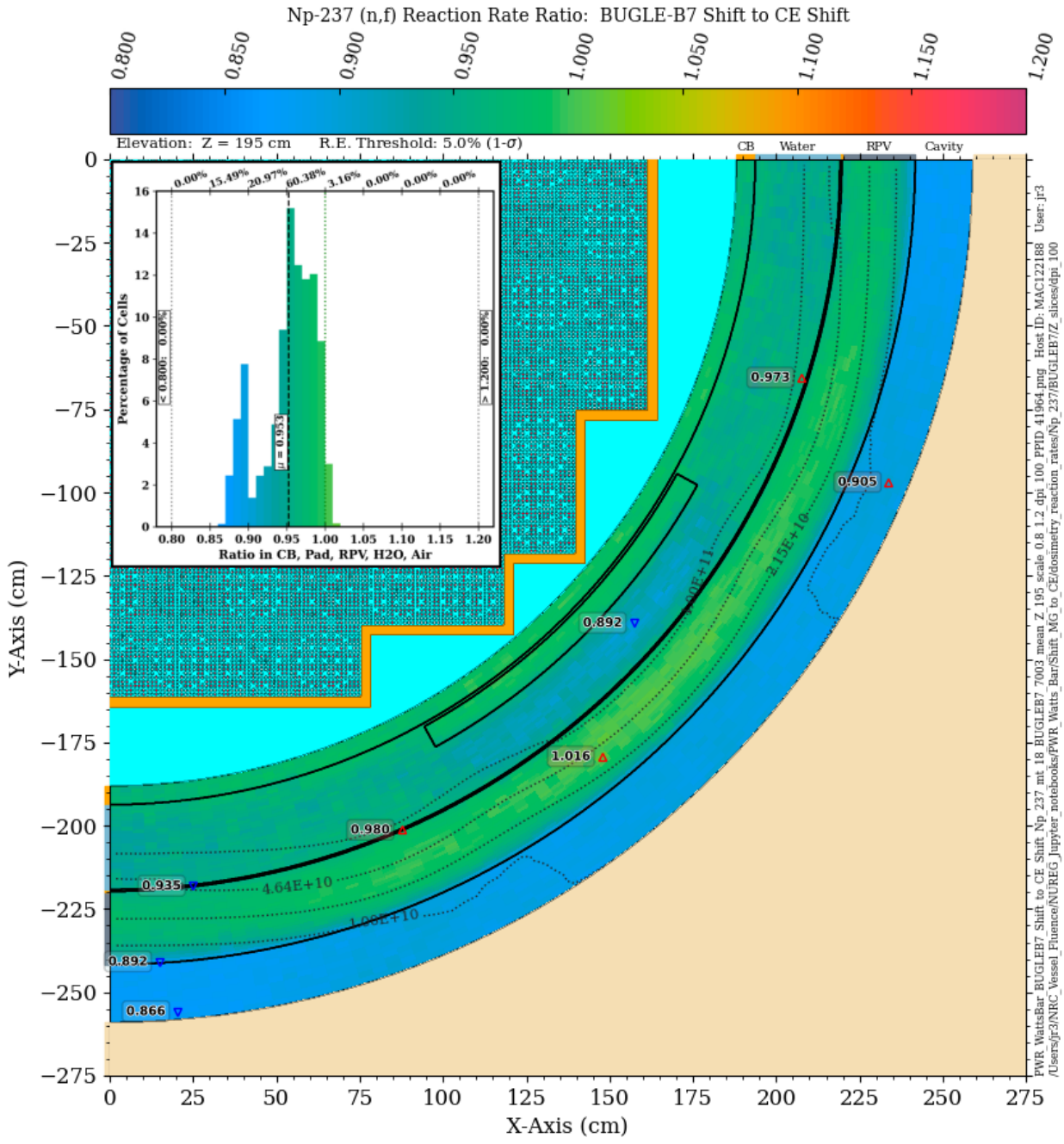

Figure 8-75 **^{237}Np (n,f) reaction rate ratio in the PWR model: BUGLE-B7 Shift/CE Shift. Plan view at Z = 195 cm** *The contour lines are the reaction rate values from the CE solution.*

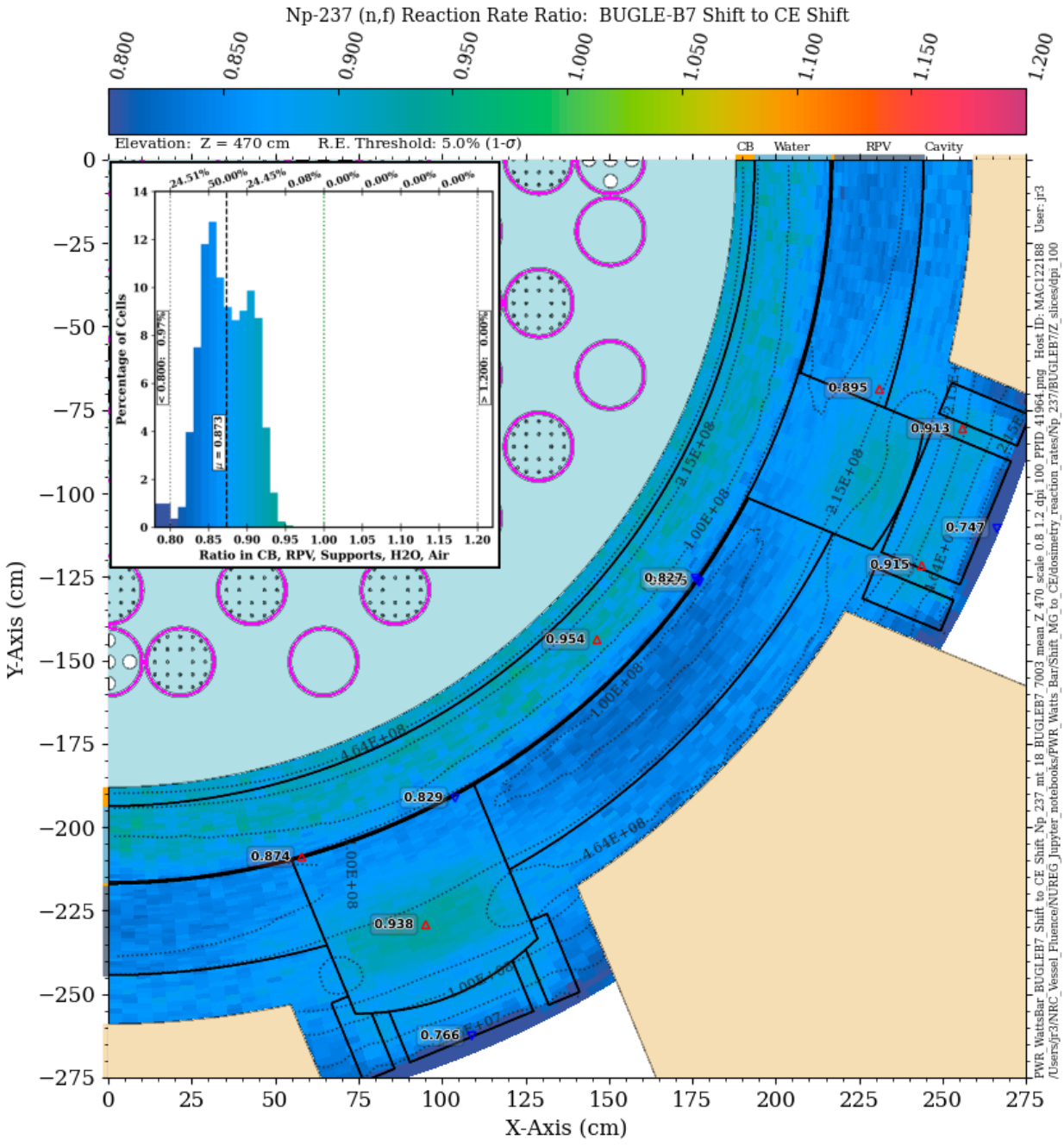

Figure 8-76 **^{237}Np (n,f) reaction rate ratio in the PWR model: BUGLE-B7 Shift/CE Shift. Plan view at Z = 470 cm** *The contour lines are the reaction rate values from the CE solution.*

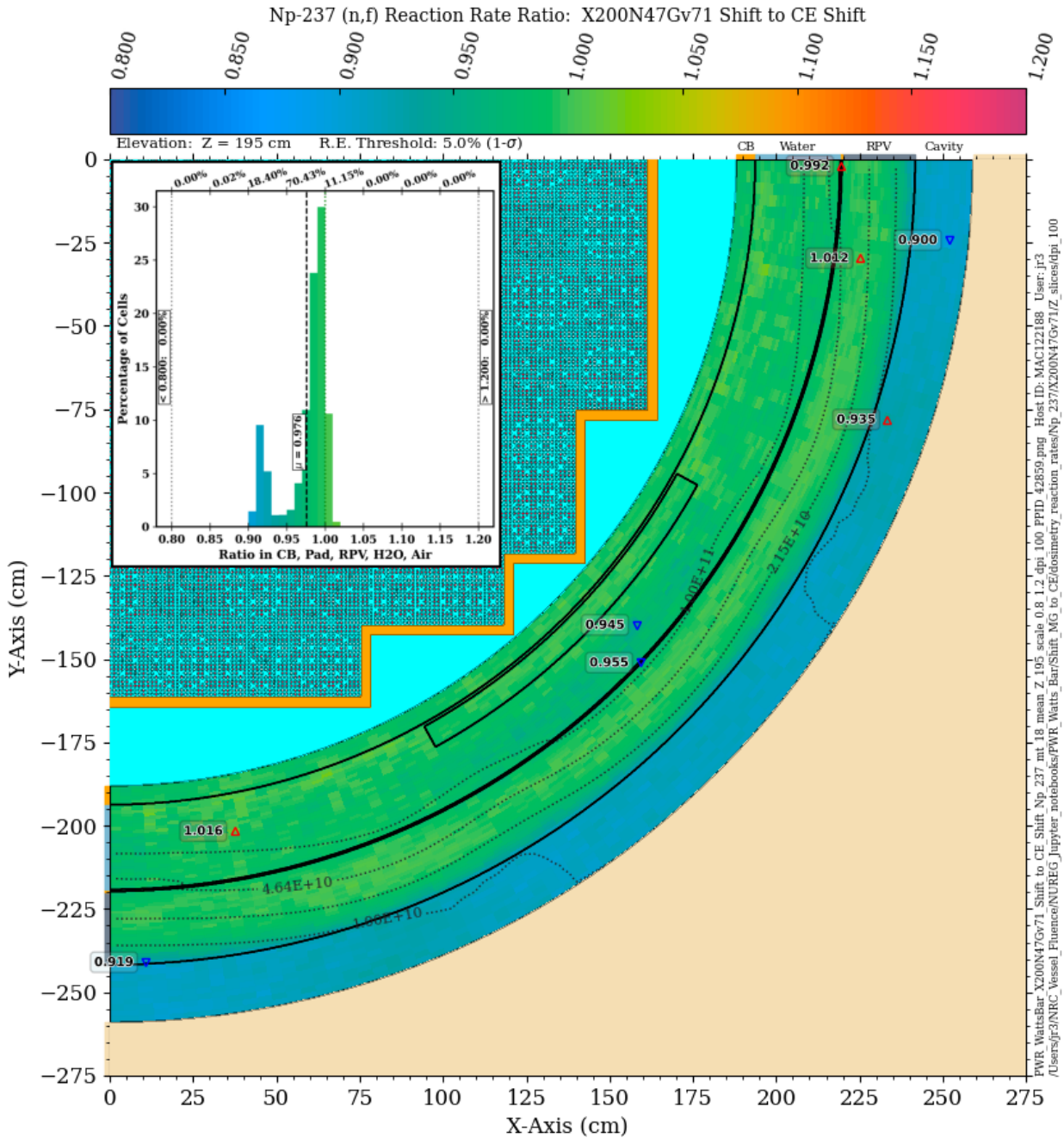

Figure 8-77 **^{237}Np (n,f) reaction rate ratio in the PWR model: 200N47Gv71 Shift/CE Shift. Plan view at Z = 195 cm** *The contour lines are the reaction rate values from the CE solution.*

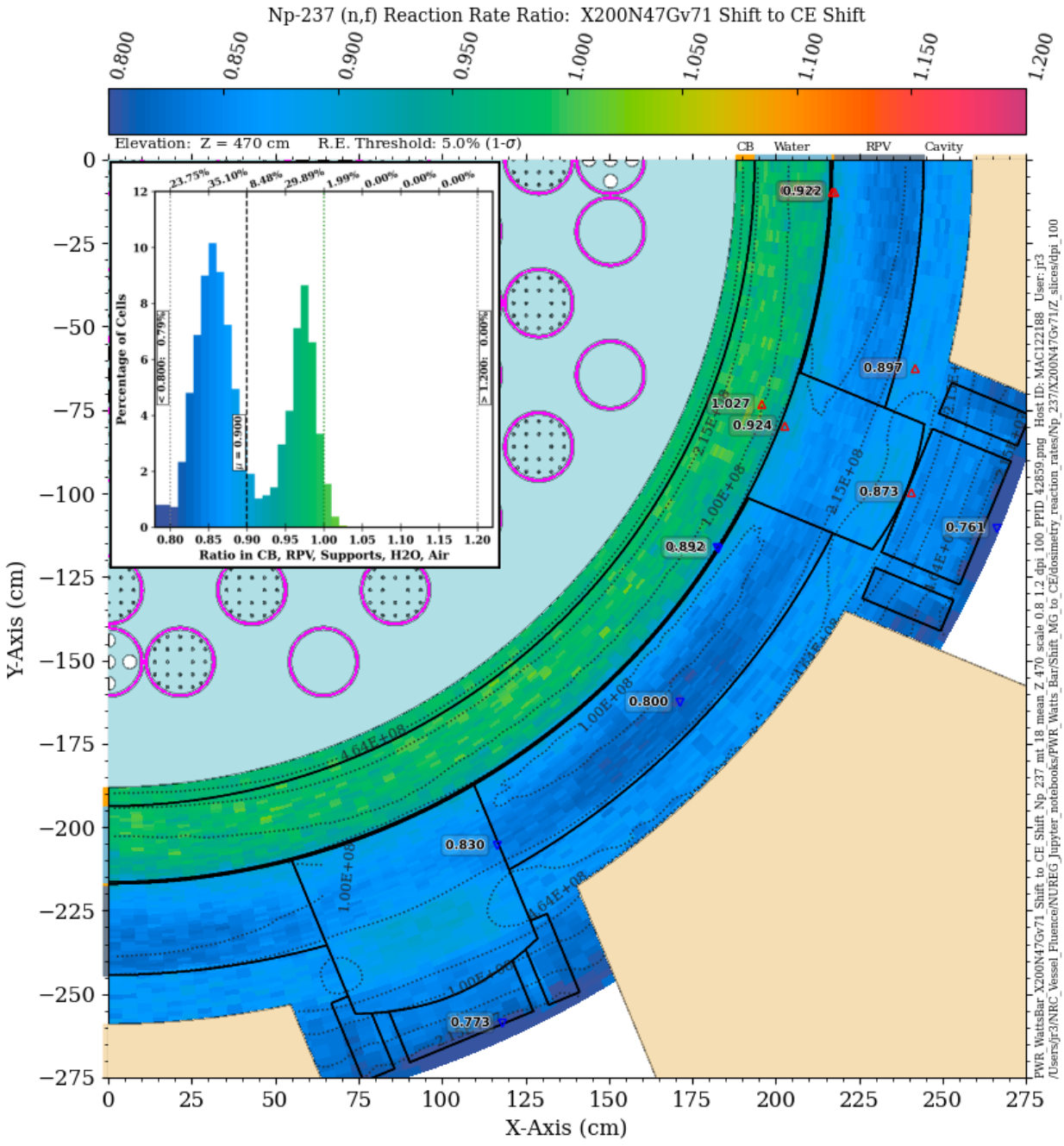

Figure 8-78 **^{237}Np (n,f) reaction rate ratio in the PWR model: 200N47Gv71 Shift/CE Shift. Plan view at Z = 470 cm** *The contour lines are the reaction rate values from the CE solution.*

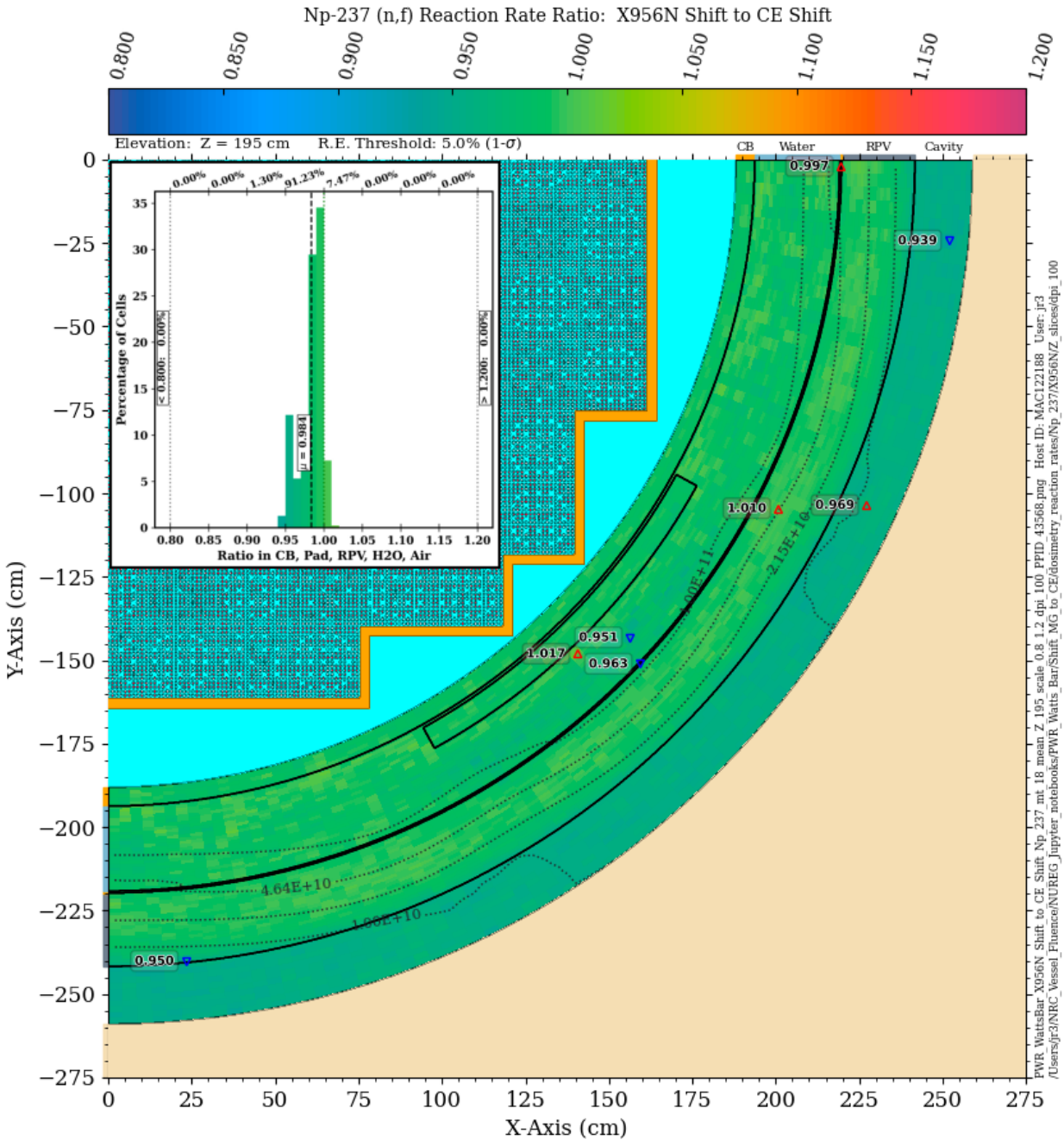

Figure 8-79 **^{237}Np (n,f) reaction rate ratio in the PWR model: X956N Shift/CE Shift. Plan view at Z = 195 cm** *The contour lines are the reaction rate values from the CE solution.*

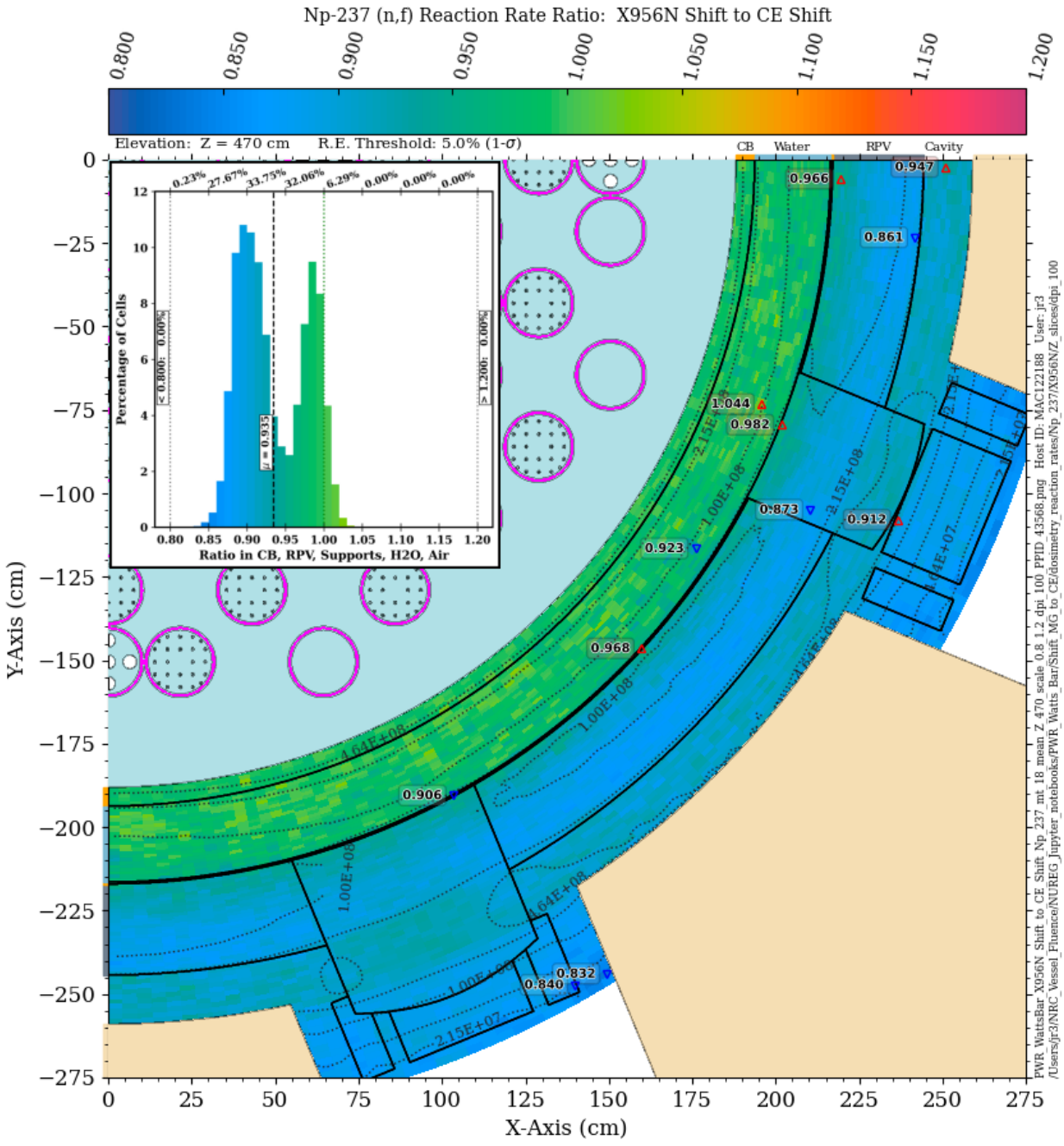

Figure 8-80 **^{237}Np (n,f) reaction rate ratio in the PWR model: X956N Shift/CE Shift. Plan view at Z = 470 cm** *The contour lines are the reaction rate values from the CE solution.*

8.5 Summary of Multigroup Studies

The analyses presented in this section provide insights into the adequacy and limitations of MG cross sections for the calculation of RPV fluence, dpa rates, and common dosimetry reactions. The results address both the traditional and extended beltline regions.

All of the MG libraries considered in this study are capable of providing accurate fast fluence estimates (i.e., values which agree very well with CE calculations) in the inner portion of the RPV within the traditional beltline region. However, with the exception of the X642N and X956N libraries which were developed specifically to improve the calculation of neutron transport through iron in the energy range of ~1 to ~3 MeV, all of the MG solutions underpredict the CE solution by ~10% at the outer surface of the RPV. Although this location is not important for RPV fluence calculations in the traditional beltline region, it is important for locations in the extended beltline region, where cavity streaming becomes an important contributor to neutron flux levels. An underprediction of the fast neutron flux at the outer surface of the RPV will result in an underprediction of the flux of neutrons that scatter from the concrete bioshield back into the cavity gap. This will result in erroneously low calculated fluxes in regions where cavity streaming is important. At the elevation of the vessel supports, all of the MG libraries except X642N and X956N underpredict the CE solution at all locations of interest, particularly in the vessel supports, where the solution differences can exceed 15% or more. In contrast, the X642N and X956N libraries provide fast fluence predictions that agree with the CE solution at the vessel support elevation within 5% in nearly all the locations of interest.

For dpa rate calculations, the results are more complex. The widely used BUGLE-B7 library underpredicts the dpa rate at all locations in the RPV at the traditional beltline elevation, with a maximum difference of more than 20% at the outer edge of the RPV. At the elevation of the vessel supports, the BUGLE-B7 solution underpredicts the CE solution by more than 20% at nearly all locations, with differences in the range of 35% at some locations in the vessel supports. Solutions using the VITAMIN-B7, X200N47Gv71, and X642N libraries overpredict as well as underpredict the dpa rate at the traditional midplane elevation, with the majority of locations agreeing with the CE solution within 5%. At the elevation of the vessel supports, these libraries produce solutions that underpredict the CE solution in all locations, with differences of 15% and more occurring in the vessel supports. The MG/CE agreement is markedly improved with the X956N library. Near the core midplane, the agreement is excellent, with differences of less than 2.5% in over 99% of the mesh tally voxels. At the elevation of the vessel supports, the MG solution again underpredicts the CE solution, but to a much lesser extent than the other libraries. The ratio values are tightly clustered with an apparent bias of ~6%.

The MG/CE agreement for the dosimetry rate calculations is strongly dependent on the reaction cross section being considered. For the three reactions with threshold energies above 2 MeV [^{27}Al(n,α), ^{63}Cu (n,α), and ^{46}Ti (n,p)], the MG/CE agreement is reasonably good at both of the elevations considered, with the exception of the ^{46}Ti (n,p) reaction rate calculated with the BUGLE-B7 and VITAMIN-B7 libraries. As noted in Section 8.4.3, the poor agreement obtained with the BUGLE-B7 and VITAMIN-B7 libraries is likely caused by differences in the ^{46}Ti (n,p) cross-section data rather than the transport cross sections.

Results for the ^{54}Fe (n,p) and ^{58}Ni (n,p) reactions—with threshold energies of 700 and 400 keV, respectively—are very similar. In each case, the BUGLE-B7 and X200N47Gv71 libraries provide good agreement with the CE solution in the traditional beltline region. At the elevation of the vessel supports, the BUGLE-B7 solutions are uniformly low, particularly toward the inner

surface of the RPV, where differences approach 10%. The X200N47Gv71 solution provides improved agreement at this elevation, with more than 92% of the tally values agreeing with the CE solution to within 5%.

For the ^{115}In (n,n′) and ^{103}Rh (n,n′) reactions, the BUGLE-B7 solutions agree well with the CE solution from the core barrel through the inner portion of the RPV at the traditional beltline location. However, at the outer edge of the RPV and in the cavity gap, the BUGLE-B7 solutions underpredict the CE solutions by up to ~10%. The agreement is degraded at the elevation of the vessel supports, where differences of 20% and more occur, particularly in the vessel supports. The X956N library solution for these two reaction rates is in excellent agreement with the CE solution at the traditional beltline elevation, with MG/CE differences of less than 5% in 99.9% of the mesh tally voxels. The agreement is degraded somewhat at the elevation of the vessel supports, but it is markedly improved relative to the BUGLE-B7 solution, with MG/CE agreement of 10% in more than 99% of the mesh tally voxels.

For the ^{238}U (n,f) reaction, the BUGLE-B7 solution consistently underpredicts the CE solution. At the traditional beltline elevation, the BUGLE-B7/CE differences are up to ~10% at the outer edge of the RPV and in the cavity gap. At the elevation of the vessel supports, the BUGLE-B7/CE agreement is further degraded, with differences of 15% or more in some locations. The MG/CE agreement at the core midplane is improved with the X200N47Gv71 library, with differences typically less than 5% except in the cavity gap, where the X200N47Gv71 solution underpredicts the CE solution by up to nearly 10%. At the elevation of the vessel supports, the solution agreement is degraded, particularly in the outer portion of the RPV and the vessel supports, where the X200N47Gv71 underprediction can reach 20%. The X956 library provides substantial improvements in the MG/CE ratios, particularly at the vessel support elevation, where the solutions agree to within 10% in more than 99% of the mesh tally cells and to within 5% in nearly 91% of the mesh tally cells.

Of all of the dosimetry reaction rates considered, the MG/CE differences are greatest at both the core midplane and the vessel support elevation for the ^{237}Np (n,f) reaction rate. This is not surprising, as the 90% energy response range for this reaction is the lowest of the nine reactions considered (Figure C-2). The BUGLE-B7 solution underpredicts the CE solution by ~10–13% throughout the cavity gap at the core midplane elevation. At the vessel support elevation, the BUGLE-B7/CE differences range from 10–20% in the RPV, nozzles, and cavity gap, with differences exceeding 20% in some vessel support locations. The X200N47Gv71 solution provides some improvement relative to the BUGLE-B7 solution, but there are still differences of 20% or more in some vessel support locations. Although the X956N solution agrees with the CE solution to within 5% in over 98% of the mesh tally cells at the core midplane elevation, the MG/CE differences with this library at the vessel support elevation are still relatively high, with differences exceeding 10% in in nearly 28% of the mesh tally cells, and differences of up to ~15% at locations in the vessel supports.

The results of the MG/CE comparisons for these 11 neutron responses (fast flux, dpa rate, and nine dosimetry reaction rates) suggest that while the widely used BUGLE-B7 library is generally adequate for the calculation of these quantities at locations radially out through the inner portion of the RPV in the traditional beltline region, it is not well suited to the calculation of most of these 11 responses at locations in the extended beltline region. In some cases, the differences between a BUGLE-B7 solution and a more accurate CE solution exceed 20%. This suggests that for a discrete ordinates calculation (which is also subject to the approximations made in

space and angle) using the BUGLE-B7 library, it may not be possible to obtain calculational results that are within the 20% uncertainty value prescribed by Regulatory Guide 1.190.

Improved agreement between MG and CE solutions can be obtained by using very fine energy-group structures that are specifically developed to accurately model neutron transport through iron over important resonance ranges. However, these very-fine-group libraries may have 10 times or more the number of groups in the BUGLE-B7 library. Because the MG libraries have 2D arrays for all the group-to-group scattering probabilities, the memory requirements for a discrete ordinates calculation scale as N^2 rather than N for a library with N groups. The computing resources required to perform 3D discrete ordinates calculations with these libraries can thus easily become prohibitive.

9 SCATTERING CROSS-SECTION EXPANSION (P_N) ORDER SENSITIVITY IN THE EXTENDED BELTLINE REGION

The angular distribution of scattered radiation in MG discrete ordinates calculations is modeled using Legendre polynomial expansions. The degree to which these expansions can adequately represent a scattering distribution is dependent on the degree of anisotropy in the MG scattering cross sections. A discussion of the causes of anisotropic MG scattering cross sections and examples of the scattering characteristics of some common nuclides and materials in LWR shielding analyses are provided in APPENDIX D.

As noted in APPENDIX D, MG scattering cross sections tend to be more anisotropic for light elements and for high-energy neutrons. Thus, scattering of neutrons within the RPV wall is less sensitive to the scattering expansion order than the scattering of neutrons within hydrogenous materials such as the coolant and the concrete bioshield. This behavior has implications for not only the penetration of neutrons through the RPV and the concrete, but also for scattering from the concrete back into the cavity gap. Consequently, it is possible that the calculation of neutron fluxes, dpa rates, and dosimetry reaction rates in the extended beltline region may be more sensitive to the scattering expansion order than similar calculations within the traditional beltline.

For RPV fluence calculations with typical LWR configurations in the beltline region, Regulatory Guide 1.190 requires a minimum P_3 expansion order. No suggestion is made as to the potential need for higher-order scattering in locations where cavity streaming is important.

It should be noted that the amount of memory required for a discrete ordinates calculation varies as $(N+1)^2$, where N is the order of the scattering expansion. Thus, a P_5 calculation requires more than twice the memory needed for a P_3 calculation, and a P_7 calculation requires four times the memory of a P_3 calculation. For this reason, as well as the increase in computational time with higher-order scattering, there is a strong incentive to avoid the use of higher expansion orders (i.e., greater than P_3) if the flux solution is relatively insensitive to the additional scattering moments.

This section describes evaluation of the effect of higher-order ($> P_3$) scattering on the fast neutron flux, dpa rate, and selected dosimetry reaction rates in the extended beltline region. In all cases, the comparisons are between P_3 and P_5 scattering.

9.1 Effect of Scattering Order on Fast Flux Levels and DPA Rates

The effect of increasing the scattering order from P_3 to P_5 has an insignificant impact on fast neutron flux and dpa rate calculations not only in the traditional beltline region (as expected), but also in the extended beltline region. Figure 9-1 illustrates the P_5/P_3 fast ($E > 1.0026$ MeV) neutron flux ratio at elevations of 200 and 465 cm. Within the RPV, nozzles, and RPV supports, the solution differences are less than 1%. The greatest difference in these solutions is seen deep in the concrete bioshield and is no more than 3%.

The dpa rate sensitivity is shown in Figure 9-2. As with the fast flux comparison, the differences between the P_3 and P_5 solutions are less than 1%. Note that because the dpa rate is only meaningful in carbon steel, the ratio data are only shown in the RPV, nozzles, and RPV supports.

These comparisons suggest that P_3 scattering expansions are adequate for calculation of fast fluence and dpa in the extended beltline region of RVs, as well as in the traditional beltline region.

9.2 Effect of Scattering Order on Dosimetry Reaction Rates

Although P_3 expansions are adequate for fast fluence and dpa calculations in the extended beltline region, it is possible that higher-order scattering may be appropriate for the calculation of neutron reaction rates with high energy thresholds. Because neutron dosimetry reactions are used to benchmark calculational methods, any decrease in the accuracy of calculating these reaction rates has implications for methods validation studies.

Section 8.4 presents comparisons of calculated reaction rates for nine commonly used dosimetry isotopes using MG and CE cross-section libraries. Three of the dosimetry reactions—^{27}Al (n,α), ^{63}Cu (n,α), and ^{46}Ti (n,p)—have energy thresholds above 2 MeV. Because angular distributions of scattered neutrons are more anisotropic at high energies (see, for example, Figure D-6, Figure D-7, and Figure D-8), it is possible that calculation of those dosimetry reaction rates may be more sensitive to higher-order scattering moments compared to fast fluence and dpa calculations.

Figure 9-3 shows the ratio of the calculated ^{27}Al (n,α) reaction rate at Z = 200 cm and Z = 465 cm. Near the core midplane, there is very little difference between the P_3 and P_5 solutions except within the bioshield. However, at the elevation of the RPV supports, there are significant differences in the solutions within the cavity gap, nozzle, and outermost portion of the RV. These differences, which can exceed 20%, could affect the accuracy of calculations for ^{27}Al dosimeters that may be placed in the extended beltline region.

Figure 9-4 shows the ratio of the calculated ^{63}Cu (n,α) reaction rate at the same elevations. The agreement near the core midplane is very good, but at the elevation of the RPV supports, there are again significant differences between the P_3 and P_5 solutions. These solution differences are less than those for the ^{27}Al (n,α) reaction, which is consistent with the lower threshold energy for the ^{63}Cu (n,α) reaction.

Figure 9-5 shows the ratio of the calculated ^{46}Ti (n,p) reaction rate at the same elevations. Consistent with the lower energy threshold of this reaction of 2.10 MeV, the solution differences at the elevation of the RV supports are again reduced, with no values exceeding 8%.

For the ^{54}Fe (n,p) reaction, which has a threshold energy of 700 keV, there are only small differences, typically less than 3% between the P_3 and P_5 solutions (Figure 9-6).

Based on these findings, it is reasonable to ask whether P_5 scattering expansions are adequate for calculation of high-energy threshold reactions. Calculations of the ^{27}Al and ^{63}Cu (n,α) reaction rates using P_7 scattering show insignificant (< 2%) differences, even at the elevation of the RPV supports.

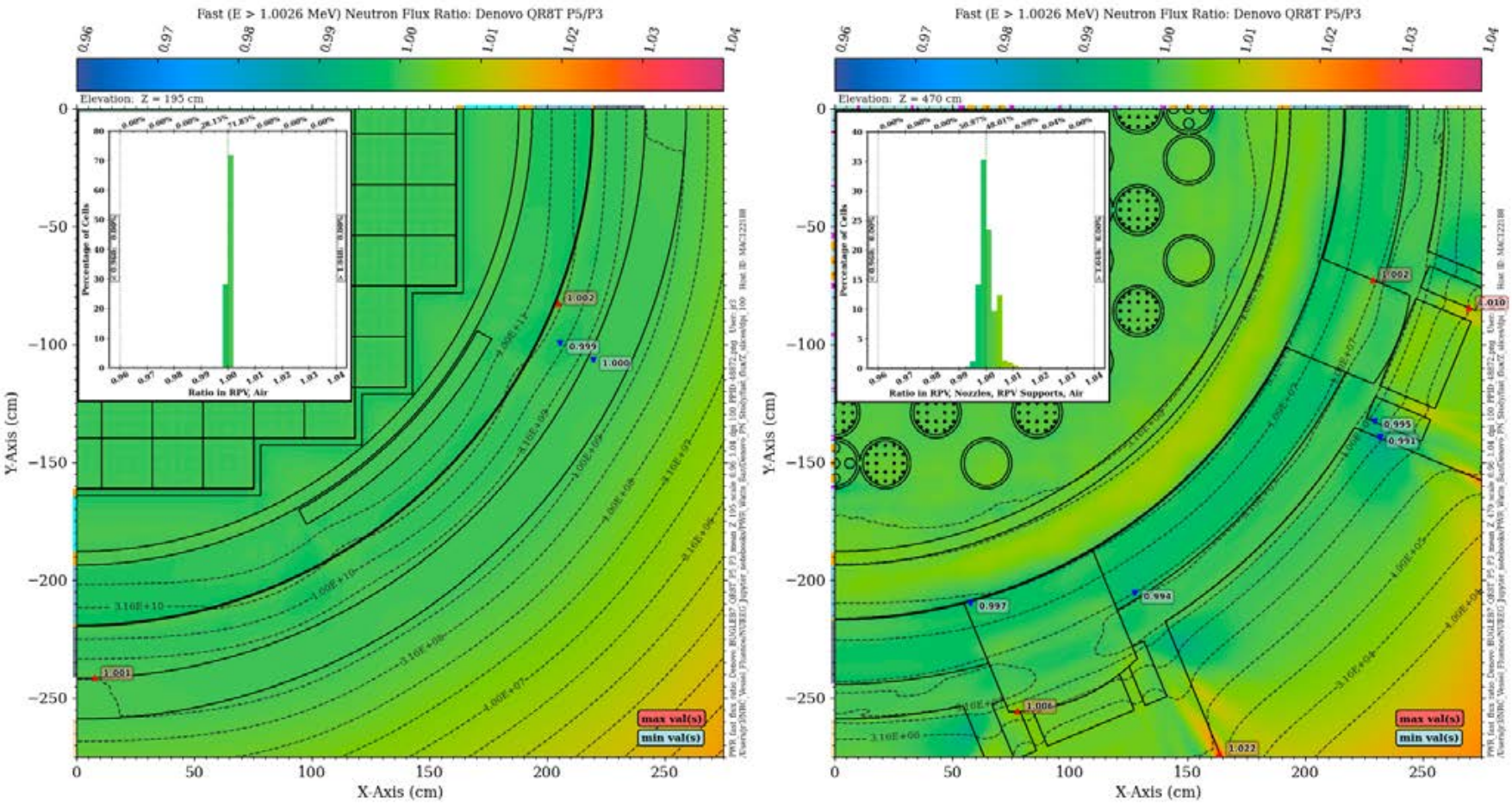

Figure 9-1 **Ratio of the fast neutron flux (E > 1.0026 MeV) from a P5 Denovo solution to a P3 Denovo solution at elevations of Z = 195 cm and Z = 470 cm**

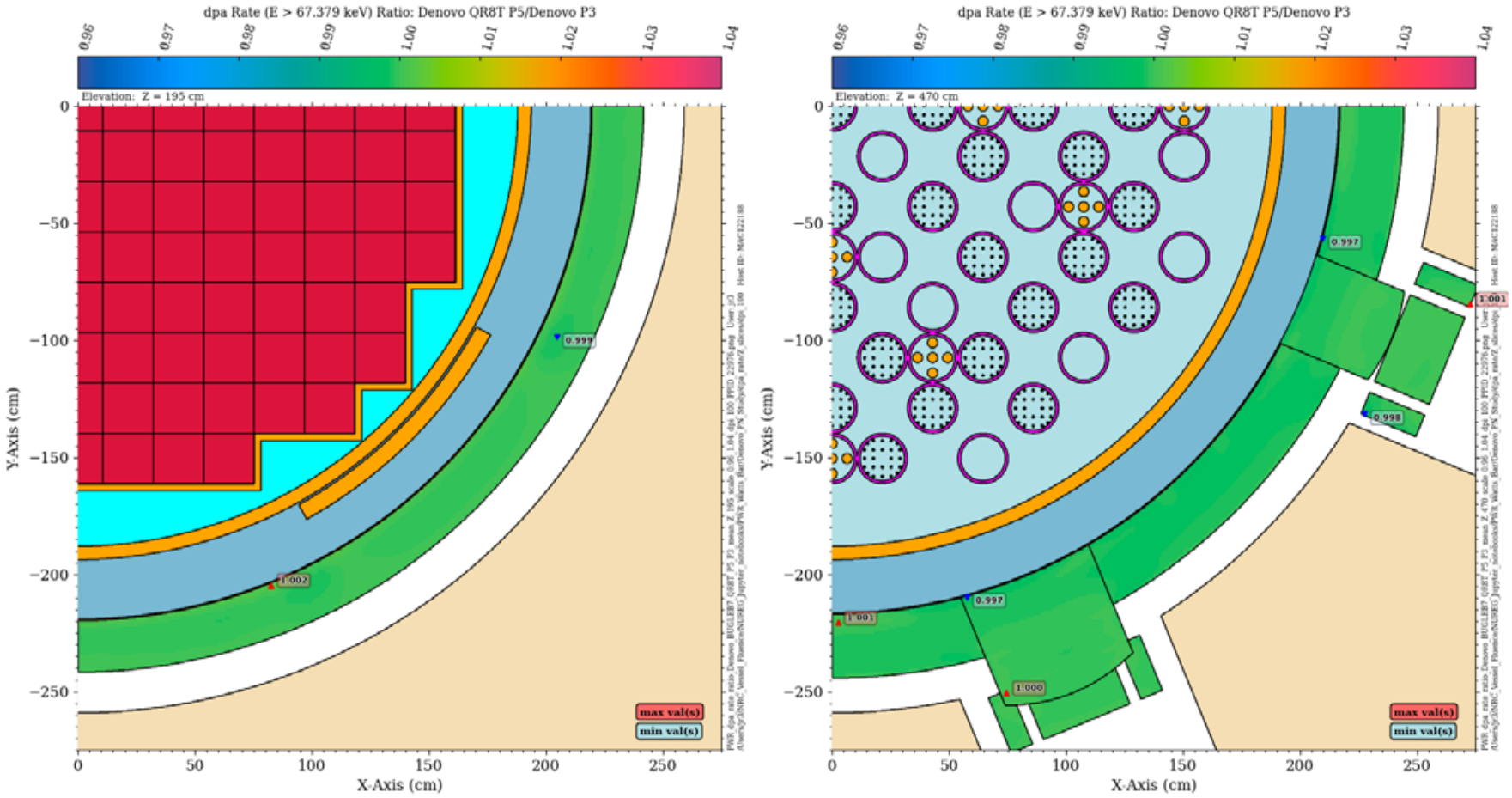

Figure 9-2 Ratio of the dpa rate for E > 67.379 keV from a P5 Denovo solution to a P3 Denovo solution at elevations of Z = 195 cm and Z = 470 cm

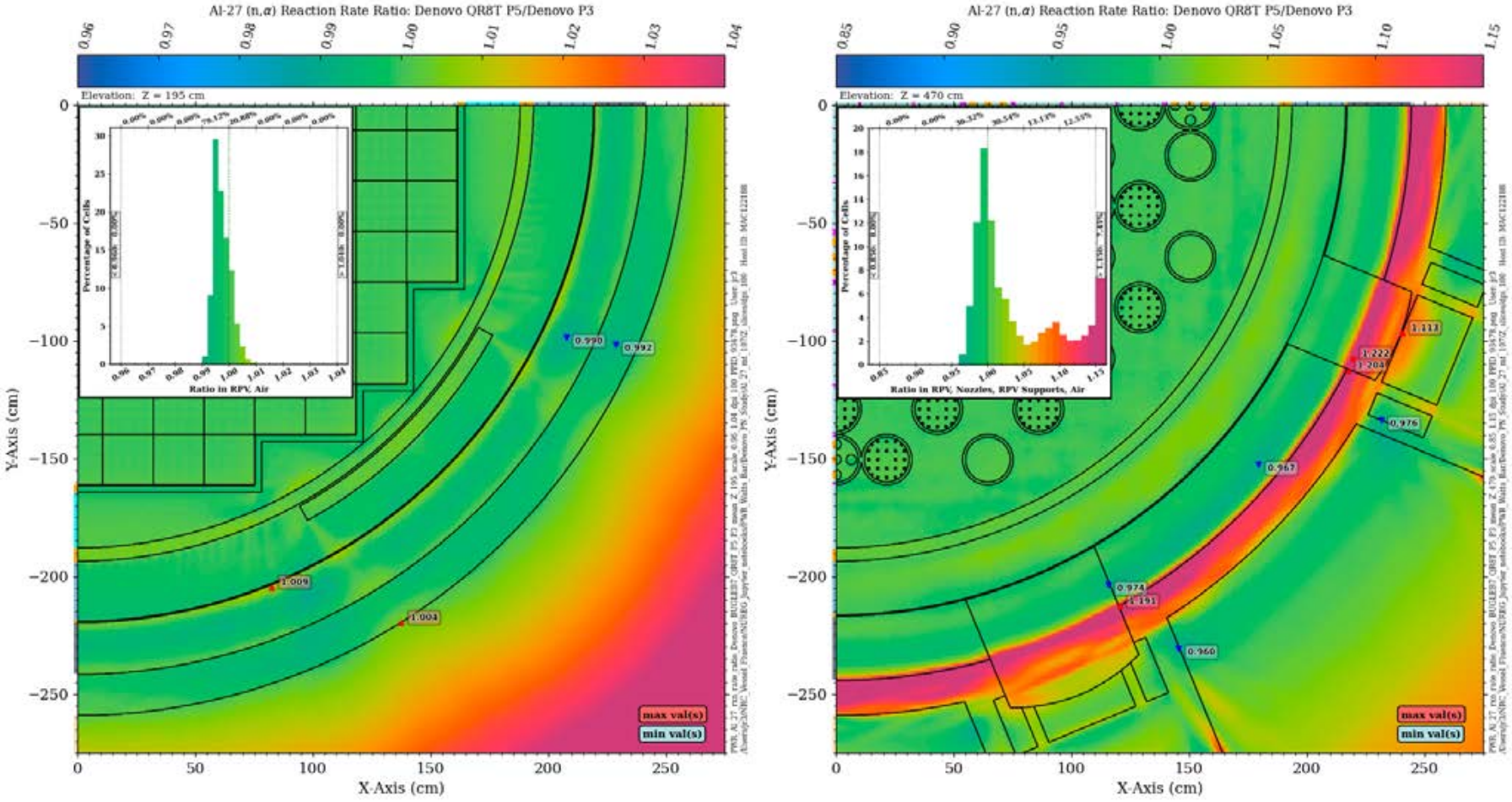

Figure 9-3 Ratio of the ^{27}Al (n,α) reaction rate from a P5 Denovo solution to a P3 Denovo solution at elevations of Z = 195 cm and Z = 470 cm *Note the change in the ratio scale between the two elevations.*

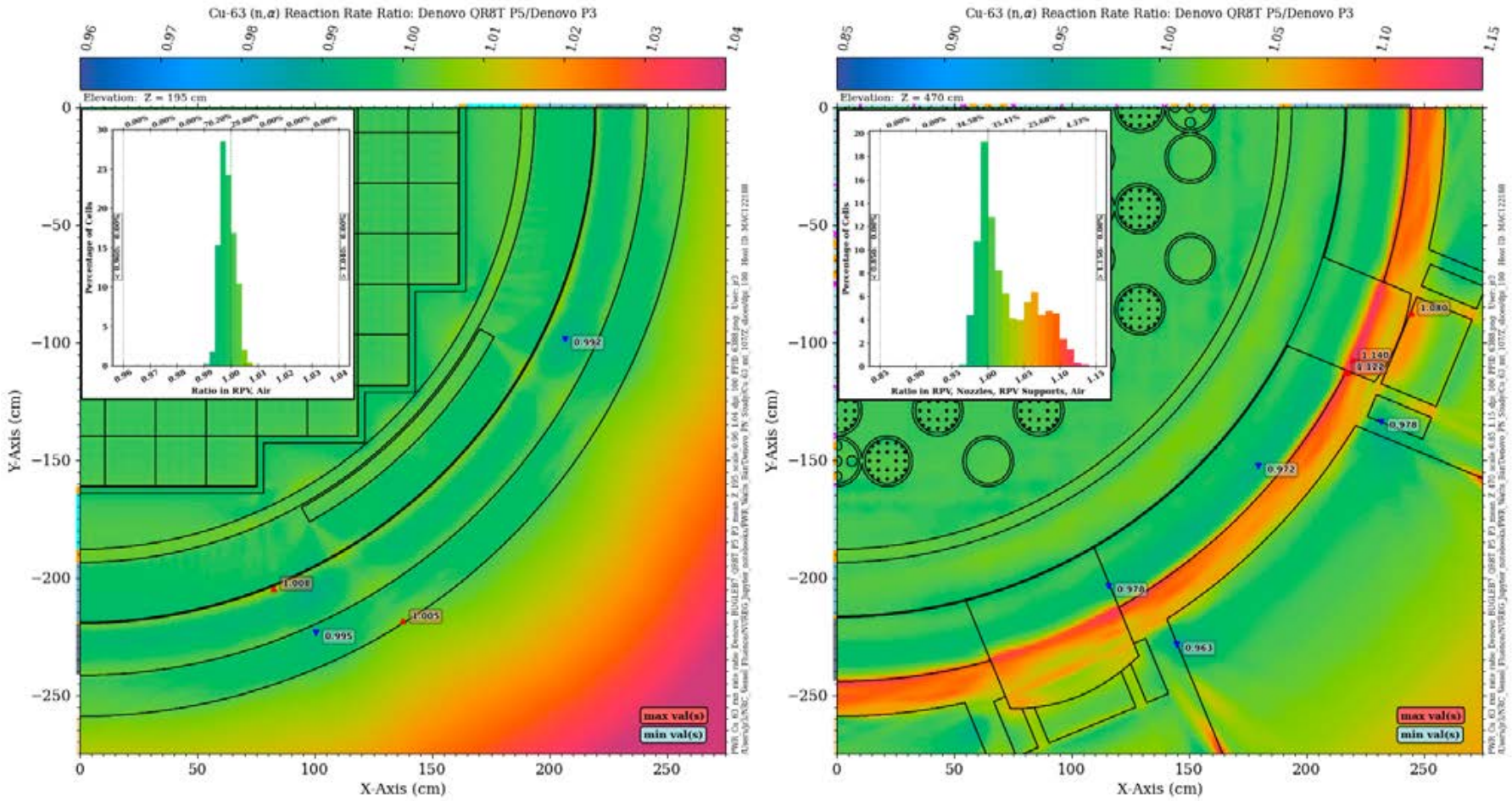

Figure 9-4 Ratio of the ^{63}Cu (n,α) reaction rate from a P5 Denovo solution to a P3 Denovo solution at elevations of Z = 195 cm and and Z = 470 cm *Note the change in the ratio scale between the two elevations.*

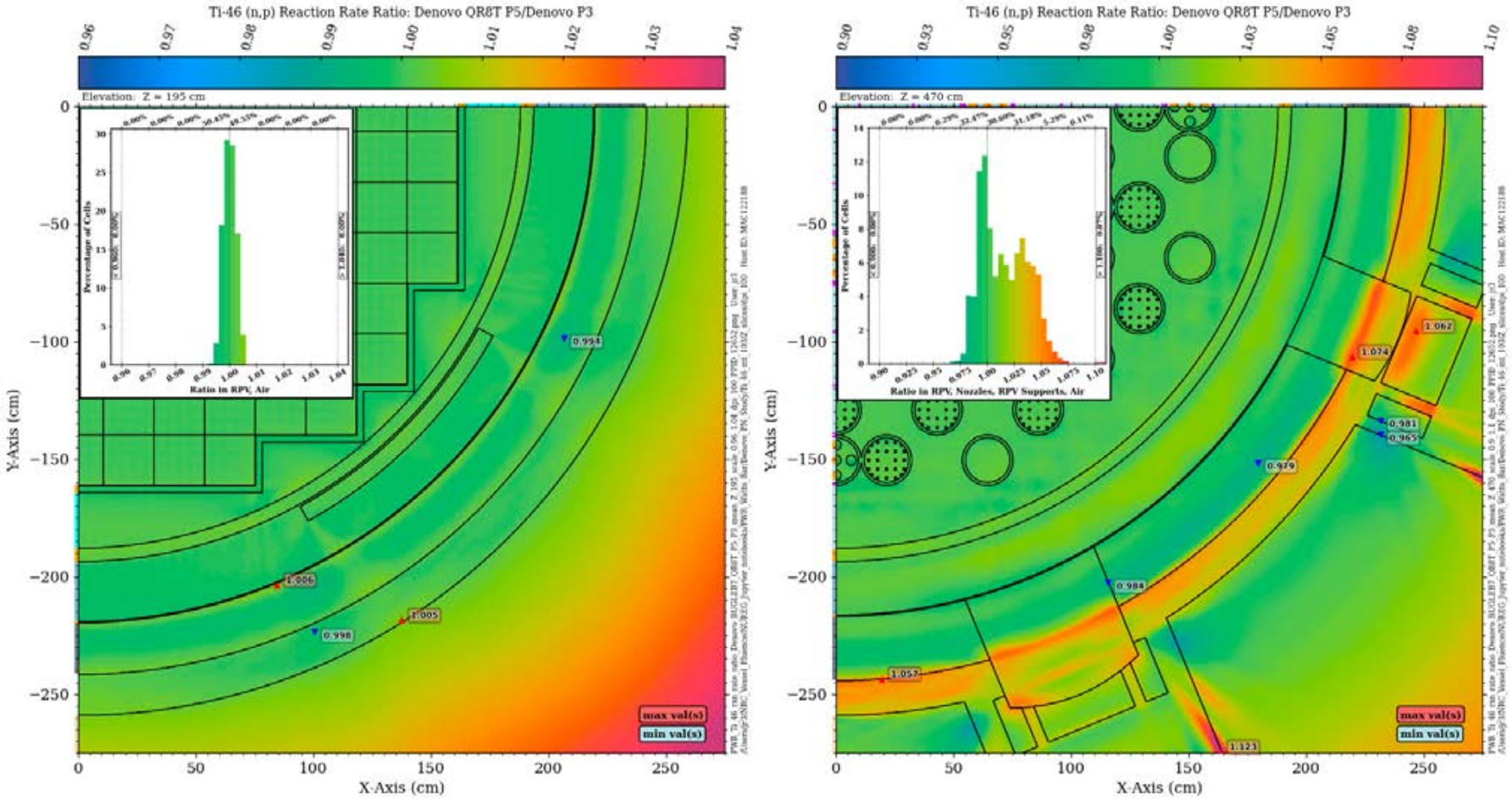

Figure 9-5 Ratio of the ^{46}Ti (n,p) reaction rate from a P5 Denovo solution to a P3 Denovo solution at elevations of Z = 195 cm and Z = 470 cm *Note the change in the ratio scale between the two elevations*

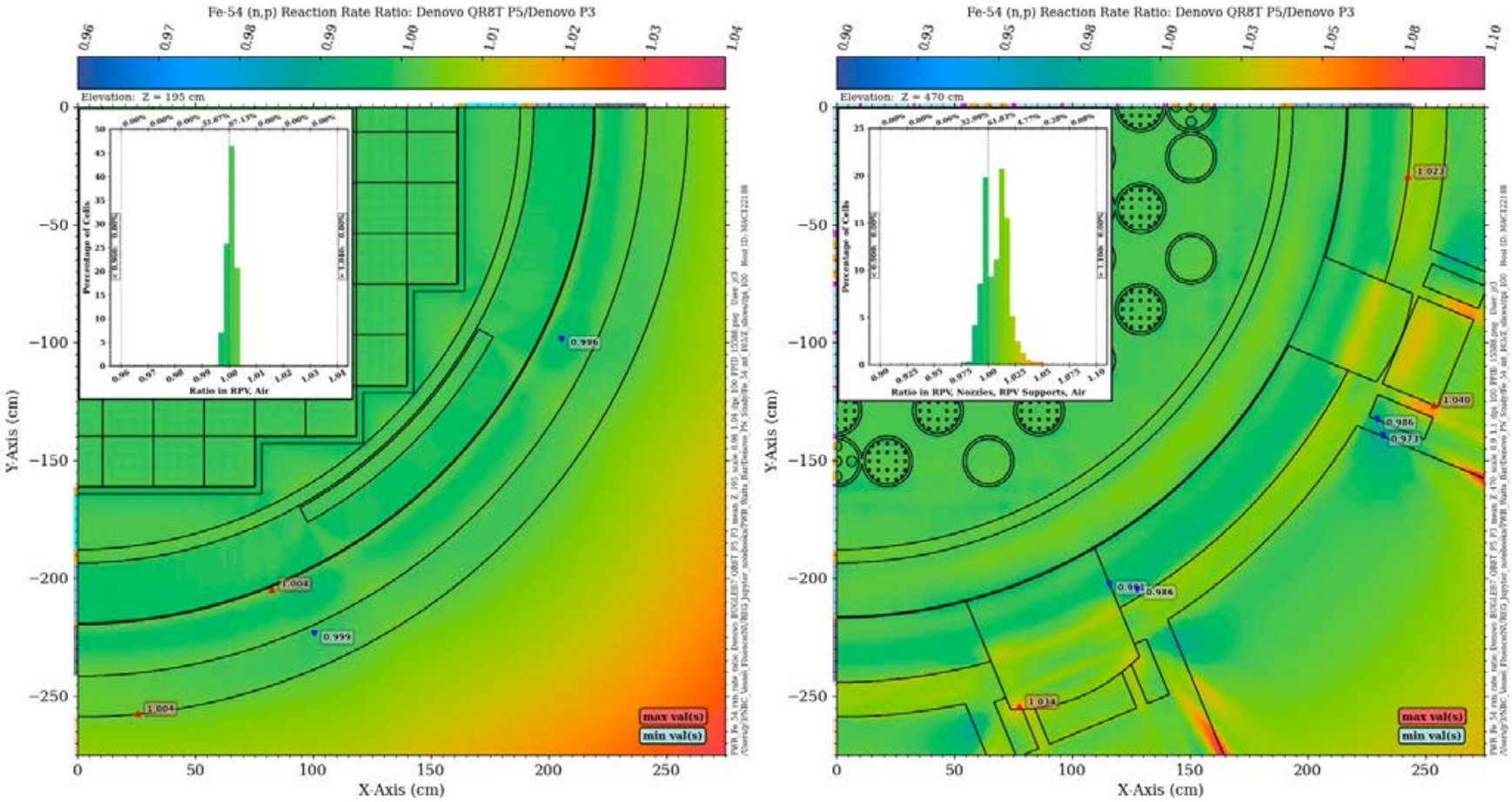

Figure 9-6 Ratio of the ^{54}Fe (n,p) reaction rate from a P5 Denovo solution to a P3 Denovo solution at elevations of Z = 195 cm and Z = 470 cm *Note the change in the ratio scale between the two elevations.*

9.3 Summary of Scattering Order Studies

The results of the analyses presented in Sections 9.1 and 9.2 can be summarized by the following points:

1. The requirement of a minimum scattering order of P_3 from Regulatory Guide 1.190 is adequate for the extended beltline region when the BUGLE-B7 MG library is used. However, this does not provide validation that P_3 scattering would be adequate for finer MG energy structures such as those considered in Section 8. Because the angular scattering limits for MG elastic scattering become narrower with finer group structures, as shown in Eq. (D-1) and Eq. (D-2) of APPENDIX D, the scattering distributions become more anisotropic. Use of P_3 scattering expansions with a fine-group library would require validation on a case-by-case basis.
2. For the analysis of cavity dosimetry in the extended beltline region, the commonly used P_3 scatting expansion may not be adequate. In fact, the sensitivity to scattering order for dosimetry calculations involving high-energy reactions can easily exceed 10% and may even exceed 20%. As with the calculation of fast fluence and dpa, use of group structures finer than the BUGLE-B7 energy structure may be even more sensitive to higher-order scattering moments and would need to be assessed on a case-by-case basis.

10 NEUTRON FLUENCE UNCERTAINTY AND BIAS ESTIMATES

10.1 Neutron Fluence Uncertainty and Bias Estimates

The overall uncertainty and bias estimates for a neutron fluence calculational methodology are described in RG 1.190 and are determined using:

(1) analytic uncertainty and bias, and
(2) calculational uncertainty and bias.

The analytic uncertainty analysis is performed by determining input parameters that may not have been used precisely. Examples of such input parameters are the core neutron source, as well as the reactor's geometrical dimensions, coolant temperatures, and material compositions. Methodology-specific parameters should also be considered, such as angular quadrature, Legendre scattering order of cross sections, and MG cross-section libraries for deterministic radiation transport calculations. A range of variation in each selected input parameter is determined, and a sensitivity analysis is performed to estimate the analytical uncertainty. Individual analytic uncertainties are typically combined using root-sum-of-squares to obtain the total analytic uncertainty. Any identified analytic biases are combined algebraically with their associated signs (plus or minus) to obtain the total analytic bias.

The calculational uncertainty is determined by comparing calculational results with measurements from benchmarks. Benchmarks may involve the use of research reactors such as the Oak Ridge National Laboratory Pool Critical Assembly benchmark [92], [93], [94], [95], VENUS-1 and VENUS-3 benchmarks [96], [97], [98], [99], [100], [101] or operating reactor benchmarks such as the H. B. Robinson Unit 2 Cycle 9 RPV benchmark [83], [102], [103]. A calculational bias may be determined from a measurement database that has been formed by combining measurements from benchmarks and measurements from operating reactors. The measurement database should have sufficient quality and quantity to allow for the estimate.

The overall uncertainty estimate may be calculated from the root-sum-of-squares of the analytical and calculational uncertainties and should be considered as the one-sigma uncertainty. The overall bias may be applied as a multiplicative factor to the calculated fluences to determine best-estimate values.

10.2 Need for Extended Beltline Benchmark Data

The uncertainty and bias estimate determination described in RG 1.190 was developed without considering the RPV extended beltline region. To determine the analytic uncertainty of the RPV extended beltline region when performing a sensitivity study, an expanded set of parameters will be required. This was not required when determining the uncertainty and bias estimate for the traditional beltline region.

The parameter studies presented in this report may serve as an example of the scope of such studies that should be carried out. These parameter studies were based on an extensive set of parameter studies using the Denovo discrete ordinates code and the hybrid transport methodology with the Shift Monte Carlo code. The studies noted that when using the widely used discrete ordinates method, there are intrinsic limitations resulting from the use of multigroup (MG) cross-section data, and to a lesser extent, from angular quadrature sets. These limitations may make it very difficult to achieve a calculation uncertainty less than 20% in extended beltline locations.

The 47-neutron-group BUGLE-B7 MG library is often used for RPV fluence estimates. Use of the BUGLE-B7 library in a Shift calculation with a reference PWR model leads to differences of 15% or more compared to a more accurate continuous energy (CE) Shift calculation in portions of the vessel supports (Figure 8-6). Even the use of the 199-neutron-group VITAMIN-B7 library results in locations in the vessel supports where the MG solution underpredicts the more accurate CE solution by nearly 20% (Figure 8-8). In addition to the fast flux underprediction, dpa rates in portions of the PWR vessel supports are underpredicted by 30% or more with the BUGLE-B7 library (Figure 8-19) and by up to 20% with the VITAMIN-B7 library (Figure 8-21).

While these results provide some indication of an analytic uncertainty for discrete ordinates calculations in the extended beltline region, specific uncertainties must be developed for other discrete ordinates codes, as the numerical techniques they employ may differ.

Section 3 notes a lack of publicly available benchmark dosimetry measurement data in the RPV extended beltline region. Without such data, a calculational uncertainty cannot be determined. This lack of data prevents a quantitative assessment of an overall uncertainty and bias estimate for the hybrid transport method as applied to extended beltline locations. However, the analytic uncertainty with the hybrid transport method will be less than that of the discrete ordinates method, as the set of “methods parameters” (e.g., angular quadrature and MG library selection) is significantly reduced when CE Monte Carlo transport simulations are used.

Extended beltline benchmark dosimetry data should continue to be pursued, but acquisition of such benchmark data for a plant design—other than the Westinghouse 4-loop design used for the PWR reference model—would require development of a new model, which is outside the scope of this project.

Uncertainty Estimation Techniques for Combining Fluence Estimates

With regard to uncertainties in RPV fluence calculations, RG 1.190 is restricted to the use of a single transport methodology:

> The NRC staff has not previously approved the combination of two methodologies for determining neutron fluence. Furthermore, the guidance provided in RG 1.190 is limited to the use of a single fluence method to determine RPV fluence for the entire irradiation period. The uncertainty analysis and methodology qualification regulatory positions do not provide any guidance for determining an accurate uncertainty estimate or qualifying the fluence estimate used from a combination of methods. As such, the staff concluded that combining fluence values from two separate methods does not adhere to the guidance contained in RG 1.190. Therefore, the staff considered this a deviation from NEDC-33178P-A, and the staff requested a supplement to the application. [104]

The licensee subsequently recalculated the fluences using a single analysis methodology.

One approach for developing an uncertainty estimation for fluence estimates that combine two or more methodologies is to use time-weighting (in effective full power years) with the analytic and calculational uncertainties and combine those using a root-weighted-sum-of-squares. However, it may be more appropriate to address this on a case-specific basis. Furthermore, if an applicant adopts an improved methodology (such as the hybrid transport method), then it would be reasonable for the applicant to apply that methodology to the entire analysis instead of combining it with fluence estimates from previous methods. This is particularly likely for fluence estimates in the extended beltline region, where previous analyses (i.e., those that cover plant lifetimes where

the extended beltline region is not a concern) might require uncertainties that exceed 30%. RG 1.190 states that if the overall fluence uncertainty exceeds 30%, then “the methodology of this regulatory guide is not applicable and the application will be reviewed on an individual basis.”

11 SUMMARY AND CONCLUSIONS

The primary objectives of this report are to identify transport phenomena that are important in calculation of RPV fluence levels in the extended beltline region and to evaluate radiation transport methodologies that are best suited to such analyses. This work makes extensive use of large 3D transport calculations employing the Denovo discrete ordinates code and the Shift Monte Carlo code. The Shift calculations all employed the hybrid transport method, which utilizes both discrete ordinates and Monte Carlo calculations and is the current state of the art in radiation transport applications.

Both PWR and BWR models were utilized in an extensive set of parametric studies. Particular emphasis was placed on identifying aspects of current methodologies that may be appropriate for traditional beltline fluence analyses, but not for extended beltline applications. Understanding those issues provides guidance on changes that might be appropriate for extended beltline analyses, either with regard to parameter guidance with discrete ordinates calculations, or with recommendations on the use of improved transport methods that have come into use since the issuance of many of the existing guidelines for RPV fluence analyses.

One of the most significant changes in radiation transport analysis methodology over the past 10 to 20 years has been the increasing use of hybrid methods These methods provide improved accuracy in modeling of the systems being analyzed and in the physics of particle transport compared with discrete ordinates methods. The hybrid methods are capable of producing well-converged, spatially detailed Monte Carlo solutions with reasonable run times (e.g., overnight solutions on computing clusters with on the order of a hundred CPUs).

The sensitivities of extended beltline fluence calculations to physical aspects of RPV models were addressed and are summarized in Section 11.1. The selection of appropriate quadrature sets and MG cross-section libraries, which are critical parameters in discrete ordinates calculations, were addressed and are summarized in Section 11.2. The MG library studies, in particular, raise important questions about the level of accuracy that can be obtained for not only fast fluence evaluations, but also for calculations used to benchmark a transport methodology against measured dosimetry data.

11.1 Sensitivity Analyses of Selected Physical Parameters

Because neutron transport paths in the extended beltline region can be significantly different from those in the traditional beltline region, it is possible that fluence calculations in the extended beltline region may be more sensitive to variations in physical parameters (e.g., coolant density, changes in the fission spectrum with increasing burnup) than are fluence calculations in the traditional beltline region.

Hybrid radiation transport calculations were performed using PWR and BWR models to address the following physical parameters:

1. Changes in the fission spectrum from BOL to EOL in the PWR and BWR models
2. Changes in the coolant temperature (and hence density) in the PWR model
3. Changes in the axially dependent VFs in the BWR model
4. Changes in the cavity gap width in the PWR model
5. Changes in the concrete composition in the PWR model
6. The presence of a steel bioshield liner in the PWR model
7. The presence of thermal insulation in the PWR model

8. Use of homogenized core geometries in the PWR and BWR models rather than explicit ones

The results of these parameter studies, which are detailed in Section 5, are summarized below. The dimensional and material parameter studies of items 4–7 were conducted for the PWR model only. This selection was made based on the significantly higher fast neutron fluence levels at end of plant life in PWRs relative to BWRs (Section 1).

11.1.1 Fission Spectrum Effects

It is well known that changes in the fraction of fissions that occur in fissile isotopes in the fuel—primarily ^{235}U, ^{238}U, ^{239}Pu, and ^{241}Pu—can lead to significant changes in the fast flux in the RPV. There are two primary causes of this effect: changes in the energy spectrum of the fission neutrons, and changes in the average number of neutrons emitted per fission ($\bar{\nu}$). There are also differences in the energy release per fission (K) among the isotopes, but those differences are relatively minor compared with the spectrum and $\bar{\nu}$ changes. The Pu isotopes have fission spectra that are shifted toward higher neutron energies, as well as higher values of $\bar{\nu}$, relative to the U isotopes. Because the ^{239}Pu and ^{241}Pu fission fractions' increase with increasing burnup, the fast neutron flux in the RPV tends to increase with increasing burnup.

For the PWR model used in this study, the fast flux in the RPV at the core midplane increases by ~23 to ~34% from BOL to EOL. The fission fractions by isotope for the BOL and EOL sources are noted in Section 5.2. At extended beltline locations, where there is increased neutron flux attenuation resulting from longer path lengths in the coolant between the core and the inner surface of the RPV, the EOL/BOL fast flux increase ranges from ~30 to ~50%.

For the BWR model used in this study, the fast flux in the RPV at the core midplane increases by ~20 to ~24% due to changes in the fission spectrum between BOL and EOL. At extended beltline locations, the fast flux increase ranges from ~22 to ~30%. It should be noted that the EOL fission fractions for ^{239}Pu and ^{241}Pu are significantly lower than in the PWR model. This is based on available fission fraction data as a function of burnup; it is likely that longer lived BWR fuel assemblies will have higher Pu isotopes than this model. In that case, the EOL/BOL fast flux ratios would be expected to increase at the core midplane elevation, and even more at the extended beltline locations.

These results suggest that accurate distributions of fissions by isotope throughout core life are particularly important for fast fluence predictions in the extended beltline region. It should also be noted that while RPV fluence levels in the traditional beltline region are dominated by the outermost pins in the outer fuel assemblies, sources further in from the peripheral edge and near the upper and lower limits of the fuel assemblies have increased importance for extended beltline locations.

11.1.2 Coolant Temperature Variation in the PWR Model

The parametric study of coolant temperature changes in the PWR model is described in Section 5.3. Reductions in coolant temperature result in a decrease in the fast flux in the RPV, nozzles, and supports due to increased neutron attenuation. In extended beltline locations, there is a more significant reduction at the inner surface of the RPV due to the longer neutron transport paths from the core to the inner surface of the RPV, as noted above for the fission spectrum study. At extended beltline locations near the outer surface of the RPV and in the nozzles and vessel supports, the temperature-related reductions are less pronounced, as the cavity streaming neutrons that dominate the flux in those regions are driven by neutrons that escape the RPV well

within the traditional beltline region. Increases in the coolant temperature in the PWR model result in fast flux changes that are essentially the inverse of those seen with temperature reductions. Because RPV locations in the extended beltline region are more sensitive to coolant temperature changes, accurate modeling of coolant temperatures throughout the RPV as a function of a plant's operating history is particularly important.

11.1.3 Void Fractions in the BWR Model

The BWR model used in this study is based on the GE14 10×10 assembly design with seven axial fuel zones. Boiling can occur in the coolant channels, resulting in changes in the coolant VF as a function of elevation and of time during a cycle. This effect was evaluated by comparing results from minimum, maximum, and average VFs by axial zone.

Changes in the RPV fast flux at the core midplane and lower elevations resulting from variation in the axial VFs are described in Section 5.4. The effects are relatively minor at elevations near or below the lower portion of the core, as the VFs in the two lowest axial zones are small and do not have significant variation between the minimum and maximum values.

Differences in the VFs between the minimum and maximum cases increase significantly compared to the two lower axial zones. This results in changes in the RPV fast flux being more significant in the upper extended beltline region than in the lower extended beltline region.

11.1.4 Reactor Cavity Gap Width

The PWR model used in this study has cavity gap widths of 17.38 and 14.75 cm at elevations below and above the elevation where the RPV thickness increases (Table 4-1 and Figure 4-1). Because cavity streaming neutrons dominate fast flux levels in the outer portion of the RPV and in the nozzles and vessel supports, changes in the cavity geometry may be expected to have a significant effect on neutron flux levels in those locations. This is particularly important for the vessel supports, where dpa rates at the end of plant life may be likely to exceed the monitoring threshold (Section 6). The cavity gap parameter study (Section 5.5) modeled increases of 10, 20, and 30 cm in the gap width. The increased gap widths have a very minor effect in the traditional beltline region, but they lead to significant fast flux increases in extended beltline locations.

11.1.5 Concrete Composition

The reactor cavity gap width study confirmed the potential for cavity gap changes to have significant impacts on fast fluence levels in the extended beltline region. A related consideration is the composition of the concrete bioshield.

The sensitivity of fast flux changes in the extended beltline region was assessed by comparing the fast flux levels for four concrete compositions. The hydrogen density, which is of primary importance for neutron scattering behavior in concrete, was varied by nearly a factor of six (Table 5-6).

Reductions in the concrete hydrogen content result in increased scatter of neutrons from the bioshield back into the cavity gap. This in turn leads to increased fast neutron flux levels in the outer portion of the RPV in the extended beltline region, in the nozzles, and particularly in the vessel supports. Conversely, higher hydrogen content in concrete results in reduced scatter into the cavity gap, with reductions in the fast flux in the regions above and below the active core.

Based on these results, it is apparent that any change in hydrogen content in the bioshield (particularly in the portion of the bioshield nearest the inner radius) during the lifetime of an NPP should be considered in calculations of fast fluence in the extended beltline region, particularly for the nozzle supports.

11.1.6 Steel Bioshield Liner

The baseline PWR and BWR models in this study have bioshields constructed of Type 04 concrete (Section 5.6) with no liner on the inner surface of the concrete (i.e., the cylindrical surface facing the RPV). Some reactor plant designs include a steel liner on the inner surface of the bioshield. The presence of a liner will affect the scattering from the bioshield into the cavity gap, as the angular distribution and average energy loss of scattered neutrons are different in steel than they are in the lighter elements—particularly hydrogen—that are the dominant constituents of the concrete.

The presence of a steel liner was assessed for two liner compositions: 304 stainless steel and carbon steel. At locations away from the nozzles in the PWR model, the presence of a steel liner made of either SS-304 or carbon steel has a minor effect on fast flux levels in the outer portion of the RPV, leading to increases less than 3%. The most significant effect of a liner is a reduction in fast flux levels of up to ~25% in the vessel supports.

11.1.7 Thermal Insulation

RPVs for PWR and BWR designs typically have a layer of thermal insulation between the RPV outer radius and the inner radius of the concrete bioshield. The effect of insulation on fast flux levels in the extended beltline region was evaluated by modeling a layer of reflective metallic insulation in the cavity gap of the PWR model. This insulation layer has a minor effect on fast flux levels in the RPV in the beltline region, where it can cause very slight increases (< 2%) in the fast flux levels at the outer surface of the RPV due to backscatter of neutrons from the insulation. At locations in the extended beltline region, the presence of thermal insulation can reduce fast flux levels in the RPV due to attenuation of the cavity streaming neutron flux by the thermal insulation. Because of reductions in cavity streaming flux levels due to attenuation in the insulation, the fast flux at locations where cavity streaming dominates the neutron flux is reduced by ~15–20%.

11.1.8 Use of Homogenized Core Geometries

It is common practice in RPV fluence evaluations to homogenize the materials within the fuel assemblies into a set of mixtures rather than having an explicit geometric representation of the fuel pins, control assemblies, guide tubes, and other components. This is a reasonable modeling approximation for fast neutron flux calculations for the traditional beltline region, as the neutron transport characteristics of the homogenized fuel assemblies are essentially identical to the explicitly modeled assemblies used when calculating fast neutron flux levels in the RPV.

The validity of this approximation for extended beltline fluence calculations was assessed using homogenized-assembly versions of the PWR and BWR models. These homogenized models were also used for the Denovo discrete ordinates calculations discussed below. The results of these assessments confirm that the use of homogenized core models is appropriate for both extended and traditional beltline fluence evaluations.

11.2 Discrete Ordinates Sensitivities in the Extended Beltline Region

Regulatory Guide 1.190 provides extensive guidance on the selection of discrete ordinates parameters (spatial, angular, and energy discretization) for RPV fast fluence calculations in the beltline region of LWR RPVs. No specific guidance is provided for fluence calculations in the extended beltline region. The sensitivity of discrete ordinates calculations in the extended beltline region was evaluated in this study using a combination of discrete ordinates (Denovo) and hybrid transport (Denovo/Shift) calculations to assess the sensitivity to angular quadrature sets and to MG cross-section libraries.

All discrete ordinates calculations were run using the ORNL Denovo code. Because other discrete ordinates transport codes have slight methodology differences, their sensitivity to the parameters studied may provide results that differ somewhat from those presented in this report. However, such differences are likely to be minor, and the overall conclusions of these parameter studies are not expected to differ greatly when other codes are used.

Regulatory Guide 1.190 discusses appropriate meshing strategies for 2D/1D flux synthesis calculations. The adequacy of the Denovo mesh used in the parameter studies was confirmed based on (1) demonstrating that the solutions were converged with respect to mesh and (2) comparisons of Denovo and Shift calculations when both codes used the same MG cross-section data. Because discrete ordinates codes typically offer a number of spatial differencing schemes, the meshing deemed appropriate for Denovo using a linear discontinuous differencing scheme may not be appropriate for other transport codes. Therefore, the parameter studies focused on angular quadrature selection and MG library effects. These studies are discussed below.

11.2.1 Quadrature Selection

Discrete ordinates calculations used for RPV fluence analyses typically employ level symmetric quadrature sets, including S8 and S16. While level symmetric quadratures have a long history and have been shown to be adequate for beltline fluence evaluations, more recent angular quadrature sets, including QR sets (Section 7), have been demonstrated to provide improved solution accuracy for (1) discrete ordinates models with material interfaces along the coordinate axes, like fuel assemblies and former plates and/or (2) streaming along or near coordinate axes, such as cavity streaming.

The initial quadrature comparisons focused on Denovo solutions using the S8 and S16 sets. Calculations with both the PWR and BWR models demonstrated nontrivial differences between S8 and S16 fast flux levels, even at the core midplane. The S8 solutions exhibited azimuthal ray effects associated with the corner fuel assemblies on the periphery of the core and at the neutron pad in the PWR model. The S8 solutions also exhibited ray effects at the jet pump risers in the BWR. The minimum and maximum S8/S16 fast flux ratios at the inner surface of the RPV vary by 9% in the PWR model and by nearly 19% in the BWR model. In addition, the S8 solution showed significant axial ray effects associated with the former plates in the PWR model.

Deviations between S8 and S16 solutions in the extended beltline region become more pronounced, particularly in the vicinity of the nozzles and the lower portion of the RPV near the lower hemispherical head in the PWR model. In the BWR model, significant S8/S16 differences occur in the shroud and in the RPV at elevations outside the axial extent of the core, particularly in regions below the bottom of the core.

Because ray effects tend to be more pronounced for higher energy neutrons, the quadrature sensitivity using S8 and S16 solutions in the PWR model was also evaluated for a high-energy threshold reaction—^{27}Al (n,α)—that is commonly used in dosimetry measurements. Results of this study show significant S8/S16 solution differences, some of which exceed 20%, even within the traditional beltline region. This is a potential concern for benchmarking of discrete ordinates calculations with dosimetry measurements, as relatively minor changes in the location of a dosimetry capsule could have a significant impact on calculated-to-measured ratios.

Further quadrature-to-quadrature comparisons were performed using a variety of QR quadratures, including QR8T, which has the same number of angles as S16, and QR16T, which served as a high-order solution. Details of these analyses can be found in Section 7.

A more stringent evaluation of quadrature effects was performed to demonstrate which quadrature sets provide the most accurate solution. This was done by comparing Denovo calculations with MG Shift calculations using the PWR model. Because both codes used the same MG library (BUGLE-B7), and the Denovo solutions had been demonstrated to be converged with respect to mesh, this comparison provided a means of effectively isolating the quadrature effects in the Denovo solution from MG effects. The results of these studies indicate that the QR sets provide superior fast flux estimates to the level symmetric S8 and S16 sets for RPV fluence calculations. The QR8T solution consistently provides closer agreement than S16 when compared with the Shift solution using MG data.

While the QR8T quadrature provides excellent agreement with the Shift solution in the traditional beltline region, it still exhibits ray effects that can produce differences of 15% or more compared to the MG Shift solution. The ray effects are reduced significantly using a QR16T quadrature, but even with that solution, there are some locations in the extended beltline region where the Denovo and Shift solutions differ by more than 10%.

11.2.2 Multigroup Cross-Section Library Considerations

One of the most significant areas of potential solution inaccuracy in discrete ordinates calculations is the use of MG cross-section libraries. With respect to RPV fluence calculations, this is particularly an area of concern for extended beltline regions, where the neutron flux spectra may be significantly different from those used to generate an MG library.

One way to examine the sensitivity of discrete ordinates calculations to the MG library selection would be to run those calculations with successively refined MG libraries. However, this approach has two limitations: (1) the vast amount of computer memory required to run a large 3D discrete ordinates calculation with an MG library that may contain hundreds of groups (compared to the 47 neutron groups in the BUGLE-B7 library), and (2) the fact that such comparisons necessarily involve substituting one approximation—a baseline MG library—with another—a refined MG library.

The method chosen to evaluate MG libraries in this study involved the use of Shift calculations. Because Shift can be run with either MG or CE cross-section data, these calculations provide a means of comparing various MG libraries with a more accurate CE solution.

In determining the impact of MG library selection for RPV fluence calculations, an extensive set of neutron response functions was considered. This set includes fast neutron flux (E > 1 MeV), neutron dpa rate, and nine dosimetry reactions based on commonly used dosimetry isotopes. This set of comparisons provides an indication of how well an MG library models neutron

interactions over a wide range of energies rather than just the fast flux. The dosimetry comparisons are important because they form the basis for calculated-to-measured ratios for benchmark calculations.

A variety of MG libraries were evaluated, including VITAMIN-B7 (199 neutron energy groups) and BUGLE-B7 (47 neutron groups). These libraries were developed specifically for LWR shielding analyses. MG libraries from the SCALE code system containing from 200 to 1,597 neutron groups were evaluated. In addition, two libraries developed specifically to address neutron transport through energy ranges of particular importance for RPV flux and response calculations were also evaluated. All calculations were performed using the PWR model.

Details of the MG study are provided in Section 8. The results can be briefly summarized as follows.

11.2.2.1 Fast Flux Calculations

All of the MG libraries considered in this study are capable of providing accurate fast flux estimates (i.e., values which agree very well with CE calculations) in the inner portion of the RPV within the traditional beltline region. Of course, those locations are of primary concern with respect to the peak damage levels in the RPV. However, with the exception of the two fine-group libraries that were developed specifically for this application—one with 642 groups (X642N) and one with 956 groups (X956N)—all of the MG calculations underpredict the CE solution by more than 10% at the outer surface of the RPV. At the elevation of the vessel supports, all of the MG libraries besides X642N and X956N underpredict the CE solution at all locations of interest, particularly in the vessel supports, where the solution differences can exceed 15%.

11.2.2.2 DPA Rate Calculations

For dpa rate calculations, the results are more complex. MG calculations using the BUGLE-B7 library underpredict the dpa rate at all locations in the RPV in both the traditional and extended beltline regions. At the core midplane, those differences range from ~5 to ~20%. At the elevation of the vessel supports, the BUGLE-B7 solution underpredicts the CE solution by more than 20% at nearly all locations of interest, with differences of up to 35% at some locations in the vessel supports. With the exception of the X956N library, all of the tested MG libraries underpredict the dpa rate at the elevation of the vessel supports, with differences of 15% and more occurring in the vessel supports.

11.2.2.3 Dosimetry Reaction Rate Calculations

The accuracy of MG calculations used for dosimetry reaction rate calculations is strongly dependent on the reaction being considered. For reactions that have energy response ranges above the resolved resonances in the iron cross section (APPENDIX A and APPENDIX C), relatively broad group structures like BUGLE-B7 might be expected to provide accurate MG solutions. As the energy response range for a reaction rate extends over lower energies, where transport of neutrons through significant resonance regions occurs, MG transport calculations would be expected to exhibit more sensitivity to a library's group structure.

The energy response ranges for the nine reaction rates considered in this study are provided in Table C-1. The three dosimetry reactions with the highest energy response ranges were ^{27}Al (n,α), ^{63}Cu (n,α), and ^{46}Ti (n,p). For these reactions, the MG/CE agreement is reasonably

good both at the core midplane and at the extended beltline vessel support elevation, except for the ^{46}Ti (n,p) reaction rate calculated with the VITAMIN-B7 or BUGLE-B7 libraries. The apparent reason for the poor VITAMIN-B7 and BUGLE-B7 results, which are discussed in Section 8.4.3, is not a function of the group structures of those libraries, but it probably is due to the differences in the ^{46}Ti (n,p) dosimetry cross-section data from these two libraries.

As noted above, for the remainder of the reactions, the MG/CE agreement became increasingly poorer as the energy response ranges of the various reactions extended to lower neutron energies. For the ^{237}Np (n,f) reaction, which has the lowest 90% energy response range, the BUGLE-B7 solution underpredicted the CE reaction rate in the cavity gap at the core midplane elevation by ~10 to ~13%, and it underpredicted the CE solution by up to 20% and more in portions of the RPV, cavity gap, and vessel supports. Even the X956N solution underpredicted the ^{237}Np (n,f) rate from the CE solution by up to 15% at the vessel support elevation.

11.2.2.4 Multigroup Library Summary

The results of the MG/CE comparisons for these 11 neutron responses (fast flux, dpa rate, and nine dosimetry reaction rates) suggest that while the widely used BUGLE-B7 library is generally adequate for the calculation of these quantities at locations radially out through the inner portion of the RPV in the traditional beltline region, it is not well suited for calculation of most of the 11 responses at locations in the extended beltline region. In some cases, the differences between a BUGLE-B7 solution and a more accurate CE solution exceed 20%. This suggests that for a discrete ordinates calculation (which is also subject to the approximations made in space and angle) using the BUGLE-B7 library, it may not be possible to obtain calculational results within the 20% uncertainty value prescribed by Regulatory Guide 1.190.

While the accuracy of MG solutions can be improved by using a very-fine-group structure, libraries with the potential to contain several hundred energy groups could increase the amount of memory required for cross-section storage by more than two orders of magnitude and would also lead to much longer run times. As such, their use may not be practical for routine RPV analyses.

11.2.3 Cross-Section Scattering Order

Regulatory Guide 1.190 requires a minimum P_3 expansion order for RPV fluence calculations with typical LWR configurations in the traditional beltline region. The sensitivity to scattering order for discrete ordinates calculations in the extended beltline region was evaluated for calculations of fast flux, dpa rate, and selected dosimetry reaction rates.

Denovo calculations using P_3, P_5, and P_7 scattering were considered. The use of P_3 scattering for fast flux and dpa rate calculations was shown to be adequate even in the extended beltline region. However, for calculation of neutron reaction rates for isotopes that have high energy thresholds [such as ^{27}Al (n,α)], P_3 calculations can easily underpredict P_5 calculations by 10% in the extended beltline region, with differences in some locations exceeding 20%. Increasing the scattering order from P_5 to P_7 in those cases was shown to result in insignificant differences, suggesting that P_5 scattering is adequate for those calculations when the BUGLE-B7 library is used.

It may be possible that for MG libraries with a finer group structure, higher scattering orders would be required. Use of P_3 (or possibly even P_5) scattering with a fine-group library would require validation on a case-by-case basis.

11.3 Recommendations on Analysis Methodology

The analyses performed in this study suggest that the discretization of the angular and energy variables in MG discrete ordinates transport calculations poses significant challenges for RPV fluence evaluations in the extended beltline region. While it may be possible to adequately address quadrature effects without a significant cost increase in computing requirements, the use of MG cross-section libraries, even those with hundreds of energy groups, was shown to produce solutions that often underpredict more accurate CE calculations in extended beltline locations, including the vessel supports in the PWR model. This underprediction is particularly noteworthy for calculation of dpa rates and of some dosimetry reaction rates.

The use of hybrid radiation transport methods provides a significant advantage in these analyses, as the Monte Carlo calculations that are the final stage of the hybrid calculational sequence are not subject to angular discretization or to the approximations made in MG cross-section libraries.

12 REFERENCES

[1] Gary L. Stevens, “Evaluation of the Beltline Region for Nuclear Reactor Pressure Vessels,” U.S. Nuclear Regulatory Commission Technical Letter Report TLR-RES/DE/CIB-2013-01, November 14, 2014.

[2] U.S. Nuclear Regulatory Commission, “Calculational and Dosimetry Methods for Determining Pressure Vessel Neutron Fluence,” Regulatory Guide 1.190, 2001. ADAMS Accession No. ML010890301.

[3] U.S. Nuclear Regulatory Commission, “Domestic Licensing of Production and Utilization Facilities,” Title 10, Code of Federal Regulations, Part 50.

[4] ASTM E185-82, “Standard Practice for Design of Surveillance Programs for Light-Water Moderated Nuclear Power Reactor Vessels,” ASTM International, 1982.

[5] U.S Nuclear Regulatory Commission, “Reactor Pressure Vessel Status Report,” NUREG/CR-1511, December 1994. ADAMS Accession No. ML082030506.

[6] IAEA Nuclear Energy Series, “Integrity of Reactor Pressure Vessels in Nuclear Power Plants: Assessment of Irradiation Embrittlement Effects in Reactor Pressure Vessel Steels,” International Atomic Energy Agency, 2009.

[7] Pavel V. Tsvetkov, Editor, Nuclear Power – Control, Reliability, and Human Factors,” Intech, 2011.

[8] James J. Duderstadt and William R. Martin, Transport Theory, John Wiley and Sons, 1979.

[9] George I. Bell and Samuel Glasstone, Nuclear Reactor Theory, Robert E. Krieger, 1982.

[10] E. E. Lewis and W. F. Miller, Computational Methods for Neutron Transport, American Nuclear Society, Inc., 1993.

[11] H. Greenspan, C. N. Kelber, and D. Okrent, Editors, Computing Methods in Reactor Physics, Gordon and Breach, 1968.

[12] R. D. Richtmyer and J. von Neumann, “Statistical Methods in Neutron Diffusion,” Los Alamos Report LMS-551, 1947.

[13] S. W. Mosher, J. C. Wagner, and D. E. Peplow, “FW-CADIS Method for Global and Regional Variance Reduction in Monte Carlo Radiation Transport Calculations,” Nucl. Sci. Eng., 176(1):37–57, 2014.

[14] H. Brockmann, “Treatment of Anisotropic Scattering in Numerical Neutron Transport Theory,” Nucl. Sci. Eng., 77(4):377–414, 1981.

[15] CCC-650, ORNL RSICC Computer Code Collection, “DOORS 3.2A, One-, Two-, and Three-Dimensional Discrete Ordinates Neutron Photon Transport Code System,” May 2007.

[16] W. A. Rhoades and R. L. Childs, “The DORT Two-Dimensional Discrete Ordinates Transport Code,” Nucl. Sci. Eng., 99(1):88–89, 1988.

[17] W. A. Rhoades and R. L. Childs, “TORT: A Three-Dimensional Discrete Ordinates Neutron/Photon Transport Code,” Nucl. Sci. Eng., 107(4):397–398, 1991.

[18] W. A. Rhoades and D.B. Simpson, “The TORT Three-Dimensional Discrete Ordinates Neutron/Photon Transport Code (TORT Version 3),” ORNL/TM-13221, Oak Ridge National Laboratory, 1997.

[19] T. M. Evans et al., “Denovo: A New Three-Dimensional Parallel Discrete Ordinates Code in SCALE,” Nucl. Technol., 171(2):171-200, 2010.

[20] CCC-842, ORNL RSICC Computer Code Collection, “PARTISN 8.29: Time-Dependent, Parallel Neutral Particle Transport Code System,” 2009.

[21] E. T. Tomlinson, W. A. Rhoades, and W. W. Engle, Jr., “Flux Extrapolation Models Used in the DOT IV Discrete Ordinates Neutron Transport Code,” ORNL/TM-7033, Oak Ridge National Laboratory, 1980.

[22] B. G. Petrovic and A. Haghighat, “Analysis of Inherent Oscillations in Multidimensional SN Solutions of the Neutron Transport Equation,” Nucl. Sci. Eng., 124(1):31–62, 1996.

[23] B. G. Petrovic and A. Haghighat, “Effects of SN Method Numerics on Pressure Vessel Neutron Fluence Calculations,” Nucl. Sci. Eng., 122(2):167–193, 1996.

[24] C. S. Davidson and C. A. Burre, “Spatial Differencing and Mesh Sensitivity in Two- and Three-Dimensional Discrete Ordinates Codes,” Nuclear Mathematical and Computational Sciences: A Century in Review, a Century Anew, American Nuclear Society, 2003.

[25] I. K. Abu-Shumays, “Compatible Product Quadrature for Neutron Transport in x-y Geometry,” Nucl. Sci. Eng. 64:299–316, 1977.

[26] I. K. Abu-Shumays, “Angular Quadratures for Improved Transport Computations,” Trans. Theory Stat. Phys., 30(2&3):169–204, 2001.

[27] J. J. Jarrell, M. L. Adams, and J. M. Risner, “Application of Quadruple Range Quadratures to Three-Dimensional Model Shielding Problems,” Nucl. Tech., 168(2):424–430, 2009.

[28] J. F. Carew and G. Zamonsky, “Uniform Positive-Weight Quadratures for Discrete Ordinate Transport Calculations,” Nucl. Sci. Eng. 131(2):199–207, 1999.

[29] J. F. Carew, K. Hu, and G. Zamonsky, “Uniform Gauss-Weight Quadratures for Discrete Ordinate Transport Calculations,” Nucl. Sci. Eng. 136(2):282–293, 2000.

[30] G. Longoni and A. Haghighat, “Development of New Quadrature Sets with the Ordinate Splitting Technique,” Proceedings of the ANS International Meeting on Mathematical Methods for Nuclear Applications, 2001.

[31] C. D. Ahrens, “Highly Efficient, Exact Quadratures for Three-Dimensional Discrete Ordinates Transport Calculations,” Nucl. Sci. Eng., 170(1):98–101, 2012.

[32] D. B. Fromowitz and G. B. Ziegler, “Development and Evaluation of High-Fidelity Product and Evenly Spaced Angular Quadratures for Three-Dimensional Discrete Ordinates Calculations with Large Air Regions,” Nucl. Sci. Eng., 182.

[33] K. Manalo, C. D. Ahrens, and G. Sjoden, “Advanced Quadratures for Three-Dimensional Discrete Ordinate Transport Simulations: A Comparative Study,” Ann. Nucl. Energy, 81:196–206, 2015.

[34] X-5 Monte Carlo Team, “MCNP – A General Monte Carlo N-Particle Transport Code, Version 5,” Los Alamos National Laboratory, February 2008.

[35] T. M. Pandya et al., “Implementation, Capabilities, and Benchmarking of Shift, a Massively Parallel Monte Carlo Radiation Transport Code,” J. Comput. Physics, 308:239–272, 2016.

[36] M. B. Chadwick et al., “ENDF/B-VII.1 Nuclear Data for Science and Technology: Cross Sections, Covariances, Fission Product Yields, and Decay Data,” Nuclear Data Sheets, 112(12):2887–2996, December 2011.

[37] M. Herman and A. Trkov, Editors, “ENDF-6 Formats Manual,” CSEWG Document ENDF-102, BNL-90365-2009, National Nuclear Data Center, Brookhaven National Laboratory, June 2009.

[38] Alireza Haghighat, Monte Carlo Methods for Particle Transport, CRC Press, 2014.

[39] S. W. Mosher et al., “ADVANTG – An Automated Variance Reduction Parameter Generator,” ORNL/TM-2013/416 Rev. 1, Oak Ridge National Laboratory, August 2015.

[40] J. C. Wagner and A. Haghighat, “Automated Variance Reduction of Monte Carlo Shielding Calculations Using the Discrete Ordinates Adjoint Function,” Nucl. Sci. Eng., 128(2):186–208, 1998.

[41] A. Haghighat and J. C. Wagner, “Monte Carlo Variance Reduction with Deterministic Importance Functions,” Prog. Nucl Energy, 42(1):25–53, 2003.

[42] B. T. Rearden and M. A. Jessee, Editors. SCALE 6.2: A Comprehensive Modeling and Simulation Suite for Nuclear Safety Analysis and Design; Includes ORIGEN and AMPX, ORNL/TM-2005/39 Version 6.2, Oak Ridge National Laboratory, April 2016.

[43] T. M. Evans, J. C. Wagner, and D. E. Peplow, “Automated Variance Reduction Applied to Nuclear Well-logging Problems,” Nucl. Tech., 168(3):799–809, 2009.

[44] Westinghouse Report WCAP-14040-A Rev. 4., “Methodology Used to Develop Cold Overpressure Mitigating System Setpoints and RCS Heatup and Cooldown Limit Curves.” ADAMS Accession No. ML050120209, May 2014.

[45] AREVA NP Inc. Report BAW-2241NP-A Rev. 2, “Fluence and Uncertainty Methodologies.” ADAMS Accession No. ML073310660, April 2006.

[46] GE Energy Nuclear Report NEDO-32983-A Rev. 2, “General Electric Methodology for Reactor Pressure Vessel Fast Neutron Flux Evaluations.” ADAMS Accession No. ML072480121, January 2006.

[47] Westinghouse Report WCAP-18124-NP-A Rev. 0, “Fluence Determination with RAPTOR-M3G and Ferret.” ADAMS Accession No. ML18099A125, February 2018.

[48] AREVA Report ANP-3127 Rev. 2, “Oconee Nuclear Station Units 1, 2, and 3 Pressure-Temperature Limits at 54 EFPY.” ADAMS Accession No. ML13305A121, September 2013.

[49] AREVA Report ANP-3300, “Arkansas Nuclear One (ANO) Unit 1 Pressure-Temperature Limits at 54 EFPY.” ADAMS Accession No. ML14241A241, June 2014.

[50] Westinghouse Report WCAP-17954-NP Rev. 0, “Indian Point Unit 3 Heatup and Cooldown Limit Curves for Normal Operation.” ADAMS Accession No. ML15061A277, December 2014.

[51] Westinghouse Report WCAP-18102-NP Rev. 1, “Beaver Valley Unit 1 Heatup and Cooldown Limit Curves for Normal Operation.” ADAMS Accession No. ML18099A125, February 2018.

[52] Westinghouse Report WCAP-18169-NP Rev. 1, “Arkansas Nuclear One Unit 2 Heatup and Cooldown Limit Curves for Normal Operation.” ADAMS Accession No. ML18215A178, June 2018.

[53] Subsequent License Renewal Application, Turkey Point Units 3, 4. Docket Nos. 50-250 and 50-251. L-2018-082 Enclosure 3 Rev. 1. “Florida Power and Light Company Turkey Point Nuclear Point Units 3 and 4 Subsequent License Renewal Application.” ADAMS Accession No. ML18113A146, April 2018.

[54] Subsequent License Renewal Application, Peach Bottom Atomic Power Station Units 2 and 3, Facility Operating License Nos. DPR-44 and DPR-54, The Second License Renewal Application.” ADAMS Accession No. ML18193A773, July 2018.

[55] Subsequent License Renewal Application, “Surry Power Station Units 1 and 2 Application for Subsequent License Renewal.” ADAMS Accession No. ML18291A828, October 2018.

[56] U.S. Nuclear Regulatory Commission, “Generic Aging Lessons Learned for Subsequent License Renewal (GALL-SLR) Report,” NUREG-2191, July 2017.

[57] D. N. Hopkins, E. T. Hayes, and A. H. Fero, “Ex-vessel Neutron Dosimetry Results in the Vicinity of RPV Supports,” PVP2007-27685, Proceedings of PVP2007, 2007 ASME Pressure Vessels and Piping Division Conference,” July 22–26, 2007, San Antonio, TX.

[58] J. Chen, F. A. Alpan, G. A. Fischer, and A. H. Fero, “Ex-vessel Neutron Dosimetry Analysis for Westinghouse 4-Loop XL Pressurized Water Reactor Plant using 3D Parallel Discrete Ordinates Code RAPTOR-M3G,” Journal of ASTM International, 9[4], 2012.

[59] E. P. Lippincott and Sr. M. P. Manahan, “Advances in Calculation of Fluence to Reactor Structures,” Journal of ASTM International, 3[3], 2006.

[60] B. W. Amiri, J. P. Foster, and L. R. Greenwood, “Dosimetry Evaluation of In-core and Above-core Zirconium Alloy Samples in a PWR,” EPJ Web of Conferences, 106, 2016.

[61] G. A. Fischer and B. C. Kim, “Retrospective Dosimetry Analysis of Top Support Plus Samples from Scrap Surveillance Capsule Material for Qualifying Calculations in the Extended Beltline Region of PWRs,” 16th International Symposium on Reactor Dosimetry, ASTM International, November 2018.

[62] 2018 Materials Programs Technical Information Exchange Meeting,” PWROG Materials Committee Update. ADAMS Accession No. ML18142A391, May 2018.

[63] A. T. Godfrey, “VERA Core Physics Benchmark Progression Problem Specifications,” Consortium for the Advanced Simulation of Light Water Reactors (CASL) Report, March 2014.

[64] Watts Bar Unit 2 Final Safety Analysis Report (FSAR), Amendment 93, Section 4, April 2009. ADAMS Accession No. ML091400651.

[65] Sequoyah Nuclear Plant Updated Final Safety Analysis Report (UFSAR), Amendment 16, May 2001.

[66] Cook Nuclear Plant Updated Final Safety Analysis Report (UFSAR), Amendment 16, May 2001.

[67] Indian Point Nuclear Generating Unit No. 3 Final Safety Analysis Report (FSAR), April 2001.

[68] Westinghouse Technology Manual. ADAMS Accession No. ML023040268.

[69] Westinghouse Technology Systems Manual. ADAMS Accession No. ML023030412.

[70] U.S. Nuclear Regulatory Commission, “PWR and BWR Pressure Vessel Fluence Calculation Benchmark Problems and Solutions,” NUREG/CR-6115, September 2001.

[71] Edwin I. Hatch Nuclear Plant Unit No. 2 Updated Final Safety Analysis Report (UFSAR), Revision 19, July 2001. ADAMS Accession No. ML012150043.

[72] U.S. Nuclear Regulatory Commission, “Review and Prioritization of Technical Issues Related to Burnup Credit for BWR Fuel,” NUREG/CR-7158, February 2013.

[73] U.S. Nuclear Regulatory Commission, “Axial Moderator Density Distributions, Control Blade Usage, and Axial Burnup Distributions for Extended BWR Burnup Credit,” NUREG/CR-7224, August 2016.

[74] M. F. James, “Energy Release in Fission,” J. Nucl. Energy, 23:517-536, 1969.

[75] I. Remec, “Study of the Neutron Flux and Dpa Attenuation in the Reactor Pressure-Vessel Wall,” ORNL/NRC/LTR-99/5, Oak Ridge National Laboratory, June 1999.

[76] Eric N. Jones, “Comparison of Regulatory Guide 1.99 Fluence Attenuation Methods,’ J. ASTM Intl., 9(4):390–398, 2012. doi:10.1520/JAI104028.

[77] 10 CFR Part 50, “Domestic Licensing of Production and Utilization Facilities,” U.S. Nuclear Regulatory Commission, 2016.

[78] U.S. Nuclear Regulatory Commission, “Radiation Embrittlement of Reactor Vessel Materials,” Regulatory Guide 1.99, Revision 2, 1988.

[79] AEC Research and Development Report, “A Summary of Shielding Constants for Concrete,” ANL-6443, Reactor Technology (TID-4500, 16th Ed., Amended), November 1961.

[80] Pacific Northwest National Laboratory Report, “Compendium of Material Composition Data for Radiation Transport Modeling,” PIET-43741-TM-963, PNNL-15870 Rev. 1, March 2011.

[81] American Nuclear Society, “Nuclear Analysis and Design of Concrete Radiation Shielding for Nuclear Power Plants,” ANSI/ANS-6.4-2006 (R2016), La Grange Park, IL

[82] A. H. Fero, “Use of SSTRs and a Multi-Component Shield Assembly to Measure Radiation Penetrating the Reactor Biological Shield in the Presence of Radiation Streaming from Other Sources,” Reactor Dosimetry: Radiation Metrology and Assessment, STP 1397, The Tenth International Symposium on Reactor Dosimetry, 12–17 September 1999, American Society for Testing and Materials, 2001.

[83] U.S. Nuclear Regulatory Commission, “H. B. Robinson-2 Pressure Vessel Benchmark,” NUREG/CR-6453, October 1997.

[84] U.S. Nuclear Regulatory Commission, “Production and Testing of the VITAMIN-B7 Fine-Group and BUGLE-B7 Broad-Group Coupled Neutron/Gamma Cross-Section Libraries Derived from ENDF/B-VII.0 Nuclear Data,” NUREG/CR-7045, September 2011.

[85] ASTM E693-17, “Standard Practice for Characterizing Neutron Exposures in Iron and Low Alloy Steels in Terms of Displacements Per Atom (DPA),” ASTM International, August 2017.

[86] ASTM E1035-18, “Determining Neutron Exposures for Nuclear Reactor Vessel Support Structures,” ASTM International, June 2018.

[87] International Rector Dosimetry File 2000 (IRDF-2002). Technical report, International Atomic Energy Agency, 2006.

[88] ASTM E844-18, “Standard Guide for Sensor Set Design and Irradiation for Reactor Surveillance,” ASTM International, July 2018.

[89] N. P. Baumann, “Gamma-ray Induced Displacements in D2O Reactors,” Proceedings of the Seventh ASTM-EURATOM Symposium on Reactor Dosimetry, Strasbourg, France, August 27-31, 1990.

[90] Materials Reliability Program (MRP): Attenuation in U.S. RPV Steels (MRP-56), Electric Power Research Institute, Palo Alto, CA, 2002.

[91] U.S. Nuclear Regulatory Commission, “Expanded Materials Degradation Assessment (EMDA),” NUREG/CR-7153, Vol. 3, October 2014.

[92] W. N. McElroy, “LWR Pressure Vessel Surveillance Dosimetry Improvement Program: PCA Experiments and Blind Test,” NUREG/CR-1861 (HEDL-TME 80-87), July 1981.

[93] I. Remec and F. B. K. Kam, “Pool Critical Assembly Pressure Vessel Facility Benchmark,” NUREG/CR-6454 (ORNL/TM-13205), July 1997.

[94] F. W. Stallmann et al., “Reactor Calculation ‘Benchmark’ PCA Blind Test Results,” NUREG/CR-1872 (ORNL/NUREG/TM428), January 1981.

[95] D. K. Min, A. L. Aronson, and J. F. Carew, “Analysis of the ORNL Pool Critical Assembly Pressure Vessel Dosimetry Benchmark Experiment,” BNL-NUREG-29047, Brookhaven National Laboratory, February 1981.

[96] R. E. Maerker, “Analysis of the VENUS-3 Experiments,” Proceedings of the Seventh ASTM-Euratom Symposium on Reactor Dosimetry, Strasbourg, France, 27-31 August 1990, ASTM, Kluwer Academic Publishers, 1992.

[97] G. Hehn and B.C. Na, “New NEA Benchmarks Reveal Decisive Improvements in Calculating Fast Neutron Fluence for Predictions of Embrittlement in Reactor Pressure Vessels,” Reactor Dosimetry, ASTM STP 1398 (J.G. Williams et al., Eds.), ASTM, West Conshohoken, PA, 2000.

[98] A. Haghighat, H. Ait Abderrahim, and G.E. Sjoden, “Accuracy and Performance of PENTRAN^{TM} Using the VENUS-3 Benchmark Experiment,” Reactor Dosimetry, ASTM STP 1398 (J.G. Williams et al., Eds.). ASTM, West Conshohoken, PA, 2002.

[99] P. D'hondt et al, “Contribution of the VENUS-Engineering Mock-up Experiment to the LWR-PV Surveillance,” Proceedings of the Seventh ASTM-Euratom Symposium on Reactor Dosimetry, Strasbourg, France, 27-31 August 1990, ASTM, Kluwer Academic Publishers, 1992.

[100] “Prediction of Neutron Embrittlement in the Reactor Pressure Vessel: VENUS-1 and VENUS-3 Benchmarks,” Nuclear Energy Agency, 2000.

[101] A. H. Fero and E. T. Hayes, “Analysis of the VENUS-1 Benchmark Using TORT and BUGLE-96,” Proceedings of the 11th International Symposium on Reactor Dosimetry. Reactor Dosimetry in the 21st Century. World Scientific Publishing Co. Pte. Ltd., 2003.

[102] M. L. Williams and M. Asgari, “Impact of ENDF/B-VI Cross-Section Data on H.B. Robinson Cycle 9 Dosimetry Calculations,” NUREG/CR-6071 (ORNL/TM-13204), October 1993.

[103] E. P. Lippincott et al., “Evaluation of Surveillance Capsule and Reactor Cavity Dosimetry from H.B. Robinson Unit-2, Cycle 9,” NUREG/CR-4576 (WCAP-11104), U. S. Nuclear Regulatory Commission, February 1987.

[104] U.S. Nuclear Regulatory Commission, “LaSalle County Station, Unit 1, Issuance of Amendment Revising Pressure and Temperature Limits (TAC No. MF3270)”, November 25, 2014. ADAMS Accession No. ML14220A517.

[105] I. I. Bondarenko, Group Constants for Nuclear Reactor Calculations, Consultants Bureau, New York, 1964.

[106] ANSI/ANS-6.1.2-2013, “Group-Averaged Neutron and Gamma-Ray Cross Sections for Radiation Protection and Shielding Calculations for Nuclear Power Plants,” American Nuclear Society, August 2013.

[107] J. Kenneth Shultis and Richard E. Faw, Radiation Shielding, American Nuclear Society, 2000.

[108] James J. Duderstadt and Louis J. Hamilton, Nuclear Reactor Analysis, John Wiley and Sons, 1976.

[109] John R. Lamarsh, Introduction to Nuclear Reactor Theory, Addison-Wesley, 1972.

[110] E. A. Attia and A. A. Harms, “A New Expansion for Highly Anisotropic Neutron-Nuclear Scattering,” Nucl. Sci. Eng., 59(4):319–325, 1975.

13 GLOSSARY

adjoint flux	The flux (see below) calculated using the adjoint form of the transport equation. The adjoint flux has the physical interpretation of representing the importance of particles to a specified response (e.g., flux or dpa rate).
discrete ordinates	A widely used method for solving the transport equation by discretizing the spatial, energy, and angular variables and solving the resulting set of algebraic equations using numerical methods. Discrete ordinates calculations are also referred to as deterministic calculations.
displacements per atom (dpa)	The mean number of times each atom in a crystal lattice structure is displaced from its lattice site as a result of radiation interactions.
fast fluence, fast flux	The fluence or flux of particles (e.g., neutrons) with energy above a specified threshold. While there is no standard definition of fast neutron flux, a commonly used energy cutoff for fast neutrons is 1 MeV. Within this report, the cutoff energy is either 1 MeV or 1.0026 MeV. The latter is used with MG cross-section libraries and with CE solutions that are compared directly with MG solutions.
fluence	The number of particles (e.g., neutrons) (dN) incident on a hypothetical sphere of cross-sectional area dA. Fluence can also be defined as the sum of the particle track lengths within the sphere. Fluence has units of inverse area (cm^{-2} or m^{-2}).
fluence rate	The number of particles entering a sphere, or the sum of the particle track lengths within a sphere per unit time.
flux	A more commonly used term for fluence rate.
hybrid	A class of techniques used to obtain a solution to the transport equation using a combination of determination and stochastic calculations.
lethargy	A measure of the amount of energy a neutron has lost as a result of scattering collisions. Lethargy is defined as $u = \ln\left(\frac{E_0}{E}\right)$ where E is the neutron energy and E_0 is the maximum neutron energy (typically 20 MeV for neutron shielding calculations)

Monte Carlo	A stochastic method of obtaining a solution to the transport equation by simulating the behavior of a large number of particle histories.

APPENDIX A AN OVERVIEW OF MULTIGROUP CROSS-SECTION LIBRARIES

MG cross-section libraries used in radiation transport analyses are generally categorized as fine group or broad group. Fine-group libraries, which typically contain hundreds of energy groups, are generated by collapsing (averaging) pointwise cross-section data over a specified set of energy groups using a standard weighting spectrum. For LWR shielding analyses, the weighting spectrum used to average the pointwise data is typically a combination of a fission spectrum, a 1/E slowing-down spectrum, and a Maxwellian thermal spectrum. Fine-group libraries include a sufficient number of groups so that differences between the flux spectrum used to produce the groupwise cross sections and the actual flux spectra in a given application should have a negligible effect on the fine-group data.

Broad-group libraries, which typically contain tens of groups, are produced by collapsing (averaging) fine-group data using flux spectra that closely approximate the spectra that are encountered in specific locations in a particular transport application. A broad-group library that is developed using appropriate weighting spectra can produce calculated fluxes more quickly, and with fewer computing resources, with little loss in accuracy compared to a fine-group calculation.

MG libraries may also be categorized as master libraries and working libraries. A master library, which is typically a fine-group library,[11] contains cross-section data for multiple temperatures to address Doppler broadening of resonances and to provide thermal Maxwellian spectra and multiple Bondarenko background cross sections for resonance self-shielding effects [105]. Working libraries contain data for a single temperature and account for energy self-shielding by applying Bondarenko factors for each isotope in a mixture based on the material composition. Working libraries are thus problem-specific in the sense that they should only be used for calculations involving models similar to those used to develop the working library. For example, the BUGLE-B7 library was developed specifically for LWR shielding applications and may not be appropriate for other types of analysis.

All MG libraries contain 1D and 2D data. The 1D data contain reaction cross sections for each energy group, while the 2D data contain group-to-group transfer matrices. Master libraries and working libraries typically contain 1D data for numerous reaction types (e.g., elastic scattering, inelastic scattering, capture). Master libraries typically contain 2D data for multiple reaction types, while working libraries contain only a single 2D transfer matrix that accounts for all processes which result in a particle in group g due to a particle interaction in group g′.

Figure A-1 shows the 1D total microscopic cross section for ^{56}Fe from three MG libraries, as well as the CE data from which the MG libraries were created. Figure A-2 and Figure A-3 show the 2D transfer matrices (for the neutron groups only) for ^{1}H in PWR core coolant and ^{56}Fe at one quarter of the distance (¼T) through a PWR RPV from the BUGLE-B7 library.

The 2D transfer matrix plots show the magnitude of the group-to-group cross section from a source group on the abscissa to a sink group on the ordinate. The group numbers on these plots start with 0, the convention used by Denovo. The far-left column of each 2D plot thus shows the cross sections for scattering from the highest energy group to all lower energy

[11] The SCALE code system contains both fine-group and broad-group master libraries.

groups. The values along the diagonal, from [0,0] to [46,46], represent the in-group cross sections. Note that all out-of-group transfers are to lower energy groups (i.e., downscattering), except in the thermal groups, where upscatter can occur.

Figure A-4 illustrates the effect of inelastic scattering in the ^{56}Fe. For all groups below group 18, downscatter can occur to only the first sink group below the source group because the maximum energy loss for elastic scattering in ^{56}Fe is only ~7%. Inelastic scattering in ^{56}Fe occurs only for energies above 862.5 keV. The inelastic scattering accounts for all downscatters of more than one group.

Fine-group master libraries appropriate for LWR shielding analyses include the VITAMIN-B7 library and the coupled 200-neutron-group 47-gamma-group libraries (XN200G47v7.0 and XN200G47v7.1) in the SCALE code system. The VITAMIN-B7 fine-group master library has 199 neutron groups and 42 gamma groups. The VITAMIN-B7 neutron group structure is the same as that of the SCALE XN200G47v7.0 library, except that it does not include an energy group from 19.64 to 20.0 MeV, as the upper energy limit of the VITAMIN-B7 library is 19.64 MeV.

The SCALE code system also contains a broad-group master library with 56 neutron groups for physics calculations, as well as a broad group coupled neutron/gamma library with 28 neutron groups and 19 gamma groups. The 28n/19g library is used primarily for discrete ordinates adjoint flux calculations to generate importance maps for hybrid radiation transport.

This appendix briefly describes the fine- and broad-group libraries that were used in this study. More details of each library can be found in the reference documents.

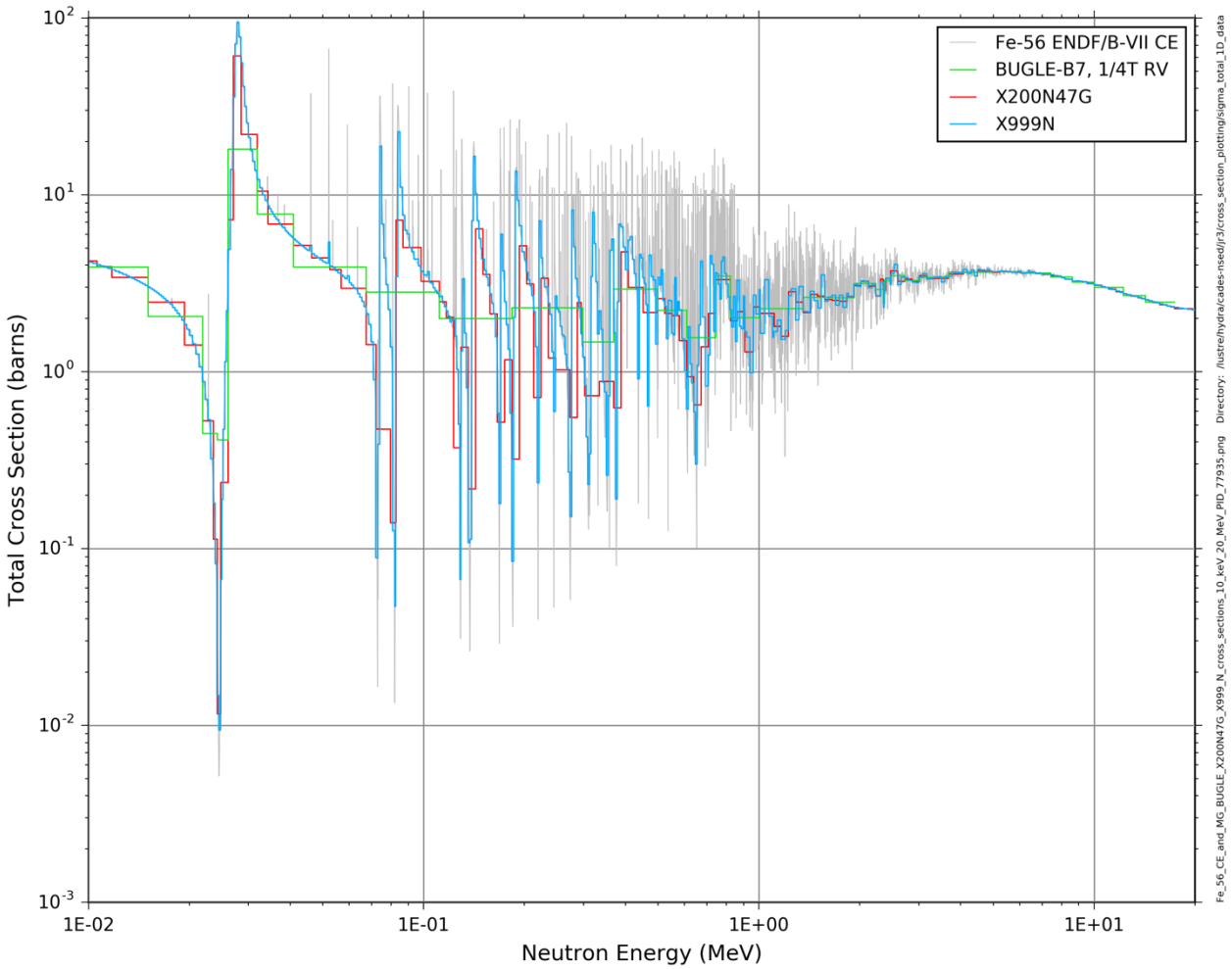

Figure A-1 Total microscopic cross section for ^{56}Fe from three MG libraries (BUGLE-B7, XN20047G, and XN999) and the SCALE ENDF/V-VII.1 CE library *The BUGLE-B7 data are for ^{56}Fe that has been collapsed from the VITAMIN-B7 library using a neutron flux spectrum at one quarter of the distance through the RPV.*

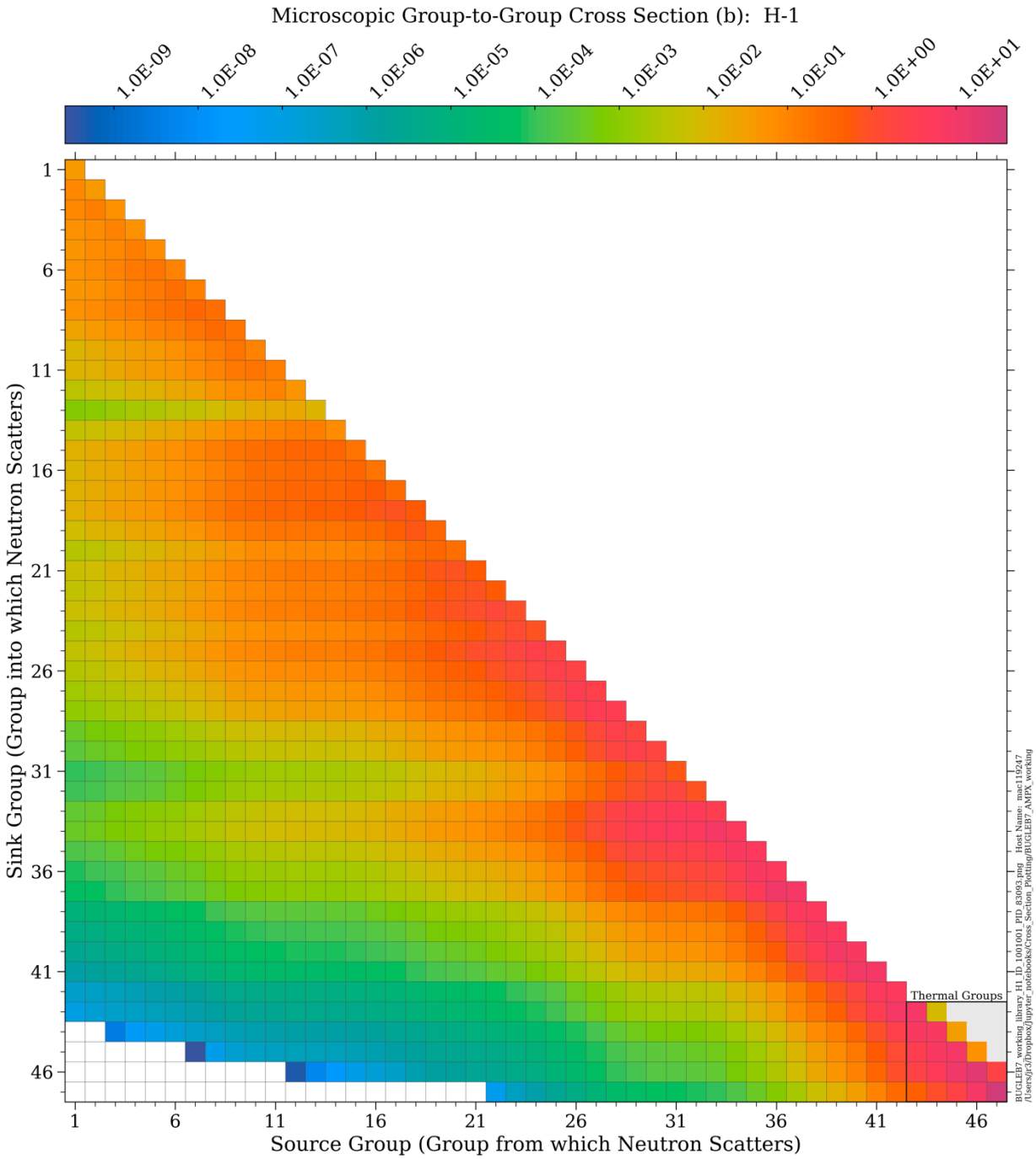

Figure A-2 Two-dimensional transfer matrix for ^{1}H from the BUGLE-B7 working library

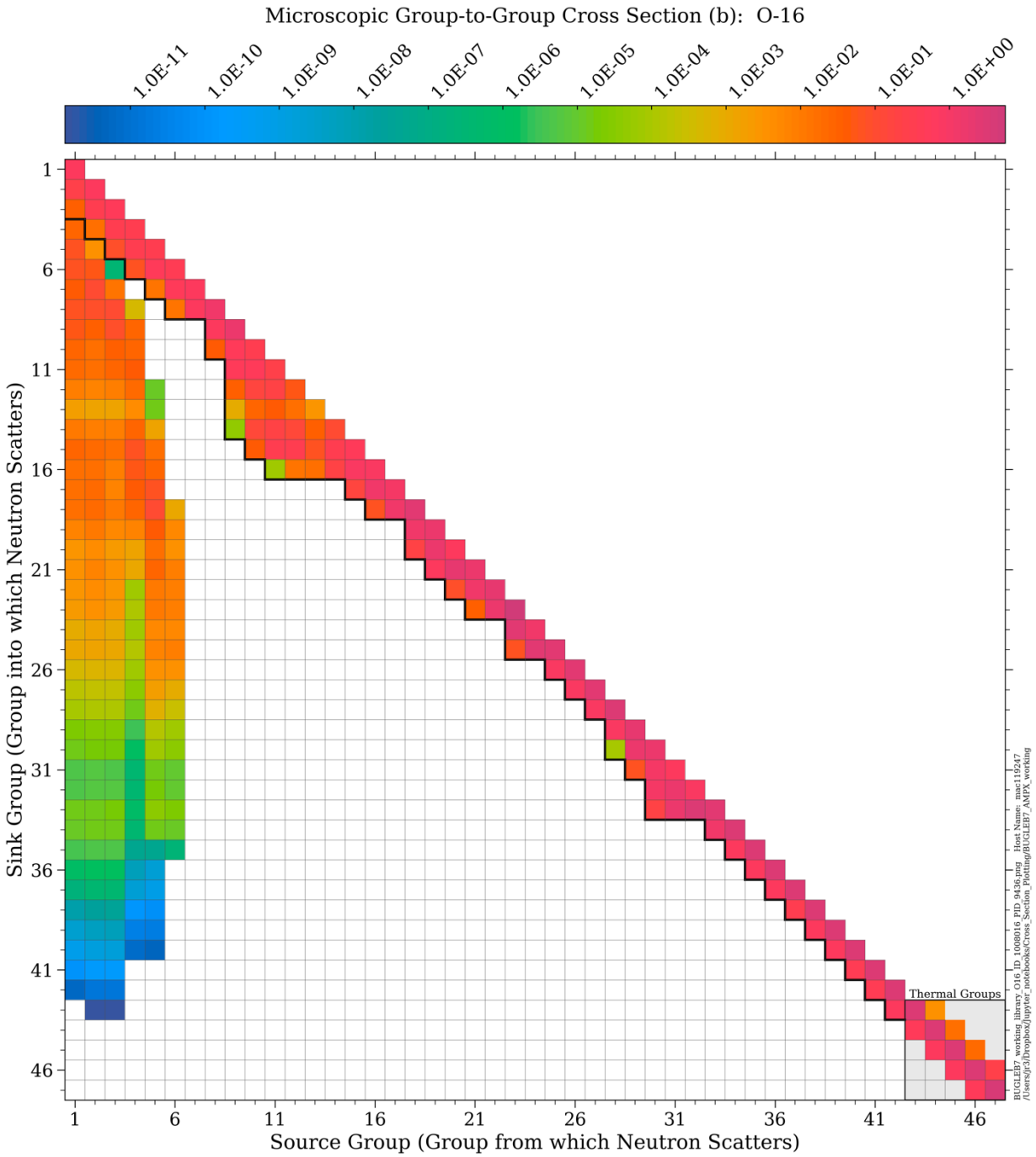

Figure A-3 Two-dimensional transfer matrix for ^{16}O from the BUGLE-B7 working library The weighting spectrum is for coolant in the core of a PWR model. *The solid black line marks the minimum group into which elastic scattering can occur. The lowest energy group in which inelastic scattering occurs in ^{16}O is group 6.*

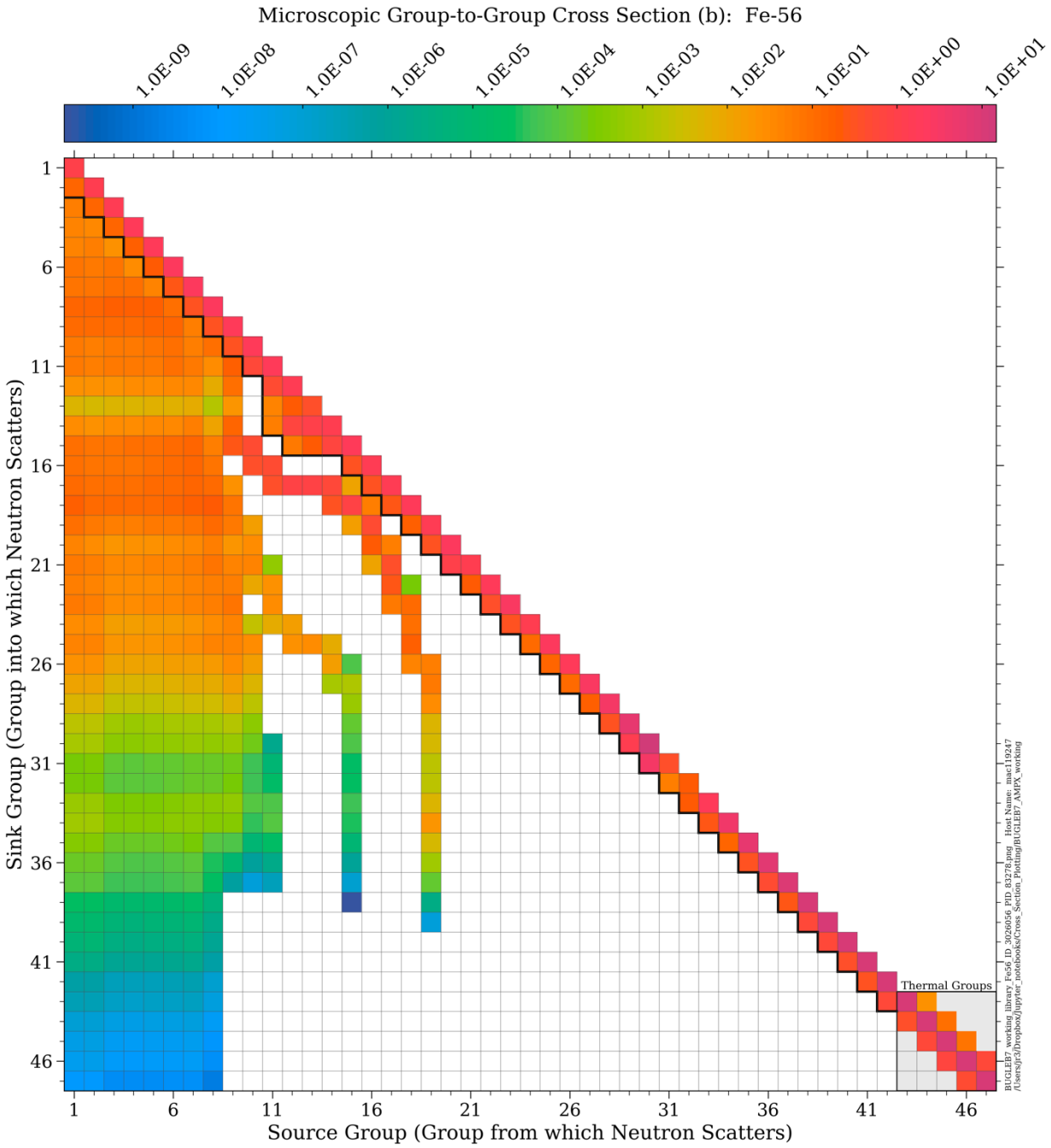

Figure A-4 Two-dimensional transfer matrix for ^{56}Fe at one-quarter of the RPV thickness from the BUGLE-B7 working library *The weighting spectrum is for the 1/4T thickness in the RPV of a PWR model. The solid black line marks the minimum group into which elastic scattering can occur. The lowest energy group in which inelastic scattering occur in ^{56}Fe is group 19.*

A.1 The XN200G47 Fine-Group Libraries

The XN200G47 libraries are part of the SCALE code system. There are two XN200G47 libraries: XN200G47v7.0, based on ENDF/B-VII.0 data, and XN200G47v7.1, based on ENDF/B-VII.1 data. The XN200G47v7.0 neutron energy group structure has 200 groups, with an upper energy limit of 20.0 MeV. The thermal energy range, which includes upscattering cross sections, has an upper boundary of 5.0435 eV and includes 36 groups. The neutron groups typically have uniform lethargy widths ranging from 0.025 to 0.25 for energies above 1.445 eV, with additional boundaries to resolve resonance minima important for shielding calculations (e.g., the ^{16}O minimum at ~2.36 MeV and the ^{56}Fe minimum at ~24.5 keV). The energy group boundaries and group lethargy widths for the XN200G47v7.0 library are listed in Table A-1. The energy group boundaries for the XN200G47v7.1 library are identical to those of the XN200G47v7.0 library, except the upper energy of the first thermal group is 5.0 eV rather than 5.0435 eV.

The neutron weighting spectrum used to generate the XN200G47 libraries is shown in Figure A-5. It consists of a 1/E slowing-down spectrum above 10 MeV, a Watt fission spectrum from 80 keV to 10 MeV, a 1/E slowing-down spectrum from 0.125 eV to 80 keV, and a Maxwellian thermal spectrum below 0.125 eV. Scattering cross sections in the XN200G47 libraries are limited to P_5 expansions for all nuclides.

A.2 The VITAMIN-B7 Fine-Group Library

The VITAMIN-B7 library was developed for use in LWR shielding applications, including vessel fluence and dosimetry analyses. VITAMIN-B7 was generated using ENDF/B, Version VII, Release 0 (ENDF/B-VII.0). The processing methodology used to generate the VITAMIN-B7 library, as well as the BUGLE-B7 library, is consistent with the guidelines specified in ANSI/ANS 6.1.2 [106].

The VITAMIN-B7 neutron energy group structure has 199 groups, with an upper energy limit of 19.64 MeV. The energy groups are identical to groups 2 to 200 of the XN200G47v7.0 library (Table A-1). The weighting spectrum used to generate the VITAMIN-B7 library is shown in Figure A-5. It consists of a fission spectrum for neutron energies above 820.8 keV, a 1/E slowing-down spectrum for energies between 0.125 eV and 820.8 keV, and a Maxwellian spectrum for energies below 0.125 eV.

The angular distribution of neutron scattering cross sections in VITAMIN-B7 is represented using Legendre polynomial expansions with P_7 order for Z values up to 30 (Zn), and P_5 order for Z values above 30.

A.3 The XN999 Fine-Group Library

The XN999 library is available for use in Denovo and Shift but is not a standard SCALE library. XN999 libraries are available for ENDF/B-VII.0 and ENDF/B-VII.1 data. Scattering expansions are limited to P_3 for all nuclides.

Table A-1 Neutron group boundaries and lethargy widths for the SCALE XN200G47v7.0 library[12] *The thermal groups are shaded in gray. The 199 VITAMIN-B7 groups are the same as groups 2–200 of the XN200G47v7.0 library*

Grp	Upper Energy (eV)	Lethargy Width	Grp	Upper Energy (eV)	Lethargy Width	Grp	Upper Energy (eV)	Lethargy Width	Grp	Upper Energy (eV)	Lethargy Width
1	2.0000E+07	0.0182	51	2.0190E+06	0.0500	101	1.4264E+05	0.0500	151	1.6702E+02	0.2500
2	1.9640E+07	0.1250	52	1.9205E+06	0.0500	102	1.3569E+05	0.0500	152	1.3007E+02	0.2500
3	1.7332E+07	0.0249	53	1.8268E+06	0.0500	103	1.2907E+05	0.0500	153	1.0130E+02	0.2500
4	1.6905E+07	0.0250	54	1.7377E+06	0.0500	104	1.2277E+05	0.0499	154	7.8893E+01	0.2500
5	1.6487E+07	0.0500	55	1.6530E+06	0.0500	105	1.1679E+05	0.0500	155	6.1442E+01	0.2500
6	1.5683E+07	0.0500	56	1.5724E+06	0.0500	106	1.1109E+05	0.1250	156	4.7851E+01	0.2500
7	1.4918E+07	0.0250	57	1.4957E+06	0.0500	107	9.8037E+04	0.1250	157	3.7266E+01	0.2500
8	1.4550E+07	0.0250	58	1.4227E+06	0.0499	108	8.6517E+04	0.0475	158	2.9023E+01	0.2500
9	1.4191E+07	0.0250	59	1.3534E+06	0.0500	109	8.2503E+04	0.0371	159	2.2603E+01	0.2500
10	1.3840E+07	0.0249	60	1.2874E+06	0.0500	110	7.9499E+04	0.0991	160	1.7604E+01	0.2500
11	1.3499E+07	0.0501	61	1.2246E+06	0.0501	111	7.1998E+04	0.0663	161	1.3710E+01	0.2500
12	1.2840E+07	0.0250	62	1.1648E+06	0.0500	112	6.7379E+04	0.1750	162	1.0677E+01	0.2500
13	1.2523E+07	0.0250	63	1.1080E+06	0.1000	113	5.6562E+04	0.0750	163	8.3153E+00	0.2500
14	1.2214E+07	0.0500	64	1.0026E+06	0.0417	114	5.2475E+04	0.1250	164	6.4760E+00	0.2500
15	1.1618E+07	0.0499	65	9.6164E+05	0.0583	115	4.6309E+04	0.1250	165	5.0435E+00	0.2500
16	1.1052E+07	0.0500	66	9.0718E+05	0.0500	116	4.0868E+04	0.1750	166	3.9279E+00	0.2500
17	1.0513E+07	0.0500	67	8.6294E+05	0.0500	117	3.4307E+04	0.0750	167	3.0590E+00	0.2500
18	1.0000E+07	0.0500	68	8.2085E+05	0.0500	118	3.1828E+04	0.1104	168	2.3824E+00	0.2500
19	9.5123E+06	0.0500	69	7.8082E+05	0.0500	119	2.8501E+04	0.0541	169	1.8554E+00	0.2500
20	9.0484E+06	0.0500	70	7.4274E+05	0.0500	120	2.7000E+04	0.0355	170	1.4450E+00	0.1057
21	8.6071E+06	0.0500	71	7.0651E+05	0.0500	121	2.6058E+04	0.0500	171	1.3000E+00	0.1443
22	8.1873E+06	0.0500	72	6.7206E+05	0.0500	122	2.4788E+04	0.0250	172	1.1253E+00	0.0411
23	7.7880E+06	0.0500	73	6.3928E+05	0.0500	123	2.4176E+04	0.0250	173	1.0800E+00	0.0377
24	7.4082E+06	0.0500	74	6.0810E+05	0.0500	124	2.3579E+04	0.0750	174	1.0400E+00	0.0392
25	7.0469E+06	0.0500	75	5.7844E+05	0.0500	125	2.1875E+04	0.1250	175	1.0000E+00	0.1319
26	6.7032E+06	0.0167	76	5.5023E+05	0.0500	126	1.9305E+04	0.2500	176	8.7643E-01	0.0912
27	6.5924E+06	0.0333	77	5.2340E+05	0.0500	127	1.5034E+04	0.2500	177	8.0000E-01	0.1588
28	6.3763E+06	0.0500	78	4.9787E+05	0.1000	128	1.1709E+04	0.1000	178	6.8256E-01	0.0880
29	6.0653E+06	0.0500	79	4.5049E+05	0.1000	129	1.0595E+04	0.1500	179	6.2506E-01	0.1620
30	5.7695E+06	0.0500	80	4.0762E+05	0.0500	130	9.1188E+03	0.2500	180	5.3158E-01	0.0612
31	5.4881E+06	0.0500	81	3.8774E+05	0.0500	131	7.1017E+03	0.2500	181	5.0000E-01	0.1888
32	5.2205E+06	0.0500	82	3.6883E+05	0.1000	132	5.5308E+03	0.2500	182	4.1399E-01	0.1210
33	4.9659E+06	0.0500	83	3.3373E+05	0.1000	133	4.3074E+03	0.1500	183	3.6680E-01	0.1210
34	4.7237E+06	0.0500	84	3.0197E+05	0.0116	134	3.7074E+03	0.1000	184	3.2500E-01	0.1671
35	4.4933E+06	0.1000	85	2.9849E+05	0.0043	135	3.3546E+03	0.1000	185	2.7500E-01	0.2007
36	4.0657E+06	0.1000	86	2.9721E+05	0.0091	136	3.0354E+03	0.1000	186	2.2500E-01	0.2012
37	3.6788E+06	0.1000	87	2.9452E+05	0.0250	137	2.7465E+03	0.0500	187	1.8400E-01	0.2043
38	3.3287E+06	0.0500	88	2.8725E+05	0.0500	138	2.6126E+03	0.0500	188	1.5000E-01	0.1823
39	3.1664E+06	0.0500	89	2.7324E+05	0.1000	139	2.4852E+03	0.1000	189	1.2500E-01	0.2231
40	3.0119E+06	0.0500	90	2.4724E+05	0.0500	140	2.2487E+03	0.1000	190	1.0000E-01	0.3567
41	2.8651E+06	0.0500	91	2.3518E+05	0.0500	141	2.0347E+03	0.2500	191	7.0000E-02	0.3365
42	2.7253E+06	0.0500	92	2.2371E+05	0.0500	142	1.5846E+03	0.2500	192	5.0000E-02	0.2231
43	2.5924E+06	0.0500	93	2.1280E+05	0.0500	143	1.2341E+03	0.2500	193	4.0000E-02	0.2877
44	2.4660E+06	0.0333	94	2.0242E+05	0.0500	144	9.6112E+02	0.2500	194	3.0000E-02	0.3567
45	2.3852E+06	0.0084	95	1.9255E+05	0.0500	145	7.4852E+02	0.2500	195	2.1000E-02	0.3704
46	2.3653E+06	0.0083	96	1.8316E+05	0.0500	146	5.8295E+02	0.2500	196	1.4500E-02	0.3716
47	2.3457E+06	0.0167	97	1.7422E+05	0.0500	147	4.5400E+02	0.2500	197	1.0000E-02	0.6931
48	2.3069E+06	0.0333	98	1.6573E+05	0.0500	148	3.5357E+02	0.2500	198	5.0000E-03	0.9163
49	2.2313E+06	0.0500	99	1.5764E+05	0.0499	149	2.7536E+02	0.2500	199	2.0000E-03	1.3863
50	2.1225E+06	0.0500	100	1.4996E+05	0.0500	150	2.1445E+02	0.2500	200	5.0000E-04	3.9120

[12] The upper energy of group 165 (the first thermal group) in the XN200G47v7.1 library is 5.0 eV.

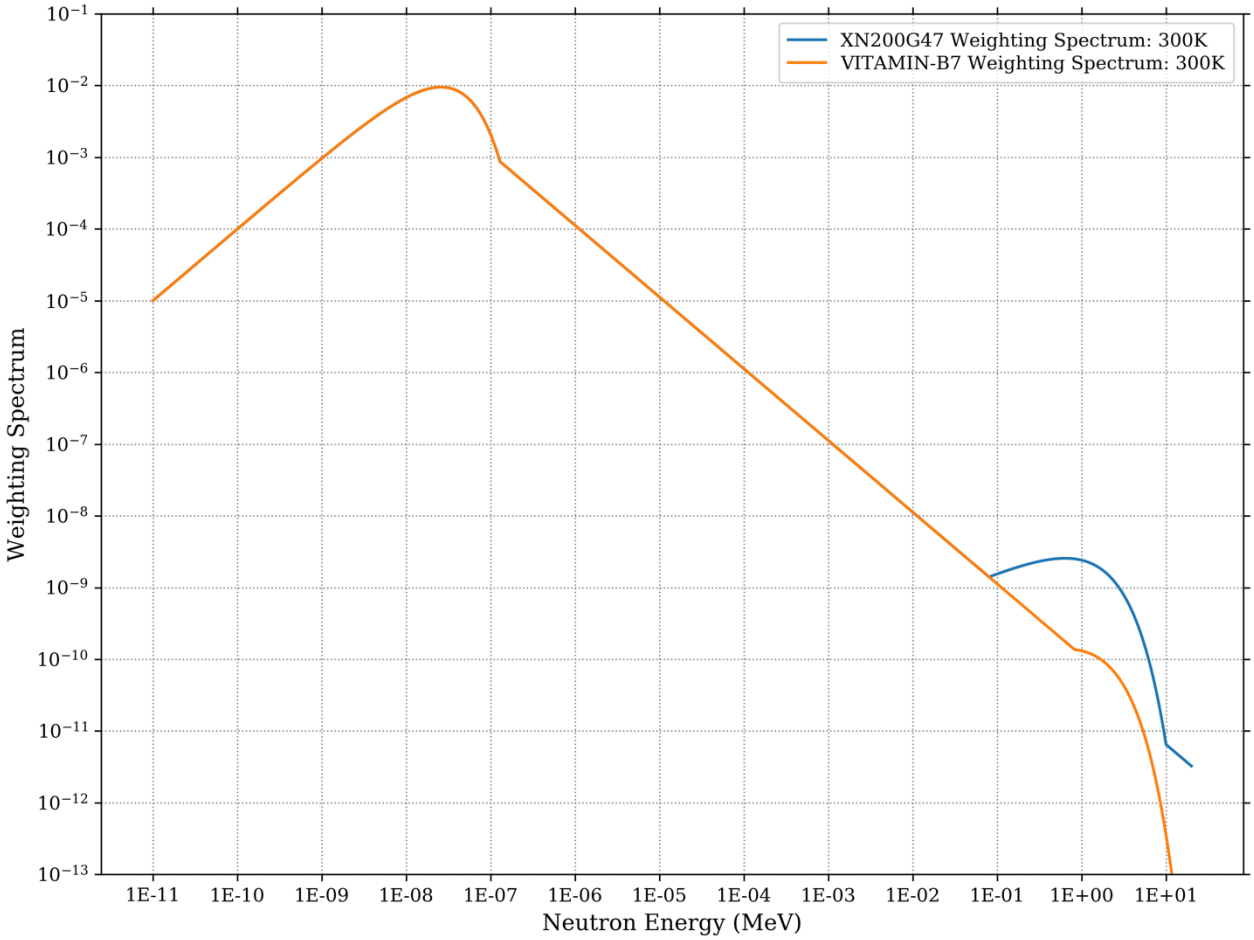

Figure A-5 The weighting spectra used to generate the VITAMIN-B7 and SCALE XN200G47 MG libraries from ENDF/B-VII pointwise data

A.4 The BUGLE-B7 Broad-Group Library

The BUGLE-B7 library is widely used in RPV fluence analyses. It includes 47 neutron energy groups with an upper energy limit of 17.332 MeV. The thermal energy range has an upper boundary of 5.043 eV and includes five groups. There are options in the BUGLE-B7 libraries to explicitly model upscatter or to apply an approach referred to as the "ANISN upscatter approximation." The energy group boundaries and group lethargy widths for the BUGLE-B7 library are listed in Table A-2.

The BUGLE-B7 library was produced by collapsing the VITAMIN-B7 library using weighting spectra from key regions of one-dimensional PWR and BWR models. These weighting spectra are representative of the following locations in the PWR and BWR models:

1. Off-center in the core region of the BWR model
2. Off-center in the core region of the PWR model
3. In the PWR downcomer region
4. Within the PWR RPV at one-fourth the vessel thickness
5. Within the PWR concrete biological shield

The fine-group (based on the VITAMIN-B7 group structure) spectra in each of these regions are shown in Figure A-6.

The angular distribution of neutron scattering cross sections in BUGLE-B7 is represented using Legendre polynomial expansions with P_7 order for Z values up to 30 (Zn), and P_5 order for Z values above 30.

Table A-2 Neutron energy group boundaries and lethargy widths for the BUGLE-B7 library
The thermal groups are shaded in gray. The fine groups correspond to the VITAMIN-B7 library

Grp	Upper Energy (eV)	Lethargy Width	Fine Groups	Grp	Upper Energy (eV)	Lethargy Width	Fine Groups
1	1.7332E+07	0.1999	2-7	26	1.8316E+05	0.5000	95-104
2	1.4191E+07	0.1500	8-12	27	1.1109E+05	0.5000	105-110
3	1.2214E+07	0.2000	13-16	28	6.7379E+04	0.5000	111-114
4	1.0000E+07	0.1500	17-19	29	4.0868E+04	0.2500	115-116
5	8.6071E+06	0.1500	20-22	30	3.1828E+04	0.2000	117-119
6	7.4082E+06	0.2000	23-27	31	2.6058E+04	0.0750	120-121
7	6.0653E+06	0.2000	28-31	32	2.4176E+04	0.1000	122-123
8	4.9659E+06	0.3000	32-35	33	2.1875E+04	0.3750	124-125
9	3.6788E+06	0.2000	36-38	34	1.5034E+04	0.7500	126-129
10	3.0119E+06	0.1000	39-40	35	7.1017E+03	0.7500	130-133
11	2.7253E+06	0.1000	41-42	36	3.3546E+03	0.7500	134-140
12	2.4660E+06	0.0417	43-44	37	1.5846E+03	1.2500	141-145
13	2.3653E+06	0.0083	45	38	4.5400E+02	0.7500	146-148
14	2.3457E+06	0.0500	46-47	39	2.1445E+02	0.7500	149-151
15	2.2313E+06	0.1500	48-50	40	1.0130E+02	1.0000	152-155
16	1.9205E+06	0.1500	51-53	41	3.7266E+01	1.2500	156-160
17	1.6530E+06	0.2000	54-57	42	1.0677E+01	0.7500	161-163
18	1.3534E+06	0.3000	58-62	43	5.0435E+00	1.0000	164-167
19	1.0026E+06	0.2000	63-66	44	1.8554E+00	0.7500	168-174
20	8.2085E+05	0.1000	67-68	45	8.7643E-01	0.7500	175-180
21	7.4274E+05	0.2000	69-72	46	4.1399E-01	1.4207	181-188
22	6.0810E+05	0.2000	73-76	47	1.0000E-01	9.2103	189-199
23	4.9787E+05	0.3000	77-80				
24	3.6883E+05	0.2159	81-84				
25	2.9721E+05	0.4841	85-94				

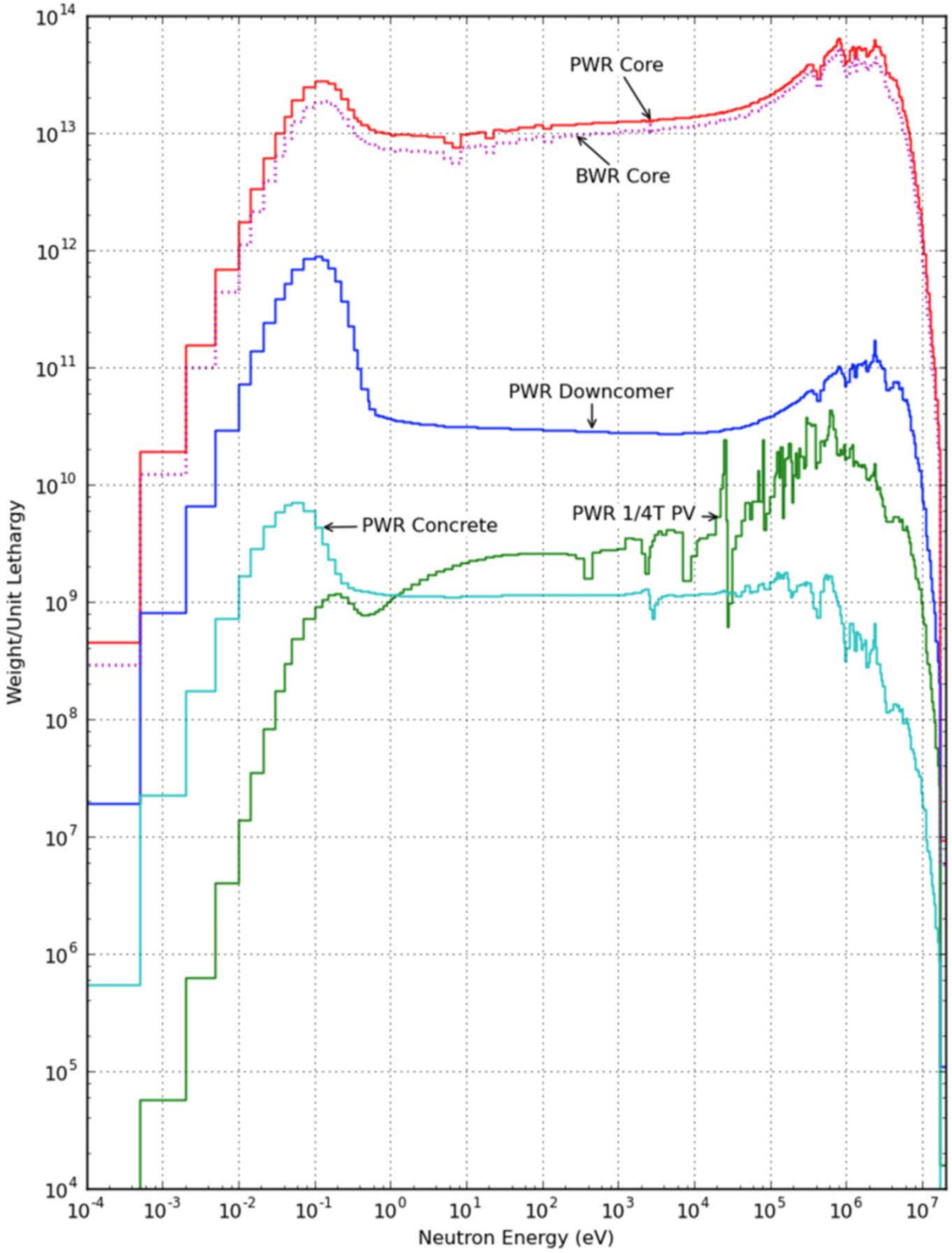

Figure A-6 The weighting spectra used to generate the BUGLE-B7 MG data for problem-specific analyses

APPENDIX B AN OVERVIEW OF THE MESH TALLIES AND PLOTTING METHODS USED IN THIS REPORT

Much of the data analysis in this report consists of plots of fast (E > 1 MeV) neutron flux distributions, dpa rates, and ratios of solutions from parametric studies. The majority of the solutions are from Shift Monte Carlo calculations with cylindrical mesh tallies. The quadrature sensitivity studies in Section 7 utilized Denovo discrete ordinates calculations and Shift calculations. For those studies, the Shift calculations used Cartesian mesh tallies with the same grid spacing as the Denovo mesh and used the same multigroup (MG) cross-section data as the Denovo calculations.

This appendix briefly describes the level of detail in the Shift mesh tallies and provides examples of the types of plots that are used to present the analysis results. Examples of typical relative errors in the Shift calculations are also presented.

B.1 Cylindrical Mesh Tallies in the PWR and BWR Models

The majority of the results presented in this report are based on cylindrical mesh tallies from continuous energy (CE) Shift calculations. The mesh tally intervals were selected to provide a high degree of spatial resolution while also providing solutions with mesh tally relative errors that are typically less than 1% in all locations of interest.
In the PWR model, the cylindrical mesh tally radial intervals are ~1 cm from the outer radius of the neutron pad to the outer radius of the RPV. In the cavity gap and the concrete bioshield the radial intervals are ~2 cm. The axial mesh intervals are ~2.5 cm over the height of the model. The azimuthal mesh intervals are uniform at 1°. Plots showing the radial, azimuthal, and axial mesh tally voxel boundaries for the PWR model are shown in Figure B-1 and Figure B-2. The Cartesian mesh in the Denovo calculations of Section 7 and Section 9 was uniform at 1 cm in X, Y, and Z. Comparison of Denovo solutions for the PWR model with Shift solutions using the identical MG cross-section library as Denovo demonstrated that this spatial mesh grid structure provides convergence with respect to mesh in the Denovo calculations.

In the BWR model, the cylindrical mesh tally radial intervals are ~2 cm over the radial extent from ~10 cm inboard of the core barrel to the inner radius of the RPV, ~1 cm through the RPV, ~3 cm in the cavity gap, and ~2 cm in the concrete bioshield. The axial mesh intervals are ~2.5 cm over the height of the model. The azimuthal mesh intervals are uniform at 1°. Plots showing the radial, azimuthal, and axial mesh tally voxel boundaries for the BWR model are shown in Figure B-3 and Figure B-4.

B.2 Fast Neutron Flux Plots

Fast neutron flux solutions are plotted using a combination of material color assignments, contour lines, and flooded contours. Contour lines are typically shown over an extent of the cylindrical mesh tallies ranging from the water region inboard of the RPV radially out into the concrete bioshield. Within the RPV and other carbon steel regions (nozzles and nozzle supports), flooded contours are used to emphasize the fast flux behavior in these key components. Maximum and minimum values of the fast flux within each distinct carbon steel component (RPV, nozzles, nozzle supports) are indicated. In some plots the mesh tally voxel boundaries are shown. For elevation plots, the top of the active fuel (TAF) and bottom of the active fuel (BAF) elevations are indicated. Example fast neutron flux plots from the PWR model are shown in Figure B-5 and Figure B-6.

B.3 DPA Rate Plots

DPA rate plots are presented in nearly the same way as fast flux plots. The sole difference is that the dpa rate contour lines and flooded contours are shown only in the carbon steel components, as the dpa cross sections from [85] apply only to iron and low-alloy steels. Example dpa rate plots from the PWR model are shown in Figure B-7 and Figure B-8.

B.4 Ratio Plots

Ratio plots are used in parametric studies to show the effect of changes in solution or model parameters. Many of the ratio plots in this report use contour lines and flooded contours only in the RPV, nozzles, and nozzle supports. Ratio plots also typically include an inset plot with a histogram of the ratio values in specified regions, which may include the RPV, nozzles, nozzle supports, and cavity gap. The abscissa labels on the histogram plots indicates which regions are included in the distribution. Numeric values on the upper edge of the ratio plot show the percentage of values that fall within each major interval of the abscissa.

An example ratio plot from a Shift parametric study is shown in Figure B-9.

Ratio plots for the Denovo parameter studies in Sections 7 and 9 are somewhat different from the ratio plots for the Shift parameter studies in Sections 5, 6, and 8. In Sections 7 and 9 the ratio of two solutions is shown over the entire plot extent. Showing the ratio for the entire extent is useful in pointing out the effects of quadrature selection. An example is shown in Figure B-10, where quadrature ray effects emanate from every corner on the peripheral fuel assemblies.

B.5 Mesh Tally Relative Errors

As noted in Section B.1 relative errors for the Shift solutions in this report are typically less than 1% in all locations of interest. Example plots showing relative errors in the fast neutron flux for the PWR model are shown in Figure B-11 and Figure B-12. These correspond to the fast flux plots in Figure B-5 and Figure B-6.

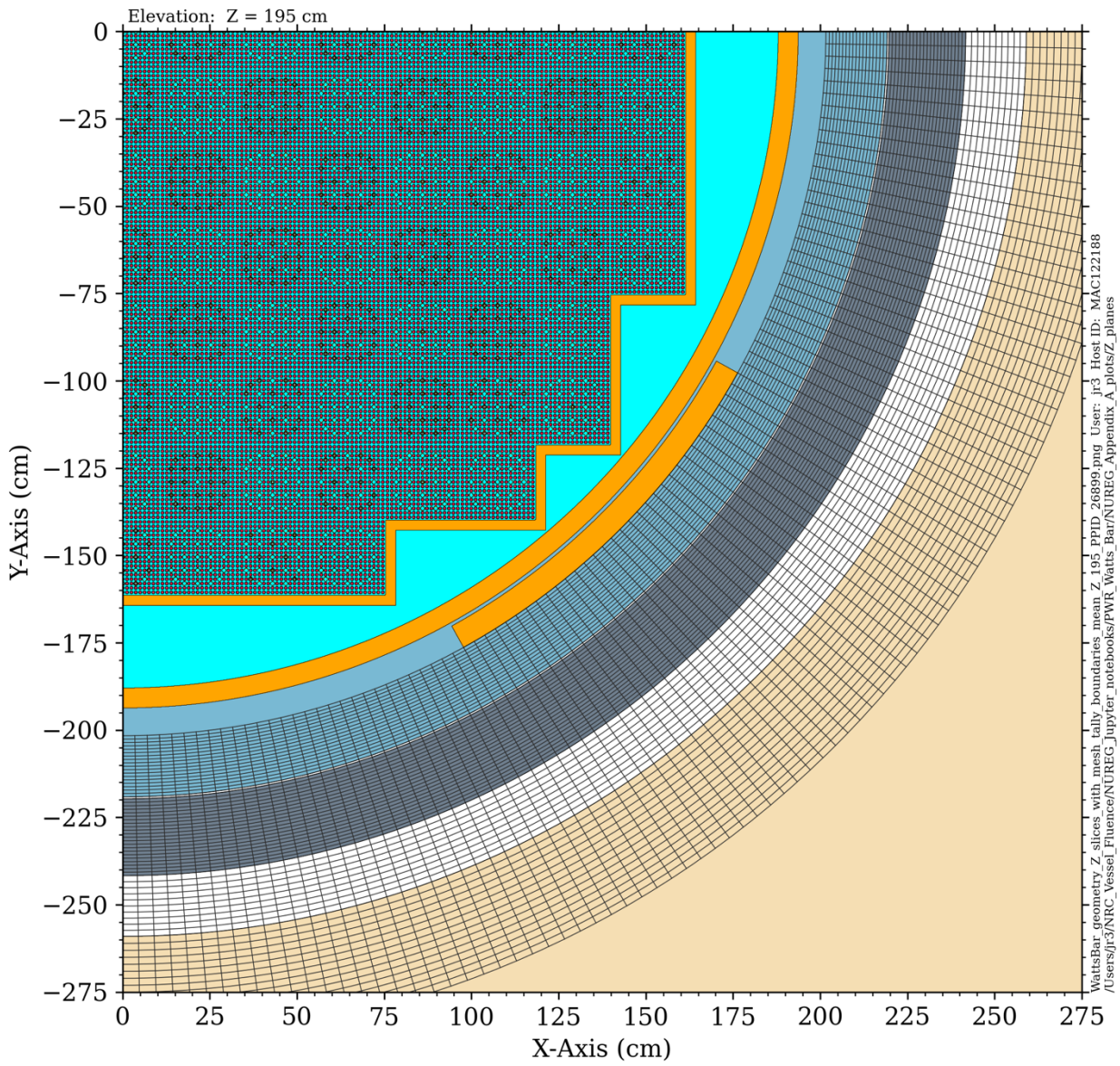

Figure B-1 Radial and azimuthal cylindrical mesh tally intervals in the PWR model. Plan view at the core midplane

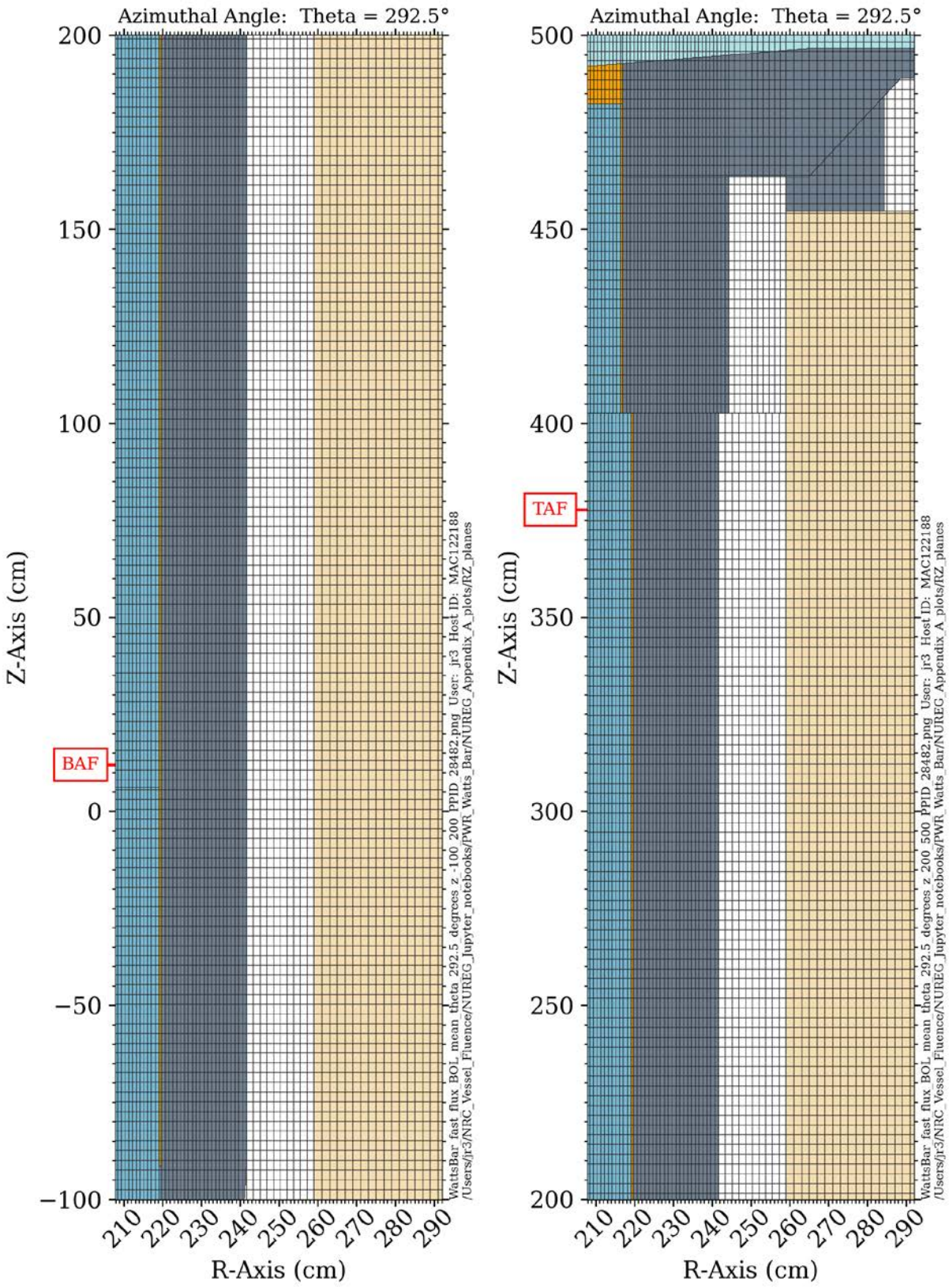

Figure B-2 Axial cylindrical mesh tally intervals in the PWR model. Elevation view at an azimuthal angle of 292.5°

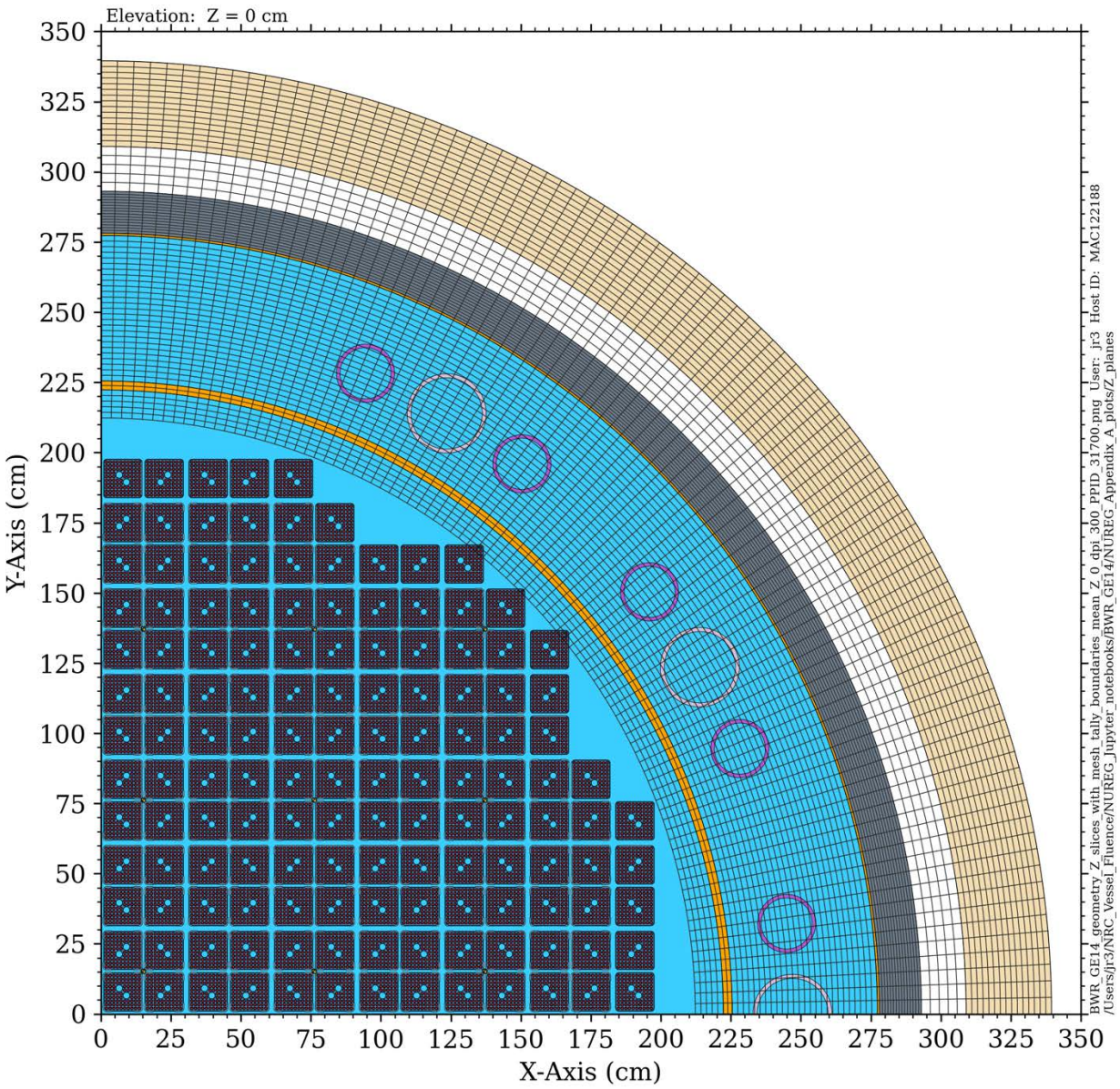

Figure B-3 Radial and azimuthal cylindrical mesh tally intervals in the BWR model. Plan view at the core midplane

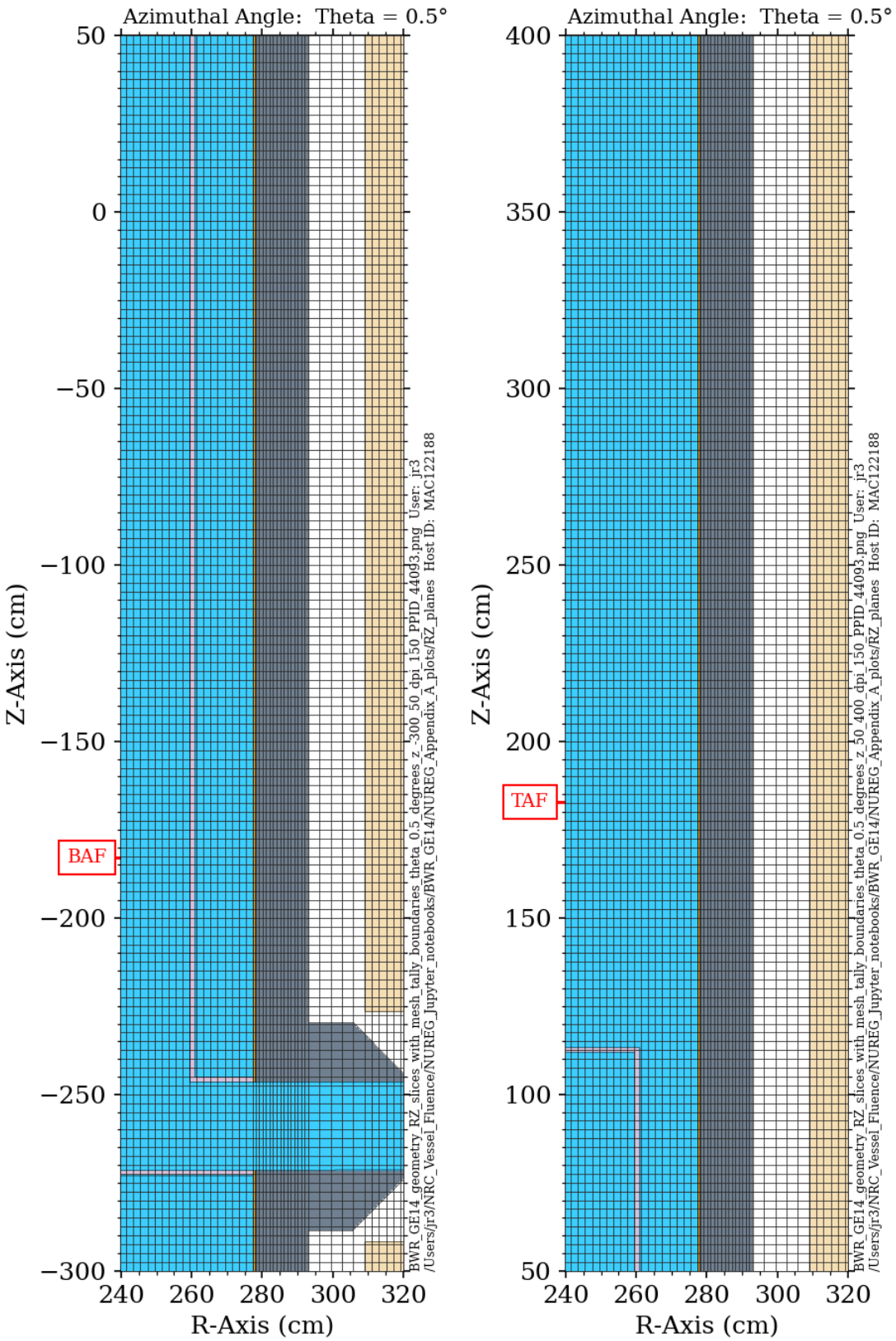

Figure B-4 Axial cylindrical mesh tally intervals in the BWR model. Elevation view at an azimuthal angle of 0.5°

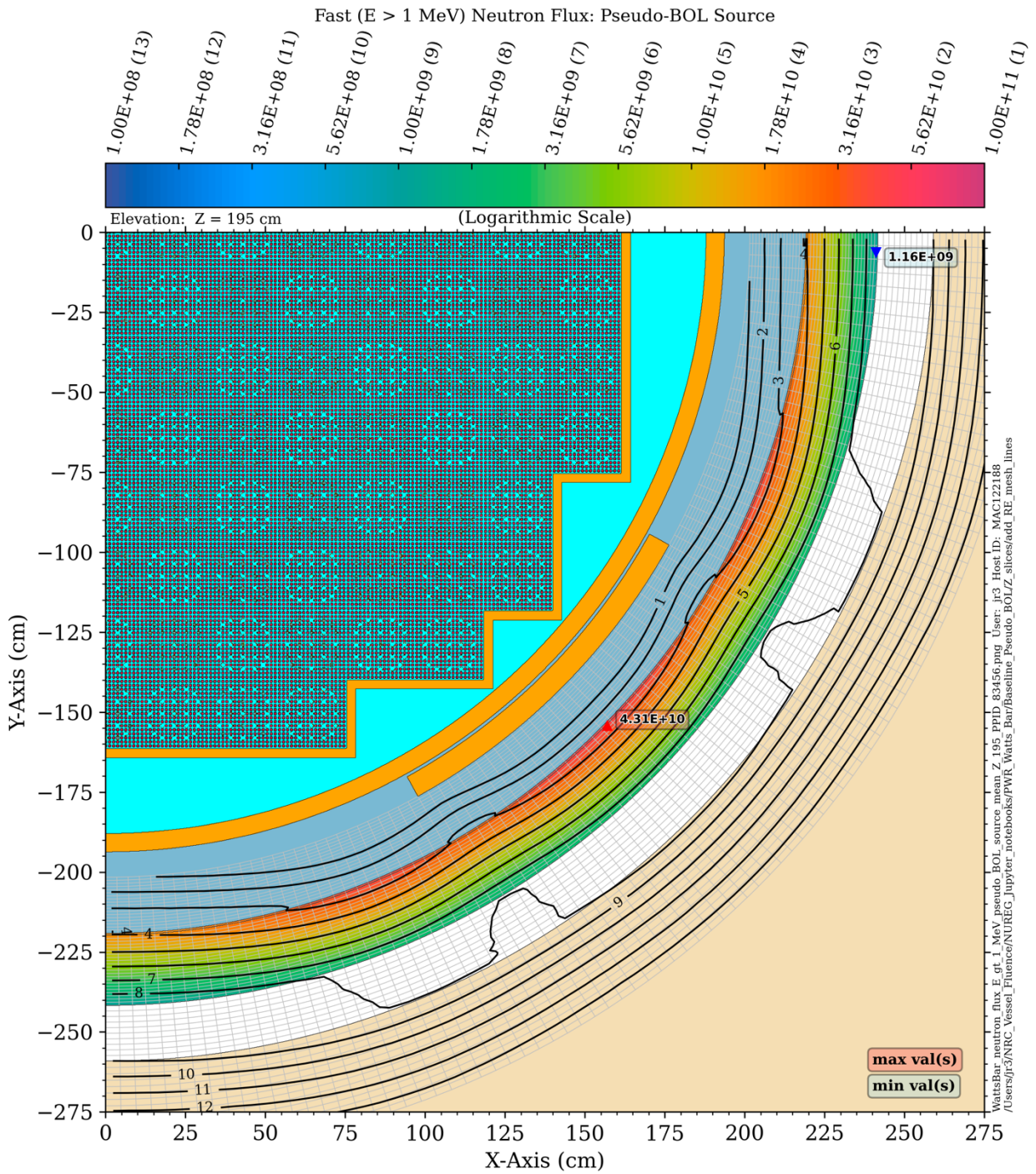

Figure B-5 **Fast neutron flux at the core midplane in the PWR model** *Regions other than the RPV are colored by material assignment Contour lines show the fast neutron flux over the full extent of the cylindrical mesh tally. Flooded contours are used to highlight the fast flux in the RPV, which is the primary region of interest. Maximum and minimum fast flux values in the RPV are indicated. The cylindrical mesh tally boundaries are shown on this plot but are not present on all plots of this type.*

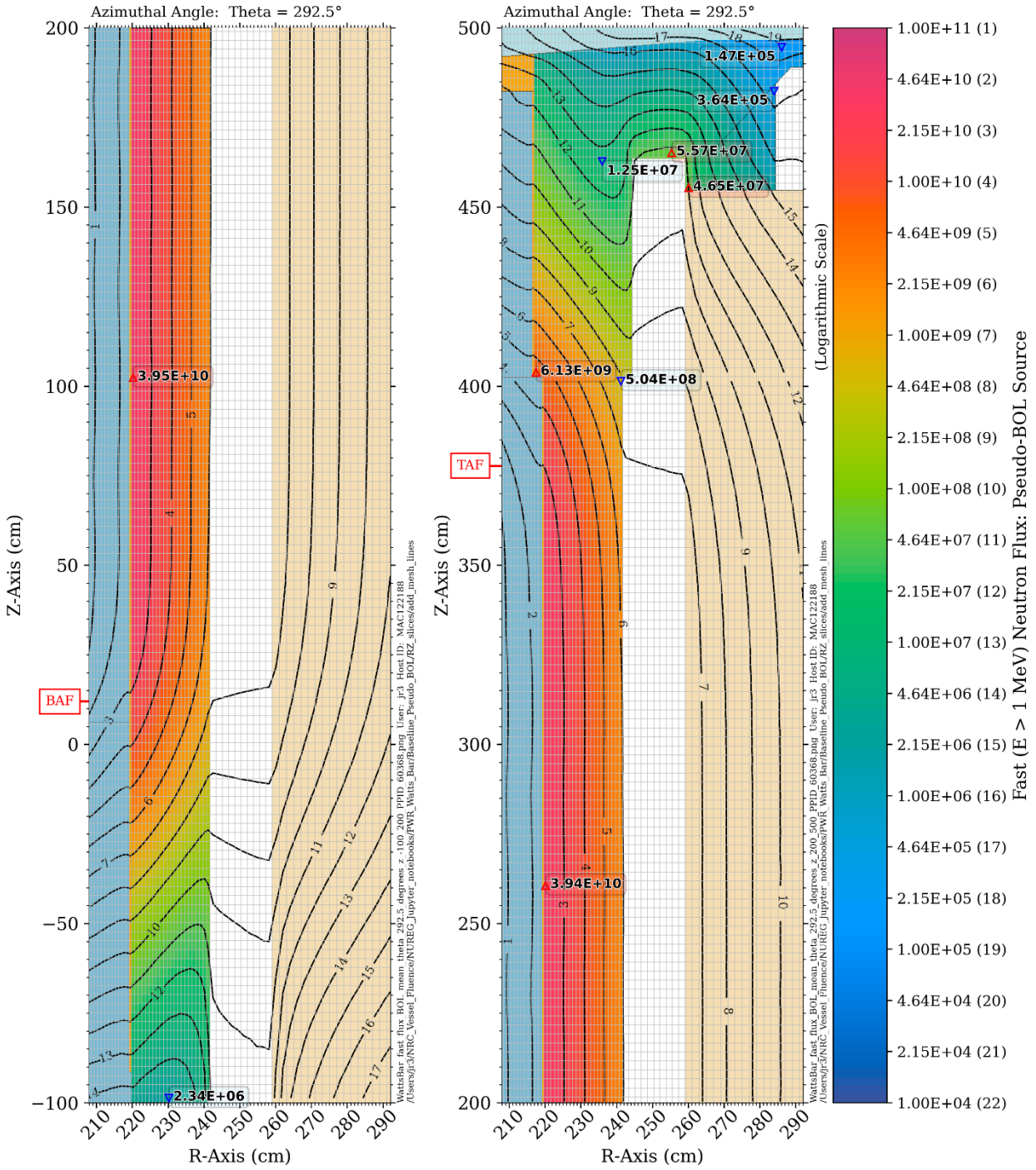

Figure B-6 **Fast neutron flux in the PWR model at an azimuthal angle of 292.5°** *Regions other than the RPV are colored by material assignment. Contour lines show the fast neutron flux in all regions. Flooded contours are used to highlight the fast flux in the RPV, which is the primary region of interest. Maximum and minimum fast flux values in the RPV, RPV nozzle, and nozzle support are indicated. Maximum and minimum values in the RPV in the right-hand-side view are indicated above and below Z = 402.59 cm, where the thickness of the RPV changes. BAF and TAF are the bottom and top elevations of the active fuel.*

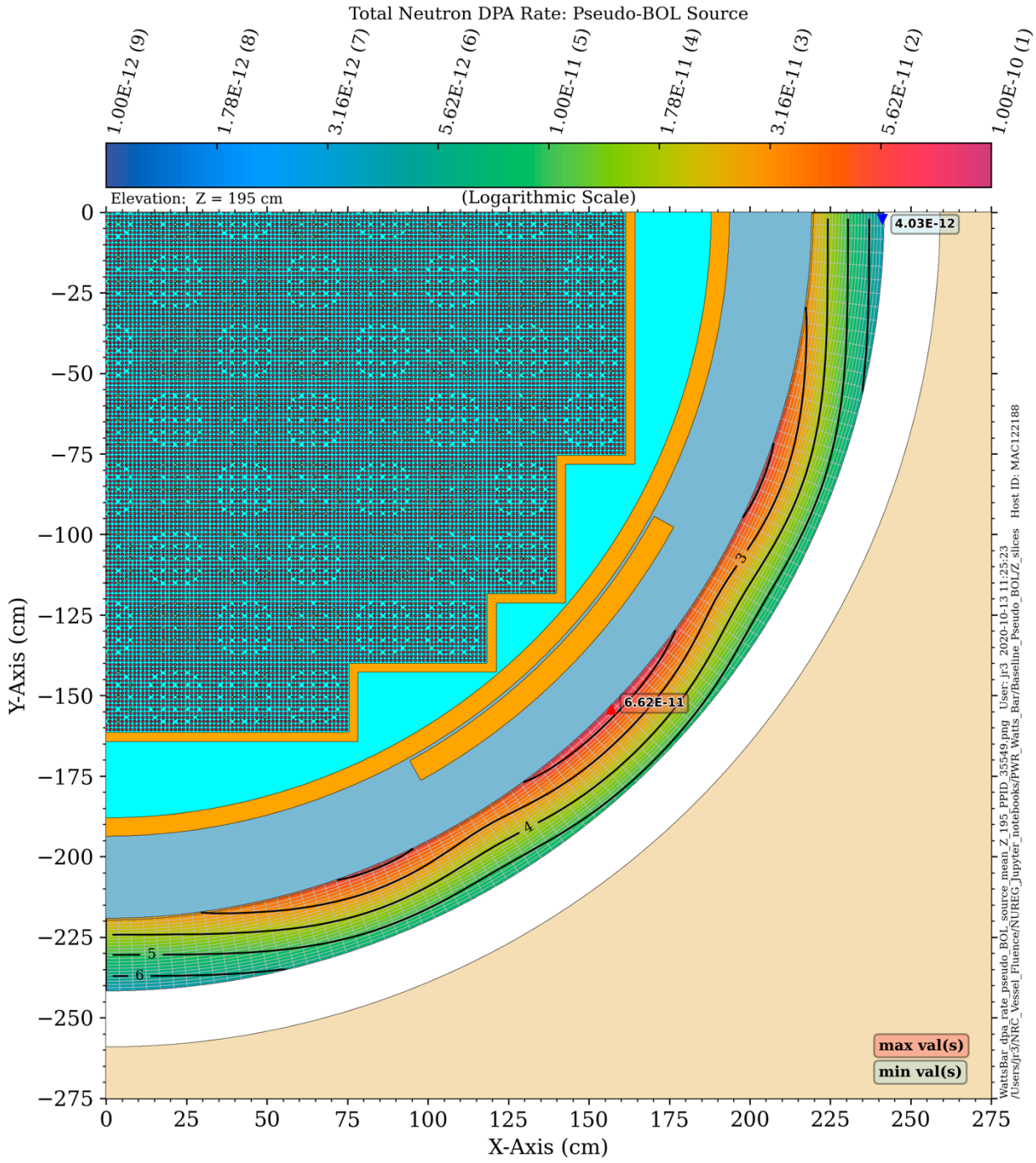

Figure B-7 DPA rate at the core midplane in the PWR model *Regions other than the RPV are colored by material assignment. Flooded contours show the dpa rate in the RPV. Maximum and minimum dpa rate values are indicated. The cylindrical mesh tally boundaries are shown only in the RPV, which is the only region where the dpa rate is meaningful at this elevation.*

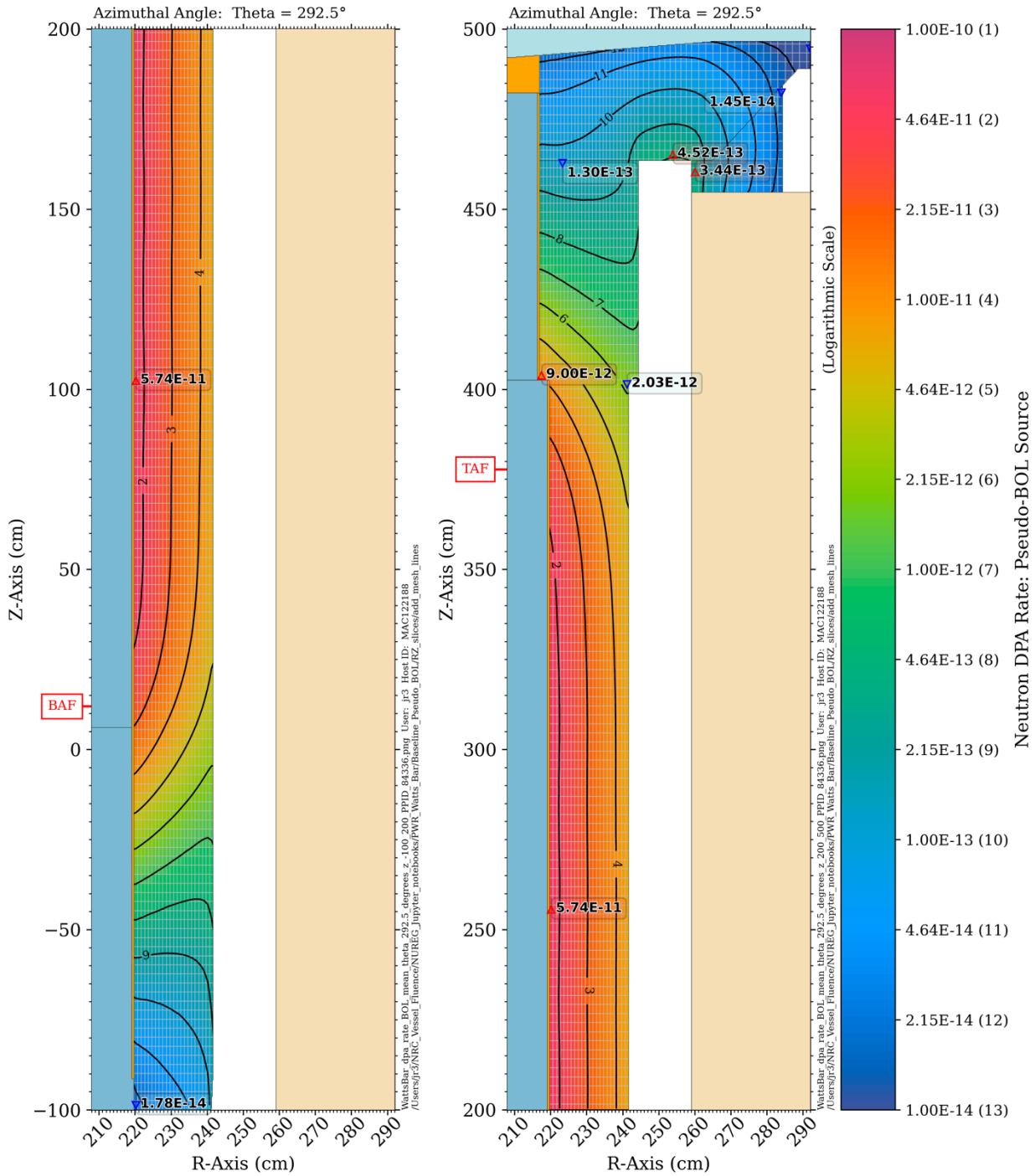

Figure B-8 **DPA rate in the PWR model at an azimuthal angle of 292.5°** *Regions other than the RPV are colored by material assignment. Flooded contours show the dpa rate in the RPV, RPV nozzle, and nozzle support. Maximum and minimum dpa rate values in the RPV, RPV nozzle, and nozzle support are indicated. Maximum and minimum values in the RPV in the right-hand-side view are indicated above and below Z = 402.59 cm, where the thickness of the RPV changes. BAF and TAF are the bottom and top elevations of the active fuel.*

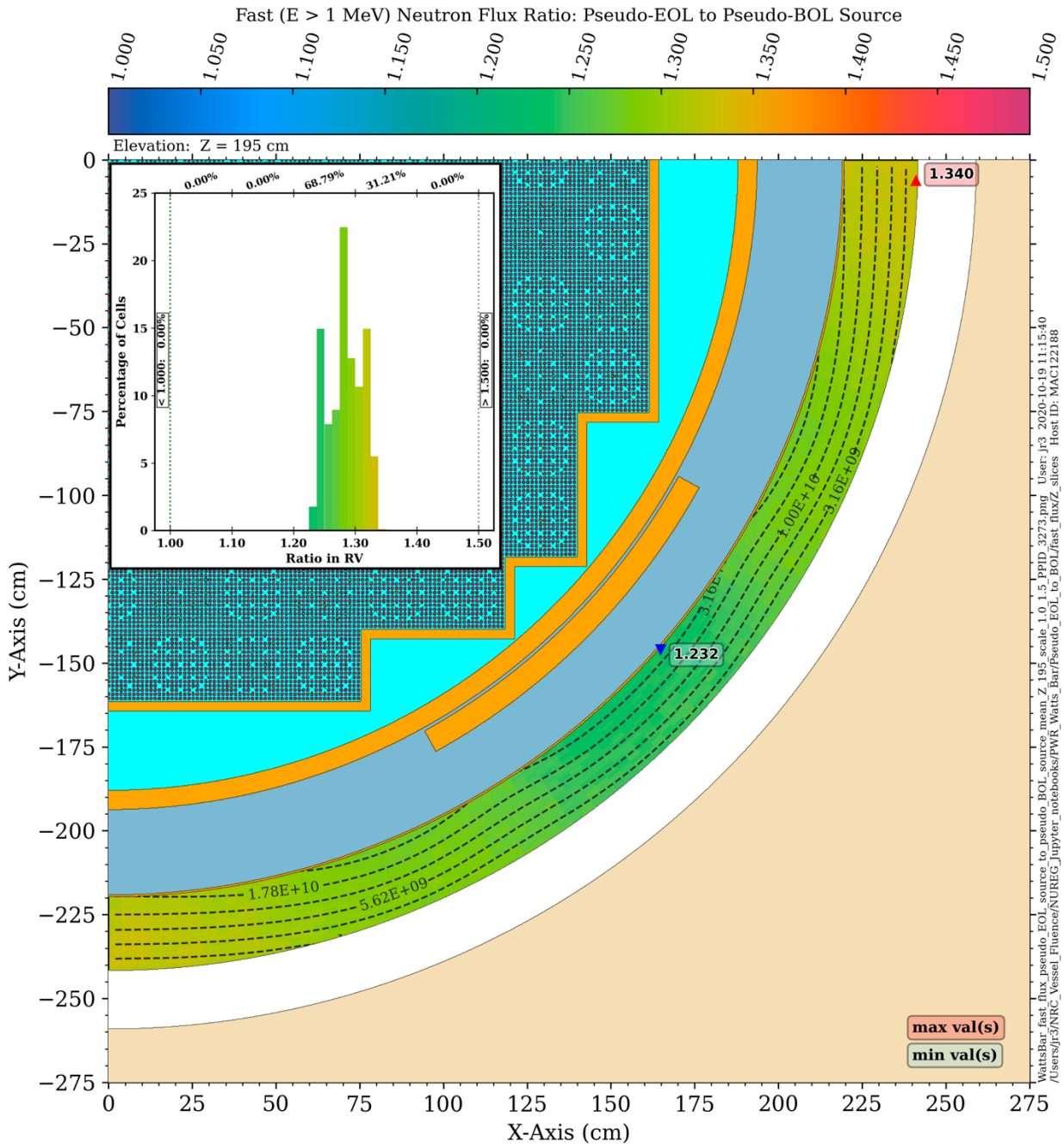

Figure B-9 Fast neutron flux ratio at the core midplane in the PWR model: pseudo-EOL source to pseudo-BOL source *Flooded contours show the fast flux ratio in the RPV. Minimum and maximum ratio values are indicated. The dashed contour lines represent the pseudo-BOL solution. The inset histogram plot shows the distribution of ratio values in the RPV.*

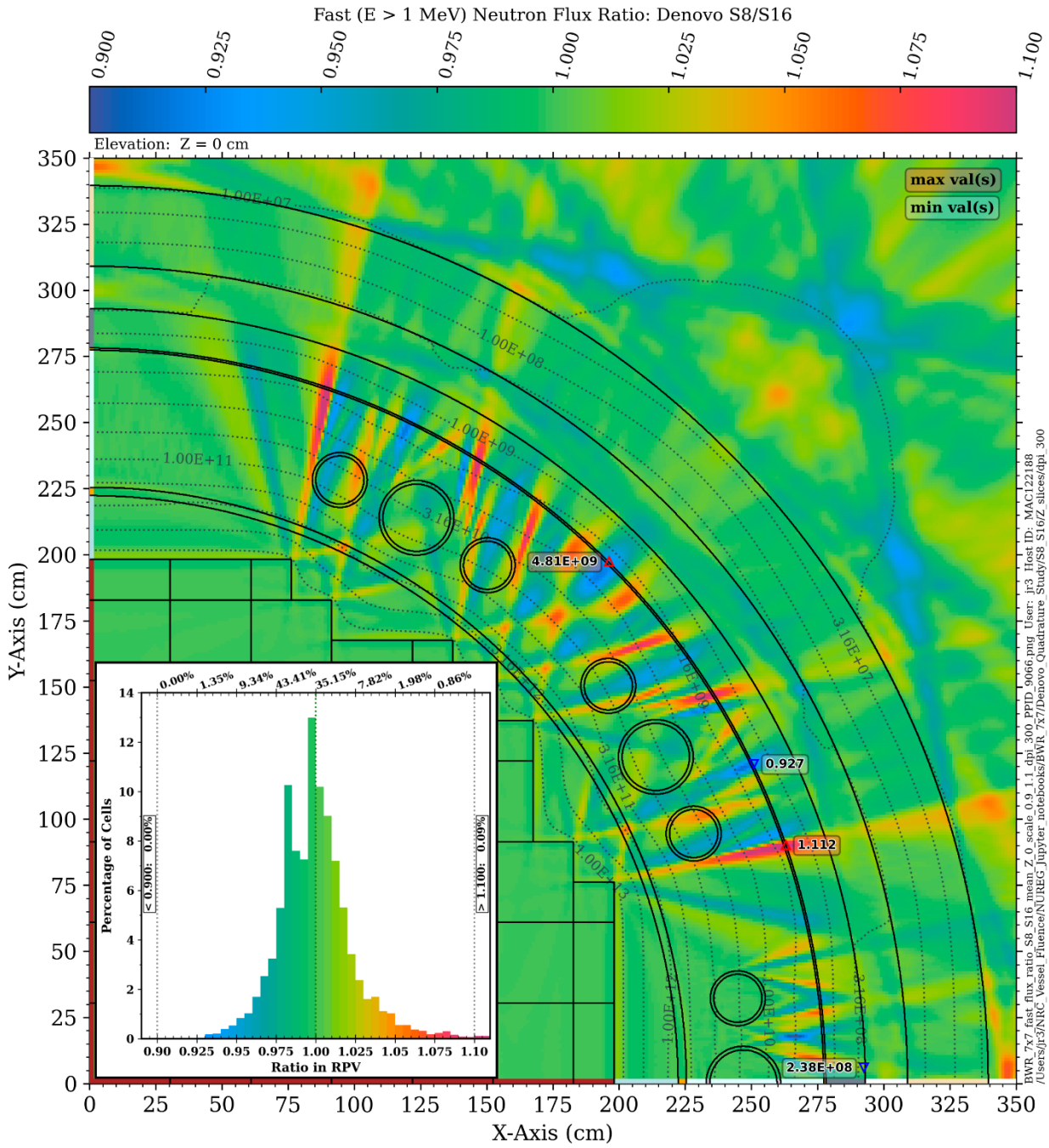

Figure B-10 Fast neutron flux ratio at the core midplane in the BWR model The flooded contours show the ratio of an S8 Denovo solution to an S16 Denovo solution
The dashed contour lines represent the fast flux from the S16 solution. Maximum and minimum values of the S16 fast flux and the S8/S16 ratio in the RPV are shown. The inset histogram plot shows the distribution of ratio values in the RPV.

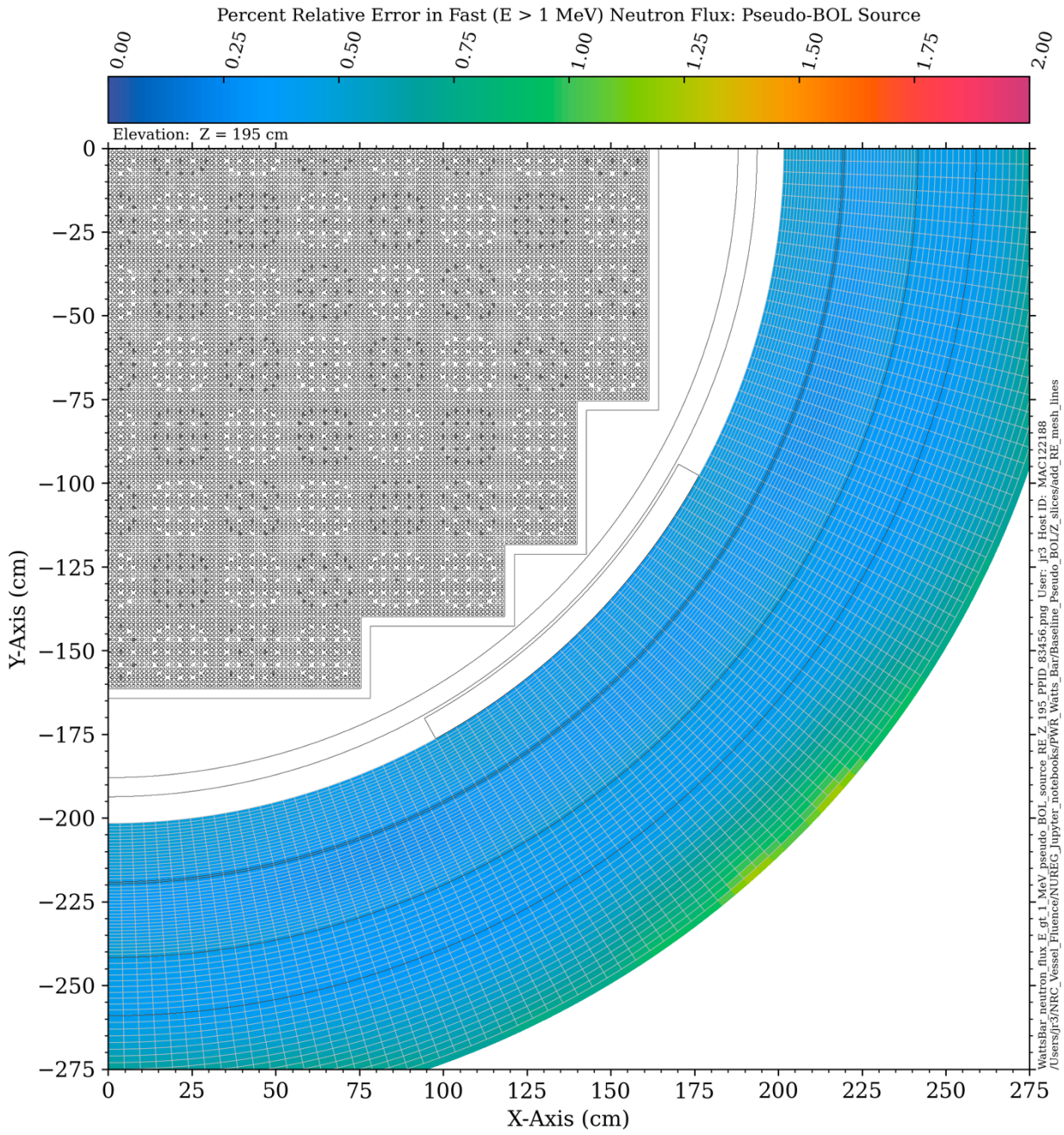

Figure B-11 Relative error in the fast neutron flux at the core midplane in the PWR model *(see Figure B-5)*

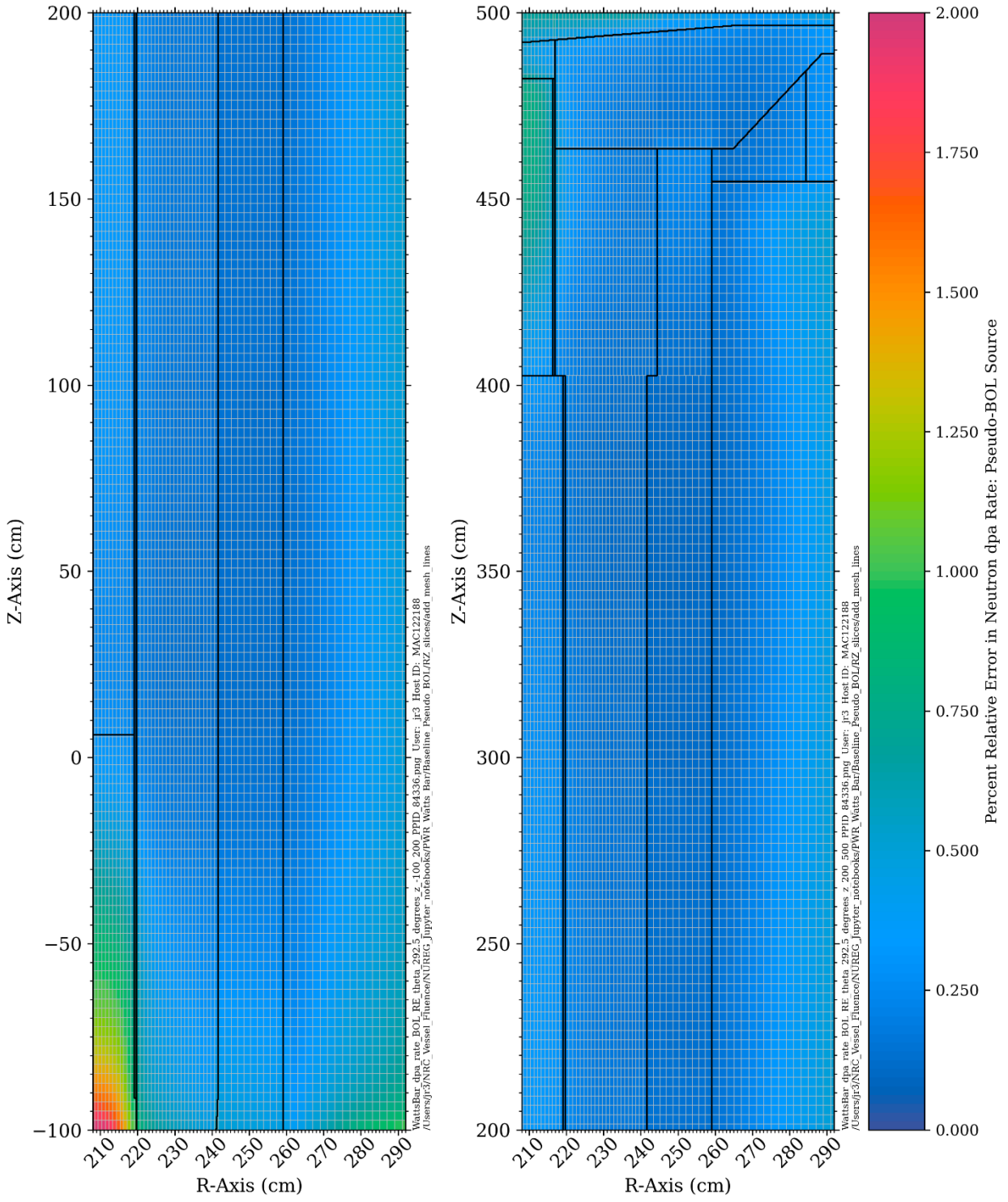

Figure B-12 Relative error in the fast neutron flux in the PWR model at an azimuthal angle of 292.5° *(see Figure B-6)*

APPENDIX C DOSIMETRY CROSS SECTIONS USED IN LWR RPV FLUENCE BENCHMARK CALCULATIONS

Benchmark calculations for RPV fluence analyses typically involve comparing measured activities of several isotopes from dosimetry capsules at specific locations in the benchmark experiment. Radiation transport calculations are then performed to estimate the isotopic activities, with the resulting calculated/measured (C/M) ratios indicating how well the transport calculations model the physical experiment.

The accuracy that can be obtained in calculating the activation of an isotopic target is dependent on both the accuracy of the neutron transport calculation and the accuracy of the cross sections for the reactions that produce the activated dosimetry isotopes.

For this analysis, nine isotopic reactions are considered that have been used in the H.B. Robinson, ORNL Pool Critical Assembly [Pressure Vessel Facility] (PCA), and VENUS-3 benchmarks [84]. These reactions are listed in Table C-1. Seven of the nine reactions are threshold reactions, with threshold energies ranging from 40.14 keV to 3.25 MeV. The remaining two are fission reactions, which have no minimum energy threshold. Characterizing a neutron field requires use of multiple dosimetry isotopes which span the desired range of neutron energies.

A commonly used set of reaction cross sections for reactor dosimetry applications is IRDF-2002 [87]. Cross sections from IRDF-2002 for the reactions listed in Table C-1 are shown in Figure C-1 and Figure C-2. Figure C-2 shows the pointwise data for energies above 100 keV and the 90% energy response ranges listed in Table C-1. For each reaction, the data symbols plotted along the abscissa indicate the threshold energies, below which the cross-section values are identically zero.

Table C-1 Dosimetry reactions that are commonly used for RPV fluence benchmark measurements and calculations

Target isotope	Reaction	Product isotope	Product half life	Reaction threshold	Energy response range (MeV)[13] [88]
^{27}Al	(n,α)	^{24}Na	14.97 h	3.25 MeV	6.45–11.9
^{63}Cu	(n,α)	^{60}Co	5.271 y	2.25 MeV	4.53–11.0
^{46}Ti	(n,p)	^{46}Sc	83.81 d	2.10 MeV	3.70–9.43
^{54}Fe	(n,p)	^{54}Mn	312.1 d	700 keV	2.27–7.54
^{58}Ni	(n,p)	^{58}Co	70.88 d	400 keV	1.98–7.51
^{115}In	(n,n′)	^{115m}In	4.485 h	339.2 keV	1.12–5.86
^{103}Rh	(n,n′)	^{103m}Rh	56.12 m	40.14 keV	0.731–5.73
^{238}U	(n,f)	F.P.	--------	--------	1.44–6.69
^{237}Np	(n,f)	F.P.	--------	--------	0.684–5.61

[13] The energy range over which 90% of the detector response occurs in a ^{235}U fission spectrum.

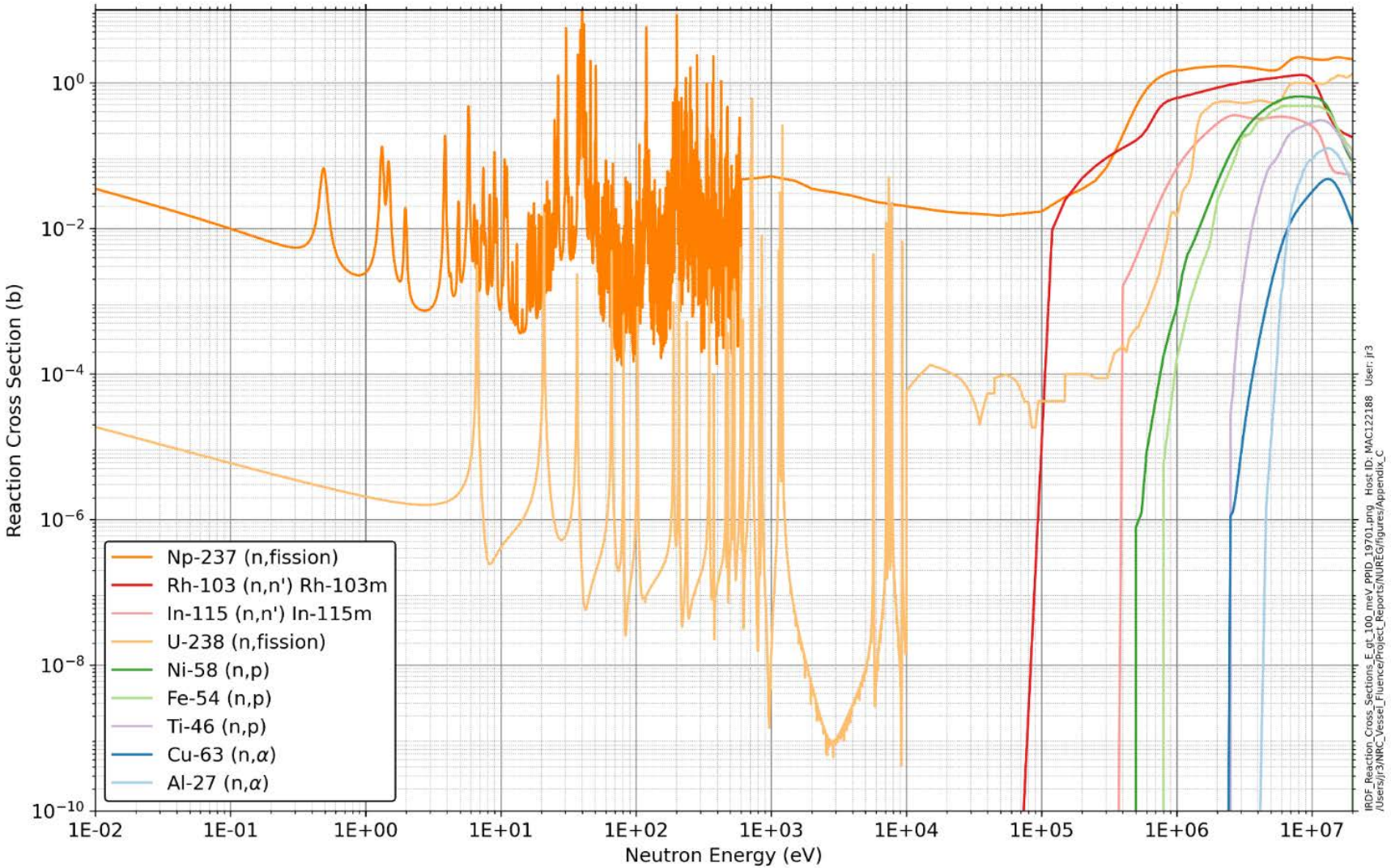

Figure C-1 Cross-section data for dosimetry reactions used in RPV benchmarks

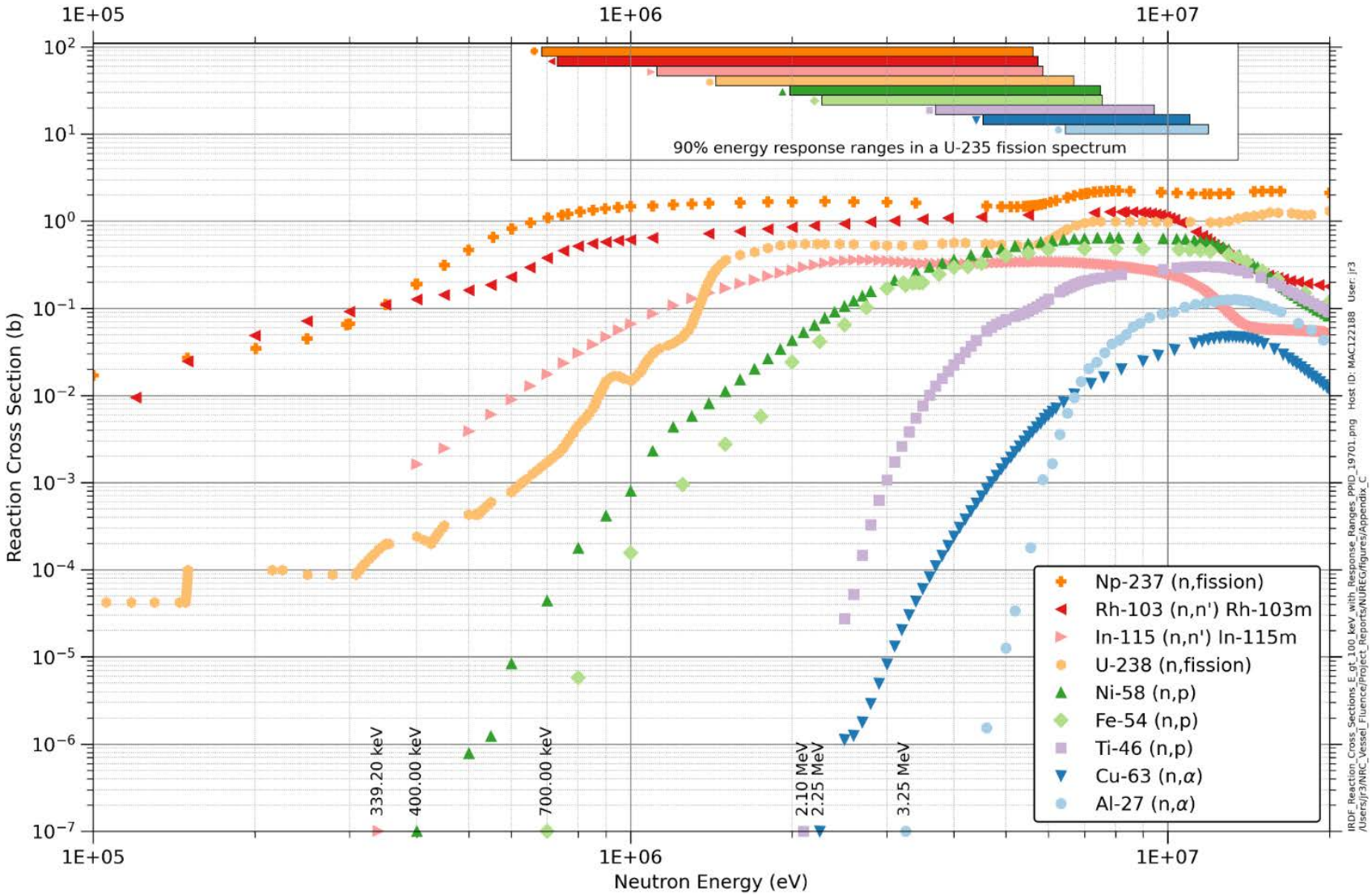

Figure C-2 Cross-section data for dosimetry reactions used in RPV benchmarks: E > 100 keV *The symbols on the abscissa indicate the reaction threshold energies for ^{115}In, ^{58}Ni, ^{54}Fe, ^{46}Ti, ^{63}Cu, and ^{27}Al.*

APPENDIX D REPRESENTATION OF ANGULAR SCATTERING DISTRIBUTIONS IN MULTIGROUP CROSS-SECTION LIBRARIES

The angular distribution of scattered radiation in MG discrete ordinates calculations is typically modeled using Legendre polynomial expansions. The extent to which these expansions can accurately model the scattering distributions is dependent on two factors: the kinematics of neutron scattering, and the MG energy boundaries. Those two factors are briefly discussed in this appendix, and examples of scattering angular distributions for some common materials encountered in LWR shielding analyses are provided. Implications of these scattering angular distributions for MG neutron transport calculations are briefly discussed.

D.1 Neutron Scattering Kinematics

A discussion of neutron scattering kinematics is well beyond the scope of this report, but a few key points can be made here. Further details can be found in the literature [107], [108], [109].

Two types of neutron scattering are of importance in typical shielding calculations: capture scattering and potential scattering. In capture scattering, the incident neutron is absorbed by the scattering nucleus, which subsequently decays by the emission of a neutron. Capture scattering can be either elastic or inelastic. With elastic scattering, the residual nucleus is left in the ground state. With inelastic scattering, the residual nucleus is left in an excited state, which returns to the ground state by the emission of a gamma ray. Potential scattering does not involve the formation of a compound nucleus and is always elastic.

The kinematics of neutron scattering events are dependent on the incident neutron energy and the scattering nucleus. Although no absolute statements can be made regarding the angular distribution of scattered neutrons as a function of the neutron energy and the specific scattering nucleus, the following behaviors are typical [14]:

1. Neutron scattering tends to become more anisotropic with increasing neutron energy for any scattering nucleus.
2. Neutron scattering tends to become more anisotropic as the mass of the scattering nucleus decreases.

Therefore, scattering anisotropy tends to be most pronounced in the scattering of high-energy neutrons from nuclei of low mass numbers. This behavior is illustrated below in Section D.3

D.2 Multigroup Energy Structures

The degree of anisotropy in MG calculations can also be dependent on the MG energy structure. This effect is not due to scattering kinematics but is rather an artifact of MG libraries. Because of energy-momentum constraints that govern the minimum and maximum scattering angles for MG neutron elastic scattering, light element scattering often produces group-to-group scattering cross sections that are highly anisotropic.

Consider the scattering of a neutron from a scattering nucleus through a scattering angle θ (Figure D-1). For elastic scattering from a source group g′ to a sink group g, the lower and upper limits (ω_{min} and ω_{max}) for the cosine of the scattering angle are given by Attia and Harms [110]:

$$\omega_{min} = \frac{1}{2}\left[(A+1)\sqrt{\frac{E_g}{E_{g'-1}}} - (A-1)\sqrt{\frac{E_{g'-1}}{E_g}}\right], \quad \text{(D-1)}$$

and

$$\omega_{max} = \frac{1}{2}\left[(A+1)\sqrt{\frac{E_{g-1}}{E_{g'}}} - (A-1)\sqrt{\frac{E_{g'}}{E_{g-1}}}\right], \quad \text{(D-2)}$$

where

A = relative mass of the scattering isotope (the mass of the isotope divided by the neutron mass)
$E_{g'-1}$ = upper energy of the source group
$E_{g'}$ = lower energy of the source group
E_{g-1} = upper energy of the sink group
E_g = lower energy of the sink group

Equations (D-1) and (D-2) are valid if

$$\alpha E_{g'-1} \leq E_g, \quad \text{(D-3)}$$

where

$$\alpha = \left(\frac{A-1}{A+1}\right)^2. \quad \text{(D-4)}$$

Note that ω_{min} and ω_{max} are restricted to the range [-1, 1]:

$$-1 \leq \omega_{min} \leq \omega_{max} \leq 1. \quad \text{(D-5)}$$

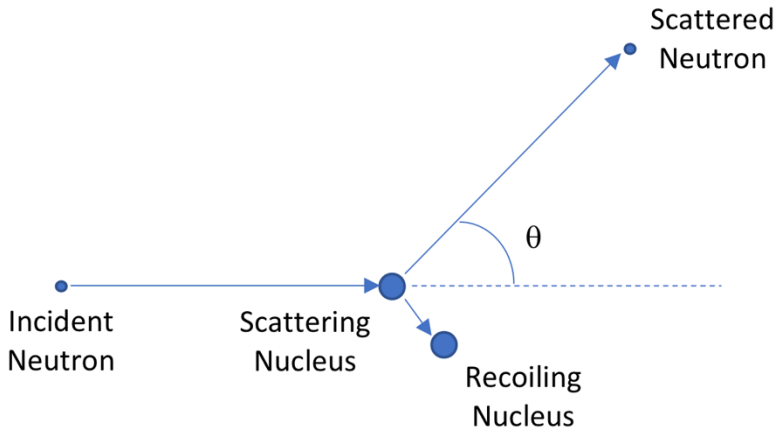

Figure D-1 Diagram illustrating the scattering angle θ (with cosine ω) for neutron scattering

The value of α provides a measure of the minimum possible energy of a neutron that scatters elastically from a nucleus of mass A. For example, neutron scattering from ^{1}H has an α value of 1.735E-7. A neutron which scatters from group 1 of the BUGLE-B7 library, with a lower energy limit of 14.191 MeV, has a minimum possible energy of 2.46 eV, which is in group 43 of the

BUGLE-B7 library. This is shown in the leftmost column of Figure A-2, where the scattering cross section from group one into groups 44 through 47 is zero.

Neutrons which undergo elastic scattering in ^{56}Fe can lose 6.9% of their energy at most in a single scatter. This behavior can be seen in Figure A-4. In all BUGLE-B7 energy groups other than groups 11–13, elastic scattering in ^{56}Fe can only occur within the scattering group or to the next group number. The exception for groups 11–13 is due to the narrow group widths of groups 12–14 (Table A-2). For neutron energies below the 862.5 eV, which is in group 19, inelastic scattering cannot occur in ^{56}Fe.

Because there is no inelastic scattering of neutrons from the isotopes of H, Eq. (D-1) and Eq. (D-2) hold for all scattering events from those nuclides. For all other nuclides, inelastic scattering is possible, and Eq. (D-1) and Eq. (D-2) are valid only for neutron energies below the lowest inelastic scattering threshold for each nuclide. Note that the lower and upper limits of the cosine of the scattering angle depend on the energy bounds of the source and sink groups, as shown in Eq. (D-1) and Eq. (D-2). Examples of scattering anisotropy for ^{1}H, ^{16}O, and ^{56}Fe can be seen in Figure D-2 through Figure D-4 for different group-to-group scattering cross sections; the true scattering anisotropy in each plot is shown by the black lines, which are obtained from MCNP calculations using CE cross-section data.

D.3 Multigroup Scattering Angular Distribution Examples

D.3.1 Scattering from a Single Nuclide: ^{1}H, ^{16}O, and ^{56}Fe

For the first example, consider the scattering of neutrons from three important nuclides in LWR shielding analyses: ^{1}H, ^{16}O, and ^{56}Fe. Legendre expansions of data from the BUGLE-B7 library are compared with scattering distributions obtained using cosine- and energy-binned current tallies for singly scattered neutrons from MCNP simulations in which a monodirectional beam of neutrons impinges on a target of the isotope being studied. This simulation provides an accurate representation of the angular scattering distribution from one BUGLE group to another. The MCNP calculations are run using CE cross-section data. The BUGLE-B7 group structure is imposed on the MCNP simulation using a neutron source with a uniform strength over the energy range of the source group, as well as tallied data with energy ranges over the sink groups. The true group-to-group scattering angular distributions from these CE MCNP calculations are shown by blank lines.

Figure D-2 illustrates the CE tally data and the Legendre polynomial expansions of the angular distributions for scattering from ^{1}H for groups 1-to-1, 1-to-2, 1-to-3, 1-to-10, 1-to-18, and 1-to-26. Because all scattering from ^{1}H is elastic, the permissible range of ω values is prescribed by Eq. (D-1) and Eq. (D-2). For each of these scattering distributions, the range of permissible ω values is quite narrow, resulting in highly anisotropic MG scattering distributions. This is reflected in the CE scattering distributions. It can also be seen that for narrow, highly peaked scattering distributions, such as for groups 1-to-10, 1-to-18, and 1-to-26, even a P_7 Legendre expansion (the highest order available in the BUGLE-B7 library) provides a poor representation of the true scattering behavior.

For each of the ^{1}H scattering distributions plotted in Figure D-2, every expansion order (with the exception of the P_1 expansion for scattering from group 1-to-18 and group 1-to-26) has regions in which the Legendre expansion produces negative cross-section values. These negative regions, which are a mathematical artifact of the Legendre expansion, can produce nonphysical behavior in MG flux solutions.

Figure D-3 shows the group-to-group scattering distributions for the same energy groups (1, 2, 3, 10, 18, and 26) for ^{16}O. Note that both elastic and inelastic scattering can occur from ^{16}O, with inelastic scattering being responsible for all scatters from group 1 to group 4 and lower energy groups (Figure A-3). Because there is no elastic scattering occurring from group 1 to groups 10, 18, and 26, it is not surprising that those scattering distributions are much less anisotropic.

Figure D-4 shows the group-to-group scattering distributions for the same energy groups (1, 2, 3, 10, 18, and 26) for ^{56}Fe. As is the case with ^{16}O, inelastic scattering of neutrons is possible for all of these group-to-group transfers and is responsible for scattering into all groups below group 2 (Figure A-4). Consequently, the anisotropy for scattering from group 1 is most pronounced for scattering into groups 1 and 2, and the higher-order Legendre expansions approximate the CE MCNP results much more closely than those from lighter elements.

In-group scattering angular distributions (as opposed to group-to-group) are shown in Figure D-5 for ^{1}H, ^{16}O, and ^{56}Fe in groups 1 and 30. These two groups have equivalent lethargy widths[14] of 0.2, so the range of permissible scattering angles in ^{1}H is equivalent for group 1-to-1 and group 30-to-30. For ^{16}O, with an inelastic scattering threshold of 6.475 MeV, Eq. (D-1) and Eq. (D-2) are valid for group 30, but not for group 7. For ^{56}Fe, the condition of Eq. (D-3) is not met for group 30 (which is below the inelastic scattering threshold of 862.5 keV), so Eq. (D-1) and Eq. (D-2) are not valid.

The following observations can be made from Figure D-2 through Figure D-5:

1. Neutron scattering from ^{1}H in MG libraries is highly anisotropic at all energies. Because of the scattering angle limitations for elastic scattering (which is the only type of scattering that occurs in ^{1}H), the range of permissible scattering angles is narrow, which is a major source of the scattering anisotropy. In addition, it can be seen that even a scatter from BUGLE-B7 group 1 to group 18 (the group with a lower energy limit of 1.0026 MeV) is a forward scatter, which means that the scattering angle is less than 90°. In fact, scattering kinematics indicate that there is no backscattering of neutrons from ^{1}H at any energy. The only way in which a neutron can change its direction by more than 90° when the scattering occurs from ^{1}H is through multiple small angle scatters.
2. For ^{16}O and ^{56}Fe, MG neutron scattering cross sections generally exhibit decreasing anisotropy as neutron energies decrease. This is seen in downscattering cross sections (Figure D-3 and Figure D-4) and in within group scattering (Figure D-5). In addition, the degree of anisotropy for a given group-to-group scattering cross section tends to decrease with increasing mass of the scattering nucleus.
3. With the exception of in-group scattering in high-energy groups and downscattering to adjacent groups, the scattering angular distributions for ^{16}O and ^{56}Fe are well represented by P_3 Legendre polynomial expansions. For ^{1}H, all of the scattering expansions show marked differences as the expansion order is increased. This suggests that the sensitivity of an MG transport calculation to scattering order should be most pronounced for transport through hydrogenous material such as water or concrete. Neutron transport through metal regions is unlikely to be sensitive to scattering expansion orders greater than P_3.

These observations are consistent with the discussion in Section D.1.

[14] The lethargy width of an energy group g in an MG library is defined as $\Delta u = ln(E_g/E_{g+1})$. MG structures are often defined based on lethargy widths.

D.3.2 Scattering from Three Common Materials in LWR Shielding Analyses: Water, Concrete, and Steel

This section addresses three common materials in LWR shielding analyses: water, concrete, and steel. The compositions of these materials are provided in Table D-1.

Table D-1 Composition of the water, concrete, and RPV steel used for the scattering angular distribution plots in Figure D-6 through Figure D-8 *Elemental compositions are listed in units of atoms/b-cm (1 b-cm = 10^{-24} cm^2)*

Element	*Water*	*Type 04 concrete*	*RPV steel*
H	*4.9540E-2*	*7.7671E-3*	
C			*9.8100E-4*
O	*2.4470E-2*	*4.4076E-2*	
Na		*1.0478E-3*	
Mg		*1.4866E-4*	
Al		*2.3882E-3*	
Si		*1.5910E-2*	*3.7100E-4*
S		*5.6343E-5*	
K		*6.9312E-4*	
Ca		*2.9151E-3*	
Cr			*1.2700E-4*
Mn			*1.1200E-3*
Fe		*3.1273E-4*	*8.1900E-2*
Ni			*4.4400E-4*

The scattering distributions for these materials are shown in Figure D-6 through Figure D-8 for the water, concrete, and RPV steel, respectively. As expected, the behavior of these distributions is consistent with those shown for ^{1}H, ^{16}O, and ^{56}Fe. The scattering distributions for water are highly anisotropic and are very sensitive to the Legendre expansion order. Consistent with the scattering distributions for ^{1}H, the higher-order expansions (greater than P_1) all have regions in which the scattering expansion has negative values. The primary constituents of Type 04 concrete by atom fraction are O, Si, and H. Type 04 concrete exhibits a high degree of anisotropy, although not as pronounced as the water. Unlike the scattering distributions for water, the concrete data exhibit very few angular regions for cases in which the expansions are negative. The RPV steel consists primarily of Fe, which has an ^{56}Fe atom fraction of 91.754%. Therefore, its scattering distributions are nearly identical to those of ^{56}Fe.

D.4 Implications for Multigroup Neutron Transport Calculations

The material discussed in Sections D.1 and D.2 and the examples provided in Section D.3 have clear implications for MG neutron transport calculations used in LWR shielding analyses. Light nuclides, particularly ^{1}H, exhibit a high degree of scattering anisotropy due to scattering kinematics. In addition, the use of MG cross-section libraries imposes restrictions on the permissible scattering angles for group-to-group transfers. Therefore, the sensitivity of a MG neutron calculation should be highest in regions that are characterized by deep penetration through hydrogenous materials, including water and concrete.

For RPV fluence calculations with typical LWR configurations in the beltline region, Regulatory Guide 1.190 requires a minimum P_3 expansion order. As shown in Figure D-4, the scattering distributions for ^{56}Fe in the BUGLE-B7 library are fairly well approximated for this case within the beltline region.

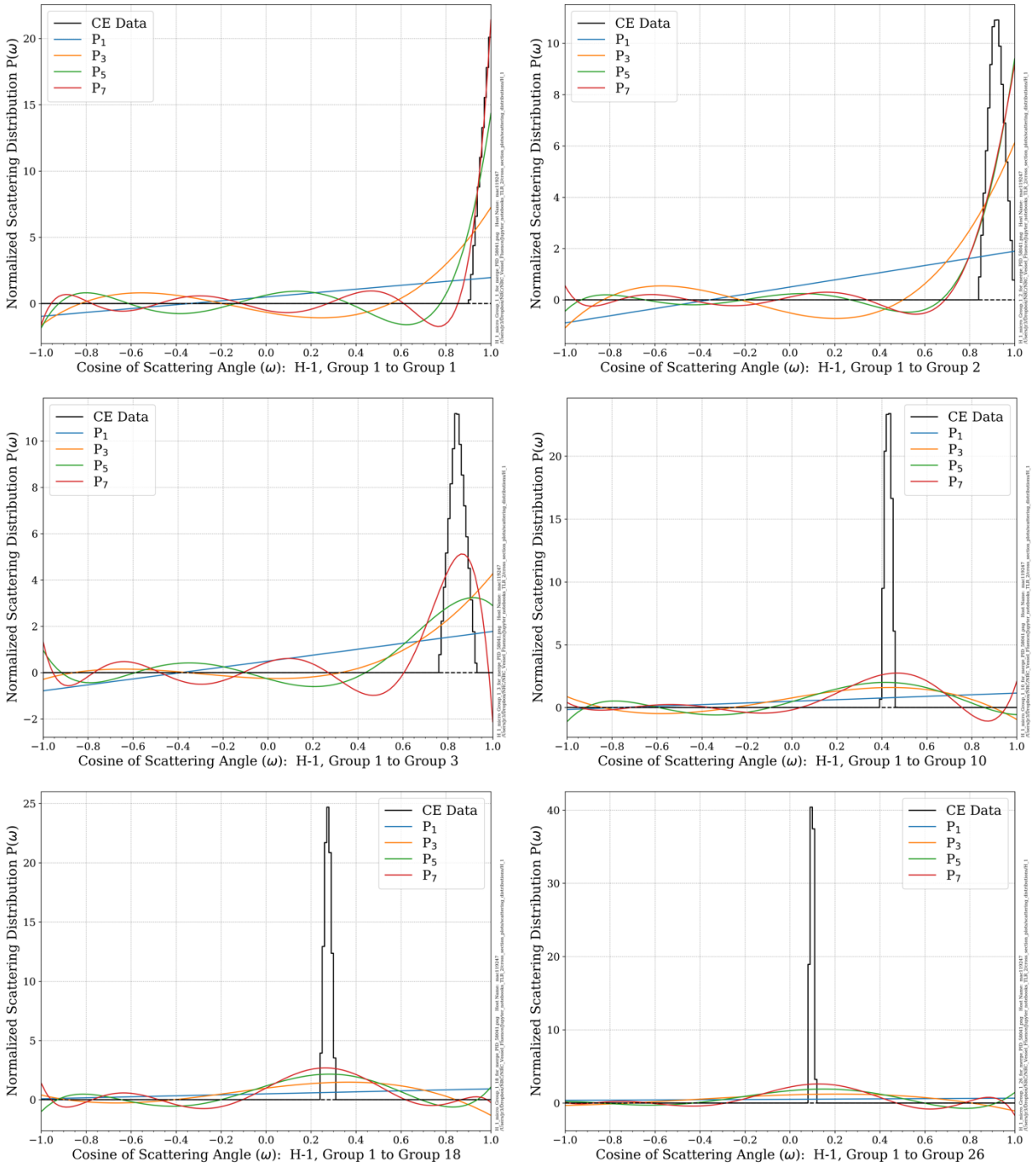

Figure D-2 Group-to-group angular scattering distributions for ^{1}H from the BUGLE-B7 library as a function of scattering order from P_1 to P_7 *The group energy boundaries and lethargy widths can be found in Table A-2. The CE data are based on cosine- and energy-binned tallies for singly scattered neutrons from an ^{1}H target.*

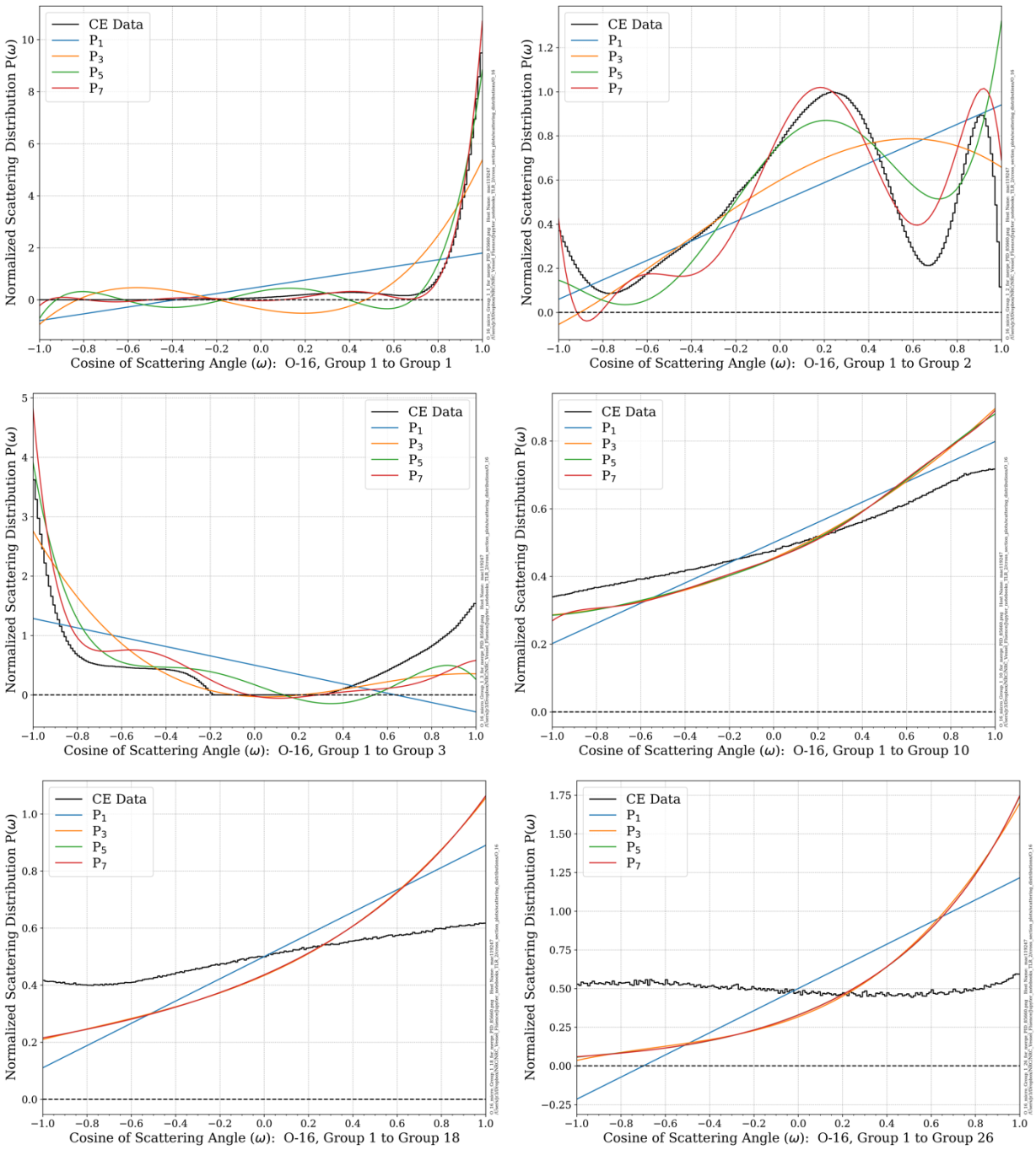

Figure D-3 Group-to-group angular scattering distributions for ^{16}O from the BUGLE-B7 library as a function of scattering order from P_1 to P_7 *The group energy boundaries and lethargy widths can be found in Table A-2. The CE data are based on cosine- and energy-binned tallies for singly scattered neutrons from an ^{16}O target.*

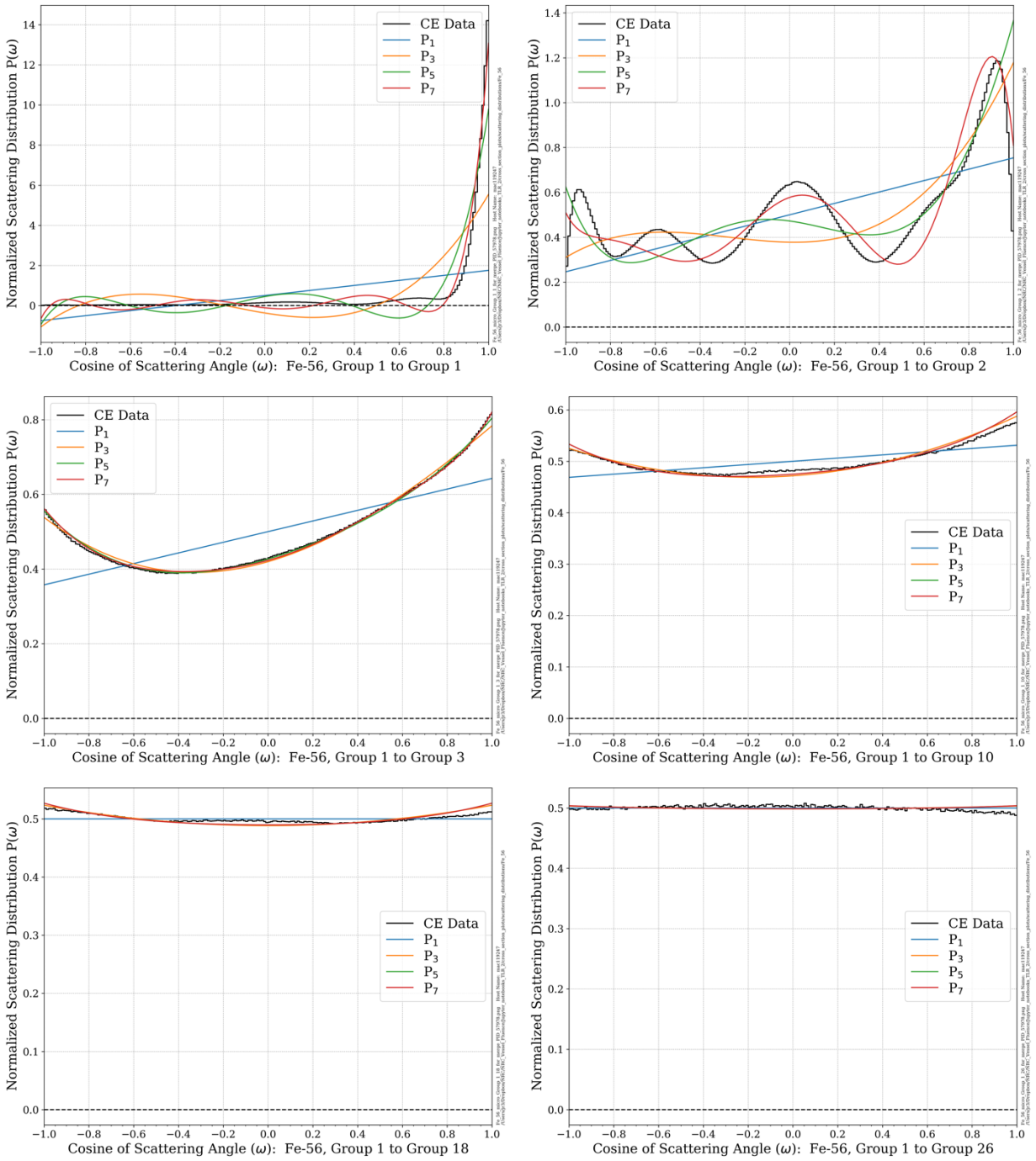

Figure D-4 Group-to-group angular scattering distributions for ^{56}Fe from the BUGLE-B7 library as a function of scattering order from P_1 to P_7 *The group energy boundaries and lethargy widths can be found in Table A-2. The CE data are based on cosine- and energy-binned tallies for singly scattered neutrons from an ^{56}Fe target.*

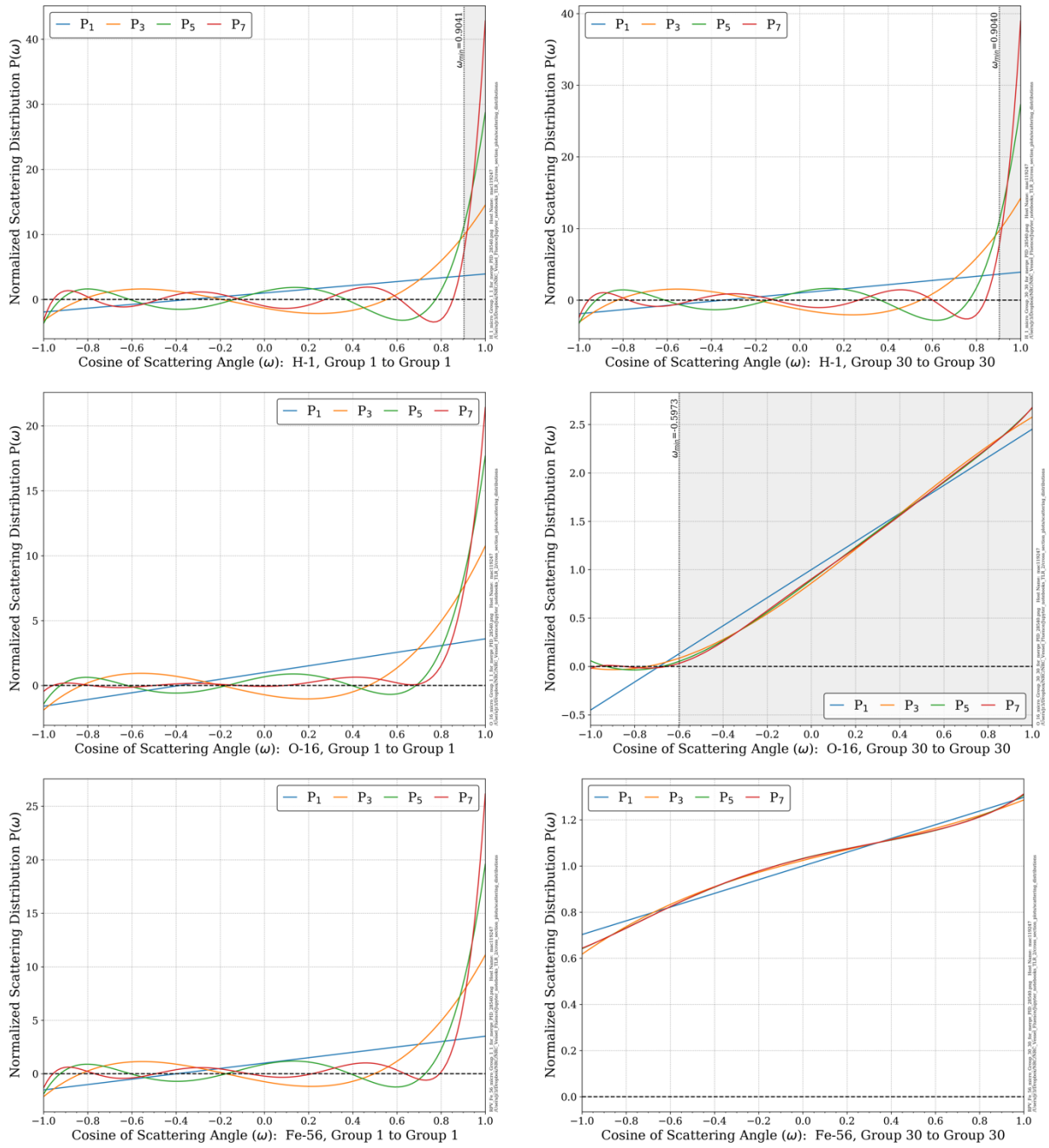

Figure D-5 In-group angular scattering distributions for ^{1}H, ^{16}O, and ^{56}Fe in groups 1 and 30 of the BUGLE-B7 library as a function of scattering order from P_1 to P_3 *The group boundaries are Group 1, 17.332–14.191 MeV; and Group 30, 31.828–26.058 keV. The areas shaded in gray for ^{1}H and ^{16}O represent the range of permissible scattering angles based on Eq. (D-1) and Eq. (D-2).*

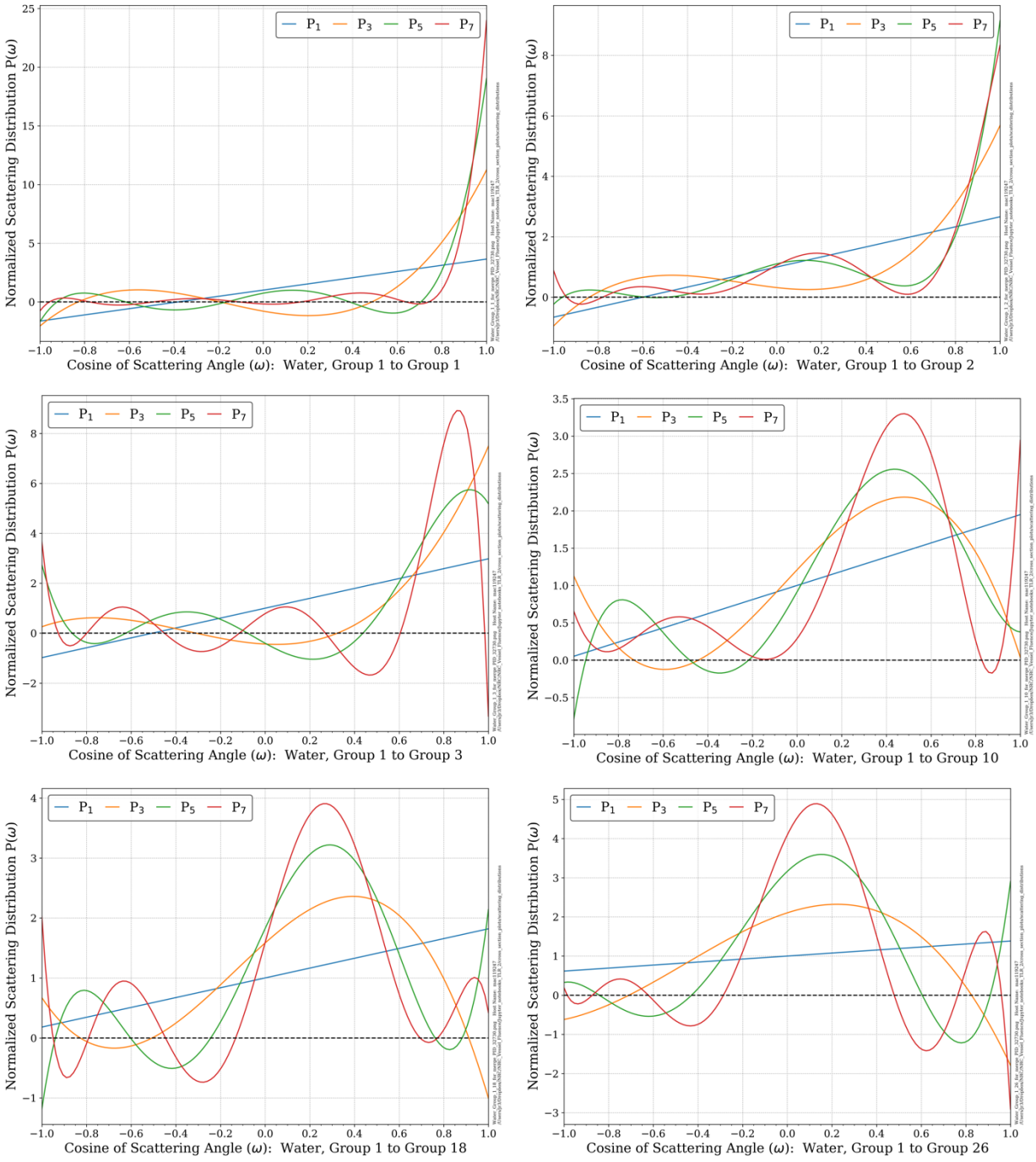

Figure D-6 Group-to-group angular scattering distributions for water from the BUGLE-B7 library as a function of scattering order from P_1 to P_7 *The group energy boundaries and lethargy widths can be found in Table A-2.*

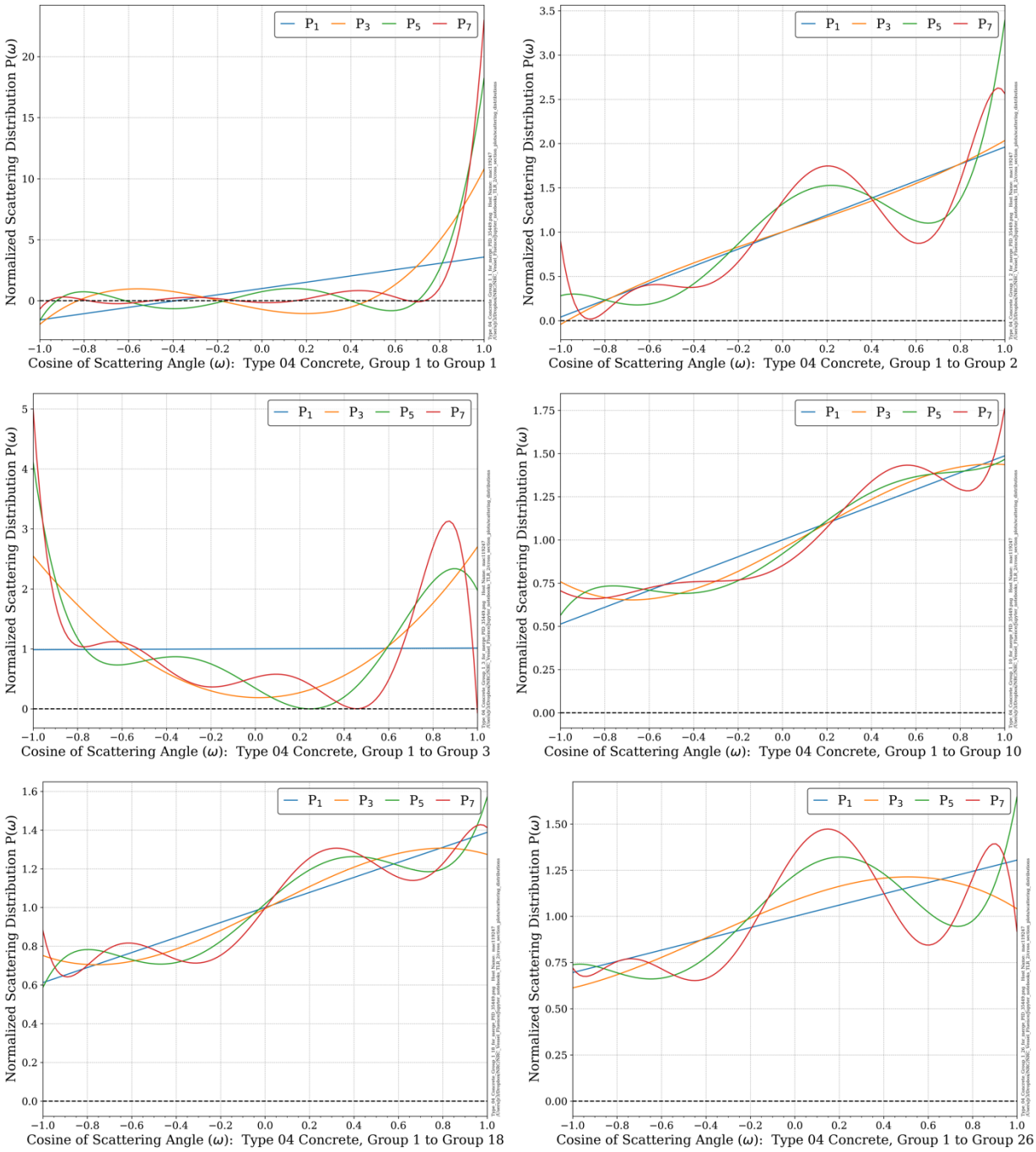

Figure D-7 Group-to-group angular scattering distributions for Type 04 concrete from the BUGLE-B7 library as a function of scattering order from P_1 to P_7 *The group energy boundaries and lethargy widths can be found in Table A-2.*

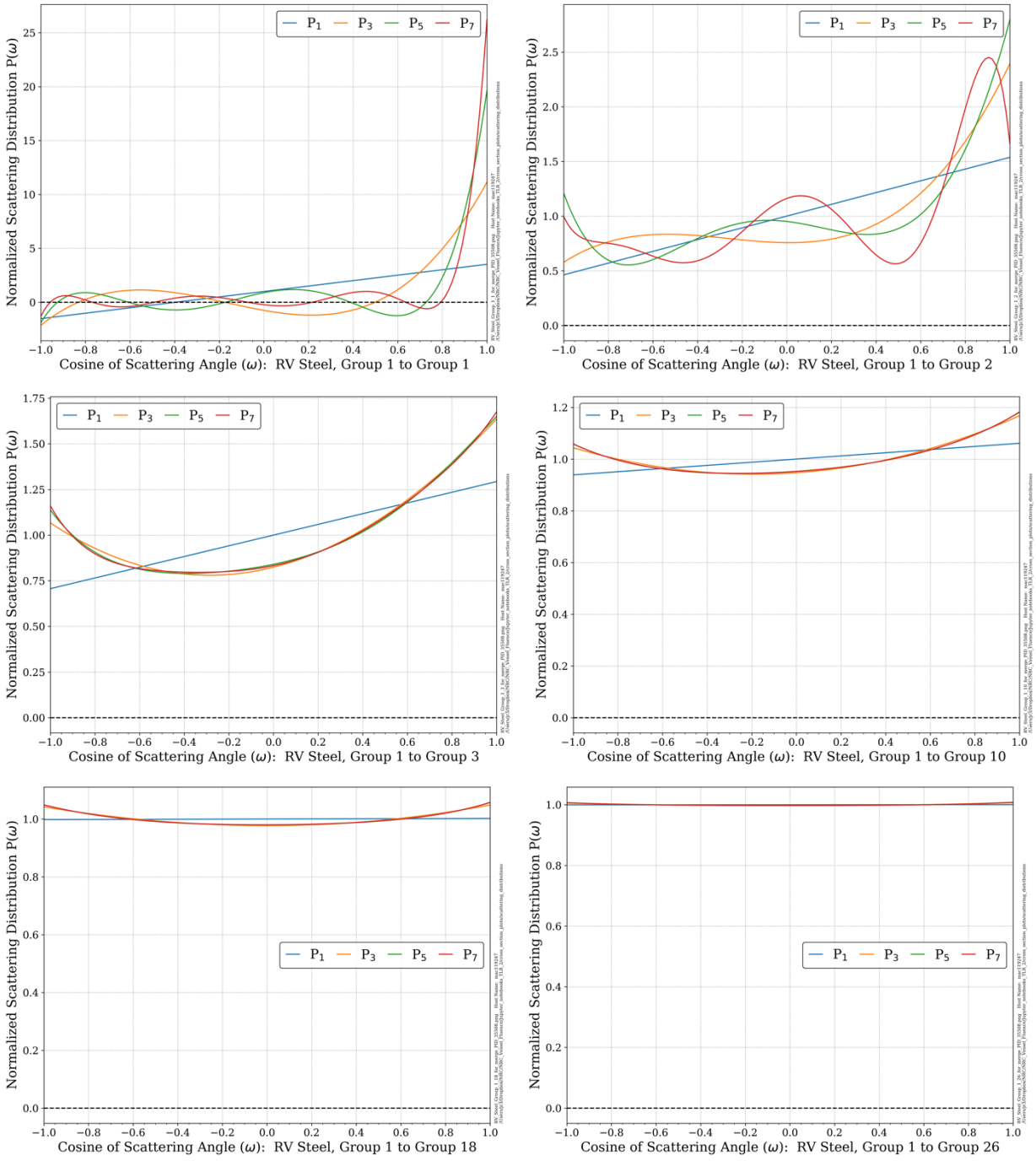

Figure D-8 Group-to-group angular scattering distributions for RPV steel from the BUGLE-B7 library as a function of scattering order from P_1 to P_7 *The group energy boundaries and lethargy widths can be found in Table A-2.*

NRC FORM 335
(12-2010)
NRCMD 3.7

U.S. NUCLEAR REGULATORY COMMISSION

BIBLIOGRAPHIC DATA SHEET

(See instructions on the reverse)

1. REPORT NUMBER
(Assigned by NRC, Add Vol., Supp., Rev., and Addendum Numbers, if any.)

NUREG/CR-7286

2. TITLE AND SUBTITLE

Reactor Pressure Vessel Fluence Evaluation Methodology for Extended Beltline Locations

3. DATE REPORT PUBLISHED

MONTH	YEAR
May	2022

4. FIN OR GRANT NUMBER

5. AUTHOR(S)

J. Risner, A. Alpan, and J. Yang

6. TYPE OF REPORT

Technical

7. PERIOD COVERED (Inclusive Dates)

8. PERFORMING ORGANIZATION - NAME AND ADDRESS (If NRC, provide Division, Office or Region, U. S. Nuclear Regulatory Commission, and mailing address; if contractor, provide name and mailing address.)

Oak Ridge National Laboratory
Oak Ridge, TN 37831-6283

9. SPONSORING ORGANIZATION - NAME AND ADDRESS (If NRC, type "Same as above", if contractor, provide NRC Division, Office or Region, U. S. Nuclear Regulatory Commission, and mailing address.)

Division of Engineering
Office of Nuclear Regulatory Research
U.S. Nuclear Regulatory Commission
Washington, D.C. 20555-0001

10. SUPPLEMENTARY NOTES

11. ABSTRACT (200 words or less)

Accurate prediction of neutron fluence and dpa in reactor pressure vessels (RPVs) has become increasingly challenging as plant life extensions and power uprates expand the area of concern with respect to neutron damage to locations in what is referred to as the extended beltline region. Current guidance on RPV fluence calculations is limited to analyses that only consider the traditional beltline region. This study evaluates the impact of multiple physical parameters on fast fluence estimates to ascertain the degree to which extended beltline fluence evaluations are more sensitive to those parameters compared with traditional beltline evaluations. In addition, key calculational parameters in the widely used discrete ordinates method are evaluated to determine their impact on extended beltline fluence estimates. Hybrid radiation transport calculations, which employ the current state of the art in radiation transport simulations, are used as benchmark solutions in the absence of measured data in extended beltline locations. These hybrid calculations utilize continuous-energy Monte Carlo calculations and eliminate the discretizations in space, energy and angle that impose accuracy limitations on discrete ordinates calculations.

12. KEY WORDS/DESCRIPTORS (List words or phrases that will assist researchers in locating the report.)

reactor pressure vessel
RPV
neutron fluence
fast fluence
neutron damage
dpa
extended beltline
discrete ordinates
hybrid radiation transport

13. AVAILABILITY STATEMENT

unlimited

14. SECURITY CLASSIFICATION

(This Page)
unclassified

(This Report)
unclassified

15. NUMBER OF PAGES

16. PRICE

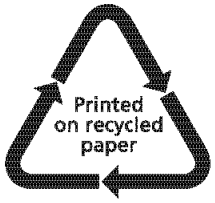

Federal Recycling Program

UNITED STATES
NUCLEAR REGULATORY COMMISSION
WASHINGTON, DC 20555-0001

OFFICIAL BUSINESS